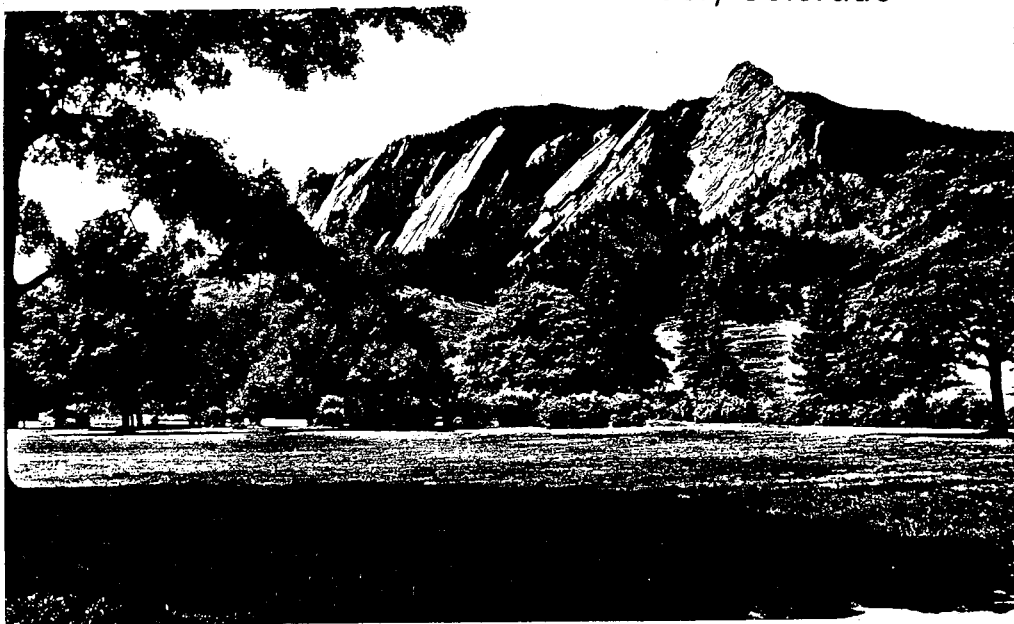# G-AP INTERNATIONAL SYMPOSIUM

August 22-24

1973

University of Colorado
Boulder, Colorado

73 CHO 764-1 AP

1973 Meeting
Condensed Program

Wednesday, August 22

0830-1200	11	High Frequency and Inverse Scattering	East Ballroom
	12	Antenna Measurements	West Ballroom
	13	Numerical Methods (1)	Chem 140
1330-1700	19	Guiding and Periodic Structures	East Ballroom
	20	Array Theory	West Ballroom
	21	Antennas	Chem 140
1615-1745	27	Panel Discussion	Chem 140
1830-2200		Reception and Banquet	Harvest House Motor Hotel

Thursday, August 23

0830-1200	31	Combined URSI/G-AP Session	Center Ballroom
1330-1700	32	Foreign Electromagnetics	East Ballroom
	33	Antenna Design	West Ballroom
	34	Numerical Methods (2)	Chem 132
	35	Scatter by Rain	Forum Room

Friday, August 24

0830-1200	39	Reflector Antennas	East Ballroom
	40	Antenna Arrays	West Ballroom
	41	Microwave Sensing	Forum Room
1330-1700	46	Array Applications	East Ballroom
	47	Plasma and Ionospheric Effects	West Ballroom
	48	Special Topics	Chem 140
	49	Electromagnetic Theory	Chem 132
1900-2100	53	Singularity Expansion Method	Forum Room

1973 G - AP

INTERNATIONAL

SYMPOSIUM

Institute of Electrical

and

Electronics Engineers

University of Colorado

Boulder, Colorado 80302

Cover design by B. Hardy. The photograph is taken from
Chautauqua Park looking southwest toward the Flatirons.
Photo by J. Roberts.

What is now Chautauqua Park was founded in 1897 by a group
of Texas teachers, headed by the president of the University
of Texas. They were searching for a summertime mecca.
Boulder was chosen and a Texas-Colorado Chautauqua Association
was formed to promote the educational, literary, artistic
and scientific professions and to establish and maintain
a summer school. An auditorium was erected and dedicated
July 4, 1898. In 1901 the Colorado Chautauqua Association
was formed. Trees were planted and tents and kerosene lamps
gave way to small, well-equipped cottages. Summertime programs
are still held at Chautauqua.

The mountains directly west of Boulder were formed during
the late Miocene and early Pliocene ages. The "Flatirons"
were formed from a sandstone conglomerate which was laid
down in an old sea bed. The bed was later folded and thrust
upward to form the visible fault. The steep dipping beds
of massive conglomerate are more resistant to erosion than
is the host granite, rendering them more protrusive.

E.C.B.

On behalf of the Steering Committee I welcome you to the 1973 IEEE Symposium on Antennas and Propagation at the University of Colorado.

Hosts for the Symposium are The Denver-Boulder Chapter of G-AP, The National Oceanic and Atmospheric Administration of the U.S. Dept. of Commerce (DOC), The Office of Telecommunications (DOC), The National Bureau of Standards (DOC), and the University of Colorado. Each of these organizations has contributed significantly in terms of both services and personnel to the planning of the Symposium and their support is gratefully acknowledged.

We have made a concerted effort to arrange the technical program so as to avoid having simultaneous sessions on similar topics. We realize, however, that it is not possible to schedule so many papers in only four days and not have a few situations in which some attendees would like to hear two (or more) papers being presented at the same time. We can only express our regret concerning this unavoidable problem.

The technical program consists of sessions on the topics currently of greatest interest to G-AP members, and of joint sessions on topics of interest to both G-AP and URSI.

We wish to express our appreciation to all session chairmen and speakers, as well as to all organizations supporting the symposium through institutional listings, for helping to make the Symposium a success.

I personally wish to express my appreciation to the members of the symposium steering committee and all its subcommittees for their efforts in the planning and organization of the Symposium.

S.W. Maley
Chairman, Steering Committee

THE PROFESSOR RONOLD W. P. KING AWARD

The Professor Ronold W. P. King Education Fund was established in April, 1972 by former students of Prof. King to further his exemplary standards in research and the teaching profession. Plans are to use this fund to present awards to young scientists or engineers who have made an outstanding contribution to the field of electromagnetics.

Professor Ronold W. P. King has attained international recognition from his over 150 journal papers and 8 books. He is a Fellow of the IEEE, the American Physical Society and the American Academy of Arts and Sciences, a corresponding member of the Bavarian Academy of Sciences and a member of many other Societies. His professional trademarks are an insistence that mathematics be forced to explain the physically real world and an emphasis on the interplay of theory and experiment with the requirement that each not only be self-consistent but that they also agree. Professor King has been at Harvard University for over 30 years and during that period of time has devoted unlimited time to the training of over 85 doctoral students. The high standards he set for his students were tempered by his understanding and encouragement.

We are pleased to announce that the first recipient of the Professor Ronold W. P. King Award is Dr. Charles Elachi. He will receive $200 in recognition of his contribution "Dipole Antenna in Space-Time Periodic Media," published in the 1972 IEEE Transactions on Antennas and Propagation.

G-AP BEST PAPER AWARD
FOR
1972

Each year the Administrative Committee (ADCOM) of the IEEE Group on Antennas and Propagation (G-AP) commissions the subcommittee on Awards to determine the outstanding papers published in its Transactions. The G-AP Best Paper Award for 1972 honors Donald E. Barrick for his paper entitled "First-order Theory and Analysis of MF/HF/VHF Scatter from the Sea, " which appeared in Vol. AP-20, No. 1, Jan. 1972, pp. 2-10.

Donald E. Barrick is currently Chief of the Sea State Studies Program Area at the National Oceanic and Atmospheric Administration's Wave Propagation Laboratory in Boulder, Colorado. He was formerly a Fellow with Battelle's Columbus Laboratories and an Adjunct Professor of Electrical Engineering at the Ohio State University. At Battelle he directed programs in radar research and analysis, and is coautho-
- Radar Cross Section Handbook. He received hi⸳ ᴿ ⌐ ⁻

TECHNICAL PROGRAM

HIGH FREQUENCY SCATTERING BY COMPLEX TARGETS*

C. A. Chuang and S. W. Lee
University of Illinois, Urbana, Illinois

P.L.E. Uslenghi
University of Illinois, Chicago, Illinois

J. W. Wright
U.S. Army Missile Command, Redstone Arsenal, Alabama

The purpose of this research is to determine the radar scatter-
ing characteristics of an airborne target with complex structure
such as an airplane. Even though this subject matter has been
studied extensively during the past twenty years[1,2] there is no
one method that is capable of producing efficient and accurate
results under all conditions. One has to devise different com-
putational schemes and employ different mathematical techniques
which depend on factors such as the particular geometry of the
target, the frequency range of interest, the acceptable error,
and computation labor.

In the present study we develop a relatively simple analytical
model of scattering from modern airplanes. Great precision of
the theoretical model is not required since we are only inter-
ested in smoothed curves of the calculated data (e.g., medians
over a small angular region). Preliminary calculation is kept
to a minimum so that repeated calculations for a wide range of
parameters may be performed for later statistical studies in
the simulation of a particular radar system.[3]

The ray-optical technique will be employed to solve the problem
as it leads to formulas that are useful for directly calculat-
ing the RCS in terms of simple functions, a feature that allows
efficient numerical computation. Furthermore, the ray-optical
method offers a convenient means for taking the shadowing
effect into account. This is accomplished by first locating
the scattering centers (specular or diffraction points) and then
adding a simple logic in the computer program to indicate which
of the bright points are in the shadow region for the aspect
under consideration.

The specific steps for computing the RCS of a complex target
are as follows. The target is first "resolved" into an ensem-
ble of components, each of which is approximated geometrically
by a simple shape. Take a jet airplane as an example. It is
usually described by 11 components, namely, a fuselage, two

wings, two wing pods, three stabilizers, and three engine ducts. Next, the backscattered field from each of these components is calculated using the ray-optical technique. Appropriate formulas for backscattered fields from well-known geometrical configurations are available in the literature, and those for the elliptical plate and the semi-infinite open-ended cylinder have been developed by the authors. The final step is then to combine the contribution from each component in a proper manner, taking into consideration the geometrical phase delay, the polarization, and the shadowing effect. Once the total back-scattered field is obtained, various radar scattering parameters, e.g., radar cross section, depolarization, and glint errors can be calculated without difficulty[4].

To test the accuracy of our theoretical model, the calculation for a typical jet airplane is compared with experimental data measured at General Dynamics with a short-pulse radar. Some results for the radar cross section are shown in Figures 1 and 2. In general, the agreement is seen to be reasonably good, leading confidence to the analytical approach described in the paper.

REFERENCES

1. J. W. Crispin, Jr., and K. M. Siegel (1968) Methods of Radar Cross Section Analysis, New York: Academic Press.

2. J. J. Bowman, T.B.A. Senior and P.L.E. Uslenghi (1969) Electromagnetic and Acoustic Scattering by Simple Shapes, Amsterdam: North-Holland Publishing Company.

3. J. W. Wright (1972) National Electronics Conference Proceedings, 27, p. 232.

4. R. Mittra, S. W. Lee, and C. A. Chuang, (1972) Analytic Radar Target Modeling, Antenna Laboratory Report 72-14, University of Illinois, Urbana, Illinois.

Figure 1. RCS in db per square meter of a jet aircraft as a
function of azimuth angle ϕ for a fixed $\theta = 90°$ for
a vertically polarized incident plane wave $(E_\phi = 0)$,
and at S band. The solid line represents the 5° -
average of the theoretical computation. The dotted
line represents the 5° - median of experimental
measurement.

3
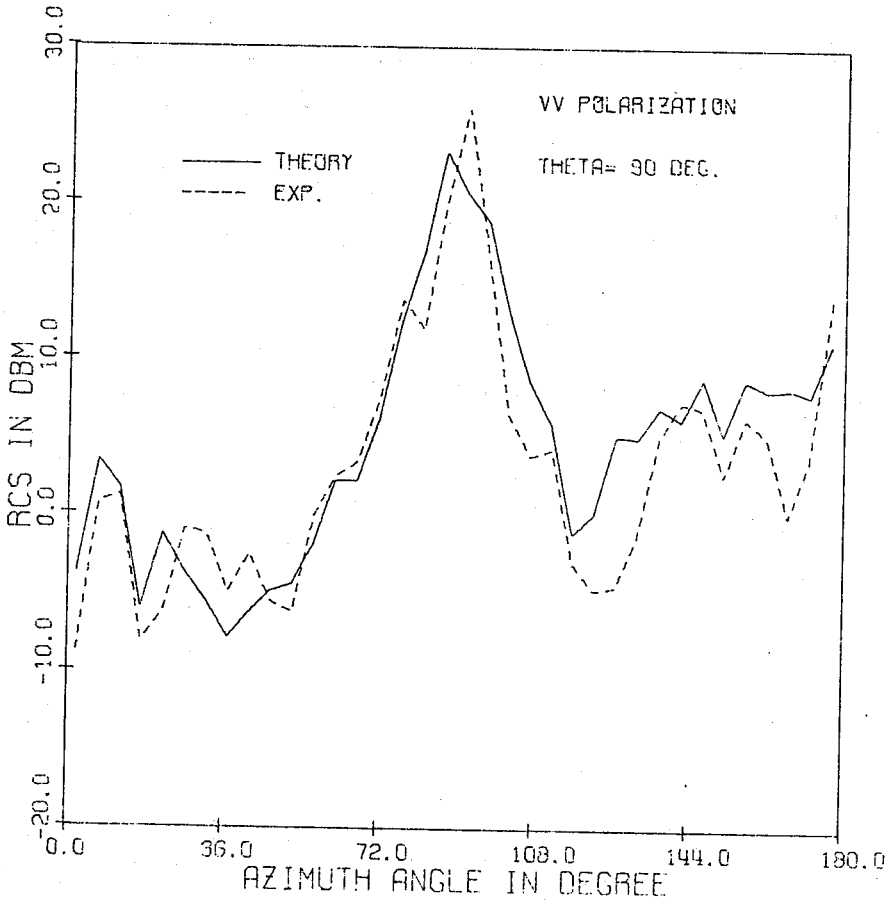
Figure 2. RCS in db per square meter of a jet aircraft as a
          function of azimuth angle ϕ for a fixed $\theta = 90°$ for
          a vertically polarized incident plane wave ($E_\phi = 0$),
          and at S band. The solid line represents the 5° –
          average of the theoretical computation. The dotted
          line represents the 5° – median of experimental
          measurement.

4

GAIN OF AN E-PLANE SECTORAL HORN - A FAILURE OF THE
KIRCHHOFF RESULT AND A NEW PROPOSAL

E. V. Jull
University of British Columbia, Vancouver 8, Canada

and

L. E. Allan
National Research Council, Ottawa 7, Canada

For three decades Schelkunoff's gain formulas [1], verified for the
pyramidal horn, have been accepted also for sectoral horns. While the
E-plane sectoral result is inherently suspect, no previous comparison
with experiment seems to have been made. Here accurate absolute gain
measurements on a typical E-plane sectoral horn reveal the conventional
expression is seriously in error. A new gain formula, almost as simple,
but yielding much closer agreement with experiment, is proposed.

Schelkunoff's formula for the on-axis gain of the E-plane sectoral horn
in Fig. 1 may be written

$$G = \frac{32ab}{\pi\lambda^2} \quad R(w) , \tag{1}$$

where

$$R(w) = \frac{C^2(w) + S^2(w)}{w^2} , \tag{2}$$

while

$$C(w) - jS(w) = \int_o^w \exp(-j\frac{\pi}{2}t^2)dt \tag{3}$$

are the Fresnel integrals and

$$w = \frac{b}{\sqrt{2\lambda\ell}} , \tag{4}$$

with λ the free space wavelength.

The solid curve in Fig. 1 was obtained from (1) for a 10 cm. band horn with
the dimensions shown. These numerical values lie roughly 0.9 dB below
the experimental values (circles) through which the dashed curve passes.
Two standard deviation error limits of about $\pm$ 0.02 dB were assigned
to these experimental values, each of which was obtained from a large
number of measurements at different separation distances between matched
identical horns on an outdoor range. Interaction was eliminated from
these results by averaging over several cycles of the response versus
distance curve and E-plane proximity connections applied. A bridge ar-
rangement compared transmission loss between the antennas with that
through an accurately calibrated attenuator.

Sources of failure in the conventional formula are a) approximations in its derivation from the assumed aperture field by the Kirchhoff method, b) errors in the assumed aperture field and c) fundamental limitations of the Kirchhoff method. Elimination of most of a), yielding the curve with long dashes in Fig. 1, accounted for only about 0.2 dB of the discrepancy. Because of the closely spaced aperture edges, errors due to b) and c) are more substantial.

In deriving a new gain formula separable aperture fields are assumed but tangential electric and magnetic fields in the aperture are not related by free space conditions, as in (1). The on-axis field of the horn is expressed, by the Kirchhoff method, as the product of the field of a two-dimensional E-plane sectoral horn and the field of an open-ended parallel-plate waveguide excited by the TE_{10} mode. The exact result [2] is then substituted for the latter, as proposed earlier [3], and the following expression for the on-axis gain of the horn is obtained

$$G = \frac{16ab}{\lambda^2(1 + \lambda_g/\lambda)} \; R(w)\exp[\frac{\pi a}{\lambda} (1 - \lambda/\lambda_g)], \qquad (5)$$

where $R(w)$ is given by (2) with

$$w = \frac{b}{\sqrt{2\lambda_g \ell}} \qquad\qquad (6)$$

and λ_g is the wavelength in the waveguide feed.

This yields the broken line in Fig. 1 which passes almost through the median of the experimental values. The oscillation in the experimental values, due primarily to double diffraction by the edges parallel to the incident magnetic field in the aperture [4], is not as simply accounted for.

This approach to antenna analysis should find application to other types of antennas.

References

1.   S.A. Schelkunoff (1943, Electromagnetic Waves, New York, Van Nostrand, p. 360).
2.   L.A. Wainstein (1969, The Theory of Diffraction and the Factorization Method, Boulder, Golem, Ch. 1).
3.   E. V. Jull (1973, IEEE Trans. AP-21, p.14).
4.   E. V. Jull (1973, IEEE Trans. AP-21, p.25).
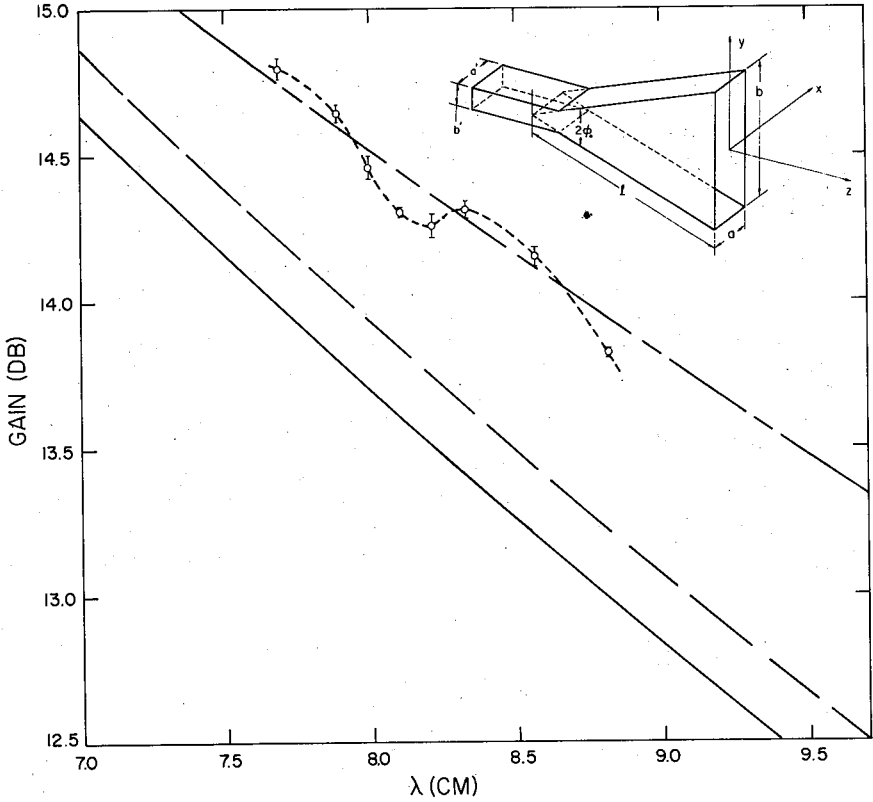
Fig. 1. Gain of an E-plane sectoral horn with $a = 7.21$ cm.,
$b = 24.0$ cm., $\ell = 42.15$ cm., $2\phi_o = 33^\circ$ and fed by
17.8 cm. of WR(284) waveguide.

————————————   Schelkunoff's equation

— — — —   Improved Kirchhoff result

— — — —   equation (5)

— ϕ — — ϕ —   measured values

7

COUPLING BETWEEN TWO WAVEGUIDES
OF FINITE LENGTH

Y. Elmoazzen and L. Shafai
Department of Electrical Engineering, University of Manitoba
Winnipeg, Manitoba, Canada, R3T 2N2

Coupling between waveguides of finite length has important practi-
cal applications in microwaves and antenna problems. In this
paper two waveguides of finite length are considered and their
coupling as well as the resulting radiated field is studied. The
exciting waveguide is assumed to be open ended near the coupled
waveguide, but terminated by a matched load at the other end. The
coupled waveguide, on the other hand, is assumed to be open ended
at both ends.

For a given excitation of the exciting waveguide, the Wiener-Hopf
technique is used to formulate the problem and a solution for the
fields inside the waveguides and in the external regions is found,
using transmission line theory. Since the exciting waveguide is
matched, the incident field at the open end of the exciting wave-
guide is the initial excitation only. Starting with this initial
excitation, the solutions of the problem of two semi-infinite
waveguides and an open ended waveguide are used to find the various
reflected, transmitted and radiated fields. The total field is
then expressed in terms of these intermediate ones and a closed
form solution for the reflected, transmitted and the radiated
fields is obtained. In particular the total radiated field is
found to be

$$\underline{P}^t(\theta) = \underline{P}(\theta) + \frac{Te^{-\gamma_m(L + \ell_2)}}{1 - R\,R_o\,e^{-2\gamma_m\ell_2}}\, e^{iKL\,\cos\,\theta}[\underline{P}_o(\theta)e^{iK\ell_2}\,\cos\,\theta$$

$$+ \underline{P}(\pi- \theta)R_o\ell^{-\gamma_m\ell_2}] \tag{1}$$

where ℓ_2 is the length of the coupled waveguide and R_o and
$\underline{P}_o$ are respectively the reflection coefficient and the radiation
field of an open ended waveguide. Also, R, T and $\underline{P}$ are
respectively the reflection coefficient, the transmission coefficient
and the radiation field of two semi-infinite waveguides separated
by a distance L [1].In this equation γ_m denotes the propagation
constant of mode m in the waveguide. It is clear that the
configuration is resonant when

$$R\,R_o\,e^{-2\gamma_m\ell_2} = 1 \tag{2}$$

the solution of which gives the complex propagation constant
$K = K_1 + iK_2$, where K_1 is the proportional to the resonant
frequency and K_2 is the loss factor.

Using equation (1), some numerical results for the radiated

fields are obtained and are shown in figures (1) and (2). Figure (1) is the radiation pattern for two parallel plate waveguides of finite length, whereas figure (2) is the radiation patterns for two finite circular waveguides. These figures show that the beam width decreases with decreasing length of the coupled waveguide.

REFERENCES

1. Y. Elmoazzen and L. Shafai (IEEE, G-MTT, Inter. Microwave Symposium, June 1973, University of Colorado)
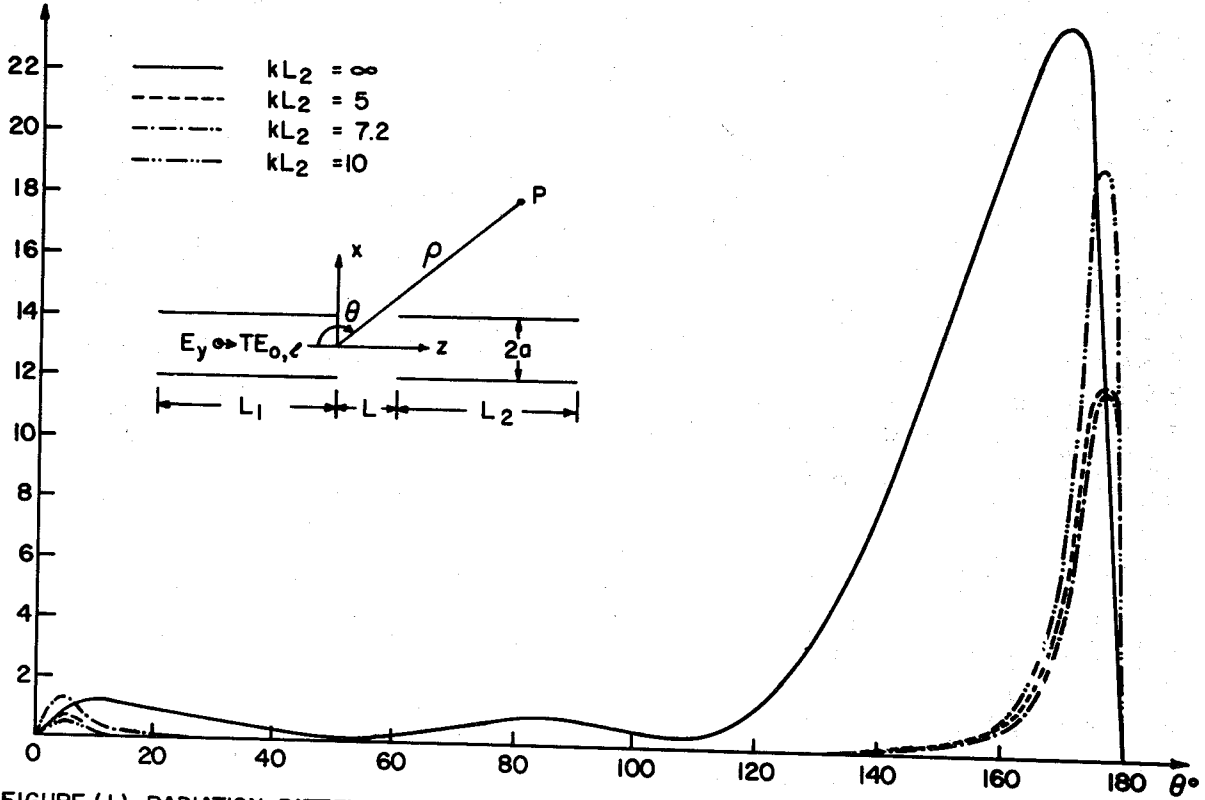
FIGURE (1) RADIATION PATTERN FOR A TWO COUPLED PARALLEL PLATE WAVEGUIDES OF WIDTH $2ka = 1.2\pi$, WITH A $TE_{0,1}$ EXCITATION AND SEPARATION DISTANCE $kL = 6$
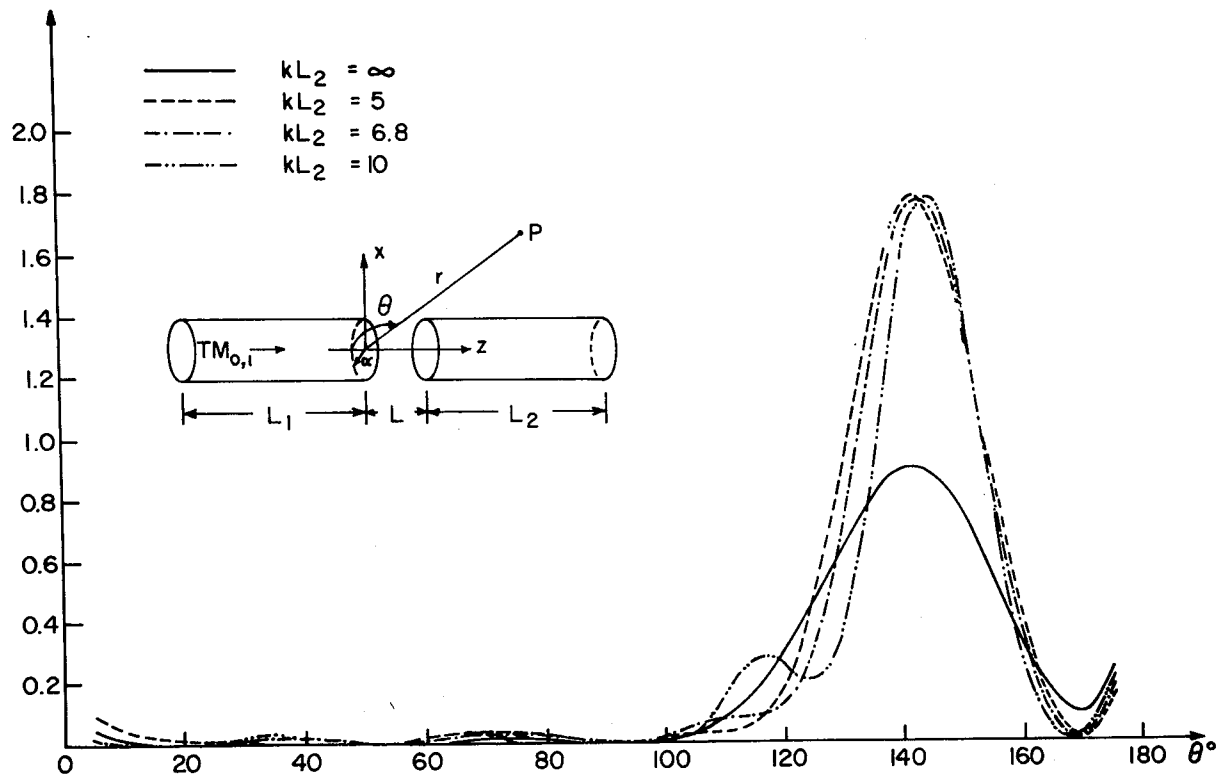
FIGURE (2) RADIATION PATTERN FOR A TWO COUPLED CIRCULAR WAVEGUIDES OF RADIUS $ka = 5$, WITH A $TM_{0,1}$ EXCITATION AND SEPARATION DISTANCE $kL = 6$

Session 11   HF and Inverse Scattering

AN INVESTIGATION OF THE APERTURE COUPLING PHENOMENON WITH APPLICATION TO EMP AND EMC PROBLEMS

R. Mittra

Electromagnetics Laboratory
University of Illinois
Urbana, Illinois 61801

The problem of estimating the coupling of an incident plane wave through an aperture, into a parallel-plate waveguide or a cavity region, is of interest in the areas of EMP hardening and EMC shielding. Though several convenient formulas are available for the small aperture problem, these are not useful for computing the early time response of an EMP pulse, or the effect of coupling of a radar signal in the GHz frequency range. Also, the high frequency techniques such as Kirchhoff approximation or GTD methods have limited applicability to the problem in question since the effects of a waveguide, or a cavity, backing the aperture, are not accounted for easily or accurately via these techniques. The conventional integral equation formulation for the aperture field does not suffer from the above limitations, though it requires the numerical solution of a pair of coupled integral equations for the two scalar components of the aperture electric field. The maximum size of the aperture that can be handled by this approach is limited by the storage capacity of the computer, and, of course, the inversion of large matrices is time-consuming. Thus, it is desirable to look for approaches that can alleviate this situation, even if partially.

In this paper a new pair of integral equations is presented for the two scalar components of the aperture electric field. The geometry of the coupling problem is shown in Figure 1. Decoupling of the original coupled equations is accomplished by incorporating an auxiliary condition on the continuity of the normal component of the electric field in the aperture. The resulting equations are then integrated to yield

$$\iint E_x(g_1 + g_2) = \frac{2}{jk_z^i} E_x^i + \sum k_{yn} A_n \, e^{jk_{xn}X + jk_{yn}Y} \tag{1}$$

$$\iint E_y(g_1 + g_2) = \frac{2}{jk_z^i} E_y^i - \sum k_{xn} A_n \, e^{jk_{xn}X + jk_{yn}Y} \tag{2}$$

where the integration is over the aperture; g_1, g_2 are the scalar Green's functions for the half-space and waveguide regions, respectively; the superscript i refers to the incident wave; and A_n are unknown constants to be determined later by applying the edge condition on the tangential component of the aperture electric field.

The above equations are generalizations of two similar equations reported in an earlier paper[1] for the thin plate problem and possess the same desirable features that make them numerically attractive. Specifically, the kernels of the two equations (1) and (2) are identical and simpler than those obtained in the conventional aperture field formulation. Thus, in addition to simplifying the computation of the matrix elements, the decoupled nature of these equations allows one to handle relatively larger size apertures with the same computer storage capacity.

Numerical investigation for the aperture field and the coupling effects for the geometry in Figure 1 has been carried out and typical results for the aperture field distributions for a $1\lambda \times 1\lambda$ square aperture are shown in Figure 2 for a normally incident plane wave with the incident E field parallel to the y direction.

The case of resonance is of particular interest in the EMP and EMC coupling problems. Thus a discussion of this case is included in the paper. Finally, comparison with some experimental data is included to illustrate the agreement with available measured results.

1.   R. Mittra, Y. Rahmat-Samii, D. V. Jamnejad and W. A. Davis, "A new look at the thin-plate scattering problem," to appear in Radio Science.

Acknowledgement
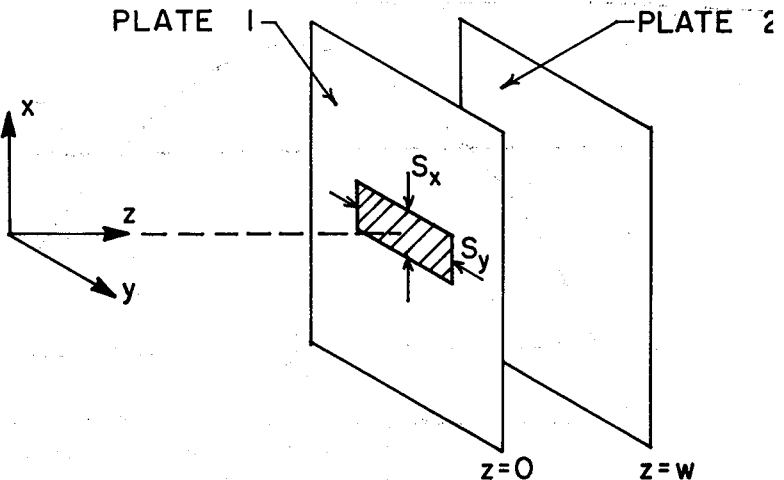
Figure 1. Aperture Coupling Problem.
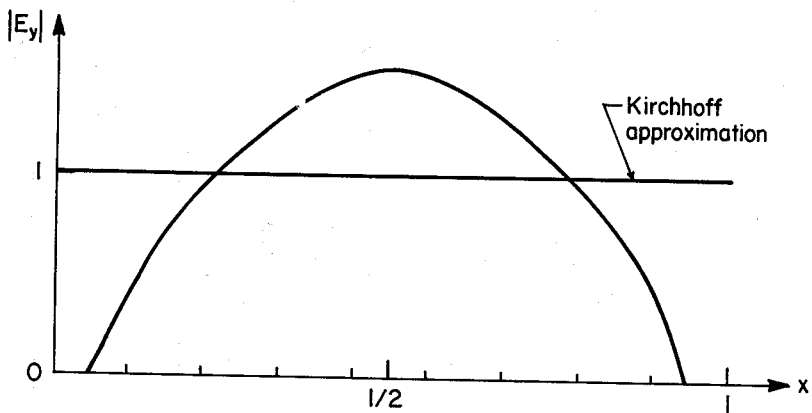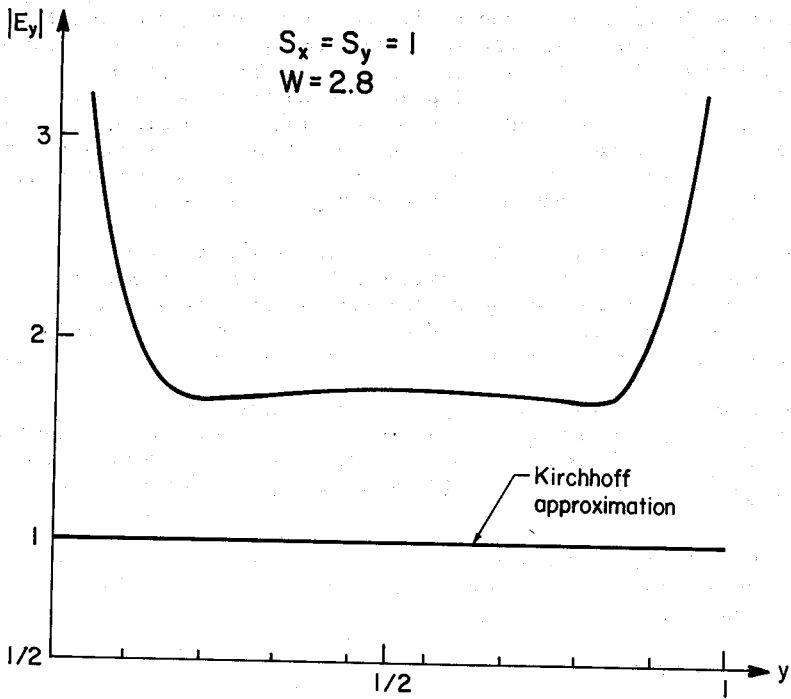
Figure 2. Amplitude plot of E_y for $w = 2.8\lambda$, $S_x = S_y = \lambda$, $E_y^i = 1$. (a) $x = \lambda/2$. (b) $y^y = \lambda/2$. Normally incident plane wave with E_y parallel to y-axis.

PROFILE CHARACTERISTICS INVERSION OF SPHERICAL TWO-BODY SCATTERING GEOMETRIES

H.P.S. Ahluwalia and W.M. Boerner
Department of Electrical Engineering, University of Manitoba
Winnipeg, Manitoba, Canada R3T 2N2

Abstract: An inverse problem of continuous wave electromagnetic scattering is considered. It is assumed that the incident and scattered fields are given everywhere and that the material surface properties satisfy the Leontovich boundary condition. Applying the novel concept of electromagnetic inverse boundary conditions it is shown how the shape and the averaged local surface impedance for spherical two-body scattering geometries can exactly be recovered. An important novel contribution is the introduction of analytic continuation methods in three dimensions.

Introduction: In inverse problems of electromagnetic scattering, the shape, the size and the averaged local material constituents of the scatterer are to be determined from the knowledge of the incident and the scattered field assuming that the laws governing the interaction are known. In a recent paper[1] a novel approach based on the concept of inverse boundary conditions for profile characteristics inversion of conducting shapes was proposed. Starting from the Leontovich condition, it was shown that two unique vector quantities $\underline{A}=\underline{E}x\underline{E}^*-\eta\eta^*\underline{H}x\underline{H}^*$ and $\underline{B}=\eta\underline{E}^*x\underline{H}-\eta^*\underline{E}x\underline{H}^*$ exist for which $\underline{A}\cdot\underline{B}=0$, $\underline{A}^2=\underline{B}^2$ and $\hat{n}\cdot\underline{A}=\hat{n}\cdot\underline{B}=0$, where $\hat{n}$ denotes the outward local normal, η the averaged local surface impedance, $\underline{E}$ and $\underline{H}$ the total electric and magnetic fields respectively, and the quantities with asterisks are complex conjugates. From these properties of the vectors $\underline{A}$ and $\underline{B}$ it is possible to derive sets of inverse boundary conditions[1] which are necessary, not locally but globally sufficient.

In the presented analysis the concept of inverse boundary conditions has been applied to the spherical mono and two-body cases. Since the application of this concept requires the knowledge of the electromagnetic fields in the vicinity of the scatterer, three-dimensional analytic continuation of the fields has been introduced.

Field Expansion and Analytic Continuation: The incident and scattered fields are expanded in terms of well established spherical vector wave functions, where the electric field is given by

$$\underline{E} = \sum_{n=1}^{\infty} \sum_{m=-n}^{n} [A(m,n)\underline{M}_{mn}^{(\nu)}+ B(m,n)\underline{N}_{mn}^{(\nu)}]$$

and $A(m,n)$, $B(m,n)$ are the expansion coefficients, $\underline{M}_{mn}^{(\nu)}$, $\underline{N}_{mn}^{(\nu)}$ denote the spherical vector wave functions, and the superscript $\nu = 1,2,3$ or 4 specifies the appropriate radial behavior of the fields.

To calculate the expansion coefficients for the general two-body case as shown in Fig.1, Bruning and Lo's approach[2] was employed and modified with the aid of the impedance boundary condition. Since the

field expansions for the multi-body case are valid only outside the Wilcox sphere, fields had to be analytically continued so that the inverse boundary conditions can be applied. Both interior and exterior analytic continuations have been employed, where the interior expansion being valid inside the sphere S' of Fig.2, can be expressed by

$$\underline{E}' = \sum_{n=1}^{\infty} \sum_{m=-n}^{n} [\alpha(m,n)\underline{M}_{mn}^{(1)'} + \beta(m,n)\underline{N}_{mn}^{(1)'}]$$

The new expansion coefficients are obtained by applying vector spherical addition theorems derived by Stein[3] and Cruzan[4] and are given by

$$\alpha(m,n) = \sum_{\nu=1}^{\infty} \sum_{\mu=-\nu}^{\nu} [A(\mu,\nu)A_{mn}^{\mu\nu} + B(\mu,\nu)B_{mn}^{\mu\nu}]$$

$$\beta(m,n) = \sum_{\nu=1}^{\infty} \sum_{\mu=-\nu}^{\nu} [B(\mu,\nu)A_{mn}^{\mu\nu} + A(\mu,\nu)B_{mn}^{\mu\nu}]$$

where the translation coefficients $A_{mn}^{\mu\nu}$, $B_{mn}^{\mu\nu}$ are of complicated form involving Wigner's 3-j symbols, and are given in references [3] and [4]. The exterior expansion is of similar form with the appropriate radial functions being interchanged in the expansion and translation coefficients.

Computational Verification: The inverse boundary conditions resulting for the perfectly electric conducting case, i.e. $\underline{E} \cdot \underline{H}$, $\underline{E} x \underline{E}^*$ and $|\underline{E}_{inc}| = |\underline{E}_{scat}|$ are compared first for the direct, the interior and exterior analytically continued expansions using a single perfectly conducting sphere as test case. As expected the approximate physical optics condition and $\underline{E} \cdot \underline{H}$ produce only one minimum along a ray of computation specifying the exact point on the proper surface locus, whereas $\underline{E} x \underline{E}^*$ produces an additional set of pseudo loci as is shown in Fig.3. In all of the tested mono and two-body cases $\underline{E} \cdot \underline{H}$ and $\underline{E} x \underline{E}^*$ specified the proper surface with greatest accuracy, where for $\underline{E} x \underline{E}^*$ the additional pseudo loci are not closed in the umbra region.

The inversion procedure for the more complicated case of imperfectly conducting scatterers is divided into three categories: η known; $\eta = \pm \eta^*$, and η unknown. In the first case, known η is substituted into $\underline{A} \cdot \underline{B} = 0$ and $A^2 = B^2$ which are simultaneously computed to recover the proper surface locus, where the two conditions display properties similar to those of $\underline{E} x \underline{E}^*$ and only at the exact point lying on the proper surface are the minima identical as is shown in Fig.4. For the case $\eta = \pm \eta^*$, the property of $\underline{A} \cdot \underline{B} = 0$ having one root η_o and of $A^2 = B^2$ having two roots η_1 and η_2 is employed. The exact point on the proper surface locus is obtained for which η_o is identical to either η_1 or η_2, thus simultaneously providing the correct value of η. Therefore, it is verified that the proper surface locus and either purely real or purely imaginary η can be recovered uniquely even if η should be inhomogeneous or dispersive. This, however, is not the case for unknown complex η in which case it must be assumed that η is homogeneous but could be dispersive which will be demonstrated with the aid of tabulated results.

Conclusions: With the introduction of improved field expansions for spherical two-body scattering and the introduction of three-dimensional interior and exterior analytic continuation, a complete verification of general spherical vector addition theorems was made possible. One apparent drawback of the presently available vector addition theorems[3,4] is that the transformed field expansions are very slowly convergent, especially in the vicinity of the scattering surface. However, the excellent results obtained prove that the novel set of inverse boundary conditions postulated in reference [1] can be applied with a high degree of confidence to the problem of profile characteristics inversion of perfectly and imperfectly conducting scatterers whose surface properties satisfy the Leontovich condition.

References
1. W.M.Boerner and H.P.S. Ahluwalia (1972 Can.J.Phys.50,3023)
2. J.H.Bruning and Y.T.Lo (1971 IEEE Trans.Ant.& Prop.19,378 and 391)
3. S.Stein (1961 Quart.Appl.Math.19,15)
4. O.R.Cruzan (1962 Quart.Appl.Math.20,23)
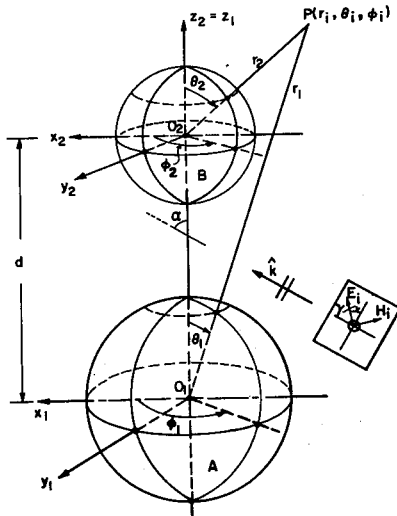
FIG. I. SPHERICAL TWO-BODY SCATTERING
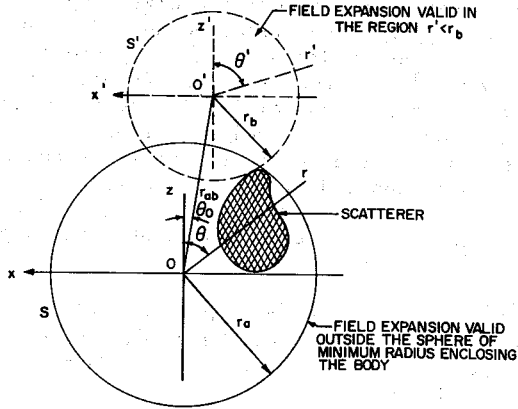
FIG. 2. ANALYTIC CONTINUATION OF ELECTROMAGNETIC FIELD
USING INSIDE EXPANSION ($\phi = 0°/\phi = 180°$ PLANE)
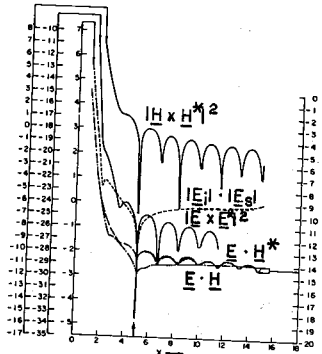
Fig. 3 Plot of $\text{Log}\{|\underline{E}_T \times \underline{E}_T^*|\}$, $\text{Log}|\underline{E}_i \cdot \underline{E}_s|$, $\text{Log}\{|\underline{E}_T \cdot \underline{H}_T|\}$, $\text{Log}|\underline{E}_T \cdot \underline{H}_T^*|$, $\text{Log}\{|\underline{H}_T \times \underline{H}_T^*|^2\}$ versus Radiant Vector $X = kR$ for the Spherical Test Case $ka = 5$, $\eta = 0$, $\theta = 22.5°$ $\phi = 0$
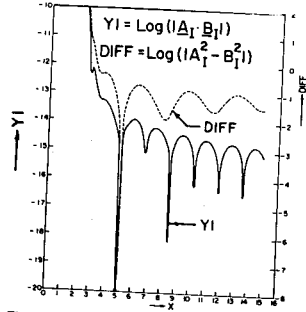
Fig. 4 Plot of YI and Diff vs Radiant Vector X for a Spherical Target of $ka = 5.0$, $\eta = 0.433 + j.25$ for $\theta = 30°$ $\phi = 90°$

18

ON AN INVERSE SCATTERING METHOD
REQUIREMENTS FOR AN EXPERIMENTAL SETUP

W. Tabbara

Laboratoire d'Electronique Générale
Ecole Supérieure d'Electricité
10, avenue Pierre Larousse
92240 Malakoff - FRANCE

The purpose of this communication is to determine un-
der what conditions the inverse scattering method described
by Lewis [1] can be applied to an experimental situation.
Symbols used here are those reported in[1] We are interested
in recovering the functions $\delta(\vec{x})$ equal to one inside the
target and to zero outside, and $\alpha(\vec{x_1})$ the cross sectional
area of the target by a plane $\vec{x_1}$ = constant. These functions
are related to $\Pi(\vec{p})$ and $\Gamma(\vec{p})$ $K(\vec{p})$ by means of a Fourier
transform, where $\Gamma(\vec{p}) = 2\sqrt{\pi}(\epsilon(\vec{p})+ \ell^*(-\vec{p})) ; \sigma = |\ell(\vec{p})|^2$
the backscattering cross section, $K(\vec{p})$ an aperture function,
and $\vec{p}$ is related to the wave number $\vec{k}$ by $\vec{p} = -2\vec{k}$.

For a monostatic experimental setup, the values of
are deduced from the measurement of the backscattered
far field. These measurements can be done in two different
ways. First, by measuring the backscattered far field at a
finite number of frequencies over a finite frequency range
at each aspect in a limited aspect band. In this case one
must determine the frequency and aspects bands over which the
measurements are done, and the number of measurements. Second
by a harmonical analysis of the impulse response of the back-
scattered far field, and by comparison with the spectrum of
the incident impulse [2] ; in this case one must determine
the spectrum width.

Numerically this is equivalent to the determination
of the truncated interval over which the Fourier integrals
will be computed and the number N of integration points. It
is obvious that N will depend on the numerical integration
method one may use. The investigation of the integrands when
the target is a sphere, a circular cylinder of finite length
or a flat back circular cone of finite length shows that the
main contribution to the integrals come from low frequency
values. But at these frequencies $\Gamma(\vec{p})$ has no physical signi-
ficance and must be replaced by $\Gamma_x(\vec{p})$ computed from the
exact solution to the problem of plane wave scattering by one
of the above mentionned targets [3] . Thus $\Gamma_x(\vec{p})$ is the ma-
thematical representation of the measured data in the whole
frequency domain and not only in the high frequency domain
as it is the case for $\Gamma(\vec{p})$. The introduction of $\Gamma_x(\vec{p})$ in
the Fourier integrals suppose that the experimental arrange-
ment is errorless. However it is possible to simulate a real

19

experiment by adding to $\Gamma_X(\vec{p})$ a parasitic signal. Then one
obtains $\delta_X(\vec{x})$, $a_X(x_i)$ which are expected to be different
from the exact values. The computations of the experimental
simulation has been carried out for a sphere of radius a, this
is possible because an exact solution is available. The re-
sults are reported on Fig. 1 where $\tau = (x_1^2 + x_2^2 + x_3^2)^{1/2}$ and on
Fig. 2.

The differences between exact and "experimental" va-
lues can be simply explained, since $\Gamma_X(\vec{p}) \sim \Gamma(\vec{p})$ when
$|\vec{p}| \ll 1$. From well known Fourier transform theorems[4]one can
state that $\delta_X(\vec{x}) \sim \alpha \delta(\vec{x})$ and $a_X(x_i) \sim \alpha' a(x_i)$ when
$|\vec{x}| \ll 1, \alpha$ and α' are constants, this can be checked on Fig. 1-
2 when $\tau/a < 0.1$ and $x_i/a < 0.1$. The experimental consequen-
ces of the occurence of α and α' is that the contour of the
obstacle will be determined with some error. The results of
the simulation can be improved if one can find a function
that accurately approximates $\Gamma(\vec{p})$ at low frequencies. This is
possible if one consider the physical optic value of the in-
duced surface currents to be true all over S and not only on
the illuminated part of it. Adachi [5] introduced the function

$$\rho_M(\vec{p}) = \frac{i}{2\sqrt{\pi}} \int_S \vec{n} \cdot \vec{p} \; e^{-i\vec{p} \cdot \vec{x}} \, d\vec{x}$$

and demonstrated that $\sigma_M = |\rho_M(\vec{p})|^2 \sim \sigma_X$ at low frequencies. One
can easily show that $\Gamma(\vec{p}) = 2\sqrt{\pi} \rho_M(\vec{p})/|\vec{p}|^2$. In the case of
the sphere $\Gamma(\vec{p})$ must be replaced by

$$\Gamma_M(\vec{p}) = 2\sqrt{\pi} \, |\rho_X(\vec{p})| \, /|\vec{p}|^2 \qquad |\vec{p}a| \leqslant 1.$$

$$= \Gamma_X(\vec{p}) \qquad\qquad |\vec{p}a| > 1.$$

the results of the computations are shown in Fig. 1 - 2, the
contour of the obstacle is more accurately determined. It is
important to notice that this improvement in the recovering
of $\delta_X(\vec{x})$ and $a_X(x_i)$ is done without increasing the value of
N or enlarging the limited frequency and aspect bands. In the
case of the sphere, the symmetry of the target reduces the
aspect band to a single value and the frequency range covers
the finite interval $[o, t_M]$ where $t = |\vec{p}a|$. The values of N
and t_M have been discussed in [6], it has been shown that
$N = t_M$ and N = 50 when $\delta_X(\vec{x})$ is recovered and N = 10 when
$a_X(x_i)$ is recovered.

It has been shown that there exists some differences
between the exact results and those given by Lewis method
when applied to an experimental situation. An extension of
physical optics induced currents to the whole surface allo-
whed us to improve the experimental results.

20

[1] R.M. Lewis (1969 I.E.E.E. Trans Ant. Prop., AP - 17
     p. 308)
[2] A.M. Nicholson et al. (1972, I.E.E.E. Trans Microwa.
     Th. Tech., MTT 20 p. 3)
[3] J.J. Bowman et al. Electromagnetic and Acoustic Scatte-
     ring by simple Shapes Amsterdam, the Netherlands : North
     Holland Publ. 1969
[4] L. Schwartz Méthodes mathématiques pour les Sciences
                  Physiques Paris France : Hermann 1961
[5] S. Adachi (1965, Proc. I.E.E.E., vol. 53 p. 1067)
[6] W. Tabbara (1973, I.E.E.E. Trans Ant. Prop., AP - 21
     p. 245

exact solution
$\gamma(\vec{x})$
$\gamma_X(\vec{x})$
improved $\gamma_X(\vec{x})$

FIG. 1

r/a

exact solution
$a(x_1)$
$a_X(x_1)$
improved $a_X(x_1)$

FIG. 2

x_1/a

22
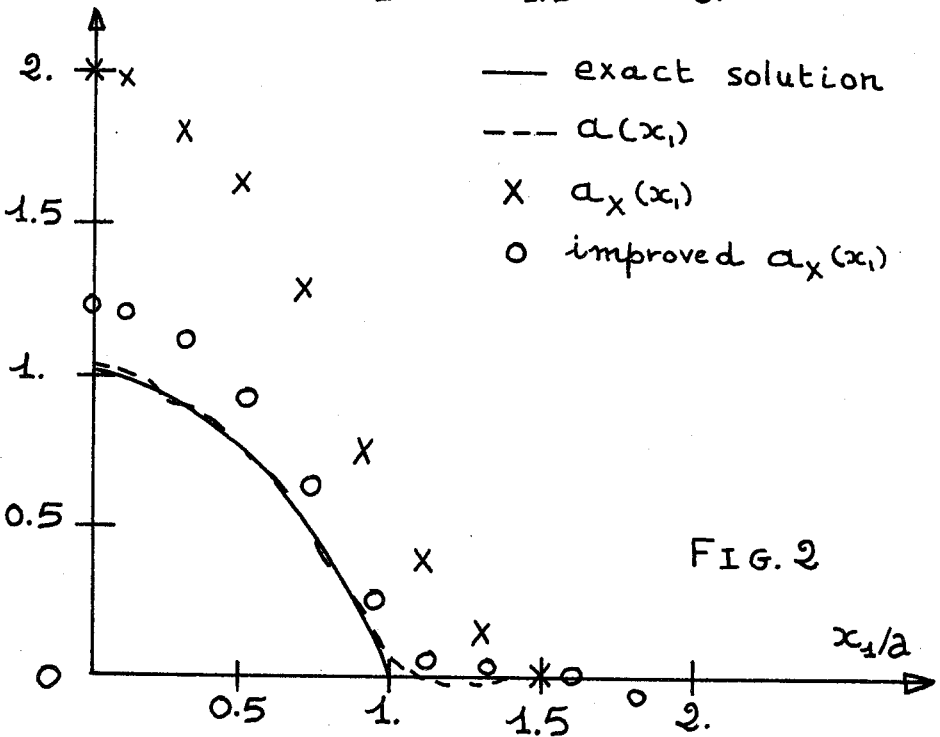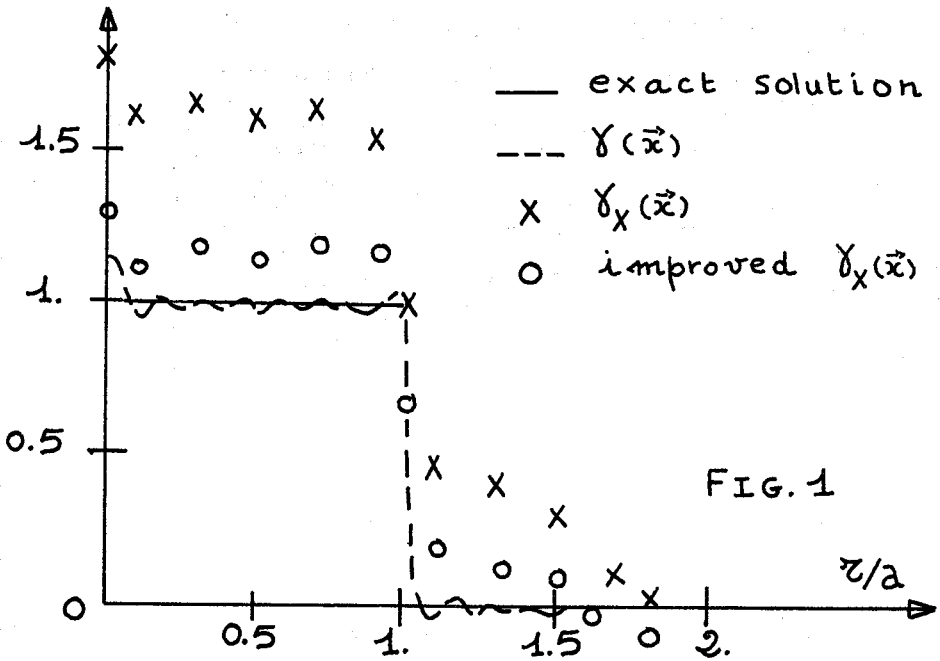
THE EQUIVALENCE OF INVERSION BY FOURIER DECOMPOSITION AND MINIMUM SQUARE ERROR INVERSION FOR SCATTERING BY CONDUCTING CIRCULAR CYLINDERS

R. C. Murphy
T. J. F. Pavlasek

McGill University
Montreal, Quebec, Canada

Solutions of the problem of plane-wave scattering by conducting circular cylinders may be found by an appropriate expansion in terms of sine-cosine eigenfunctions. The scattered part of the total field is given by an expansion of the form (1):

$$E_z^s = E_0 \sum_n j^n a_n H_n^{(2)}(k\rho) e^{jn\phi} \tag{1.1}$$

When this is specialized to the far field by taking the proper limit of the radial terms, we can define the far-field pattern of the scattering:

$$g(\phi) = \sum_n a_n e^{jn\phi} \tag{1.2}$$

This Fourier series representation of a piecewise continuous far-field pattern function is the optimal representation (2), since the square error $\|g-g'\|^2$ achieves a minimum value of zero when g' is constructed from an orthogonal basis set, such as $\{\exp(jn\phi)\}$ and the appropriate multipliers a_n. Since $\{\exp(jn\phi)\}$ is complete, we find (Parseval's equation):

$$\|g\|^2 = \sum_n a_n^* a_n \tag{1.3}$$

If we choose as an inversion procedure the recovery of the a_n by the analysis of the far-field pattern g,

$$a_n = \frac{1}{2\pi} \int_0^{2\pi} g(\phi) e^{-jn\phi} d\phi \tag{1.4}$$

we can also demonstrate

$$\sum_n a_n^* a_n = \|g(\phi)\|^2 \tag{1.5}$$

provided we use the discrete form of the δ-function

$$\sum_n \frac{1}{2\pi} e^{jn(\phi'-\phi)} = \delta(\phi'-\phi) \tag{1.6}$$

This shows the optimality of inversion by Fourier decomposition provided the far-field pattern function is suitably behaved. This technique has been used by several authors (3,4,5) for reconstructing the near field from given far-field pattern data. The dashed line in Fig.1 shows the mode coefficients $a_n^* a_n$ plotted for cylinders of radius 0.25λ, 0.5λ, 1.0λ, and 2.0λ. They are normalized so that $\|g\|^2 = 1$, and for $n \geq 1$, are counted twice to account for the $+\&-$ values.

Let us now inquire into a method of optimizing the inversion process for near-canonical scatterers. If the far-field pattern $g(\phi)$ is the result of a linear operation on the near field

$$g = Tf \qquad\qquad (2.1)$$

then it may not be possible to find f such that

$$g_\delta = Tf \qquad\qquad (2.2)$$

where g_δ is a measured far-field pattern containing possible errors. By forming the square-error performance index

$$F(f) = \|Tf - g_\delta\|^2 = \langle Tf - g_\delta, Tf - g_\delta \rangle \qquad (2.3)$$

we have a quantity which may be minimized by variational techniques:

$$\left.\frac{\partial F(f + \epsilon\eta)}{\partial \epsilon}\right|_{\epsilon=0} \equiv 0 \;\rightarrow\; \langle \eta, T^*Tf - T^*g_\delta \rangle \equiv 0 \text{ for all } \eta. \qquad (2.4)$$

Consequently,

$$T^*Tf - T^*g_\delta \equiv 0 \qquad\qquad (2.5)$$

describes the minimum square error process by which an element in the space of f is matched to an arbitrary g_δ.

For the cylindrical scattering problem the g=Tf form is given by the Fredholm equation of the 1$\underline{^{st}}$ kind

$$g(\phi) = \left[-\frac{k^2 a}{E_0 4\omega\epsilon}\right]\int_0^{2\pi} J_z(\theta) e^{jka \cdot \cos(\phi - \theta)} d\theta \qquad (2.6)$$

where $J_z(\theta)$ is the surface current distribution on the cylinder. The operator T*T then takes the form

$$T^*TJ_z(\theta) = \left[\frac{2\pi k^4 a^2}{E_0^2 16\omega^2\epsilon^2}\right]\int_0^{2\pi} J_z(\theta')\, J_0(2ka \cdot \sin\frac{\theta'-\theta}{2}) d\theta' \qquad (2.7)$$

which is equivalent to the eigenvalue problem

$$\lambda\Phi(\theta) = \int_0^{2\pi} K(\theta, \theta')\, \Phi(\theta')\, d\theta' \qquad (2.8)$$

The eigenfunctions of (2.8) are the set $\{\exp(jn\theta)\}$, and the eigenvalues are given by

$$\lambda_n = C \cdot 2\pi J_n^2(ka) \qquad\qquad (2.9)$$

where C is the bracketed factor before the integral in (2.7). These eigenvalues are plotted as the solid line in Fig.1 for the four cylinders. They have been normalized so that $\Sigma\lambda_n = 1$, and are also counted twice for $n \geqslant 1$.

The equivalence of the eigenvalue form and the direct expansion form is shown by calculating $\|g(\phi)\|^2$. Substituting (2.1) into (1.4), we find

$$a_n = \frac{1}{2\pi} \int_0^{2\pi} \left[Tf(\theta) \right] e^{-jn\phi} \, d\phi \qquad (3.1)$$

By forming the sum (1.3), we can show

$$\sum_n a_n^* a_n = \left[\frac{k^4 a^2}{E_0^2 \cdot 16 \omega^2 \epsilon^2} \right] \int_0^{2\pi} \int_0^{2\pi} J_z^*(\theta) J_z(\theta') J_0(2ka \cdot \sin\frac{\theta'-\theta}{2}) d\theta d\theta' \qquad (3.2)$$

Subsituting the expansion for $J_z(\theta)$ (1),

$$J_z(\theta) = \left[\frac{2E_0}{\omega \mu \pi a} \right] \sum_n \frac{j^{-n} e^{jn\theta}}{H_n^{(2)}(ka)} \qquad (3.3)$$

we find

$$\sum_n a_n^* a_n = \frac{1}{(2\pi)^2} \int_0^{2\pi} \sum_n \frac{2\pi J_n^2(ka)}{|H_n^{(2)}(ka)|^2} d\theta = \sum_n \left| \frac{J_n(ka)}{H_n^{(2)}(ka)} \right|^2 = \sum_n a_n^* a_n \qquad (3.4)$$

The coefficients $a_n^* a_n$ may be calculated from the λ_n by multiplying by a factor proportional to $1/|H_n^{(2)}(ka)|^2$.

The equivalence of the two techniques is important for the following reason: Inversion programs have an inherent limitation of accuracy which arises from measurements, quadratures, etc. Because of the equivalence, the performance of near-field reconstruction will deteoriate with loss of data accuracy in such a way that the characteristics of the near field are preserved for small errors. Fig.2 shows the reconstructed near field for three levels of Gaussian noise added to the exact pattern data. The reconstruction is at $\rho=1.35\lambda$ in a system with $a=1.1\lambda$. While the very substantial noise of case (c) results in a noisy near-field pattern, the characteristic shape is retained.
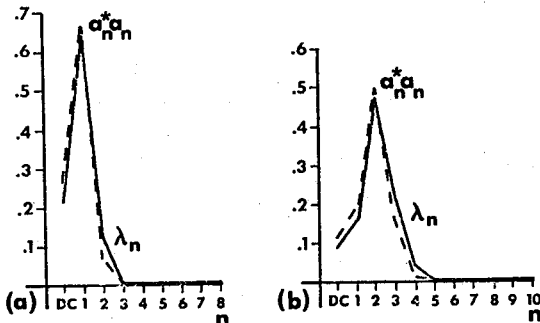
Fig.1 (a,b): Normalized coefficients $a_n^* a_n$ (dashed line) and eigenvalues λ_n (solid line) for cylinders of 0.25λ-radius (a) and 0.50λ-radius (b).
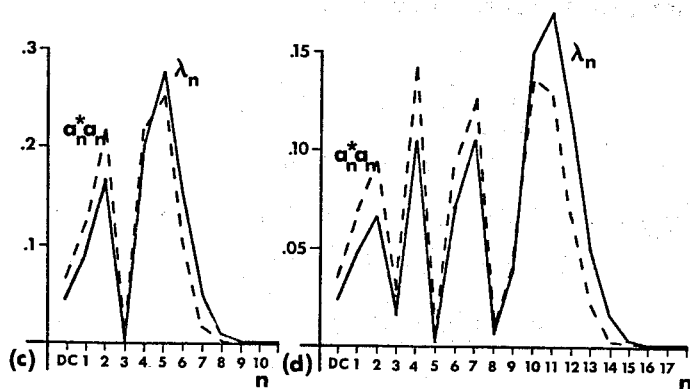
Fig.1 (c,d): Normalized coefficients $a_n^* a_n$ (dashed line) and eigenvalues λ_n (solid line) for cylinders of 1.0λ-radius   (c) and 2.0λ-radius (d).
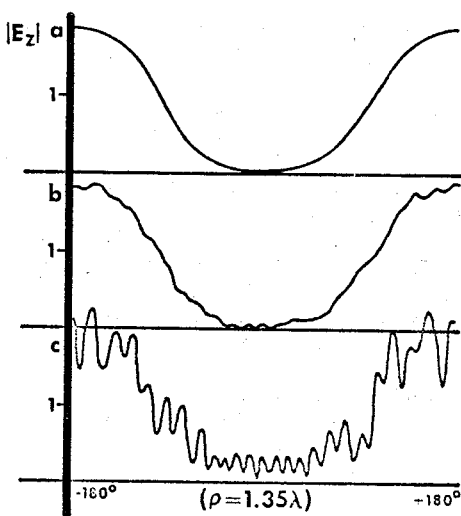
Fig.2: Azimuthal field reconstruction at $\rho = 1.35$ for a 1.1λ-radius cylinder. The exact pattern data has been modified by the addition of Gaussian noise: (a) $\mu = 0.0$, $\sigma = 0.0005$; (b) $\mu = 0.0$, $\sigma = 0.005$; (c) $\mu = 0.0$, $\sigma = 0.05$.

1. R.F.Harrington (1961,"Time Harmonic Electromagnetic Fields", McGraw-Hill, N.Y.)
2. W.Kaplan (1952,"Advanced Calculus", Addison-Wesley, Reading, Mass.)
3. W.A.Imbriale and R.Mittra (1970, IEEE Trans.G-AP, AP-18, pp 633-642)
4. J.-C.Bolomey (1968, Rev.Cethedec, 5,#2, pp 21-37)
5. H.S.Cabayan, R.C.Murphy, and T.J.F.Pavlasek (1973, IEEE Trans.G-AP, AP-21, pp 346-357)

COMPLEX NATURAL RESONANCES OF AN OBJECT
IN DETECTION AND DISCRIMINATION

D.L. Moffatt
J.H. Richmond
R.K. Mains

ElectroScience Laboratory
Dept. of Electrical Engineering
Ohio State University
Columbus, Ohio 43212

It was suggested in 1965 [1], that the scattering function of an
object (that function which when multiplied by the incident field yields
the scattered field) could be represented in the frequency domain at
low frequencies as a rational function of the complex variable s. The
suggested representation was therefore that of a lumped constant network.
Hill [2] used such a representation and a linear difference equation [3]
to demonstrate, via a predictor-correlator processing, both size and
shape discrimination and detection capabilities for those objects (sphere
and thin prolate spheroids) whose complex natural resonances can be ob-
tained analytically.

In this paper, procedures are demonstrated for obtaining the comple
natural resonances of an arbitrary object via numerical solutions of an
integral equation formulation [4]. The natural resonances of various thi
wire structures, some of which are first order models of aircraft shapes,
are shown. Using these natural resonances, size and shape discrimination

27

via predictor-correlator processing is demonstrated. Finally,

procedures for obtaining the complex natural resonances directly from

scattered field data [5] are discussed.

REFERENCES

1. Kennaugh, E.M. and Moffatt, D.L., "Transient and Impulse
    Response Approximations," Proceedings of the IEEE, Vol. 53,
    No. 8, August 1965, pp. 893-901.

2. Hill, David A., "Electromagnetic Scattering Concepts Applied
    to the Detection of Targets Near the Ground," Report 2971-1,
    (Dissertation), September 1970, The Ohio State University
    ElectroScience Laboratory, Department of Electrical Engineering;
    prepared under Contract No. F19628-70-C-0125 for Air Force
    Systems Command, Laurence G. Hanscom Field, Bedford, Massachusetts 01730.

3. Corrington, M.S., "Simplified Calculation of Transient Response,"
    Proceedings of the IEEE, Vol. 53, No. 3, March 1965, pp. 287-292.

4. Richmond, J.H., "Radiation and Scattering by Wire Structures in
    Active and Passive Media", Report 2902-9, in preparation, The
    Ohio State University ElectroScience Laboratory, Department of
    Electrical Engineering; prepared under Grant No. NGL 36-008-138
    for National Aeronautical Space Administration, Langley Research
    Center, Hampton, Virginia.

5. Moffatt, David L., "Time Domain Electromagnetic Scattering from
    Highly Conducting Objects," Report 2971-2, May 1971, The Ohio State
    University ElectroScience Laboratory, Department of Electrical
    Engineering; prepared under Contract No. F19628-70-C-0125 for Air
    Force Cambridge Research Labs, Air Force Systems Command, U.S. Air
    Force, Bedford, Massachusetts 01730.

UTILIZATION OF PHASE INFORMATION
IN RADAR TARGET IDENTIFICATION[*]

Y. T. Lin and A. A. Ksienski
The Ohio State University ElectroScience Laboratory
Department of Electrical Engineering
Columbus, Ohio 43212

Previous results [1] have shown that reliable target identification can be accomplished by utilizing low frequency radar scattering data. The band of discrete frequencies used extended from the Rayleigh range through the first resonance. Only the amplitudes of the radar returns had been used, however, for the identification process. It would be reasonable to expect that the introductions of phase information would approximately double the information content of the radar returns and would thus significantly improve the quality of identification processes, or, alternatively, could provide the same reliability of classification as with amplitude alone, utilizing half as many frequencies.

Phase information was therefore introduced and the performance will be presented using amplitude and phase data. The above identification performance will be compared to that using amplitude alone. The comparison criterion used was probability of misclassification in the presence of noise and errors. Several classification techniques were used and the performance differences will be discussed.

Several geometrical shapes were used as targets with the accent placed on high performance aircraft.

1. Lin, Y. T. and Ksienski, A. A., "Airplane Identification From Low Frequency Scattering Data", presented at the International Symposium, 1972 G-AP at College of William and Mary and Williamsburg Conference Center, December 11-14, 1972. p. 218.

OPTICAL BACKSCATTERING
FROM INHOMOGENEOUS PARTICLES

C. L. Brockman Jr.
Hughes Aircraft Co.
Canoga Park, California 91304

N. G. Alexopoulos
Electrical Sciences and Engineering Department
University of California
Los Angeles, California 90024

Inhomogeneous dielectric scatterers are known to occur in nature. Examples range from bacteria at the microscopic level to planets and atmospheres at the macroscopic level. The problem of scattering from such particles is difficult to solve exactly. Depending on the wavelength and the size of the particle, approximations such as geometric optics or Rayleigh scattering have been used. However, results obtained by geometric optics are particularly difficult to correlate with exact solutions even when they do exist. This is because the exact series solutions usually converge slowly at high frequencies.

In this paper, optical backscattering by a certain class of spherically inhomogeneous particles will be examined. The dependence of the dielectric constant with radius treated here is:

$$\epsilon = \epsilon_0 g^2 (\tfrac{r}{a})^{2m} = \epsilon_0 g^2 \rho^{2m}. \tag{1}$$

g and m are real constants with $m > -1$, $g > 0$; r is the radial distance from the center of the particle; and a is the outer radius of the sphere. This dependence is somewhat general since the parameters g and m are arbitrary. Yet, the wave equation has been solved for this dependence, and the TE_r and TM_r radial wavefunctions $S_n(\rho)$ and $T_n(\rho)$ may be expressed as Bessel functions of the following kinds [1] :

$$S_n(\rho) = \rho^{\frac{1}{2}} J_{\frac{n+\frac{1}{2}}{m+1}} \left[(\tfrac{g k_0 a}{m+1}) \rho^{m+1} \right]$$

$$T_n(\rho) = \rho^{m+\frac{1}{2}} J_{\frac{[(n+\frac{1}{2})^2 + m^2 + m]^{\frac{1}{2}}}{m+1}} \left[(\tfrac{g k_0 a}{m+1}) \rho^{m+1} \right]$$

With these results an exact solution for the backscattering of a plane linearly polarized wave in terms of a Mie type series may be developed. A Watson transformation is applied to the series, which results in two types of contributions. The first of these is a series of line integral contributions through saddle points of the integrands obtained in the transformation. The sec-

ond is a residue series which is responsible for surface wave contributions, such as creeping waves.

The leading terms of the ray contributions obtained from the exact solution compare well with the corresponding results obtained from geometric optics. In addition, the first correction term to geometric optics is available. Results obtained thus far are summarized below.

The electric field contribution by rays reflected off the front surface of the sphere is given by:

$$E_{dr} = \frac{a}{2r} \left(\frac{g-1}{g+1}\right) \left[1 + \frac{i}{x}\left(\frac{m}{g^2-1} - \frac{1}{2}\right)\right] e^{-jk_0(r-2a)} \ , \qquad (2)$$

where $x=k_0 a$ and where the field is linearly polarized, but the direction has been omitted. This result collapses to the result obtained by Scott[2] for the metallic sphere ($g=\infty$), and is an improvement in the result obtained by Inada and Plonus [3] for the dielectric sphere.

Rays will now be considered which are refracted into the sphere, reflect p times inside while circulating N times about the center, and then exit the sphere in the backscatter direction. These will be defined as glory rays because such rays have been identified with the glory phenomena. The glory phenomena is most often seen by air passengers, and appears as a bright set of colored rings about the shadow of the airplane on the clouds. Glory rays of a given order p can only exist for very specific values of N, m and g. In Fig. 1, the typical behavior of the scatter angle δ relative to the backscatter angle is shown as a function of the incidence angle α . Several curves are shown for fixed p, N, and g at various values of m, where δ may be found by geometric optics, and is:

$$\delta + 2N\pi = 2\alpha + \frac{p+1}{m+1}(\pi - 2\beta) \ , \qquad (3)$$

where α and β are the incidence and transmission angles at the edge and are related by Snell's law. Fig. 1 shows that there may be 0, 1 or 2 backscattered rays depending on the number of intercepts at $\delta = 0$. The value of α at which $\frac{d\delta}{d\alpha} = 0$ is defined as the rainbow angle, and is:

$$\cos \alpha_0 = \sqrt{\frac{g^2-1}{(\frac{p+1}{m+1})^2-1}} \ . \qquad (4)$$

This corresponds to a condition obtained by Sir Isaac Newton for the rainbow when m=0 [4] . As m changes from m_3 to m_2, Fig. 1 shows that two glory rays merge and form a single return. It may be shown that a backscattered rainbow can only exist for g>1, and that a rainbow does not exist at all for most values of g less than 1. In fact, there will typically be one glory ray or less for a given p or N.

An examination of the integrand obtained in the Watson transformation for the existence of saddle points was made. Saddle points do exist at incidence angles α_p for which the derivative of the exponential part of the integrand vanishes. This leads to a result identical to (3) (with δ =0) as a condition. The glory rays are seen to correspond to the steepest descent contribution of the integration through these saddle points. Further, if both the first and second derivatives of the exponential part vanish, then both (3) and (4) are obtained as conditions. Thus, contributions from the second order saddle point represent backscattered rainbows. Evaluation of the saddle point integral for a glory ray of reflection order p and circulation order N gives the following scalar part of the electric field contribution:

$$E_g = \frac{ax^{\frac{1}{2}}}{2r}(-1)^N \sqrt{\frac{\pi M \cos\alpha_p \sin^2\alpha_p}{M - (\frac{p+1}{m+1})}} \cdot$$

$$\left[\frac{4M}{(M+1)^2}(\frac{1-M}{1+M})^p(-1)^p(1+j\frac{f_e}{x}) + \frac{4M\,g^2}{(M+g^2)^2}(\frac{M-g^2}{M+g^2})^p(1+j\frac{f_m}{x})e^{\frac{j(p+1)\phi}{x}}\right]$$

$$\cdot \exp\left[-j\left[k_0(r-2a\cos\alpha_p(1-M\frac{p+1}{m+1})) - \frac{p\pi}{2} - \frac{\pi}{4}\right]\right], \qquad (5)$$

where $M = g\cos\beta_p/\cos\alpha_p$, and f_e, f_m and ϕ are functions of α_p and β_p. The above result holds unless $\alpha_p \approx 0$, in which case the ray is incident along the axis. For the TE_r part of the incident field, the applicable result near α_p =0 is:

$$E_{aE} = \frac{a}{4r}(-1)^{N+1}\frac{4\,g^2 j}{(g-2N)(g+1)^2}(\frac{g-1}{g+1})^p e^{-j\left[k_0(r-2a(1-g\frac{p+1}{m+1}))-p\frac{\pi}{2}\right]}$$

A similar result may be obtained for the TM_r part. Saddle point integration may be extended to the rainbow and the double glory ray cases with similar results. A general tabulation of the dependence of the scatter amplitude on x is given in Table 1 for each ray contribution. These results correlate with other treatments [3,5,6].

The surface wave contributions may be shown to depend on $x^{-1/3}$. In the geometric optics limit, these are smaller contributions than the ray optics terms and are not considered here.

1. C.T. Tai (1958 Applied Scientific Res. B7, p. 129)
2. J.M.C. Scott (1949 A.E.R.E. Report T/M.30, p.13)
3. H. Inada and M.A. Plonus (1970 IEEE Trans. AP18, pp. 89-99)
4. C.R. Boyer (1959, The Rainbow, Yoseloff Ltd.,p.249)
5. H.M. Nussenzveig (1969 J. Math. Phys. 10, pp.82-176)
6. R.G. Kouyoumjian, L. Peters, D.T. Thomas (1963 IEEE Trans. AP11, p. 699)
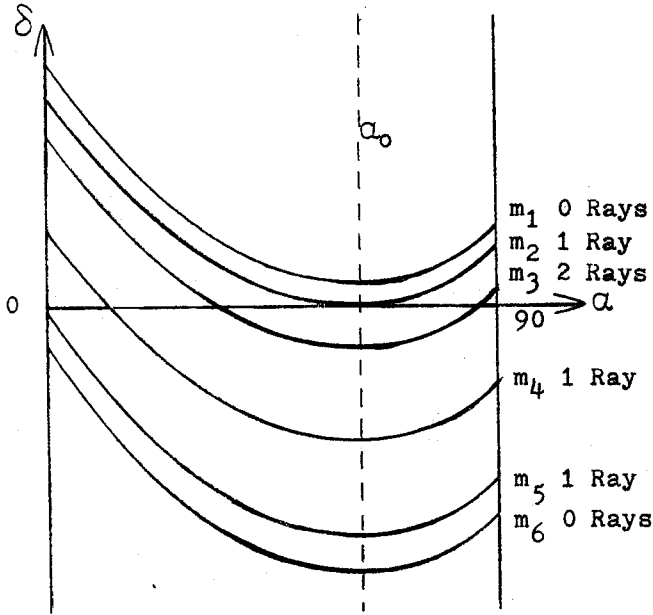
Figure 1. General Behavior of δ With α for Various m.

Table 1. Dependence of the Leading Term on
$x=k_o a$ for Various Rays

Ray Type	E Field Dependence
Front Axial Ray	x^0
Internal Axial Ray $(2N=\frac{p+1}{m+1})$	x^0
Single Glory Ray	$x^{\frac{1}{2}}$
Backscattered Rainbow Ray	$x^{2/3}$

33

Session 12   Antenna Measurements

THE IMPEDANCE OF A CAVITY-BACKED SLOT ANTENNA

Stuart A. Long*
Gordon McKay Laboratory
Harvard University
Cambridge, Massachusetts 02138

H. G. Booker's [1] extention and generalization of Babinet's prin-
ciple to take into account the vector nature of the electromagne-
tic field is often applied to slot antennas. For a slot which is
free to radiate on both sides of a large, thin, highly-conducting
sheet, Babinet's principle can be applied and the resulting imped-
ance of the slot is well approximated by $Z_S = (Z_0/2)^2 Y_D$ where Y_D
is the admittance of the complementary dipole and Z_0 is the wave
impedance of the surrounding medium. In most applications, how-
ever, a unidirectional radiation pattern is desired and some sort
of cavity backing is added. Once this step has been taken the re-
quired symmetry is destroyed, Babinet's principle can no longer be
applied, and the impedance of the cavity-backed slot depends crit-
ically on the size of the cavity.

An experimental investigation has been carried out to determine
the driving-point impedance of a cavity-backed slot antenna as a
function of frequency and the parameters of the cavity. Measure-
ments were first made on a simple slot, open on both sides, which
conformed well with Booker's assumptions. The results obtained
showed good agreement with that predicted through Babinet's prin-
ciple and the known admittance of a linear dipole [2]. A cavity
backing was then added to this slot and a detailed study was made
of the resulting impedances.

The impedance in each case was measured using a voltage and cur-
rent probe technique developed by Scott and Smith [3]. An imaging
plane was used perpendicular to the plane of the slot which bi-
sected the slot lengthwise. Thus the measured impedance $Z_{s/2}$ is
exactly one half the value that would have been measured for the
complete slot.

Figures 1 and 2 show the experimentally measured resistance and
reactance of a cavity-backed slot as a function of a normalized
cavity depth. The cross section of the cavity was chosen so that
only the dominant TE_{10} mode would propagate and the cavity depth
then normalized to the guide wavelength of that mode. The imped-
ance was measured for each of several normalized antenna lengths
$2h/\lambda$, and justification of the normalization of the cavity depth
is shown by the resistance of each curve as it approaches zero
near the value $z_0/\lambda_g = 0.5$.

Figures 3 and 4 show the experimental impedance of the same cavi-
ty-backed slot but as a function of the normalized length $2h/\lambda$ of

34

the antenna. Measurements were made for each of several cavities with different depths including $\lambda_g/4$. Even in this, the most ideal case, the relation to the impedance of the open slot is not a simple proportion.

Figures 5 and 6 show the measured impedance as a function of frequency for several cavity depths. The impedance is noted to display very sharp resonances and is highly dependent on the frequency. A change in frequency results in both a change in the normalized cavity depth and the normalized antenna length.

A mathematical model is being derived to relate the impedance of the cavity-backed slot to that of the open one. This model will take into account both the depth and the cross-sectional size of the cavity and will provide an analytic expression which gives the same impedance behavior as those experimentally measured as a function of the parameters of the cavity and the slot.

References:

1. H. G. Booker (1946 J.I.E.E. (London), 93, Part IIIA, p. 620).

2. R. W. P. King (1971, Tables of Antenna Characteristics, Plenum, p. 46).

3. L. D. Scott and G. S. Smith (1973 IEEE Trans. Ant. Prop., AP-21, July -- to be published).
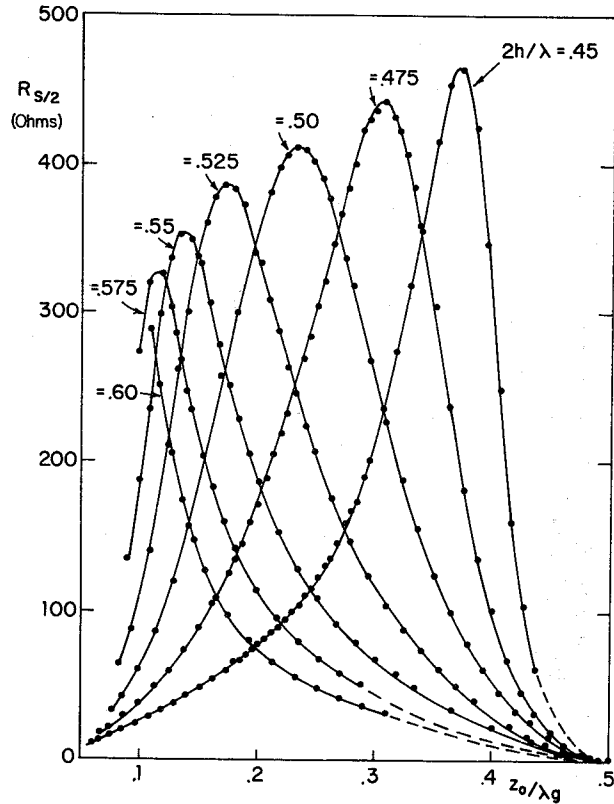
FIG. 1 RESISTANCE VS. NORMALIZED CAVITY DEPTH
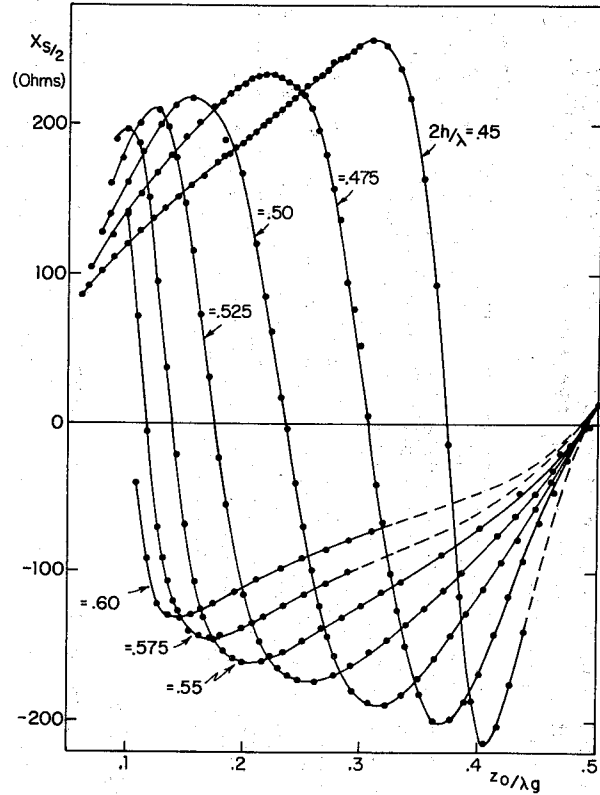
FIG. 2 REACTANCE VS. NORMALIZED CAVITY DEPTH
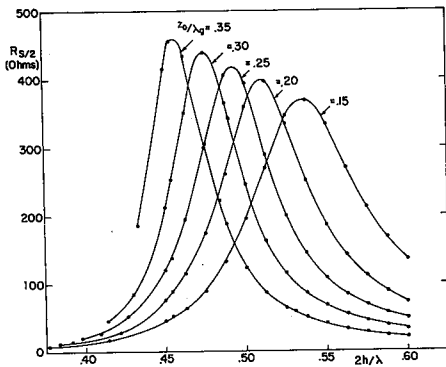
FIG. 3 RESISTANCE VS. NORMALIZED ANTENNA LENGTH
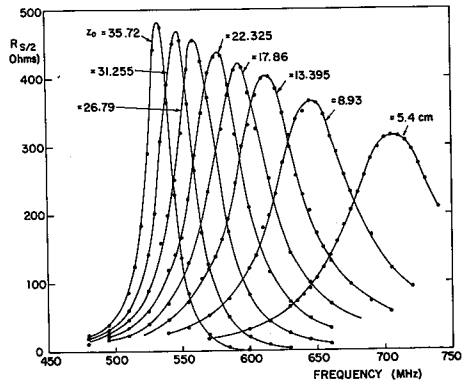
FIG. 5 RESISTANCE OF CAVITY-BACKED SLOT ANTENNA
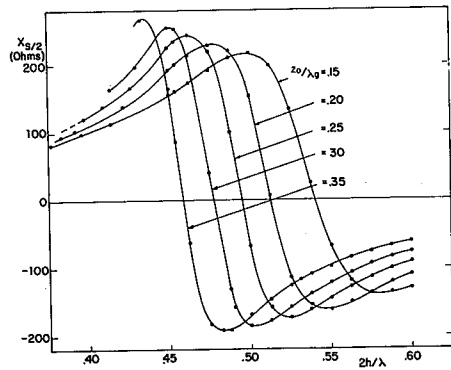
FIG. 4 REACTANCE VS. NORMALIZED ANTENNA LENGTH
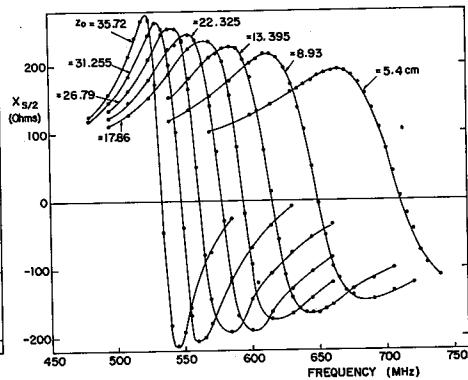
FIG. 6 REACTANCE OF CAVITY-BACKED SLOT ANTENNA

THE VLF PERMITTIVITY OF DEEP ANTARCTIC ICE MEASURED IN-SITU
WITH AN ELECTRICALLY SHORT DIPOLE PROBE

J. C. Rogers
Geophysical Institute, University of Alaska

I. C. Peden
Department of Electrical Engineering
University of Washington, Seattle

This report presents for the first time the results of an in-situ measurement of the dielectric and loss properties of deep Antarctic ice as functions of vertical depth. During the austral summer of 1969-70, a short dipole probe and encapsulated instrumentation were used in the 2164 m deep drill hole at Byrd Station to obtain measured probe admittances at 5 discrete VLF frequencies over the depth range of the drill hole.[1,2,3] Figure 1 summarizes some relevant physical aspects of the measurement.

The input admittance of the fluid-sheathed probe can be related unambiguously to the relative complex permittivity ($\varepsilon^* = \varepsilon'-j\varepsilon''$) of the ice external to the sheath. A simple 3-element equivalent circuit whose frequency-independent capacitor components were experimentally determined provides a means to reduce the data to the desired permittivity parameters of the ice.[1,2] Direct measurements were made down to the 1500 m level, and the subsequent dielectric properties extrapolated to the bottom of the ice sheet. The latter procedure was necessitated by closure of the lower 30% of the drill hole before the experiment could be performed.[3]

Figure 2 illustrates the results at two of the measurement frequencies as functions of depth over the direct measurement range. The imaginary or loss part ε'' of the complex permittivity, is fairly constant over the first 1000 m, departing significantly from this behavior at greater depths. The relationship between the shapes of these curves and the temperature profile measured by Gow et. al. is discussed.[4] Clearly, the dielectric and loss properties of the ice at 2.5 kHz are different from the 10 kHz values.

It is of interest to compare the measured permittivity of the ice sheet with the expected behavior of pure polycrystalline ice at the same frequencies and temperatures. Calculations for pure ice can be based on a Debye relaxation mechanism, and the resulting permittivity presented in the form of a semi-circular Cole-Cole plot; temperature determines the radius of the curve, and frequency the position of individual points at the given temperature.[5] Figure 3 compares calculated values for pure ice at -26.9° with those measured at 150 m where the temperature was the same; similar compari-

sons are reported for other depths. The close relationship between the temperature of the ice and its complex permittivity is apparent from examination of all the measured results.

An extrapolation procedure was worked out for the complex permittivities at greater depths, and justified by projecting the 1350 m values to 1500 m for comparison with measured results; details and an evaluation of the procedure are presented. Figure 4 illustrates the resulting permittivities as functions of depth at 2.5 kHz and compares the real and imaginary parts of ε^* with values calculated for pure polycrystalline ice at the appropriate temperature.

Finally, the new in-situ permittivity data are compared with the effective bulk average values obtained by Peden et. al. from surface measurements of the amplitude and phase of the VLF near-fields surrounding the 34 km dipole antenna formerly in operation near Byrd Station.[6] At any particular VLF frequency, the latter technique resulted in an averaging of the permittivities over the entire vertical profile of the ice sheet in ways that can now be better understood. The drill hole temperature data provide the means to interpret and compare the results of the two measurement techniques in ways that are shown to be consistent.

The complex permittivity parameters resulting from the in-situ measurement at Byrd Station are the most accurate presently available for the ice mass covering the interior of Antarctica. They have important applications to radio science research in the polar regions and will be of interest to glaciologists as well. The technique is well suited to use in the drill holes that result from the removal of glacial ice cores. Comparison of the new values with those resulting from previous work further suggests that the temperature range in deep ice masses may be estimated from surface measurements of the VLF electromagnetic fields.

REFERENCES

1. J. C. Rogers, I. C. Peden (IEEE Transactions on Antennas and Propagation, November, 1973 - forthcoming).
2. J. C. Rogers, I. C. Peden (1972 G-AP International Symposium, 72 CHO 704-7AP, p. 33).
3. I. C. Peden, J. C. Rogers (1971 IEEE Transactions on Geoscience Electronics, GE-9, No. 4, p. 224).
4. A. J. Gow, H. T. Ueda, D. E. Garfield (1968, Science, Vol. 161, p. 1011).
5. S. Evans (1965, Journal of Glaciology, Vol. 5, No. 4, p. 773).
6. I. C. Peden, G. E. Webber, A. S. Chandler (1972 Radio Science 7, No. 6, p. 645).
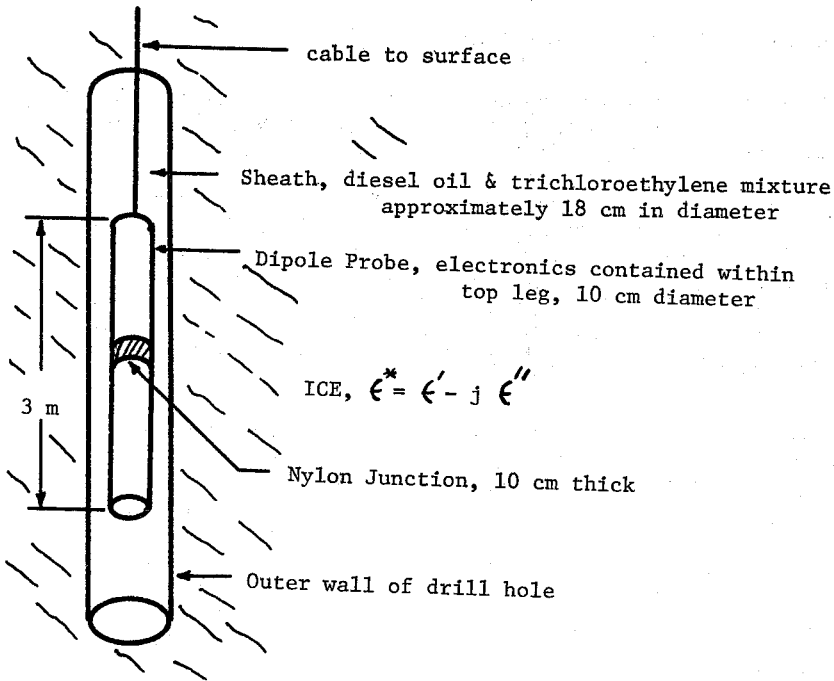
FIGURE 1.   SKETCH OF ELECTRICALLY SHORT DIPOLE WITH FINITE
JUNCTION REGION SURROUNDED BY A CONCENTRIC FLUID SHEATH USED
TO MEASURE THE COMPLEX PERMITTIVITY OF THE SURROUNDING ICE
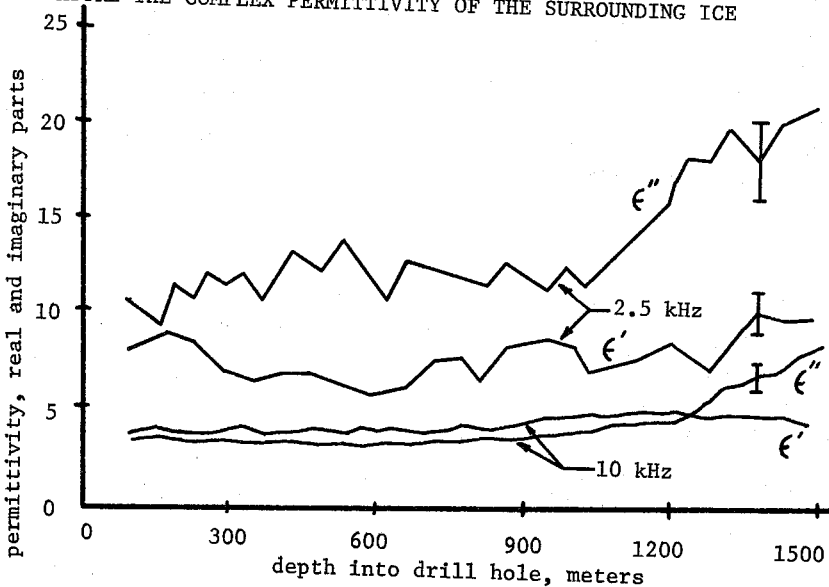
FIGURE 2.   MEASURED REAL AND IMAGINARY PARTS OF COMPLEX PERMITTIVITY
VERSUS DEPTH FOR 10 KHZ AND 2.5 KHZ
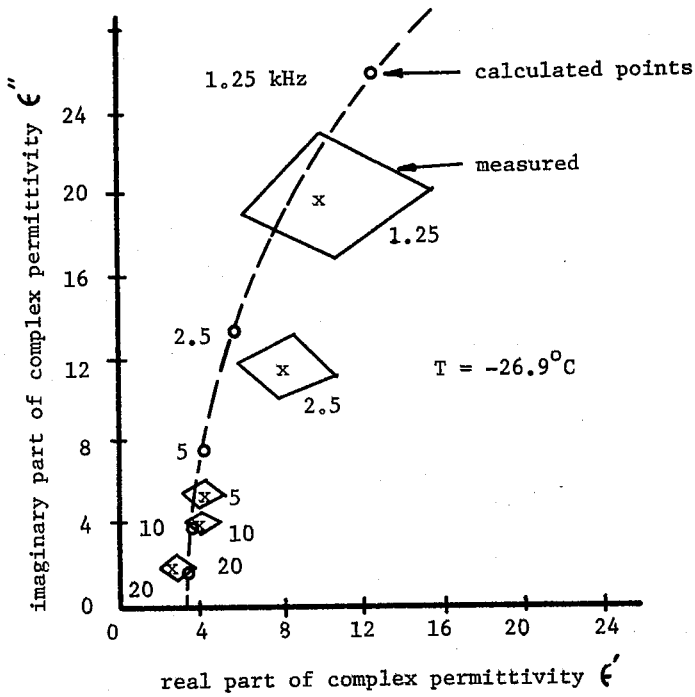
FIGURE 3. MEASURED COLE-COLE PLOT FOR A DEPTH OF 150
METERS BELOW ICE SURFACE
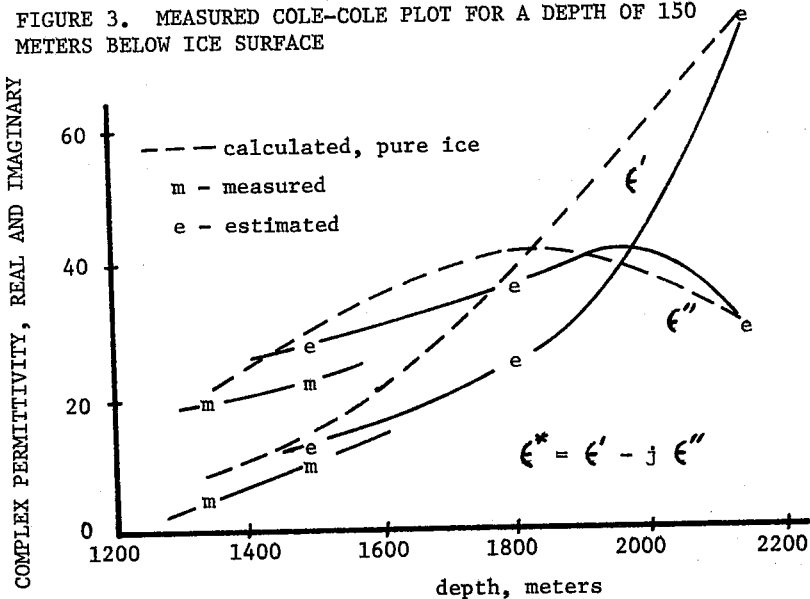
FIGURE 4. COMPLEX PERMITTIVITY AT 2.5 KHZ: MEASURED TO
1500 METERS, PROJECTED TO 2164 METERS

MEASUREMENT OF RF SCATTERING DATA USING A NETWORK ANALYZER

Werner J. Stark
Harry Diamond Laboratories
Washington, D.C.

The theory of scattering of electromagnetic radiation by a conducting body is often described in terms of scattering at the resonant frequencies of the body. This formulation of the theory is not in a convenient form for computing the scattering of an electromagnetic pulse, since in this case one requires the results to the scattering problem over a wide range of frequencies. Such a solution may be difficult to obtain in some cases, and experimental data may be required as an aid in the solution to scattering of an electromagnetic pulse.

Taking an experimental approach one can use either pulsed or continuous wave (CW) techniques. A comparison of the advantages and disadvantages of the two techniques indicates that the CW approach may be best suited for the study of RF scattering problems. The present work consists of an investigation in the application of CW techniques to a simple scattering problem, namely that of the current induced at the center of a thin conductor parallel to a finite conductivity ground plane, illuminated with an RF field whose E-field component is parallel to the conductor. An analytical solution to this problem can be obtained[1,2] for certain geometries and conditions of interaction for the conductor. The experiment was designed so that these conditions were applicable.

A block diagram for the instrumentation is shown in Figure 1. Typical results for the measured and computed induced current are shown in Figure 2. The results show that application of network analyzers to the study of scattering problems can be a very useful technique.

1. J. N. Bombardt (Time-Harmonic Analysis of the Induced Current on a Thin Cylinder Above a Finitely Conducting Half-Space, EMP Interaction Notes, Note 111, June 1972).

2. J. R. Wait (Theory of Wave Propagation Along a Thin Wire Parallel to an Interface, Radio Science, Vol. 7, Number 6, June 1972).

TRANSMITTING
ANTENNA

REFERENCE
ANTENNA

CURRENT
PROBE

| HP 8601A GENERATOR/ SWEEPER | TRANSMITTER AMPLIFIER | | LINEAR AMPLIFIER | LINEAR AMPLIFIER |

VTO

RG 9/U
COAXIAL
CABLES

HP 8407
NETWORK
ANALYZER

REFERENCE

TEST

BRAIDED SHIELD

AMPL.   PHASE

DISPLAY
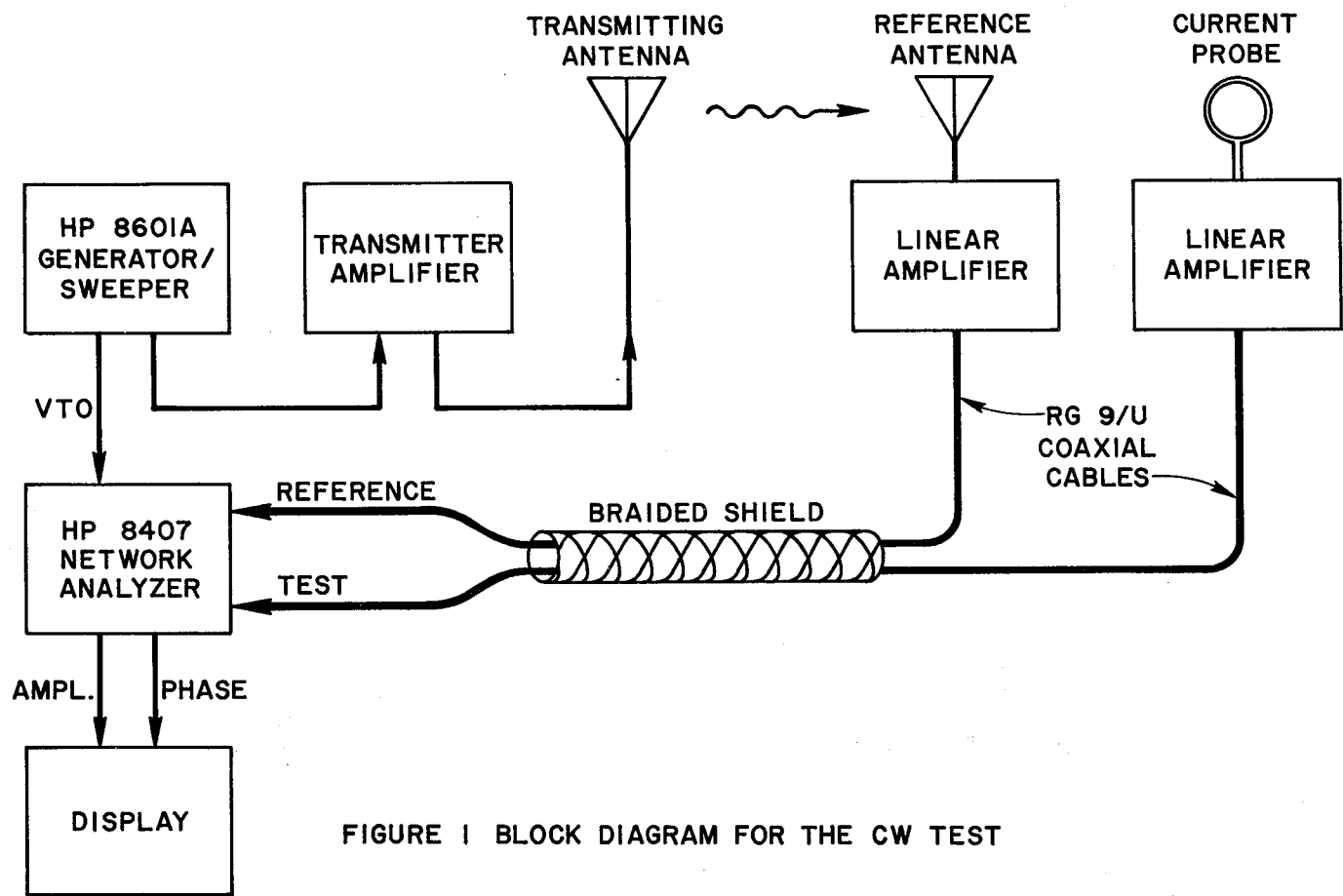
FIGURE I BLOCK DIAGRAM FOR THE CW TEST
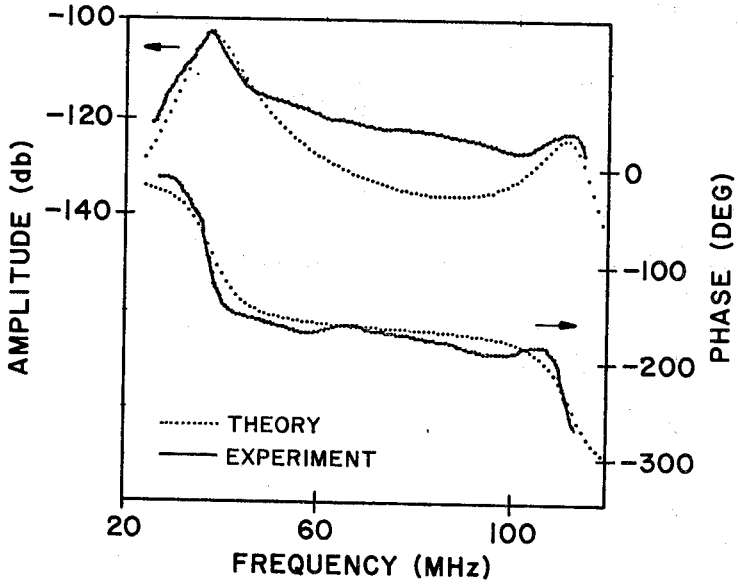
FIGURE 2   FREQUENCY SPECTRUM OF THE CURRENT
AT THE CENTER OF THE CONDUCTOR
RELATIVE TO THE INCIDENT FIELD.

AUTOMATED RADAR CROSS-SECTION MEASUREMENTS

W. B. Weir
L. A. Robinson
D. Parker
J. L. Huber
Stanford Research Institute
Menlo Park, California   94025

INTRODUCTION

A new technique for measuring the radar cross section (RCS) rapidly over wide frequency bands has been developed. The technique is based on the nonconventional use of a Hewlett-Packard automatic network analyzer. This instrument rapidly and accurately measures scattering parameters at discrete frequencies over a wide band and corrects for system errors before presenting the measured results. By incorporating suitable wideband antennas and appropriate calibration targets and techniques, the automatic network analyzer was adapted to make RCS measurements of various targets over an octave at both VHF and at S-band. Targets with RCS values greater than -30 dBsm can be measured. Typically, the background clutter, antenna cross coupling, and system errors in the absence of a target are reduced by the system measurement technique to an equivalent value of -45 dBsm.

MEASUREMENT TECHNIQUE

The RCS measurement technique using the automatic network analyzer may be viewed as an automated form of the two-antenna RCS measurement method.[1] A digital computer is used in the measurement system to control the measurement equipment as well as to perform the data processing. At each discrete frequency for which RCS measurements are to be obtained the system measures the characteristics of the measurement equipment (such as mismatch errors due to reflections from the signal source and the receiver input, errors due to finite isolation between the reference and receiver channels, and the losses and phase deviations of the cables that connect the antennas to the network analyzer). These characteristics are stored in the computer memory and subsequently subtracted from the measured data during data processing. In addition to the system errors, cross coupling between the transmitter and receiver antennas and clutter from fixed obstacles such as supports for the target are measured, saved, and subsequently subtracted from the received target-plus-clutter signal to obtain the back-scattered signal from the target alone. This is equivalent to

the process of balancing a bridge in the absence of a target and then measuring the degree of unbalance in the presence of a target in the conventional two-antenna RCS measurement technique.

The actual value of the target RCS is determined by first measuring, at each discrete frequency, the signal return from a reference target of known RCS. The results are stored and subsequently compared with the signal return from the target of unknown RCS. The reference target used is a sphere. The equations for back-scattering from a sphere as a function of sphere diameter and wavelength, and from which the sphere RCS can be calculated, are programmed in the computer and apply in the Rayleigh, resonance, and optical regions.[2]

Figure 1 shows the overall block diagram of the automated RCS measurement system. The complex values of the parameters measured during the determination of the target RCS are indicated on the figure (n = frequency index).
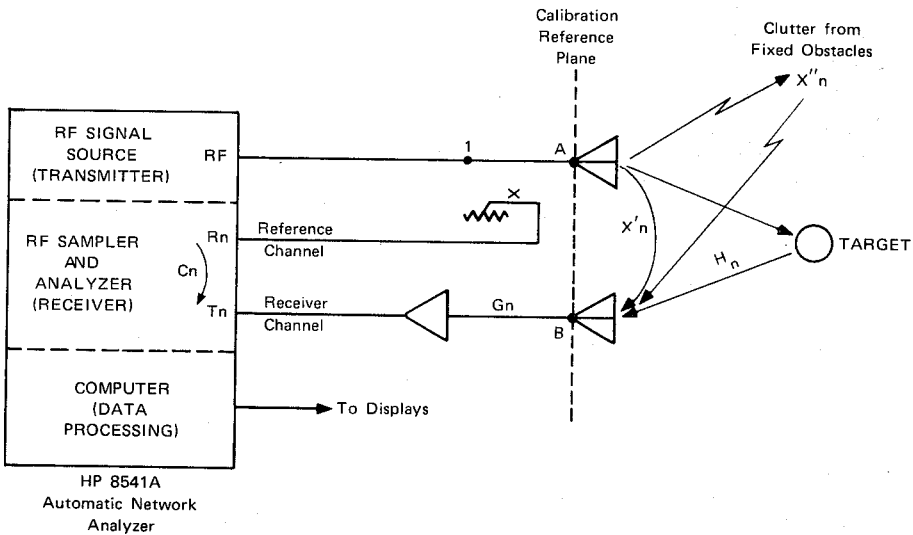
FIGURE 1   AUTOMATED RCS MEASUREMENT SYSTEM

The computer sets the RF signal source sequentially at a number of preselected frequencies and at each frequency the network analyzer measures the complex ratio T_n/R_n for five different sets of measurements. The first two measurements are used to characterize and eliminate the internal cross talk between the transmitting and receiving channels of the analyzer. A third measurement is used to characterize the antenna cross coupling, reflections from the target

supporting structures, and other background clutter in the absence
of a target. This data is stored and later subtracted from the data
obtained with a target. The fourth measurement is of a target
with known RCS (sphere for example) to calibrate the system so
absolute values of RCS can be obtained. The final measurement is
of the unknown target and the RCS is found directly from the
relationship

$$\sigma_{n(t)} = \frac{\left|H_{n(t)}\right|^2}{\left|H_{n(s)}\right|^2} \sigma_{n(s)}$$

where $\sigma_{n(s)}$ is the RCS of the reference target calculated by the
computer; $H_{n(t)}$ is the complex ratio of the received signal at
Port B (Figure 1) to the transmitted signal at Port A with the
unknown target; and $H_{n(s)}$ is a similar ratio for the known target.

MEASURED RESULTS

Measured RCS data in S-band for both a 6-inch and a 12-inch diameter
sphere are shown in Figure 2. For these measurements the 12-inch
sphere was used as a reference target. The measured data points
indicated for the 12-inch sphere were obtained by remeasuring and
processing the signal return from it as if it were an unknown
target. Results for a 20-inch diameter sphere in the VHF range
are shown in Figure 3. Examples of measured data for spheres have
been presented here primarily because the theoretical RCS of spheres
can be calculated and compared with measured data. Results for
other targets in the VHF and S-band ranges for which the theoretical
RCS is not easily calculated will be presented as well as a descrip-
tion of the range used to make these measurements.

Some variations are indicated between the measured and theoretical
data for a 6-inch sphere. These variations would have been signi-
ficantly reduced and the system sensitivity increased if the signal
source of the network analyzer had been frequency stabilized. A
stabilized source was not available at the time the measurements
were obtained.

CONCLUSIONS

A new technique has been developed and reduced to practice for
rapidly making RCS measurements over a wide band in the 100 MHz to
18 GHz region. The bandwidth of any set of measurements is
limited only by the bandwidth of the transmitting and receiving
antennas. The capability of the H-P automatic network analyzer
for measuring the scattering parameters of an electrical network
was extended to measuring scattering parameters of objects in
free space by incorporating two antennas and certain calibration
procedures in the measurement system. Improved sensitivity and
accuracy can be obtained with stabilized systems now available.

Session 12   Antenna Measurements

REFERENCES

1. G. T. Ruck (1970 Radar Cross Section Handbook, Chap. 11,
    p. 893, Plenum Press).

2. T.B.A. Senior (1965 Univ. of Michigan, EE Department Report
    7030-1-7).
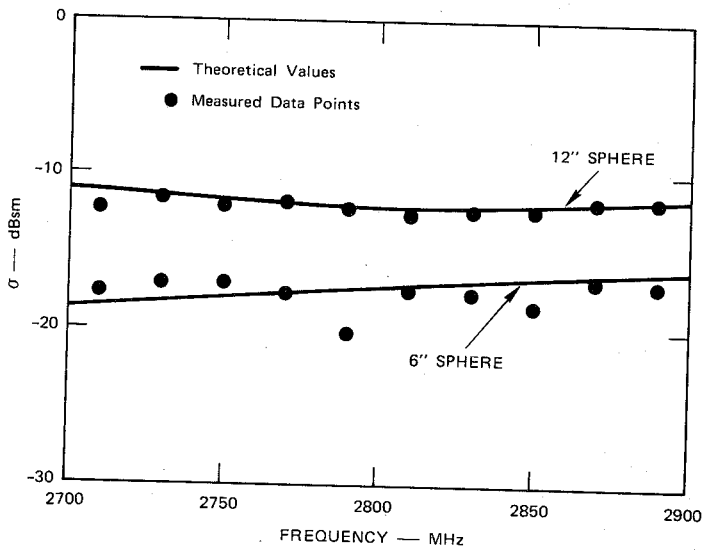
FIGURE 2   MEASURED RCS DATA FOR A 12-inch AND A 6-inch
           SPHERE

           The 12-inch sphere was the reference target.
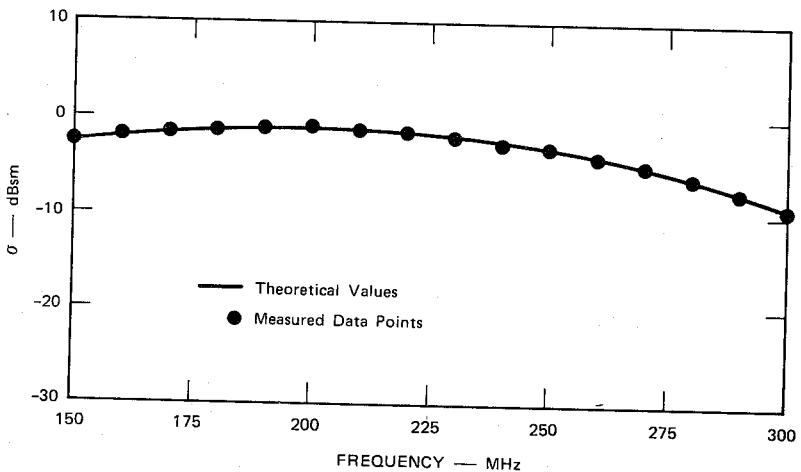
FIGURE 3   MEASURED RCS DATA FOR A 20-inch SPHERE

           The 20-inch sphere was also used as the reference target.

48

MILLIMETER WAVELENGTH RADAR CROSS SECTION MEASUREMENTS

R. B. Dybdal and C. O. Yowell
Antennas and Propagation Department
Electronics Research Laboratory
The Aerospace Corporation

ABSTRACT

Radar cross section (RCS) measurements performed at 93 GHz are reported for flat plate targets and a scaled sphere-cone target. RCS predictions based on common asymptotic methods agree well with measured results for these targets. This frequency range is shown to be useful in making scaled model measurements on targets which are large in terms of wavelengths.

INTRODUCTION

In recent years, millimeter wavelength technology has undergone, considerable progress; however, the number of radar cross section (RCS) measurements performed in this frequency range is limited. The purpose of this paper is to report some measurements of flat plate targets and a scaled model target. These measurements were performed at 93.07 GHz.

The measured RCS values for these targets agree well with results predicted by common asymptotic methods. These measurements indicate that common RCS prediction techniques may be used, at least for the size targets measured. More complex targets are sometimes composed of an aggregate of simple shapes, and thus a phasor sum of returns may be used for an overall RCS estimate. This is particularly true for millimeter wavelength RCS because of the specular nature of the scattering and the inherent separation of scattering centers.

The millimeter wavelength regime is also advantageous in making scaled model measurements on targets whose dimensions are large in terms of wavelengths. The normal far field criteria, when target dimensions are specified in wavelengths, results in a range which is directly proportional to wavelengths. Thus, a higher frequency results in a shorter range requirement. Additionally, the models at the higher frequencies are physically smaller and may be easily constructed and maneuvered.

Session 12 Antenna Measurements

MEASUREMENT FACILITY

The measurements reported here were performed in the
Aerospace Corporation 90-ft, quasi-tapered anechoic chamber.
The reflectivity and background RCS levels of this facility have
been recently reported (Ref. 1). The tiltable rear wall of this
chamber is particularly useful in reducing background RCS levels
at these frequencies. The measurements were made at a 50'
range and the $2D^2/\lambda$ far field criterion limits target dimensions to
6'' for this range. The 6'' dimension corresponds to a 50 wave-
length target.

The electronics for the radar system have been converted from
equipment originally constructed for measuring the atmospheric
phase structure function (Ref. 2). This transmitting and
receiving equipment is phase-locked; the receiver yields a -130
dBm sensitivity. System linearity exceeds 80 dB.

The radar uses a quasi-monostatic antenna system. Two 6'' dia-
meter paraboloids with absorber-lined tunnels are used as
antennas. The mutual coupling between the antennas was meas-
ured and adequate isolation is achieved with only a few inches
separation because of the small wavelength. Since nulling cir-
cuitry is not required to achieve transmitter-receiver isolation,
and with the availability of millimeter wavelength frequency
sweepers, swept frequency measurements could be easily achieved
using a tracking receiver.

RCS MEASUREMENTS

The measured RCS of square and circular disks at 93.07 GHz are
shown in Figs. 1 & 2 respectively. The dimensions of the plates
were chosen to provide peak specular levels of -10 dBsm. These
plates were constructed from available 1/16'' aluminum stock and
no special care was given to dimensional tolerances. These
plates were measured using horizontal polarization, since the
2 lb. test monofilament line used for support has a peak specular
return of -20 dBsm for vertical polarization.

The measured values for the flat plates correspond well with
results predicted from common asymptotic techniques. Calcu-
lations were performed using diffraction formulations (Ufimtsev)
to estimate polarization differences. As expected, polarization
differences become apparent only for low RCS levels. For such
levels, measurement accuracy is compromised by the background
RCS clutter. For more complex targets the response from other
scattering centers fills in the lower levels, too. For these
reasons, simpler physical optics models are applicable for RCS
predictions.

When the target dimensions are large in terms of wavelengths,
target alignment becomes critical. The scattering behavior of
the target in the specular region provides a means of electrically

aligning the target. For the flat plate targets, the ratio of the peak specular return to the peak of the first lobe from the specular should be 13.3 and 17.6 dB for the square (sin X/X distribution) and circular (J_1(X)/X distribution) disks, respectively. These levels provide a convenient means of target alignment.

Scaled model measurements have been illustrated by a sphere-cone target. The model, having a 4" length, a 1/2" nose radius and a 2" base diameter, was measured. The measured result, again using horizontal polarization, was given in Ref. 1. A calculated response, using an approximate physical optics response, is also given in the technical report (Ref. 1) and gives close correspondence with the measured RCS pattern.

CONCLUSIONS

The feasibility of millimeter wavelength RCS measurements has been demonstrated. There are few RCS measurements published for this frequency range so it is established here that, for the size targets measured, common asymptotic RCS predictions correspond well with measured results. This frequency range has also been found useful in making scaled measurements on targets which are large in terms of wavelength.

ACKNOWLEDGMENT

The millimeter wave radar used for these measurements was developed and maintained by R. D. Etcheverry, and the RCS measurements were performed by L. U. Brown.

REFERENCES

1. R. B. Dybdal and C. O. Yowell, "VHF to EHF Performance of a 90-Foot Quasi-Tapered Anechoic Chamber," The Aerospace Corporation, TR-0073(3230-40)-2, 28 December 1972; also IEEE Trans. AP-21, July 1973.

2. R. D. Etcheverry, G. R. Heidbreder, W. A. Johnson, and H. J. Wintroub, "Measurements of Spatial Coherence in 3.2-mm Horizontal Transmission," IEEE Trans. AP-15, 136-141, January 1967.

3. H. E. King, F. I. Shimabukuro and J. L. Wong, "94 Gc Measurement of Microwave Absorbing Material," The Aerospace Corporation, TR-669(6230-46)-5, March 1966.
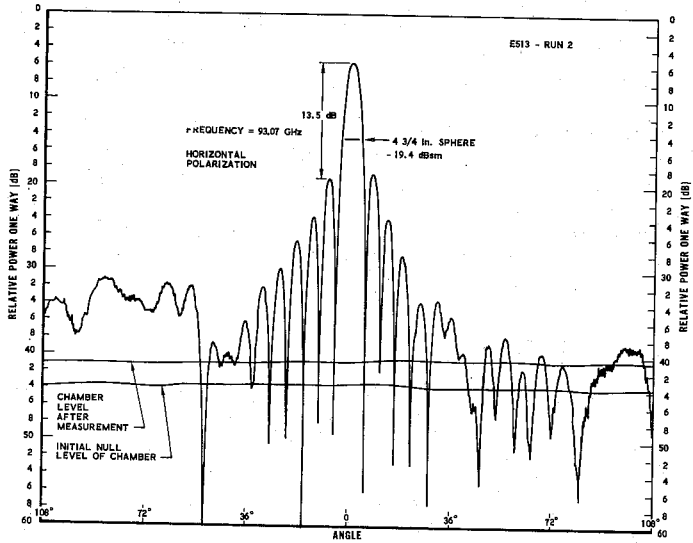
Fig. 1 RCS Of - 10 dBsm (0.667" Side) Square Plate
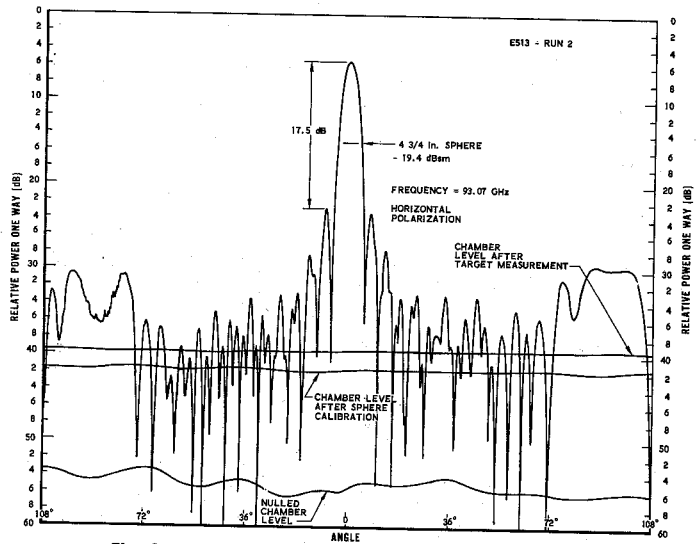
Fig. 2 RCS Of -10 dBsm (0.75" diam) Circular Disk

BROADBAND CORRELATION SWEEP INTERFEROMETER

K. HILTY, STUDENT MEMBER, IEEE

During the last few years the Microwave Laboratory, Swiss
Federal Institute of Technology, Zurich has been planning
a sweep interferometer system for the observation of the
radiosun. This system will allow to localize and trace
radiobursts over a frequencyband from 100-1000 MHz. The
angular resolution is 1 min of arc in the zenith.

For one dimensional observation with a fan beam the fol-
lowing system (Fig.1) is proposed.
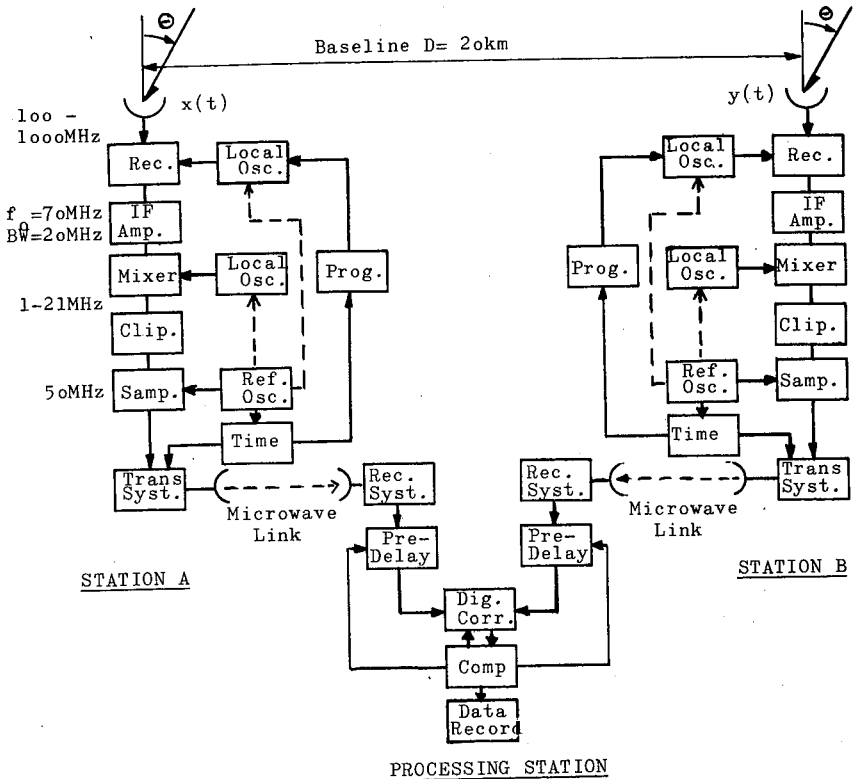
Fig.1 Broadband Correlation Sweep Interferometer

It consists of two identical receiving stations A and B,
20 km apart, and a central processing station. The pa-
noramic receiver (1) in the front end of each station,
followed by an i-f amplifier with a bandwidth of 20 MHz,
is the crucial component. A second mixer transfers this

The author is with the Microwave Laboratory, Swiss
Federal Institute of Technology, Zurich, Switzerland.

Figure 1 shows a principle plane cut of the difference channel.
The solid line is the recorded far field plot and the X's are the
computed far field points determined from near field measurements.
The results are seen to be in excellent agreement. It should be
emphasized that no fitting of data has been made (other than nor-
malization of the peak of the main beam) and the results are of
completely independent measurements conducted several weeks apart.

The near field technique yields a set of far field points which
are normally drawn on a Calcomp plotter as point to point straight
line segments. Figure 2 shows this Calcomp output superposed
on the sum channel far field data. Here the point-to-point nature
of the near field result is noticeable near some sidelobe nulls.
This feature, if bothersome to the observer, can be corrected by
further data filtering. By reducing the angular coverage the reso-
lution of any region of the pattern can be improved.

Figure 3 shows a detailed plot of the difference pattern null.
Here the angular coverage has been reduced to $\pm 2.5°$. It should be
emphasized that no fitting of the angular settings was made. The
zero azimuth angle is established by an independent optical bore-
sighting on both the far field and the near field using a refe-
rence mirror. Note that the near field result and the far field
result indicate that the antenna difference pattern null occurs
some $.05°$ to the right of the optical boresight, and the near and
far field results agree to within 0.1 milliradian.

Off-axis pattern cuts were also measured on the far field range
and obtained from the near field data. Figure 4 shows typical
results for the sum channel. These results are all the more
striking when it is remembered that in cuts taken off the prin-
ciple axis small angular inaccuracies can lead to relatively
large errors when data points fall on the steep slopes of lobes.

The results reported here prove that all parameters of the far
field pattern of a high performance antenna can be measured as
accurately on a near field range as on a conventional far field
range. The great efficiency with which data is collected on a
near field range offers a marked reduction in the costs (both
temporal and fiscal) of pattern determination. Added benefits
accrue from the fact that the antenna need not be moved to remote
and often physically inconvenient far field mount, but can
instead be tested in a laboratory or in the production facility.
The vagarities of weather conditions that have so often plagued
far field measurements are no longer a problem.

Even greater economies of data recording should be possible on
electronically steerable phased array antennas. In its present
mode of operation the speed of data taking is limited by the time
required to mechanically position the near field probe. An elec-
tronically steerable antenna could be cycled through a number of
beam positions as the probe traverses the distance between data
points thus recording in a single run up to ten antenna patterns
simultaneously.
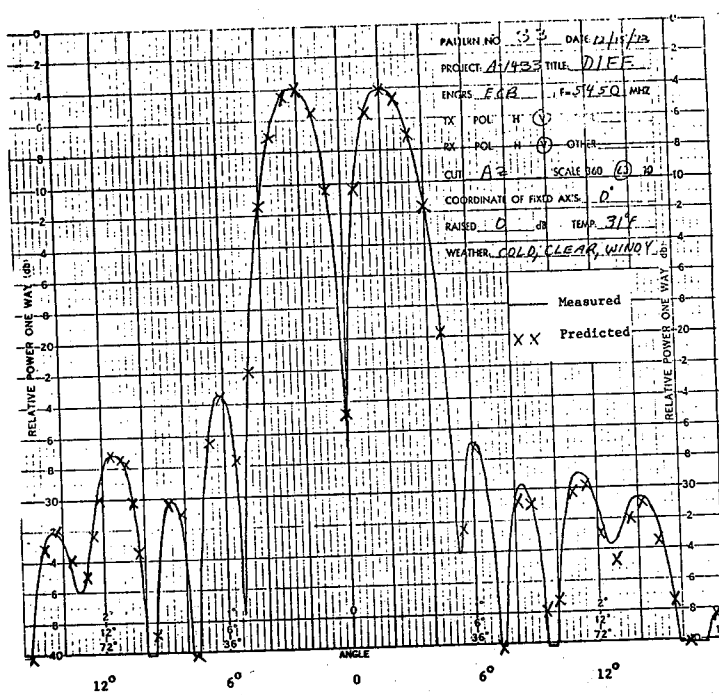
Figure 1. Comparison of measured far-field pattern
predicted from near-field measurements,
monopulse difference pattern.
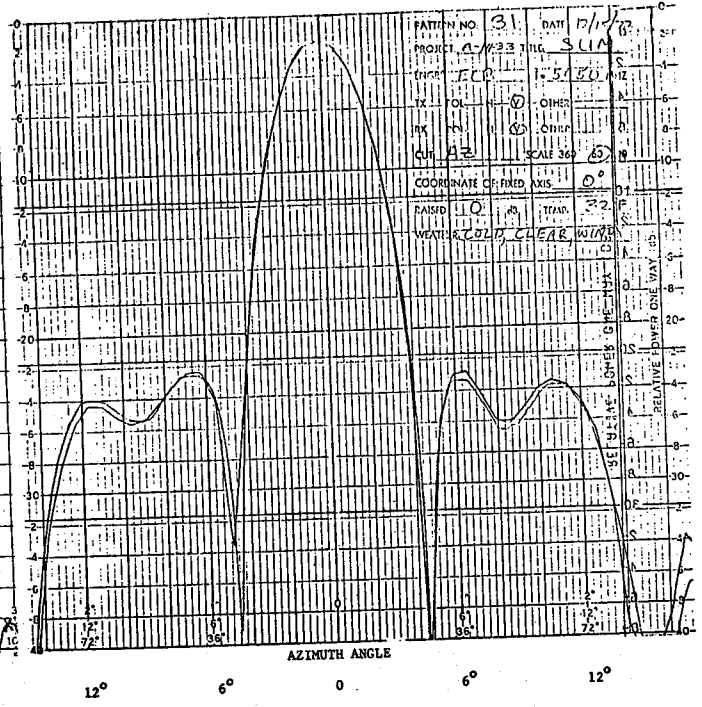
Figure 2. Comparison of measured far-field pattern
and far-field pattern predicted from
near-field measurements, monopulse sum
pattern.

Session 12 Antenna Measurements

The near field technique has the distinct advantage of offering
an almost unlimited degree of flexibility in data format. Once
the near field results are stored on magnetic tape the far field
output is obtainable at any future time in any format desired.
The presentation can take the form of pattern cuts as already
shown, three dimensional plots, or tabular summaries. The engineer
could alternatively exercise a program that printed out the loca-
tion (in azimuth and elevation) of all sidelobes above some
selected level.

It is strongly felt that the accuracy, economy, and flexibility
of the near field technique in measuring far field antenna pat-
terns will make it increasingly popular as an acceptable proce-
dure at all levels of pattern determination.
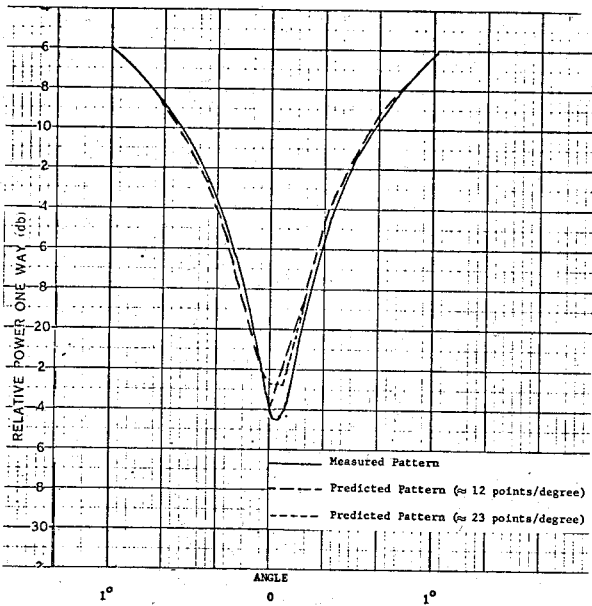
Figure 3. Comparison of measured and pre-
dicted difference pattern.
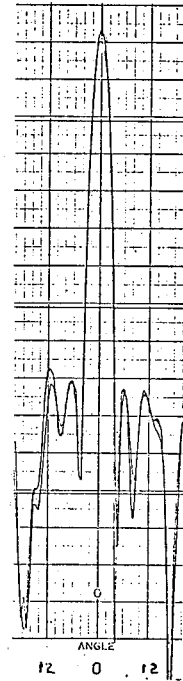
Figure 4. Off-axis cut
(2°).

A HOLOGRAPHIC METHOD FOR DETERMINING ANTENNA NEARFIELD DISTRIBUTIONS FROM PHASE AND INTENSITY MEASUREMENTS ON A SPHERICAL SURFACE

E. L. Rope, R. A. Hayward, and G. Tricoles
General Dynamics Electronics Division, P. O. Box 81127,
San Diego, California 92138

A holographic method[1] for determining fields near transmitting antennas is described. The method utilizes phase and intensity values that are measured on a spherical surface, centered at the antenna. The nearfield distribution is then computed from the measured data by evaluating the Kirchoff integral formula,[2] for each rectangular field component,[3] over the measurement surface, with the antenna absent. The amplitudes of the fields are determined from the measured intensity on the assumption that the fields are tangential to the measurement surface and that the tangential electric components are related to the tangential components by the intrinsic impedance. The integrands are the complex conjugates of the fields determined from the measurements; this choice generates a convergent reconstructed wave, a real image of the nearfield distribution.[4]

To evaluate the accuracy of the method, the farfield radiation patterns of the antennas were also measured and compared with patterns that were computed from the reconstructed nearfield distributions. In addition, the fields near the antennas were measured. Several nearfield probes were utilized, and although the measured data agreed generally with the computed nearfields, the measured results depended on the nature of the probe antenna. Therefore the comparison of measured and computed farfield patterns seems the more reliable test.

Several parameters were varied to evaluate the effects of approximations and of the procedures for measurement and calculation. For example, measurements were made on several circles with distinct radii ranging from the region of Fresnel diffraction to that for Fraunhofer diffraction. The reflections by the probe into the transmitting antennas were measured to establish a criterion for minimum radius. Data were measured with four distinct probes. The extent of the measurement surface was varied, as were sampling intervals.

Surface integration was compared with integration on a circu-
lar path. When a surface integral is done, the computed near-
field distribution spans an area, but, whe the integral is on
an arc, the nearfield is calculated on a line.

Some typical results are shown in Figures 1 and 2. In addi-
tional calculations for two distinct excitation conditions, we
found the intensities at the computed beam peaks agreed with
those measured. That is, normalization was preserved.
Measurements were made for a transmitting antenna that was
an array of four, reduced-height, rectangular waveguides.
The array length was 2.2 wavelengths in the E-plane, with the
apertures spaced by half the free space wavelength, which was
1.875 cm; see Figure 2. The array was connected through a
corporate feed to the source, with phase shifters, attenuators,
and tuning devices for each element. Several excitation con-
ditions were considered by attenuating various numbers of
elements. These cases were: all four elements radiating;
two distinct pairs radiating; and a single element radiating.
In addition, a single element radiated when a small ground
plane covered the remaining three elements; see Figure 1.

The method is contrasted with earlier work. For scalar,
acoustic waves, Napier and Bates formed holograms with a
radiated reference beam, measured intensity fringes, and
computed nearfield phase and amplitude for a line distribu-
tion that represented the radiating source, which has aperture
diameter four wavelengths.[5] The method is contrasted with
work of Ransom and Mittra, who numerically analyzed a method
for locating defective elements in phased arrays.[6] Intensity
distributions near small arrays have been formed in optical
reconstructions[7] and by electronic spectrum analysis of
spatial interference fringes.[8]

REFERENCES

1. D. Gabor, Nature 161, p. 777 (1948).
2. S. Silver, Microwave Antenna Theory and Design, McGraw Hill, p. 164.
3. J. R. Wait, IEEE Trans. Vol. E-13, p. 98 (1970).
4. H. M. Smith, Principles of Holography, Wiley-Interscience.
5. P. J. Napier and R. H. T. Baks, Int. J. Engng. Sci. 9, pp. 1193-1208 (1971).
6. P. L. Ransom and R. Mittra, Proc. IEEE 59, pp. 1029-1030 (1971).
7. E. L. Rope and G. Tricoles, Digest of 1969 IEEE Conference on Laser Engineering and Applications. p. 9 (1969) IEEE Catalog No. 69 C 27.
8. E. L. Rope and G. Tricoles, Proceedings of Array Antenna Conference, U. S. Naval Electronics Laboratory Center 7D 155 (1972).
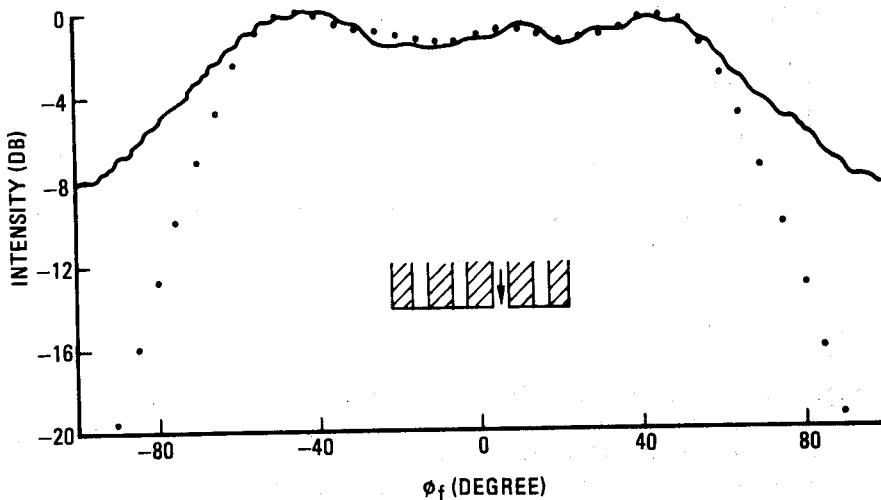
Figure 1. E-plane, farfield pattern of array with one element radiating and the others covered to form a finite ground plane. The curve represents measured values and the dots represent computations that utilize reconstructed nearfields.
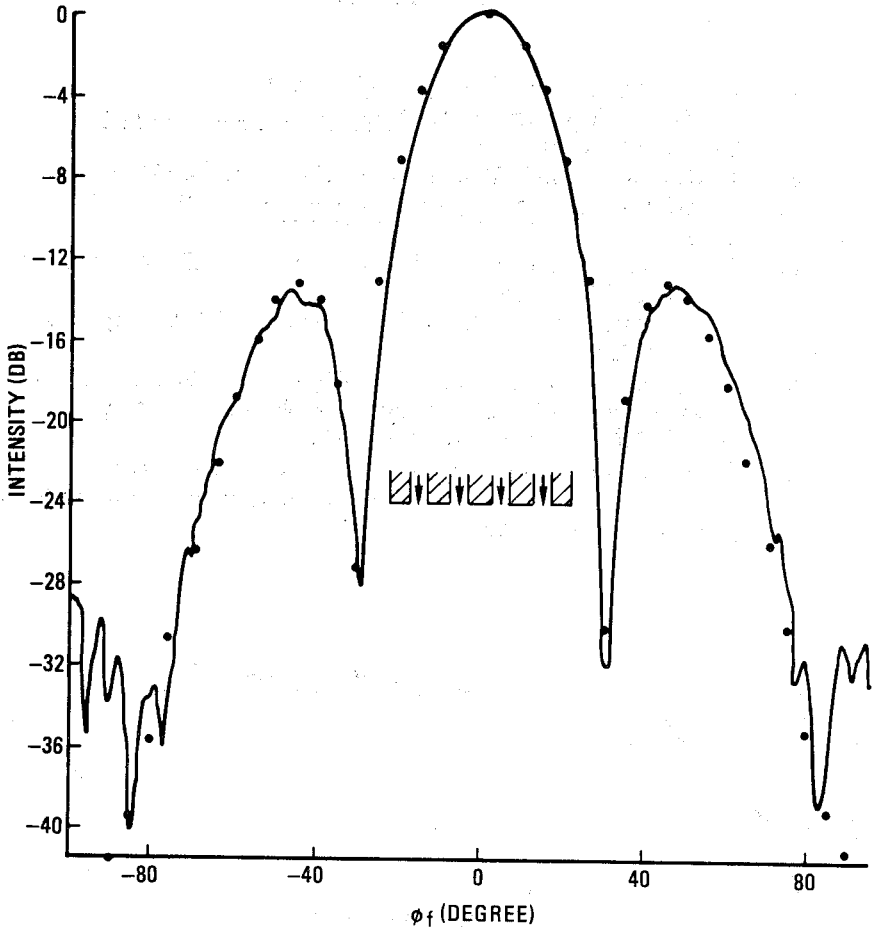
Figure 2.   E-plane, farfield pattern of four element array, width
2.2 wavelength. Frequency 16.00 GHz. All four elements
were excited equally and in-phase. The curve represents mea-
sured value, and the dots represent computations that utilize
reconstructed nearfields. The inset diagram shows metallic
walls as shaded regions.

NUMERICAL DIFFICULTIES ASSOCIATED WITH INTEGRO-DIFFERENTIAL EQUATIONS FOR HOLLOW CYLINDRICAL STRUCTURES*

W. A. Davis

Electromagnetics Laboratory
University of Illinois
Urbana, Illinois 61801

It can be shown that the E-equation formulation of the problem of plane wave scattering by a finite hollow cylinder gives rise to a pair of coupled integral equations for the surface current harmonics with $e^{j\phi}$ variation. The equations are

$$E_\phi^{inc}(z) = \int_z K_1(z,z') \, J_\phi(z') - (d/dz) \int_z K_2(z,z') \, J_z(z') \, dz' \quad (1)$$

$$E_z^{inc}(z) = [k^2 + (d/dz)^2] \int_z K_3(z,z') \, J_z(z') \, dz'$$

$$\quad (2)$$

$$+ (d/dz) \int_z K_2(z,z') \, J_\phi(z') \, dz'$$

The numerical solution of the above equations has been investigated by the author and it has been discovered that the conventional moment method of solution of these equations is plagued by numerical error propagation and often leads to erroneous results. The cause of this difficulty is traced to the numerical derivative of the coupling terms in (1) and (2). It has been found that the results for the computed currents J_z and J_ϕ are strongly dependent on how these derivatives are numerically interpreted. The paper describes a method of circumventing this problem by working with two new equations, one of which has an uncoupled form. For normal incidence, the results obtained by using the new equation have been compared with those reported by Kao (1970), who used a transform technique, and good agreement has been found. The paper shows that the new uncoupled equations are also stable for other angles of incidence, including axial and near-axial cases. Finally, the paper discusses other integro-differential equations for thin structures that are susceptible to numerical difficulties and includes suggestions for alleviating these problems.

1. C. C. Kao (1970 Radio Science 5, p. 617).

SOME WEAKNESSES OF DELTA FUNCTION TESTING
IN METHOD OF MOMENTS SOLUTIONS TO POCKLINGTON-TYPE MODELS
OF THIN-WIRE STRUCTURES

L. Wilson Pearson
Naval Weapons Laboratory
Dahlgren, Virginia 22448

and

Chalmers M. Butler
Department of Electrical Engineering
University of Mississippi
University, Mississippi 38677

INTRODUCTION

The subsectional collocation particularization of the method
of moments, as suggested by Harrington [1], has been used by many
workers with several forms for the basis variation over the in-
terval of the pulse. Notable forms are flat-topped pulses, tri-
angular pulses, and piecewise-sinusoidal pulses [2,3]. Further,
Richmond has used piecewise sinusoidal functions in his "reaction
matching" technique [4]. This corresponds to Galerkin's method
with piecewise sinusoidal basis set.

The present paper reports results obtained when an attempt
was made to solve an array of parallel linear elements using
piecewise sinusoidal bases and collocation testing in the method
of moments. The formulation used is that of coupled Pocklington
integral equations with flat end caps on the elements accounted
for by way of the quasi-static formulation given by Taylor and
Wilton [3]. The feed to the array is an annular "frill" of
magnetic current after Tsai [5]. Thus, the equations solved cor-
respond to an array of monopoles above a conducting ground with
one or more of the elements fed through a coaxial aperture in the
ground. Attention is restricted for the purposes of this paper
to the case of a driven element and a single parasitic element as
shown in Figure 1. Details of the solution technique are given
in references [3] and [6].

SAMPLING OF FEED FIELD FOR THE POCKLINGTON MODEL

The highly-peaked nature of the feed to the driven element
of an antenna array makes it difficult for point-matching to
adequately sample the integral equation in the feed region.
Figure 2a shows amplitudes of current distribution solutions on
an array comprising quarter-wave monopoles. The number of bases
on the two elements is varied in tandem. Figure 2c gives $|I(0)|$
for each solution as a function of $\Delta z = h/N-1$. Current amplitude
is seen to be approximately proportional to Δz and hence the
location of the second match point on the element. Figure 2b

explains this behavior. It gives the magnitude of the feed field
in the vicinity of the feed. The dashed lines connect the first
match point value at z = 0 with the second match point value at
z = Δz. Clearly, the collocation solution cannot distinguish be-
tween a feed distribution which would follow the dashed line cor-
responding to the value of N and the actual feed distribution.
The magnitude of the current is proportional to the integral of
E^{feed} w.r.t.z and hence the approximate proportionality to Δz is
simply the variation in the area under the triangles formed by
the dashed lines in Figure 2b. The triangles represent the ef-
fective feed field as seen by the collocation solution.

Figure 3 shows the amplitude of current distribution so-
lutions for an array similar to the one for Figure 2 but with the
feed diameter ten times that of the element diameter. This feed
produces a field which is more slowly varying with z and that it
is adequately sampled is seen from the match points located in
Figure 3b. The adequate sampling yields the well converging cur-
rent solutions given in Figure 3a. The number of bases on the
parasite is six for this example. No appreciable change in the
solutions is seen if this value is taken as four.

The validity of solutions derived for resonant length ele-
ments where the feed is adequately sampled is established through
a comparison with the work of King [8] as given in Figure 4.

CONVERGENCE IN THE PRESENCE OF NON-RESONANT LENGTH ELEMENTS

Figure 5 demonstrates the rapid convergence as a function of
the number of bases on the parasite. The N_D value used is short
of convergence in terms of feed sampling. Feed sampling effects
are consistent, nevertheless, and the value of thirty is com-
putationally efficient in the program used.

Figure 6 gives the current solutions for an array which
is identical save for a shortened parasitic element. The rapid
convergence of the parasite current present for the resonant ele-
ment is seen to vanish for the non-resonant element case. The
reason lies in the behavior of the axial electric field scattered
from the parasite as given qualitatively in Figure 7. It is seen
that the scattered field is highly peaked at the breakpoint be-
tween pulses, and this is precisely where the match-points must
lie in the collocation solution. Hence, the collocation testing
does not adequately represent the average scattered field and an
intolerably high error field results. Table 1 gives an average
value for E^{err} as a function of N_p for the examples of Figures 5
and 6. The error for the non-resonant case is seen to vary
strongly with N_p while the error remains low for the resonant
case. The variation in the error field with N_p is due to the
variation in "ripple" amplitude in the scattered field as the
slope discontinuity between pulses changes with Δz.

Figure 8 gives the average ripple of the scattered field as

a function of element length with Δz held constant in terms of wavelength. It is seen that the rippled behavior of the scattered field is minimum at h = λ/4 as one would expect. This minimum occurs because the sinusoidal form for the pulse tops in the bases is nearly exact on a resonant element and the slop discontinuities between pulses are minimized for the resonant element.

CONCLUSIONS

Slope discontinuities between basis pulses in a subsectional technique can cause scattered field anomolies which result in poor convergence of the solution. Potential remedies lie either in using some average means of testing such as the Galerkin method which Richmond has shown to be satisfactory or in using a pulse top function which allows the derivative of the current distribution to be continuous at breakpoints.

Feed sampling considerations also limit the utility of collocation solutions to thin-wire structures. A potential remedy lies in using mixed testing functions comprising a distributed function over the feed region and delta functions over the remainder of the structure. The difficulty is circumvented through the use of a Hallen-type integral equation formulation.

REFERENCES

1. R.F. Harrington, Field Computation by the Method of Moments, McMillan, 1968.
2. C.M. Butler (1972 Spring URSI Proceedings, p. 123.)
3. C.D. Taylor and D.R. Wilton (1971 IEEE Trans. Ant. and Prop., AP-20, p. 772.)
4. J.H. Richmond and N.H. Geary (1970 IEEE Trans. Ant. and Prop., AP-18, p. 414.)
5. L.L. Tsai (1972 IEEE Trans. Ant. and Prop., AP-20, p. 115.) See also C.M. Butler and L.L. Tsai (1973 IEEE Trans. Ant. and Prop., AP-21, p. 115.)
6. L.W. Pearson, "Two Method of Moments Solution Techniques for the Planar Dipole Array Problem," M.S. Thesis, U. of Miss., Ch. III.

Non-resonant Case			Resonant Case	
N_p	ε_p		N_p	ε_p
10	0.117		2	0.071
15	0.096		4	0.051
20	0.078		6	0.044
25	0.060		8	0.041
30	0.038			
35	—			

Table 1. Average Error Field Compared for Resonant and Non-Resonant Cases

CONFIGURATION OF THE STUDY ARRAY
Figure 1

CONVERGENCE OF RESONANT PAIR
SOLUTION WITH $N_D=30$ AND N_P VARIED
Figure 5

CONVERGENCE OF RESONANT PAIR
SOLUTION WITH $N_D= N_P$
Figure 2

CONVERGENCE OF NON-RESONANT
PAIR SOLUTION FOR $N_D=30$ AND N_P VARIED
Figure 6

CONVERGENCE OF RESONANT PAIR
WITH OVERSIZED FEED SOLUTION
Figure 3

QUALITATIVE PLOT OF FIELDS
INTERACTING AT PARASITE AXIS
Figure 7

COMPARISON OF SOLUTIONS USING PRESENT THEORY
AND FIRST ORDER KING-MIDDLETON THEORY
Figure 4

AVERAGE RIPPLE AS A FUNCTION OF
PARASITE LENGTH
Figure 8

69

APPROXIMATION OF THE SOMMERFELD'S INTEGRAL FOR FAST CONVERGENCE

W. C. Kuo and K. K. Mei
Department of Electrical Engineering and Computer Sciences
and the Electronics Research Laboratory
University of California, Berkeley, California 94720

Introduction:

The Sommerfeld's integral for a horizontal dipole over the ground and observation point in the ground is given by, (only horizontal component is considered here)[1]

$$\Pi_{xE} = -\frac{2}{\varepsilon} \int_0^\infty J_0(\mu r) \, e^{\mu_E z - \mu h} \frac{\lambda \, d\lambda}{\mu_E + \mu} \tag{1}$$

where

$$z < 0, \quad \mu_E = \sqrt{\lambda^2 - k_E^2} \quad, \text{ and } \quad \mu_0 = \sqrt{\lambda^2 - k^2}$$

The approximation for the integral for both the source and observation point above the ground is done essentially by approximating μ_E by $jk\sqrt{\varepsilon}$.[2,3] The same approach, however, cannot be repeated for Eq. (1).

Expansion and Interpolation:

In Eq. (1) we realize that the contribution of the integral comes mainly from the integral for $\lambda < k$, since the term $e^{-\mu h}$ decays for $\lambda < k$. It is therefore possible to approximate the term $e^{\mu_E z}$ for $\lambda < k$ by its Taylor's expansion

$$e^{\mu_E z} \simeq e^{j\sqrt{k_E^2 - k^2}\, z} \left(1 + \frac{z}{j\sqrt{k_E^2 - k^2}} \frac{\mu^2}{2!} \right) \tag{2}$$

Unfortunately the above approximation grows quadratically as λ increases while the left hand side of Eq. (2) is actually a decaying function. Furthermore, it grows rather rapidly before the $e^{-\mu h}$ is able to suppress the integrand and thus contributes to the error of integration. An improvement of Eq. (2) is to reapproximate by

$$e^{\mu_E z} = e^{j\sqrt{k_E^2 - k^2}\, z} \left(1 + \frac{z}{j\sqrt{k_E^2 - k^2}} \frac{\mu^2}{2} \right) + e^{z_0 \mu} \left(1 + z_0 \mu + \frac{(z_0 \mu)^2}{2} \right) \tag{3}$$

where we have add to Eq. (2) a term $e^{z_0 \mu}$ and subtract its second order Taylor's expansion. In Eq. (3) z_0 is chosen such that $\dfrac{(z_0 \mu)^2}{2}$ is identical to $\exp(j\sqrt{k_E^2 - k^2}\ z)[z\mu^2/(j2\sqrt{k_E^2 - k^2})]$ to that the total expansion is now only of linear growth. There are considerable improvement by using this technique.

Further improvement may be obtained if we use curve-fitting technique. Retaining $e^{z_0 \mu}$ as one of the interpolating function,

$$e^{\mu_E z z} = a_0 e^{z_0 \mu} + a_1 + a_2 \mu + a_3 \mu^2 \tag{4}$$

The coefficients are found by enforcing Eq. (4) at four points, namely, $\lambda = \lambda_0$, λ_1, λ_2, and λ_3. The choice of λ_i's depends on k, k_E, and z.

With the approximation of Eq. (4), we are able to transform Eq. (1) into

$$\Pi_{xE} = \frac{2}{\varepsilon} [a_0 I_z + a_1 I_0 + a_2 I_1 + a_3 I_2] \tag{5}$$

where

$$I_z = -\int_0^\infty J_0(\lambda r)\ e^{-\mu(h - z_0)}\ \frac{\lambda\ d\lambda}{jk\sqrt{\varepsilon_1^0 + \mu}} \tag{6}$$

$$I_0 = -\int_0^\infty J_0(\lambda r)\ e^{-\mu h}\ \frac{\lambda\ d\lambda}{jk\sqrt{\varepsilon_1^0 + \mu}} \tag{7}$$

$$I_1 = -\ \frac{\partial I_0}{\partial h} \tag{8}$$

$$I_2 = \frac{\partial^2 I_0}{\partial h^2} \tag{9}$$

By a similar procedure as that for z above the ground, I_0 is reduced to:

$$I_0 = \frac{e^{-jkR''}}{R''} + jk\sqrt{\varepsilon_1^0}\ e^{jk\sqrt{\varepsilon_1^0}\ h} \int_{h - j\infty}^h \frac{e^{-jk\sqrt{\varepsilon_1^0}\ \xi}}{R_\xi''}\ e^{-jkR_\xi''}\ d_\xi \tag{10}$$

where $R'' = \sqrt{r^2 + h^2}$ and $R_\xi'' = \sqrt{r^2 + \xi^2}$. From Eqs. (8) and (9), I_1, I_2 are easily obtained. I_z is obtained by replacing h in Eq. (10) with (h-z).

Some results of Eq. (5) are compared with those calculated from exact Sommerfeld's integral, Eq. (1), and from plane wave approximation. These comparisons are shown in Figs. 1 to 3.

References:
1.A.Sommerfeld(Partial Differential Equation in Physics,Academic

Press,N.Y.,1964).
2.W.C. Kuo and K.K. Mei(Horizontal Array over a Lossy Ground,The
    1972 USNC/URSI-IEEE Spring Meeting,Washington,D.C.,April 13-
    15,1972).
3.W.C. Kuo and K.K. Mei(ERL Report,Electronics Research Lab.,U.C.
    Berkeley,Report No. ERL-71-4,Dec.1971).
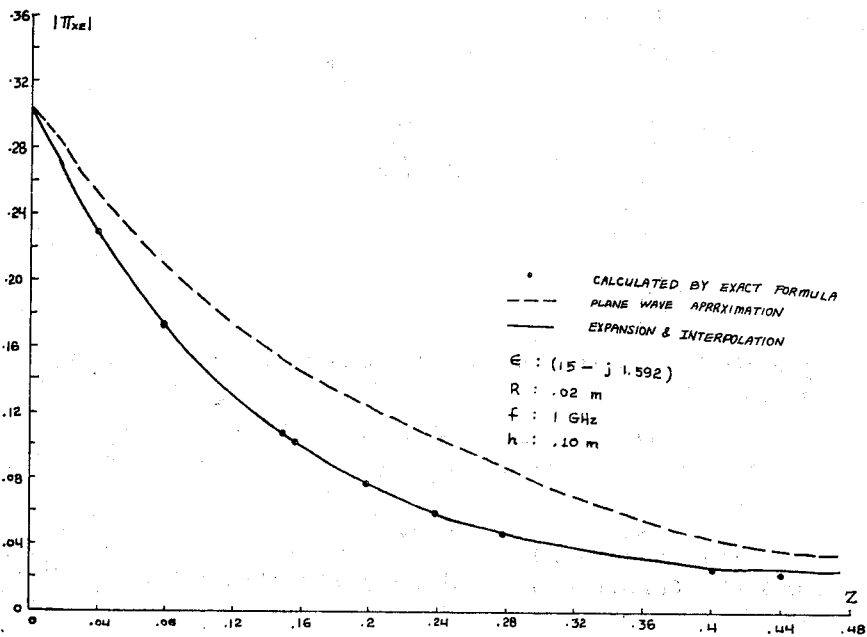
Fig. 1   Comparison of the magnitudes of
          between plane wave approximation
          and approximation equation (5).
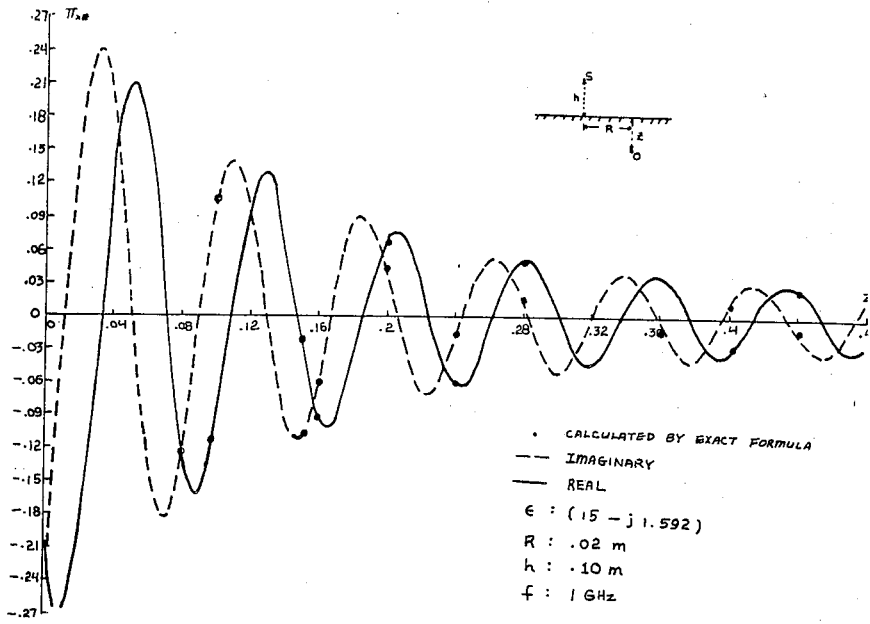
Fig. 2 vs. z with r fixed.
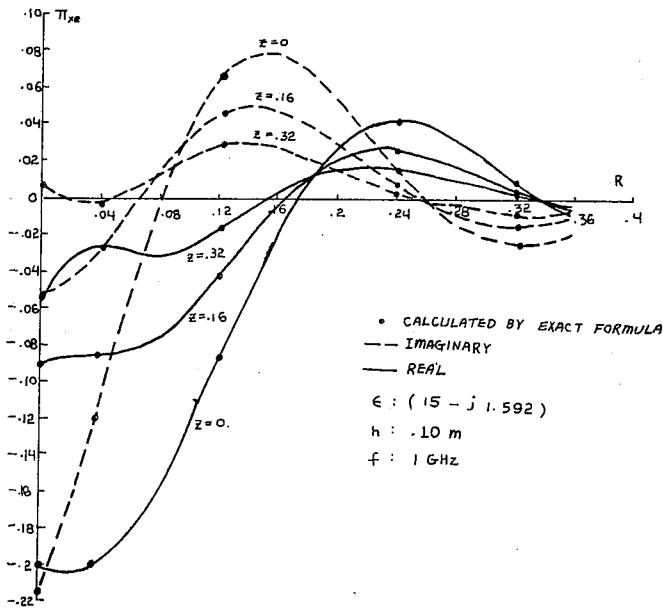
Fig. 3 vs. r with z fixed.

A DIRECT APPROACH TO THE NUMERICAL EVALUATION OF EM FIELDS DUE TO
SOURCES BURIED BENEATH THE EARTH'S SURFACE

James E. Lindsay, Jr., Department of Electrical Engineering,
University of Wyoming, Laramie, Wyoming, and
Robert R. Morgan, Exxon Minerals Department, Houston, Texas.

The potential integral solutions of Sommerfeld for the vector poten-
tial due to buried vertical and horizontal electric or magnetic dipoles
are readily available and well known (Sommerfeld, 1949). Approximate
evaluations of these integrals can be made for the far and near zone cases
utilizing such procedures as the saddle point method of integration or
quasi-static approximations (Wait, 1961; Bannister, 1968). The expressions,
once obtained, are then limited to these cases.

A direct procedure is presented which is not limited to the quasi-
static case but allows transition to the other cases of interest. The
approach to be discussed is based upon first obtaining the expressions
for the electric and magnetic fields in terms of these integrals. It is
found that representation in terms of circular cylindrical coordinates
leads to a considerable simplification. These expressions contain four
basic integrals, each involving a Bessel function of the first kind of
either zero or first order. The range of integration is along the positive
real axis. The integrals are then evaluated by breaking the interval into
two ranges, one involving a finite interval, the other an infinite interval.
Asymptotic forms are encountered in the integral over the infinite interval
and it is evaluated directly. Polynomial approximations for the factor
multiplying the Bessel function in the integrand then allow direct evalua-
tion of the integral over the finite interval in terms of Lommel functions.

1. A. Sommerfeld (1949), "Partial Differential Equations," Academic
        Press, New York, N. Y.

2. James R. Wait (1961), "The Electromagnetic Fields of a Horizontal
        Dipole in the Presence of a Conducting Half-Space," Canadian
        Journal of Physics, Vol. 39, pp. 1017-1028.

3. Peter R. Bannister, William C. Hart (1968), "Quasi-Static Fields of
        Dipole Antennas Below the Earth's Surface," USL Report No. 870,
        Electromagnetic Systems Planning Branch, Radio Communications
        System Division, U.S. Navy Underwater Sound Laboratory, Fort
        Trumbull, New London, Connecticut 06320.

RECURRENT GREEN'S FUNCTIONS FOR
MULTIPLE SCATTERING PROBLEMS

J.C. Bolomey
Laboratoire d'Electronique Générale
Ecole Supérieure d'Electricité
10, avenue Pierre Larousse
92240 Malakoff - FRANCE

A.   Wirgin
Laboratoire de Physique   Mathématique
Université de Toulouse III
118, Route de Narbonne
31400   Toulouse - FRANCE

Numerous studies of multiple scattering problems have been published in the litterature. They can be divided into two main classes. The first class includes those in which, in order to solve an N body problem, one supposes known the solutions for each isolated body. Historically, this was the first approach that was employed (1) (2) (3). It was subsequently abundantly re-utilized (for example (4) (5) (6)). By means of various methods (self consistent, for example) the characteristic quantities of the N body problem are expressed as a function of these same quantities for each body considered separatedly. These quantities can be superficial current densities or scattering diagrams. In this way one obtains systems of coupled integral equations of the second kind which can be solved by iteration. The convergence is in general slow except in the case of small obstacles, of obstacles separated by large distances or of obstacles located in dissipative media (7).

In the studies of the second class, one tends to consider the N bodies as a single "composite" obstacle. The usual formulation, based on the use of the free-space Green's function leads, as before, to systems of coupled integral equations. The transition from systems of the first class to those of the second class can be assured by means of appropriate transformations. For loose coupling the problem can be solved by perturbation techniques (7). Otherwise, numerical solutions are obtained with the help of computers (8) (9) (10) In numerous cases, the central memory capacity of the computer is insufficient and it becomes necessary to employ peripheral memory. The system of integral equations is then solved by partitioning.

The object of this communication is to describe a third approach which possesses certain advantage at the numerical resolution stage. In this approach, the N body problem is treated as a succession of intermediate problems in which

intervene an increasing number of obstacles. This approach is
recurrent in the sense that the solution of the n body problem
is deduced from that of the n - 1 body problem. In this way
one profits from the effort invested in the resolution of the
preceding problem. The rather arbitrary partitioning of the
global system in the conventional approaches is replaced by a
"natural" partitioning in which each block corresponds to a
well defined physical problem. The result is a gain of time
in the sense that the solutions of each of the intermediate
problems are known once the solution of the global problem is
obtained. If, for the given problem, the number of obstacles
constitutes a parameter which is used for obtaining a result
fixed in advance (e.g., synthesis of gratings), the recurrent
technique permits the interruption of the resolution process
as soon as this result is attained. If one wishes to introdu-
ce supplementary obstacles, it is not necessary to start from
the beginning the resolution process.

        The following discussion is restricted to time--harmo-
nic problems involving spatial cylindrical symmetry. The im-
plicit time factor is $e^{+i\omega t}$. The N perfectly conducting scat-
tering bodies are exposed to radiation emitted by given ap-
plied sources of density ρ . The obstacles occupy the regions
Ωi whose frontiers are $\Gamma_i (i = 1,2... N)$.   denotes the spa-
ce exterior to the first n obstacles. The Dirichlet (E - wave)
and Neumann (H - wave) problems are distinguished by the in-
dex ν whose value is -1 and +1 respectively.

        In order to solve this problem recurrently, one con-
siders an n - body problem (n $<$ N) with which is associated
the Green's function defined by :

$$(\Delta + k^2) \, G^{(n)}(x;x') = -\delta(x-x') \quad ; \, (x,x') \in (\omega_n \times \omega_n)$$

$$\delta_{\nu,-1} \, G^{(n)}(x;x') + \delta_{\nu,1} \, \partial_n G^{(n)}(x;x') = 0 \quad ; \, x \in \Gamma_1 \cup \Gamma_2 ... \cup \Gamma_n$$

in which k is the propagation constant within ω_n, ∂_n the
normal derivative at the frontier of an obstacle, δ (x - x')
the Dirac distribution, Δ the two-dimensional Laplace an ope-
rator and $\delta_{\nu,\pm} 1$ the Kronecker symbol. In addition, $G^{(n)}$ sa-
tisfies the usual finite energy and radiation conditions. It
follows that $G^{(n)}$ is identical to the total field at x due to
a line source localized at x' in the presence of n perfectly
conducting obstacles.

        From the consideration of two successive problems,
one easily obtains the following recurrence relation between
successive Green's functions:

$$G^{(n)}(x;x') = G^{(n-1)}(x;x') + \int_{\Gamma_n} [\ \delta_{\nu,-1}\ G^{(n-1)}(x;y)\ \partial_{n_y} G^{(n)}(y;x') + \cdots$$

$$\cdots - \delta_{\nu,1}\ G^{(n)}(y;x')\ \partial_{n_y} G^{(n-1)}(x;y)\ ]\ d\Gamma(y)$$

where $G^{(0)}(x;x') = i/4\ H_0^{(1)}(\ k|x-x'|\ )$ and $H_0^{(1)}$ designates the zero-order Hankel function of the first kind. According to the polarization state, one establishes the integral equations

$$\tfrac{1}{2}\partial_{n_x} G^{(n)}(x;x') = \partial_{n_x} G^{(n-1)}(x;x') + \int_{\Gamma_n} \partial_{n_x} G^{(n-1)}(x;y)\ \partial_{n_y} G^{(n)}(y;x')\ d\Gamma(y)\ ;$$

$$\nu = -1$$

$$\tfrac{1}{2}\partial_{n_{x'}} G^{(n)}(x;x') = \partial_{n_{x'}} G^{(n-1)}(x;x') - \int_{\Gamma_n} \partial_{n_x} G^{(n)}(y;x')\ \partial_{n_y} G^{(n-1)}(y;x)\ d\Gamma(y)\ ;$$

$$\nu = +1$$

wherein $\int$ denotes a principal value integral, $x \in \Gamma_n$ and $x' \in \omega_m$.

The successive resolution of these equations for n = 1,2... N leads to the determination of the recurrent Green's functions. The solution of the complete problem is obtained from the quadrature :

$$u(x) = \iint_{\omega_N} G^{(N)}(x;x')\ \rho(x')\ d\Omega(x')$$

This method is easily generalized to the case in which the incident radiation is constituted by one or more plane waves. The method has been applied in our laboratory to the calculation of blaze effects produced by gratings constituted by a finite ensemble of scatterers. Details concerning the obtained numerical results and the organization of the calculations will appear in a forth coming publication. It appears, at present, that the increased complexity at the program conception stage is largely compensated by the interest presented by the knowledge of the solutions of intermediate problems.

(1) K. Schwarzschild (1902 Math. Ann. 55, p. 177)
(2) F. Zaviska (1913 Ann. Phys. 40, p. 1023)
(3) W.V. Ignatowsky (1914 Ann. Phys. 44, p. 369)
(4) V. Twersky (1962 Journal Opt. Soc. of Am. 52, p. 145)
(5) R.F. Millar (1965 Proc. Camb. Phil. Soc. 61, p. 777)
(6) I.P. Skal'skaya (1963 Soviet Physics Tech. Phys. 8, p. 179)
(7) H. Hönl, A.W. Maue, K. Westpfahl (Theorie der Beugung,

p. 363 - 372 Springer Ed, Berlin).

(8)   R.V. Row (1955 Journ. Appl. Phys. 26, p. 666)
(9)   M.G. Andreasen (1965 I.E.E.E. Trans AP - 13, p. 303)
(10) V.P. Kopaleishvili, R.S. Popovidi (1972 - Rad. Eng. Electron. Phys. 17, p. 1074).

SCATTERING BY A DIELECTRIC RECTANGULAR CYLINDER

Tommy C. Tong

National Bureau of Standards

Boulder, Colorado

Introduction

The problem concerning scattering by a perfectly con-
ducting rectangular cylinder was solved by Mei and
Van Bladel[1,2] about a decade ago. Later Richmond[3,4]
considered dielectric cylinders of arbitrary cross
section shapes. But his method, which essentially
represents the field inside the dielectric by the
equivalent current, is limited to thin cylinders.
It is the purpose of this paper to extend Mei and
Van Bladel's method to the case of a dielectric
cylinder.

Formulation of the Integral Equations

We are considering a homogeneous dielectric rectangular
cylinder upon which a plane wave is incident normally.
Without loss of generality, let us assume that the
incident wave is TM polarized (E-wave) and time varia-
tion $e^{j\omega t}$. From the Helmoholtz equation, the Green's
theorem plus the boundary conditions, we can derive
the following coupled integral equations

$$E_z^i(\underline{r}) = \frac{E_z(\underline{r})}{2} + \lim_{\sigma \to o} \int_{S-\sigma} \left[G_1(\underline{r},\underline{r}') \frac{\partial E_z(\underline{r}')}{\partial n'} \right.$$

$$\left. - E_z(\underline{r}') \frac{\partial G_1(\underline{r},\underline{r}')}{\partial n'} \right] dS' \quad (1)$$

$$0 = \frac{E_z(\underline{r})}{2} - \lim_{\sigma \to o} \int_{S-\sigma} \left[G_2(\underline{r},\underline{r}') \frac{\partial E_z(\underline{r}')}{\partial n'} \right.$$

$$\left. - E_z(\underline{r}') \frac{\partial G_2(\underline{r},\underline{r}')}{\partial n'} \right] dS' \quad (2)$$

$$\underline{r},\underline{r}' \ \epsilon \ S$$

where $G_i(\underline{r},\underline{r}') = \frac{-j}{4} H_0^{(2)}(k_i |\underline{r}-\underline{r}'|)$,

σ = a small segment of S containing
the point $\underline{r}'$,

$$k_i = \omega\sqrt{\mu_i \varepsilon_i}, \quad i = 1,2,$$

$H_o^{(2)}(\ )$ = zeroth order Hankel function of second kind,

$E_z^i(\underline{r}), E_z(\underline{r})$ = the incident and the total electric fields,

μ_1, μ_2 = the permeabilities and

$\varepsilon_1, \varepsilon_2$ permittivities of free space and the dielectric cylinder respectively,

S = surface of the cylinder, and

$\hat{n}$ = unit outward normal to S.

The integral equations for the TE polarization (H-wave) can be obtained easily from Eqs. (1) and (2) by invoking the concept of duality.

Numerical Results

The numerical results for the surface fields are presented in Fig. 1 and Fig. 2 for the E-wave, and Fig. 3 and Fig. 4 for the H-wave for different values of the relative dielectric constant $\varepsilon_r, (\varepsilon_r = \varepsilon_2/\varepsilon_1)$ for a square cylinder. The plots for very high dielectric constant are also included and can serve as a check on the numerical results. The results for these limiting cases agree very well with those obtained by Mei and Van Bladel.

Concluding Remarks

Although the numerical results presented here are limited to normal incidence and the surface fields, the computer program can handle oblique incidence and compute the scattered field pattern.

References

1.   K. K. Mei and J. G. Van Bladel (1963 IEEE Trans. on Antennas and Propagation, AP-11, p. 185).

2.   K. K. Mei and J. G. Van Bladel (1963 IEEE Trans. on Antennas and Propagation, AP-11, p 52).

3.   J. H. Richmond (1965 IEEE Trans. on Antennas and Propagation, AP-13, p. 334).

4.   J. H. Richmond (1966 IEEE Trans. on Antennas and Propagation, AP-14, p. 460).
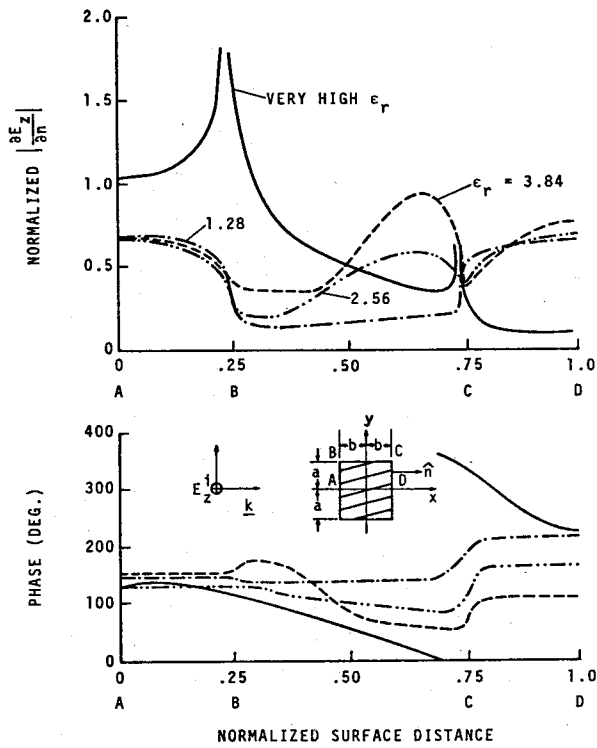
Fig. 1. Normalized $\left|\dfrac{\partial E_z}{\partial n}\right|$ for a square cylinder (ka = kb = 1.0) for E-wave.
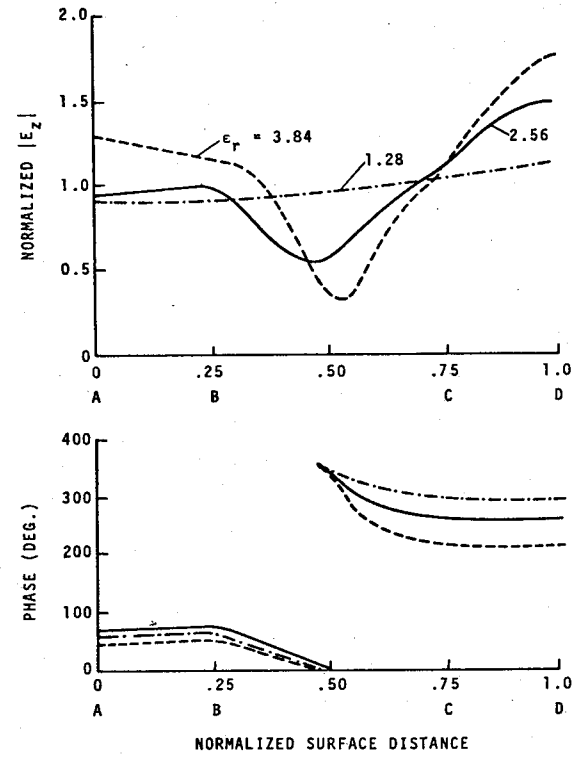
Fig. 2. Normalized $|E_z|$ for a square cylinder (ka = kb = 1.0) for E-wave.
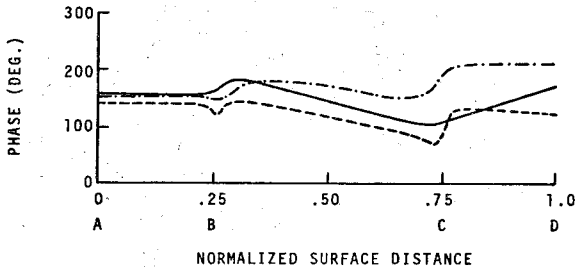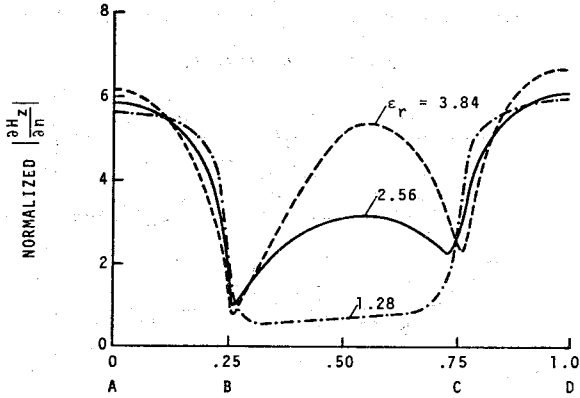
Fig. 3. Normalized $\left|\dfrac{\partial H_z}{\partial n}\right|$ for a square cylinder (ka = kb = 1.0) for H-wave.
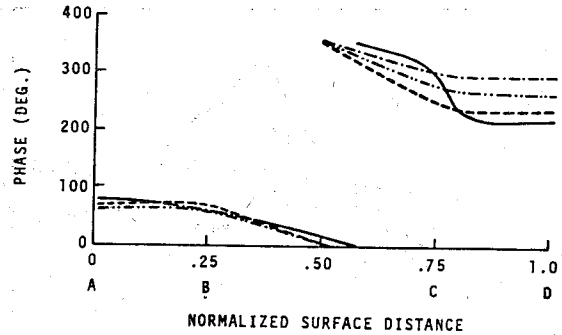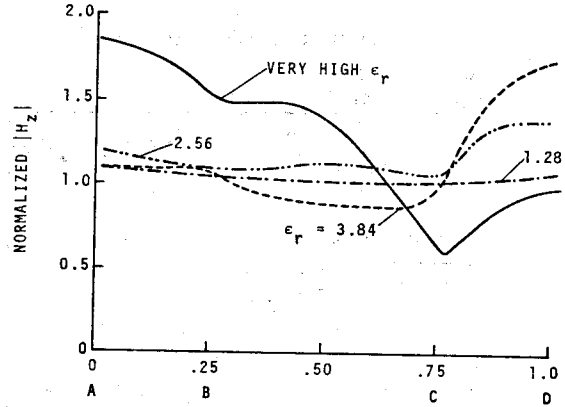
Fig. 4. Normalized $|H_z|$ for a square cylinder (ka = kb = 1.0) for H-wave.

ELECTROMAGNETIC SCATTERING FROM A PERFECTLY

CONDUCTING RECTANGULAR BOX

L. L. Tsai,
University of Mississippi,
University, Mississippi   38677

and

D. G. Dudley,
University of Arizona,
Tucson, Arizona   85721

A study is made of the interaction of a plane wave incident on a
perfectly conducting rectangular box. The problem is three-
dimensional with no rotational symmetry. A solution is
accomplished by application of the method of moments to the
magnetic field integral equation. The results obtained are the
currents induced on the box surface, the fields in the vicinity
of the box, and the radar cross section. To produce the solution,
the vector integral equation is first separated into coupled
scalar integral equations. The currents are then obtained by
inversion of a matrix formed from pulse expansion and delta function
weighting. One major limitation is the matrix size necessary to
specify adequately the variations of the currents. Consequently,
symmetry properties are employed to reduce the matrix size. It
is shown that for the case of broadside incidence on any face,
this reduction is by a factor of eight, or equivalently, con-
sideration is reduced to one octant of the box. Broadside radar
cross section computed from currents thus obtained shows excellent
agreement with experimental results in the literature, both for
the case of a cube and a flat plate with finite thickness, up
through second resonance ($> 1 \lambda$). Also presented are three-
dimensional computer plots of the frequency domain surface
currents. The directions of current flow and singular behavior
near edges together with the fields in the vicinity of the box
should constitute valuable diagnostic tools in frequency domain
analysis and should be amenable to transient analysis through
numerical Fourier inversion techniques.

THE FIELD DISTRIBUTION IN A RECTANGULAR APERTURE BY A MOMENT METHOD SOLUTION

R. J. Spiegel and D. E. Young
The Boeing Aerospace Company
Seattle, Washington 98124

The field distribution in a rectangular aperture is investigated by use of the method of moments. A rectangular aperture cut into an infinite, perfectly conducting screen of zero thickness is considered. The coordinate system is chosen with the origin located at the center of the aperture and oriented so that the screen lies in the x-y plane. The electromagnetic field incident upon the aperture is assumed to emanate from a monochromatic source with $e^{-j\omega t}$ time dependence.

It is well known that both the normal component of $\overline{E}$ (E_z) and the tangential components of $\overline{H}$ (H_x and H_y) in the aperture are equal to their respective components of the incident field [1]. Therefore, to completely specify the field in the aperture, it only becomes necessary to determine the tangential components of $\overline{E}$ (E_x and E_y). The derivation of the necessary equations generally follows a procedure described by Tai [2], where the analytic approach involves the use of the vector Green's theorem along with a Green's function which satisfies the Neumann boundary condition on the plane of the screen. The resulting set of coupled integral equations are given by

$$H_x^{inc} = \frac{4jK^2}{\omega\mu_o} \iint\limits_A E_y(x',y') G_o(\overline{R/R'}) dx'dy'$$

(1a)

$$- \frac{4j}{\omega\mu_o} \iint\limits_A \left[E_x(x',y') \frac{\partial^2 G_o(\overline{R/R'})}{\partial x' \partial y'} - E_y(x',y') \frac{\partial^2 G_o(\overline{R/R'})}{\partial x'^2} \right] dx'dy'$$

$$H_y^{inc} = \frac{-4jK^2}{\omega\mu_o} \iint\limits_A E_x(x',y') G_o(\overline{R/R'}) dx'dy'$$

(1b)

$$+ \frac{4j}{\omega\mu_o} \iint\limits_A \left[-E_x(x',y') \frac{\partial^2 G_o(\overline{R/R'})}{\partial y'^2} + E_y(x',y') \frac{\partial^2 G_o(\overline{R/R'})}{\partial x' \partial y'} \right] dx'dy'$$

where $G_o(\overline{R/R'}) = e^{jK|\overline{R}-\overline{R}'|}/4\pi|\overline{R}-\overline{R}'|$ and $|\overline{R}-\overline{R}'| = \sqrt{(x-x')^2 + (y-y')^2}$. The quantities H_x^{inc} and H_y^{inc} refer to the tangential component of the magnetic field existing on the surface of the aperture, when the aperture is replaced by a conducting surface to form a solid infinite conducting screen.

The integral equations (1) are solved by the application of the
method of moments [3], in which the aperture is divided into N
square subsections. The unknown field components, E_x and E_y, are
written in terms of pulse expansion functions, while delta
functions are chosen as the testing functions. The original equat-
ions are thus approximated by a system of 2N linear equations in
which the self coefficients are calculated by expanding the Green's
function into a series and performing the resultant integrals
analytically for each term. The off-diagonal coefficients are
evaluated using a Gaussian quadrature approximation for the integ-
rals. The unknowns associated with the system of equations are
easily solved by well known numerical procedures.

Figures (1)-(4) show plots of the normalized magnitude of the x-
component of the electric field in a square aperture with sides of
length ℓ. The source field is a normally incident plane wave with
an E-field oriented in the x-direction. An electrically small
aperture ($\ell/\lambda = .002$) is considered in Figures (1) and (2), while
an electrically larger aperture ($\ell/\lambda = 1$) is given in Figures (3)
and (4). For both cases, the solid curves represent the solution
when the aperture is divided into 100 square subsections, and the
X's which are superimposed on the solid curves, show the solution
for a 36 square subsection case. As would be expected, the coarser
grid solution begins to deviate from that of the finer grid when
the aperture becomes electrically larger.

<div align="center">References</div>

[1]   H. A. Bethe, Phys. Rev. 66, 163 (1944).

[2]   C. T. Tai, Dyadic Green's Functions In Electromagnetic Theory,
      International Textbook Co., Scranton, Penn., Chap. 4, 1971.

[3]   R. F. Harrington, Field Computation by Moment Methods, The
      Macmillan Co., N. Y., 1968.
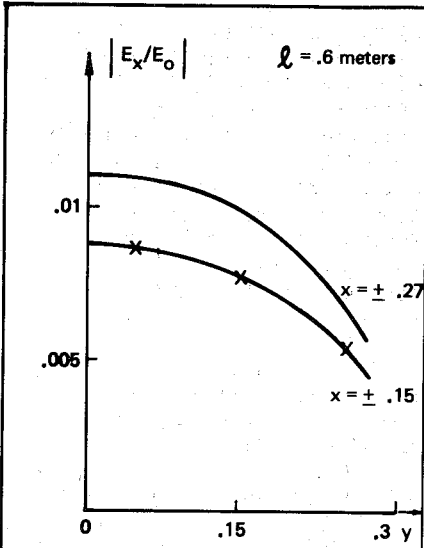
Figure 1. Aperture E-field in the direction perpendicular to the incident E-field for λ = 300 meters.
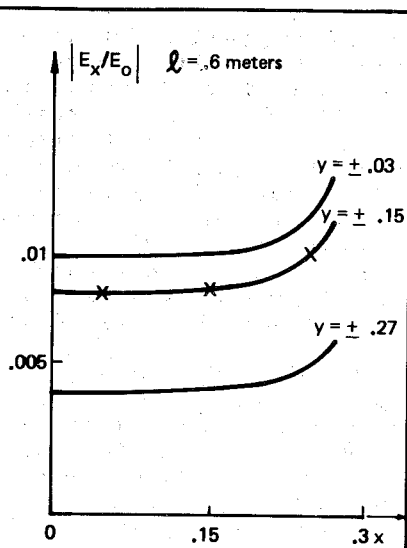
Figure 2. Aperture E-field in the direction parallel to the incident E-field for λ = 300 meters.
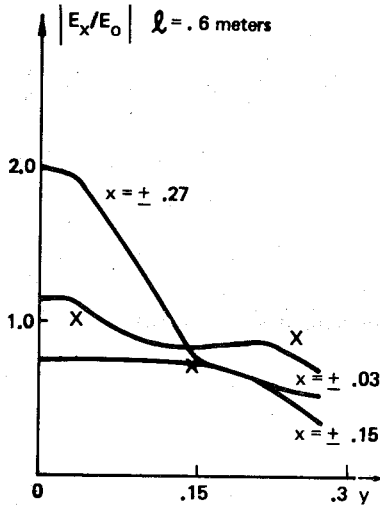
Figure 3. Aperture E-field in the direction perpendicular to the incident E-field for λ = 0.6 meters.
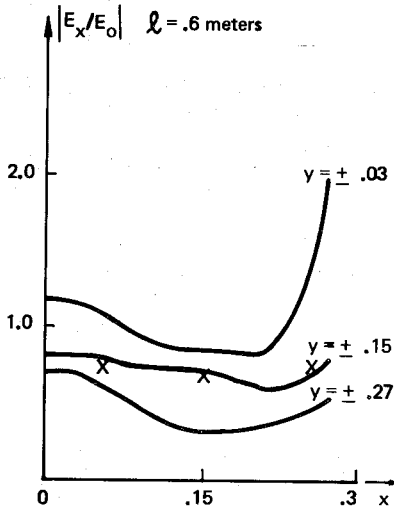
Figure 4. Aperture E-field in the direction parallel to the incident E-field for λ = 0.6 meters.

RCS OF A THIN PLATE

Y. Rahmat-Samii
Electromagnetics Laboratory
University of Illinois
Urbana, Illinois 61801

In a recent work[1] it has been shown that the problem of plane wave diffraction by a thin, flat plate lying in the x,y plane can be formulated in terms of two integral equations for J_x, J_y, the two components of the surface current density on the plate. These equations have the form

$$\iint_A J_x \phi \, ds' = \frac{1}{jk_z^i} H_y^i + \sum_n k_{nx} A_n e^{j(k_{xn}x + k_{yn}y)} \tag{1a}$$

$$\iint_A J_y \phi \, ds' = \frac{-1}{jk_z^i} H_x^i + \sum_n k_{yn} A_n e^{j(k_{xn}x + k_{yn}y)} \tag{1b}$$

where $\phi = (e^{-jkr}/r)$; $k = 2\pi/\lambda$; $k_z^i = z$ component of the wavenumber of incident plane wave; A_n's are unknown coefficients; $k_{xn}^2 + k_{yn}^2 = k^2$.

It is observed that the two scalar components J_x and J_y are uncoupled in (1a) and (1b) and the integral equations have identical kernels that contain no partial derivatives of the Scalar Green's function ϕ. Consequently, for numerical computation, (1) is preferable rather than the corresponding E-integral equation which leads to two coupled integral equations with more complicated kernels.

The object of this paper is to present the result of RCS calculation of thin plates using the new equation and to compare these results with the RCS data based on PO, GTD and variational formulations.

The numerical solution of (1) is carried out in a conventional manner by transforming the integral equations into corresponding matrix equations. The unknown constants A_n's are determined by imposing the boundary condition on the normal component of the surface current at the edge of the plate, viz., $\bar{J} \cdot \bar{\nu} = 0$, where $\bar{\nu}$ is normal to the bounding contour of the plate. This procedure is similar to that followed in connection with Hallen's approach to the thin wire problem, generalized here to accommodate the two-dimensional nature of the plate. Extensive numerical studies indicate that the equations (1a) and (1b) are numerically well-conditioned and their uncoupled nature allows one to handle plate sizes larger than would be possible using the E-integral equation.

Session 13   Numerical Methods (1)

The radar cross-section of the plate may be obtained in a standard
manner from the knowledge of the surface current density distribution
on the plate.   Computed results for a $1\lambda \times 1\lambda$ square plate are shown
in Figure 1 where the RCS data from GTD and PO   formulations
also are plotted for convenience of comparison.   kote that all three
curves are in close agreement with each other for aspect angles in
the range $0 < \theta < 20$.   For θ between 20° and 65° both the GTD and
physical optics solutions differ from the numerically rigorous
integral equation solutions, though the deviation is less for the
GTD solution than the physical optics results.   Beyond 80° the GTD
results deviate substantially from the integral equation solution.
This is not totally unexpected, however, since it is well known
that the GTD method is not applicable in the neighborhood of
grazing angles of incidence.

Figure 2 is a plot of the RCS data of a square plate, as a function
of its size, for $\theta = 0^{\circ}$, i.e., the normal incidence case.   The
results may be compared with those obtained by using the variational
technique and the experimental data given in Ruck.[2]   It is evident
that the integral equation solutions are in better agreement with
the measurements than the variational solution.

References

1.   R. Mittra, W. A. Davis and D. V. Jamnejad (1972 URSI Fall Meeting,
     p. 93-94).
2.   G. T. Ruck, D. E. Barrick, W. D. Stuart and C. K. Krichbaum
     (1970 Radar   Cross Section Handbook, G. T. Ruck, Ed., Plenum, p. 524).

Acknowledgement
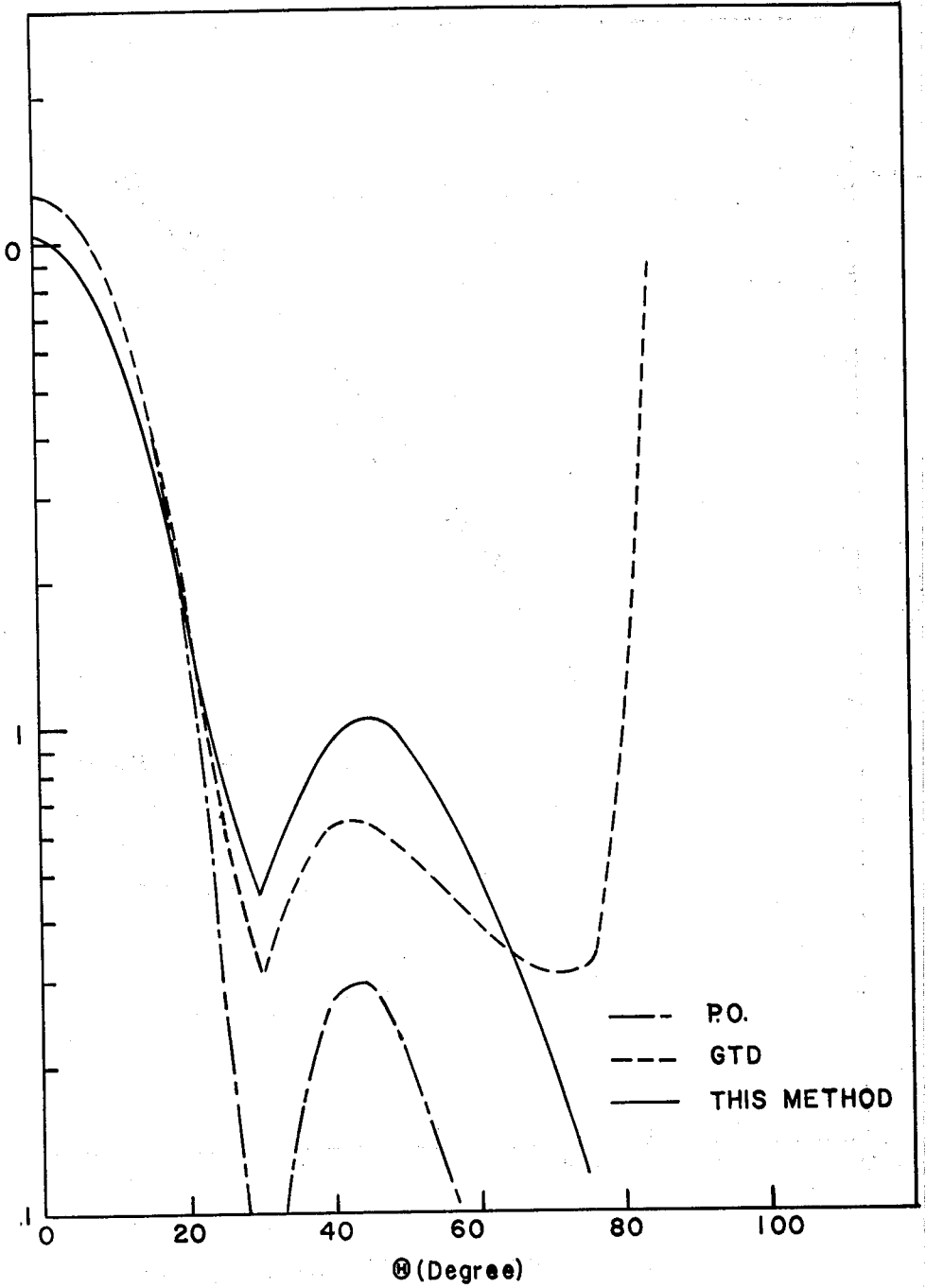
Figure 1.   RCS of $|\lambda x|\lambda$ flat plate.
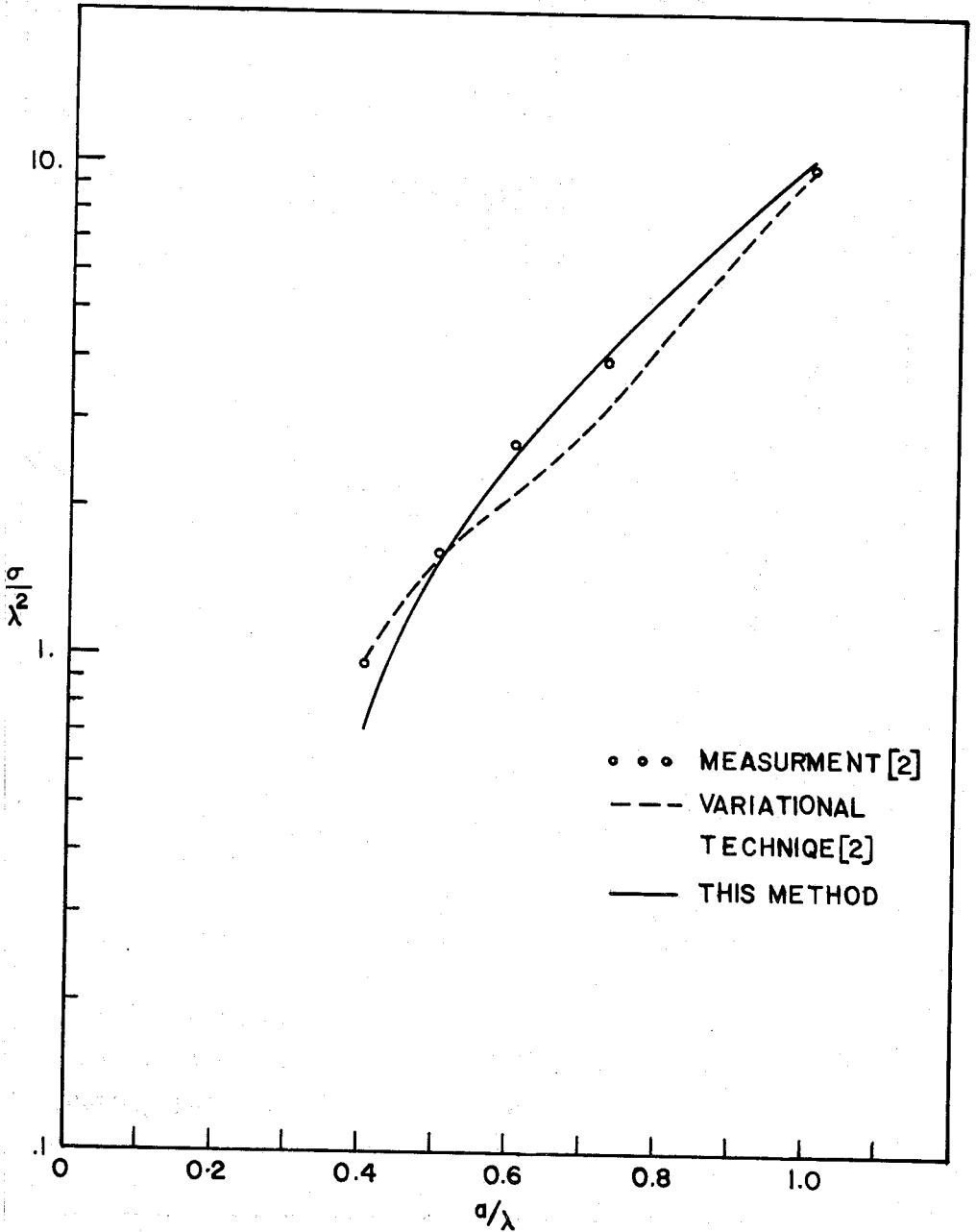
Figure 2. RCS for normally incident plane wave.

A GENERAL-PURPOSE INTERACTIVE ANTENNA ANALYSIS PROGRAM

William L. Cook and Geoffrey Hyde
COMSAT Laboratories
Clarksburg, Maryland 20734

SUMMARY

An interactive computer program (GAP) has been developed
to solve a wide class of antenna problems on an IBM 360/65
computer, including the analysis of antenna performance
and generation of antenna surfaces, in problems where the
interior fields can be treated by geometric optics methods.
The ray-tracing methods used account for the polarization,
energy density, pathlength (phase) and wavefront curvature
information associated with each ray, so that the resulting
surface currents and aperture field distributions are
accurate within the basic geometric optics approximation.
Up to six surfaces (regular or deformed) may be used in
the ray-trace analysis. Rays which miss reflectors and/or
the aperture plane, or are blocked, are accounted for.
Far-field patterns are computed from either "wavefront"
approximations in the aperture plane or current distribu-
tions on the final reflector surface using standard inte-
gral representations. The user is given a wide choice of
options for input of fields and surfaces and outputs both
of far-field and intermediate fields and currents.

INTRODUCTION

By means of an interactive preprocessor, accessed by the
antenna designer through a remote terminal, the problem
may be described in engineering terms. Most of the input
data is given as answers to questions asked by the program
to prompt the designer (see Figure 1). The program accepts
inputs in a wide variety of forms. Reflecting surfaces
can be described as general second order polynomials with
appropriate constants, surfaces of revolution, or by means
of discrete element descriptions. This permits any surface
including deformed surfaces to be described. Radiation
fields can be described analytically in terms of Fortran
statements input by the user or retrieved from a built-in
library or by specifying the amplitude and polarization
components of each ray (point-by-point description).
There is complete freedom in the choice of origin and ori-
entation of the coordinate systems (rectangular, circular
cylindrical, spherical and spherical-tilde) chosen to
describe these inputs. In all cases the GAP program
handles all necessary coordinate and polarization trans-
formations.

91

Session 13 Numerical Methods (1)

NEAR FIELD DETERMINATION

The theory of geometrical optics is employed to trace in-
cident radiation fields (either transmitted or received)
through an antenna system having multiple reflecting sur-
faces. Surfaces may be defined by listing the coefficients
of polynomial equations, or by modelling the surface with
a large number of grid points connected by triangular or
quadrilateral discrete elements (see figure 2). Surface
deformations are described in terms of three translational
and three rotational components of displacement at each
grid point. The assumed elastic displacement function for
a triangular surface element is of the form

$$w = a_0 + a_1x + a_2y + a_3x^2 + a_4xy + a_5y^2 + a_6x^3$$

$$+ a_7(x^2y + xy^2) + a_8y^3$$

where the nine coefficients are evaluated in terms of the
nine corner displacements contributing to bending, after
the rigid body displacement of the element has been sub-
tracted out. This representation is analogous to that used
in the finite element approach in structural mechanics,
and provides the capability for determining the effects
of structural distortions on the radiation patterns, and
for modelling cut-outs and surface boundaries of arbitrary
geometry, feed support structures, and reflecting surfaces
defined in terms of measured data.

There is no limitation on the number of rays used in defin-
ing a radiation field. Each ray is defined in terms of
18 quantities which define the previous point of reflection;
the direction of the ray; the cross-sectional area, cumula-
tive pathlength and phase of the ray at that point; six
components of polarization; and the second derivatives of
the wavefront. This latter information is used in updating
the values of amplitude and cross-sectional area at each
reflecting surface. The effects of blockage and spillover
are accounted for (in a simple ray-trace manner, i.e. no
edge effects).

FAR-FIELD DETERMINATION

An efficient and accurate algorithm has been developed for
determining the far-field radiation pattern, based on a
non-regular spacing of points on the aperture plane, which
eliminates the lengthy running times commonly associated
with two-dimensional interpolation and numerical integra-
tion. The complex far-field amplitude is given by:

$$F(\theta,\phi) = \int_y \int_x E(x,y) e^{j\frac{2\pi}{\lambda}\sin\theta(x\cos\phi + y\sin\phi)} dxdy$$

where x and y are rectangular aperture plane coordinates, θ and ϕ are the spherical far-field coordinates, and where E(x,y) is the complex electric field on the aperture plane. Since the cross-sectional area and the derivatives of phase associated with each point in the aperture field have been determined, the far-field pattern may be approximated by summing the individual effects of each aperture plane point, i.e.

$$F(\theta,\phi) \simeq \sum_{i=1}^{n} 4E_i e^{-ja_i} \frac{\sin(\alpha\epsilon_i)}{\alpha} \frac{\sin(\beta\epsilon_i)}{\beta}(\cos\gamma + \sin\gamma)$$

where,

$$a_i = \psi_i - x_i \left.\frac{\partial\psi}{\partial x}\right|_{x=x_i,y=y_i} - y_i \left.\frac{\partial\psi}{\partial y}\right|_{x=x_i,y=y_i}$$

$$\alpha = \frac{2\pi}{\lambda} \sin\theta \, \sin\phi - \left.\frac{\partial\psi}{\partial x}\right|_{x=x_i,y=y_i}$$

$$\beta = \frac{2\pi}{\lambda} \sin\theta \, \sin\phi - \left.\frac{\partial\psi}{\partial y}\right|_{x=x_i,y=y_i}$$

$$\gamma = \alpha x_i + \beta y_i$$

in which E_i and ψ_i are the field amplitude and phase, and $(2\epsilon_i)^2$ is the cross-sectional area of the ray tube at point (x_i,y_i). An analogous algorithm based on surface current distributions is also provided. The contour plot in figure 3 shows the far-field pattern created by a distorted parabolic reflector whose discrete element model is shown in figure 2.

CORRECTING SUBREFLECTORS

A method called the "Create" algorithm has been developed. In it, equations for generating points on a pathlength-correcting subreflector have been mechanized so that a point on the surface is generated for each member of the incident ray family to be focussed. The surface is output in the discrete element format so that it can be used as input in subsequent analyses or as input to automatic 3-D surface cutting machinery. A discrete element model of a subreflector generated for a toroidal main reflector is shown in figure 4

```
PLEASE TYPE CONTROL DECK FOR GAP PROGRAM
LAST CARD MUST BE "BEGIN BULK"

title= torus antenna analysis
ifield=5
surface 1=3
method=wavefront(%)
output farfield
begin bulk


CONTROL DECK SUMMARY:

APERTURE METHOD
DEFORMED MODE
POLARIZED FIELDS
VARIABLE AMPLITUDE
1 REFLECTING SURFACES
APERTURE SYSTEM IS THE BASIC SYSTEM
BULK DATA WILL NOT BE SAVED
BULK DATA WILL NOT BE FETCHED
NO SYMMETRY INVOLVED


ENTER "MODIFY", "DELETE" OR "PROCEED"
proceed


DO YOU WANT GAP TO GENERATE SURFACE    3 ?
no
IS SURFACE    3 AN "EQUATION" OR A "LIST" OF ELEMENTS?
equation
WHAT IS THE EQUATION TYPE: "1" OR "2"?
2
EQUATION IS: A+BZ+CX+DZZ+EZX+FXX+G
PLEASE LIST ALL SIX COEFFICIENTS
-112780.04  -187.7534  0.  0.  2.  1.
WHAT ANGLE(IN DEGREES) DOES THE ROTATION AXIS MAKE WITH THE Z AXIS?
95.5
WHAT IS THE COORDINATE SYSTEM OF THE EQUATION?
0
WHAT IS THE COORDINATE SYSTEM OF THE LIMITS?
0
DEFINE THE LIMITS ON X
12. 132.
DEFINE THE LIMITS ON Y
-90. 90.
DEFINE THE LIMITS ON Z
-250. -70.
ANY CHANGES SINCE LAST CHECKPOINT?
no
```

Figure 1.   Sample Input
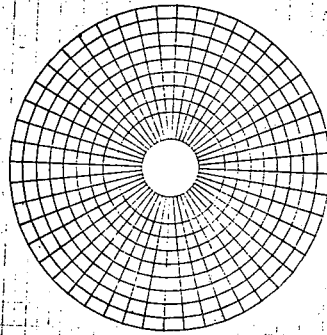
Figure 2.   Model of Parabolic
Dish
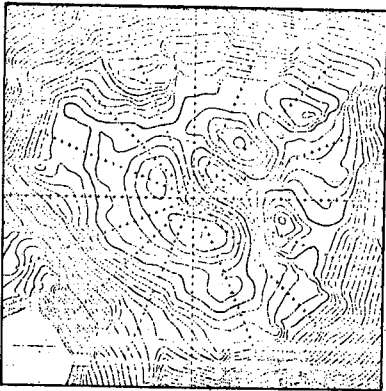
Figure 3.   Far-Field Patterns
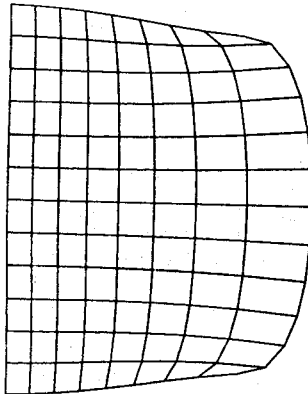
Figure 4.   Created Subreflector

94

INPUT IMPEDANCE OF A VERTICAL $\lambda/2$ DIPOLE NEAR A CYLINDRICALLY SYMMETRIC SURFACE CONTOUR

Ronald R. Lentz
Visiting Fellow
C. I. R. E. S.
Univ. of Colorado/NOAA

For high frequency coastal surface-wave radars it is often important that the transmitted signal be very pure (with noise sidebands <100 dB , Barrick [1]) in order that the Doppler shifted returns from targets be observable. In order to excite the surface wave it is sometimes convenient to put the transmitting antenna over the water or at least on the beach near the water. When the antenna is over the water the passage of water waves under the antenna will affect its input impedance, which will cause the transmitted power to vary introducing "noise" side-bands into the transmitted signal. A simplified model of a sea surface will be used to examine the effect of the surface on the input impedance of a $\lambda/2$ dipole. The surface is assumed to be symmetric about the z axis on which the vertical dipole is located, i.e. the surface is described by $z = f(\rho)$ as shown in Fig. 1.

The compensation theorem of Monteath [2] has been used to compute the input impedance. It states that

$$Z' - Z = \frac{1}{I_o^2} \oiint_S (\overline{E} \times \overline{H}' - \overline{E}' \times \overline{H}) \cdot \hat{n}\, ds$$

where the primed letters indicate the quantities after changes have been introduced in the medium bounded by the surface S . The unprimed letters are the values before changes have been introduced in the medium. I_o is the strength of the current generator feeding the antenna. For the present case, $\overline{E}$ and $\overline{H}$ are the fields radiated by the dipole in free space and $\overline{E}'$, $\overline{H}'$ are the fields radiated by the dipole in the presence of the surface. Since the surface is perfectly conducting, the last term in the integral vanishes. The tangent-plane approximation is used to compute $\overline{H}'$, i.e. it is double the free space value. From symmetry the φ integration can be eliminated, leaving the integration over the ρ variable which is done numerically. Only the portion of the surface within a radius of a few wave-lengths of the antenna has any appreciable effect upon the input impedance. All of the integrations were truncated between $\rho = 2\lambda$ to 4λ . The method was tested on a dipole over a

perfectly conducting plane and is in excellent agreement with the result of Shelkunoff and Friis [3].

Fig. 1 shows the input resistance of the dipole when it is located above a trough and above a crest. The surface is sinusoidal although it need not be so. The results indicate that an automatic antenna matching device is required to maintain a steady radiated field if the antenna is mounted over the water.

The above method can also be used to estimate the disturbing effect of non-planar terrain on geological measurements made using the input impedance of an above-ground antenna. The result shown in Fig. 2 is for a perfectly conducting hill of varying radius of curvature. The program has been extended to include non-perfectly conducting ground.

<div align="center">REFERENCES</div>

1. D. E. Barrick (Private communication).
2. G. D. Monteath (1951 "Application of the compensation theorem to certain radiation and propagation problems," Proc. I. E. E. (London) 98, pp 23-30.)
3. S. A. Schelkunoff and H. T. Friis (1952 Antennas Theory and Practice, Wiley, p. 413.)
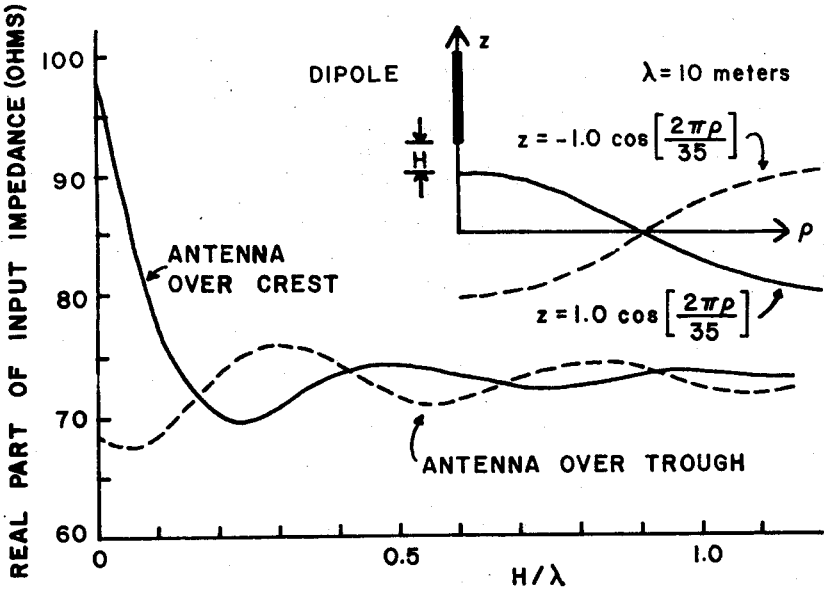
FIG. I. INPUT RESISTANCE OF DIPOLE OVER CREST
AND TROUGH VS. HEIGHT OF DIPOLE
ABOVE CREST
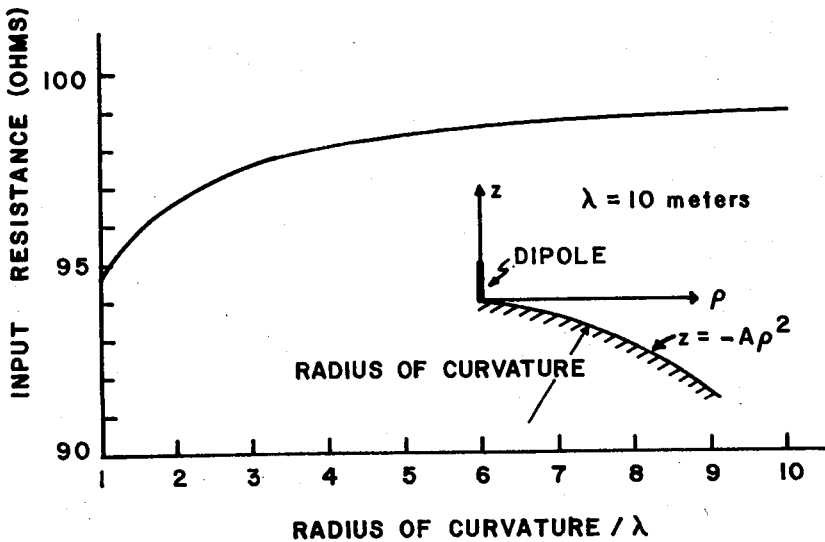
FIG. 2. INPUT RESISTANCE OF DIPOLE OVER PARABOLIC
SURFACE VS. RADIUS OF CURVATURE

The resultant equivalent network is shown in Fig. 3. By means of this network representation, the total (100%) power conversion condition has been shown to be related to half-wavelength resonances in the corrugation region. The results of the equivalent network analysis can thus be used to design these gratings with specific blaze requirements. To have the total power conversion point occur at a specified incidence angle θ_i or a specified wavenumber k, it is only necessary to solve for the grating profile parameters (d,h) which satisfy the above resonance condition, subject to the constraint $kd \sin\theta_i = \pi$.

REFERENCES

1. D. Y. Tseng (Ph.D. Dissertation, Polytechnic Institute of Brooklyn, June 1967).
2. D. Y. Tseng, A. Hessel, A. A. Oliner (1969 Alta Frequenza 38N, Special Issue, p. 82).
3. A. Wirgin, R. Deleuil (1969 J. Opt. Soc. Am. 59, p. 1348).
4. A. Hessel, J. Shmoys, private communications.
5. J. A. DeSanto (1971 J. of Math. Phys. 12, p. 1913).
6. H. J. Carlin, A. B. Giordano, Network Theory: An Intro-duction to Reciprocal and Non-Reciprocal Circuits, Prentice-Hall, (1964).

1780-1
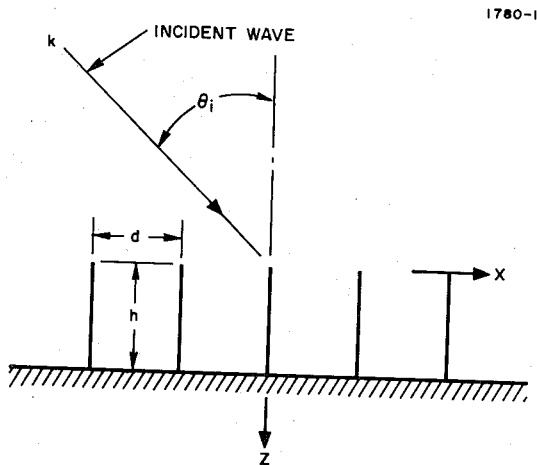
Fig. 1   Rectangular corrugation gratings which exhibit total (100%) power conversion into a diffracted spectral order.
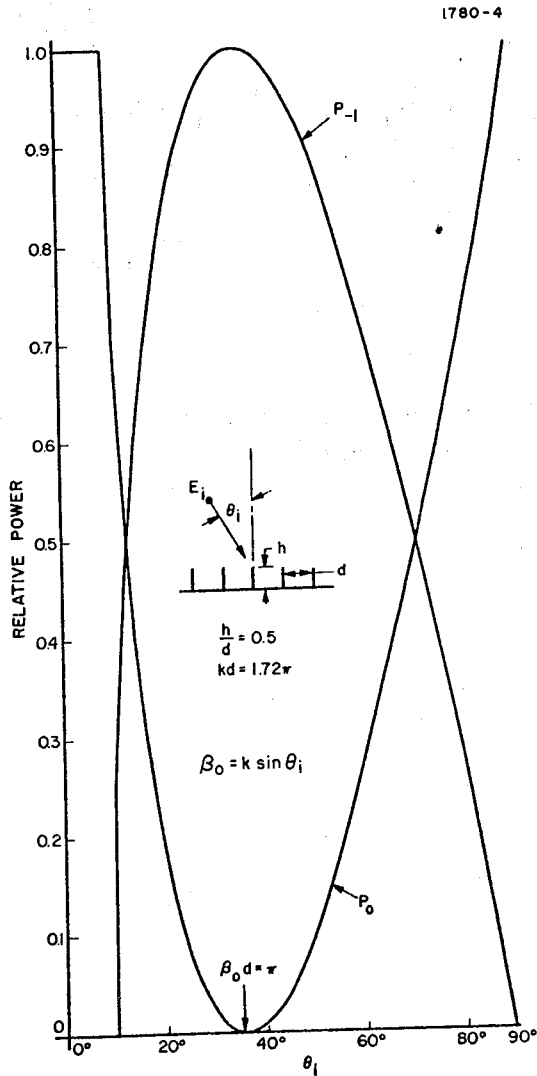
Fig. 2   Power distribution in n = 0 and -1 spectral orders as a function of incidence angle. Total (100%) power conversion exhibited at $\beta_0 d = \pi$. (Incident power normalized to unity.)

1780-3
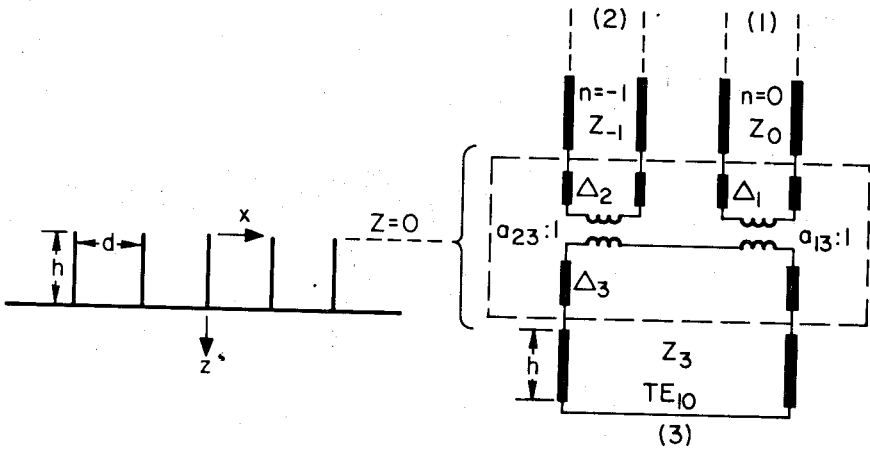
Fig. 3   Transverse equivalent network representation of
          corrugated grating.

THE SIGNIFICANCE OF THE "ZWISCHENMEDIUM" IN FIELDTHEORY, RADIATION FROM THE PARALLEL PLATE WAVEGUIDE AND SCATTERING AT AN ANGLE.

Prof. Dr.-Ing. G. Piefke
Fachgebiet Theoretische Elektrotechnik
Technische Hochschule Darmstadt, BRD

Summary

1. Advantages of the "Zwischenmedium"

The "Zwischenmedium" according to Piefke (1) allows in some cases a precise calculation by means of the orthogonal expansion. This may lead to simple eigenfunctions and to a solution in closed form of the integrals (expansion-integrals) arising from the orthogonal expansion, as well as to a good convergence. This means a reduction of numeric calculations. Moreover, the use of the "Zwischenmedium"-principle enables one to divide a difficult problem into several smaller ones, in analogy to the modular principle used in technology.
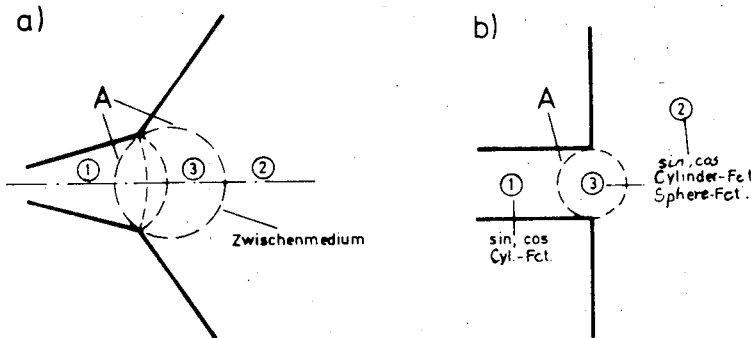
Fig.1: Transition between 2 conical horns and as a special case the circular flanged waveguide.

The problem shown in Fig. 1a will have a precise solution on the condition of continuity only on the surface A of the sphere, which was introduced as "Zwischenmedium" 3. The sphere as "Zwischenmedium" 3 in Fig.1b leads to sphere-functions instead of the complicated spheroid-functions. The planar problem being analogous to Fig.1b is the flanged parallel plate waveguide (see numeric example Fig.3). In this case the "Zwischenmedium" is a cylinder and as eigenfunctions you have only sin-, cos- and cylinder-functions instead of the Mathieus's functions.
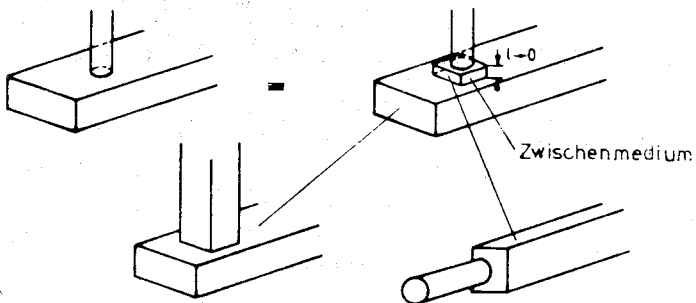
Fig.2: Rectangular waveguide with attached circular waveguide. Partitioning by a "Zwischenmedium".

Fig.2 shows the division of the problem into two problems, which can be solved separately. After formation of the scattering-matrices the solution of the problem is gained by chaining (modular principle).

2. Examples
2.1 Radiation from a flanged waveguide
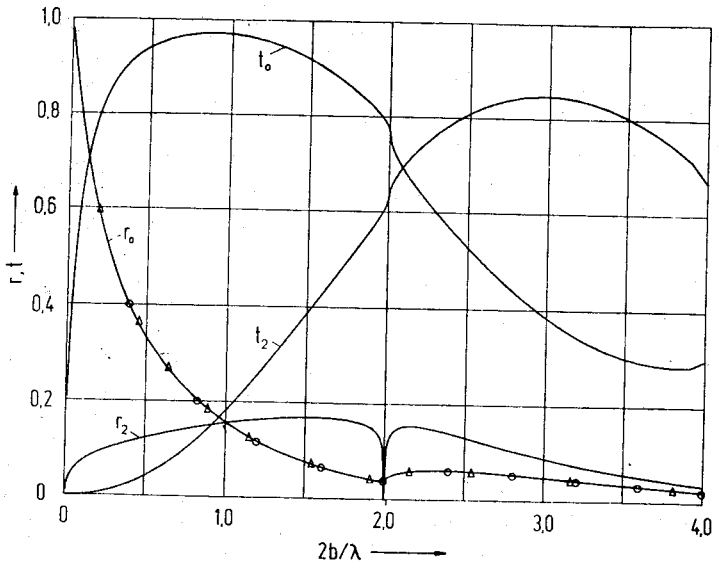
Fig.3: Magnitude of the reflection coefficient r and transmission coefficient t for the TEM excitation. r_o, t_o (TEM-mode) r_2, t_2 (TM$_{20}$-mode)

    b height of the waveguide
    o Mittra
    Δ Früchting

106

The mathematical method is the same as described for Fig.1b. Fig.3 shows the numerical solutions according to (2) and in comparison with Mittra (3), Früchting (4). Best convergence with ratio L : N = 2. Graphs in Fig.3 are calculated with N = 6. L number of waves in medium 2, N number of waves in medium 1. L + N number of waves in medium 3 (compare Fig.1b).

2.2 Scattering of a planar wave at an ideally conducting angle

Fig.4 shows the division of the total area into three media. Components of the field of the incident wave are E_z, E_ϕ, H_ρ (E-wave).
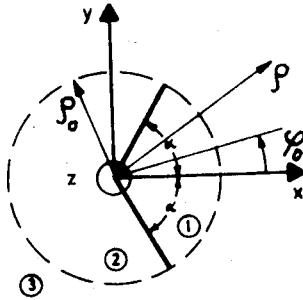
Fig.4: Location of the angle in the coordinate-system. "Zwischen-medium" 2.

ϕ_0 angle of incidence of the wave

$f_n = \dfrac{2\rho_0}{\lambda_0}$ normated frequency

λ_0 wavelength in vacuum

Calculation for the H-wave is analogous. Eigenfunctions are trigonometric- and cylinder-functions. The expansion is developed from media 1 and 2 to medium 3. The expansion-integrals are solvable in closed form. Good convergence at ratio L : N = $(\pi - \alpha)/\alpha$. N number of waves in medium 1, L number of waves in medium 2. L + N number of waves in medium 3. Fig.5 shows some numerical results for the scattering-field. 18 waves in medium 3 were taken into consideration.
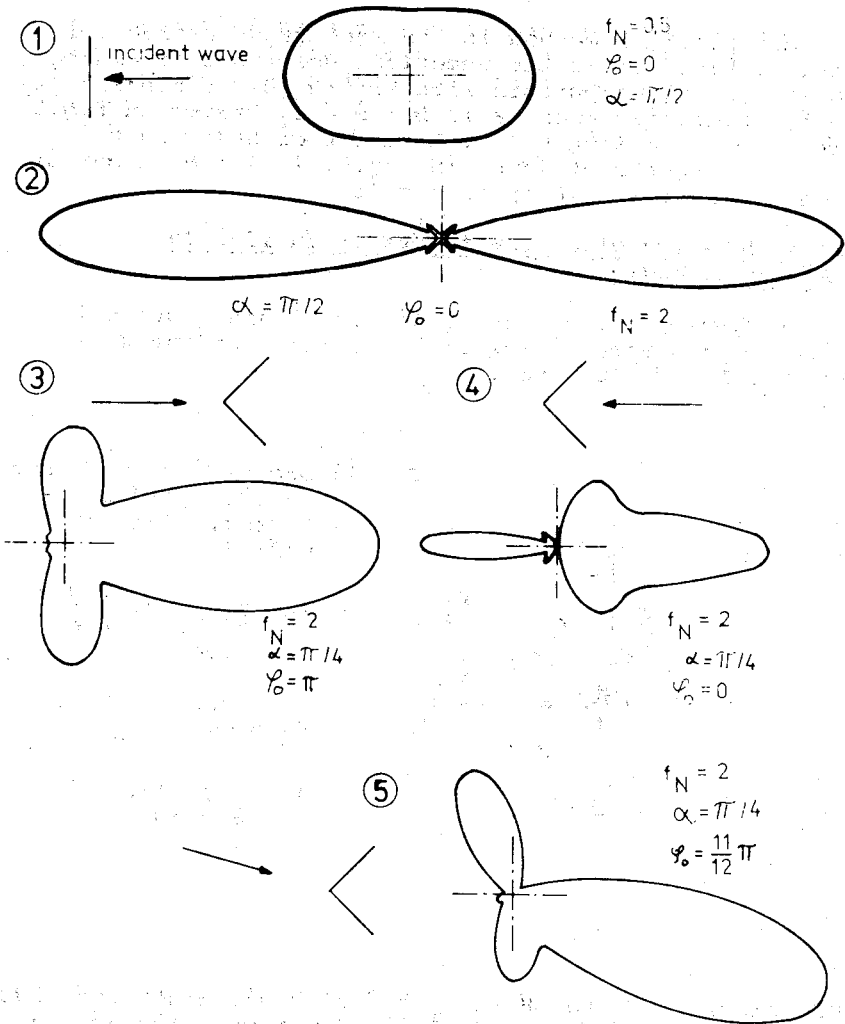
Fig.5: Scattering field at an angle

References

1. G.Piefke (1970 Archiv für Elektronik und Übertra-
   gungstechnik 24, p.523)

2. F.Reisdorf, W.Schminke (1973 Proceedings of IEE,
   to be published)

3. H.Früchting (1970 Nachrichtentechnische Zeitschrift
   23,p.80)

4. T.Itoh, R.Mittra (1971 Proceedings of IEEE 59,p.1131)

VARIANCE AND CORRELATION OF CUTOFF EIGENMODES
IN A ROUGH-WALLED CYLINDRICAL WAVEGUIDE

H.S. Cabayan

Gulf Radiation Technology, Inc.
San Diego, California

R.C. Murphy
McGill University
Montreal, Quebec, Canada

We are interested in the problem of determining statis-
tics of the characteristic cutoff frequencies of a cir-
cular cylindrical waveguide when the walls of the wave-
guide are not smooth, but are described by a random
variable with a particular correlation length. We shall
find solutions of the Helmholtz equation

$$(\nabla^2 + k^2)\Psi = 0 \qquad (1.1)$$

subject to the boundary condition at the rough conduc-
ting surface

$$\Psi(\Gamma) = 0 \qquad (1.2)$$

The surface belongs to an ensemble of surfaces which
can be described by

$$\Gamma = \Gamma_0 + \epsilon r \qquad (1.3)$$

where Γ_0 is the unperturbed surface and r is a random
variable with $\langle r \rangle = 0$. It is assumed that r is real and
homogeneous, and that $\langle r(\phi) r(\phi') \rangle = \eta(|\phi - \phi'|)$, where ϕ
is the angle to a point on the waveguide surface. See
Figure 1. ϵ is a small number.

With any particular boundary, the waveguide problem
determines a set of eigenfunctions and the eigenvalues
associated with them. More importantly, the cutoff
eigenfunctions and eigenvalues can be determined for
which there is no z-propagation of the field. At cutoff,
with $k_z = 0$, the wavenumber k is a function of the geome-
try. In order to study the statistics of the cutoff
wavenumber with an imposed random boundary condition,
we can expand it in a power series:

$$k = k_0 + \epsilon k_1 + \epsilon^2 k_2 + \cdots \qquad (1.4)$$

Likewise, the field itself can be expanded in a power
series:

$$\Psi = \Psi_0 + \epsilon \Psi_1 + \epsilon^2 \Psi_2 + \cdots \qquad (1.5)$$

The random boundary condition can be handled as
follows: The field at any point on the rough conducting
surface is zero, so if we expand the field in a Taylor

series to account for boundary roughness, it equals
zero also:

$$\Psi(\Gamma_0 + \epsilon r) = \Psi(\Gamma_0) + \epsilon r \frac{\partial}{\partial} \Psi(\Gamma_0) + \cdots = 0 \qquad (1.6)$$

By subsituting (1.4) and (1.5), the Helmholtz equation
becomes:

$$\left[\nabla^2 + k_0^2 + 2\epsilon k_0 k_1 + 0(\epsilon^2)\right]\left[\Psi_0 + \epsilon\Psi_1 + \epsilon^2\Psi_2 + \cdots\right] = 0 \qquad (1.7)$$

Inserting (1.5) into (1.6), the boundary condition
takes the form:

$$\Psi_0(\Gamma_0 + \epsilon r) + \epsilon\Psi_1(\Gamma_0 + \epsilon r) + 0(\epsilon^2) = \Psi_0(\Gamma_0) + \epsilon\Psi_1(\Gamma_0) + \epsilon r\frac{\partial}{\partial n}\Psi_0(\Gamma_0) + 0(\epsilon^2) = 0 \qquad (1.8)$$

Re-arranging, and setting each order of ϵ to zero, we
get for the first two orders of ϵ:

$$(\nabla^2 + k_0^2)\Psi_0 = 0$$
$$\Psi_0(\Gamma_0) = 0 \qquad \qquad \text{Problem A: unperturbed.} \quad (1.9)$$

$$(\nabla^2 + k_0^2)\Psi_1 + 2k_0 k_1 \Psi_0 = 0$$
$$\Psi_1(\Gamma_0) + r\frac{\partial}{\partial n}\Psi_0(\Gamma_0) = 0 \qquad \text{Problem B: } 1^{\underline{st}} \text{ order} \quad (1.10)$$
$$\text{perturbation.}$$

Solving Problem A, we find solutions to the cylindrical
waveguide at cutoff. The TM wavefunctions are given by:

$$\Psi_{0np(cutoff)}^{TM \begin{bmatrix} o \\ e \end{bmatrix}}(\rho, \phi, z) = J_n(\frac{x_r}{;} \frac{o}{-})\begin{Bmatrix} \sin n\phi \\ \cos n\phi \end{Bmatrix} \qquad (1.11)$$

with $k_0^2 = (x_{np}/a)^2$ where x_{np} is the $p^{\underline{th}}$ root of $J_n(x)$.
These wavefunctions will be used in the solution of
Problem B.

Problem B provides the operator equation necessary to
solve for Ψ_1 and k_1. To obtain an expression for k_1, we
make use of the divergence theorem,

$$\int_S (\Psi_1 \nabla^2\Psi_0 - \Psi_0\nabla^2\Psi_1) \, dS = \oint_{\Gamma_0} (\Psi_1 \frac{\partial\Psi_0}{\partial n} - \Psi_0 \frac{\partial\Psi_1}{\partial n}) c \, \vdots \qquad (1.12)$$

By making appropriate subsitutions from (1.9) and
(1.10), and by noting that Ψ_0 on Γ_0 is zero, we obtain:

$$k_1 = \frac{-1}{2k_0 (\Psi_0, \Psi_0)} \int_0^{2\pi} a r(\phi) \left[\frac{\partial\Psi(\rho, \phi, z)}{\partial\rho}\right]_{\rho = a}^2 d\phi \qquad (1.13)$$

where

$$(\Psi_0, \Psi_0) = \int_S \Psi_0^2 \, dS \qquad (1.14)$$

The mean value of k_1 is zero since $\langle r(\phi) \rangle = 0$. Neglecting
terms of order ϵ^2, the variance of k is

$$\sigma_k^2 = \langle (k - \langle k \rangle)^2 \rangle = \epsilon^2 \langle k_1^2 \rangle \qquad (1.15)$$

We may now write the expression from which both auto-
correlation and cross-correlation quantities may be
calculated for the eigenmodes of the cylindrical wave-
guide:

$$\left\langle k_{1 \atop np} \; k_{1 \atop qr} \right\rangle = \frac{1}{4 k_{o \atop np} \; k_{o \atop qr} \; (\Psi_{o \atop np}, \Psi_{o \atop np}) \; (\Psi_{o \atop qr}, \Psi_{o \atop qr})} \int_{o}^{2\pi}\!\!\int_{o}^{2\pi} a^2 \left\langle r(\phi) \, r(\phi') \right\rangle$$

$$\cdot \left[\frac{\partial}{\partial \rho} \Psi_{o \atop np}(\rho,\phi)\right]_{\rho=a}^{2} \left[\frac{\partial}{\partial \rho}\Psi_{o \atop qr}(\rho',\phi')\right]_{\rho=a}^{2} d\phi \, d\phi' \qquad (1.16)$$

Equation (1.16) was evaluated for two types of correlation function $\left\langle r(\phi) r(\phi') \right\rangle = \eta(|\phi-\phi'|)$. The first choice was the δ-function $\delta(|\phi-\phi'|)$ and the second an exponential form normalized at the endpoints of the endpoints of the interval $[0,2\pi]$ and symmetric within this interval:

$$\eta\,(|\phi-\phi'|) = \left[e^{-a_c|\phi-\phi'|} + e^{a_c(|\phi-\phi'|-2\pi)}\right] \Big/ \left[1 + e^{-2\pi a_c}\right] \qquad (1.17)$$

here $a_c = 1/\theta_c$, where θ_c is the correlation length in radians, chosen as $\pi/6$ for this study. Thus the exponential correlation function is quite narrow, but not nearly as narrow as the δ-function.

The evaluation of (1.16) requires a coordinate transformation which necessitates the separate treatment of the even and odd wavefunctions for $n \geqslant 1$. For example, correlations of the 4 lowest frequencies involve the 21 product pairs of:

$$\left\{ k_{01}, k_{02}, k_{11}^{e}, k_{11}^{o}, k_{21}^{e}, k_{21}^{o} \right\}$$

Table 1 shows the computed correlation values found by adding components:

$$\left\langle k_{11} \; k_{11} \right\rangle = \left\langle k_{11}^{e} \; k_{11}^{e} \right\rangle + \left\langle k_{11}^{e} \; k_{11}^{o} \right\rangle + \left\langle k_{11}^{o} \; k_{11}^{e} \right\rangle + \left\langle k_{11}^{o} \; k_{11}^{o} \right\rangle$$

The numbers listed should be multiplied by a^4 for computing correlation coefficients, and by $\epsilon^2 a^4$ for computing variances as in (1.15). While the numbers shown in the table differ only by a factor equal to the ratio of the integrated correlation functions, it should be noted that for $n=q \geqslant 1$ the individual even/odd correlations are dependent on n, but that the dependency cancels when the components are summed.

The reader is referred to Keller (1) and Boyce (2) for statistical expansion methods and the random eigenvalue problem. Chen (3) develops the boundary expansion technique which separates the problem as in (1.9) and (1.10). The authors (4) have used a similar analysis for computing field correlations in scattering by rough conducting cylinders. Harrington (5) was our reference for waveguide field theory.

MODES		δ-function	exp-function
k_{01}	k_{01}	1.85	1.93
k_{01}	k_{02}	4.23	4.43
k_{01}	k_{11}	5.87	6.15
k_{01}	k_{21}	7.87	8.24
k_{02}	k_{02}	9.71	10.17
k_{02}	k_{11}	13.47	14.11
k_{02}	k_{21}	18.06	18.91
k_{11}	k_{11}	18.69	19.57
k_{11}	k_{21}	25.05	26.24
k_{21}	k_{21}	33.58	35.16

Table 1: Intramode and intermode correlation as compu-
          ted in (1.16) for the δ-function and exponen-
          tial (1.17) surface correlation functions.
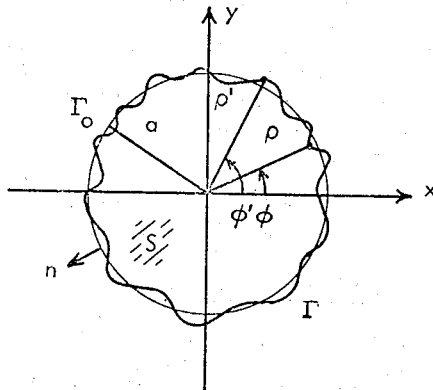
Figure 1: Cross-section schematic of cylindrical
          rough-walled waveguide.

1. J.B.Keller (1968 Proceedings of the Symposium on Tur-
    bulence in Fluids and Plasmas, Brooklyn Poly. Inst.,
    Brooklyn, N.Y. 131-142)
2. W.E.Boyce (1968 "Probabilistic Methods in Applied
    Mathematics", A.T.Bharucha-Reid, Ed., Academic Press)
3. Y.M.Chen (1968 J.Math.Phys. 9 439-450)
4. H.S.Cabayan and R.C.Murphy ($\overline{1}$973 IEEE/G-AP Trans.
    To be published in Nov. issue)
5. R.F.Harrington (1961 "Time-Harmonic Electromagnetic
    Fields", McGraw-Hill)

SCATTERING LOSS IN A CLADDED FIBRE OPTICAL WAVEGUIDE

G.L.Yip,J.Martucci and G.W.Farnell

Department of Electrical Engineering
McGill University
Montreal,P.Q.,Canada.

The objective of the present paper is to present a theoretical model to account for losses due to discrete scattering centres within a cladded fibre optical waveguide. Our discussions here are confined to a consideration of the radiation loss from a scattering centre in a cladded fibre operating in the dominant HE_{11} mode.

Assuming Raleigh theory is valid,the radiation fields from the scatterer can be calculated from a point electric dipole parallel to the incident transverse electric field and with the same induced current moment. Snyder(1969),and Clarricoats and Chan(1972) pointed out that the formulation of Green's function for open-bounded cylindrical hybrid-mode structures is extremely complex,and,because of the small dielectric difference between the $core(\varepsilon_0\varepsilon_1)$ and the $cladding(\varepsilon_0\varepsilon_2)$,they used the expression for the power radiated from an infinitesimal dipole into an infinite $medium(\varepsilon_0\varepsilon_1)$ as an approximation. However,for the simpler case of a transversely-oriented dipole on the axis of a dielectric rod,the Green's function is available(Yip,1970). We now extend the previous analysis to the case of a cladded fibre. The radiation loss for a dielectric scatterer calculated from this exact solution is found to be considerably higher than that obtained from the infinite medium approximation. In a long fibre,there will be many scattering centres,and the cumulative difference in the calculated transmitted power levels can be quite appreciable.

The dependence of the radiation loss on the dielectric difference$(\delta\varepsilon=\varepsilon_1-\varepsilon_2)$,the spatial distribution of the radiated power as well as other pertinent data will also be presented.

Session 19 Guiding and Periodic Structures

CIRCULAR BENDS IN DIELECTRIC FRAME BEAM WAVEGUIDES

P.F.Checcacci, R.Falciai, A.M.Scheggi
Istituto di Ricerca sulle Onde Elettromagnetiche
Firenze - Italia

It is well known that beam waveguides cannot be made to follow a curved path like tubular waveguides but bends can be obtained by the use of prisms or mirrors. However curvatures with large radii (like those encountered to follow the ground contour or to avoid obstacles along the path) can be achieved by lateral displacements of the elements in a lens beam waveguide or by a sequence of small angle changes at each aperture of an iris waveguide (1,2,3,4). This of course implies an increase of the losses.

The present communication is concerned with an investigation on circular bends in beam waveguides constituted by dielectric frames (5) along with some design considerations for the transition between straight and curved sections of the guide.

An uniform bending of the guide axis is also here obtained by tilting each frame by a small angle; however due to the phase correction performed by the dielectric frame the losses introduced by the bending can be made lower than those of an analogously curved iris guide.

On the basis of the analogy between open resonators and beam waveguides the diffraction losses of a planar F.P. resonator with tilted mirrors have been evaluated for different amounts of tilting and by varying the Fresnel number. Such losses have been compared with those evaluated for the same resonators in the presence of a rim along the edges of the mirrors. It turned out that for suitable values of the rim thickness the losses for the tilted rimmed resonator are much lower than those in the absence of the rim and this decrease is due to the rims placed at the largest-distance edges of the mirrors thus limiting the field spill-over caused by the tilting. The

rims placed at the nearest-distance edges have a negligible effect as the field at that side is practically zero. Hence this rim could be suppressed; however when considering the corresponding beam waveguides this rim is maintened for constructive convenience and the curved section results constituted by a number of frames tilted one with respect to the other by the same angle.

The numerical computations have allowed to assess in a number of cases the maximum permissible amount of tilting (and hence minimum radius of curvature of the waveguide) and the corresponding optimum frame dimensions in view of acceptable losses.

Losses due to mode conversion which add to the diffraction losses due to bending have also been evaluated when considering the design criteria for connecting a straight into a curved section of the waveguide.

1. D.Marcuse: (1965, Bell Syst. Tech. J. 44, p.2065)
2. G.Goubau: (Academic Press 1968 - Advances in Microwaves, pp.110-123)
3. J.W.Mink: (1969, IEEE Trans MTT-17, p.48)
4. J.W.Mink: (1971, Electronics Letters 7, p.527)
5. P.F.Checcacci, R.Falciai, A.M.Scheggi: (1972, IEEE Trans MTT-20, p.608)

Session 19 Guiding and Periodic Structures

FIELD DISTRIBUTIONS INSIDE THE CONICAL WAVEGUIDE

L. J. Du
Department of Electrical Engineering
University of Louisville
Louisville, Kentucky 40208

Analytical expressions for the electromagnetic fields inside a perfectly conducting conical waveguide of semi-infinite extent have been well known [1],[2]. If the apex of the cone coincides with the origin of the coordinate system and the polar axis is the longitudinal axis of symmetry of the cone, then conical surface will coincide with surface of constant colatitude angle θ_0 as shown in Fig. 1. The permissible TE fields are

$$E_r = 0$$

$$E_\theta = \frac{1}{r}\hat{H}_\nu^{(2)}(kr)\frac{m}{\sin\theta}P_\nu^m(\cos\theta)\sin m\phi$$

$$E_\phi = \frac{1}{r}\hat{H}_\nu^{(2)}(kr)\frac{\partial}{\partial\theta}\left[P_\nu^m(\cos\theta)\right]\cos m\phi$$

$$H_r = \frac{1}{j\omega\mu}\left[\frac{\partial^2}{\partial r^2}+k^2\right]\hat{H}_\nu^{(2)}(kr)\,P_\nu^m(\cos\theta)\cos m\phi \tag{1}$$

$$H_\theta = \frac{1}{j\omega\mu}\left[\frac{1}{r}\frac{\partial}{\partial r}\hat{H}_\nu^{(2)}(kr)\right]\frac{\partial}{\partial\theta}\left[P_\nu^m(\cos\theta)\right]\cos m\phi$$

$$H_\phi = \frac{1}{j\omega\mu}\left[\frac{1}{r}\frac{\partial}{\partial r}\hat{H}_\nu^{(2)}(kr)\right]\frac{-m}{\sin\theta}P_\nu^m(\cos\theta)\sin m\phi$$

where

$$\hat{H}_\nu^{(2)}(kr) = kr\,h_\nu^{(2)}(kr)$$

$h_\nu^{(1)}(kr)$ is the spherical Hankel function of order ν, k is the wave number $2\pi/\lambda$ and $P_\nu^m(\cos\theta)$ is the associated Legendre function of order ν and degree m. m is an integer and ν is the solution of the equation

$$\left.\frac{d}{d\theta}P_\nu^m(\cos\theta)\right|_{\theta=\theta_0}=0. \tag{2}$$
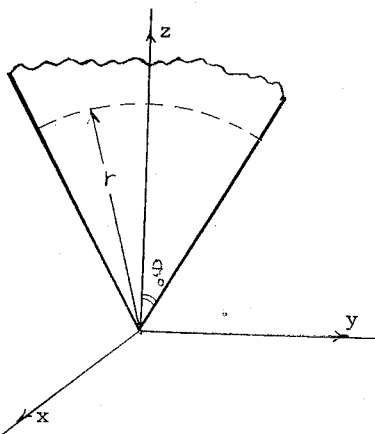
Fig. 1. Geometry of conical waveguide.

116

The permissible TM fields are

$$E_r = \frac{1}{j\omega\epsilon}\left[\frac{\partial^2}{\partial r^2} + k^2\right] \hat{H}_\nu^{(2)}(kr)\, P_\nu^m(\cos\theta)\,\cos m\phi$$

$$E_\theta = \frac{1}{j\omega\epsilon}\left[\frac{1}{r}\frac{\partial}{\partial r}\hat{H}_\nu^{(2)}(kr)\right]\frac{\partial}{\partial\theta}\left[P_\nu^m(\cos\theta)\right]\cos m\phi$$

$$E_\phi = \frac{1}{j\omega\epsilon}\left[\frac{1}{r}\frac{\partial}{\partial r}\hat{H}_\nu^{(2)}(kr)\right]\frac{-m}{\sin\theta}\,P_\nu^m(\cos\theta)\,\sin m\phi$$

$$H_r = 0 \tag{3}$$

$$H_\theta = \frac{1}{r}\hat{H}_\nu^{(2)}(kr)\frac{-m}{\sin\theta}\,P_\nu^m(\cos\theta)\,\sin m\phi$$

$$H_\phi = \frac{1}{r}\hat{H}_\nu^{(2)}(kr)\left[-\frac{\partial}{\partial\theta}\,P_\nu^m(\cos\theta)\right]\cos m\phi$$

where ν is the solution of the equation

$$\left. P_\nu^m(\cos\theta)\right|_{\theta=\theta_0} = 0. \tag{4}$$

     Because of the difficulties involved in solving equations (2) and (4) numerical results for the field structure are still unknown. Recently, a simple iterative procedure for evaluating the exact eigenvalue ν was developed [3] by making use of the recurrence relations and the integral representation for the associated Legendre functions [4]:

$$P_\nu^m(\cos\theta) = (-1)^m\left(\frac{2}{\pi}\right)^{\frac{1}{2}}\frac{\Gamma(\nu+m+1)}{\Gamma(\nu-m+1)\,\Gamma(m+\frac{1}{2})\,\sin^m\theta}$$

$$\int_0^\theta \cos\left(\nu+\frac{1}{2}\right)\chi\left[\cos\chi - \cos\theta\right]^{m-\frac{1}{2}}d\chi. \tag{5}$$

     The two transverse electric field components as well as the two transverse magnetic field components have the same dependence on r as indicated in (1) and (3). If we are concerned only with the distributions on a constant radius spherical cross-section field components will depend only on the factors which are functions of the coordinates θ and ϕ. Numerical methods were used to find the value of ν and to calculate these factors to determine the field intensities across such a spherical cross-section inside the cone. Some of the results are shown in Fig. 2 where lines of electric field are sketched. The radial coordinate

TE_{11}	TE_{12}	TE_{21}	TE_{22}
$\nu = 3.184$	$\nu = 9.864$	$\nu = 5.605$	$\nu = 12.419$

TM_{11}	TM_{12}	TM_{21}	TM_{22}
$\nu = 6.836$	$\nu = 12.910$	$\nu = 9.373$	$\nu = 15.615$
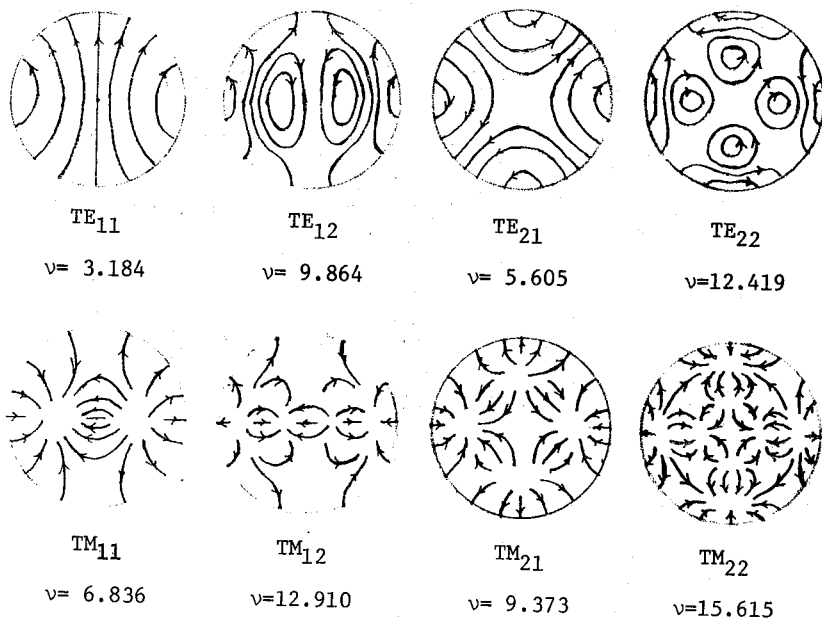
Fig. 2. Field distributions inside a cone with flare
          angle $\theta_0 = 30$ degrees.

corresponds to the polar angle θ. The flare angle θ_0 of the cone
is 30 degrees. These modes are designated TE_{mp} or TM_{mp} having m
field variations in one azimuthal circuit and p field variations
from polar axis to the cone wall.

       These distributions are quite similar to the
corresponding planar cros-sectional mode patterns in cylindrical
waveguide due to the fact that the Bessel functions $J_m(\rho)$ and the
Legendre function $P_\nu^m(\theta)$ varies similarly as functions of their
respective arguments especially when the arguments are small [3].
In the transmission region where kr>>1 the waves behave
asymptotically as spherical waves in unbounded medium. The radial
field components become negligible and the wave inpedance
approaches to the intrinsic impedance of the medium $\sqrt{\mu/\epsilon}$ for both
TE and TM modes. The transverse magnetic field is perpendicular
to the transverse electric field and they are in phase also. This
is the same relation as that of the cross-sectional field
structure inside the cylindrical waveguide. There is no clear
cut cut-off radius to separate the transmission region and
attenuation region inside the cone [1], [5]. In the attenuation
region the transverse magnetic field is still perpendicular to the
transverse electric field except the phase relationship between
them is rather complicated. This is quite different from the
situation in cylindrical waveguide where the phase angle between

the orthogonally oriented transverse electric and magnetic fields
is 90 degrees when the modes are operated with frequency below
cut-off.

References

1. M.G.Schorr and F.J.Beck,Jr.(1950 J. Appl. Phys. 21,p. 795).
2. R.F.Harrington(1961 Time-Harmonic Electromgnetic Fields,McGraw-
   Hill,p.279).
3. M.S.Narasimhan(1973 IEEE Transactions AP-21,p.8).
4. W.Magnus and F.Oberhettinger(1954 Formulas and Theorms for the
   Functions of Mathematical Physics,Chelsea,p.67).
5. W.L.Barrow and L.J.Chu(1939 Proc. I.R.E. 27,p.51).

A CROSS-CORRELATION ANALYSIS OF THE INPUT
ADMITTANCE AND BLINDNESS PHENOMENON OF PHASED ARRAYS

A. I. Zaghloul and R. H. MacPhie
Department of Electrical Engineering
University of Waterloo, Waterloo, Ont., Canada

The Fourier transform relationship between the cross-correlation
function and the cross spectral-density is applied to antenna
arrays in order to calculate the input admittance of the array
elements. We consider the cross-correlation function between the
total array function $f_a(x)$ and the central element function $f_e(x)$:

$$R_{ea}(\xi) = \frac{1}{a} \int_{-a/2}^{a/2} f_a(x+\xi)\ f_e^*(x)\ dx \tag{1}$$

where a is the aperture width of the element. The element-array
cross power density pattern is related to the cross-correlation
function R_{ea} by the following modified Fourier transform:

$$P_{ea}(u) = \frac{1}{2\pi\eta(u)} \int_{-\infty}^{\infty} R_{ea}(\xi)\ e^{ju\xi} d\xi , \tag{2}$$

where $u = k_0\sin\theta$ (k_0 being the free-space wave number and θ the
angle measured from the broadside direction) and $\eta(u)$ is the plane
wave intrinsic impedance in the u direction. The total power per
unit length of the element is given by:

$$P_{ea} = a \int_{-\infty}^{\infty} P_{ea}(u)\ du . \tag{3}$$

Equating this with the power per unit length fed to the element
leads to an expression for the input admittance.

In this paper we apply this method to find the input admittance and
hence the active reflection coefficient of two types of arrays:
(a) an infinite slot array with its elements periodically spaced
and (b) the same array subjected to element positioning errors of
the inter-element spacing type studied in [1]. As is shown in
Fig. 1, the slots are infinite in the y direction and there is a
dielectric slab of thickness t covering the array. For narrow
slots the functions f_e and f_a are shown in Fig. 2a while Fig. 2b
illustrates their cross-correlation function R_{ea}. In this figure
$u_0 = k_0\sin\theta_0$ where θ_0 is the main beam direction. Proceeding from
(2) and (3) we derive the input admittance for the element. If the
array is periodic (the δ's in Figs. 1 and 2 are all zero), this
also yields the input admittance for the array, a result which is
in agreement with the admittance obtained by the unit-cell method
[2]. For arrays having positioning errors with the variance of the
δ's equal to σ^2, the input admittance to the whole array is shown
to be proportional to the mean of the element input admittances.
Although this is a statistical quantity, for infinite arrays it
becomes deterministic (variance approaches zero) and it can be used

to determine the active reflection coefficient of the array.

Several examples are calculated with different combinations of the parameters B (nominal element spacing), t and σ. Fig. 3 shows the reflection coefficient curves for arrays with B = 0.5λ, t = 0.2λ and σ= 0, 0.05, 0.1 and 0.2. For the ideal periodic array (σ = 0), a unity reflection coefficient point (blind spot) is noticed at θ_0 = 44°, while as σ increases this peak is replaced by a dip preceded and succeeded by reflection coefficient peaks less than unity. For σ = 0.2 the curve becomes fairly smooth and the blind spots disappear. For infinite periodic arrays the blindness is due to a resonance effect which causes the input susceptance to be +∞ [3]; the positioning errors have the effect of deresonating the system and the susceptance varies smoothly from a finite positive peak to finite negative peak, passing through zero on the way.

An important result of the analysis by the cross-correlation techniques is that for a finite periodic array, the variation of the reflection coefficient with scanning angle shows a dip at the position of "blindness" whereas two peaks appear just before and after this dip. This makes the array blind on each side of the critical angle, but not blind at the angle itself. The width of the dip in the reflection coefficient curve depends on the number of elements in the array and it approaches zero as the array becomes infinite. This variation of the input admittance for different array sizes is shown in Fig. 4 where the peak susceptances correspond to peaks in the reflection coefficient curve and the near zero susceptance corresponds to a dip.

This method, involving the cross-correlation between the aperture fields of different elements, includes explicitly the mutual coupling effect which plays an important role in the scanning pattern of phased arrays. It can be applied not only to periodic and non periodic, but to finite as well as infinite array configurations. This approach also clarifies the nature of the blindness for large finite periodic arrays. The array is blind before and after this angle and has a very small reflection coefficient at the point of "blindness".

References:

1.   A. I. Zaghloul and R. H. MacPhie (1972 IEEE Transactions, AP-20, p. 637).

2.   G. H. Knittel, A. Hessel and A. A. Oliner (1968 Proceedings of the IEEE 56, p. 1822).

3.   A. A. Oliner (1969 Alta Frequenza XXXVIII N. Speciale, p. 221).
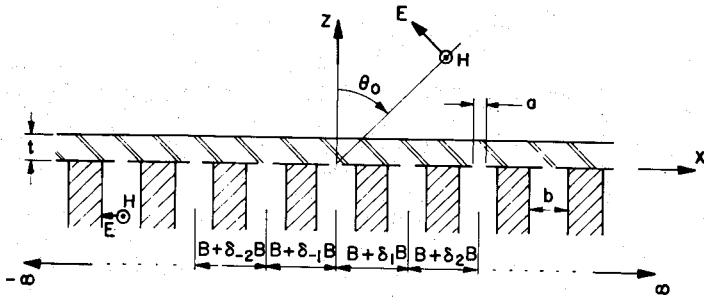
Fig. 1.   Infinite Slot Array Subject to Positioning Errors.
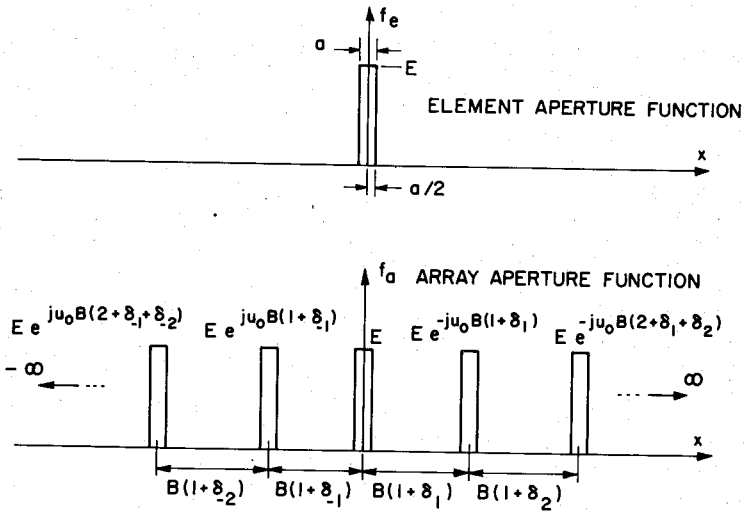
Fig. 2a.   Element and Array Aperture Functions.
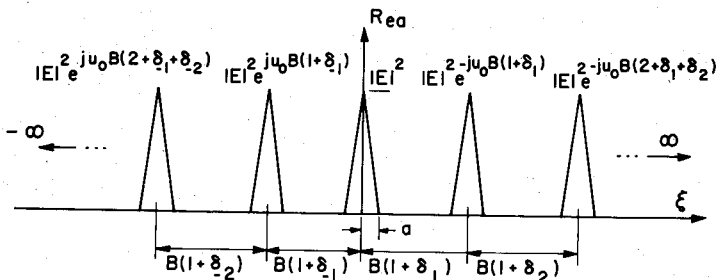
Fig. 2b.   Cross-correlation Function of f_e and f_a.
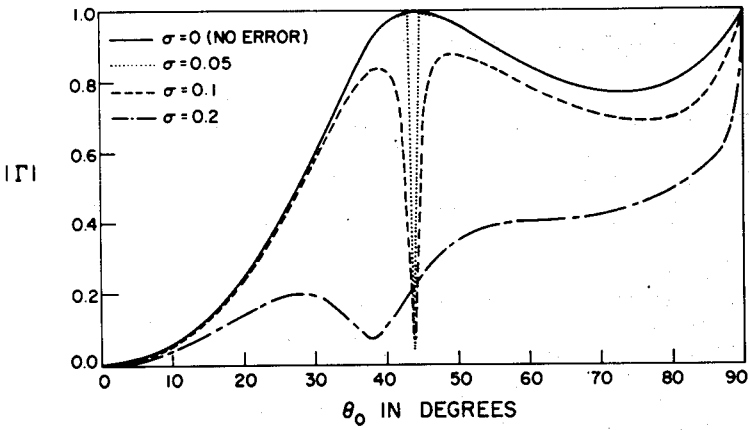
Fig. 3. Variation of Reflection Coefficient with Scanning Angle
for Arrays with B = 0.5λ, and t = 0.2λ.
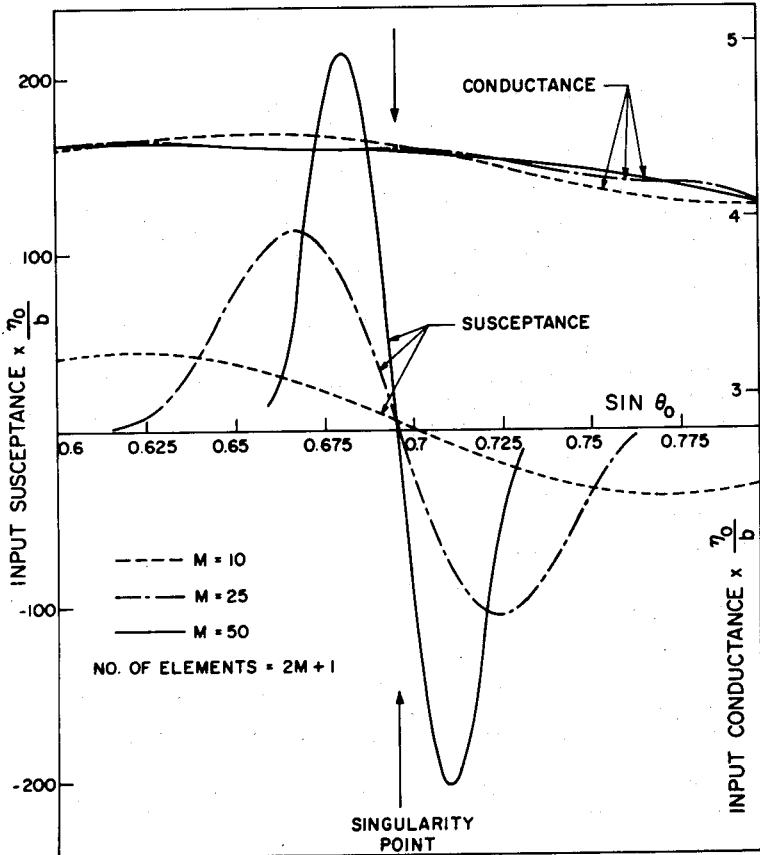
Fig. 4. Input Admittance Variation Near the "Blindness" Point
for Finite Periodic Arrays with B = 0.5λ and t = 0.2λ.

Session 20   Array Theory

IMPEDANCE MATCHING OF PHASED ARRAY ANTENNAS FOR ALL EXCITATIONS BY
CONNECTING NETWORKS

Dietrich E. Bergfried, Weinschel Engineering Co., Gaithersburg, Md.
and
Walter K. Kahn, George Washington University, Washington D.C.

Introduction

In phased arrays of closely spaced radiators, the mutual coupling
effects among the antennas cause variations of the active impedances,
when the array is scanned. This undesired impedance variation can
theoretically be eliminated by a lossless matching network inserted
between the array and its feeding generators [1,2]. However no
constructive matching technique, that permits the calculation of the
circuit elements required, has been published. In this paper such a
technique that achieves this complete match, which can in principle
be applied to any array, will be presented. As such it constitutes
a constructive proof that any array can be matched by means of a
lossless reciprocal network.

Interconnecting susceptances for wide angle array matching were
introduced by Hannan, Lerner and Knittel [3]. The susceptances con-
nected between the elements introduce phasing dependent signals
(equivalently, phasing dependent susceptances) into the feed lines,
which cancel the signals coupled by the mutual impedances. The
special symmetry of the infinite array implies that the real and
imaginary parts of the mutual impedance matrix $[Z]$ are simultaneously
diagonalized by the conventional uniform amplitude and linear pro-
gressive phase excitation. The complex active impedance for this
excitation may therefore be matched by Hannan's technique [2]. In
general, the real and imaginary parts of $[Z]$ have different eigen-
bases. However the imaginary part of $[Z]$ can be cancelled by an
interconnecting network. The remaining real impedance matrix may
then be matched by a generalization of Hannan's technique to be
described in this paper.

The Matching Process

A typical interconnecting network is shown in Fig. I for the example
of a five element array. One connecting susceptance is inserted for
every mutual impedance between any two elements in the array. These
susceptances are connected a quarter wavelength away from the antenna
terminal plane where all mutual impedances are inverted into mutual
admittances, and can be modified with shunt interconnections. The
complete network consists of N elements to ground, (N-1) first
order connections between direct neighbours, (N-2) second order
connections, etc. up to one Nth order connection. In the most
general case all connecting susceptances, even the ones of the same
order, may be different.
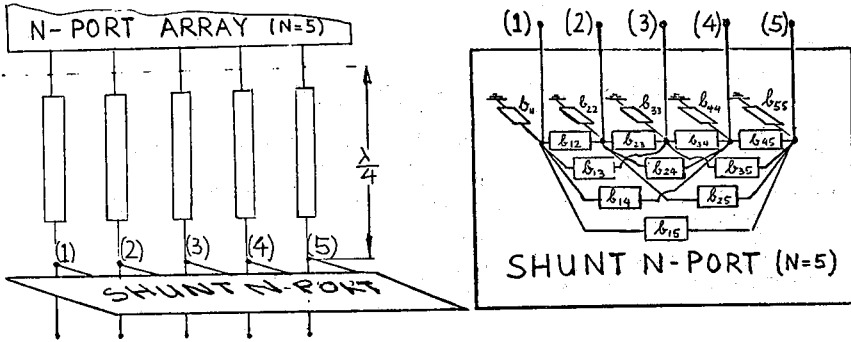
Fig. I Typical Shunt Interconnecting Network

Let the N element array be represented by its mutual impedance matrix [Z]. The voltages and currents at the array ports are then related by the matrix equation

$$\underline{V} = [Z] \, \underline{I}$$

i.e., the voltages at each port depend in general on the currents at every other port. For the special case in which the currents in the antennas are proportional to one of the eigenvectors of [Z], all components of the vectors $\underline{V}$ and $\underline{I}$, i.e., the voltages and currents at each element are related by the same constant, the eigenvalue. For this excitation all ports are decoupled and identical, and the complicated N-port can be represented as N decoupled one-ports.

Since every excitation of a linear network can be considered as a linear combination of eigenexcitations, the goal is to match the network for its eigenexcitations. It will then automatically be matched for any other excitation. If the terminals of the shunt connecting network, are ordered in the same ordering scheme as the antenna ports, the matrices [Z] and the susceptance matrix [B] correspond. The elements of [Z] however are complex, while the elements of [B] are real.

The first step in the matching procedure involves cancellation of all reactive components of the mutual impedances, so that the remaining mutual impedance matrix contains only real coefficients. This is accomplished, if a set of interconnecting susceptances is used in the reference plane a quarter wavelength from the antenna terminal plane with normalized susceptances numerically equal to the reactive parts of the corresponding mutual impedance coefficients.

The remaining real mutual impedance matrix Re [Z] is symmetric for reciprocal antennas. Consequently, a real orthogonal set of eigenvectors can be found by any one of the standard methods and combined into a modal matrix [M].

125

The transformation

$$[\widetilde{M}]\ Re\ [Z]\ [M] = diag\ [\widehat{Q}(o),\dots\widehat{Q}(N)]$$

(2)

will therefore diagonalize the residual real mutual impedance matrix.
The eigenvalues which appear on the principal diagonal are the real
impedances $\widehat{Q}(n)$ associated with the eigenexcitations of the residual
network. The network Re [Z] will now be matched by a generalization
of Hannan's technique.

The complete matching circuit that comprises three sets of inter-
connecting networks separated by two quarterwave transformers is
shown in Fig. IIa.
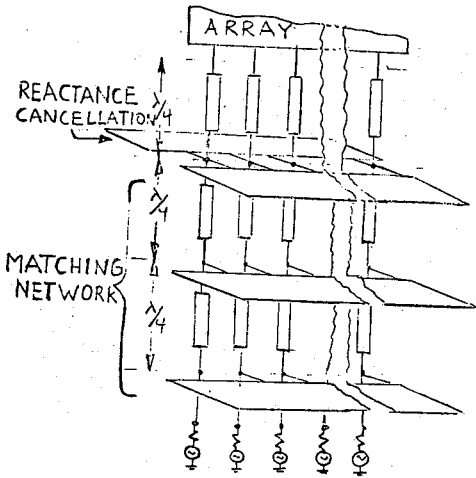
Fig. IIa Complete Matching Network
          for an N-Element Array
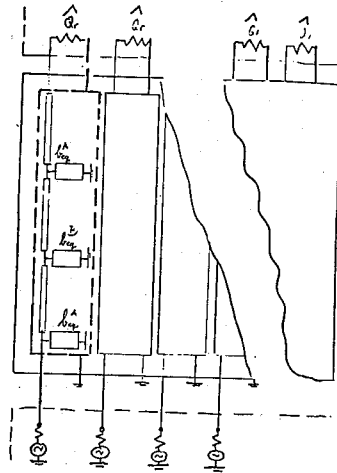
Fig. IIb Equivalent Circuit
          for the Eigenexci-
          tation

The elements b_{ij} of the susceptance matrices [B] of each shunt
N-port are defined such that the transformation

$$[\widetilde{M}]\ [B]\ [M] = diag.\ [beq(o)\dots beq(n)]$$

(3)

will diagonalize the matrix [B].

For this choice of elements and any eigenexcitation of the network
Re [Z] the 2N-port matching network can be represented as N de-
coupled and identical two-ports as shown in Fig. IIb. Each two-port
comprises three shunt susceptances separated by quarter wavelength
transmission lines and is equivalent to a π type matching network.
The two outer susceptances beq^A may be chosen to be identical and
act as shunt elements to the π. The element in the center, which
has a different value than the outer ones, is connected between
two quarterwave transformers which act as inverters [4]. The in-
verter interchanges series and parallel connections and thus trans-
forms the shunt susceptance into a series reactance.

The values of the equivalent shunt susceptances, derived from the
transformation in the normalized admittance plane, are found from
the real eigenvalues $\hat{Q}$ as

$$beq^A = \sqrt{\hat{Q}(n)} \tag{4}$$

$$beq^B = \sqrt{\frac{1}{\hat{Q}(n)}} \tag{5}$$

When all equivalent shunt susceptances for the eigenexcitation are
determined, the values of the connecting elements can be obtained
from the inverse operation of eq. 3.

The matching procedure is completely general and can be applied to
arbitrary arrays with arbitrary matrices. The only stipulation is,
that one interconnecting susceptance is used for each mutual impe-
dance and that the mutual impedances and connecting susceptances
are ordered in the same matrix form. This insures that the two
matrices have a common eigenbasis.

The matching network becomes very elaborate even for moderate size
arrays since $3 \cdot \frac{N(N+1)}{2}$ interconnecting susceptances are required to
match an N element array. It can, however, serve as a guideline to
evaluate simpler matching networks which neglect higher order mutual
coupling effects.

References

1. D.M. Sazonov and B. A. Mishustin, 1968 Radio Engineering, Vol. 13,
   No. 8.
2. P. W. Hannan, 1967 Radio Science 2, p. 361-369.
3. Hannan, Lerner, Knittel, 1965 IEEE Transactions AP 13, p. 28-34.
4. H. A. Wheeler, Wheeler Monographs #1.

A SHORT, HARDENED, PHASED ARRAY ELEMENT

William H. Schaedla
RCA Missile and Surface Radar Div., Moorestown, N. J.

Environmental restrictions, such as weather considerations and nuclear hardening, often play an important role in phased array radiating element design. This paper describes the design approach used and the results achieved for a phased array element restricted by such considerations.

The element was designed for operation over a 1/4 hemisphere scan volume and a 10% bandwidth at D-Band (JCS designation). Thermal and mechanical considerations required the use of a highly capacitive, beryllium oxide window at the element aperture. In order to keep the overall length of the element to a minimum, the waveguide-to-coax transition was designed to provide element matching, as well as to act as a TE_{10} waveguide mode launcher. The element design was achieved using the following design sequence: 1. A waveguide aperture, consistent with the environmental requirements, which minimized the frequency and scan impedance variation was designed by computer analysis. 2. A launcher was designed which, when combined with this waveguide aperture, provided an acceptable element match. 3. This composite design was tested in array simulators and slight corrections were made, as necessary, to correct for deviations due to the practical application of the idealized design.

The element is shown in Figure 1. It consists of a 7.6" x 1.9" rectangular waveguide casting, an N-type coax-to-waveguide end launcher, and a 0.188" thick beryllium oxide window set in a thick inductive iris to form the radiating aperture.

The radiating aperture was designed using a versatile computer analysis based upon a mode-matching technique[1,2]. This computer analysis accurately predicts the array impedance (or admittance) for an infinite array of waveguide elements incorporating an aperture iris of arbitrary thickness and an arbitrary set of internal and external dielectric steps. An inductive iris and BeO window combination which minimized the impedance mismatch with scan and frequency was selected using this program. The resulting impedance characteristic is shown in Figure 2. The coax-to-waveguide launcher was experimentally designed to give an impedance looking into the waveguide port that approximated the conjugate of the aperture impedance as a function of frequency.

The element design was tested in two array simulators[3], a single cell simulator and a wide H-plane scan simulator, which simulate 26°-29° and 36°-40° of H-plane scan respectively. These two simulators were used to check the aperture design and to correct for the practical implementation of 1) the BeO window mounting technique and 2) the trenched ground plane design incorporated

for rain runoff. The single cell simulator was used to test the total element design and to make small corrections for higher-order mode interactions between the aperture and coax-to-wave-guide transition. Good agreement between theoretical and experimental results was achieved.

The final element design provides a VSWR of less than 3:1 over 98% of the scan/frequency domain. The resulting impedance characteristic is shown in Figure 3. Seventy-two elements were manufactured for use in a fractional array. Amplitude and phase tracking measurements on these units indicated RMS phase and amplitude variations of less than 1.5 degrees and 0.16 dB respectively over the frequency band. The average dissipative loss was less than 0.2 dB.

References
1. G.F. Farrel and D.H. Kuhn (1966 IEEE Trans. AP-14, pp. 652-654)
2. J.J. Campbell and B.V. Popovich (1972 IEEE Trans. AP-20, pp. 421-427)
3. P.W. Hannan and M.A. Balfour (1965 IEEE Trans. AP-13, pp. 342-353)

FIGURE 1: ARRAY ELEMENT

FIGURE 2:   APERTURE IMPEDANCE

for rain runoff. The single cell simulator was used to test the
total element design and to make small corrections for higher-
order mode interactions between the aperture and coax-to-wave-
guide transition. Good agreement between theoretical and experi-
mental results was achieved.

The final element design provides a VSWR of less than 3:1 over
98% of the scan/frequency domain. The resulting impedance
characteristic is shown in Figure 3. Seventy-two elements were
manufactured for use in a fractional array. Amplitude and phase
tracking measurements on these units indicated RMS phase and
amplitude variations of less than 1.5 degrees and 0.16 dB
respectively over the frequency band. The average dissipative
loss was less than 0.2 dB.

References
1. G.F. Farrel and D.H. Kuhn (1966 IEEE Trans. AP-14, pp. 652-
    654)
2. J.J. Campbell and B.V. Popovich (1972 IEEE Trans. AP-20,
    pp. 421-427)
3. P.W. Hannan and M.A. Balfour (1965 IEEE Trans. AP-13,
    pp. 342-353)

FIGURE 1: ARRAY ELEMENT

FIGURE 2:   APERTURE IMPEDANCE

FIGURE 3:   ELEMENT IMPEDANCE

EDGE EFFECTS IN CONFORMAL ARRAYS

J. Shapira, L. B. Felsen, A. Hessel

Department of Electrical Engineering & Electrophysics
Polytechnic Institute of Brooklyn

This paper is concerned with edge effects in two-dimensional conformal arc arrays of identical, equispaced, axial, narrow slits in large conducting circular cylindrical surfaces; the slits are fed by TEM mode parallel plate guides. The analysis is carried out by two alternative approaches. In the first, an "element-by-element" multiple scatter approach, the scattering matrix is synthesized by inversion of the mutual admittance matrix, and yields numerical results for the coupling coefficients and element patterns in the matched array environment; the admittance matrix is calculated via the ray procedures described previously[1]. The numerical results obtained in this manner are in turn employed to validate the second, "periodic structure" approach. In the latter, it is assumed that the excited element launches a directly radiated wave (space wave) as well as periodic structure creeping waves propagating along and guided by the match terminated array structure[2]. These creeping waves are multiply reflected (and scattered) from the array edge discontinuities, thereby giving rise to edge effects. The second approach provides physical insight into the mechanism of mutual coupling and of element pattern formation in finite, conformal arrays. Either approach may be generalized to accommodate unequal elements and/or spacing, and variable curvature, but these aspects are not pursued here.

Figure 1 depicts the array geometry. Numerical results for the coupling coefficients s_{ij} in three arc arrays of 11, 31 and 51 elements are shown in Figs. 2 a, b, c, for the following parameter values: $kr_0 = 105$, $d/\lambda = 0.6$, $b/\lambda = 0.4$; all slits are matched to free space for in-phase excitation in an active full ring array environment. The quantities plotted are $|s_{ji} + \delta_{ji}|$, where δ_{ji} is the Kronecker delta, while the reflection coefficients $|s_{ii}|$ in the excited elements are marked by crosses. For ease of comparison, each figure contains a plot (and its asympote) of the full ring array coupling coefficients. For convenience, this curve is referenced to an $i = 0$ excited element.

In order to interpret the results, it is necessary to isolate the effect of a single-edge discontinuity. To this end, the coupling coefficients for the full ring array $\overline{s}_{ji} = \overline{s}|_{j-i}$ are subtracted from the s_{ji} of the 51 element array to form the difference quantity Δ_{ji}, associated with waves reflected from the edge discontinuities. In view of the decay of the creeping waves, this array is expected to be sufficiently large for damping out the interaction between the two end effects. From the plot of $|\Delta_{ji}|$ in Fig. 3 it is noted that in the central portion of the array and particularly when the center element is excited, a standing

wave pattern with pronounced dips is present, evidently formed
by an interference between waves reflected from the two array
edges and traveling in opposite directions. It will be shown that
the edge discontinuity can be represented in terms of an equiva-
lent source, the amplitude of which is determined from numerical
results.

With the known excitations of the driven and the equivalent sources,
the coupling coefficients in a finite array are evaluated in terms
of contributions from multiply reflected periodic structure creep-
ing rays traveling along the array face.   To verify the validy of
the periodic structure approach, the entire scattering matrix of
the 11 element array was reproduced and an agreement with the
values calculated directly by matrix inversion was obtained to
within an accuracy of 2%. Furthermore, an explanation of the
trends in Figs. 2a, b, c, is easily given in terms of this model.

Figure 4 presents the E-plane realized gain patterns of the 1st,
2nd, 3rd, 4th, and 16th (central) element in a 31 element arc
array having the same parameters as those of Fig. 2b. The $\phi=0$
direction of each pattern is referenced to broadside of the
excited element.   An interesting feature of the patterns of the
first two elements near the edge is the absence of the dip to the
right of broadside of the excited element and also the absence or
reduction of the ripple, characteristic of the element pattern of
a full ring array (also shown in Fig. 4).   These features of the
element patterns will be explained with the help of the periodic
structure model.

1.   J. Shapira, L. B. Felsen and A. Hessel (1972 URSI
      Fall Meeting Digest, pp 60-61.)

2.   J. C. Sureau and A. Hessel, (1971 IEEE Trans. AP-19
      pp. 64-74.)
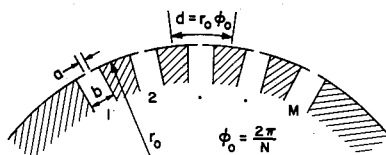
Fig. 1. M element arc slit array on a conducting circular cylinder
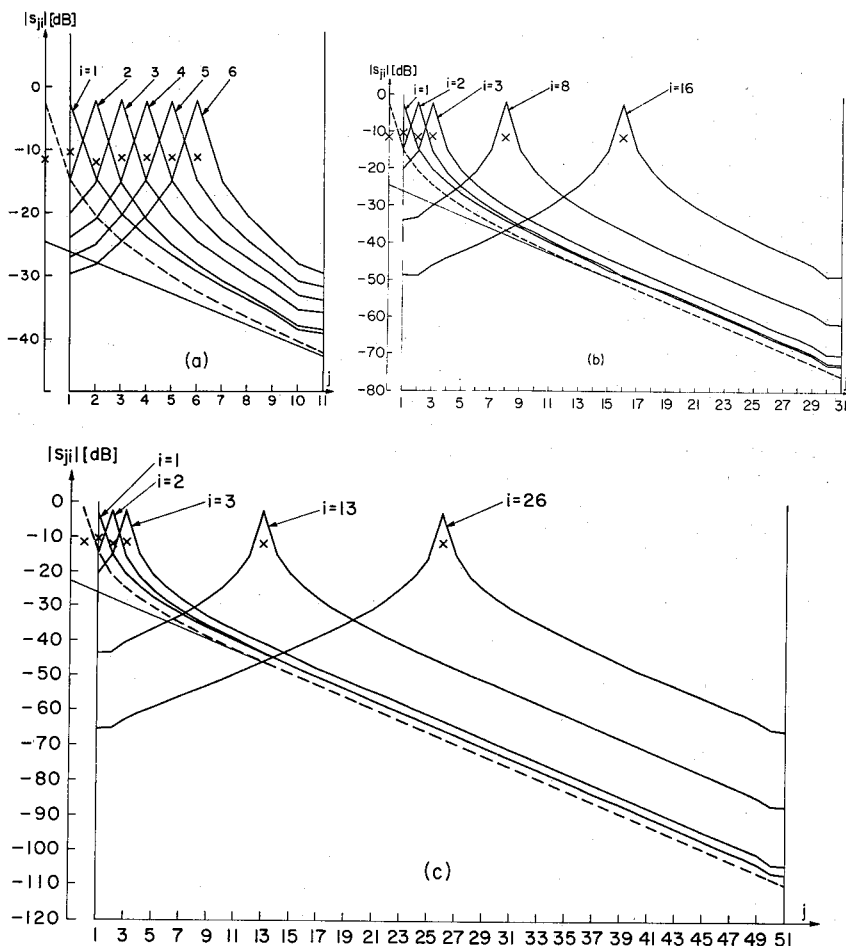
Fig.2. Coupling coefficients for finite arc arrays of parallel-plate-
guide-fed slits on a conducting circular cylinder. (a) 11 ele-
ment array (b) 31 element array (c) 51 element array

134
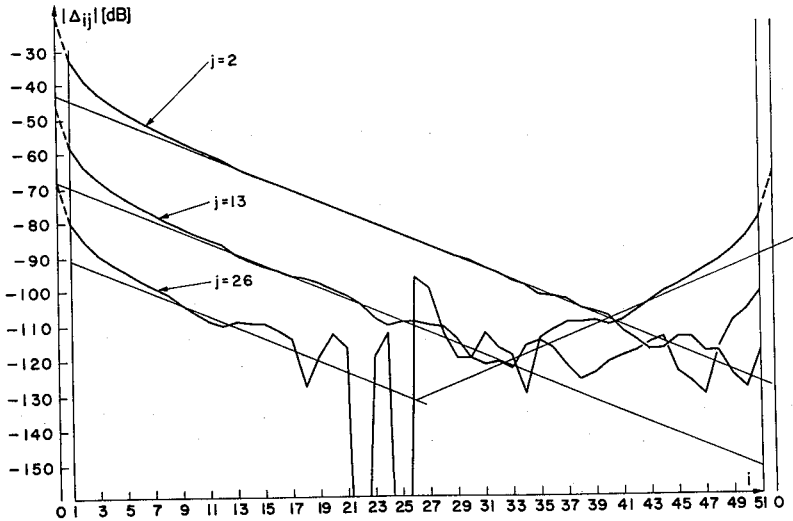
Fig. 3. Effect of array finiteness on coupling coefficients (array parameters as in Fig. 2(c))
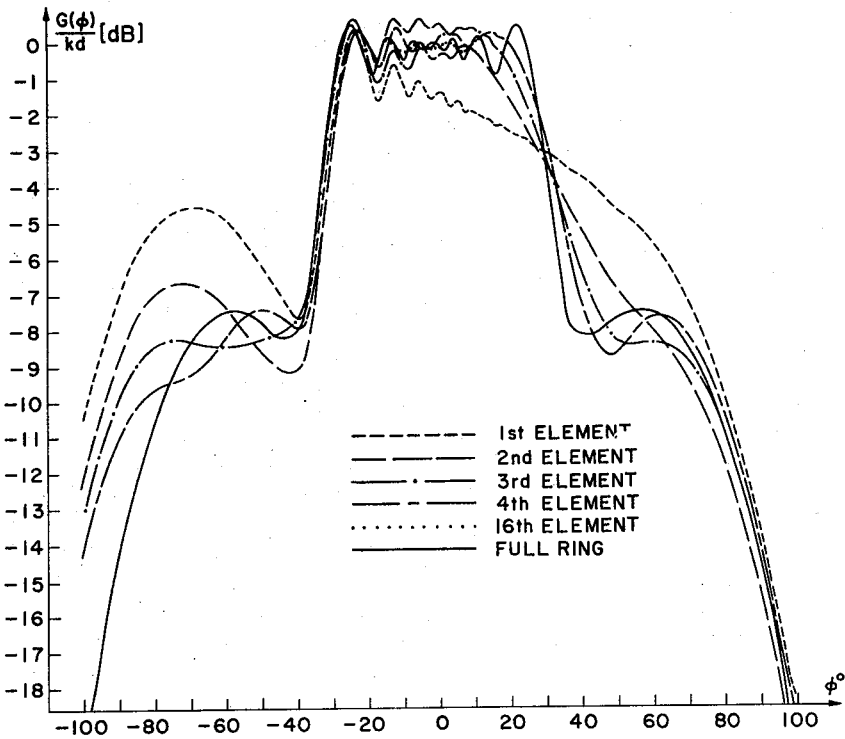
Fig. 4. Realized gain patterns for various elements (array parameters as in Fig. 2(b))

PATTERNS AND GAIN OF FINITE ARRAYS OF APERTURES

Q. Balzano, L. R. Lewis, K. Siwiak
Raytheon Company
Missile Systems Division
Bedford, Massachusetts 01730

ⁱ ˎ

This paper presents a method of evaluating the gain and
patterns of finite arrays of waveguides with arbitrary cross-
section, that includes mutual coupling. A multimode represen-
tation of the aperture fields is used to determine the performance
of arrays of rectangular, circular and annular feedguides.

A mutual admittance matrix describing the coupling between
modes in the elements is determined by enforcing the continuity
of tangential fields at the apertures via Galerkins's method. [1,2,3]
Application of this method to the continuous wave number spectrum
conserves power, as in the case for the discrete spectrum of
infinite arrays. In this fashion, element and array gain calcula-
tions automatically take into account reflections at the aperture
plane.

A simple method to characterize arbitrary lossless and
decoupled feeding of these canonic apertures has been developed;
an example of which is the stripline fed cavity backed slot array.
As a result, a matching network consisting of an ideal transformer,
a shunt susceptance and a length of transmission line correctly
accounts for this arbitrary feed. This network addition results
in an augmentation of the aperture mutual admittance matrix, from
which the aperture fields and reflection coefficients at the gener-
ators are readily determined.

This analysis has been applied to a triangular grid array of
59 elements shown in Figure 1. The apertures are cavity backed
rectangular slots fed by strip transmission line, where the isolated
element has a VSWR of 2.4. A comparison between computed and
measured reflection coefficients at the generators are shown in
Figure 2. Typical agreement is within 15 percent, and a departure
from the isolated element case is noted. Measured and calculated
E and H-plane element patterns for element No. 2 (see Figure 1)
are shown in Figures 3 and 4. The E-plane patterns of Figure 3
compare very well for $|\theta| < 70$ deg. The H-plane patterns of
Figure 4 are in excellent agreement out to $|\theta| \approx 80$ deg. The
ground plane edge extending $\approx 1\lambda$ from the edge elements causes
these departures.

For this size array and spacing, element-to-element gain variation, both computed and measured, is in some cases in excess of 1.5 dB.   This gain nonuniformity significantly affects patterns and efficiency of the array, resulting in overall gain losses.

It is concluded that, in order to approach full aperture gain, a careful selection of the external geometry of small arrays is required.

REFERENCES

1.   Borgiotti (May, 1968, IEEE PGAP, AP-16, pp. 329-334).
2.   Steyskal (1972 G-AP Int. Syp. Dig., p. 165).
3.   Balzano, Siwiak, Lewis (AFCRL Final Rept. Contract No. F19628-72-C-0202).
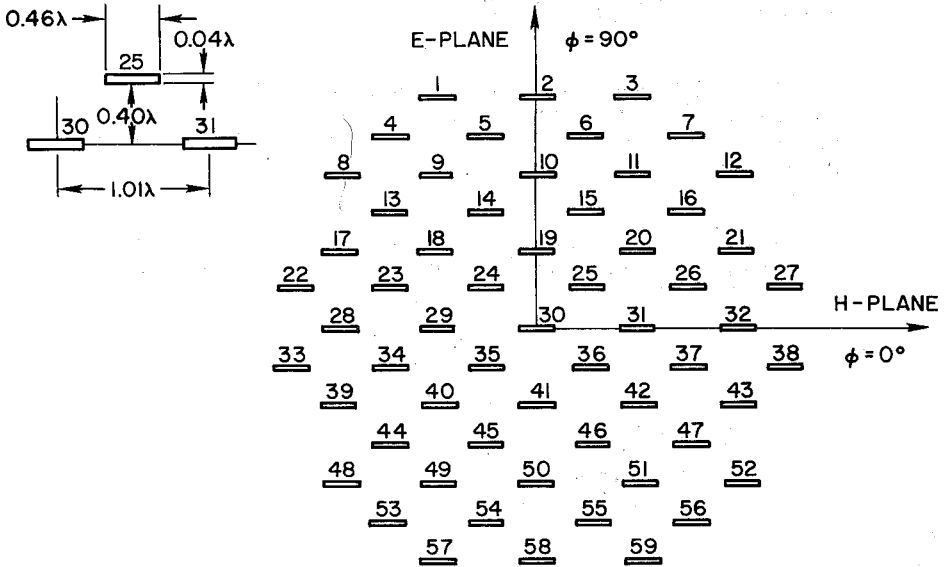
Figure 1 - 59 Element Array of Rectangular Slot Elements

$|\Gamma|$ = CALCULATED (MEASURED)

2
0.427 (0.34)

3
0.431 (0.40)

6
0.483 (0.55)

7
0.472 (0.40)

10
0.474 (0.34)

11
0.543 (0.46)

12
0.352 (0.33)

15
0.452 (0.52)

16
0.454 (0.44)

19
0.468 (0.36)

20
0.463 (0.51)

21
0.482 (0.43)

25
0.463 (0.49)

26
0.457 (0.45)

27
0.356 (0.37)

30
0.504 (0.37)

31
0.487 (0.52)

32
0.559 (0.44)
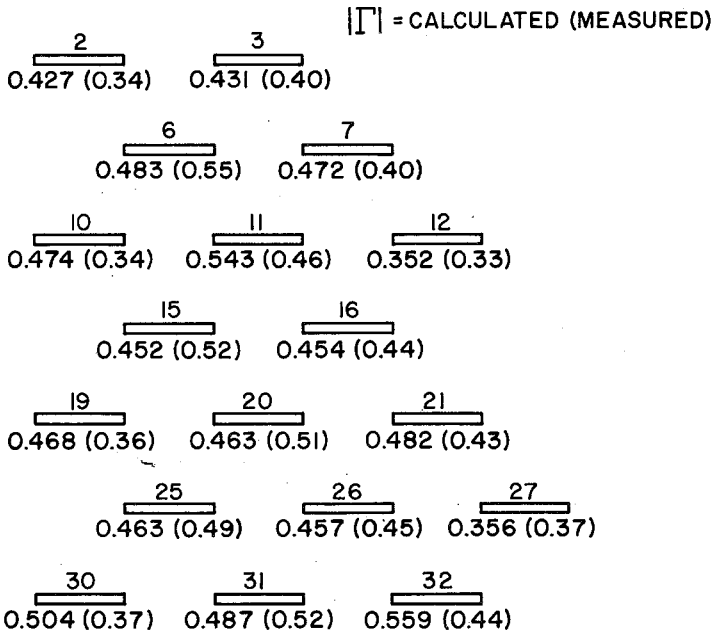
Figure 2 - Measured and Calculated Reflection Coefficients (Γ) for a
Quadrant of the 59 Element Array
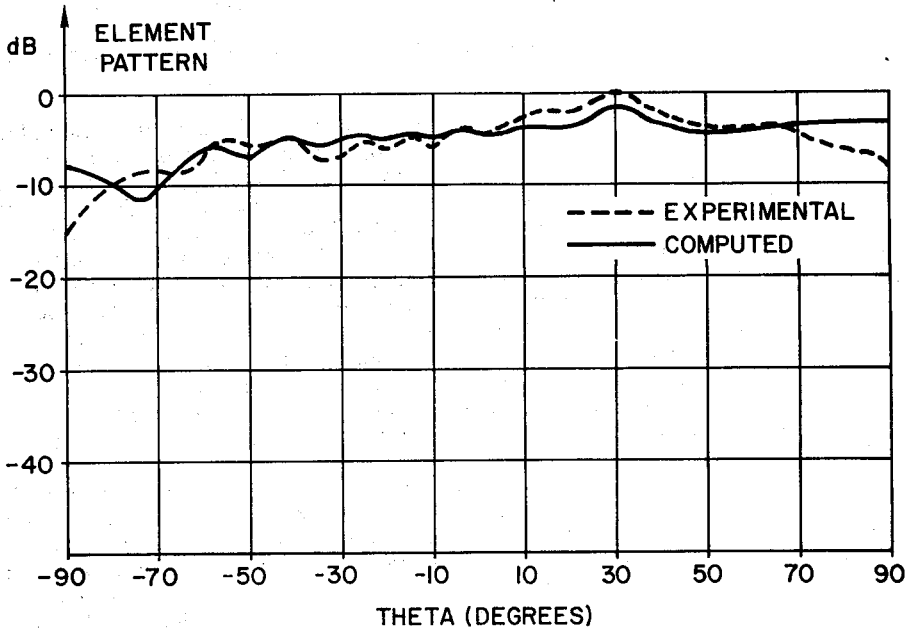
Figure 3 - E-Plane Pattern of Element No. 2
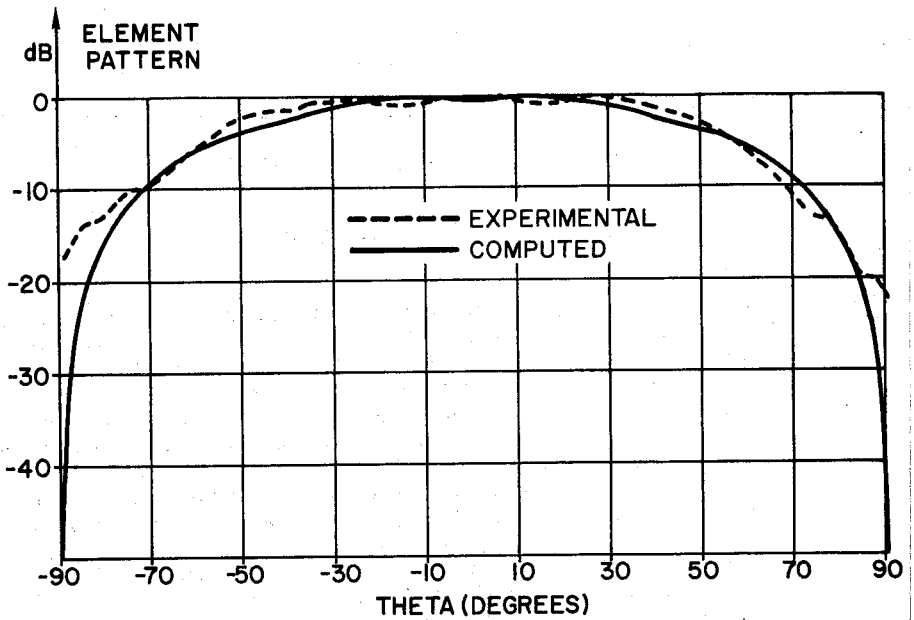
Figure 4 - H-Plane Pattern of Element No. 2

FAR FIELD COMPUTATIONS OF CONICAL ARRAYS

A.G. Cha and J.K. Hsiao, U.S. Naval Research Laboratory

In recent years, there has been considerable interest in cylindrical arrays because of advantages such as a 360° azimuth coverage, an almost constant azimuthal beamwidth, space saving and minimum interference with vehicle operations [1]. However, in many radar applications, the cylindrical array does not provide adequate coverage at large elevation angles. It has been suggested that conical arrays may be employed in cases where large elevation angle coverage is important. The use of a conical array is analogous to tilting back the planar array faces to extend the high elevation angle coverage at the expense of the coverage below the horizon. It is the object of the present paper to treat the conical array problem analytically as there seems to be little analytical work on the subject.

Figure 1 shows the coordinate system of the conical array under consideration. It is assumed that there are M rows of circular arrays on the conical surface and each row has an identical number of elements. Note the far field of a conformal array in general can not be factored into the product of an element pattern function and an array pattern function due to the fact that each individual antenna in the array has a different orientation. The appropriate expression for the far field of a conical array can be written as

$$\bar{V}(\theta,\varphi) = \sum_{m=1}^{M} \sum_{n=-N}^{N} \alpha_{mn} \, \bar{V}_{mn}(\theta''_{mn},\varphi''_{mn}) e^{jk\bar{R}_{mn} \cdot (\hat{R}-\hat{R}_o)} \tag{1}$$

$$\hat{R} = (\sin\theta\cos\varphi, \, \sin\theta\sin\varphi, \, \cos\theta)$$

$$\hat{R}_o = (\sin\theta_o\cos\varphi_o, \, \sin\theta_o\sin\varphi_o, \, \cos\theta_o)$$

In Eq. (1), α_{mn} is the excitation coefficient of the element in the m-th row and n-th column, $\bar{V}_{mn}$ is the far field vector of the mn-th element ($\bar{E}$ or $\bar{H}$), $\bar{R}_{mn}$ is the position vector of the mn-th element, k is the free space wave number, θ and φ are the spherical coordinate variables. It has been assumed in writing Eq. (1) that only 2N+1 elements on each row are excited. The exponential factor in Eq. (1) represents a phase shift needed to make the field of each element in phase in the direction of maximum radiation (θ_o,φ_o). The far field expression $\bar{V}_{mn}$ ($\theta''_{mn},\varphi''_{mn}$) of the mn-th element is assumed to be known in the (x''_{mn},y''_{mn}, z''_{mn}) coordinate system. For instance, if the thin slot in Fig. 2b is the radiator placed at the origin of the (x'',y'',z'') coordinate system of Fig. 1, the far field for

the slot is known in the double primed coordinates as

$$\bar{H} = \sin \theta'' \; \hat{\theta}'' \tag{2}$$

where the maximum field strength has been normalized and the factor $e^{j(\omega t - kR)}/R$ has been omitted. Two problems would have to be solved before Eq. (1) can be used. First, one must resolve each set of unit vectors $(\hat{\theta}''_{mn}, \hat{\phi}''_{mn})$ in terms of the unit vectors $\hat{\theta}$ and $\hat{\phi}$ in order to perform the vector addition in Eq. (1). Second, the double primed coordinate variables θ''_{mn} and ϕ''_{mn} must be expressed as functions of θ and ϕ. A systematic way toward solving these two problems has been developed by the authors whereby the far field expression of a radiator in any coordinate system may be derived from the far field expression of the radiator in some other coordinate system. Using this technique, the far field of the conical array in Fig. 1, with thin slots aligned on the conical surface as in Fig. 2a, is

$$H_\theta = \sum_{m=1}^{M} \sum_{n=-N}^{N} \alpha_{mn} \cos \theta \sin (\phi - \phi_{mn}) e^{jk\bar{R}_{mn} \cdot (\hat{R} - \hat{R}_0)} \tag{3}$$

$$H_\phi = \sum_{m=1}^{M} \sum_{n=-N}^{N} \alpha_{mn} \cos (\phi - \phi_{mn}) e^{jk\bar{R}_{mn} \cdot (\hat{R} - \hat{R}_0)} \tag{4}$$

where ϕ_{mn} is the azimuthal angle at which the mn-th element is located. Equations (3) and (4) have been calculated for an array with M=18, N=25, TC=20°, RB=19.6λ, DZ=0.524λ and DFI=1.5°, where TC is the cone angle, RB is the radius of the base circle of the cone, DZ is the projected element apacing along the z-axis and DFI is the azimuthal angular element spacing. Figures 3-5 show some of the computed results for Eqs. (3) and (4). Figure 3 shows H_ϕ in the elevation plane $\phi=0$ with the main beam steered at two different elevation angles. The other component H_θ is not shown as $H_\theta=0$ in the elevation plane $\phi=0$, as can be seen from Eq. (3). Figure 4 shows H_ϕ in the azimuthal plane $\theta=90°$. Again it is seen from Eq. (3) that $H_\theta=0$ in this plane. The above calculations were made for a uniformly illuminated array. Figure 5 shows H_θ and H_ϕ in the conical cut $\theta=70°$ for an array with cosine excitation coefficients in the azimuth direction and uniform excitation coefficients in the vertical direction. It is seen that tapering the illumination leads to a reduced sidelobe level similar to the situation found with planar arrays.

References

1. Proceedings of the Conformal Array Antenna Conference
   (1970, held at NELC, San Diego).

(a)

(b)
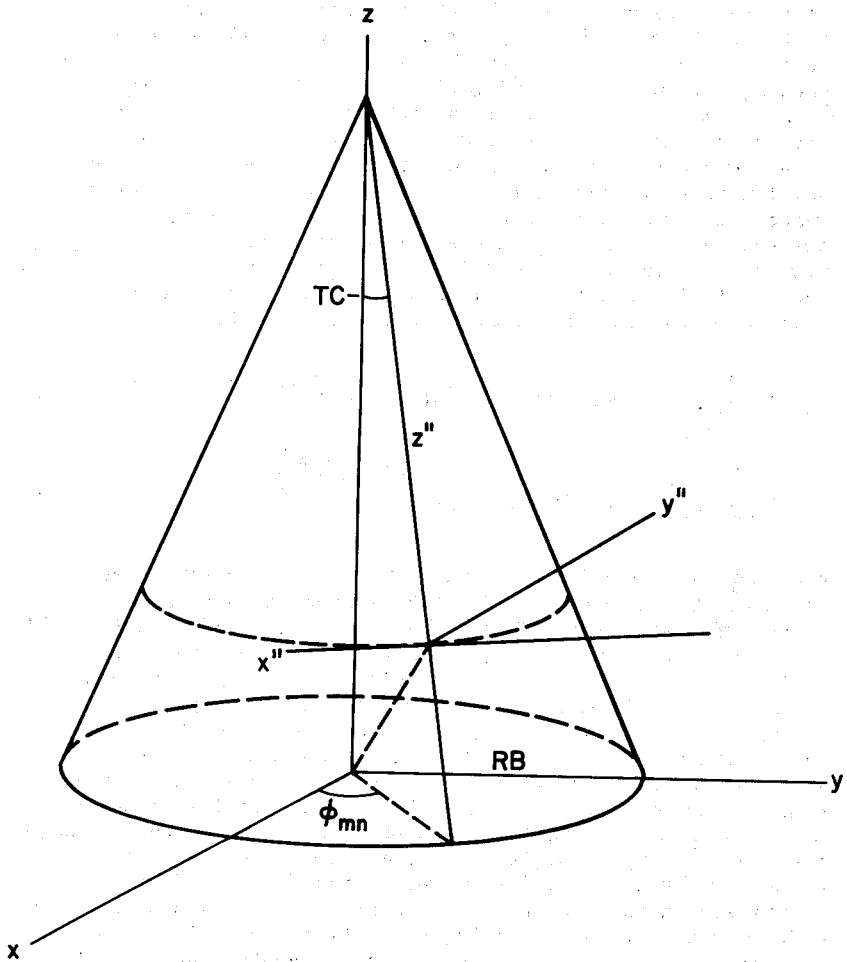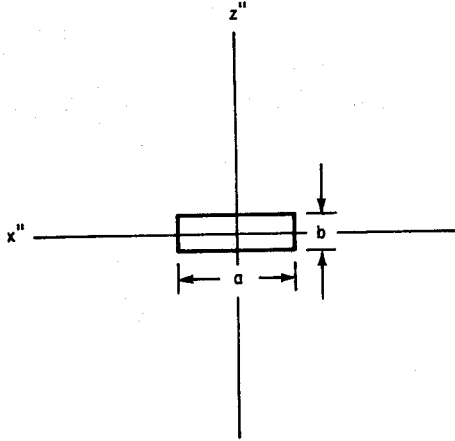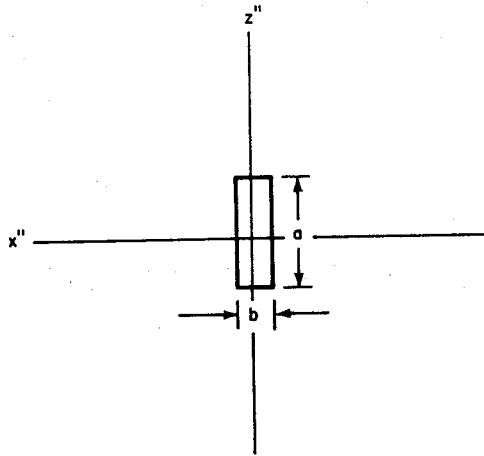
SURFACE WAVE EFFICIENCY RESULTS FOR SOURCES IN PROXIMITY TO GROUND*

R. J. Lytle, F. J. Deadrick, E. K. Miller, D. L. Lager, and J. A. Landt
Lawrence Livermore Laboratory

This paper is concerned with the relative hf surface wave launching
efficiency of dipole, monopole, Beverage, and Lambda antennas, and
arrays of these antennas. The theoretical study is based upon com-
puter modeling of wire antenna elements in the presence of the ground.
The computer model is founded upon matrix methods of solving integral
equations. Interaction of the elements among themselves and with the
ground is included in the model. Ranges of validity of the approxi-
mate procedure have been established by comparison with Sommerfeld
integral evaluations.

Enhancement of the overall surface wave launching efficiency can be
achieved for the different antenna types by determining good feed
point locations, preferred wire configurations, and desired wire
spacings, among other factors. This paper presents results indicative
of our studies concerning these factors. A standard comparison model
has been used for each situation studied. The standard parameters are
P_{input} = 1 watt, Range = 100 km, Flat earth model, Mixed-path propa-
gation: d_{land} = 200 m, d_{sea} = 99.8 km, and f = 10 MHz.

Representative study results indicate that a diamond shape configuration
for a Lambda antenna is a more effective surface wave launcher than a
skewed or parallel wire configuration (see Figure 1). Beverage antennas
work much more efficiently with closely spaced multiple wire elements
than with a single wire element (see Figure 2). This is due to a
decrease in the near field ground losses (and a consequent rise in the
surface wave field) for multiple wire excitation. Off-base feeding of
a monopole can enhance the surface wave achieved with base feeding
(not shown). Broadside arrays of antennas with a significant vertical
extend (e.g., vertical dipoles, monopoles, Lambdas) are most effective
with an interelement spacing of ~ 20 m (e.g., see Figure 3). Wave
tilt effects should be considered for optimum system utilization (not
shown). The tilt angle is of course different for the transmit and
receive situations.

FIG I

LAMBDA   ANTENNA   CONFIGURATION   STUDY

Center Leg   length = $\frac{3}{2}\lambda$
in all cases

Maximum Wire Separation
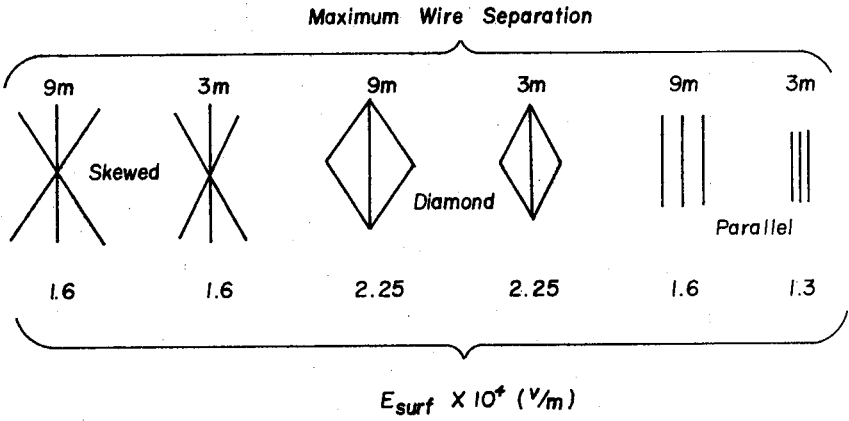
DIAMOND CONFIGURATION   PATTERNS
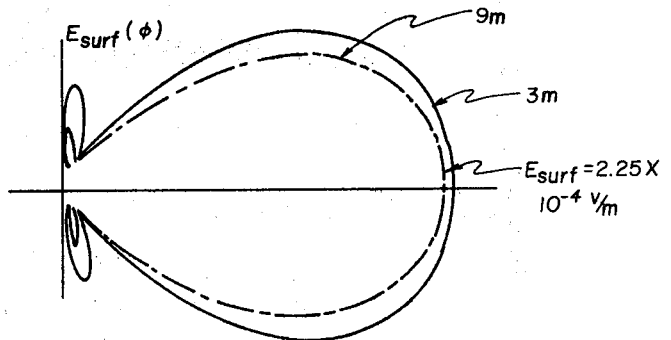
FIG 2

N PARALLEL BEVERAGE ANTENNAE

HEIGHT = 2.5 m, LENGTH = 40 m

$Z_L = 400\,\Omega$, $\epsilon_r = 9$, $\sigma = 10^{-2}$

$f = 10MHz$

SEPARATION DISTANCE (m)

FIG 3

N Vertical ½λ Dipoles

⅓ λ High

$\epsilon_r = 9$, $\sigma = 10^{-2}$

$f = 10\,MHz$
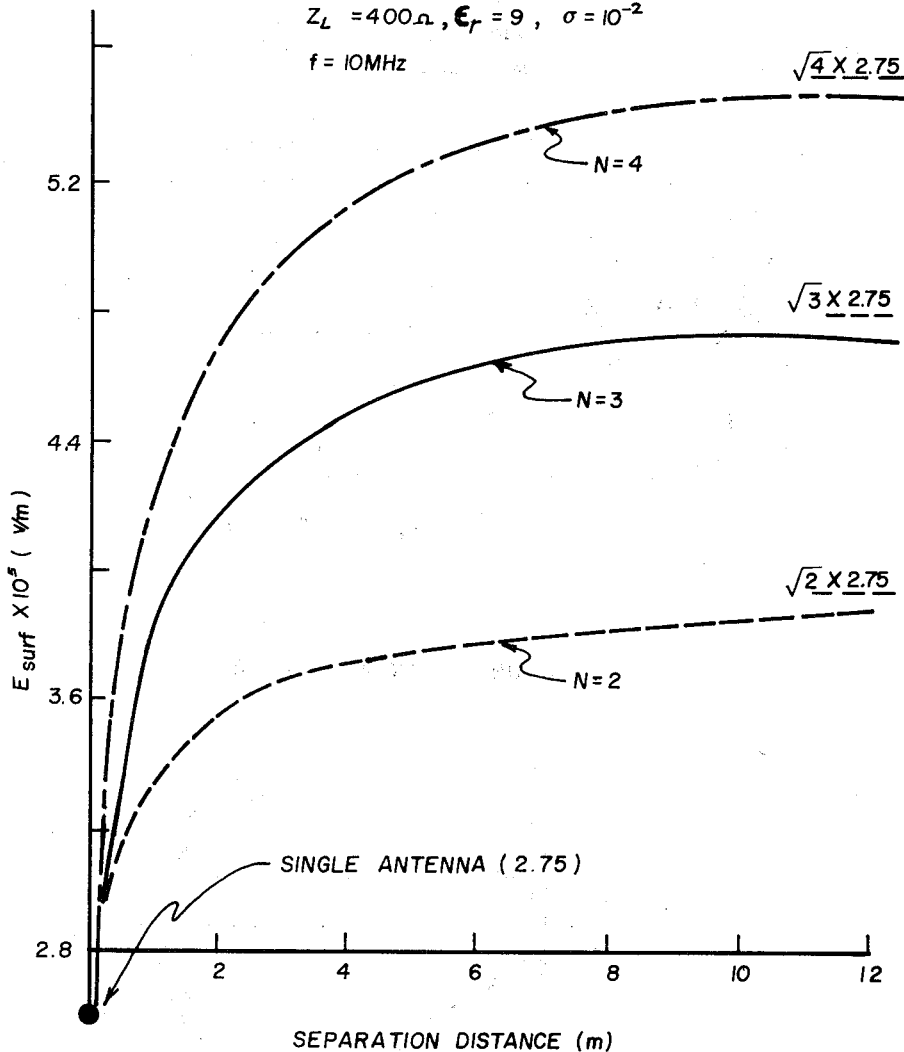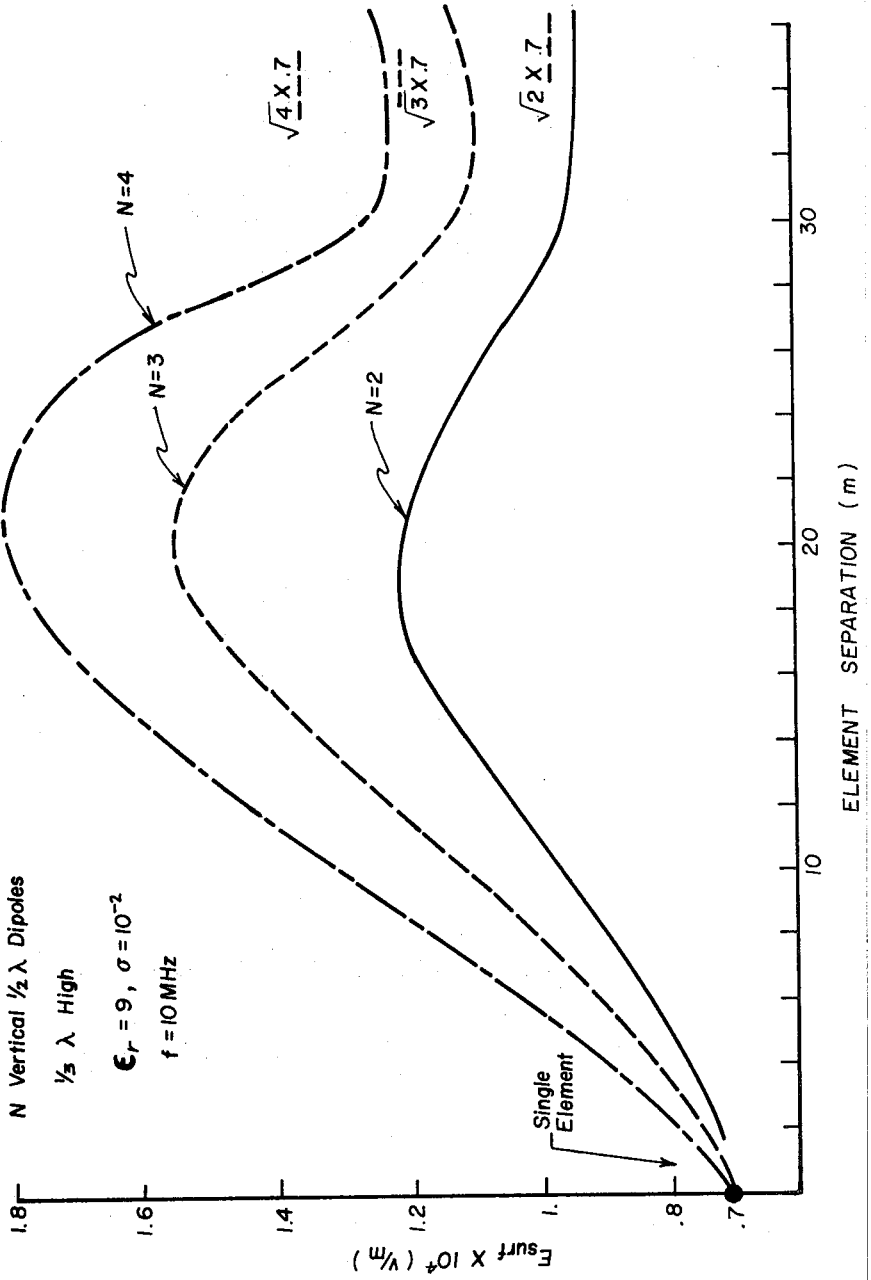
MODE ANALYSIS OF ELECTROMAGNETIC FIELDS
OF A LOADED CIRCULAR LOOP ANTENNA

Hsi-Tien Chang

The Dikewood Corporation

1009 Bradbury Drive, S. E.

Albuquerque, New Mexico 87106

The current distribution on a circular loop located on the plane $z = 0$ with the major radius "a" and minor radius "b" may be decomposed into Fourier series [1].

$$I(\phi) = \sum_{n=-\infty}^{\infty} I_n e^{-in\phi} \tag{1}$$

If the Green's function is also Fourier expanded in cylindrical coordinates (ρ, ϕ, z),

$$G(\rho - a, \phi - \phi', z) = \frac{e^{-ik|\vec{r} - \vec{r'}|}}{4\pi |\vec{r} - \vec{r'}|} = \sum_{n=-\infty}^{\infty} a^{-1} G_n(\rho, z) e^{-in(\phi - \phi')} , \tag{2}$$

one can show that the electric and magnetic fields in space may be written as follows:

$$\vec{E}(\rho, \phi, z) = \sum_{n=-\infty}^{\infty} I_n \vec{N}_n(\rho, \phi, z) = \sum_{n=-\infty}^{\infty} I_n \vec{N}_n(\rho, z) e^{-in\phi} ; \tag{3}$$

$$\vec{H}(\rho, \phi, z) = \sum_{n=-\infty}^{\infty} I_n \vec{M}_n(\rho, \phi, z) = \sum_{n=-\infty}^{\infty} I_n \vec{M}_n(\rho, z) e^{-in\phi} , \tag{4}$$

Here, the electric mode $\vec{N}_n$ and the magnetic mode $\vec{M}_n$ are independent of the source function and the loading impedance. For each mode, I_n may be regarded as the excitation factor. If the fields in eqs. (3) and (4) are normalized to their respective low frequency limits at the center of the loop, then these modes satisfy the following relations:

$$\vec{N}_n = \frac{1}{ik} \nabla \times \vec{M}_n ; \tag{5}$$

$$\vec{M}_n = \frac{1}{-ik} \nabla \times \vec{N}_n . \tag{6}$$

Consider the plane $z = 0$ for example. One can determine that

$$N_{\rho_n}(\rho,0) = \left(\frac{4\pi n}{k}\right)\left[\frac{\partial G_n(\rho,0)}{\partial \rho}\right] + 2\pi ka\left[G_{n+1}(\rho,0) - G_{n-1}(\rho,0)\right]; \quad (7)$$

$$N_{\phi_n}(\rho,0) = \left(\frac{4\pi n^2}{ik\rho}\right) G_n(\rho,0) + 2\pi i ka\left[G_{n+1}(\rho,0) + G_{n-1}(\rho,0)\right]; \quad (8)$$

$$M_{z_n}(\rho,0) = 2\pi a\left[\frac{\partial G_{n+1}(\rho,0)}{\partial \rho} + \frac{\partial G_{n-1}(\rho,0)}{\partial \rho}\right] + \frac{2\pi a}{\rho}\left[G_{n+1}(\rho,0) + G_{n-1}(\rho,0)\right]$$
$$+ \frac{2\pi na}{\rho}\left[G_{n+1}(\rho,0) - G_{n-1}(\rho,0)\right] \qquad (9)$$

and for small ρ,

$$G_n(\rho,0) = \frac{e^{-ika(1+\rho^2/4a^2) + in\pi/2}}{4\pi}$$
$$\left\{\left(1 + \frac{\rho^2}{4a^2}\right) J_n(k\rho) - \frac{\rho^2}{8a^2}(3 + ika)\left[J_{n+2}(k\rho) + J_{n-2}(k\rho)\right]\right.$$
$$\left. + \frac{\rho}{2a}i\left[J_{n+1}(k\rho) - J_{n-1}(k\rho)\right]\right\} \qquad (10)$$

It turns out, as one would have expected from considerations of symmetry, that only the first order mode contributes to the electric field and only the zero order mode contributes to the magnetic field at the center of the loop. At a given frequency, the higher order modes gradually become important as the observation point moves away from the center. On the other hand, the peak field of a given mode at one location increases as the frequency increases. Nevertheless, the higher the order of the mode, the smaller the field strength for a large n. So, it is only necessary to sum up with a limited number of modes in order to obtain a reasonably accurate field distribution. For example, one needs about four modes for ka = 1 and about fourteen modes for ka = 50 at locations on $\rho = a/4$ (Figure 1). However, when ρ is close to a, a lot of modes have to be considered [2]. If ρ is now greater than a, the number of modes needed will again decrease as ρ increases since there is another symmetry point at infinity.

The mode method is rather convenient for calculating the fields at low frequencies because only a few modes are required. Even at the intermediate frequencies, a limited number of modes will be sufficient to describe the field pattern as long as the observation point is not very close to the source. This mode method is also applicable to other types of antennas exhibiting symmetry. Here, the mode structures $\mathbf{N}_n$ and $\mathbf{M}_n$ depend only on the coordinate

149

system being chosen and may be calculated in advance even if the antenna properties are unknown. Although, the Fourier coefficient G_n is complicated and in many cases must be calculated by tedious numerical integrations, one needs only to calculate it once. Actually, one may consider these mode formulas for $\mathbf{N}_n$ and $\mathbf{M}_n$ as some kind of special functions and tabulate them in advance. As the loading impedance and the source function of the antenna are determined, one can calculate the excitation factor I_n either analytically or numerically and compute the field immediately.

References:

1. R. E. Collin and F. J. Zucker (1969, Antenna Theory Part 1, McGraw-Hill, Ch. 11).

2. R. L. Fante, J. J. Otazo and J. T. Mayhan (1969, Radio Science, 4. p. 697).
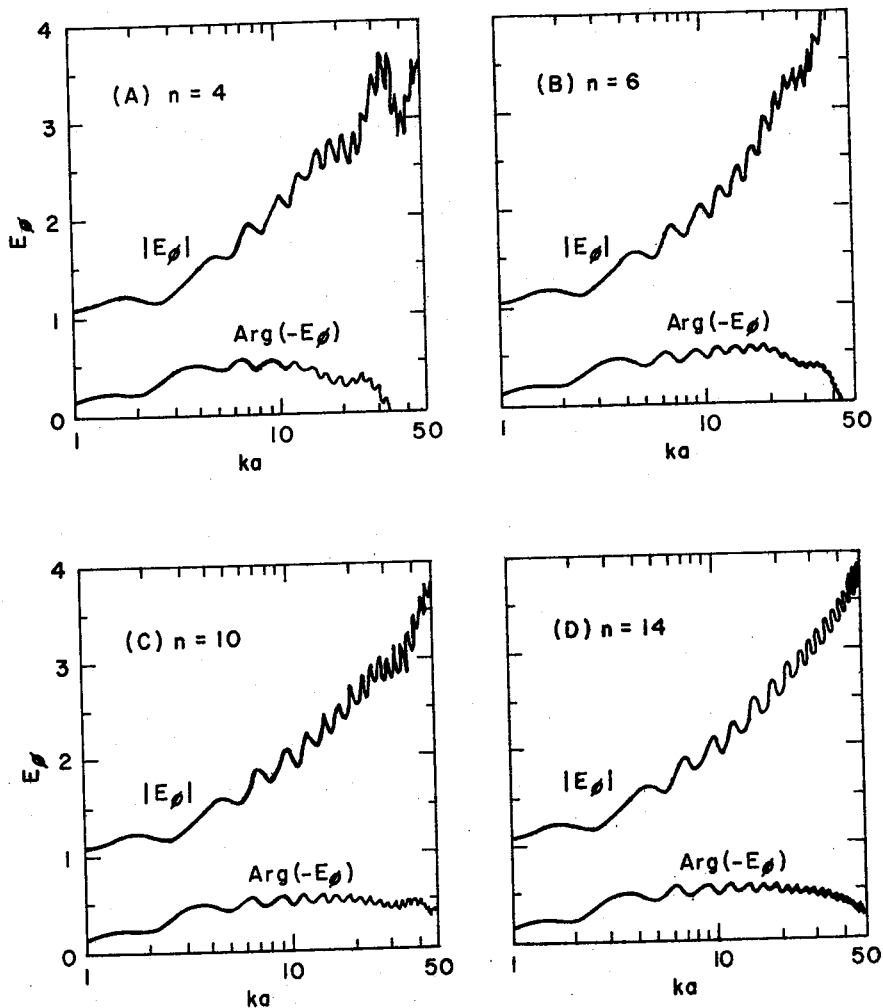
Figure 1. Normalized E_ϕ for b/a = 0.02, ρ = a/4, ϕ = 0 and n is the number of modes taken in the summation. The load of the antenna is a uniform resistance, R = 120π [ln(8a/b) - 2].

ON FERRITE BAR ANTENNA AND ITS GAIN LIMITATION

SOJUN SATO AND YOSHIYUKI NAITO

TOKYO INSTITUTE OF TECHNOLOGY

1. INTRODUCTION

Ferrite bar antenna is widely used as a small ante-
nna of MF and HF band receiver, because the permeabi-
lity of ferrite can be made large and the loss of fer-
rite small in that frequency range.

At higher frequencies, however, the permeability of
ferrite decreases and its loss increases. Recently
the diepersion relation and the limit relation of per-
meability of ferrite have been formalized.[1][2]

This physical limitation of the permeability should
affect the characteristics of the devices utilizing
ferrite, and surely on ferrite bar antenna. So far
the authors have found the characteristic limitations
of the electromagnetic wave absorber[3]   and the tran-
smission type balun.[4]

In this paper, the authors would like to discuss
the characteristic limitation of ferrite bar antenna,
that is, to discuss the merit of using ferrite as a
function of frequency and find the upper limit of usa-
ble frequency.

2. EFFECTIVE PERMEABILITY

Let's consider the ferrite bar antenna, shown in
Fig.1, of which shape is prolate spheroid and wounding
coil is very fine.

The effective permeability $\overset{\bullet}{\mu}_e$ is difined as the
ratio of electromotive force V to V_0 (without ferrite)
in case of plane wave incidence, that is

$$\overset{\bullet}{\mu}_e = V \ / \ V_0 . \qquad (1)$$

In case of low frequency, the equation (1) can be
expressed approximately by using a demagnetizing fact-
or ν of the prolate spheroid as follows:

$$\overset{\bullet}{\mu}_e = \frac{\overset{\bullet}{\mu}_r}{1 + \nu(\overset{\bullet}{\mu}_r - 1)} \qquad (2)$$

In general case, the effective permeability can be
obtained through the analytical calcuations by use of
the prolate spheroidal coordinates and its wave funct-

ions. The formulation or the method to get the solution is tedious and so omitted here, and only some examples of numerical calculations are presented.

Fig.2 shows the difference between the exact values and ones from the approximate equation (2) as a function of frequency. It is assumed that l =100mm, d =10 mm and μ_r is also real. In this case, the value of the imaginary part μ_e'' increases as the value of μ_r becomes greater and frequency higher, but still μ_e''/ μ_e' is less than 10^{-2}. The differences in the cases of other parameters of l/d and complex values of μ_r are very similare to Fig.2, and so the equation (2) can be used as a good approximation of the effective permeability if the error less than 10% is permitted and if the frequency is lower than 500 MHz.

In regard to the frequency dispersion of the relative permeability μ_r of general ferrite, it has been found that it can be expressed.

$$\mu = 1+ \frac{K}{1+j\,f/f_1} \equiv 1+ \frac{S}{f_1 + jf} \quad (3)$$

in the frequency region of interest, where f_1 is equal to $S/(\mu_i-1)$ and μ_i is the initial permeability at D.C.

The value of S is considered to express the "goodness" of the quality of ferrite. About this value of S the following limit law has been obtained experimentally.

$$S \leqq 10 [GHz] \quad (4)$$

Substituting the equation (3) into (2), μ_e is expressed as equation (5)

$$\mu = 1+ \frac{S'}{f_1' + jf} \quad (5)$$

where $S'=(1-\nu)S$ $f'=f+\nu S$

When l/d is greater than 10, the value of ν is smaller than 0.02. And so the value of S' is close to that of S. Therefore S' satisfies equation (4), too.

3. AVAILABLE POWER OF BAR ANTENNA

The equivalent circuit of bar antenna is shown in Fig.3, where L and R are propotional to the real and the imaginary part of μ_e, respectively, that is

$$L=L_1 \mu_e' \quad R=\omega L_1 \mu_e'' \quad (6)$$

and r is the resistance of a loop. The available power from the bar antenna is expressed as

$$P = \frac{|V|^2}{4(r+R)} = \frac{|\mu_e|^2 V_0^2}{4(r+\omega L_1 \mu_e'')} \quad (7)$$

Without ferrite, this becomes

$$P_0 = \frac{V_0^2}{4r} \quad (8)$$

The ratio of P to P_0 is the parameter to express the merit of using ferrite bar, and can be formulated as follows:

$$P/P_0 = \frac{|\dot{\mu}_e|^2}{1 + \frac{\omega L}{r}\mu_e''} \equiv \frac{|\dot{\mu}_e|^2}{1 + Q_l\mu_e''} \qquad (9)$$

where

$$Q_l = \frac{\omega L_l}{r}$$

In the equation described above, it may be considered that the value of Q_l is constant. Substituting (5) into (9), we obtain

$$P/P_0 = \frac{(1/\chi_{ie} + 1)^2 + (f/S')^2}{(1/\chi_{ie})^2 + (f/S')^2 + Q_l f/S'} \qquad (10)$$

where $\chi_{ie} \equiv S'/f'$ (effective susceptibility at D.C.)

Fig.4 shows the relation of P/P_0 to f/S' in case of $Q_l=50$. It is understood from this figure, that at every frequency f there exists the value of χ_{ie} that makes P/P_0 maximum. This maximum value of P/P_0 is drawn in the same figure and can be expressed as follows

$$(P/P_0)_{max}=1+ \frac{2S'}{Q_l f - S' + \sqrt{(Q_l f + S')^2 + 4f^2}} \fallingdotseq 1+\frac{S'}{Q_l f} \qquad (11)$$

The value χ_{ie} which makes P/P_0 maximum at frequency f is

$$\chi_{ie} = \frac{S'}{Q_l f} \qquad (12) \quad \text{or} \quad f_l = Q_l f - \nu S \qquad (13)$$

Roughly speaking, when the frequency is low, the merit to use ferrite bar is large and when frequency increases, the merit becomes very little. One of the numerical example is as follows

```
Q_l =50      (Usual Wounding Coil's Q)
S'=5[GH ]    (Usual Ferrite's S')
```

Frequency [MHz]	Merit
1	100
10	10
100	2

These calculations have been performed using the approximation equation (5) for $\dot{\mu}_e$ which is applicable for the frequency lower than 500MH . According to the statement above, the ferrite is useful only below 100 MH , where the equation (2) is applicable and so this conclusion is regorous.

REFERENCES
1. Y. Naito (1970. Proceedings of International Con-
           ference on Ferrite P.558)
2. Y. Naito (1973. Trans. of IECE of Japan (c) 2
           P.113)
3. Y. Naito & K. Suetake (1971. Trans. on MTT, 1
                    P.65)
4. S. Sato & Y. Naito (1972. Trans. of IECE of Japan
                    (c) 10 P.544)

FIG.1 STRUCTURE OF FERRITE   FIG.3 EQUIVALENT CIRCUIT.
BAR ANTENNA
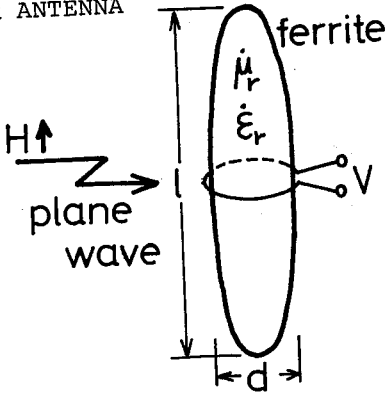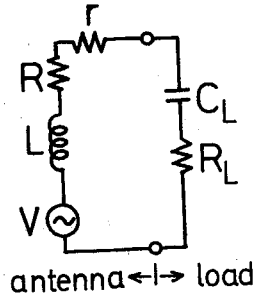
FIG.2 FREQUENCY DEPENDENCY
OF $\left| \dfrac{\dot{\mu}_e^{(2)} - \dot{\mu}_e^{(1)}}{\dot{\mu}_{e^{(2)}}} \right|$
WHERE $\dot{\mu}_e^{(1)}$ IS APPROXIMATE
VALUE BY (2) AND $\dot{\mu}_e^{(2)}$ IS
EXACT VALUE.
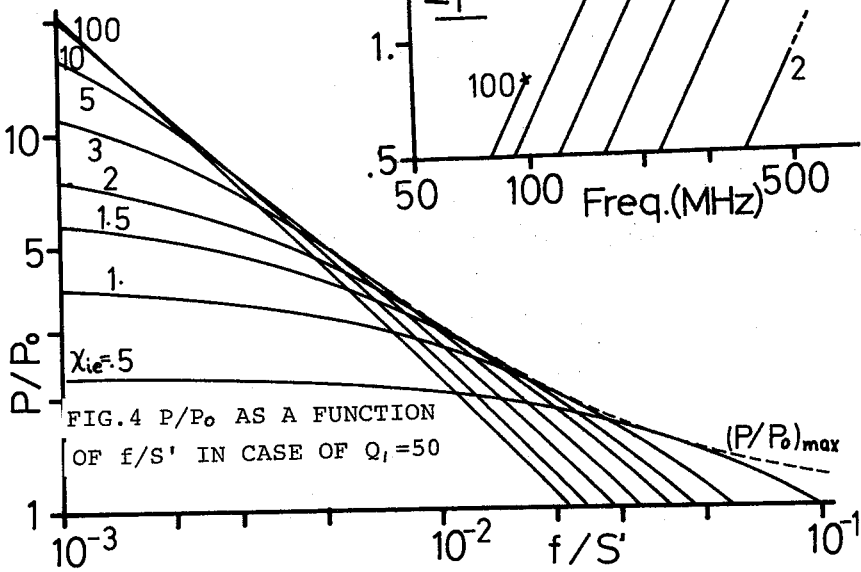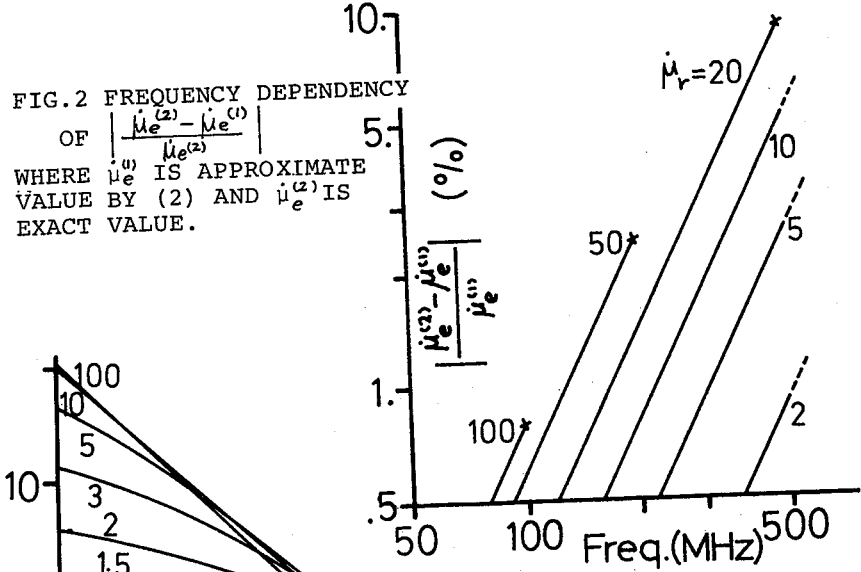
FIG.4 P/P₀ AS A FUNCTION
OF f/S' IN CASE OF $Q_l = 50$

CURRENT DISTRIBUTIONS ON
ELECTRICALLY THICK TUBULAR ANTENNAS

W. Chang and D.V. Otto
Dept. of Electrical Engineering
The University of Auckland
Private Bag, Auckland
New Zealand.

This work follows from [1] where singular integral equation
theory has been used to obtain leading terms of the total
current distribution on thick tubular antennas. Two forms of
the integral equation for the current on a perfectly conducting
tubular transmitting antenna, as shown in Figure 1, have been
investigated, namely,

$$\int_{-1}^{1} \left[\frac{dI(t_o)}{dt_o} \cdot \frac{d}{dt} G_o(t-t_o) + H^2 I(t_o) G_o(t-t_o) \right] dt_o = hF(t), \qquad (1)$$

and

$$\int_{-1}^{1} I(t_o) G_o(t-t_o) dt_o = C \cos (Ht)$$

$$+ \frac{1}{k_o} \int_{0}^{t} F(t_o) \sin \{H(t-t_o)\} dt_o , \qquad (2)$$

where the source function for delta-function excitation with no
rotational variation is

$$F(t) = -\frac{2\pi i}{hZ_o} \delta(t) + \frac{2\pi iA}{Z_o} \left. \frac{\partial G_o(t,r')}{\partial r'} \right|_{r'=a}$$

and $A = k_o a$, $H = k_o h$, $t = {}^z/h \leq 1$.

To solve (1) and (2), the logarithmic term in both the kernel
and the source function is isolated and the non singular parts
approximated by finite Chebyshev expansions.

In the case of (1), the variable

$$\phi(t) = \frac{dI(t)}{dt} + H^2 \int_{0}^{t} I(t_o) dt_o$$

is introduced and the equation is cast into a singular integral

156

equation with a Cauchy kernel having $\phi(t)$ as the unknown. This
equation is then solved using a technique analagous to the
standard for such an equation as given in [2]. $\phi(t)$ is
obtained as the solution of the principal part of the equation
already given in [1], plus a Chebyshev series (whose coefficients
arise explicitly as well as implicitly through a matrix inversion
process from the series expansions of the kernel and the source
function) multiplied by an edge singularity factor
$[1-t^2]^{-\frac{1}{2}}$.   Integration of $\phi(t)$ then yields the total current.

In the case of (2), differentiation with respect to t gives a
singular integral equation with a Cauchy kernel. The current
is expressed as a logarithmic term (arising from the nature of
the source function) plus a finite Chebyshev series multiplied
by the factor $[1-t^2]^{\frac{1}{2}}$.   A matrix inversion yields the
coefficients of the series and the constant C.

Current distributions thus obtained are shown in Figures 2 and
3, for two of the cases considered. Ten-term Chebyshev series
expansions were used for the non-singular parts of the kernel
and source function. A computation partitioning the total
current into its interior and exterior components was carried
out and the results are also displayed in these figures. For
the case $a = \lambda/2$, $h = \lambda/4$ good agreement with the results of
D.C. Chang [3] has been obtained.

For thick, short antennas ($a \geq \lambda/2$, $h \leq \lambda/4$), a fair approx-
imation for the kernel is simply

$$G_o(t) \simeq \frac{1}{\pi A} \left\{ -\ln\left|\frac{ht}{8a}\right| + Ci(2A) - \ln|4A| - \gamma + \left(\frac{Ht}{2}\right)^2 \ln\left|\frac{Ht}{2}\right| \right.$$

$$\left. + i\left\{ \frac{\pi}{2} \left(\frac{Ht}{2}\right)^2 - Si(2A)\right\} \right\}$$

Using this, and assuming the non-singular part of the current
to be of the form, constant multiplied by
$[1-t^2]^{\frac{1}{2}}$, the value of the constant can be obtained from
either (1) or (2) without necessitating digital computation.
This approximate solution is currently being researched.

References:

1. D.V. Otto (1971 IEEE Trans. Antennas and Propagation AP-19,
   p. 532).

2. N.I. Muskhelishvili, Singular Integral Equations (1953
   2nd ed. Groningen Holland: Noordhoff, Transl. J.R.M. Radok).

3. D.C. Chang (1967 Radio Science 2, p. 1043).
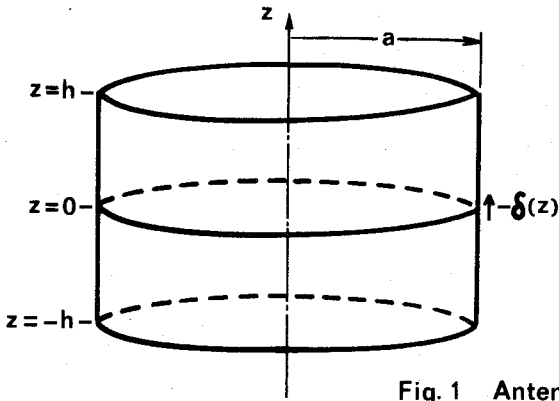
Fig. 1 Antenna Geometry
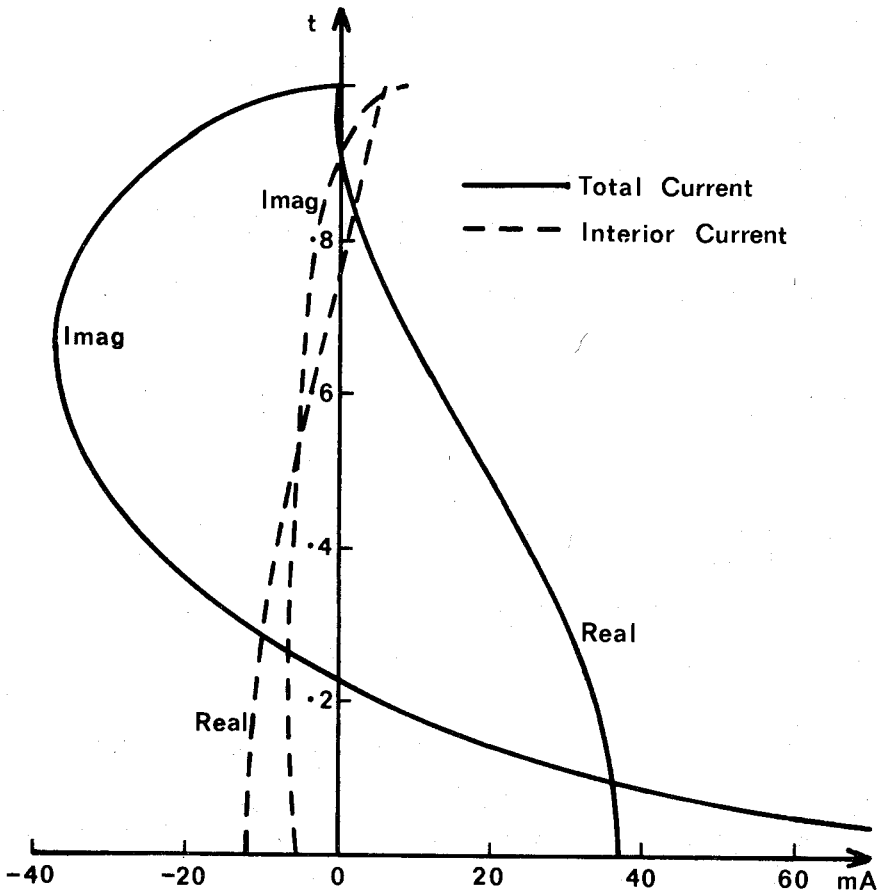
Fig. 2 Current Distributions $a = \lambda$ $h = \lambda/2$
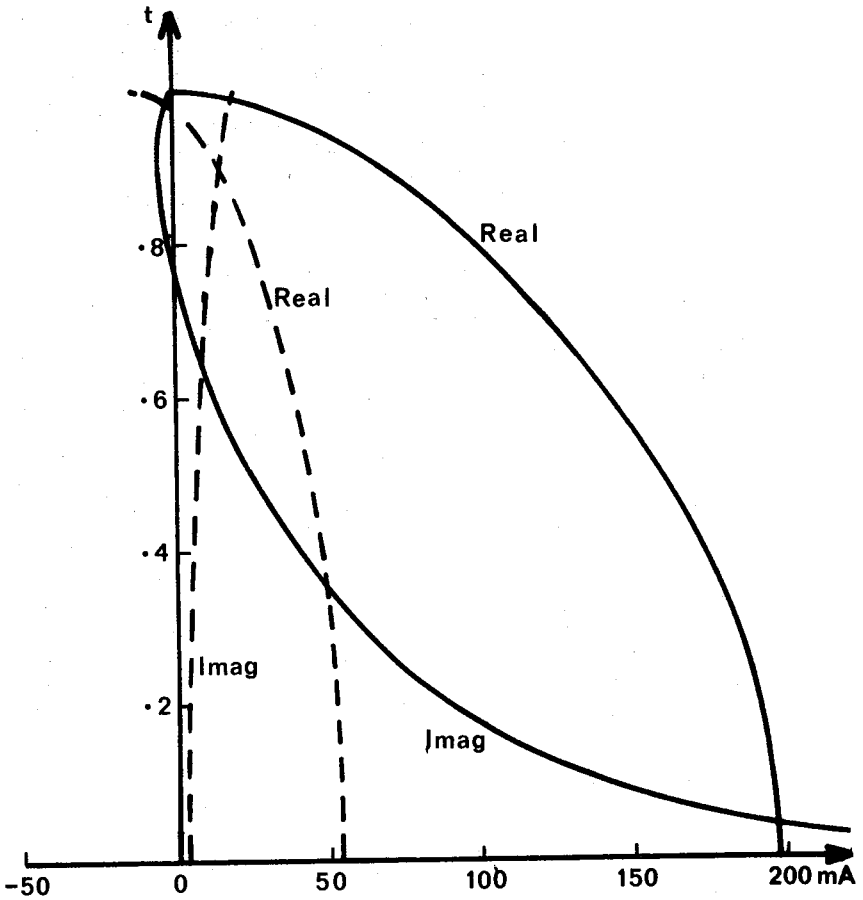
Fig. 3   Current   Distributions   a = 2λ h= λ /4

A TWO WAVELENGTHS OPEN-END CIRCULAR
LOOP ANTENNA AND ITS APPLICATION TO ARRAYS.

Ken-ichi Kagoshima Toshio Sekiguchi

Department of Electronics
Tokyo Institute of Technology
Tokyo Japan

INTRODUCTION

Impedance loading on an antenna is simple and effective technique to improve its characteristics. For example, resistance and reactance loading to a dipole[1],[2], whose current has only traveling wave component, makes its band wide, a small circular loop with resistance load[3], whose far field pattern is originally omnidirectional, becomes uni-directional and a scattering loop antenna with symmetrical load[4] makes its back scattering cross section minimum. These ideas are based on that the current on an antenna is controlled to satisfy the desired object with load.

However, it has not been clear how to determine the load impedance analytically to satisfy the desired performances. By using the fact that the imput impedance, VSWR and directivity of a loop antenna are expressed by the product between the values of unloaded loop and complex linear function of a load impedance Z_L, we have recently derived the formulas for the load making VSWR minimum or directivity maximum and obtained many useful numerical data[5]. According to the results, the directivity of a circular loop antenna with load at $\varphi=\pi$ becomes maximum and is 6.6 [dB] when its circumference is two wavelengths and the load impedance is infinite. (An unloaded loop has maximum directivity of 4.5 [dB] when its circumference is 1.5-wavelength[6].)

In this paper numerical and experimental data, for the 2-wavelength loop with a short circuited parallel line of quarter wavelength as an infinite load are shown and this type of loop is applied to broadside and endfire arrays. It can be shown numerically that the arrays of open end 2-wavelength loops have significant features compared with an unloaded loop.

A LOADED CIRCULAR LOOP ANTENNA

Theoretical analysis of a circular loop antenna loaded at $\varphi=\pi$ shown in Fig. 1 has been accomplished by various ways[5][6][7], and current distribution, input impedance and far field pattern obtained numerically and experimentally. Among these analyses, the Fourier expansion method is the most rigorous and simplest one. By this method, imput impedance Y_{in} and directivity normal to the loop surface G are shown as follows;[5]
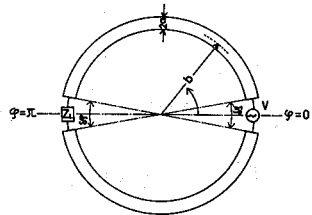
Fig. 1 Geometry of a
    circular loop
    loaded at $\varphi=\pi$

(1) $Y_{in} = \dfrac{(Y_0^2 - Y_\pi^2)Z_L + Y_0}{Y_0 Z_L + 1}$

(2) $G = G_0 \dfrac{Re(Y_0)\,|1+(Y_0+Y_\pi)Z_L|^2}{Re[\,(1+Y_0^* Z_L^*)\{Y_0+(Y_0^2-Y_\pi^2)Z_L\}\,]-Re[Z_L Y_\pi Y_\pi^*]}$

where Z_L is a load impedance, Y_0, Y_π are the admittances of the un-loaded loop at $\varphi=0$, $\varphi=\pi$ respectively and G_0 is directivity of the unloaded loop antenna.
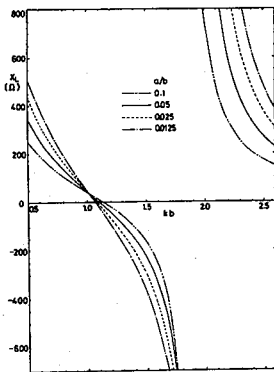
Fig. 2 Optimum load
reactance
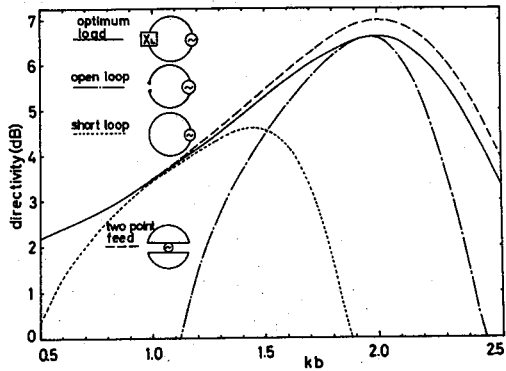
Fig. 3 Directivity of a loaded
loop antenna

We will determine the optimum load reactance making directivity G maximum as an example of optimization of the load impedance. We consider a pure reactance instead of the impedance loading to avoid the decreasing of efficiency by ohmic loss. First, substitute $Z_L=jX_L$ into equ.(2) and differentiating it with respect to X_L and we can get an quadratic equation for the load reactance X_L, which makes G maximum. Moreover, this equation always has a root[5]. Fig. 2 shows the optimum load reactance and Fig. 3, directivity of the loop antenna with various load reactances. We have obtained the result here that the maximum directivity is 6.6 [dB] (a/b= 0.05) when the circumference of a loop is two wave-lengths and the value of re-actance is 2400 [Ω] which will be approximately considered infinite. It is interesting that this load reactance
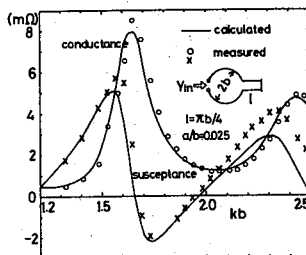
Fig. 4 Input impedance
of a loop with
infinit reactance
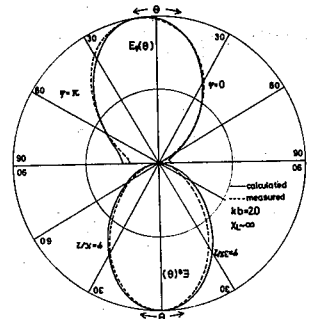
Fig. 5 Far field pattern
of a loaded loop

also makes the absolute value of the ratio of the odd mode to the
even mode of the current maximum[5].

Experimental value of imput impedance and far field pattern of
the loop antenna with a short circuited parallel line of quarter
wavelength as a load reactance are shown in Fig. 4 and Fig. 5.

ARRAYS OF 2-WAVELENGTH LOOP CIRCULAR ANTENNA

In section 2, we found that 2-wavelength circular loop opened
at $\varphi=\pi$ has high directivity. We apply this antenna to array
antennas to get high directivity.

BROADSIDE ARRAY

A broadside array of circular
loop whose circumference is about one
wavelength is used as a UHF TV trans-
mitting antenna and its current dis-
tribution was theoretically obtained[8].
If a 2-wavelength open-end loop used
as an element of a same array instead
of one wavelength loop, the direc-
tivity becomes higher by 2.0 [dB]
without reflector and by 1.3 [dB]
with reflector compared with the one
wavelength loop array.[Fig. 6]
Input admittance Y_{in} is about 5.0
[m℧] and is real. Fig. 7 indicates
that frequency characteristics of the
input admittance are comparatively
good.
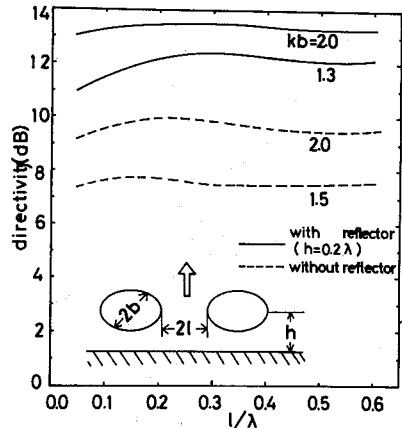
Fig. 6 Directivity of 2 elements
broadside array of unload
and loaded loop

END-FIRE ARRAY

For an end-fire
array, it is better to
use a two point feed
method shown in Fig. 3.
The two point feed
loop antenna is con-
sidered to be a
special case of the
one loaded at $\varphi=\pi$.

In Fig. 8, the
far field pattern of
two element array is
shown when each
element is excited by
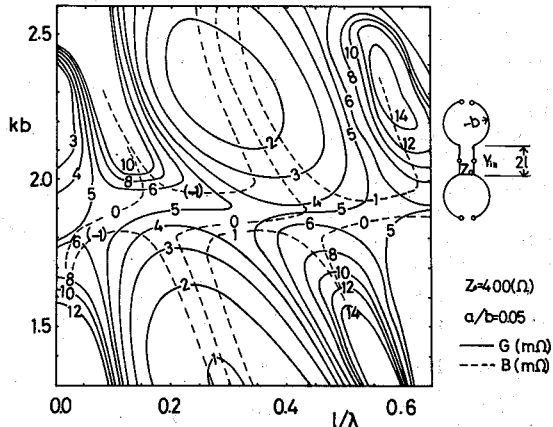
Fig. 7 Input admittance of
2 elements broadside array

162

optimum voltage. Main beam of the 2-wavelength loop array becomes
sharper and back lobe a half, compared with those of one wavelength
loop array. Directivity of two element Yagi-Uda array is shown in
Fig. 9. One wavelength loop works better than 2-wavelength loop
as a reflector and a double loop reflector consisting of 1.2- and
2-wavelength loop is much better than the other.
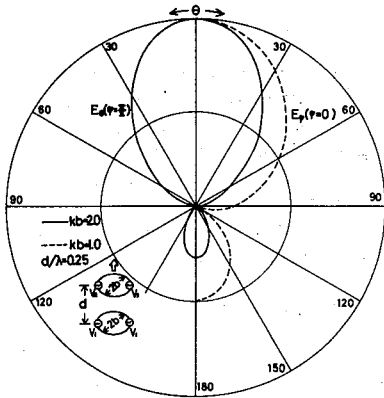
Fig. 8

Far field
pattern of
optimum
excitation
array

Fig. 9 Directivity of
2 element Yagi-Uda
array

CONCLUSION

    Main beam of an unloaded 2-wavelength circular loop is tilted,
but a loop loaded at $\varphi=\pi$ radiates normal to the surface of it and
the directivity becomes high. We applied this 2-wavelength open-end
loop to arrays which have higher directivity than those consisting
of one wavelength loops. Two wavelengths circular loop is moderate
in size at UHF band and will be expected to be a practical antenna.

REFERENCE

(1) E.E. Altshuler, IEEE Trans., AP-9, 4, P 324, 1961
(2) D.P. Nyquist and et. al., IEEE Trans., AP-16, 1, P 21, 1968
(3) M. Mikkaichi and et. al., J. Inst. Telev. Eng. Jap. Vol 22, 5,
    P 379, 1967
(4) J.L. Lin and et. al., IEEE Trans., AP-16, 3, P 299, 1968
(5) K. Kagoshima and et. al., J. Inst. Electron. Commun. Eng. Jap.,
    Vol 56-B, 1973, to be published
(6) N. Inagaki and et. al., J. Inst. Electron. Commun. Eng. Jap.,
    Vol 53-B, P 135 1970
(7) K. Iizuka, IEEE Trans. AP-13, 1, P 7, 1965
(8) K. Kagoshima and et. al., J. Inst. Electron. Commun. Eng. Jap.
    Vol 56-B, 1973, to be published

FLUSH-MOUNTED, SCANNING END-FIRE ANTENNA WITH CORRUGATED SURFACE WAVE STRUCTURES

O. K. Kim and K. M. Chen

Department of Electrical Engineering and Systems Science
Michigan State University, East Lansing, Michigan 48823

I.   Introduction

A flush-mounted, scannable end-fire antenna using corrugated surface wave structures has been studied for the communication between a supersonic aircraft and a space or ground station. The end-fire radiation is obtained by mounting two corrugated surface wave structures on the opposite sides of a wedge or a finite body as shown in Fig. 1. The beam scanning can be accomplished by adjusting the input power to each surface wave structure and varying the tooth height and width of the corrugated structure.

II.   Surface Fields of a Single Corrugated Surface Wave Structure

The surface fields on a finite corrugated structure mounted on a finite conducting plane as shown in Fig. 2 have been determined based on a theoretical analysis and an experimental observation. The surface fields are:

Region 1:   Uniform corrugated surface

$$\left.\begin{aligned}
H_{x1} &= H_o \cos\left(\frac{\pi x}{a}\right) e^{-a_1 y - j\beta_1 z} \\[2mm]
E_{z1} &= -\frac{ja_1}{\omega\epsilon_o} H_{x1}, \qquad E_{y1} = -\frac{\beta_1}{\omega\epsilon_o} H_{x1}
\end{aligned}\right\} \tag{1}$$

where the phase constant β_1 and the attenuation constant a_1 of the surface wave are related by

$$\left(\frac{\pi}{a}\right)^2 - a_1^2 + \beta_1^2 = k_o^2 \tag{2}$$

and from the transverse resonance condition,

$$a_1 = \frac{d}{D} k_o \tan k_o h . \tag{3}$$

Region 2:   Tapered Corrugated Surface

$$\left.\begin{aligned}
H_{x2} &= H_o \cos\left(\frac{\pi x}{a}\right) e^{-a_2(z)y - j\beta_2(z)z} \\[2mm]
E_{z2} &= -\frac{ja_2(z)}{\omega\epsilon_o} H_{x2}, \qquad E_{y2} \doteq -\frac{\beta_2(z)}{\omega\epsilon_o} H_{x2}
\end{aligned}\right\} \tag{4}$$

where

$$a_2(z) \doteq a_1 \frac{L + T - z}{T}$$

$$\beta_2(z) \doteq \sqrt{k_o^2 + a_1^2 (\frac{L + T - z}{T})^2 - (\frac{\pi}{a})^2} \doteq \beta_1 \quad \left.\right\} \quad (5)$$

Region 3:   On Finite Ground Plane

$$H_{x3} \doteq \frac{\omega \epsilon_o}{2} \cos (\frac{\pi x}{a}) \{ \int_o^L E_{z1}(z')H_o^{(2)}[k_o(z-z')]dz'$$

$$+ \int_L^{L+T} E_{z2}(z')H_o^{(2)}[k_o(z-z')]dz'\} \quad (6)$$

$$E_{y3} = \sqrt{\frac{\mu_o}{\epsilon_o}} H_{x3} \, , \qquad E_{z3} = 0 \, .$$

The surface fields have been probed carefully with the obtained results shown in Fig. 3.   Theoretical results are in good agreement with the experimental results.   It is interesting to note that the surface fields stay rather uniform over the corrugated surface and then decay rapidly in the surrounding ground plane.   When the corrugated structure is excited by a waveguide, the surface fields remain the variation of $\cos (\pi x/a)$ in the x-direction over the corrugated surface and the ground plane.

III.   Radiation Field of a Single Corrugated Surface Wave Structure

Based on the surface fields obtained in Section II, the radiation field of a single corrugated surface wave structure was calculated. Theoretical and experimental radiation patterns are shown in Fig. 4.   A sharp beam with low side lobe level was obtained.   With a finite ground plane, the beam was tilted and only a near end-fire radiation could be achieved.

IV.   Radiation from Two Corrugated Surface Wave Structures Mounted on Opposite Sides of a Wedge

When two identical corrugated surface wave structures are mounted on the opposite sides of a wedge or a finite body, a perfect end-fire radiation can be obtained.   This end-fire radiation has a sharp main beam with a satisfactory side lobe level.   The beam can be scanned over a finite angle around the end-fire direction by adjusting the input power to each of the two corrugated structures.   The beam scanning is shown in Fig. 5.   A wider scanning off the end-fire direction can be accomplished by changing the slow surface wave over the corrugated structure to a fast wave with the help of varying the tooth height and width of the corrugated structure.
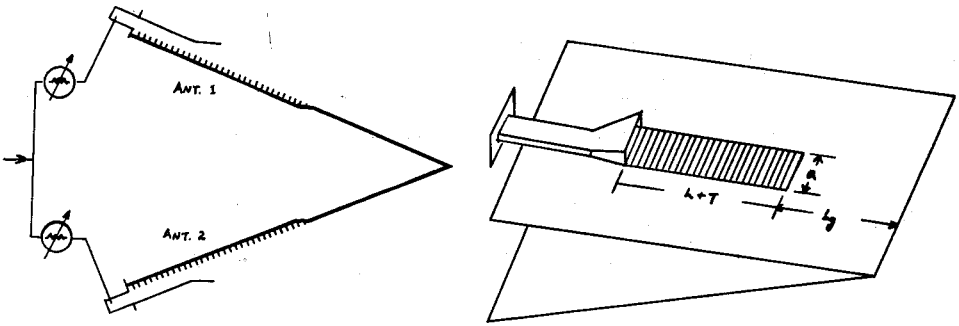
Fig. 1.   Geometry.
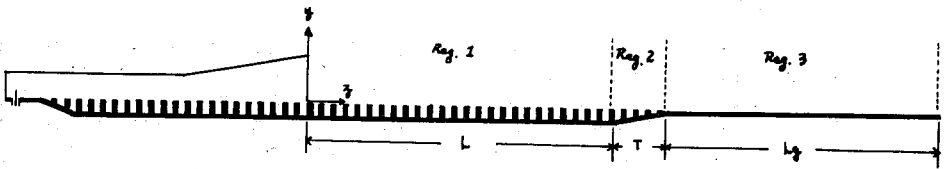
Fig. 2.   Single Corrugated Structure (L = L_g = 10 λ_o,
T = 0. 5 λ_o at 9 GHz).
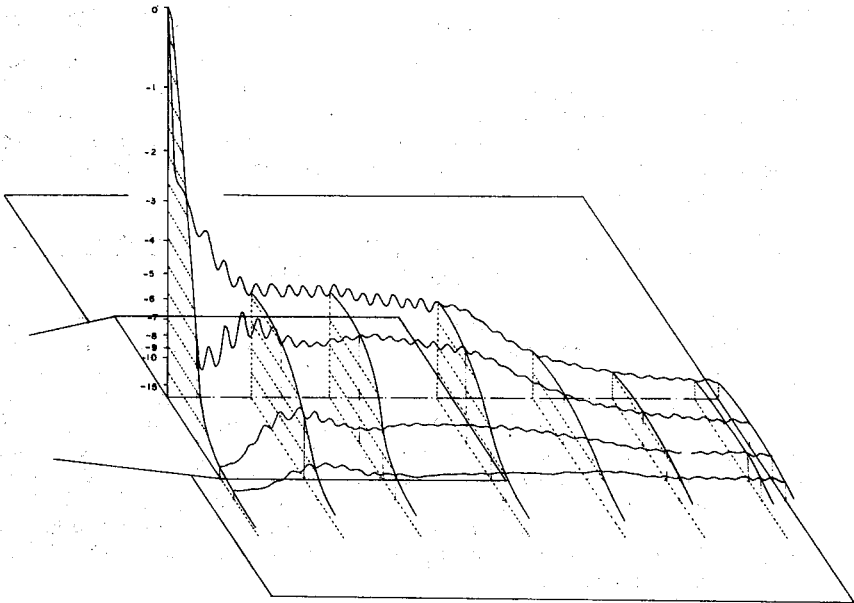
Fig. 3.   3-Dimensional Surface Field at 8 GHz.

f = 7 GHz   f = 8 GHz   f = 9 GHz

E-plane patterns

f = 7 GHz   f = 8 GHz   f = 9 GHz
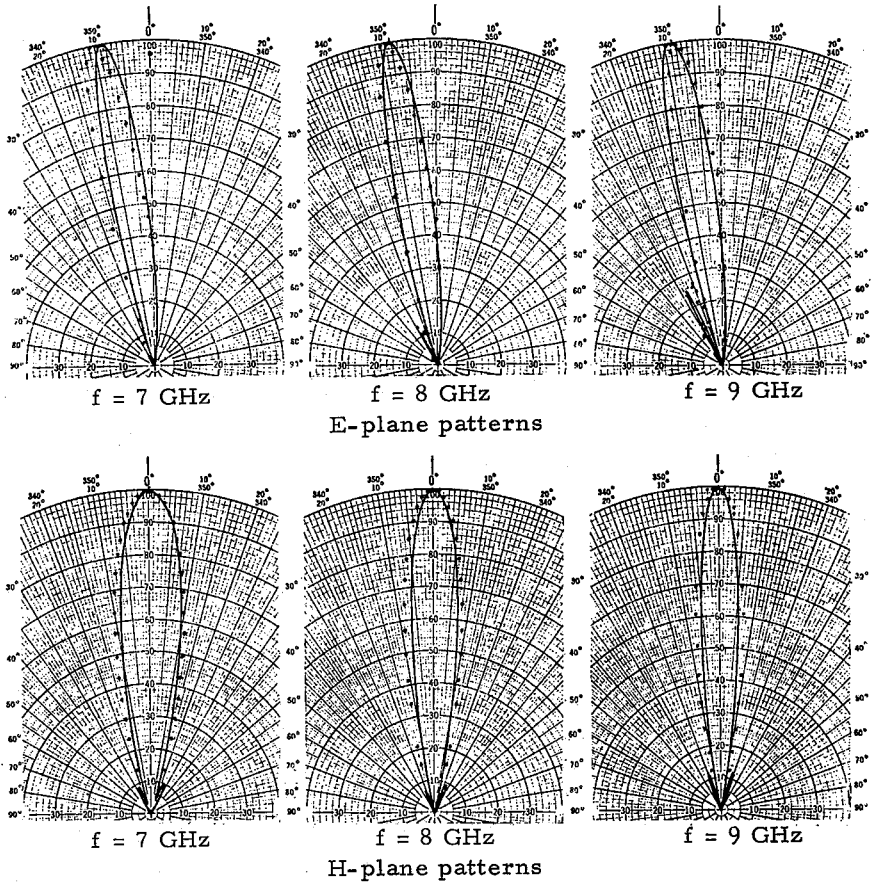
H-plane patterns

Fig. 4.   Radiation power patterns of a single corrugated structure
           (···· theory; —— experiment).

Ant. 1 = 0 db   Ant. 1 = 0 db   Ant. 1 = 0 db
Ant. 2 = 0 db   Ant. 2 = 10 db   Ant. 2 = 20 db
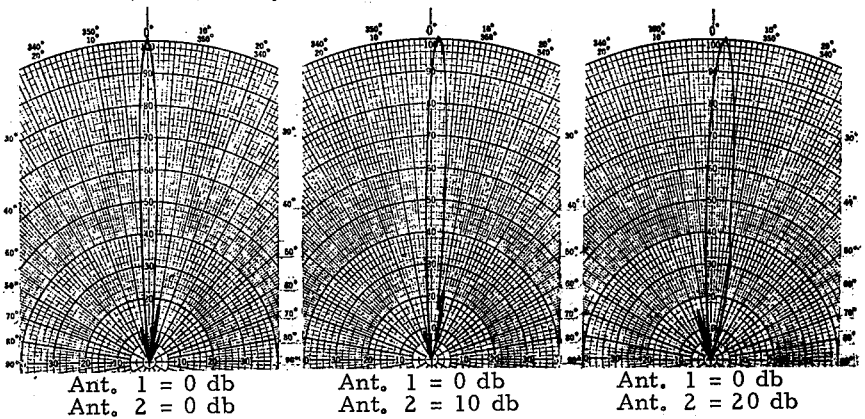
Fig. 5.   Scanning of Beam (E-plaue patters at f = 9 GHz).

A Rigorous Formulation of the Illumination Matching Principle

Giorgio V. Borgiotti – ELETTRONICA S.p.A.
Via Tiburtina Km. 13.700 – 00131 Roma – Italy

According to a widely accepted proposition in antenna theory, the
illumination of an aerial (i.e. the electric and magnetic field tangential
to the antenna surface, existing when the antenna is connected to a transmitter)
should be the complex conjugate of the field in which the antenna is immersed,
in order to maximize the antenna absorption area [1] .
This formulation of the"Illumination Matching" (I.M.) principle although
heuristically appealing, on the basis of readily found counterexamples can
be shown not to be correct in the general case.

In this paper a rigorous formulation of the I.M. principle is provided,
and the exact conditions, the antenna illumination must satisfy for gain maxi-
mization are established. The study has been limited to planar antennas, focu-
sing particularly the attention to the case of a planar aperture horn feed im-
mersed in the receive focal field of a microwave optical system.

The Fourier Transform (F.T.) Technique [2] and the use of functions
having the property of being orthogonal in both a finite and an infinite domain
[3] have provided the essential tools for this study. The peculiar properties
of double orthogonal functions make them ideally suitable to approximate functions
defined in a limited domain G of a certain space, by using functions which are
the F.T. of functions defined in a limited domain A of the space of the conjugate
variables. The maximization of the antenna efficiency leads to a linear approxi-

mation problem exactly of this type, provided G is identified with the
"visible space" of the wavenumber plane, and A with the antenna aperture.
The power transfer efficiency between the receive field and the antenna
can always, in principle, be made as close to unity as desired, by choosing
an aperture illumination whose F.T. "matches" in some sense the F.T. of the
received field on the aperture plane. This solution may lead to illuminations
very different from those expected on the basis of conventional I.M. principle
(valid rigorously only for apertures with unconstrained size).
Practical limitations of the formal solution thus established are due to the
possibly reactive (supergaining) character of the distributions.

[1] R.C. Hansen (editor) "Microwave Scanning Antennas" Academic Press 1964
    ch. 2, pp. 191-193.

[2] G.V. Borgiotti, "Fourier Transform Method in Aperture Antenna Problems"
    Alta Frequenza n. 11, Vol. 32, Nov. 1963 pp. 808-816.

[3] G.D. Boyd, A. Kogelnik, "Generalized Confocal Research Theory" B.S.T.J.
    July 1962, pp. 1347-1369.

Session 21 Antennas

APPLICATIONS OF VARIATIONAL METHODS AND HANKEL TRANSFORMS IN
APERTURE ANTENNAS

K. S. KUNZ, Research Professor of Physics
B. K. SINGARAJU, Electrical Engineering Department
New Mexico State University, Las Cruces, New Mexico 88003

Summary

Aperture admittance

This paper considers a uniform waveguide radiating into free space through an aperture in an (infinitely conductive) infinite baffle or ground plane.[1] The electric and magnetic fields in the waveguide are represented by vector mode functions $\vec{e}_{mn}$ and $\vec{h}_{mn}$ and one requires continuity of the tangential components of the fields at the aperture. Thus for a single incident mode described by $\vec{e}_{pq}$ and $\vec{h}_{pq}$ one has

$$A_{pq}\vec{e}_{pq} + \sum_{m,n} B_{mn}\vec{h}_{mn} = \vec{E}_t(x,y) \tag{1}$$

$$A_{pq}Y_{pq}\vec{h}_{pq} - \sum_{m,n} B_{mn}Y_{mn}\vec{h}_{mn} = \vec{H}_t(x,y) \tag{2}$$

where $\vec{E}_t(x,y)$ and $\vec{H}_t(x,y)$ are tangential components of the external fields in the aperture ($z = 0$). Here Y_{mn} is the mn mode admittance, A_{pq} is the complex amplitude of the incident mode, and B_{mn} the amplitude of the mn reflected mode. Letting Y_T denote the terminal admittance, one may write

$$Y_T = \frac{\int_s ds[\vec{E}_t \times \vec{I}]\cdot\hat{z}}{[\langle \vec{E}_t,\vec{e}_{pq} \rangle]^2} \equiv F[\vec{E}_t] \tag{3}$$

where

$$\vec{I} = \vec{H}_t + \sum_{m,n}{}' \langle \vec{E}_t,\vec{e}_{mn} \rangle Y_{mn}\vec{h}_{mn} \tag{4}$$

Here s denotes the surface of the aperture, $\hat{z}$ the direction of propagation, and the prime on the summation sign indicates that $m,n \neq p,q$. It is also defined that

$$\langle \vec{E}_t,\vec{e}_{pq} \rangle = \int_s ds[\vec{E}_t \cdot \vec{e}_{pq}] \tag{5}$$

It is easy to show that Y_T is stationary with respect to small but orbitrary variations in $\vec{E}_t$.

For the special case of a circularly cylindrical waveguide and an incident field given by the single transverse magnetic mode TM_{01} one can obtain an approximation for Y_T by assuming that the transverse field in the aperture is just that due to the TM_{01} mode. One then finds that

$$Y_T = (\tau_{01})^2 \omega \varepsilon \int_0^\infty d\kappa \; \kappa \left[\frac{\kappa^2 J_0^2(\kappa a)}{\left[\kappa^2 - \left(\frac{\tau_{01}}{a} \right)^2 \right] \sqrt{k_0^2 - \kappa^2}} \right] \qquad (6)$$

where τ_{01} is the first zero of the zeroth order bessel function of the first kind and the square root is taken such that

$$\mathrm{Re}\sqrt{k_0^2 - \kappa^2} \; \geq \; 0 \qquad (7)$$

$$\mathrm{Im}\sqrt{k_0^2 - \kappa^2} \; \leq \; 0 \qquad (8)$$

One can write

$$Y_T = (\tau_{01})^2 \omega \varepsilon \int_0^\infty d\kappa \; \kappa \; F_1(\kappa) F_2(\kappa) \qquad (9)$$

where

$$F_1(\kappa) \equiv \frac{1}{\sqrt{k_0^2 - \kappa^2}} \quad \overset{\tilde{h}_0}{\longleftrightarrow} \quad f_1(\rho) \qquad (10)$$

and

$$F_2(\kappa) \equiv \frac{\kappa^2 J_0^2(\kappa a)}{\left[\kappa^2 - \left(\frac{\tau_{01}}{a} \right)^2 \right]^2} \quad \overset{\tilde{h}_0}{\longleftrightarrow} \quad f_2(\rho) \qquad (11)$$

In the above $\overset{\tilde{h}_0}{\longleftrightarrow}$ implies that each side is a zeroth-order Hankel transform of the other.

By taking the Hankel transforms of zeroth order of $F_1(\kappa)$ and $F_2(\kappa)$ one finds that

$$f_1(\rho) = \frac{j \, e^{-jk_0\rho}}{\rho} \qquad (12)$$

and

$$f_2(\rho) = \begin{cases} \dfrac{\pi}{4} (\tau_{01}) J_1(\tau_{01}) Y_0(\tau_{01}) J_0\!\left(\rho \, \dfrac{\tau_{01}}{a} \right) & \rho \leq a \\[4mm] 0 & \rho \geq a \end{cases}$$

$$(13)$$

Using the Parseval's theorem for Hankel transforms, and substituting in numerical values for $\tau_{01}, J_1(\tau_{01})$, and $Y_o(t_{01})$, one finds that Y_T is given by

$$Y_T = 2.89k_o \int_o^a d\rho e^{-jk_o\rho} J_o\left(\rho \frac{\tau_{01}}{a}\right)$$

(14)

This integral yields Schwarz functions[2] and leads to the following expansion:

$$\frac{Y_T}{Y_o} = 2.89(k_o a)e^{-jk_o a} \sum_{n=o}^{\infty} \frac{\left[\left\{1-\left(\frac{2\cdot4}{k_o a}\right)^2\right\} \frac{k_o a}{2}\right]^n}{n!(2n+1)}$$

$$[J_n(k_o a) + jJ_{n+1}(k_o a)]$$

(15)

where Y_o is the free space admittance.

It is easy to show that $\frac{Y_T}{Y_o}$ is zero when $2a/\lambda = .765227$. This checks well with the result obtained by Marcuvitz[3]. In the high-frequency case, i.e., $k_o a \gg 1$, one can show that

$$\frac{Y_T}{Y_o} \simeq 1$$

(16)

Electric field external to the waveguide
Using the vector mode functions, the only nonzero component of the electric field external to the waveguide is given by

$$E_\rho = \frac{\tau_{01}}{\sqrt{\pi}\, J_1(\tau_{01})} \frac{d}{d\rho} \int_o^\infty d\kappa\, \kappa \left[\frac{J_o(\kappa a)J_o(\kappa\rho)}{\kappa^2-\left(\frac{\tau_{01}}{a}\right)^2}\right] e^{-jz\sqrt{k_o^2-\kappa^2}}$$

(17)

Here the integration with respect to κ over the interval $0 \le k \le k_o$ yields the radiated field and the integration over the interval $k_o \le k < \infty$ yields the near field. Using the product expansion for the Bessel function $J_o(\kappa a)$, and the approximation

$$\sqrt{k_o^2-\kappa^2} \simeq k_o\left(1-\frac{\kappa^2}{k_o^2}\right)$$

(18)

which fits at $\kappa = 0$ and $\pm k_o$, the radiated field can be approximated

by

$$E_{\rho_{Rad}} \simeq - \frac{a^2}{\sqrt{\pi} \, \tau_{01} J_1(\tau_{01})} \frac{d}{d\rho} \int_o^{k_o} d\kappa \, \kappa \, J_o(\kappa\rho) e^{-jk_o z\left(1 - \frac{\kappa^2}{k_o^2}\right)}$$

(19)

This integral yields Lommel functions and thus (19) can be written as

$$E_{\rho_{Rad}} \simeq - \frac{a^2}{\sqrt{\pi} \, \tau_{01} J_1(\tau_{01})} \frac{d}{d\rho} [U_1(k_o z, k_o \rho) - jU_2(k_o z, k_o \rho)]$$

(20)

where

$$U_1(k_o z, k_o \rho) = \sum_{n=o}^{\infty} (-1)^n \left(\frac{2k_o z}{\rho}\right)^{2n+1} J_{2n+1}(k_o \rho)$$

(21)

and

$$U_2(k_o z, k_o \rho) = \sum_{n=o}^{\infty} (-1)^n \left(\frac{2k_o z}{\rho}\right)^{2n+1} J_{2n+2}(k_o \rho)$$

(22)

are Lommel functions of two variables[4]. It is interesting to note that Lommel first introduced these functions to describe the diffracted field due to a circular aperture.

References

1. B. K. Singaraju (1973 "Applications of Variational Methods and Hankel Transforms in Aperture Antennas," D.Sc. Dissertation, Electrical Engineering Dept., New Mexico State University).

2. Y. L. Luke (1962 "Integrals of Bessel Functions," McGraw-Hill, New York).

3. N. Marcuvitz (1951 "Waveguide Handbook," McGraw-Hill, New York).

4. A. Papoulis (1968 "Systems and Transforms with Applications in Optics, Mcgraw-Hill, New York).

RADIATION FROM WIDE-FLARE CORRUGATED E-PLANE SECTORAL HORNS

M.S.Narasimhan and V.Venkateswararao
Department of Electrical Engineering
Indian Institute of Technology, Madras
Madras-600036, INDIA

An analytical and experimental investigation of the radiation properties of wide-flare corrugated E-plane sectoral horns ($10° \leqslant \alpha_o < 70°$, where α_o is the half-flare angle) excited in the HE_{11} mode with improved E-plane radiation patterns and suppressed side-lobe levels (over a broad bandwidth) is described in this paper. Given the flare-length and half-flare angle of the horn, the far-field radiation pattern is determined by two methods, one of which involves aperture field-integration, based on vector diffraction formula, over a constant-phase surface at the mouth of the horn and the other of which employs an expansion of the aperture field in terms of free-space cylindrical TE and TM wave functions. Good agreement is obtained between the two methods and with measured radiation patterns for several values of α_o. Given the flare length, variation of on-axis gain with α_o of the horn is analytically investigated and the design procedure for determining optimum α_o, in order to obtain maximum on-axis gain, is also indicated. Furthermore, design details concerning wide-flare corrugated E-plane sectoral horns exhibiting low input VSWR and improved radiation characteristics are also presented.

Reference

1. M.S.Narasimhan and V.Venkateswararao ('Radiation chracteristics of corrugated E-plane sectoral horns' to appear in IEEE Trans. Antennas and Propagation,May 1973)

PUBLICATIONS AS AN AID TO THE G-AP MEMBER
L. J. Ricardi
Lincoln Laboratory, Massachusetts Institute of Technology

Of the many services that the Institute of Electronical Electrical
Engineers and the Group on Antennas and Propagation have to
offer their members, publications is undoubtedly the most expen-
sive and hopefully the most rewarding. These publications are
well organized and readily available. An "unbiased" committee
recently evaluated all Transactions of the IEEE and found the
Transactions on Antennas and Propagation to be the leading pub-
lication in the field of antennas and one of the best group trans-
actions in general. Ultimately the quality of this and our other
publications are left to the reader, the G-AP membership and
those practicing engineers that use the G-AP publications. The
following will discuss the services, policies and directions in
which they are changing, with regard to the Transactions, News-
letter, Symposium Digest and Standards.

Considering first the services of the Transactions, those who
benefit from their publication, include the authors, readers and
reviewers. It is a means for the authors to obtain a formal
review of their work by very capable specialists in an appropriate
discipline. Their work is disseminated to that body of people in
the world that are presumably interested in reading about their
accomplishments. And, as I am well aware, the recognition that
the authors receive contributes considerably to the advancement
of their careers.

The readers benefit from the new ideas, methods and theories
that are presented in these publications. It is hoped that, both in
the past and more so in the future, the application of this infor-
mation will be more easily transferred to the practicing engineer.
The reviewers benefit from their efforts in several ways including
recognition, a forced critique of the material they read as opposed
to a casual scanning of it, the review of material in advance of its
formal publication, and the ability to improve their own writing
and increase their detailed knowledge.

The Symposium Digest provides information similar to that
obtained in the Transactions but with far less detail and formality.
The Digest however provides the reader with a record of those
presentations made at a symposium and those people with whom
he could discuss those subjects of interest to him. In general
terms, it provides him with much of the material presented at
the symposium without requiring that he attend it. If he does
attend the symposium then the digest represents a very good guide

as to how he should allocate his time in attending the presentations.

The IEEE Standards and in particular those written and sponsored by G-AP are constantly in revision and generation. Whenever a significant set of Standards are complete they are published in the Transactions for the entire membership to use. They represent a great deal of effort on the part of those people who take the time to write them and review them. It is certainly rewarding to them and could serve as a means of obtaining a common language among all practitioners.

The previously discussed publications deal with the technical aspects of the Group activity. The Newsletter serves to transmit information of a social and administrative nature among all members of the Group. All members are encouraged to express their views on various subjects relating to the policies and administrative procedures of the Group and its officers can reply to the questions raised or present the policies as they see them. It is a very powerful means of communicating with your fellow worker.

Next, let us consider some of the important policies of each of these publications. The Transactions editor considers for publication all manuscripts submitted to him for that purpose. They are distributed directly to reviewers or to the associate editors depending upon the subject and the individual work load at the time of submission. All papers and most all communications are reviewed by at least two reviewers; all communications are reviewed by at least one reviewer. Comments and corrections are handled entirely by the Editor. Although I make the final decision as to whether a paper should be published, the associate editors and the reviewers contribute substantially in the formulation of that decision.

As you probably know, an individual may comment on a published paper in the correspondence section of the Transactions. If these comments are cirtical, they are first submitted to the original author for rebuttal. He may, or may not, comment as he desires. If he does comment his rebuttal is then sent to the individual who made the criticism. At this time, the criticism may be withdrawn. In this case nothing is published. If it is not withdrawn it may not be modified and the original comment and rebuttal are published side by side in the same issue of the Transactions. The purpose behind this procedure is to eliminate unnecessary attacks on personalities and publication of entertaining, as opposed to technical, writing in the Transactions. Needless to say, I would be most happy to publish a jointly prepared comment by the author and his critic.

Authors often submit papers in more than one part for various reasons. I will not review any paper that is submitted with the intent of having more than one part unless all parts are included in the initial submission. In general, I do not approve of multipart papers but will accept them if a satisfactory explanation accompanies the submission of the original or revised manuscripts.

The format for preparation of manuscripts is adequately described on the inside of the rear cover of a late issue of the Transactions. Authors are urged to follow these guidelines in the preparation of their original manuscript. The permissible length of a paper or communication is probably best obtained by reviewing past issues of the Transactions. In any case, the author should make every effort to keep his presentation succinct and clear. When preparing his manuscript, especially the revised version of it, the author should proofread it very carefully and remove all errors. All author alterations of the galley proof must be paid for by the Group as a publication expense. I feel that it is wrong that the members of the Group be assessed indirectly for the carelessness of an author in the preparation of his manuscript. Consequently, all author alteration charges for changes at variance with his manuscript as it was submitted for publication, will be levied on the author if they exceed a reasonable level.

It is well known that all authors are asked to pay a voluntary charge of $60 per page for the publication of their work. This is far less than it would cost him to publish the work and disseminate it in any other fashion. It is also less than the average cost of about $80 to publish a page in the Transactions. Since more than sixty percent of the authors pay the voluntary charge, I feel that authors should try very hard to support the Group by honoring the page charge. At the present time, the charge is voluntary and failure to honor it will in no way affect publication of the authors manuscript.

The Newsletter is designed to cover a broad category of subjects with the particular exclusion of technical information. The membership is urged to submit gripes or criticisms of the Transactions, the Newsletter, or any other publication, or the manner in which the Group is being organized, administered or directed. Instructions for submitting letters, comments, etc. to the editor of the Newsletter are included on the inside of the rear cover of the Transactions and in the Newsletter.

Finally, copies of the Standards have been published in previous issues of the Transactions on Antennas and Propagation and can be obtained from the IEEE Headquarters at a nominal fee. Directions and forms for procuring these and other G-AP documents, are

usually found in the rear pages of the Transactions.

The Group membership has on many occassions criticized the Trans-
actions as being too "theoretical" as opposed to containing informa-
tion applicable to the needs of the practicing engineer. Toward
this end, I have urged the authors of papers with which I have become
familiar, either through company reports, informal discussions,
presentations at symposiums, or recommendation of fellow colleagues,
to submit a document to me for publication in the Transactions. I
have allowed the review of experimental papers to be less critical
in an effort to encourage publication of the paper under review and
those that may be written by the readers of these papers. I have
insisted that theoretical papers present a connection to engineering
applications and that they at least contain some calculated values
or information of immediate interest and utility. In short, I have
insisted that the theoretical papers be as good or better than they
have been in the past and that the experimental papers be immediately
useful to the G-AP readers.

The review period has been shortened somewhat and the time between
original submission and publication can be as little as four months;
it need be no more than seven months. The latter limit may require
the author to prepare a revision of this original manuscript in approx-
imately four weeks.

The Newsletter will attempt to introduce topics of a social economic
flavor with a decided interest in promoting the newest activities of
the IEEE. The editor is constantly pleading for news and I would
like to see comments and criticisms of the Transactions appearing
in each issue of the Newsletter. This type of interaction between
myself and the readers may help improve the quality and applica-
bility of the papers that appear in the Transactions.

Session 27 Panel Discussion

AD COM INITIATIVES - 1973

Carlyle J. Sletten
Air Force Cambridge Research Laboratories
L. G. Hanscom Field
Bedford, Massachusetts

ABSTRACT

My main function on this panel is to advocate and explain
current initiatives G-AP is taking to make our organization more
responsive to member needs. Some of the actions or ideas being
implemented and considered are:

1. Active solicitation by session Chairman and Editor of
Transactions of applications papers.

2. Outstanding Speakers program for local Chapter talks.

3. Newsletter expansion for job seekers and better coverage
of news and views.

4. Listing of company or laboratory contacts.

5. Shaping educational policies to aid practitioners and
provide continuing education.

6. Society status to our members.

7. Some tangible benefits such as IEEE low cost insurance
and Washington representation on economic interests.

This is a good occasion to discuss options available to G-AP management.
Based on an appraisal of the kind of economic force field we are in and
the diverse interests of members in engineering, teaching, research and
development, scientific management, etc., some policies and goals will
be proffered.

PANEL DISCUSSION ON
"HOW CAN THE G-AP BE MORE USEFUL TO ITS MEMBERS?"

A. F. Sciambi, Jr.
Philco-Ford Corporation
Western Development Laboratories Division
Palo Alto, California

The major function of the G-AP is to provide a forum for the dis-
semination of technical information that is principally scientific
and educational. The majority of the members of the technical com-
munity are practicing engineers (as opposed to pure scientists) and
the information which is presented in the Transactions, at symposia
and at the regional meetings should be directed toward the discussion
and solution of engineering problems. Since engineers are people
who skillfully manage or carry through some enterprise, usually with
the constraints of both time and money, it is of paramount importance
that the exchange of information be of a practical engineering
nature rather than purely theoretical discussions. It is of little
value, either technically or educationally, to present a theoretical
dissertation which cannot be practically applied or one which requires
many hours of study to even understand. This almost assuredly defeats
any educational purposes for which the discussion may have been in-
tended.

In order for published material to be of significant engineering
value, theory should be supported by experiment, or at least a graphi-
cal presentation, disadvantages as well as advantages should be dis-
cussed and mathematical treatments should be supported by example.
Those papers which provide these desirable ingredients should be given
first priority and should constitute the bulk of the information
reported.

Most practicing engineers have elected to leave the full time aca-
demic world to practice their art in industry. As such, their time
is devoted to the development and manufacture of products for which
their employers have committed their resources. This is a full time
job and leaves little time for the detailed study required to under-
standing articles dealing with general theory. Thus, to serve their
needs and to recognize their practical accomplishments, the G-AP
should realign its course and serve firstly the engineering community
and secondly the academic community.

MAKING G-AP RELEVANT

W. A. Imbriale
TRW Systems Group, Redondo Beach, Calif.

The decline in membership in the G-AP certainly indicates that we have come to important and unavoidable crossroads. Do we want to serve only the "high class" theoretician and university-type people, or do we want to branch out and include the "working" technician? Can we do both? Much of the criticism leveled at G-AP by the working engineer concerns the influence of colleges and universities in G-AP affairs, particularly as it affects publication policy. Many joint advisor-student thesis papers on a topic of interest to perhaps half a dozen people in the entire world have become a standard G-AP syndrome, they complain. The papers don't relate to the problems the average engineer is concerned with. Is this true? Is this what we want? Certainly the feedback of the general membership is sought. There is also a definite need for industrial feedback so that the problems of industry influence, in some manner, the topics of concern in the profession. In any event, we should try to accommodate the working engineer as well as we can by including more applications-minded papers in the transactions and at the conferences. The most useful G-AP paper award is a great idea. Perhaps this will encourage authors to consider including useful data with their papers. We need more ideas of this caliber.

Another reason for the declining membership is that students and young engineers are not motivated to become part of the E.M. community. They often fail to see the relevance of E.M. theory in the present and future problems of society. Electromagnetics is a dead field, they say.

Our traditional technologies are narrow, to say the least. We need to
expand our horizons to include new emerging fields and also to be
sensitive to the problems of society.

As members of G-AP, should we continue to promote only the
scientific and educational activities, or must we also serve the
professional welfare of the membership? Again, can we do both? Our
participation in professional activities, to be sure, takes a minor role
as compared with programs of the entire IEEE, but it need not be zero.
Areas where G-AP can contribute include the establishment of a code of
ethics and standards for the profession and gathering data for industrial
profiles.

Doing a better job of serving the interests of the working engineer,
broadening the scope of the technology, and promoting professional
activities are just a few of the many ways G-AP can better serve its
membership.

ELECTROMAGNETIC PROBING OF THE MOON

Gene Simmons for the SEP TEAM

Massachussetts Institute of Technology
University of Toronto
Raytheon
National Aeronautics and Space Administration

In December 1972, the Apollo 17 Crew performed a simple electromagnetic and interferometry experiment on the surface of the Moon. They laid out on the surface two orthogonal, resonant, half-wave dipole transmitting antennas. They mounted on the Lunar Roving Vehicle a receiver with three small orthogonal, concentric magnetic loop antennas. They recorded on magnetic tape the field strength as a function of distance from the transmitter for each of the two transmitting antenna orientations, for each of the three receiving antennas, and for each frequency (1, 2.1, 4, 8.1, 16 and 32.1 M Hz). The Astronauts brought the magnetic tape back to earth for data analysis and interpretation.

The interpretation of the observed data is based on the theoretical solutions of the wave equation for the EM fields in the vicinity of an interface between media with different electric and magnetic properties and for a dipolar source.

The properties of the media are completely general and are contained in the usual reflection coefficients. We have obtained solutions of the general integrals in terms of normal modes, by use of the geometrical optics approximation, and by direct numerical integration. The direct integration uses large amounts of computer time but provides a check on the other solutions. The geometrical optics approximation is fast in computation and valid for lossy, or thick, layered media. The normal mode solution is best for thin, low loss, layered media.

In preparation for the lunar experiment, we tested the experiment concept and equipment on the Gorner Glacier (Switzerland), Athabasca Glacier (Alberta), and several glaciers in the Juneau (Alaska) icefields. Glaciers were chosen for those tests because of their relatively high electrical resistivity ($\sim 10^7 \Omega m$). These particular glaciers were chosen because their properties and geometry were known from previous investigations. The thickness and properties of the ice obtained from the observed interference patterns matched closely the known values. But, in addition to the expected features, we observed many other interferences of short spatial wavelength that we attribute to scattering by crevasses, air pockets, and large boulders. Surface topography also produced interference patterns with wavelengths of 3-6 meters. On the basis of our glacier experiences with scattering, we were surprised to find that the lunar data is essentially free of similar scattering.

The theoretical solutions were adequate for the interpretation of
the glacier data. They were also tested against the surface fields
measured for simple layered, scaled models in an analogue tank at
GHz frequencies.

The theoretical expressions for layered media have been used to
interpret the Apollo 17 Lunar data. Our preliminary models of the
electrical properties are based on the vertical magnetic field com-
ponent. The patterns calculated for the models match closely the
observed interference patterns for each frequency and each trans-
mitting antenna orientation. The loss tangent of the Moon is less
than 0.01 and may be as low as 0.001. From these values of loss
tangent, we infer that no liquid water is present in the outer few
kilometers.

Two basically different models of the dielectric constant satisfy
the observations. We emphasize that the theory for neither of
these models is yet complete. For one model, we suggest that the
dielectric constant varies continuously with depth from a value
of 3 1/2 at the surface to about 5 at a depth of 40-50 meters
where it increases discontinuously to 6-6 1/2. It does not in-
crease more for at least 2 kilometers. For the other model, we
suggest the presence of a shallow, dipping interface at a depth
that varies from 40 meters near the touchdown point of the Lunar
Module to about 20 meters at a distance 1 1/2 kilometers to the
west. The dielectric constant of the upper layer is 3 1/2 to
4, of the lower layer 5 to 6. In this second model, there is a
probable increase of dielectric constant at a depth of 300 meters.

RADIO FREQUENCY SOUNDING ON GLACIERS

AND ON THE MOON

D. W. Strangway,[1] R. D. Watts,[1] J. D. Redman,[2] A. P. Annan,[2]

J. R. Rossiter,[2] G. R. Olhoeft[3] and A. L. Frisillo[1]

ABSTRACT

In most geologic environments the electrical conductivity is
sufficiently high that useful electromagnetic sounding is restricted
to low frequencies where diffusion of energy into the earth is
dominant. In some environments the resistivity is sufficiently high
that it is possible to get considerable depths of penetration using
frequencies in the 1 Mhz to 100 Mhz range so that one can deal with
conventional wave propagation. One such material is ice which behaves
as a dielectric with a frequency-dependent loss. The dielectric constant
is typically about 3.2 - 3.3 and the loss tangent is typically $\frac{0.2 - 0.4}{f}$
where f is in Mhz. By measuring the field strength as a function of
distance from a fixed transmitter it is possible to detect interference
between the surface wave, the subsurface wave and any reflections. This
gives a determination of dielectric constant, loss tangent and depth to
reflectors.

A series of experiments using frequencies of 1, 2, 4, 8, 16 and 32 Mhz
have been conducted on two glaciers - the Athabasca glacier in western
Canada and the Juneau icefields in Alaska. The results can be summarized
as follows:

[1]NASA-JSC, Houston, Texas 77058
[2]Department of Physics, University of Toronto, Toronto, Canada
[3]Lockheed Electronics Company, Houston, Texas 77058

A. Atahbasca glacier - bare ice

  1) dielectric constant measured is 3.2 $\pm$ .1 (at 1, 2 and 4 Mhz)

  2) loss tangent measured behaves roughly as 0.25/f (at 1, 2
     and 4 Mhz)

  3) depth to bottom of ice determined with a precision of a
     few meters in 200 to 300 (at 2 and 4 Mhz)

  4) strong glacier scattering detected at 8, 16 and 32 Mhz
     with very clear crevasse "signals"

B. Juneau Icefields - snow covered

  1) at 1 Mhz the glacier behaves like a halfspace with the
     dielectric constant and loss tangent typical of the
     underlying ice

  2) at 2 Mhz the data indicates the presence of the snow layer
     on the surface by attenuation of the interference

  3) at 4 Mhz there is almost no interference. This is a result
     of the snow layer, which is thin enough that it will not
     support reflections but at the same time effectively
     decouples the receiver from waves in the ice layer below

  4) at 8 and 16 Mhz layers can be detected below the ice surface

  5) at 8 and 16 Mhz only a very small number of crevasses
     are detected while much scattering is present at 32 Mhz

  6) by comparison with seismic data the bottom of the ice can
     be detected when it is less than about 200 m thick.

The interpretation of the results from the glaciers has been done with the use of theoretical curves developed both from a geometrical optics approach and from mode theory. Scale model studies at 6 cm wavelength have been used to confirm the theory, to study antenna patterns and to demonstrate the signature expected over crevasses and other scattering objects.

These results have led to the basis for interpreting the data collected on the moon during the Apollo 17 mission. Studies on lunar samples which are typical dielectrics show that the dielectric constant of the soil is about 3.0 and increases significantly on compaction in a vacuum. The loss tangent is fairly low and with considerable measurement precautions to insure that there is no moisture present the loss tangent is in the range .005 - .05 and is essentially frequency independent. Rocks have a higher dielectric constant, typically in the range from 5 - 9 and somewhat higher in loss tangent.

The lunar data can be interpreted as due to 1) a regolith of soil with dielectric constant about 3.0 - 4.0, about 20 m thick and dipping slightly to the east, 2) a solid rock layer extending to a depth of at least 1.5 kilometers. A weak reflector at about 300 m coincides with a change in seismic velocity and is probably the result of a change from fractured rock to more solid rock.

OPTICAL INTERACTION WITH BIOLOGICAL MATERIALS

Curtis C. Johnson
Department of Biophysics and Bioengineering
University of Utah
Salt Lake City, Utah 84112
(801) 581-8496

Optical radiation plays a very significant role in mankind. On the whole, man is very well adapted to the sun's optical and infrared radiation and depends on it for warmth and the processing of food through photosynthesis. Optical hazards to man are few, and mostly come from artificial sources such as lasers. The ultra-violet portion of the spectrum can cause superficial cell damage (sunburn).

Despite the important role of optical energy in the animal and plant world, its use in medical and biological applications has been limited. Examples include quantitative biochemical analysis in the clinical chemistry laboratory, optical and electron micros-copy, endoscopy (including the use of coherent fiberoptic bundles for probing in the body), spectroscopy, and holography. New principles, techniques, and devices, such as lasers, light-emitting diodes, fiberoptics, optical data processing, holography, integrated optical circuits, phototransistors, etc., are now available which are expanding the use of light in biological applications.

Of particular interest in this paper is optical propagation in biological materials. We will not generally be concerned with cell damage and hazardous effects that are confined to the UV spectrum or high intensities. These are described elsewhere.[1] Optical propagation in natural biological materials is dominated by scattering, because the cellular structure creates medium inhomogeneities of the order of an optical wavelength. There is optical absorption caused by a variety of biochemical molecules which create a variable absorption as a function of wavelength. These combined scattering and absorption properties will be dis-cussed for some selected biomaterials, and an analytical foundation will be laid for describing these effects.

Very little is known about the optical properties of most biological materials. There is considerable data on hemoglobin solutions and whole blood, some data on skin, with increasing inter-est in cellular scattering. Ultraviolet irradiation has been a subject of interest for many years due to the hazards involved.[2,3]

Light is commonly used to determine the oxygen content in blood. The normal healthy pink appearance of a person compared to a grey color or "blue baby" is a common diagnostic tool based on optical spectroscopic effects in blood. Erythrocytes (red blood

cells) contain hemoglobin molecules, Hb, which are easily oxygen-
ated to oxyhemoglobin molecules HbO_2. An important parameter is
oxygen saturation OS, defined as the ratio of HbO_2 to total
hemoglobin. There is an index of refraction discontinuity between
the erythrocyte and its surrounding plasma medium (about 1.40 to
1.35), thus scattering occurs which complicates the optical
measurement of OS of hemoglobin contained inside the erythrocyte.
A strong absorption band is centered at 414.5 nm, called the Soret
band, with minor absorption peaks in the 550-nm region. Oxyhemo-
globin HbO_2 has low absorption in the red portion of the spectrum
compared to Hb. Thus blood "looks" red when oxyhemoglobin molecules
are predominant. Observers have noted that there is a greater net
absorption when hemoglobin is packaged in erythrocytes (whole
blood) as compared to being in solution (hemolyzed blood). The
increased absorption is due to erythrocyte scattering effects.

Small organisms such as cells, bacteria, etc., scatter light
in characteristic patterns. These scattering patterns can be used
to identify the type and concentration of species. For example,
the detection of bacteria in urine represents an important medical
application. If it were possible to make a rapid determination of
bacterial count in urine greater than 10^4/ml, it would expedite
enormously the time-consuming clinical laboratory procedure involv-
ing culturing the bacteria for many hours. A more direct bacterial
counting capability, one which is simple, effective and rapid, is
available via the technique of laser light scattering. Light
scattering photometer instruments record the scattered intensity
variation with scattering angle from cells in solution illuminated
by a laser beam.[4,5] The features (amplitude and angular positions
of maxima and minimal) in the light scattering pattern give a
precise measure of the size, shape, structure, and size distribu-
tion of the ensemble of scattering particles. In addition, measured
changes in the light scattering pattern can be employed to monitor
the effects of variation of conditions (heat, nutrient changes,
drug treatment, etc.) on bacterial suspensions.

The detection of bacterial concentrations of 10^5/ml is
routine by this technique. At these concentrations and lower, the
intensity of the scattered light at any angle relative to the back-
ground light is approximately proportional to the number and density
of cells, especially when the cell size distribution is narrow.
Thus, calibration of the light scattering patterns in terms of cell
concentration is straightforward. In specimen solutions such as
urine, appreciable background light may be scattered from various
materials other than the bacteria, materials such as tissue cells,
granules, cell debris, leukocytes, erythrocytes, and various crystals.
Bacterial concentrations of 10^5/ml are clearly detectable.

Optical (particularly ultraviolet) effects in skin have been
studied extensively.[6] A comprehensive paper by Hardy, *et al.*,[7]

establishes the scattering and absorbing properties of skin. The
transmittance versus wavelength characteristics for skin in the
ultraviolet-to-infrared regions show transmission rising very
rapidly as wavelength is increased above 0.3 μ. The skin heavily
absorbs UV radiation, providing a protection for the underlying
tissues that are damaged by UV. The inefficiency in this protection
gives rise to sunburn. Beyond 1.4 μ, the transmission curves follow
closely the transmission characteristics of water. Skin reflectance
in the near infrared is determined by scattering sites in skin and
the transmission characteristics of water.

Early theoretical concepts focused on a purely homogeneous
absorbing medium with no scattering. Pure absorption obeys the
simple one-dimensional exponential Lambert-Beer law. For a sample
thickness d, optical density becomes

$$OD = Ckd$$

where concentration C is expressed in moles cm^{-3}, and k, defined as
the *specific absorption coefficient* for the material, has the dimen-
sions cm^2 $mole^{-1}$. Note that for a purely absorbing material
described by the Lambert-Beer law, a plot of OD versus d results in
a straight line, the slope of which is proportional to the specific
absorption coefficient for the absorbing medium and the concentra-
tion. OD measurements can be used to determine the concentration
of molecular species, knowing k and d.

The historical analytical approach to the scattering problem
originated with the work of Schuster[8] in his attempt to describe
optical scattering through atmospheres of distant stars. This work
was subsequently modified by Kubelka.[9] Schuster's two-flux theory
is one-dimensional and applies only to diffuse flux. The scatterers
in the material are characterized by an absorption cross section σ_a,
a backscattering cross section σ_s^-, and a scatterer volume density
ρ. Schuster's expressions for reflectance and transmittance for a
slab medium are:

$$R = \frac{\sigma_a + \sigma_s + \sigma}{\sigma_s^-}\left(\frac{1 - e^{2\rho\sigma d}}{1 - Ae^{2\rho\sigma d}}\right)$$

$$T = \left(\frac{1 - A}{1 - Ae^{2\rho\sigma d}}\right)e^{\rho\sigma d}$$

where

$$A = \frac{\sigma_a + \sigma_s^- + \sigma}{\sigma_a + \sigma_s^- - \sigma}$$

More sophisticated attempts to describe wave scattering and absorption effects can be categorized into either a "phenomenological" approach based on Schuster's work and progressing into neutron transport theory and radiative transport theory, or an "analytic" approach based on Maxwell's field equations and dealing with averaged field quantities. Twersky has developed the basic theoretical approach, with some useful applications to cell scattering.[10,11] An optical diffusion theory has emerged from the phenomenological approach as a means of describing some of the observed phenomena in biological materials with a promising degree of quantitive precision and with analytical simplicity.[12,13] Quantitative comparisons between the optical photon diffusion theory and experimental results on whole blood have been very encouraging.

The light absorbing and scattering properties of biological materials have been utilized to make important material property measurements. In a clinical chemistry laboratory, various reagents are combined with specific biologically important ions and molecules to generate new colored compounds especially suited to optical measurements. A vast and automated technology has been developed based on this procedure. Optics technology has also been applied to making important measurements on natural biological tissue, such as the propagation of light through the skin and underlying tissue to measure blood volume (photoplethysmography) or anatomy (transillumination), and optical spectrophotometric techniques to measure oxygen content in blood (oximetry).

References

1. S. M. Michaelson (Apr. 1972 Proc. IEEE 60, pp. 389-421).
2. G. Moreno, M. Lutz, and M. Bessis (1969 Int. Rev. Exp. Path. 7, pp. 99-137).
3. F. Daniels, Jr., J. C. Van der Leun, and B. E. Johnson (July 1968 Sci. Amer., pp. 38-46).
4. P. J. Wyatt (October 1968 Appl. Opt. 7, pp. 1879-1896).
5. P. J. Wyatt (1969 Nature 221, p. 1257).
6. F. Urbach, ed. (1969 The Biologic Effects of Ultra-Violet Radiation, Pergamon).
7. J. D. Hardy, H. T. Hammel, and D. Murgatroyd (Sept. 1956 J. Appl. Physiol. 9, pp. 257-264).
8. A. Schuster (Jan. 1905 Astrophys. J. 21, pp. 1-22).
9. P. Kubelka (May 1948 J. Opt. Soc. Amer. 38, pp. 448-457).
10. V. Twersky (1964 Proc. Am. Math. Soc. Symp. on Stocastic Processes in Math. Phys. and Eng. 16, pp. 84-166).
11. V. Twersky (Aug. 1970 J. Opt. Soc. Amer. 60, pp. 1084-1093).
12. C. C. Johnson (Apr. 1970 IEEE Trans. Biomed. Eng. BME-17, pp. 129-133).
13. R. J. Zdrojkowski and N. Pisharoty (Apr. 1970 IEEE Trans. Biomed. Eng. BME-17, pp. 122-128).

Session 31   Combined URSI/GAP

ELECTROMAGNETIC INTERACTIONS WITH BIOLOGICAL MATERIALS

Arthur W. Guy
Department of Rehabilitation Medicine
School of Medicine
University of Washington
Seattle, Washington 98195

The need for a thorough understanding of the biological effects
of electromagnetic energy has never been so acute as it is today.
This situation exists in spite of the fact that during the period
after World War II through the late fifties, extensive EM bioeffects
research had been carried out. This work was in part conducted by
the medical profession for a better understanding of the uses of EM
energy for diathermy (1)(2), and in part was stimulated and funded
by the Tri-Services to provide data for the safe operation of radar
systems (3). This early work indicated that electromagnetic energy
could indeed produce biological damage through tissue heating at
incident power density levels of greater than 100 mW/cm^2. It was
felt at that time that the relation of the threshold and degree of
thermal damage or deleterious effects in the tissue to the incident
power density was sufficient to quantify the hazards and to set a
safety exposure standard generally accepted at 10 mW/cm^2 for con-
tinuous exposure which was considered to be a safe order of magni-
tude lower than that known to produce biological damage. During
the period from this time to the time of the passage of the Radiation
Control for Health and Safety Act of 1968, research in the United
States on the subject had become almost non-existent, while that
in the Soviet Union and East European countries continued. At the
time of the formulation of the Radiation Control Act, it became
apparent that the Soviet and East European results showed that in
addition to thermal effects, there was the possibility of either
thermal or athermal effects from much lower power levels, especially
to the central nervous system (CNS). This prompted the setting of
a far more conservative safety standard for continuous 8 hour
microwave exposure in these countries of 10 µW/cm^2. This was
initially somewhat discounted in the Western countries (3) (4),
since the research protocols, instrumentation and exposure situa-
tions were poorly defined in the Soviet and East European literature
and sharp differences exist between researchers in the United States
and the Soviet Union in their physiological interpretations and
techniques. Additional but limited research results in this country
corroborated and refuted some of the Soviet work, but has added fuel
to a growing controversy on whether there are hazards due to low level
EM radiation (5) (6). There has been a severe lack of dosimetry
in connection with most of the low level work, however, where little
is known about the actual energy absorbed by the tissues. Recent
theoretical and experimental studies on EM power absorption charac-
teristics in biological tissues has indicated much higher and possibly
thermal levels of power absorption in animals exposed to low level
microwave radiation (7) (8).

An understanding of the biological effects observed and
measured in man, animals and biological specimens exposed to elec-
tromagnetic fields requires a complete description of the fields
and possible heating patterns induced in the tissues by the outside
sources. These induced fields are complex functions of the types
of sources, frequency, and subject size and they may differ by many
orders of magnitude depending on exposure conditions, even though
the measured values of outside field parameters usually specified
in safety standards are the same. Above 200 MHz the combination
of curved surfaces and high dielectric constant of tissues can
produce very high localized and frequency dependent internal absorp-
tion deep in the tissue due to focusing of the power with values
as shown in Fig. 1 for a spherical tissue model. Below 200 MHz the
absorbed power in exposed subjects drops sharply with frequency.
In this range magnetic fields can produce far greater absorbed
power densities in man than electric fields of the same energy
density, whereas the reverse may be true in small animals. Intern-
ally placed metal or highly conducting probes can produce intense
localized absorption due to the fringing of fields near sharp edges
or points. Internal fields and power absorption density may be
directly measured in vivo by implanted electromagnetically trans-
parent probes or indirectly measured in electrically equivalent
phantom models of the subject and in the bodies of sacrificed animals.
This is done by thermographically observing related temperature
changes in bisected sections of the model or animal after a short
exposure to a high level of radiation. Measurements by these methods
show power absorption density thresholds of 4 mW/gm for latency
changes in evoked responses in the brains of cats exposed for
15 minutes and 138 mW/gm for opacity formation in the lenses of
rabbits exposed for 100 minutes. Auditory sensations have been
evoked in both man and cats exposed to narrow (<30 µsec) microwave
pulses with incident energy densities 20 to 40 µjoules/cm^2 or greater,
regardless of pulse width or peak power.

REFERENCES

1. H.P. Schwan, "Biophysics of diathermy," in Therapeutic Heat and
    Cold, S. Licht, Ed. New Haven, Conn.:Licht, 1965, sec. 3, pp.
    63-125.

2. J.F. Lehmann, "Diathermy," in Handbook of Physical Medicine and
    Rehabilitation, Krusen, Kottke, Ellwood, Eds. Philadelphia,
    Pa.:Saunders, 1971.

3. S.M. Michaelson, "The tri-service program-A tribute to George
    M. Knauf, USAF (MC)," IEEE Trans. Microwave Theory Tech.
    (Special Issue on Biological Effects of Microwaves), vol. MTT-19,
    pp. 131-146, Feb. 1971.

4. H.P. Schwan, "Interaction of microwave and radio frequency radi-
    ation with biological systems," IEEE Trans. Microwave Theory
    Tech. (Special Issue on Biological Effects of Microwaves),
    vol. MTT-19, pp. 146-152, Feb. 1971.

5. S.M. Michaelson, "Human exposure to nonionizing radiant energy-potential hazards and safety standards," Proc. IEEE, vol. 60, no. 4, pp. 389-421, Apr. 1972.

6. A.H. Frey, "Biological function as influenced by low-power modulated RF energy," IEEE Trans. Microwave Theory Tech., (Special Issue on Biological Effects of Microwaves), vol. MTT-19, pp. 153-164, Feb. 1971.

7. C.C. Johnson and A.W. Guy, "Nonionizing electromagnetic wave effects in biological materials and systems (Invited paper)," Proc. IEEE, vol. 60, no. 6, pp. 692-718, June 1972.

8. A.W. Guy and S.F. Korbel, "Dosimetry studies on a UHF cavity exposure chamber for rodents," IMPI Symp., Ottawa, Canada, May 1972.
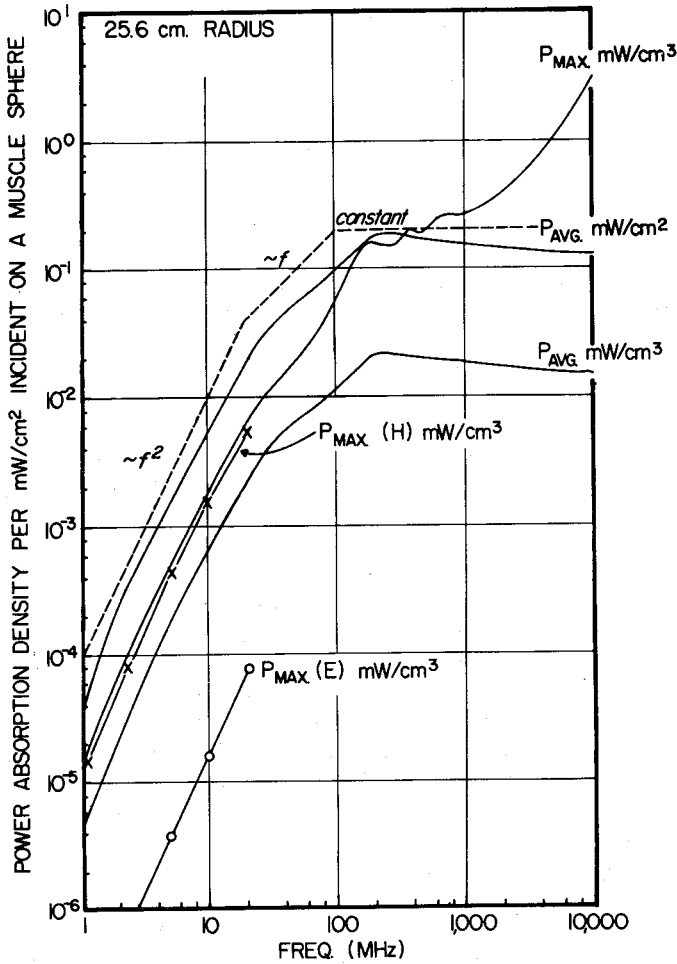
Fig. 1 Characteristics of power absorption density in a 25.6 cm radius spherical model of man exposed to plane wave radiation. Solid curves illustrate maximum and average value per unit volume and average value per unit area. Absorbed power density due to electric (E) and magnetic (H) field components in the HF frequency range are shown as separate curves. The dashed lines roughly illustrate frequency dependence of average absorbed power density.

ELECTROMAGNETIC DIRECTION FINDING EXPERIMENTS
FOR LOCATION OF TRAPPED MINERS

R. G. Olsen and A. J. Farstad
Westinghouse Electric Corporation
Georesearch Laboratory
8401 Baseline Road
Boulder, Colorado 80303

The Coal Mine Health and Safety Act of 1969, passed by Congress in the wake of the disaster at Farmington, West Virginia, led to an extensive study by the National Academy of Engineering of the problems involved in the coal mine safety[1].   One of the results of this report and subsequent research conducted by the U.S. Bureau of Mines has been the investigation of electromagnetic techniques for the location of trapped miners after a mine emergency.   The Westinghouse Georesearch Laboratory has been involved in both the theoretical and field studies relating to this problem [2].

A compact personal beacon transmitter has been developed which can be attached to and powered by a miner's lamp battery. A compatible lightweight loop antenna package has also been developed which can be easily carried on a miner's belt. This antenna can be quickly deployed on the mine tunnel floor. For the purpose of calculating its electromagnetic fields on the earth's surface, the loop can be considered to be a magnetic dipole buried in the earth. (The earth is assumed to be homogeneous and to have a conductivity of σ mhos/m.) The surface of the earth is assumed to be uniformly sloping and the transmitter dipole oriented as in Figure 1.   The fields on the earth's surface can be computed by using a superposition of the fields of a vertical magnetic dipole[3] and of a horizontal magnetic dipole[4] in proportions which depend on the slope of the terrain.

In the case of level terrain a null in the horizontal magnetic field occurs on the surface directly above the dipole[5]. This null is designated as the apparent source location and is the criteria by which the source is located. The criteria was tested at two hardrock mines and two coal mines in the fall of 1972. The apparent source locations were compared to actual locations determined by conventional surveying techniques. It was found that due to nonlevel terrain the apparent and actual source locations differed by up to 13 meters. This discrepancy can be

resolved by an examination of the fields of a source beneath uniformly sloping terrain.

Figure 2 shows the experimental and theoretical results for a case where the hill slope is 15° (H$_0$ is the horizontal field, and H$_z$ is the vertical field.) The null is displaced downhill by an amount which depends on the depth of the source, the ground conductivity and the hill slope.

These results can be used to improve the location technique. If the apparent source location is known along with the ground conductivity, hill slope, and approximate source depth, the theoretical null offset can be used to obtain the actual source location.

REFERENCES

1.   G. Meloy, G. V. Keller, et al (1969 Mine Rescue and Survival, Nat. Acad. Eng.)

2.   D. B. Large, L. Ball and A. J. Farstad (1973 IEEE Trans. Comm. Tech., vol. COM-21, No. 3, pp. 194-202).

3.   J. R. Wait (1971 Proc. IEEE, Vol. 59, No. 6, pp. 1033-1035).

4.   A. K. Sinha and P. K. Bhattacharya (1966 Radio Science, Vol. 1 (New Series), No. 3, pp. 379-395).

5.   J. R. Wait and L. L. Campbell (1953 Jour. Geophysics Res., Vol. 58, No. 2, pp. 167-178).
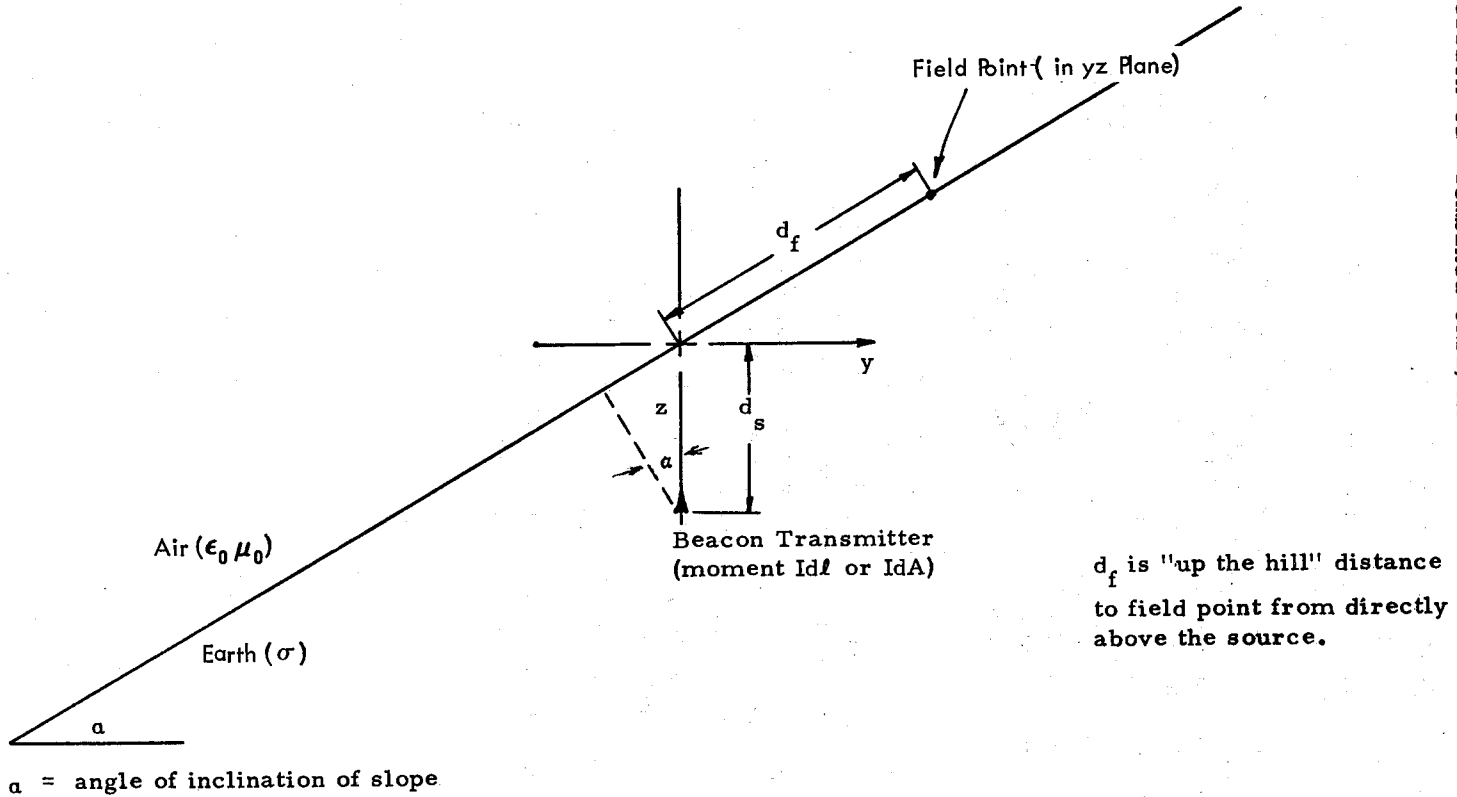
Figure 1   Dipole Located Beneath a Uniformly Sloping Interface and Coordinate System
in Which Fields are to be Referred
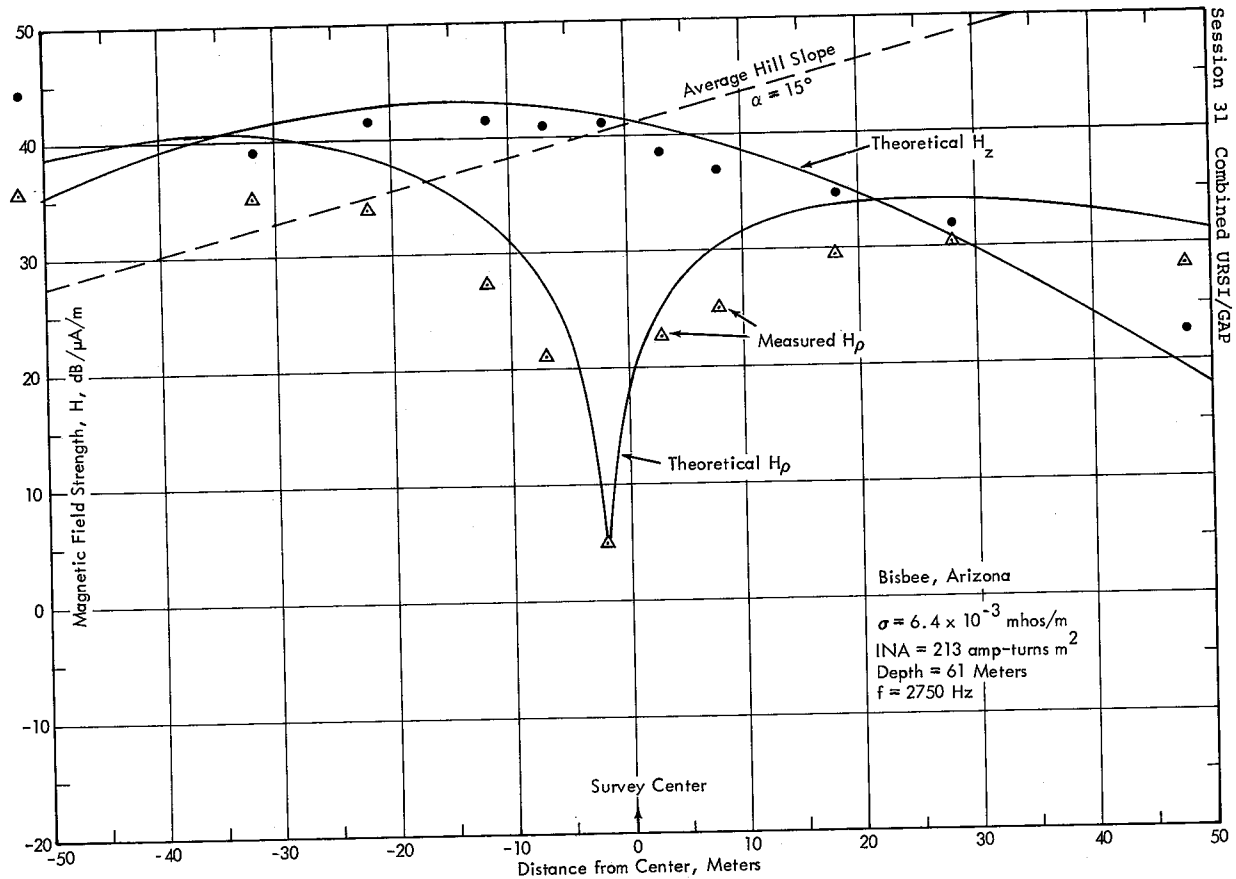
Figure 2   Electromagnetic Surface Pattern from Buried VMD
(Along Hill Slope)

BISTATIC MEASUREMENT OF METEOROLOGICAL AND PROPAGATION
PARAMETERS WITH A HIGH-RESOLUTION K_U-BAND SCATTER SYSTEM

U.H.W. LAMMERS
Air Force Cambridge Research Laboratories
Bedford, Massachusetts, U.S.A.

and

R.L. OLSEN
Communications Research Centre
Department of Communications
Ottawa, Ontario, Canada

Forward scatter in the troposphere has been used for more than two
decades as a means to communicate at meter and centimeter wave-
lengths over distances beyond the horizon. The increasing number
of space and terrestrial links operating at increasingly higher
frequencies has created a need to determine the probability of
interference as a function of separation between services. With
the improved resolution of narrow-beam antennas, bistatic systems
can also be used to investigate meteorological parameters of the
troposphere. By the use of synchronized antenna scanning at both
ends of the path, it is possible to study propagation mechanisms
and to examine tropospheric structure and motion with an angular
resolution previously not available[1,2]. In the experiment
described, measurements of transmission loss at 15.7 GHz have been
taken over a 500 km path and meteorological data obtained over a
surface area 200 km long and 100 km wide at the center of the path.

Figure 1 illustrates the computer-controlled motion of the common
volume of the antenna beams (center at P) during a great circle
plane raster scan (xz plane) and a midpath plane raster scan (yz
plane). Other types of scans are performed in addition to the
xz plane and yz plane rasters to analyze particular characteristics
of the troposphere, to measure cross-path wind speeds, and to
simulate long-distance interference situations.

A typical recording of a great circle plane raster is given in
Figure 2. It consists of 20 individual scans and lasts 10 minutes.
Several horizontally stratified layers are visible in the height
range between 8 and 13 km. Effectively no signals are received in
those portions of the scans which are below the radio horizons
(the dashed lines in Figure 2). Three-dimensional scanning of the
bistatic system with high spatial and doppler resolution permits
discrimination between turbulent scatter, hydrometeor scatter, and
ducting. Also the effect of antenna sidelobe coupling can be
determined.

Continuous recordings of cross-path wind speed, which are difficult
to obtain with conventional meteorological instrumentation, have
been obtained from upper levels of the troposphere over extended

periods of time. Figure 3 displays 48 hours of wind data taken
every 15 minutes during even hours. The radiosonde data are in
good agreement with the scatter data, considering the substantial
horizontal drift which radiosondes quite often exhibit.

A complete map of the midpath plane wind field, implicit in the
doppler shifts recorded, is shown in Figure 4. The cross-path wind
is unidirectional and leads to the typical y-dependent frequency
offsets (positive in one half, negative in the other half of the
display). The sharp wind shear zone at around 12 km height,
clearly visible in a number of scans, is of particular interest.

In Figure 5 cumulative distributions of the median transmission
loss that can be expected for a K_u-band scatter system operating
over a 500 km path are displayed. These results can be applied
to the situation of interference between space and terrestrial
systems sharing the same frequencies. More realistic conditions
have also been examined by transmitting part of the time with a
wide-beam antenna typical of those used in terrestrial systems.

References

1. R.L. Olsen and U.H.W. Lammers (1973 AGARD Conf. Proc. 127, p. 14-1).
2. U.H.W. Lammers and J.W.B. Day (1973 Radio Science 8, to be
published).
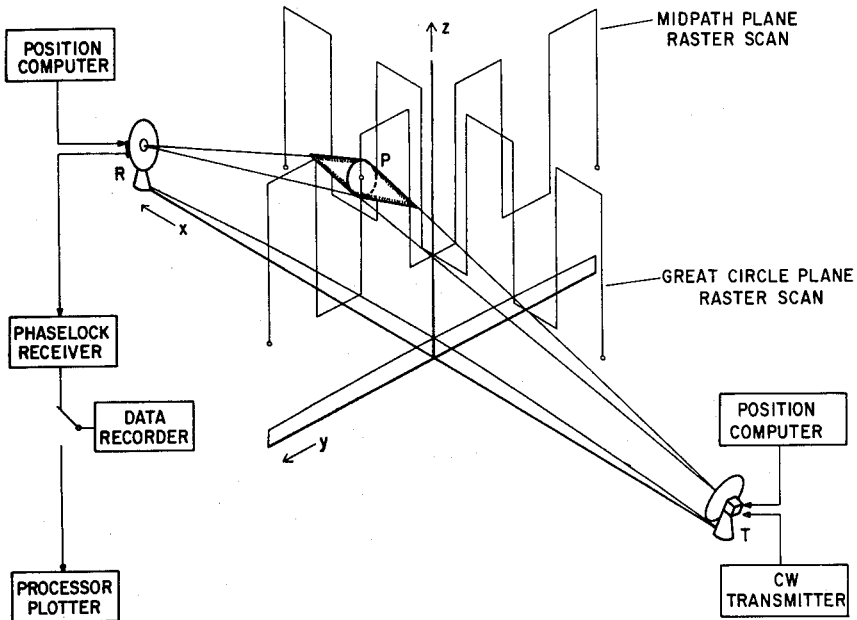
Fig. 1 Geometry and block diagram of scanning bistatic scatter
        system.
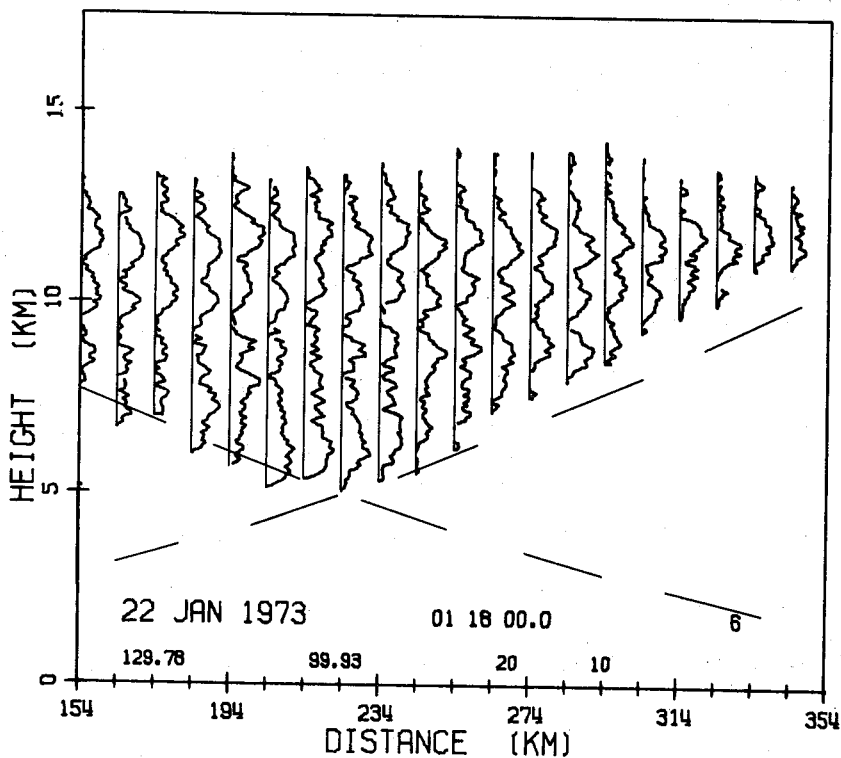
Fig. 2 Great circle plane raster scan; horizontal scale of
        received power is 30 dB between adjacent base lines.
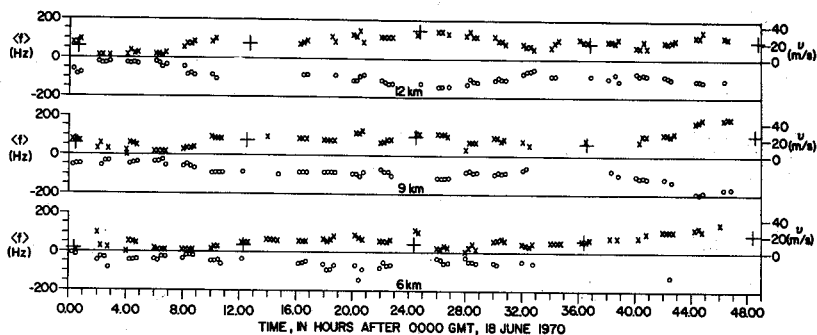
Fig. 3 Comparison of scatter and radiosonde measurements of cross
        path wind speed at three heights. Scatter measurements at
        10 km off path o upwind side, x downwind side, + radio-
        sonde measurements.
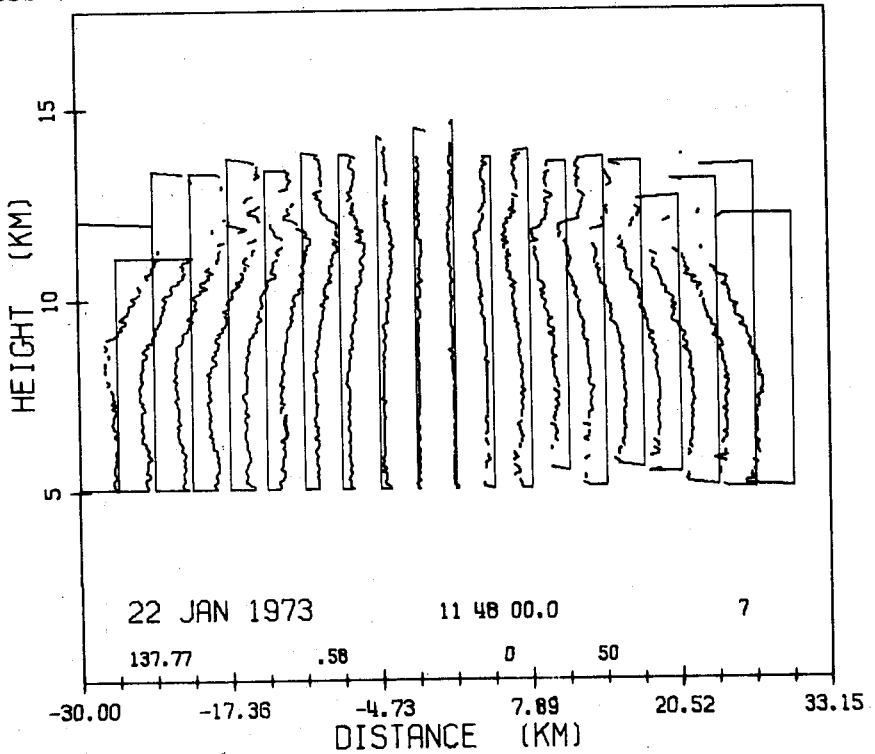
Fig. 4   Midpath plane raster scan; horizontal scale of doppler
shift of the received signal is 200 Hz between adjacent
base lines.
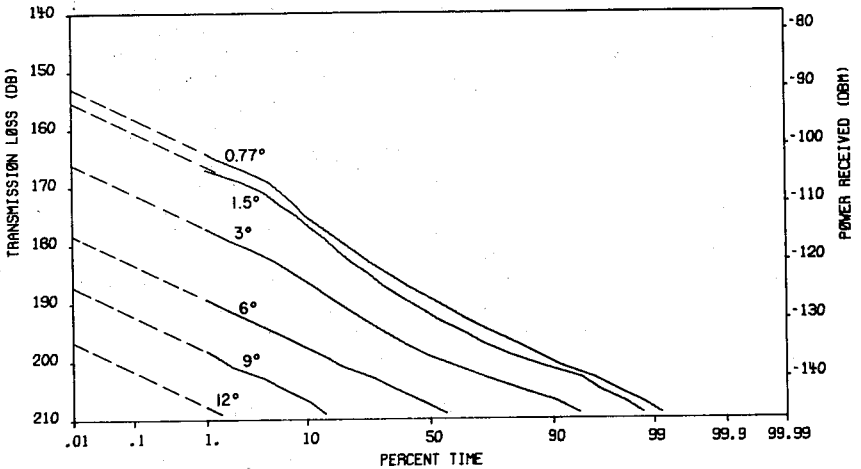
Fig. 5   Cumulative distributions of one-minute median transmission
loss at 15.7 GHz for a 500 km overland path. The effect
of receiving antenna elevation angle is shown for a period
from September 1972 to February 1973. Transmitter eleva-
tion angle is 0.33°; antenna gains are 60 dB.

Session 32 Foreign Electromagnetics

REVIEW OF CURRENT ELECTROMAGNETICS RESEARCH IN NEW ZEALAND

R.H.T. Bates, University of Canterbury, New Zealand.

In New Zealand most of the research associated with electro-
magnetic waves is concerned with the upper atmosphere.
This work is regularly reported to Commissions III, IV and
VIII of URSI, and a detailed account was given to the 17th
General Assembly. I am largely ignorant of the details of
these investigations and so I only list them briefly with
the most recent, pertinent, major publications. I accord the
same treatment to work on magneto-telluric observations and
to studies of the electronic properties of materials.

My main concern is with the type of electromagnetics research
which is of chief interest to engineers. Significant
contributions are being made in the electrical departments of
the country's two engineering schools.

Ionospheric Research The Physics and Engineering Laboratories
(PEL) of the Department of Scientific and Industrial Research
(DSIR) operate a number of experimental stations and conduct
work in several areas (1-3). They measure ionograms on a
routine basis and they carry out experimental studies of the
aurora, the F-Region and the vagaries of radio transmissions
from satellites. They make computer models of the ionosphere.
Studies of sporadic-E formation, jet currents and X-ray
particle precipitation are conducted at Otago University
(4,5). At Canterbury University the emphasis is on radar
studies of meteor trails, observational techniques for back-
scatter from the ionosphere and attempts at correlating
electron densities and drifts with stratospheric warming in
polar regions (6-9). At the Radio Research Centre of Auckland
University they are concerned with several aspects of the
ionosphere: electron content, effective slab thickness,
ionogram analysis and electron densities of irregularities
(10). They also investigate the Exosphere and make commun-
ication studies using rotation interferometers (11).

Magnetospheric Research Observations of VLF and MHF emissions,
and dispersion analyses to determine source regions, are
made at Otago University (12,13). Detailed experimental
studies, some in collaboration with the Radioscience Labor-
atory of Stanford University, are carried out by PEL on
Whistler emissions and VLF propagation (14).

Terrestrial Radio Noise DSIR are surveying man-made and
natural radio noise in Antarctica. The contribution to radio
noise by Whistler and VLF emissions is being studied jointly
by PEL and Otago University (15).

Magneto-Telluric Research At the Christchurch Geophysical
Observatory of DSIR, earth potentials are measured between

pairs of electrodes spaced N-S and E-W. Magnetic observations made nearby are combined with the measured potentials to deduce the profile of ground conductivity with depth, down to some hundreds of km (16).

Materials Research At the Victoria University of Wellington, studies are made of electronic properties of disordered materials, particularly metal alloys and amorphous semi-conductors. Measurements are made using several spectrometers covering the electromagnetic spectrum from the low infrared to the near ultraviolet (17,18).

Electrical Engineering Electromagnetics Research
Auckland University Research is being pursued in the following areas (19-29): electrically thick antennas, thin wire antennas, antennas and probes in waveguides, VHF propagation along High Tension transmission lines, radio propagation studies for fire detection in exotic pine forests.

The work on thick antennas is being handled from the stand-point of singular integral equation theory. Hollow cylinders and open-ended hyperboloids are now understood. The solid cylinder is presently being studied.

A new theory for thin wire antennas has been formulated, being one which synthesises key aspects from other current theories to produce a simple and direct solution.

A solution with rigorously established error bounds has been obtained for hollow cylindrical antennas in rectangular waveguides.

Extensive experimental work on the characteristics of a VHF surface wave on a stranded galvanised open wire transmission line is in progress. A novel modelling technique is being used to check the theoretical work. The effect of nearby objects on the VHF wave propagation is being investigated.

Optimum modes of radio propagation in exotic pine forests are being sought. Initial experimental work on the electrical characterisation of the trees has been carried out and a detailed mathematical model is being formulated.

Canterbury University A time domain antenna range, employing a TDR and subnanosecond pulses, is controlled by a hybrid computer. The interface apparatus associated with the comput-er is particularly convenient for interacting with experiments on-line. The pulse and frequency responses of antennas are displayed simultaneously (30). Models have been tested of antenna systems capable of faithful transmission of very wide bandwidth signals (31). The known theories of the input impedance of the infinite monopole have been checked exper-imentally (32). A method has been developed for inferring the radiation patterns of wide-beam aperture antennas from near

field measurements. The modal distribution in the mouth of a waveguide antenna has been estimated (33).

Computational algorithms have been deduced from Pauli wedge diffraction theory for the design of cuts in the perimeters of reflector antennas, for positioning nulls in radiation patterns (34). An accurate method for computing diffraction by arbitrarily deformed wedges has been developed (35) and new secondary diffraction coefficients for the geometrical theory of diffraction have been found (36).

A method of radiation pattern measurement, incorporating a reference radiated down the pattern range, has been demonstrated experimentally using acoustic antennas. Only the magnitude of the radiated field is measured, but its phase can be inferred because the method makes use of holographic principles. Imperfections, having relative amplitudes of less than 5%, in aperture distributions are found easily (37). By invoking certain function theoretic properties of Fourier transforms, which were originally proposed for use in astronomy (38), it has been shown how to identify certain small imperfections in aperture distributions when no reference is radiated and when one is given only the magnitude of the radiation pattern (39,40).

The null field method (41,42) has been perfected for computation of the characteristics of waveguides (43) and thick antennas (44). The latter complements Otto's work at Auckland. Point matching methods have been put into proper perspective by detailed computational comparisons of a number of techniques (45). Computationally convenient, specialised solutions for dielectric wedges have been found (46) and generalised computational approaches to azimuthal surface waves (47) and to diffraction (48) have been developed. A number of research areas in radio science have been reviewed recently (49).

References

1.R.S.Unwin,F.B.Knox(1971 Radio Science 6,p.1061)
2.W.L.Ecklund,R.S.Unwin(1971 Nature(Phys. Sci.)232,p.54)
3.G.A.M.King(1971 J.Atmos.Terr.Phys. 33,p.1223)
4.R.L.Closs(1971 Radio Science 6,p.339)
5.P.J.Edwards(1969 Proc.Astr.Soc.(Aust.) 1,p.290)
6.W.J.Baggaley(1972 Mon.Not.R.astr.Soc. 159,p.203)
7.W.J.Baggaley,D.W.Hughes(1972 Nature(Phys. Sci.)237,p.224)
8.G.J.Fraser,A.Kochanski(1970 Ann.Geophys. 26,p.675)
9.H.A.von Biel(1971 J. Geophys. Res. 76,p.8365)
10.J.E.Titheridge(1972 Planet. Space Sci. 20,p.353)
11.M.L.Heron(1972 J. Atmos. Terr. Phys. 34,p.139)
12.R.L. Dowden,G.McK.Allcock(1971 J.Atmos.Terr.Phys.33,p.1125)
13.R.J.Offen(1972 Planet. Space Sci. 20,p.135)
14.F.A.McNeill(1970 J. Geophys. Res. 75,p.4230)
15.G.McK.Allcock,J.C.Mountjoy(1970 J. Geophys. Res.75,p.2503)

16.P.J.Gill(1971 N.Z.J.Geol. Geophys. 14,p.547)
17.D.Beaglehole,E.Erlbach(1972 Phys. Rev. B 6,p.1209)
18.D.Beaglehole,M.Wihl(1972 J. Phys. F 2,p.43)
19.D.V.Otto(1967 Radio Science 2,p.1031)
20.D.V.Otto(1968 Radio Science 3,p.862)
21.D.V.Otto(1968 Radio Science 3,p.1050)
22.D.V.Otto(1969 Trans. IEEE AP-17,p.101)
23.D.V.Otto,J.H.Richmond(1969 Trans. IEEE AP-17,p.98)
24.D.V.Otto(1969 Trans. IEEE AP-17,p.234)
25.D.V.Otto(1971 Trans. IEEE AP-19,p.532)
26.H.P.Nguyen(1968 Electron. Lett. 4,p.354)
27.D.T.Nguyen(1968 Electron. Lett. 4,p.475)
28.D.T.Nguyen(1968 Can. J. Phys. 46,p.1311)
29.A.G.Williamson,D.V.Otto(1972 Electron. Lett. 8,p.545)
30.R.H.T.Bates,G.A.Burrell(1970 Proc. AICA-IFIP Conf.,
   .Presses Academiques Européenes, Brussels,p.554)
31.R.H.T.Bates,G.A.Burrell(1972 Trans. IEEE AP-20,p.684)
32.G.A.Burrell(1972 Proc. IREE Australia 33,p.393)
33.A.R.Jamieson,R.H.T.Bates(1973 Proc. IEE 120,p.183)
34.G.L.James,V.Kerdemelidis(1973 Trans. IEEE AP-21,p.19)
35.J.D.Hunter,R.H.T.Bates(1970 J. Engng. Math. 4,p.119)
36.J.D.Hunter,R.H.T.Bates(1972 Int. J. Electron.32,p.321)
37.P.J.Napier,R.H.T.Bates(1973 Proc. IEE 120,p.30)
38.R.H.T.Bates,P.J.Napier(1972 Mon.Not.R.astr.Soc.158,p.405)
39.R.H.T.Bates(1971 Int.J.Engng.Sci. 9,p.1107)
40.P.J.Napier,R.H.T.Bates(1971 Int.J.Engng.Sci. 9,p.1193)
41.R.H.T.Bates(1968 Proc. IEE 115,p.1443)
42.R.H.T.Bates(1969 Trans. IEEE MTT-17,p.294)
43.F.L.Ng,R.H.T.Bates(1972 Trans. IEEE MTT-20,p.658)
44.R.H.T.Bates,C.T.Wong(1973 Appl.Sci.Res.21, in press)
45.R.H.T.Bates,F.L.Ng(1973 Int.J.Num.Methods Engng. 6,p.155)
46.R.H.T.Bates(1973 Int. J. Electron. 34,p.81)
47.R.H.T.Bates,F.L.Ng(1971 Alta Frequenza 40,p.658)
48.R.H.T.Bates,F.L.Ng(1972 Proc. IEE 119,p.1568)
49.R.H.T.Bates et al(1972 Canterbury Engng. J.(3)p.2)

CURRENT ELECTROMAGNETIC RESEARCH IN DENMARK

P.L. Christiansen
Laboratory of Applied Mathematical Physics
Technical University of Denmark
Lyngby, Denmark

Eight research projects have been selected to give an impression of current electromagnetic research in Denmark. This activity owes a great deal to the Laboratory of Electromagnetic Theory founded in 1954 by Professor Lottrup Knudsen at the Technical University of Denmark. Thus a majority of the following authors outside this place has earlier been affiliated with the laboratory.

> Studies in hereditary electromagnetism. P.W. Karlsson, Physics Laboratory II, Technical University of Denmark, Lyngby, Denmark.

The problem considered consists in establishing boundary conditions for the field vectors as well as conditions upon quantities appearing in the constitutive equations, such that the electromagnetic field (1) is uniquely determined, and (2) has a finite velocity of propagation. A theorem of this kind was proved by Rubinowicz in 1926 for constant material parameters. As a generalization, we have considered constitutive equations involving hereditary terms, i.e., integrals, with material-describing kernels, of independent field variables over the past at the position in question, or over the "past" hypercone in four-dimensional space-time; the materials may be non-linear, anisotropic, inhomogeneous and non-stationary. For this case, conditions implying (1) as well as (2) have been found.

> Wave propagation in stratified, moving media. S. Berntsen and G. Johannsen, Electrical Department, Danish Engineering Academy, Aalborg, Denmark.

In recent years numerous authors have examined wave propagation in stratified media of different structure. Wong and Cheng (1) thus calculated the scattered fields from a circular cylinder coated with an inhomogeneous plasma by means of a stratification technique using 4×4 transmission matrices in order to avoid large numbers of simultaneous equations. Kong (2) treated a plane n-layer structure, in which the layers are in relative motion, in a similar manner.

The present work is a general investigation of the 4×4 matrix method, which seems only applicable in rectangular and circular structures. If the layers are moving with different velocities no common rest frame obviously exists, but a Lorentz-invariant formulation can easily be obtained. A suitable choice of inertial frame for each layer turns out to facilitate the computation. The formalism will also be applied to wave guides.

1. W.C. Wong and D.K. Cheng (1968 Proc. IEE 115, p. 1446).
2. J.A. Kong (1971 Can. J. Phys. 49, p. 2785).

Propagation in an evaporation duct. H. Bach, Laboratory
of Electromagnetic Theory, Technical University of Denmark,
Lyngby, Denmark.

The propagation in an atmospheric superrefractive layer above
the sea is investigated. Here an evaporation duct, in which the
refractive index first decreases with height and later increases
again, is known to exist. A smooth profile is modelled by means
of two parabolic segments and a semi-infinite line with a slope
corresponding to standard atmospheric conditions.

The eigenvalues of the corresponding mathematical problem is
determined by numerical means, and curves for attenuation fac-
tors and height-gain functions are computed. The results show
good agreement with results obtained by means of the phase in-
tegral method.

The technique has been used in connection with propagation in
an evaporation duct above a rough sea surface. It turns out
that the attenuation due to leakage and due to scattering losses
is of the same order of magnitude in practical cases.

Future work on bringing the computer programs into a form which
is suitable for radar forecasting is planned.

A comparative study of diffraction processes in geometrical
diffraction theory. P.L. Christiansen, Laboratory of
Applied Mathematical Physics, Technical University of
Denmark, Lyngby, Denmark.

The literature shows an increasing number of time-harmonic solu-
tions to scattering problems concerning halfplanes and wedges
with various boundary conditions at the bounding halfplanes.
From the far field expansion of these solutions diffraction
coefficients describing the diffraction process at the edge of
the scatterer can be extracted and used in the geometrical dif-
fraction theory.

In the present work the scalar diffraction process at a wedge
with two different surface impedances is analysed. When the
wedge reduces to a halfplane with the same surface impedance on
both sides the description of the diffraction process can be
generalized to the plasma case where two modes of propagation
exist outside the halfplane. The diffraction coefficient then
describes the process by which an incident ray produces a dif-
fracted ray of the same mode as the incident ray. The diffraction
process by which the mode is converted can also be handled by
these considerations.

The possibility of a prediction of the (unknown) diffraction
coefficients for a wedge in a plasma is discussed.

Numerical determination of radiation patterns for wire
antennas on conducting bodies. N.C. Albertsen, J.E. Hansen,
and N.E. Jensen, Laboratory of Electromagnetic Theory,
Technical University of Denmark, Lyngby, Denmark.

In contract with the European Space Research Organization, a
theoretical formulation has been developed for the determination
of radiation patterns of thin wire antennas on conducting bodies.
Using this formulation a computer program has been constructed
with the purpose of analysing the radiation from monopole antennas
on a small scientific satellite body of cylindrical shape on which
a number of straight, passive antennas may also be attached.

The method uses a combination of two integral equations for the
unknown current distributions. An integral equation for the
electric field is applied for the passive and driven wire antennas.
For the satellite body itself, a magnetic field integral is used.
This procedure exploits the individual properties of electric and
magnetic field integral equations. The complete electromagnetic
problem is in this way formulated in terms of simultaneous integral
equations which are solved numerically by the method of moments.

A number of test runs for monopoles on cylinders has been made.
The results agree well with radiation patterns obtained experi-
mentally in the Anechoic Chamber at the Technical University.

Theoretical investigation of a double grid reflector antenna
system for satellite communication*. J. Jacobsen and
O. Sønder, Terma Elektronisk Industri A/S, Aarhus, Denmark.

A new type of reflector antenna with polarization cleaning pro-
perties has been investigated. This antenna is particularly in-
tended for transmission of two signals with orthogonal polariza-
tions within the same antenna beam (dual polarization mode trans-
mission). For this application a high degree of polarization
purity is required.

The double grid reflector consists of two orthogonal sets of thin,
parallel metallic plates. The edges of the two sets of plates lie
on two slightly displaced paraboloidal surfaces with parallel focal
axes. Each surface is illuminated by a feed horn located at the
focal point for the surface and linearly polarized parallel to the
plates. Thus each horn is focused with respect to the correspond-
ing grid surface but defocused with respect to the other, such
that the unwanted cross-polarized field does not radiate in the
direction of the focal axes of the system.

The analysis was carried out by means of a modified version of the
physical optics method. This version uses the scattering matrix
for an infinite plane model of the double grid structure.

The polarization cleaning effect has been computed. A reduction
of the cross-polarized field from -32 dB (solid reflector) to -53
dB (double grid reflector) below the maximum of the principal
field was found. An experimental verification has been planned.

Riometer measurements in the polar region. P. Stauning,
Ionosphere Laboratory, Danish Meteorological Institute,
Lyngby, Denmark.

Since the International Geophysical Year (1957/58) the riometer
(Relative Ionospheric Opacity - meter) measurements of cosmic
noise absorption have been a valuable tool for investigations of
geophysical disturbances causing absorption of HF-radio waves in
the ionosphere.

Presently the Ionlab riometer project comprises a set-up of 14
riometers at various observatories in Greenland, at Faroe Islands
and at Spitsbergen. The riometer net is primarily intended to
provide data for studies of the relations of absorption events
in the auroral and polar regions to the energetic particle radi-
ation produced during solar flare events and during magneto-
spheric substorms. The data are also used for investigation of
problems related to the HF-radio communication in Greenland.

In the time up to the International Year of Magnetospheric Studies
(1975/76) the number of Ionlab riometer observatories will be
further increased to enable a detailed analysis of the temporal
and geographical development of polar absorption events. When
combined with satellite particle data, such a riometer set-up may
prove a unique tool for investigations of the complicated struc-
ture of the geomagnetic field extending from the polar cap into
the outer magnetosphere and tail regions.

Radio echo sounding of polar ice*. P. Gudmandsen, Laboratory
of Electromagnetic Theory, Technical University of Denmark,
Lyngby, Denmark.

Radio echo sounding of the inland ice in Greenland is carried out.
The program comprises development of suitable apparatus and meas-
uring techniques as well as surveying the inland ice.

At present two pulse radars at 60 MHz and 300 MHz installed in a
C-130 Hercules aircraft are used for the sounding. The echo
records are continuous films of intensity modulated oscilloscopes.

For the interpretation of the records studies are made of the re-
fractive properties of the layered medium of polar ice with densit
variations and surface ondulations. Also the total two-way absorp
tion of the inland ice has been calculated based on a theoretical
model of the temperature profile of the ice.

Extensive scattering of the radio waves occurs in some areas of
Greenland for unknown reasons and makes the sounding very diffi-
cult. Remarkable stratifications are observed on the records for
the greater part of Greenland. The origin of the layer echoes is
still unknown but play an important role in glaciological studies
of the flow of the ice.

The current development concerns the introduction of new technique
to overcome propagation problems in Greenland and Antarctica.

Review of current electromagnetics research in Canada

R.A. Hurd

The review covers electromagnetic research
in Canada from January 1972 to the present. Owing to
the large amount of work done, the subjects considered
are limited to antennas, waveguides and scattering,
for the most part. Current methods of analysis are
also discussed.

REVIEW OF CURRENT ELECTROMAGNETICS RESEARCH
IN JAPAN

S. Adachi

Department of Electrical Engineering
Tohoku University, Sendai, Japan

Electromagnetics researches which have been carried out in
Japan in these several years, particularly in very recent years
are reviewed.   The related fields are propagation, diffraction,
scattering of electromagnetic waves, and radiation from antennas.
Instead of making the all-around review, an emphasis will be
placed on high lights in research fields such as:

    Propagation in random or non-linear media
                    Multiple-scattering
                    Laser beam propagation

    Diffraction and scattering
                    Analyses based on various methods aided
                    by electronic computers
                    Resonance, diffraction, reflection, scattering
                    of beam waves
                    Remote sensing

    Electromagnetic fields in moving media

    Antennas
                    Analysis of linear-antenna arrays
                    Synthesis theories of various arrays
                    Beam shaping of aperture antennas
                    Antennas in plasmas

Session 32 Foreign Electromagnetics

REVIEW OF CURRENT ELECTROMAGNETIC RESEARCH IN GERMANY

by H.-G.Unger, Technische Universität Braunschweig, Germany

Antenna research in Germany has resulted in extremely short
helical antennas with guiding discs to maintain circular
polarization over wide bands and beam widths. The near field
patterns of various antennas are studied experimentally and
theoretically with the theory leading to a geometrical
representation of power flow and effective area in the
receiving mode. Mutual coupling effects in arrays have been
calculated and measured and a theory for decoupling and
matching networks developed.

For solving field problems in waveguide and resonator circuits
a mode matching method and a method using a "Zwischen"medium
was developed and the former applied to quasioptical directional
couplers in oversized rectangular waveguide. The analysis of
tapered waveguide transitions in natural coordinates has been
improved and cut-off as well as multi-mode horns are investi-
gated with horn-mode expansions. For the circular electric
(H_{01}) mode in round waveguide with dielectric lining taking
into account the low loss character of the E_{11}-mode has led
to extremely low curvature loss for the H_{01}-mode.

For optical fibres and integrated optics applications fields
and waves in graded index slab and round waveguides as well as
rectangular dielectric waveguides are analyzed and wave disper-
sion characteristics calculated. Different mathematical models
allow to study wave propagation through randomly curved monomode
or multimode round fibres with homogeneous or graded index cores
in considerable detail. Excitation of such fibres with coherent
as well as incoherent light in the multimode case is measured
and calculated. For Multimode and graded index fibres pulse
dispersion is studied experimentally.

Topics of electromagnetic research in Austria
E.Ledinegg, Graz

§ 1. Introduction

Electromagnetic research in Austria is closely connected with
the Universities and Technical Universities in Wien, Graz and
Innsbruck, respectively. Although there are numerous problems under
investigation, only a relatively small part is concerned with
signal engineering, antenna theory and wave propagation. Informa-
tion on research in power engineering (developments and theoretical
contributions in electromotor and generator manufacture), which is
of great importance for our country, will not be given in this paper.
Firstly, because these activites are not of special interest to
the AP-Symposium and in the second place, I feel not competent to
give this information.

Although the microscopic behaviour of the electromagnetic field
and its interaction with electrons does not belong to the actual
subject of this report, I may briefly refer to the research in
quantum electrodynamics done in Graz and Wien. In particular, I
mention the activities of the Institute of Theoretical Physics of
the University of Graz which holds a leading position in our
country in the field of quantum physics. At present main topics of
research in this institute are non linear effects in electrodynamics
and investigations in mega Gauß physics /1/,/2/,/3/,/4/. Recently,
coherence problems - up to a technical application of the induced
emission only in optics of interest - have been treated thoroughly
in electrodynamics too. Based on correlation functions of higher
order introduced by R.Glauber /5/ in quantum electrodynamics, several
investigations have been carried out at the Institute of Theoretical
Physics of the Technical University of Graz. Field conditions be-
longing to a coherence of degree n have been investigated and the
disturbance of coherence caused by interaction of an electromagnetic
field with charged particles was evaluated /6/,/7/,/8/.

Finally, I want to mention the investigations in magnetohydrodynamics carried out mainly at the Institute of Physics of the University of Innsbruck. They published several papers which are of interest also from the viewpoint of classical electrodynamics /9/,/10/.

Problems of wave propagation and antenna theory are investigated mainly in Graz (Technical University) and Innsbruck. These activities are co·ered in what follows.

§ 2. Wave propagation

This paragraph gives some information on activities concerning in turn free propagation, partially guided propagation and propagation in wave guides. Since the basic investigations by G.Goubau and F.Schwering on beam waveguides /11/, a great number of theoretical and experimental contributions have been published on iteration of wave packets by periodical phase corrections. G.Goubau considered a representation of the electromagnetic field in the half space by superposition of TM and TE waves which is abstractly formulated with no reference to a source distribution. B.Schnizer /12/ showed that Goubau's representation is equivalent to a boundary value representation of the electromagnetic field in the half space Eq.(1) derived by the author /13/:

$$\vec{E} = -\int_F \overleftrightarrow{L}_{P_A} \frac{\partial \Psi}{\partial z_Q} \vec{E}_o \, df \tag{1}$$

with

$$\left(\overleftrightarrow{L}_{P_A}\right)_{i,\kappa} = \frac{1}{k^2} \nabla_i \nabla_\kappa + \delta_{i,\kappa} \quad , \qquad \Psi = -2 \, \psi_{(+)} \tag{1a}$$

$$\psi_{(+)} = r_+^{-1} \cdot \exp\left(-ikr_+\right)$$

where

$$r_+^2 = (x - x_Q)^2 + (y - y_Q)^2 + (z + z_Q)^2$$

$$2\vec{E}_o = \vec{E}_{+,o} - \vec{E}_{-,o} \tag{1b}$$

can be realized by a surface distribution of electric and magnetic dipoles.

Another problem in wave propagation where the field should be related analytically to the source is concerning the single wire line (Harms - Goubau -waveguide) developed by G.Goubau, 1950. There, Sommerfeld's surface wave on a cylindrical wire is considered as power carrier. The surface wave is excited by a horn /14/ which operates as a type-converter between a concentric feeder and the G-line. In several papers by W.Papousek, W.Jank and the author, the properties of transmission and conversion by the horn have been described analytically. Introducing appropriate horn parameters, conversion ratios of any size could be obtained /15/,/16/,/17/,/18/. A characteristic quantity is the type-conversion coefficient

$$
\left(\eta\, \eta^{x} \right)_{Abs} = \int_{0}^{\pi/2} \eta\, \eta^{x}(\vartheta)\, \frac{d\vartheta}{\sin^{2}\vartheta}\; \frac{\left| H_{\varphi}^{(A)}(a_{o}) \right|^{2}}{\int_{a_{o}}^{\infty} H_{\varphi}^{(A)} H_{\varphi}^{(A)\,x}\, \varrho'\, d\varrho'} \tag{2}
$$

where

$$
\eta\, \eta^{x}(\vartheta) = \frac{H_{\varphi}^{(s)}\, H_{\varphi}^{(s)\,x}}{H_{\varphi}^{(A)}\, H_{\varphi}^{(A)\,x}} \tag{2a}
$$

$H_{\varphi}^{(s)}$ = H_φ -component of the radiation field

$H_{\varphi}^{(A)}$ = H_φ -component of the surface wave at the aperture

$H_{\varphi}^{(s)}$ and $H_{\varphi}^{(A)}$ follow from an integral equation which was evaluated by Schwinger's principle.

Quite recently, problems of VLF-propagation between earth and ionosphere have acquired some interest. E.g., some authors investigated mode conversion phenomena considering simplified models for the earth-ionosphere waveguide. In this connexion I may refer to a paper by F.Reder and the author /19/ concerning mode conversion at the terminal, whereby the direction of the incident wave was assumed to form an arbitrary angle with the terminal. Earth and ionosphere were considered as ideal electric and magnetic conductors, respectively. If one considers a TE-mode

$$
\vec{E} = -i\omega \left(\nabla \times \vec{Ve_{3}} \right)
$$

then one obtains from the representations of the transmitted and
scattered field:

(transmitted wave)
$$V^{(1)} = \sum_{\nu=0}^{\infty} R_\nu(z) \int_0^\pi h_\nu(\beta) e^{i \varkappa_\nu^{(1)}(x \sin\beta + y \cos\beta)} d\beta$$

(reflected wave)
$$V^{(2)} = \sum_{\nu=0}^{\infty} Q_\nu(z) \int_0^\pi g_\nu(\beta) e^{-i \varkappa_\nu^{(2)}(x \sin\beta + y \cos\beta)} d\beta$$

(3)

and the conditions of continuity a system of two integral equations
which was solved by iteration. R_ν and Q_ν mean the modes in day
and night region, respectively. One obtains a mode-splitting for
order as well as for direction.

Using realistic models of the earth-ionosphere waveguide, one
gets to a complicated three layer problem which is even more in-
volved if one takes into account the geomagnetic field. For an
analytical treatment of wave propagation in an anisotropic model -
- where the source is a vertical electric dipole located between
earth and ionosphere - one can apply the method of reflection
matrix (J.R.Wait) /20/ as well as the method of Arbel and Felsen
/21/. Apart from approximations, the evaluation of the occurring
integral representations in principle yields contributions from
branch cuts, and the residue series represent non-orthogonal
modes. For this reason, B.Schnizer and the author tried to apply
a conductivity approximation concept for the anisotropic ionosphere
which has been introduced by Monteath and J.R.Wait (see also
Wait and Spies /22/). From the rigorous Arbel-Felsen integral
representations for the two layer problem earth - anisotropic
ionosphere, an evaluation with the saddle point method yields a
tensor relation between the tangential field of $\vec{H}$ and $\vec{E}$ along the
ionospheric boundary:
$$\vec{H}_{tg} = \overleftrightarrow{\sigma} \, \vec{E}_{tg}$$

(4)

with
$$\overleftrightarrow{\sigma} = \begin{pmatrix} \sigma_{11} & \sigma_{12} \\ -\sigma_{12} & \sigma_{22} \end{pmatrix} , \quad \sigma_{11} = \sigma_{22}$$

(4a)

218

The elements σ_{ik} of the derived surface tensor are functions of the characteristic parameters of the anisotropic ionosphere (plasma frequency, collision frequency and gyromagnetic frequency). By reducing the three layer problem to a boundary value problem also mixed-path problems can be treated in a relatively simple manner./23/.

§ 3. Antenna theory

  Research in this field is done mainly at our Institute (Institute of Theoretical Physics of the Technical University of Graz). We investigated spatial extended antennas with and without ground reaction as well as antenna arrays. Besides investigations on cylindrical antennas and their ground reaction /24/, W.Timischl /25/,/26/ could extend the theory of active and passive torus antennas with reference to the work of E.Hallén, I.E.Storrer and T.T.Wu. In particular, he evaluated the current density distribution on the antenna up to terms of order $(a/s)^2$, (a = radius of the cross-section, 2s = length of the antenna). From the field representation by a vector potential

$$\epsilon \vec{E} = \kappa^2 \vec{A} + \text{grad div } \vec{A} \tag{5}$$

with

$$\vec{A} = \frac{1}{4\pi\epsilon} \int_V \vec{L} \frac{e^{-i\kappa r}}{r} d\vec{x}_Q$$

one obtains two integro-differential equations which could be transformed into Fredholm integralequations. This result was received by introducing torus coordinates and considering the tangential field of $\vec{E}$ and its surface condition

$$\vec{E}_t^{(A)} + \vec{E}_t^{(i)} = 0 \tag{6}$$

with

  $E_t^{(A)}$ = applied electric tangential field

  $E_t^{(i)}$ = induced electric tangential field

With torus antennas, loop antenna systems can be constructed which

sometimes show marked directional properties. Loop antenna arrays
up to a number of 100 loops have been investigated by W.Papousek
and the author /27/,/28/,/29/ taking into account also the ground
reaction in the frame of a conductivity approximation concept. We
computed radiation patterns with the help of a second-order saddle
point approximation as well as by rigorous integration /30/ (only
possible for horizontal characteristics). Occurring contributions
from branch cuts equally could be evaluated by a saddle point
approximation. The consideration of such antenna arrays has been
suggested by H.Brueckmann /27/. He expected that the poor ra-
diation power of a loop (compared to an electric dipole antenna)
might be compensated by its low ground losses and by using arrays
of large numbers of loops.

Finally, the validity of the surface impedance concept in
connection with the ground reaction was investigated in a paper
by W.Papousek and W.Ninaus /31/. They considered an electric dipole
above earth and calculated the ratio $H_\psi /E_\varphi = \sigma$ along the surface
of the earth in its dependence on frequency and ground conductivity
by numerical evaluation of the Sommerfeld integrals.

Apart from Graz, investigations in the VLF-region are also carried
out in Innsbruck (Electronics Laboratory of the Institute of Physics
of the University). The main interest is directed to wave propagation
below the surface of the earth and to developments of ground-buried
antennas showing high effective radiation resistances. The head
of this research group, N.Nessler, published several papers from
which some of them are listed in the references /32/,/33/,/34/,/35/.

Session 32 Foreign Electromagnetics

References

/1/ P.Urban, K.Wittman: Photonabsorption eines Elektrons
     in hohen homogenen Magnetfeldern, Act.Phys.Austr.,
     35, 9 (1972).

/2/ H.G.Latal: Megagaußphysik, Act.Phys.Austr., 34, 65 (1971).

/3/ T.Erber, H.G.Latal, P.Urban: Fourieranalyse von Fluß-
     kompressionsfeldern, Act.Phys.Austr., 34, 337 (1971).

/4/ T.Erber, H.G.Latal, J.E.Kennedy, S.M.Prastein: Analysis
     of flux compression experiments I,II,III, Act.Phys.Austr.,
     36, 171, 257 (1972).

/5/ R.J.Glauber, The quantum theory of optical coherence,
     Phys.Rev., 130, 6 (1963).

/6/ E.Ledinegg: Klassische und Quantentheorie kohärenter
     und nichtkohärenter elektromagnetischer Felder,
     Act.Phys.Austr., 20, 1-4 (1965).

/7/ E.Ledinegg: Zur Kohärenz n-ter Ordnung in der
     Quantenelektrodynamik, Z.f.Physik, 191 (1966).

/8/ W.Bulla: Kohärenzstörung durch Wechselwirkung mit
     wasserstoffähnlichen Atomen, Act.Phys.Austr., 36,
     368 (1972).

/9/ E.J.Powers, D.E.Smith: An experimental study of drift
     wave turbulence using digital spectral analysis
     techniques, Int.Congress Waves and Instabilities in
     Plasmas, Innsbruck, April 1973, Univ.Innsbruck.

/10/ S.P.Mishra, K.P.Singh, P.K.Shukla, K.D.Misra: Generation of
     plasma waves and their conversion into electromagnetic wave
     by various natural plasma sources, Congress Waves and In-
     stabilities in Plasmas, April 1973, Innsbruck.

/11/ G.Goubau, F.Schwering: I.R.E. Transactions on Antennas
     and Propgation, AP-9, 1961.

/12/ B.Schnizer: Zur Äquivalenz der Bessel-Fourierdarstellung
     mit dem Randfeldfunktional des elektromagnetischen
     Feldes des Halbraumes, Act.Phys.Austr., 22, 1-4 (1966).

/13/ E.Ledinegg: Zur Darstellung des elektromagnetischen
     Feldes im Halbraum, Z.f.ang.Phys., 17, 4 (1964).

/14/ G.Goubau: Surface waves and their application to trans-
     mission lines, J.appl.Phys., 21, (1950).

/15/ E.Ledinegg: Theoretical studies on TAHA-antennas and
     surface wave launchers, Final Technical Report, European
     Research Office, London, 1961.

Session 32 Foreign Electromagnetics

/16/ E.Ledinegg, W.Papousek: Anregung der Goubauschen
      Eindrahtleitung durch ein Stufenhorn, Arch.elektr.
      Übertr., 24, 2 (1970).

/17/ E.Ledinegg: Die Stufenhornanregung der Eindrahtleitung
      als Transformationsvierpol, A.E.Ü., 24, 5 (1970).

/18/ G.Jank: Zur Theorie der Umwandlung Lecherwelle - Ober-
      flächenwelle durch ein n-Stufenhorn, Act.Phys.Austr., 31,
      (1970).

/19/ E.Ledinegg, F.Reder, Dependence of mode conversion at
      terminator on its angle with direction of wave propa-
      gation. Flat-earth model with infinite wall conductivities,
      Act.Phys.Austr., 32, (1970).

/20/ J.R.Wait: Electromagnetic waves in stratified media,
      Perg.Press, Oxford 1962.

/21/ E.Arbel, L.B.Felsen: Theory of radiation from sources
      in anisotropic media, Part I, Vol.6, Perg.Press (1963).

/22/ J.R.Wait, K.P.Spies: Characteristics of the earth-ionosphere
      waveguide for VLF-radio waves, NBS, Techn.Note 300,(1964).

/23/ E.Ledinegg, B.Schnizer: An equivalent surface conductivity
      tensor for the boundary between atmosphere and the
      anisotropic ionosphere, AEÜ, (1973), (in press).

/24/ E.Ledinegg, F.Reder: Current distribution on a horizontal
      cylindrical antenna with rigorous allowance for ground
      reaction, Act.Phys.Austr., 27, (1968).

/25/ W.Timischl: Über die Bestimmung der auf einer Zylinder-
      antenne durch ein elektrisches Feld induzierten Strom-
      verteilung, Act.Phys.Austr., 34 (1971).

/26/ W.Timischl: Näherungsweise Berechnung der Stromverteilung
      auf torusartigen Antennen mit kleinem Drahtquerschnitt,
      AEÜ, 26 (1972).

/27/ E.Ledinegg: Low-Frequency Loop Antenna Arrays, Final Technical
      Report, European Res.Office, London, (1969).

/28/ E.Ledinegg, W.Papousek, H.L.Brueckmann: Low-Frequency
      Loop Antenna Arrays: Ground reaction and mutual
      interaction, IEEE Trans.on Ant.and Prop., Vol.AP-21,1,
      (1973).

/29/ E.Ledinegg, W.Papousek, W.Ninaus: Low-frequency loop
      antenna arrays: Radiation field of systems of horizontally
      and vertically oriented loops, AEÜ (in press).

/30/ W.Papousek: Über strenge Lösungen von Sommerfeld-Integralen
      bei Dipolantennen, Act.Phys.Austr., 30 (1969).

Session 32 Foreign Electromagnetics

/31/ W.Papousek, W.Ninaus: Zur Formulierung von Problemen
     elektromagnetischer Wellenausbreitung über die Erde mit
     Hilfe eines konstanten Oberflächenwiderstandes,
     Act.Phys.Austr., 33, (1971).

/32/ W.Bitterlich: Magnetische Dipolantennen für Feldstärke-
     messungen im LF- und VLF-Bereich. Internat. Elektr.
     Rundsch. Berlin, Vol.21, No.9 (1967).

/33/ N.Nessler: Die Ausbreitung langer elektromagnetischer
     Wellen durch homogene und inhomogene feste Medien,
     Thesis, Innsbruck University (1967).

/34/ N.Nessler, W.Bitterlich: Überlegungen zur Eichung einer
     Ferritstabantenne für Meßzwecke. Intern. El.Rundsch.,
     Berlin, Vol.25 (1971).

/35/ N.Nessler, W.Bitterlich: Die Messung der Leitfähigkeit
     und der Dielektrizitätskonstanten eines schwach leit-
     fähigen homogenen Mediums mittels Wellenausbreitung,
     Act.Phys.Austr., 29, (1969).

        Additional pertinent papers in the field of applied

        electrodynamics not reviewed in the survey:

/36/ B.Schnizer: General properties of fields and beam
     dynamics in a linac gap, CERN 69-3, March 1969,
     Genevy.

/37/   G.Schiffner: A scanning spherical mirror interferometer
     for the analysis of CO_2 laser radiation, Appl.Opt., Vol.9,
     (1970).

/38/ McElroy J.H., Schiffner G.; Reynolds R.S.: Temperature-
     dependent etalon effects in laser systems, Appl.Opt.,
     Vol.10 (1971).

/39/ G.Schiffner, W.Hansi: Prediction of CO_2 laser signatures.
     IEEE J.ofQuantum Electronics, 1973

RADIATION CHARACTERISTICS OF THE
RING-LOADED CORRUGATED CONICAL HORN

- BROADBANDING OF THE
CORRUGATED HORN -

Fumio TAKEDA and Tsutomu HASHIMOTO
Mitsubishi Electric Corporation
Kamimachiya, Kamakura-City, Japan 247

The corrugated horn is very useful as a primary radiator in antennas for satellite-communication earth stations and radio telescopes, because it has a rotationally symmetrical main beam and low sidelobes. But the useful frequency bandwidth, in which the corrugated horn is effective for the improvement of antenna properties, is limited by frequency characteristics of the aperture field and VSWR at the transformer between the horn and connecting waveguide. In the conventional corrugated horn, the useful bandwidth is restricted to about one octave[1]. For the improvement of a transformer between corrugated and homogeneous waveguides, the ring-loaded corrugated waveguide (shown in Fig. 1)[2] was devised by authors and it has been shown that it is very effective for broadbanding of the transformer. In this paper, the application of the ring-loaded corrugated waveguide to horns is investigated, and radiation characteristics of the ring-loaded corrugated horn are theoretically and experimentally clarified. The useful frequency bandwidth in the ring-loaded corrugated horn is 1.35 times broader than that in the conventional one.

The amplitude distribution at the aperture of the ring-loaded corrugated horn shown in Fig. 3 (insert) can be approximated by the field distribution of the ring-loaded corrugated waveguide with a large fin diameter. In the case of $a \gg \lambda$, $\lambda \gg p$, $k > \beta_0$, the field distributions for EH_{11} mode in the ring-loaded corrugated waveguide are given as follows;

$$Ex = Eo \left\{ J_0(k_0 r) + \gamma J_2(k_0 r) \cos 2\theta \right\},$$
$$Ey = Eo\, \gamma\, J_2(k_0 r) \sin 2\theta,$$
$$k = 2\pi/\lambda, \quad \beta_0 = 2\pi/\lambda_g, \quad k_0 = \sqrt{k^2 - \beta_0^2}, \qquad (1)$$
$$\gamma = J_0(k_0 a)/J_2(k_0 a),$$

where λ and λ_g are wavelengths in free space and the waveguide, respectively, p is the slot pitch, Ex and Ey are the field components in the x and y directions, respectively. Ex and Ey are determined by only a variable $k_0 a$ as well as those in the conventional one[3]. For instance, when $k_0 a = 2.405$, Ex is expressed with $J_0(2.401\, r/a)$ which is approximately Gaussian function and Ey=0, and then the radiation pattern of the corrugated horn is rotationally symmetric and its sidelobes are very low, and when $k_0 a = 1.841$, Ex and Ey coincide with those of TE_{11} mode in homogeneous circular waveguide. Therefore, in order to broaden the bandwidth in which the desirable aperture field is obtained, it is required that, over wide frequency range, $k_0 a$ is between 2.405 and 1.841.

The variable k_0a for EH_{11} mode can be derived from the following boundary conditions;

$$\overrightarrow{Y_{S1}} + jBd_1 + \overrightarrow{Y_{S2}} = 0 \quad \text{at } r=b_1,$$
$$\overleftarrow{Y_{S2}} + \overrightarrow{Y_C} = 0 \qquad \text{at } r=a , \qquad \Big\} \quad (2)$$

$\overleftarrow{Y_{S1}}$: The slot admittance as seen from $r=b_1$ toward the bottom of slot,

$\overrightarrow{Y_{S2}}$: The slot admittance as seen from $r=b_1$ toward the wave-guide-axis,

$\overleftarrow{Y_{S2}}$: The slot admittance as seen from $r=a$ toward the bottom of slot,

$\overrightarrow{Y_C}$: The admittance as seen from $r=a$ toward the waveguide-axis,

Bd_1: Shunt susceptance for change in the slot width.[4]

In Fig. 2, the computed results of k_0a in the ring-loaded and the conventional corrugated waveguides are plotted. In the ring-loaded corrugated waveguide, $k_0a=2.405$ at $ka=6.0$ and $k_0a=1.841$ at $ka=17.4$, and frequency characteristic of k_0a is more flat than that in the conventional one. This means that the desirable aperture field is obtained over a 2.9:1 bandwidth. On the other hand, it is well known that the broadbanding of the transformer can be achieved by the expanding the frequency range in which $\overrightarrow{Y_{S2}}$ is capacitive susceptance[2]. In the ring-loaded corrugated waveguide, $\overrightarrow{Y_{S2}}=0$ at $ka=6.54$ and $\overrightarrow{Y_{S2}}=j\infty$ at $ka=17.4$. This shows that good performance in the transformer is obtained over a 2.7:1 bandwidth. From the above considerations, it is found that the useful frequency bandwidth in the ring-loaded corrugated horn is about 1.35 times broader than that in the conventional one.

Radiation patterns and input VSWR of the ring-loaded and the conventional corrugated horns were measured. The aperture dimensions of these horns are chosen as well as those in Fig. 2. In Fig. 3, the radiation patterns at $\overrightarrow{Y_{S2}}=0$ and $|\overrightarrow{Y_{S2}}|=\infty$ are shown, and in Fig. 4, the variations of the beamwidths at -10dB and VSWR are shown. Fig. 4 (a) also shows the comparison between theoretical and measured values of the beamwidths. Theoretical results quite agree with the experimental results, and in the ring-loaded corrugated horn, the useful frequency bandwidth, in which E- and H-plane patterns are nearly identical and good VSWR characteristic is obtained, is 1.35 times broader than that in the conventional corrugated horn.

In conclusion, the frequency broadbanding of the corrugated horn can be achieved by applying the ring-loaded corrugated waveguide to the horn. The useful frequency bandwidth in the ring-loaded corrugated horn is 1.35 times broader than that in the conventional corrugated horn.

REFERENCES

1. A. F. Kay (1964 TRG Science Report 5, AFCRL Project 4600, Contract No. AF19 (604)-8057).
2. Y. Takeichi, T. Hashimoto, F. Takeda (1971 IEEE Trans. MTT-19, No. 12, PP. 947-950).

3. M. Mizusawa, F. Takeda, S. Betsudan (1973 The Transaction of
    the Institute of Electronics and Communication Engineers of
    Japan, 56, No. 1, PP. 11-13).
4. N. Marcuvitz (1951 WAVEGUIDE HANDBOOK, McGraw-Hill, New York,
    PP307-308).
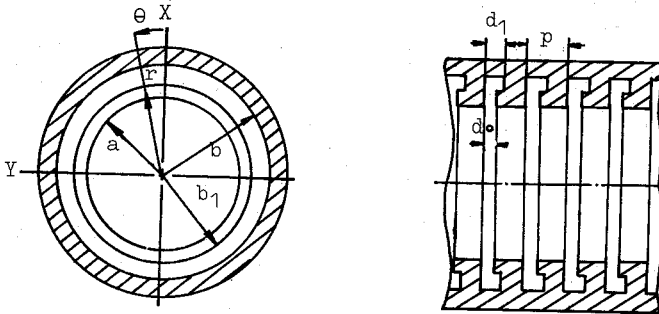
Fig. 1 Ring-loaded corrugated waveguide.

Fig. 2 Frequency characteristics of k_oa.

$\overline{Ys_2} \simeq 0, ka = 6.54$　　　　$|\overline{Ys_2}| \simeq \infty, ka = 17.1$

(a) Ring-loaded corrugated horn.

$\overline{Ys_2} \simeq 0, Ka = 8.71$　　　　$|\overline{Ys_2}| \simeq \infty, Ka = 17.0$

(b) Conventional corrugated horn.

Fig. 3 Radiation patterns.

(a) Ring-loaded　　　　(b) Conventional
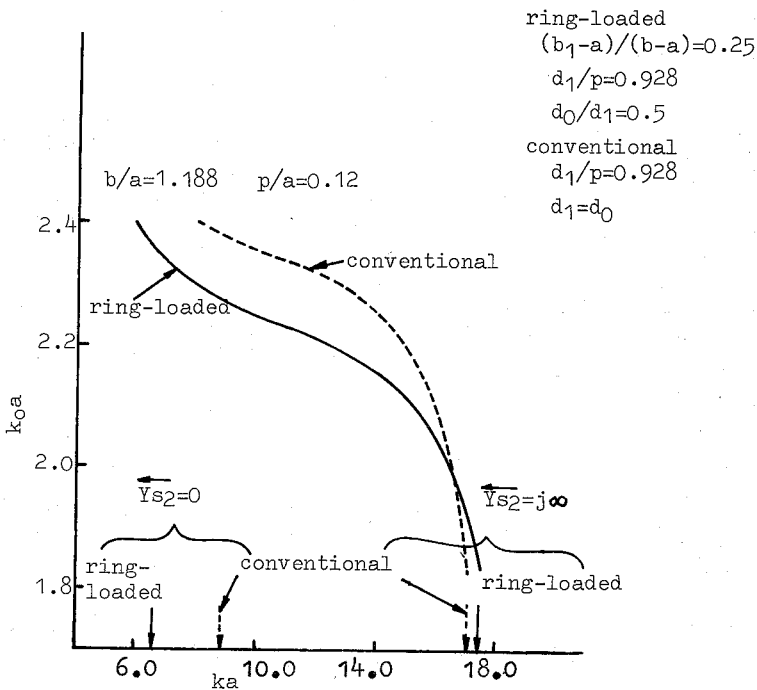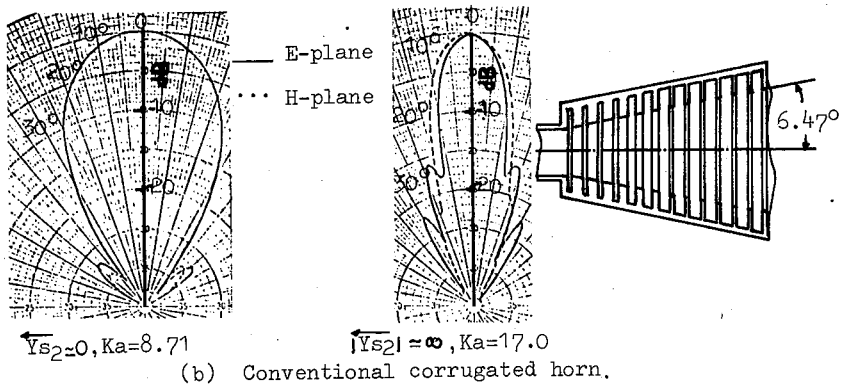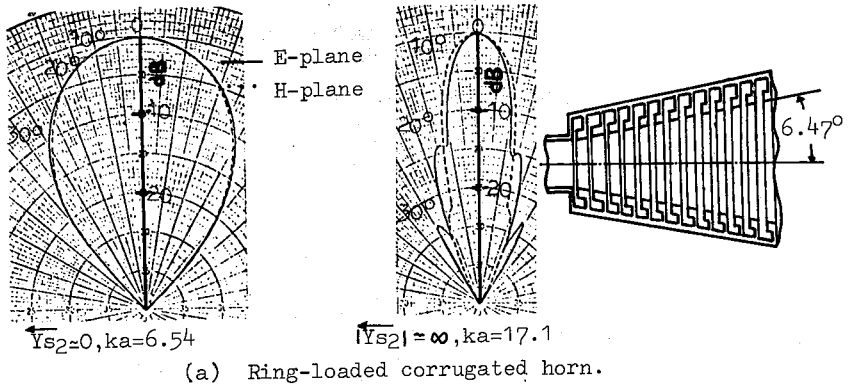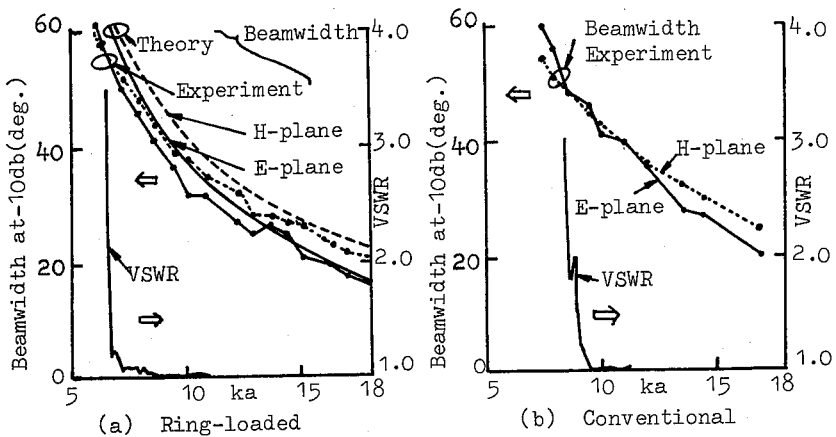
Fig. 4 Beamwidths and VSWR vs.ka.

CIRCULAR WAVEGUIDE APERTURE WITH A CURVED CORRUGATED DISK AS A PRIMARY FEED

P.S.Neelakantaswamy and D.K.Banerjee
Department of Electrical Engineering
Indian Institute of Technology
Madras-36,India

Introduction:

Recently several investigations have been carried out on a class of feed structures consisting of a circular waveguide with a flat corrugated disk at the aperture [1,2]. The so-called 180 deg. corrugated conical horn [1] and waveguide feed structures based on multichoke concept are examples for this category of feed types [2].

Presently, a modified feed structure having a circular waveguide with a curved (convex or concave) corrugated disk at the aperture is studied. The waveguide carries the dominant TE_{11} mode. For identical corrugation dimensions and disk diameters the far-field patterns of the flat or curved types are compared both theoretically and experimentally.

Theoretical formulation:

Clarricoats and Saha [3] have surveyed in detail the radia-tion behaviour of corrugated conical horns and several addi-tional results have also been reported on this subject [1,2,4]. In all these cases the feed with a flat corrugated circular disk at the circular waveguide aperture has been studied as a special case of conical scalar horns with 90 deg. flare angle. In the present investigation, curved or flat corrugated disks (fig.1) are assumed to be represented equivalently by dielectric coated ground planes. The far-zone field components due to TE_{11} mode excited aperture on this assumed "equivalent dielectric coated plane can be obtained by the method indicated by Knop and Cohn [5]. The pattern distortion due to the diffracted E-field along the coated ground plane can also be incorporated in the expressions for the far-field components based on edge diffra-ction method [6]. The dielectric constants of the equivalent coating of flat and convex curved corrugated surfaces are res-pectively given by eqns.(1) and (2) of ref.7.

The resulting far-zone field pattern in the elevation plane (y-z plane) is given by

$$E_\theta^T = E_\theta^a f(\theta) + E_{\theta 1}^d + E_{\theta 2}^d \tag{1}$$

and in the equitorial plane (x-z plane) by

$$E_\phi^T = E_\phi^a g(\theta) \tag{2}$$

where E_θ^a and E_ϕ^a represent the primary field components due to the open-ended circular waveguide aperture given by (5) and (8) of ref.6. The functions $f(\theta)$ and $g(\theta)$ denote the pattern modifi-cation due to dielectric coating and are given by (16) and (17) of ref.5.

$E_{\theta 1}^{d}$ and $E_{\theta 2}^{d}$ refer to edge diffracted field components given by

$$E_{\theta 1}^{d} = E_{\theta 1}^{c} \exp(jk_{o}b\sin\theta)\ V_{B}(b,\ \pi/2 - \theta_{1} + \theta,\ 3/2)$$

$$E_{\theta 2}^{d} = E_{\theta 2}^{c} \exp(-jk_{o}b\sin\theta)\ V_{B}(b,\ \pi/2 - \theta_{1} - \theta,\ 3/2)$$

(3)

where

$$E_{\theta 1}^{c} = E_{\theta}^{a}\ f(\theta)\quad \text{at}\quad \theta = +(\ \pi/2 - \theta_{1})$$

$$E_{\theta 2}^{c} = E_{\theta}^{a}\ f(\theta)\quad \text{at}\quad \theta = -(\ \pi/2 - \theta_{1})$$

Here, θ_{1} is the angle of the disk-edge (fig.1), b is the disk diameter and $k_{o} = 2\pi/\lambda$. $V_{B}(r, \psi, n)$ refers to the plane wave diffraction function defined by (3) in ref.8.

Results and Discussion:
Using the expressions (1) and (2) the far-field patterns computed for the feed structures of fig.(1) for a frequency of 9.477 GHz (except for the concave corrugated type) are presented in fig.3. The feed structures of fig.1 were fabricated and pattern measurements were carried out at a frequency of 9.477 GHz. These results are also given in fig.3. For concave corrugated type, we have at present no theoretical results and only the experimental results are presented in fig.2. Also, for a different corrugation dimensions and disk diameter, the theoretical results obtained by the present method is compared with the results of Lambrechtse [4] obtained by 90 deg. flare angle conical scalar horn principle (frequency 14 GHz).

From the results it can be observed that the simple closed form expressions obtained by the present method, represents the field patterns very closely; the effect of concave curvature is the improved pattern symmetry. The convex curvature type has almost identical characteristics as the flat one. It was also observed that these feed structures present a measured VSWR of less than 1.5 over the waveguide band.

References:
[1] M.E.J. Jeuken,et.al.(1972 Nachrichtentech.Z. 8, p.374)
[2] R.Wohlleben, et.al. (1972 Electronics Letters,8,p.474)
[3] P.J.B.Clarricoats and P.K.Saha (1971 Proc.IEE. 118,p.1167)
[4] C.W.Lambrechtse (1969 Report ETA-31 Eindhoven University of Technology,Netherlands)
[5] C.M.Knop and G.I.Cohn (1964 Radio Science,68D, p.363)
[6] C.A.Balanis (1970 IEEE Trans.AP-18, p.561)
[7] P.S.Neelakantaswamy and D.K.Banerjee (1972 Electronics Letters, 8, p.534)
[8] C.A.Balanis (1970 IEEE Trans. AP-18, p.352)

Guide diameter (2a) = 2·61 Cm   Corr. teeth
Disk diameter (b) = 12·0 Cm   width (t) = 0·2 Cm.
Disk radius of   Corr. Depth
   curvature (R) = 15·0 Cm   (d) = 0·7 Cm.
Corrugation groove   No. of grooves = 11
   width (g)   = 0·2 Cm   No. of teeth   = 12
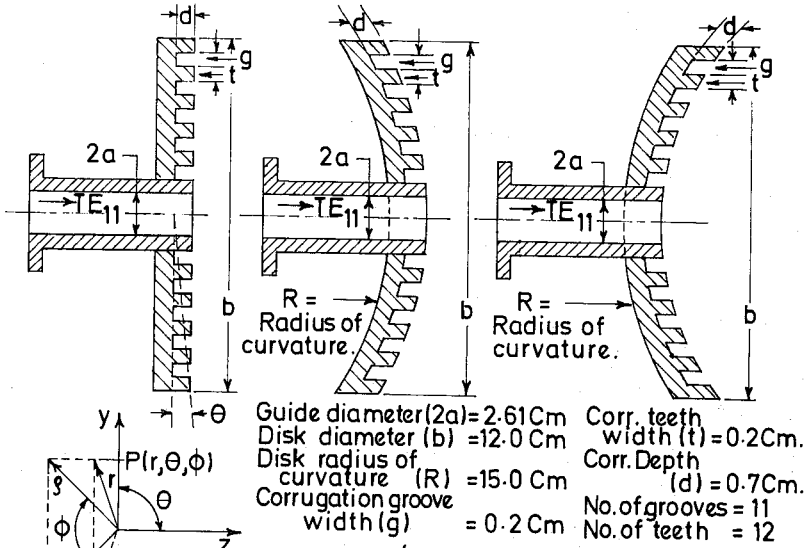
Fig. 1. The Different Feed
          Structures.

Power (db)

Vertical
Plane

Horizontal
Plane

ⓐ   ⓑ   ⓐ   ⓑ

——— Theory
x x x x Experimental
●—●—●—● Experimental

Feed dimensions =
      Vide Fig. 1.
   f = 9·477 GH$_z$

(a) = Open wave-guide
         aperture.
(b) = Concave corrugated
         Disk-loading.

← θ Degrees →

80   60   40   20   0   20   40   60   80
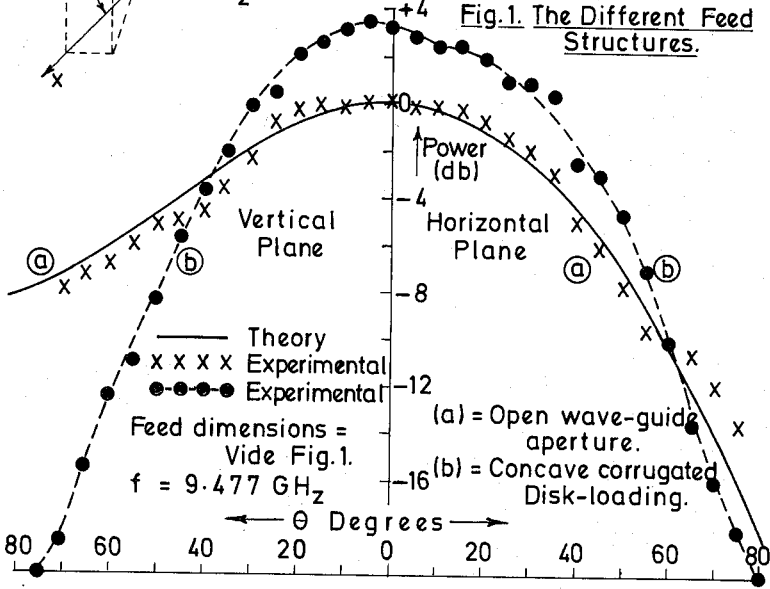
Fig. 2. Field Patterns of (a) and (b)
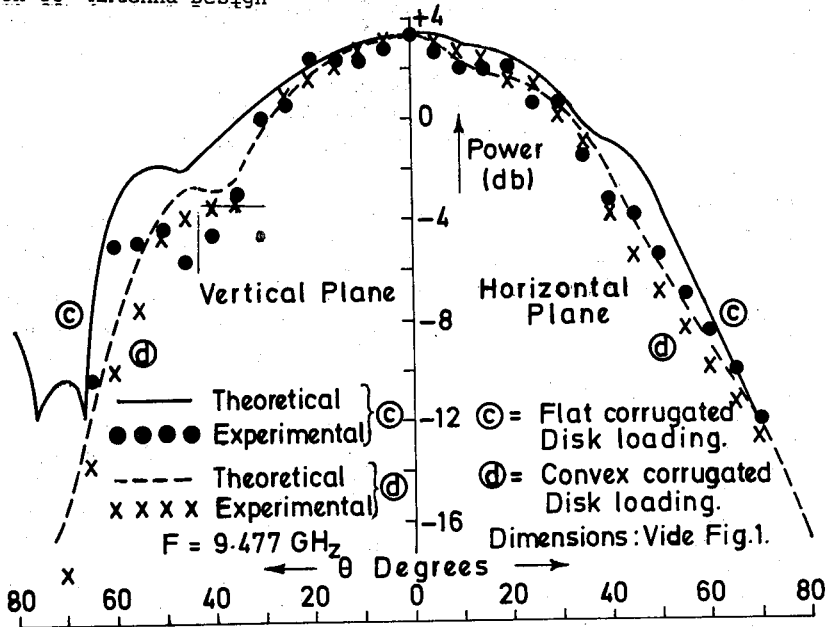
Fig.3. Field Patterns of (c) & (d)
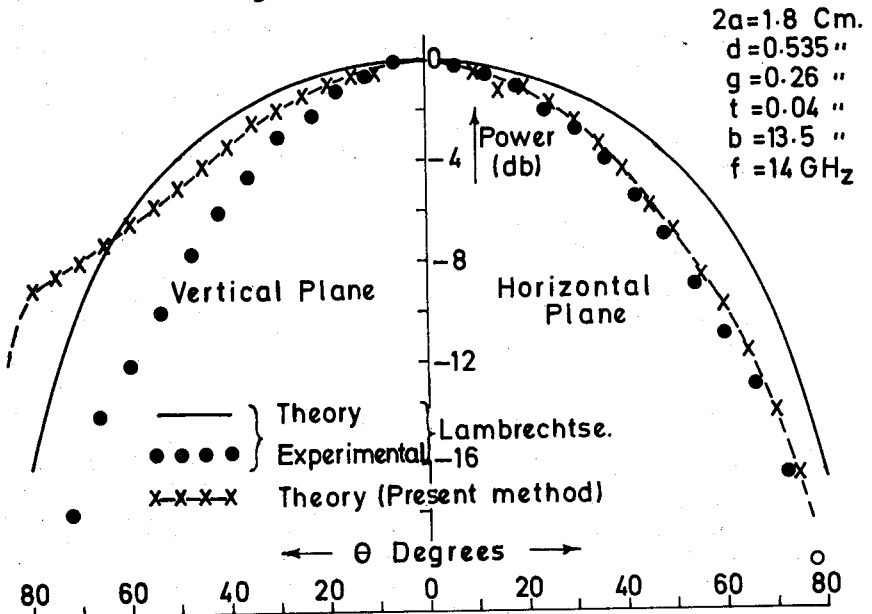
Fig.4. Field Patterns of Feed-Flat corrugated type.

ON HIGH-PERFORMANCE MONOPULSE FEED USING CORRUGATED WAVEGUIDE

T. B. Vu
School of Electrical Engineering
University of New South Wales
Kensington, Sydney, Australia

This paper discusses experimental models of single-port multimode monopulse feeds using corrugated circular waveguide. The design is based on conventional systems using a conical horn feed where the difference pattern is derived from the TM_{01} mode. With the corrugated models, however, the sum or reference signal is provided by the natural modes of the corrugated waveguide.

The theory of corrugated circular waveguide has been discussed in the literature (1), (2). Briefly speaking, the corrugated wall allows the waveguide to support modes having both E_z and H_z components. These so-called hybrid modes can be looked upon as linear combinations of conventional TE and TM modes which propagate in a smooth waveguide. It can be shown that the radiation pattern of a hybrid mode possesses cylindrical symmetry, i.e. the pattern of the dominant hybrid mode HE_{11} is similar to that of Potter's TE_{11}-TM_{11} combination which achieves complete beamwidth equalization in all planes and at least 30db sidelobe suppression (3). Thus, with an appropriate combination of HE_{11} and the next higher-order hybrid mode HE_{12} one can achieve an overall antenna efficiency obtainable with a correct combination of TE_{11}, TM_{11}, TE_{12} and TM_{12} in a smooth waveguide. The advantage of the corrugated model is therefore obvious. As the number of modes is effectively halved, the useful bandwidth of the corrugated horn is much wider than that of its conventional counterpart. This has also been confirmed by experimental results (4).

These properties make corrugated waveguide particularly attractive, not only for the design of high-efficiency feeds for large radio-telescopes, but also for single-port multimode monopulse feeds. A detailed discussion of corrugated horn as high-performance monopulse feed can be found in the literature (5), and it suffices to mention here that its wide-band characteristics make it well suited for commercial satellite tracking applications where a single feed is used for both the transmit and receive band. In addition, the problem of processing the error signals will be simpler for the general case of elliptically polarized signals. In this case, both TE_{01} and TM_{01} must be used to provide information on the target position, and with a corrugated horn, the relative power pattern of these two modes are identical. It is also important to note that only two hybrid modes need be used to shape the sum pattern. As a result, optimization of both the sum and difference mode can be achieved without greatly sacrificing the bandwidth. Lastly, the effect of spurious modes is also less significant in a corrugated waveguide.

In order to obtain a systematic examination of the performance of

the corrugated horn, two types of single-port multimode monopulse feeds have been designed and tested. In both cases, the difference signal is derived from the TM_{01} mode, but the first type uses only the dominant mode HE_{11} to provide the reference signal, while the second type attempts to optimize both the sum and the difference mode. Fig. 1 shows a model of the first type where the corrugated waveguide is flared out into a cone so as to achieve the required beamwidth. The main parameter here is the flare angle. Fig. 2 shows a model of the second type. In this case, the performance of the horn depends greatly on the relative phases and amplitudes of the HE_{11} and HE_{12}. The phase relationship is basically governed by the horn length, whereas the amplitude ratio is determined by the degree of discontinuity at the step junction. Experimental results have shown that, if only HE_{11} is used, the useful bandwidth is of the order of 40%, i.e. the pattern symetry and the sidelobe suppression will be satisfactory within this band. Thus, this type of feed would be suitable for wideband applications. The main drawback is that the HE_{11} pattern is much narrower than the TM_{01} pattern, so that the spill-over loss can be quite high. This is clearly seen from the radiation patterns shown in Figs. 3 and 4. For horns of the second type where both the sum and difference channel are to be optimized, the normal approach is to choose the size of the feed aperture so as to obtain the best difference illumination. The sum pattern is then broadened with the aid of the HE_{12} mode. Sample radiation patterns of this type of feed are shown in Fig. 5. The feed is here designed to illuminate the paraboloidal reflector from the primary focus. The sum pattern is designed to approximate the ideal pattern required for uniform illumination or for maximum efficiency. It is noted that the beamwidth of the sum pattern can be varied simply by varying the amount of HE_{12} power. This is done in practice by varying the degree of discontinuity at the step junction. The bandwidth achievable in this case is of the order of 10%. Thus, independent optimization of the sum and difference mode can be achieved without having to greatly sacrifice the bandwidth. For both types of horns the resultant hybrid mode is first converted to TE_{11} in the smooth circular waveguide of the mode coupler shown in Figs. 1 and 2. This is then coupled to the first rectangular port through slots cut on the waveguide wall. The TM_{01} mode is allowed to propagate down the smooth circular waveguide and then coupled to the second rectangular port through a circular waveguide to coaxial to rectangular adapter.

References.

1. B.M. Thomas (1971, Proc. Inst. Elect. Engrs.,118,p.1539).
2. P.J.B. Claricoats and P.K. Saha (1971, ibid.,118,p.1167).
3. P.D. Potter (1963, Microwave J., VI,p.71).
4. T.B. Vu (1973, International J. Electronics, 34,p.391)
5. T.B. Vu (1973, ibid., 34,p.   ).
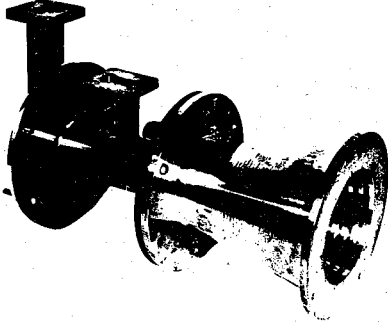
Fig.1 Monopulse feed
with HE$_{11}$ as sum mode
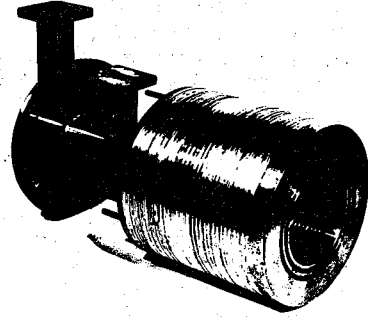
Fig.2 Dual-hybrid-mode
monopulse feed

Fig.3 Sample sum pattern
of feed of Fig.1

——— H-plane

— — — E-plane
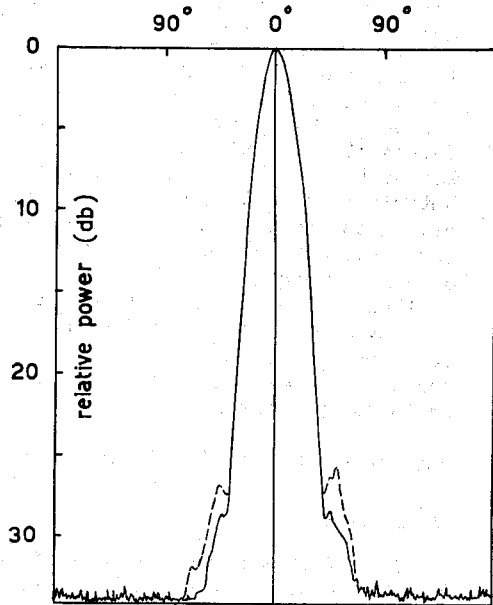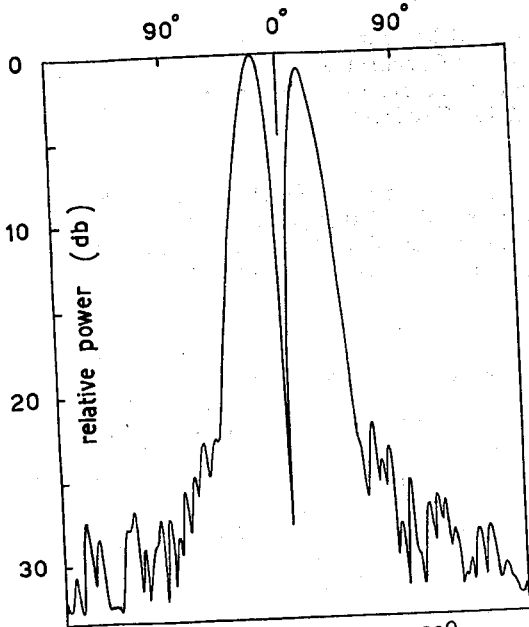
Fig.4 A typical
difference pattern
of feed of Fig.1
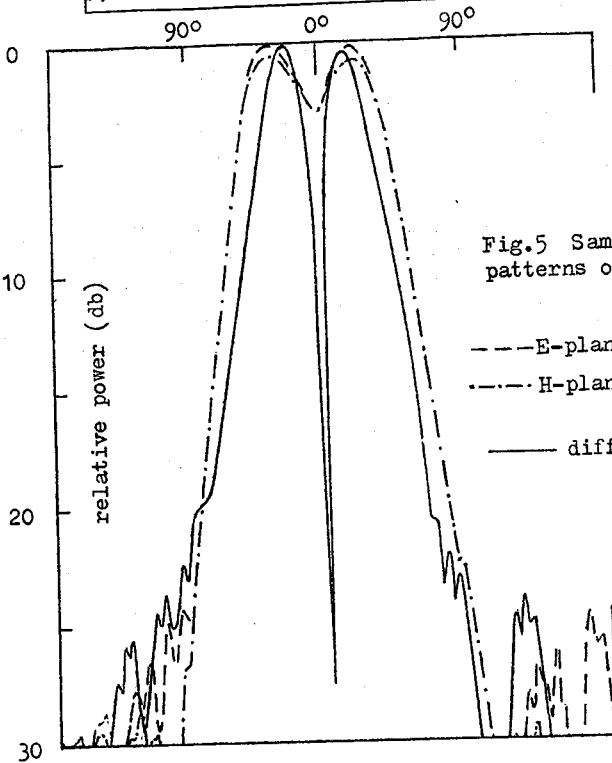
Fig.5 Sample radiation
patterns of feed of Fig.2

– – –E-plane ⎫
                ⎬ sum pattern
·–·–·H-plane ⎭

———— difference pattern

Session 33   Antenna Design

A DUAL-FREQUENCY COAXIAL FEED FOR A PRIME FOCUS ANTENNA

Gary H. Schennum
Philco-Ford Corporation
Western Development Laboratories Division
Palo Alto, California

The need in microwave systems for antennas with a dual-frequency
capability has led to the development of multifrequency, multipurpose
antennas. This paper describes one type of dual-frequency feed which
will be used in the Viking Orbiter High Gain Antenna subsystem shown
in Figure 1.

The feed (Figures 2 and 3) consists of an X-band center channel sur-
rounded by the S-band outer channel. The X-band channel is transmit
only, operating at a frequency of 8415 ± 20 MHz; the S-band channel
transmits and receives at 2295 ± 5 and 2115 ± 5 MHz, respectively.
The X-band channel is excited by sidewall coupling from the WR112
rectangular input, with circular polarization provided by a dielectric
quarter-wave plate keyed at 45° to the input waveguide slot. Circular
polarization at S-band is produced by driving four equal-amplitude
orthogonal probes in phase quadrature. The depth of the S-band cavity
was adjusted to obtain high isolation (>30 dB) between the X-band trans-
mit and S-band receive frequencies.

The aperture sizes of the S- and X-band feed channels were chosen to
obtain a 12.5 dB taper at the dish edge. To calculate the required aper-
ture sizes, computer programs were written for an open-ended circular
waveguide and for a coaxial cable operated in the TE_{11} coaxial mode.
The excellent correlation between the predicted and measured patterns
is shown in Figures 4 and 5.

The 58-inch parabolic dish was constructed of graphite epoxy skins with
an aluminum-honeycomb core. Reflectivity tests were conducted which
showed that the graphite epoxy skins were highly reflective, thus pre-
cluding a metallic parabolic surface. The dish and the support struts
together weigh less than 11 pounds.

The design details and the primary and secondary RF performance will
be described in the presentation.
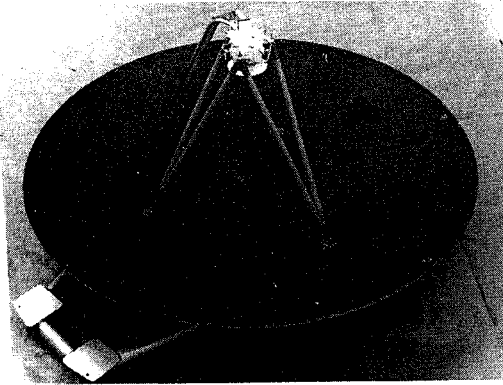
Figure 1   The Viking Orbiter
High Gain Antenna
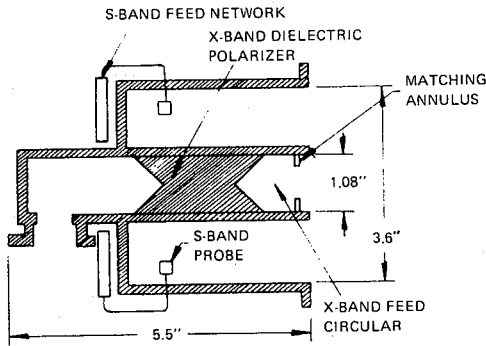
Figure 2   S/X-Band Feed Schematic
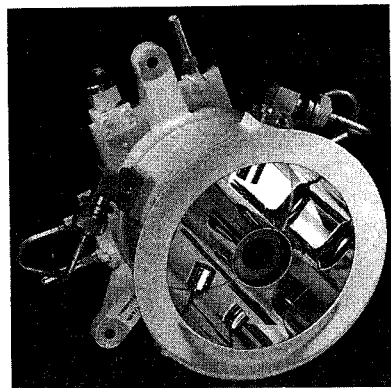
Figure 3   Oblique View of
Dual-Frequency
Coaxial Feed

237
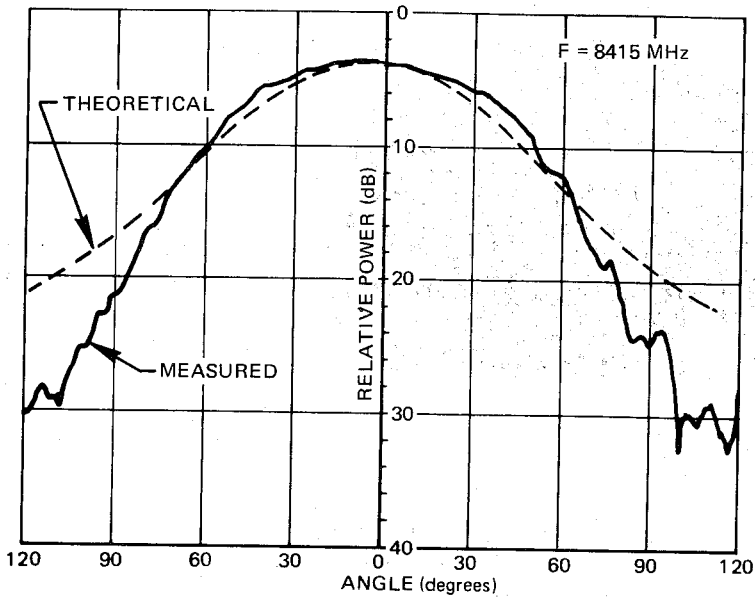
Figure 4 X-Band Feed Pattern - Circular Polarization
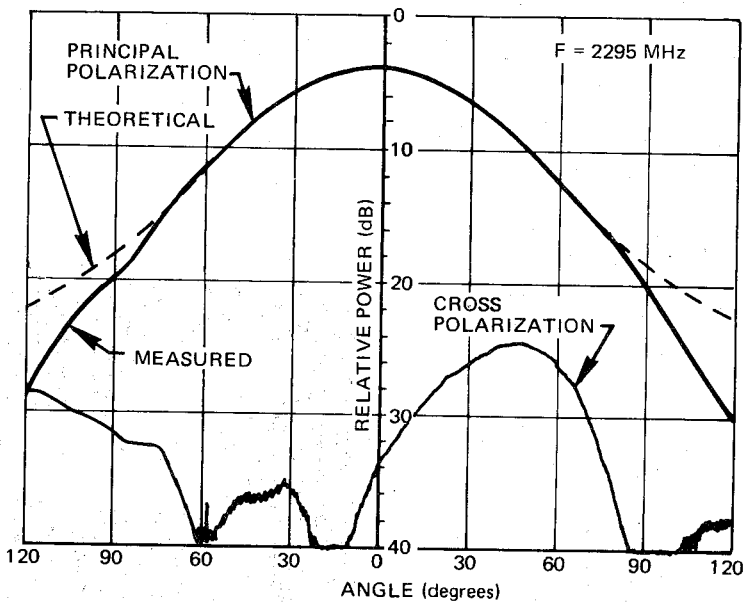
Figure 5 S-Band Feed Pattern - Circular Polarization

MEASUREMENTS OF 20 GHz TRANSMISSION
THROUGH A WET RADOME

by

IAIN ANDERSON
Bell Telephone Laboratories
Crawford Hill Laboratory
Holmdel, New Jersey   07733

INTRODUCTION – Large ground station antennas of pro-
posed[1] 18-30 GHz domestic satellite systems may be
enclosed within radomes. An experiment to study the
effects of rain on transmission through such radomes
is in operation at Crawford Hill, Holmdel, N.J. This
paper presents the experimental results obtained to date.

EXPERIMENT – Figure 1 shows the experiment designed to
measure the 20 GHz transmission due to rain on the
surface of a radome section. A (Gaussian) beam, which
is launched by the transmitting antenna, intercepts a
portion of the radome surface and is then detected at
the receiving antenna. Each antenna has a two-foot
diameter aperture and is similar in design to the
enclosed, periscope type described by Crawford and
Turrin[2]. The dimensions of the radome support structure
have been chosen so that, in the absence of wind, the
water flow characteristics on the surface of the section
approximate that on the corresponding section of a 90-
foot diameter radome. To allow transmission measure-
ments of the radome material under dry conditions the
wooden structure tips in the vertical plane to clear the
antenna beam. The radome material used in the experiment
is believed to be typical of present radome technology
and consists of a 0.03 inch thick, water repellent
laminate. The transmission loss of this material under
dry conditions is 0.5 dB at 20 GHz.

The transmission loss due to the heaviest of rains on
the short (30 foot) path is negligible. To eliminate
errors caused by rain on the antenna weather covers,
suitable rain shields are attached to each antenna. The
transmitted field is vertically polarized and is focused
to give approximately a planar phase front over the
circular test area of the radome surface. A 50 dB
dynamic range, with an accuracy of ±5% is provided
by the measuring system which consists of a 30 mW
modulated Gunn oscillator, crystal detector and tuned
amplifier. The rain rate is measured by a capacitor-
type rain gauge[3] and this, together with the signal
output from the tuned amplifier, is continuously recorded.

RESULTS – The experiment has been operational since
October 1972 and since then there has been comparatively
little change in the radome surface when examined under
dry conditions. An almost unnoticeable thin grime film
has accumulated on the surface and this has increased
the dry radome transmission loss by approximately 0.1 dB.
There has, however, been a drastic change in the wetting
properties of the surface and this has been accompanied
by a large increase in the radome transmission loss
during periods of rain.

Figure 2 shows the transmission loss as a function of
rain rate for the periods October 6-7, November 8-9, 1972
and March 16-17, 1973. Inspection of the radome surface,
during these periods, revealed that the water run-off
occurred in both rivulet and laminar flow. Rivulet flow
dominated during the October rain and laminar flow
dominated during the March rain. This suggests that the
grime accumulation greatly increased the wettability of
the surface. The November results are an intermediate
example. The solid curve is predicted by Gibble's
result[4] and assumes laminar flow conditions on a 90-foot
diameter radome. Evidently the transmission loss, for a
given rain rate, is steadily increasing with time and
approaching the value predicted by considerations of laminar
flow.

CONCLUSIONS – The results demonstrate that a non-wetting
radome surface is essential to achieve small transmission
losses in rain. In the particular sample examined, how-
ever, it appears that the non-wetting nature of the
surface is significantly degraded in time, presumably
by atmospheric pollution or weathering. Latest measure-
ments are in good agreement with Gibble's result for
rain rates up to 5 mm/hr. The experimental results
indicate that transmission losses through a 90-foot
diameter radome, that has weathered for six months in
central New Jersey, may range from 6-8 dB for rain rates
of 3-40 mm/hr.

1. L. C. Tillotson (1968 BSTJ 47, p. 2111).
2. A. B. Crawford and R. H. Turrin (1969 BSTJ 48, p. 1605).
3. R. R. Seibel (1972 Rev. Sci. Instrum. 43, p. 1081).
4. D. Gibble (1964 IEEE International Conv. New York City).

FIG.I RADOME EXPERIMENT

WOODEN STRUCTURE
WITH RADOME SECTION

TRANSMITTING
ANTENNA

13'

45' RAD.

25'

RECEIVING
ANTENNA

SIDE VIEW

SUPPORT POLES

RAIN SHIELD

RAIN SHIELD

AXLE

6'
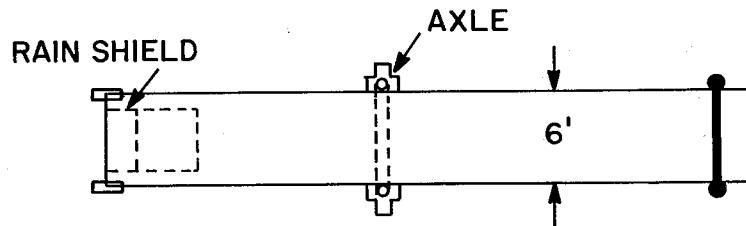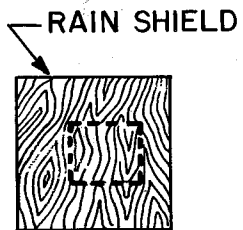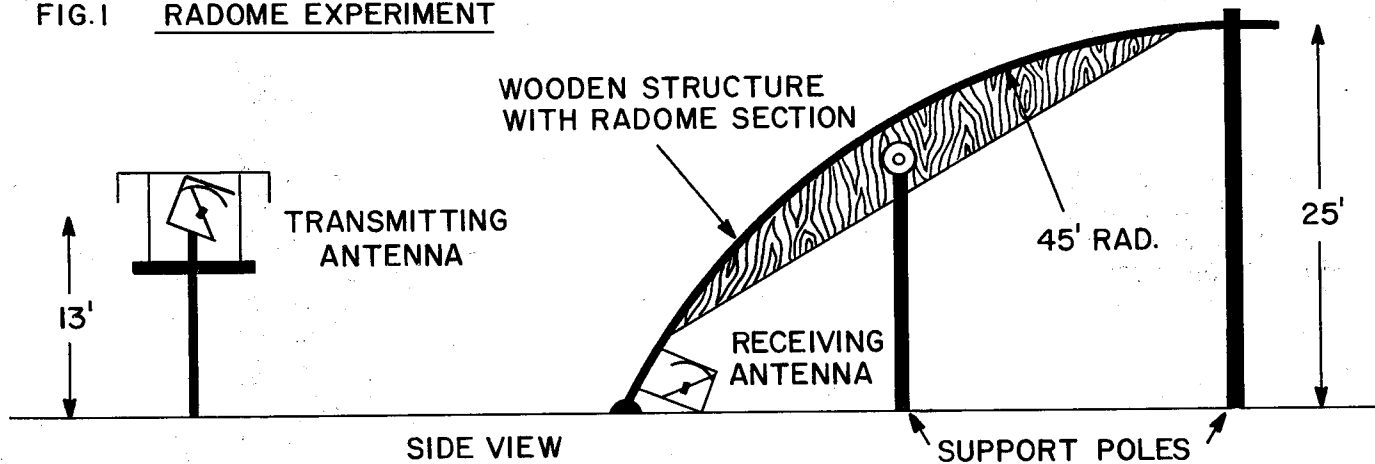
TOP VIEW

(ANTENNAS NOT DRAWN TO SCALE)

FIG. 2 RADOME TRANSMISSION VS RAINRATE
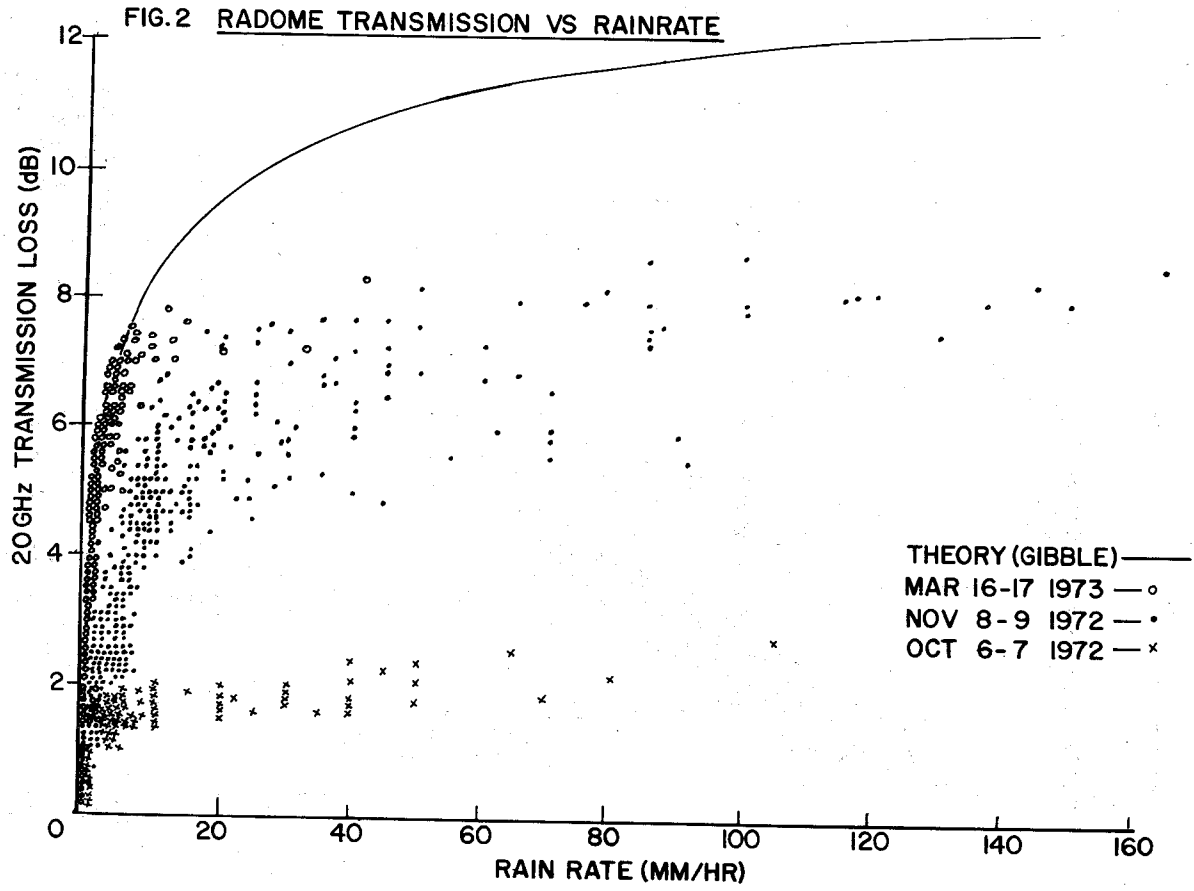
UHF ANTENNAS IN CONCRETE

R. G. FitzGerrell and L. L. Haidle
U. S. Department of Commerce
Office of Telecommunications
Institute for Telecommunication Sciences
Boulder, Colorado 80302

The antennas discussed in this paper are full-scale electrical models of hardened antennas for long-range ground-to-air communication links at UHF. Environmental factors affecting this class of antennas are seismic waves, atmospheric shock waves, thermal radiation, blast-product erosion, and radio-active debris. The electrical and mechanical requirements imposed by these environmental factors are evident in -the antenna design and performance tests.

This paper describes some results of an 8-month study to determine the power gain and input VSWR of buried annular slots and above ground conical monopole antennas, primarily designed using empirical methods, encapsulated in properly dried refractory concrete. Power gain versus elevation angle and input VSWR were measured as functions of the following parameters:

(1) Annular slot dimensions,
(2) Frequency from 225 MHz to 400 MHz,
(3) Annular slot burial depth in refractory
      concrete from 0 m to 1 m,
(4) Debris (topsoil) depths from 0 m to 1.2 m, and
(5) Debris moisture content (conductivity and di-
      electric constant).

The antenna of primary interest was the annular slot. Two of these antennas, differing in linear dimensions by a scale factor of 1.5 were used in this study. The smaller antenna was designed and fabricated for a previous study {1} by the Institute for Telecommunication Sciences (ITS). Shown in Figure 1, it was to have optimum low-angle gain and input VSWR characteristics at 392.5 MHz when buried 1 m below ground level in refractory concrete. Since the larger antenna differed from the smaller one by only a 1.5 scale factor, its optimum characteristics were expected near 262 MHz.

The antenna of secondary interest was a right circular conical monopole fed against a 35.5 cm diameter ground plane. This antenna was encapsulated in a refractory concrete hemisphere with the ground plane just covering the base of the casting. Three models of the encapsulated monopole were measured. Since the conical element consisted of a cage structure of wires to define the surface of the cone, the models differed in the number of wires forming the cone and the position of the antennas over ground. One model was placed atop a wire mesh cylinder used to simulate a steel pipe with a 35.5 cm outer diameter. The overall height of this model was 1.2 m. It was the only one of the three monopole models included in the debris tests.

The very large number of measured data points led to the decision to present most of the final results in contour plot form. Rectangular arrays of measured data points were processed by a digital computer, resulting in

power gain or VSWR plotted as lines of equal amplitude versus the parameters represented by the ordinate and abcissa of the array. That is, the computer processed an array of measured data points by means of programs which scanned the array, interpolated between data points, and produced relatively smooth contour lines through all points of equal amplitude called for by the programmer.

Figure 2, a typical plot of data produced by this antenna performance study, shows power gain versus elevation angle and mean slot radius measured in units of wavelengths in the refractory concrete medium (ε = 6.5, tanδ = 0.005 at 300 MHz). This figure is plotted from data measured using the two annular slot antennas buried 0.33 m deep in refractory concrete.

Because of the many parameters involved in the performance measurements, it is difficult to draw simple conclusions. The measured data fairly well describe the power gain versus elevation angle and input VSWR for two types of hardened antennas as functions of frequency over the 225 MHz to 400 MHz band. Pertinent mid-band performance characteristics are as follows:

Small Annular Slot, 0.33 m Burial Depth

 Power gain = -7 dB at Ψ = 10°
 VSWR = 1.4 referred to 50 ohms

Large Annular Slot, 0.33 m Burial Depth

 Power gain = -15 dB at Ψ = 10°
 VSWR = 1.5 referred to 50 ohms

Encapsulated Monopole III

 Power gain = -1 dB at Ψ = 10°
 VSWR = 4.0 referred to 50 ohms

Conical Monopole (for comparison)

 Power gain = -3 dB at Ψ = 10°
 VSWR = 2.0 referred to 50 ohms

This antenna is a 27.7 cm high 90° conical monopole fed against a 76 cm diameter ground plane resting on test range ground.

In general, increased burial depth or debris depth reduces power gain. The effect of debris is not pronounced for encapsulated monopole III until the debris rises above the feedpoint of this antenna which is 1 m above ground. The power gain then decreases at a more rapid rate with debris depth than it does for the annular slots. The effect of debris and burial depth on annular slot VSWR is almost negligible, assuming that the burial depth is 0.33 m or greater. The VSWR of encapsulated monopole III improves at lower frequencies as debris rises above the feedpoint.

These antennas may have applications where debris and great mechanical strength are not important design criteria. These antennas are certainly not fragile. The annular slot could be placed in roadways, runways, or in supersonic aircraft since it has no profile extending beyond the ground plane and the dielectric is a strong high temperature material. The encapsulated monopoles are much smaller than the annular slots, exhibit higher power gains, have narrower bandwidths, and tend to be less rugged primarily because of the hemispherical profile above the ground plane.

1} R.G. FitzGerrell, L.L. Haidle (January 1972, IEEE Trans. Antennas Propagat., Vol. AP-20, pp. 56-62).
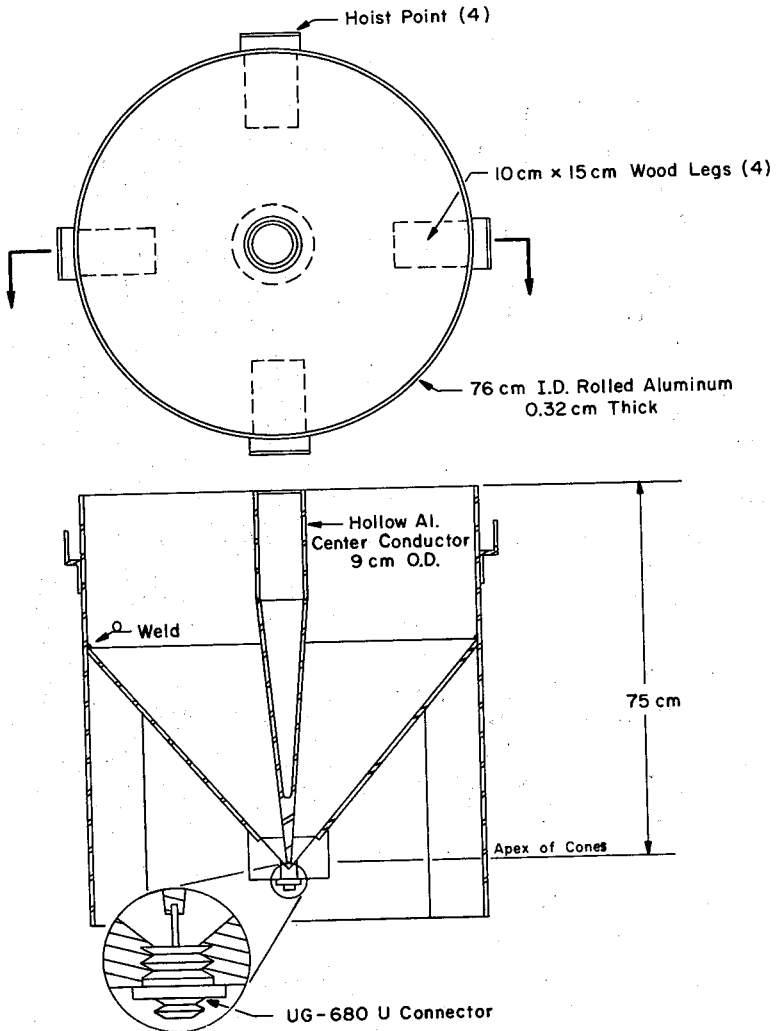
Figure 1. Top and cross section views of the small annular slot
antenna. The space between conductors above the apex
of the cones is filled with refractory concrete ($\epsilon_r = 6.5$,
tan $\delta = 0.005$ at 300 MHz).

245
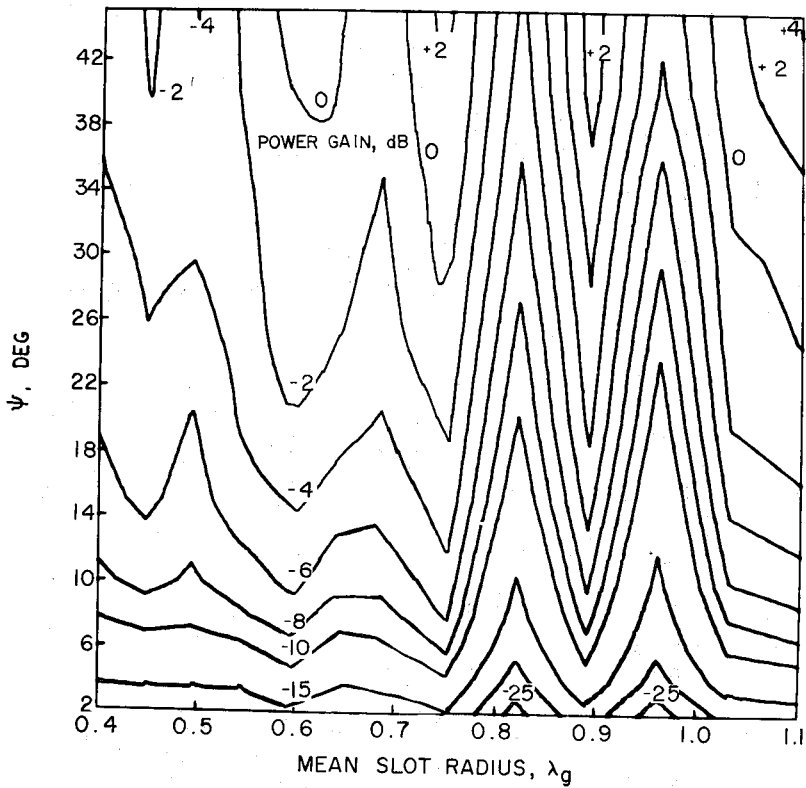
Figure 2. Power gain versus elevation angle and mean slot radius
for an annular slot antenna, buried 0. 33 m deep in re-
fractory concrete, which differs dimensionally from the
small annular slot shown in Figure 1 by a scale factor
between 1. 0 and 1. 5.

EXPERIMENTAL INVESTIGATION OF THE IMPEDANCE OF A HORIZONTAL LINEAR ANTENNA ABOVE A DISSIPATIVE HOMOGENEOUS EARTH[1]

Ahmed Abul-Kassem
S.W. Maley
David C. Chang
J.R. Wait

Department of Electrical Engineering
University of Colorado
Boulder, Colorado   80302

Introduction

An experimental study has been conducted of the influence of a dissipative earth on the characteristics of a horizontal linear antenna. The study was conducted in the laboratory at microwave frequencies using a simulated earth. One of the objectives of the investigation was an evaluation of the feasibility of using antenna impedance measurements to determine the electrical parameters of the earth. Previous investigations[1-6] have treated some aspects of this problem and have provided some data for comparison.

Experimental equipment

The laboratory equipment used in this investigation consisted of a tank containing material to simulate the earth. The material used was dry sand mixed with powdered graphite. The conductivity of the mixture was varied by varying the concentration of the graphite. The tank was 17 wavelengths square and 6-1/2 wavelengths deep. The frequency used throughout the investigation was 4.106 GHz. The tank was sufficiently large that it could be considered infinite without noticeable error. The tank was made of plywood on all sides except one vertical side which was an aluminum sheet used as a ground plane for the horizontal monopole antenna. The results of the measurements were monopole impedance but because of the symmetry they could be interpreted as dipole impedance after multiplication by two. The experimental equipment is sketched in Figure 1. The monopole was excited from a slotted coaxial line which was coupled to a 4.1666 GHz generator through an adjustable coupling with an associated short-circuiting plunger used to achieve impedance matching. A probe in the slotted section of coaxial line was used for impedance measurements. The length of the monopole and its height above the simulated earth were adjustable. The coaxial line exciting

the monopole measured 0.118 cm. radius for the inner con-
ductor and 0.320 for the inside radius of the outer con-
ductor. This resulted in a sufficiently small annular
aperture at the base of the antenna that the radiation
from the aperture was considered to effect the results
negligibly. The details of the impedance matching and
the measurement procedure are given by Abul-Kassem.[7]

Measurements

Several sets of preliminary measurements were made with
the laboratory equipment before the simulated earth was
put in place. In one case a non-reflecting absorber was
used in place of the simulated earth. The measurements
were then compared with the theoretical and experimental
impedances for antennas in free space. In another case a
metallic sheet was used in place of the simulated earth
and the impedance measurements were compared with theo-
retical and experimental results for an antenna over a per-
fectly conducting plane. These preliminary sets of mea-
surements produced results in reasonable agreement with
previous investigations thereby giving confidence in the
experimental equipment and measurement technique.[7]

Next antenna impedance measurements were made over a sim-
ulated earth. The electrical parameters of the simulated
earth were determined by placing the material in a long
(many wavelengths) section of C-band waveguide and mea-
suring the impedance using a slotted line. The electri-
cal parameters were then easily calculated from the mea-
sured impedance. The results for three mixtures of sand
and graphite are given in the table below.

	Conductivity	Dielectric Constant	Loss Tangent
mixture 1	0.17	3.30	0.22
mixture 2	0.28	4.18	0.29
mixture 3	0.68	6.25	0.47

Each of the numbers in the above table is an average of
a number of measurements.

Measurements were made of antenna impedance for the three
above mentioned mixtures of sand and graphite, for various
values of antenna length and for various values of height
above a simulated earth. Antenna admittance as a function
of antenna length, h, for a height, d, above the simulated
earth is shown in Fig. 2. These results show the impor-
tance of using an antenna of near resonant length. An-
tenna admittance as a function of height above the simu-
lated earth for an antenna of nearly resonant length is
shown in Fig. 3. These results show the importance of
placing the antenna close to the earth. Experiments for
longer lengths resulted in the curves for the different

mixtures being closer together and thus less effective
for the determination of the earth's parameters. A
monopole a quarter wavelength or slightly less in length
appears best suited to spread the curves apart and thus
best suited for probing the earth.

Conclusions

The results of the measurements indicate that the earth
has significant influence on the antenna impedance when
the antenna is near resonant length and when the antenna
is near the ground. Furthermore, if the antenna imped-
ance is measured when it is close to earth of unknown
electrical parameters, it is possible to determine the
parameters from the impedance. This appears to be a
practical method if the antenna is nearly of resonant
length and if the spacing between the antenna and ground
is not greater than about one-tenth wavelength.

The values of the earth's parameters resulting from such
measurements are weighted averages of the actual values
in the near vicinity of the antenna to a depth dependent
upon the frequency and the earth's conductivity.

References

1. Bhattacharyya, B. . (1963 IEEE Trans. AP-11,pp. 261-
    266).

2. Chang, D.C. and J.R. Wait (1970 IEEE Trans. AP-18,
    pp. 182-188).

3. Proctor, R.F. (1950 IEEE (London), 97, pp. 188-190).

4. Sommerfeld, A. and F. Renner (1942 Wireless Engineer
    19, pp. 351-359, 409-414, 457-462).

5. Wait, J.R. (1969 Antenna Theory, R.E. Collin and
    F.J. Zucker (editors), McGraw Hill, pp. 386-435.

6. Miller, E.K. et al. (1971 Analysis of Wire Antennas
    in the Presence of a Conducting Half-space, Lawrence
    Radiation Lab. Report, Pt. 1 and 2).

7. Abul-Kassem, Ahmed Said (Experimental Study of the
    Characteristics of a Horizontal Antenna Above a
    Dissipative Homogeneous Earth. M.S. Thesis,
    Electrical Engineering Dept., University of Colorado,
    1972).
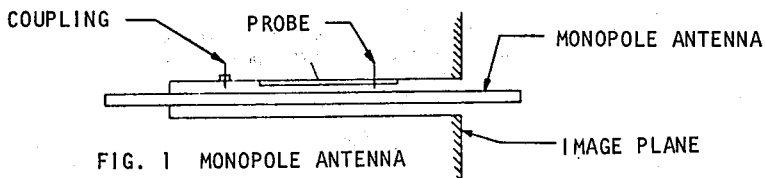
FIG. 1   MONOPOLE ANTENNA
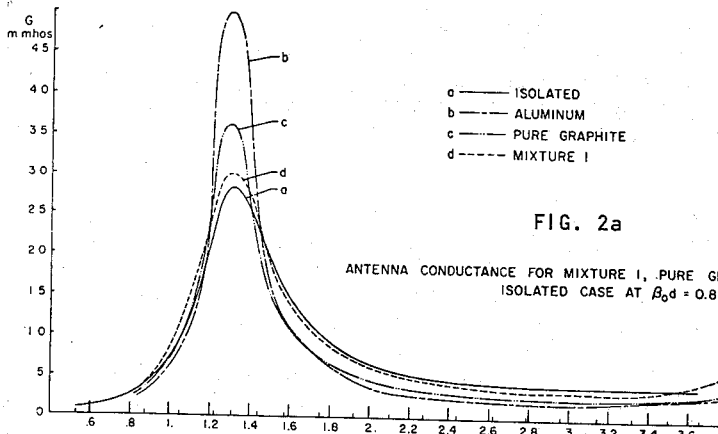
FIG. 2a

ANTENNA CONDUCTANCE FOR MIXTURE I, PURE GRAPHITE, ALUMINUM, AND ISOLATED CASE AT $\beta_o d = 0.88$.

a ——— ISOLATED
b ——— ALUMINUM
c ——— PURE GRAPHITE
d ——— MIXTURE I
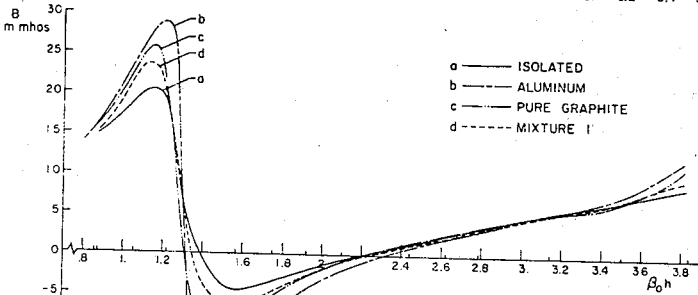
FIG. 2b

ANTENNA SUSEPTANCE FOR MIXTURE I, PURE GRAPHITE, ALUMINUM, AND ISOLATED CASE AT $\beta_o d = 0.88$.

a ——— ISOLATED
b ——— ALUMINUM
c ——— PURE GRAPHITE
d ——— MIXTURE I

G - CURVES

a ——— ALUMINUM
b ——— MIXTURE 3
c ——— MIXTURE 2
d ——— MIXTURE

B - CURVES
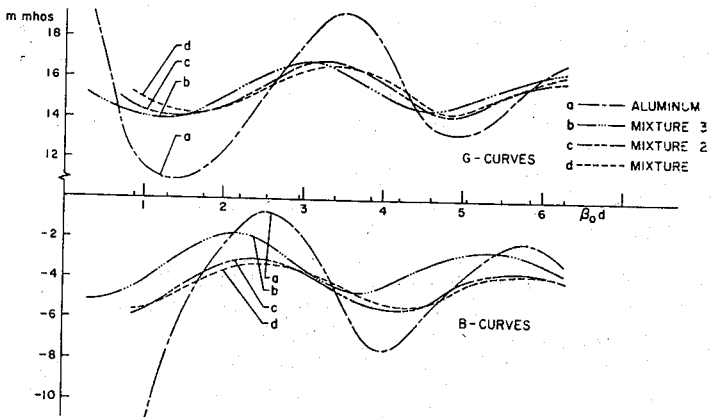
FIG. 3   ANTENNA ADMITTANCE FOR DIFFERENT MIXTURES AND PERFECT CONDUCTOR FOR $\beta_o h = 1.57 (h = \lambda/4)$.

UNI-MOMENT METHOD OF SOLVING ANTENNA
AND SCATTERING PROBLEMS

Kenneth K. Mei

Department of Electrical Engineering and Computer Sciences
and the Electronics Research Laboratory
University of California, Berkeley, California 94720

Summary

It has been shown by this investigator and numerous others
[1] [2] [3] that exterior boundary value problems involving
localized inhomogeneous media are most conveniently solved using
finite difference or finite element equations together with
harmonic expansions or integral equations which satisfy the
radiation condition. The coupled equations are partly full and
partly sparse. And, methods used to solve them, such as iteration
or banded matrix methods are not very successful. The "Uni-
moment Method" alleviates the difficulties by decoupling the
difference or finite element equations from the exterior problems.
This is done by solving the interior problems many times so
that N linearly independent solutions are generated. The
continuity conditions are then enforced by solving a much smaller
matrix. Two methods of generating solutions of interior
solutions are presented, namely, "the shooting method" and "the
Ricardi Transformation".

The shooting method is a fast and easy way to generate
solutions of wave equations in a closed region by assigning the
values of the potential on two adjacent rows in a finite difference
mesh. The five point difference equations then become a initial
value problem which can be solved by step marching. The method
is unstable and its use is limited to small dimension finite
difference region. However, where applicable the method is extremely
fast and most easy to implement.

The Ricardi Transformation involves transformation of the
wave equation into a Ricardi type differential equation which is
non-linear but also becomes an initial value problem. The step
marching solutions of the Ricardi Transformed equations are stable
and therefore may be used to solve larger dimension problems.
The method involves inversion of many small matrices, so it
requires somewhat more complex programming than the shooting method.

The Uni-moment method solves problems in inhomogeneous media
as easily as it does those in homogeneous media. In many cases,
excluding the thin wire problems, the Uni-moment method is found
to be faster than the conventional moment method in solving homog-
eneous problems.

Several results of antennas and scattering obtained by the Uni-moment Method will be discussed.

References

1. K. K. Mei, R. Stovall and D. Tremain (1971 URSI Meeting, p. 82).

2. P. Silvester and M. S. Hsieh (1971 Proc. Inst. Elec. Engr. 12, p. 1743).

3. B. H. McDonald and A. Wexler (1973 IEEE Trans. MTT, 12, p. 841).

A TECHNIQUE TO COMBINE THE GEOMETRICAL THEORY
OF DIFFRACTION AND THE MOMENT METHOD*

W.D. Burnside, C.L. Yu and R.J. Marhefka
The Ohio State University ElectroScience Laboratory
Department of Electrical Engineering
Columbus, Ohio 43212

Abstract - For many years, The Geometrical Theory of Difraction (GTD) has been applied to antenna and scattering problems for which the structure is large in terms of wavelength. GTD solutions have mainly been concerned with pattern computations with little information concerning antenna impedance and/or aperture distributions. This is especially true for wire-type antennas. On the other hand, The Method of Moment (MM) has been applied to such problems for which the structure is small in terms of wavelength. This paper presents a technique which can be used to combine these two solutions such that a whole host of new problems can be handled.

Summary - Morita[1] has shown that one can apply MM to infinite planar structures by first subtracting out the surface current density associated with the incident and reflected fields. Similarly, Tew and Tsai[2] have shown that one can use fewer current samples by first subtracting out the physical optics currents. However, both of these approaches still require a large number of current samples around the point of diffraction.

The following discussion illustrates how one can vastly reduce the number of current samples by including a diffraction current term which is based on GTD solutions. Consider the scattering by a simple wedge for a TE plane wave incident as shown in Fig. 1a. At the field point (ρ,ψ), the incident and reflected fields are easily computed using geometrical optics; whereas, the diffracted field is given by[3]

$$H_z^d = [v_B(\rho,\psi-\psi_0,n) + v_B(\rho,\psi+\psi_0,n)]$$

assuming the incident field is normalized at the wedge tip. If the field point is not in the vicinity of the shadow boundary $(\psi\pm\psi_0=180°)$, the diffracted field can be expressed by

$$H_z^d \simeq D(\psi,\psi_0,n)\ \frac{e^{-jk\rho}}{\sqrt{\rho}} \qquad \text{for } \rho > \lambda/4 \qquad ,$$

where D is a composite diffraction coefficient. Using this form, one can define a surface current density on the wedge as

(1) $\vec{J}^{GTD} = (\hat{n}{\times}\hat{z})[H_z^i + H_z^r + H_z^d] \simeq \vec{J}^i + \vec{J}^r + (\hat{n}{\times}\hat{z}) D \dfrac{e^{-jk\rho}}{\sqrt{\rho}}$

for $\rho > \lambda/4$. Note that D is, now, assumed to be an unknown constant. Of course, D is known using GTD, but it will be shown that one can solve for D using MM simply by knowing the form of the diffraction current. Once this is verified, the approach can be extended to a whole host of new problems where the diffraction coefficients are not known at the outset.

As presented by Harrington[4], the H-field integral equation is given by

$$J = - \left[H_z^i + \hat{z} \cdot \nabla \times \int_C J \; \frac{H_0^{(2)}(k|\rho-\rho'|)}{4j} \; d\vec{\ell}' \right]$$

where C is the perfectly conducting surface over which one wishes to find the total surface current density (J). Considering the 90° wedge structure of Fig. 1b, the total surface current density can be defined by

$$J = \begin{cases} J_y^{GTD} & y_c \leq y \leq \infty \\ J_y^{MM} & 0 \leq y < y_c \\ J_x^{MM} & 0 \leq x < x_c \\ J_x^{GTD} & x_c \leq x \leq \infty \end{cases}$$

where J^{GTD} is defined by Eq. (1) which is only valid away from the diffraction edge. The Moment Method current (J^{MM}) around the edge can be defined by simple basis functions such as

$$J^{MM} = \sum_{n=1}^{N} \alpha_n \; P_n(\ell-\ell_n) \qquad ,$$

where $P_n(\ell-\ell_n)$ are orthogonal pulse functions with weight α_n. By applying a point matching technique at the midpoint of each of the N pulse current segments, one obtains[4]

(2) $L_n(J) = \sum_{m=1}^{N} \ell_{mn} \; \alpha_m + L_n(J_y^{GTD}) + L_n(J_x^{GTD}) = g_n$ for $1 \leq n \leq N$,

where

$$\ell_{mn} = \begin{cases} \hat{z} \cdot \nabla \times \int_{d\ell_m} \dfrac{H_0^{(2)}(k|\rho_n-\rho_m|)}{4j} \; d\vec{\ell}' & \text{for } m{\neq}n \\ 1/2 & \text{for } m{=}n \end{cases}$$

$$g_n = - H_z^i(x_n, y_n)$$

$$L_n(J^{GTD}) = J^{GTD} + \hat{z} \cdot \nabla \times \int_{C_{GTD}} J^{GTD} \frac{H_o^{(2)}(k|\rho_n - \rho|)}{4j} d\vec{\ell}'$$

Substituting Eq. (1) into Eq. (2) one finds that

$$(3) \quad \sum_{m=1}^{N} \ell_{mn} \alpha_m + L_n(J_x^i + J_x^r + D_x \frac{e^{-jkx}}{\sqrt{x}}) +$$

$$+ L_n(J_y^i + J_y^r + D_y \frac{e^{-jky}}{\sqrt{y}}) = g_n \quad \text{for } 1 \le n \le N .$$

Since the incident and reflected currents (J^i and J^r) are known, one can transfer them to the source side. In addition, since the operator (L_n) is linear and with D_x and D_y being complex constants, one obtains N equations given by

$$(4) \quad \sum_{m=1}^{N} \ell_{mn} \alpha_m + D_x L_n (\frac{e^{-jkx}}{\sqrt{x}}) + D_y L_n (\frac{e^{-jky}}{\sqrt{y}}) = g_n' \quad \text{for } 1 \le n \le N$$

where

$$g_n' = - H_z^i(x_n, y_n) - L_n(J_x^i + J_x^r) - L_n(J_y^i + J_y^r) .$$

By introducing two additional matching points in the GTD current region as shown in Fig. 1b, one obtains two additional equations using Eq. (4). This provides the necessary linear equations to solve for the N+2 unknowns [N current pulse functions (α_n's) plus two diffraction constants (D_x and D_y)]. This system of simultaneous linear equations can be easily solved using numerical matrix inversion techniques.

A comparison of the total surface current density along the x wall of Fig. 1b between the above approach and the exact solution is shown in Fig. 2. Just four current samples were used around the edge for these calculations plus two unknown diffraction constants. Thus, only 6 unknowns were found to successfully predict the total surface current density on an infinite wedge structure.

The oral presentation will, also, include the effects of variations in the various parameters, a means of computing the diffraction surface current density around the shadow boundary, a similar solution obtained for curved surfaces by applying GTD current forms, and comparison of results for several problems using various techniques.

REFERENCES

1. N. Morita (1971, IEEE Trans., AP-19, p. 358).
2. M.D. Tew and L.L. Tsai (1972, GAP, Int. Sym.).
3. P.M. Russo, R.C. Rudduck, and L. Peters (1965, IEEE Trans., p. 219).
4. R.F. Harrington (1968, Field Computation by Moment Methods, MacMillan).
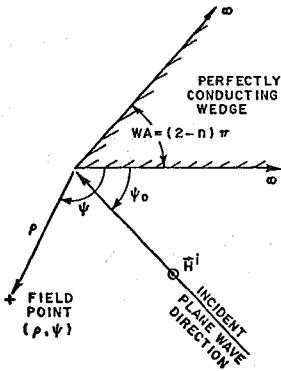
Fig. 1a. Basic wedge geometry.
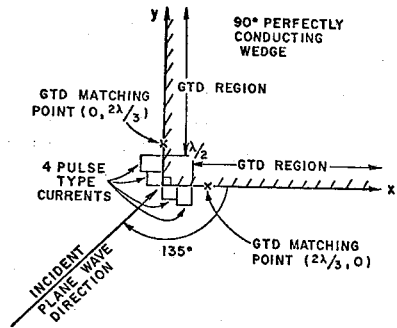
Fig. 1b. Geometry of wedge problem applied to compute currents of Fig. 2.
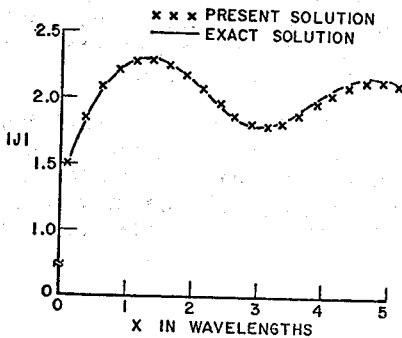
Fig. 2a. Magnitude of surface current density.
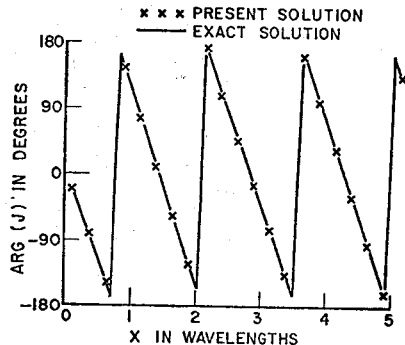
Fig. 2b. Phase of surface current density.

A NEW METHOD FOR COMBINING MOMENT METHODS
WITH THE GEOMETRICAL THEORY OF DIFFRACTION

Gary A. Thiele and Thomas Newhouse, The Ohio
State University ElectroScience Laboratory,
Dept. of Electrical Engineering, Columbus, Ohio

In recent years the analysis of antennas and antennas on metallic
bodies wherein the body is not large in terms of the wavelength
has been greatly facilitated by advances in the solution of inte-
gral equation formulations via the method of moments. Such tech-
niques may be referred to as low frequency methods. They are
limited only by computer storage as to the size of structure that
may be analyzed. On the other hand, the geometrical theory of
diffraction (GTD) is best suited to structures that are arbitrarily
large in terms of the wavelength. However, direct calculation of
the impedance of a wire antenna on a large finite structure, for
example, is not practical with GTD alone.

To combine these two techniques, we have considered the problem of
a monopole near a conducting wedge although any other wire antenna
of arbitrary configuration could readily be used. The problem may
be described in the usual matrix formulation $[Z']$ $(I) = (V)$ where,
however, $[Z']$ is a generalized impedance matrix modified by the
energy diffracted by the wedge. For example, if Z_{ij} represents the
field at segment j due to segment i, then Z'_{ij} represents that field
plus the field from segment i diffracted to segment j by the wedge.
Solution of the matrix equation yields the currents on the monopole
in the presence of the wedge and thus the impedance is obtained
directly. Far-field patterns are then obtained by appropriately
summing the field from the monopole and that diffracted by the wedge.
Experimentally confirmed results will be presented.

Session 34 Numerical Methods (2)

NUMERICAL SOLUTION OF SCATTERING PROBLEMS –
AN ALTERNATIVE TO THE MOMENT METHOD

Louise Jones and R. E. Kleinman
University of Delaware

The present paper describes a new integral equation for
scattering problems which provides the basis for numerical solution
by direct iteration. The Neumann problem for the field exterior
to a smooth closed finite surface for the three dimensional Helmholtz
equation is considered. A Fredholm integral equation of the second
kind for the unknown field on the surface is derived as the contin-
uous limit of a representation of the field in the exterior domain.
This equation differs from the commonly employed form in that the
singularity in the kernel is cancelled and the solution may be
obtained by straightforward iteration. The convergence of the
Neumann series is proven for sufficiently small k for all convex
scatterers. The iteration procedure has been programmed for rota-
tionally symmetric scatterers with plane wave incidence along the
axis of symmetry. The resultant surface field was then used to
compute the backscattering cross section. Results have been ob-
tained for spheres, prolate and oblate spheroids and cone spheres.
A remarkable feature of these results is that they remain valid
for frequencies beyond the radius of convergence of the low fre-
quency expansion. The computed cross sections of spheres agreed
with the exact results for values of ka $\leq$ 2.6 (and possibly
higher) while the low frequency expansion diverges for $|ka| > 1$.
Similar results were observed for those prolate spheroids for
which exact answers are available where again the computed values
remain accurate deep into the resonance region. The speed and
economy of the computation suggest that this method may be pre-
ferable to the moment method for numerical solution of scattering
problems in the resonance region.

THE MOMENT METHOD AS A PERTURBATION TECHNIQUE
IN ELECTROMAGNETIC PROBLEMS

Y. L. Chow and D. P. S. Seth
Electrical Engineering Department
University of Waterloo, Waterloo, Ontario (Canada)

For many applications of the moment method, the boundary condition
is matched on all surfaces with little consideration of the a priori
information. When the structure under study can be interpreted as
a perturbation of another structure for which an accurate solution
exists, the a priori solution of the latter structure can be used to
improve the convergence of the moment method solution of the former.
In other words, the moment method becomes a perturbation technique.

As examples, the perturbation technique is applied to a disc-loaded
tubular dipole and a solid cylindrical dipole. As seen in Fig. 1
they both are perturbations of the tubular dipole for which the
accurate King-Sandler solution [1] is available. For either
example, a 10x10 matrix is needed giving a current accuracy of 0.5%,
while at least a 20x20 matrix is needed on a regular application
of the moment method. Similar fast convergence is also reported
by Tew and Tsai [2] in a simpler problem of TM scattering by a
finite strip.

Unlike Tew and Tsai, we formulate the perturbation technique in
a general manner. With the general formulation, it is clear how
perturbation technique is to be applied not only to the dipole
examples but other electromagnetic problems of any excitation.

For the general formulation, let us assume that the moment method
is to be used to solve the following scalar equation

$$\tilde{L}_p J_p = E_p \tag{1}$$

where $\tilde{L}_p$ is an integral operator, including the Green's function,
integrating an unknown current component J_p over the surface of the
"perturbed" structure p to cancel the tangential excitation $(-E_p)$.
For the two perturbed examples in Fig. 1 we may identify J_p as
the longitudinal current along the tubular sections, and the
radial current on the disc or the solid end.

Let us assume another equation

$$\tilde{L}_c J_c = E_c \tag{2}$$

where $\tilde{L}_c$ is the same integral operator but integrating the a priori solution over the "unperturbed" structure c to cancel the tangential excitation $(-E_c)$. We may identify the structure c to the equivalent tubular dipole in Fig. 1.

As shown in Fig. 1 we divide the surfaces p and c into unperturbed region 1, to-be-deleted region 2 and the added (perturbed) region 3. We may define the restricted operators as

$$\tilde{L}_c = \tilde{L}_1 + \tilde{L}_2 \tag{3}$$

and

$$\tilde{L}_p = \tilde{L}_1 + \tilde{L}_3 \tag{4}$$

where $\tilde{L}_1$ integrates over only region 1 and similarly $\tilde{L}_2$ and $\tilde{L}_3$. We may also define the restricted parameters which have values on their own region and identically zero elsewhere. That is

$$J_c = J_1 + J_2, \quad E_c = E_1 + E_2 \tag{5}$$

and

$$J_p = J_1 + J_1^\dagger + J_3^\dagger \ , \quad E_p = E_1 + E_3 \quad . \tag{6}$$

It is observed in the above that in the presence of the extra tangential excitation $(-E_3)$ there is a small perturbed $J_1^\dagger$ in addition to the unperturbed J_1 on region 1. There is also a small perturbed $J_3^\dagger$ on region 3 where the current is zero before.

With the substitution of the restricted (5) and (3) into the known (2) we can express conveniently, without cross terms,

$$\tilde{L}_1 J_1 + \tilde{L}_2 J_2 = E_1 + E_2 \tag{7}$$

resembling the $\nabla.\vec{E}$ operation in Cartesian coordinates. Similarly with (6) and (4) substituted into unknown (1), we get

$$\tilde{L}_1(J_1 + J_1^\dagger) + \tilde{L}_3 J_3^\dagger = E_1 + E_3 \tag{8}$$

We now define two corresponding weighting function sets W_{1m} and W_{3m} with indices m. Taking the inner product of both W_{1m} and W_{3m} to (8) we get

$$<W_{1m}[\tilde{L}_1(J_1 + J_1^\dagger) + \tilde{L}_3 J_3^\dagger]> = <W_{1m}E_1> \tag{9}$$

$$<W_{3m}[\tilde{L}_1(J_1 + J_1^\dagger) + \tilde{L}_3 J_3^\dagger]> = <W_{3m}E_3> \ . \tag{10}$$

260

with two cross terms between different restricted W and g dropped
to zero. Taking the inner product of W_{1m} alone to (7), we get

$$<W_{1m} \tilde{L}_1 J_1 + W_{1m} \tilde{L}_2 J_2> = <W_{1m} \ \tilde{E}_1> \tag{11}$$

With (11) subtracted from (9), together with the rearranged (10),
we get the reduced pair,

$$<W_{1m} \tilde{L}_1 J_1^\dagger> + <W_{1m} \tilde{L}_3 J_3^\dagger> = <W_{1m} \tilde{L}_2 J_2> \tag{12}$$

$$<W_{3m} \tilde{L}_1 J_1^\dagger> + <W_{3m} \tilde{L}_3 J_3^\dagger> = <W_{3m} E_3> - <W_{3m} \tilde{L}_1 J_1> \tag{13}$$

where all the terms on the right-hand sides are known, and the
unknowns at the left are the small perturbed $J_1^\dagger$ and $J_3^\dagger$. With the a
priori known J_1 in (11) subtracted, the moment method matrix from
(12) and (13) is found to be faster convergent in this study, as
well as by Tew and Tsai [2].

The physical interpretation of the inner product $<W_{1m} \tilde{L}_2 J_2>$ is that
it is the weighted electric field effect on region 1 due to the
current J_2. Evidently therefore (12) indicates that on region 1,
the missing effect due to the deleted region 2 must be compensated
by the extra effects introduced by the perturbed currents $J_1^\dagger$ and $J_3^\dagger$
As both $J_1^\dagger$ and $J_3^\dagger$ are usually evanescent, their distribution, as
well as effects, are highly localized. Hence the inner products
$<W_{1m} \tilde{L}_1 J_1^\dagger>$ and $<W_{1m} \tilde{L}_3 J_3^\dagger>$ need not be integrated over the whole
region 1 but only its smaller evanescent region. This reduces
the matrix size and further improve the convergence.

The physical interpretations of the inner products in (13) are
similar. Therefore it is evident that the pertubation technique
can be applied not only to the dipole problems but to any other
problems for which an equivalent "unperturbed" structure of known
solutions can be found.

For the perturbation technique formulated in (12) and (13), an equiva-
lent "unperturbed" structure is to be such that the unperturbed,
deleted and added regions 1, 2 and 3, can be defined.

References:

1. R. W. P. King, R. B. Mack and S. S. Sandler (Arrays of
    Cylindrical Dipoles, New York: Cambridge University Press,
    1968).

2. M. D. Tew and L. L. Tsai (A method toward improved convergence
    of moment method solutions, 1972 Proceedings IEEE, p. 1436).

RADIUS a

c

TUBULAR DIPOLE
(UNPERTURBED GEOMETRY)

(a)

② ③ ①

RADIUS a

DISC RADIUS
= 2a

p

ANNULAR DISC LOADED
TUBULAR DIPOLE

(b)

③ ② ①

RADIUS a

p

Δh

2h

Δh

SOLID DIPOLE WITH
FLAT ENDS

(c)
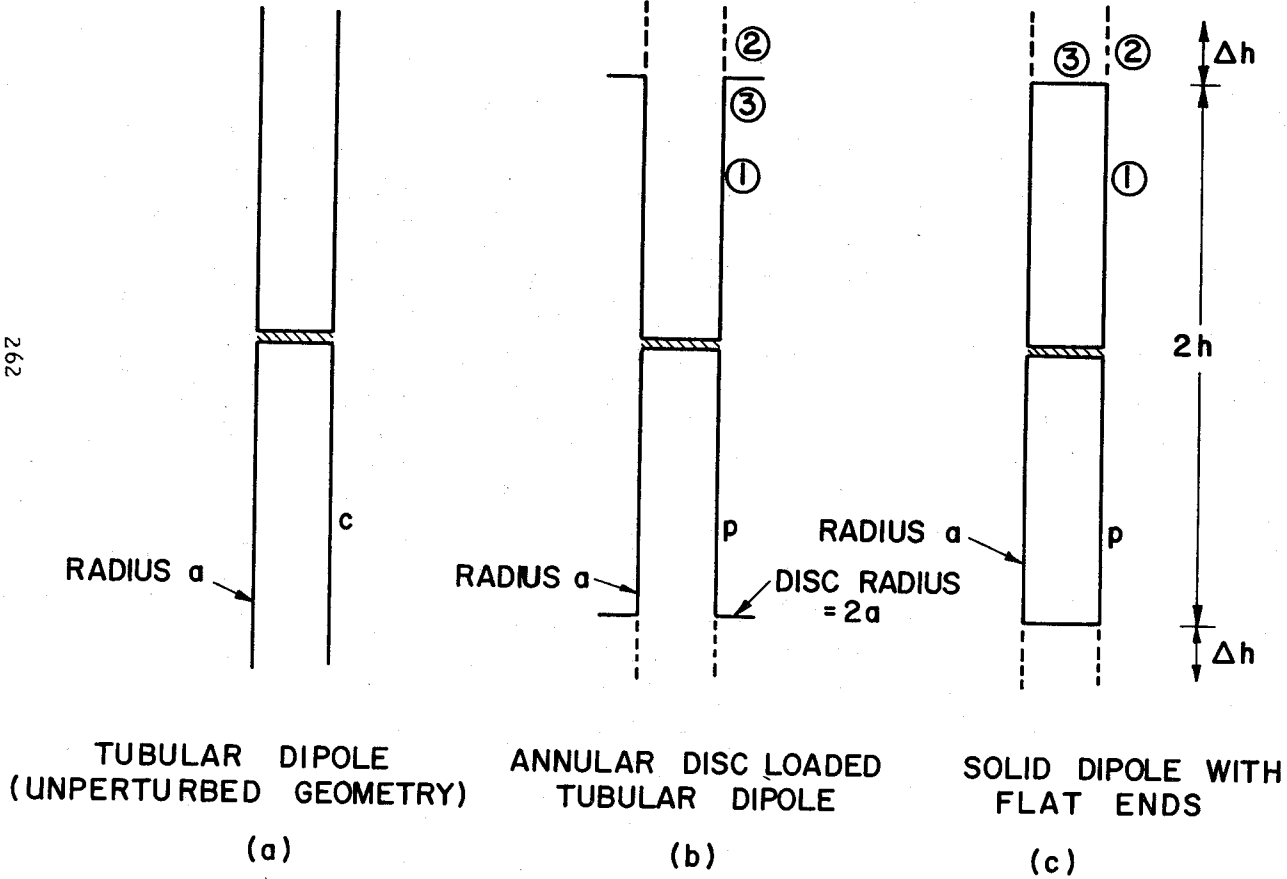
FIGURE 1

PROPOSED NUMERICAL SOLUTION FOR THE

EM RADIATION AND SCATTERING PROBLEMS

By J. Perini

Syracuse University
Syracuse, New York

SUMMARY

Introduction – The method of moments [1], [2] has been widely
used in the solution of electromagnetic scattering and radiation
problems for the past several years. Because of the required
matrix inversion in its implementation, the method can only be
applied to problems of a few wavelengths in size. Because of
the nature of the known matrix inversion techniques of today,
it is difficult to take advantage of any redundancies that
occur in the matrix elements except for those due to some
geometrical symmetry. Usually the amount of programming
required to take advantage of redundancies in general offsets
the accrued space savings for the variables.

In this presentation I propose to solve the same class of
problems using a technique based on optimization theory that I
believe has demonstrated through problems already solved, a
promise of substantial savings on fast access computer memory
(core) requirements. The price paid, at this state, is an
increase in running time. There are indicators, however, that
one order of magnitude improvement is within reach, putting
this technique side-by-side with the method of moments, as far
as running times are concerned.

The Technique – It is well known [1] that scattering and
radiation problems can be reduced to an integral equation. To
simplify our presentation, let us assume that the scatterer is
a straight perfectly conducting wire. If x is the coordinate
along the length L of the wire, we can write

$$-E_t^i(x) = \int_0^L I(x')K_1(x,x')dx' \tag{1}$$

where $K_1(x,x')$ is the known Green's Function and E_t^i is the
tangential component of the incident field on the wire surface.
Let us now approximate $I(x')$ by a series of "pulse" functions
$p(x)$ defined in the following way

$$p(x) = 1 \qquad -\frac{\Delta x}{2} < x < \frac{\Delta x}{2}$$

$$= 0 \qquad \text{otherwise} \tag{2}$$

If the length $(0,L)$ is divided in N intervals of length Δx and if $I_n = I(n\Delta x) = I(x_n)$, $n = o,1,2,...N$, we can write

$$I(x) \overset{\sim}{=} \sum_{n=0}^{N} I_n p(x-x_n) = \sum_{n=1}^{N-1} I_n p(x-x_n) \tag{3}$$

The last summation takes already into consideration the usual boundary condition $I(0) = I(L) = 0$. If (3) is substituted in (1) and the integration carried out, we have

$$-E_t^i(x_k) = \sum_{n=1}^{N-1} I_n K(x_k,x_n) = \sum_{n=1}^{N-1} I_n K_{k,n} \tag{4}$$

where $K(x_k,x_n) = K_{k,n}$ is the result of the indicated integration on K_1 in (1). This is now a linear equation in the N-1 unknowns I_n. Instead of writing equation (4) for the N-1 points x_k as done in the method of moments, we choose to define an error function e in the following way:

$$e = \sum_{k=1}^{N-1} e_k = \sum_{k=1}^{N-1} \left| E_i^t(x_k) + \sum_{n=1}^{N-1} I_n K_{k,n} \right|^2 \tag{5}$$

e is proportional to the mean square of the error in matching the boundary conditions due to the present approximations. The solution of the problem is the set of values $I_n(n=1,2,3,...N-1)$ that minimizes (5). It is easily seen that e is quadratic in I_n and therefore a unique minimum will exist. The techniques used to find this minimum are the subject of optimization theory [3]. One of the most obvious procedures to apply to the problem is the steepest descent which consists of successive steps in the direction opposite to the gradient until the "bottom of the valley" is found. The most successful technique used so far in this problem is called Continued PARTAN [3], which has improved the running time over the steepest descent by at least one order of magnitude. There is no room in this presentation to discuss the merits and details of these different techniques. For those interested, I highly recommend references [3] and [4]. An examination of (5) will show some of the advantages of this method over the matrix inversion techniques:

a) The elements $K_{k,n}$ have to be stored in an (N-1) x (N-1) array if a matrix inversion is contemplated. If we are willing to recompute these elements every time that we need them, the present technique will require only an array (N-1) x 1 in size. Therefore, a (N-1) improvement factor in core requirements has been achieved over the matrix inversion technique. When reciprocity applies, only approximately half of the $K_{k,n}$ have to be stored; but the fact that they are complex numbers doubles the total number of terms to be stored again.

b) If any redundancies on $K_{k,n}$ occur either due to symmetries or just by coincidence, schemes can be developed to take advantage of this in further reducing the (N-1) x 1 array

size. Since $K_{k,n}$ is really a function of the distance between X_k and X_n many terms of $K_{k,n}$ are redundant.

c) Because the function $K_{k,n}$ decreases rapidly with the increase of the distance between X_k and X_n and then oscillates between small values, $K_{k,n}$ can be considered constant over large numbers of Δx's introducing further redundancies in the problem.

These three points have only been explored on the surface and should receive much more attention if the full potentialities of this method are to be realized.

One aspect of the present formulation which is worth mentioning is derived from the quadratic behavior of e and is the following. In all the search methods for the minimum of e, a so-called one dimensional search has to be performed at almost every step. This is a time-consuming procedure which is totally avoided here, since the one dimensional search is reduced to finding the minimum of a quadratic $y = at^2 + bt + c$ on which all the coefficients are a function of the known parameters of the problem [5]. A direct calculation rather than a search is performed with the consequent savings in running time.

A last point which can be taken advantage by both methods is to change the computation procedures for $K_{k,n}$ [1] to more efficient methods such as the near field of a wire antenna with assumed sinusoidal current distribution [6]. If the antenna is short enough, this is the same as a triangular pulse. Reductions on the computation time of the $K_{k,n}$ by a factor of over ten have been reported.

Comparative Results - Tables I and II show comparison runs between the method of moments and the optimization technique proposed here. Note the advantage of this method when the number of segments is large. Note also how the core requirements increase for each method. Due to the continued PARTAN technique used here, we required a (N-1) x 7 matrix instead of (N-1) x 1.

The running times are still high. Work in this area is progressing at this time. It is possible to show that if the initial guess for a run with 2N segments can be obtained by interpolating the results from a run with N segments and if the run with 2N segments converges in $\frac{2N}{k}$ iterations then an improvement of approximately k times in the running time can be achieved. There are reasons to believe so far that k=10 is a realizable figure.

Conclusions - From the results of Tables I and II, it is obvious that this technique has great potential in reducing the core requirements to solve scattering and radiation problems. The running time is still high but I believe it is a price one is glad to pay when the alternative is that of not to being able to solve the problem at all. Further work is this area will very probably bring the running times within more attractive limits.

TABLE I

Single Straight Conductors Normally Excited By a Plane Wave

(Hirasawa, Stewart)

Number Wavelengths	Number of Segments	Core K Required	Exec Time	Number Iterations
.5	10	10	.0009	13
.5	10	9	.0004	Moments
1.	20	10	.0023	23
1.	20	9	.0006	Moments
2.	40	10	.0148	55
2.	40	11	.0019	Moments
5.	100	11	.3568	227
5.	100	28	.0225	Moments

TABLE II

Scattering Involving Multiple Conductors

(Hirasawa, Stewart)

Number Conductors	Configuration	Conductor Length	Total # Segments	Core K Required	Exec Time	Number Iterations
4	In Line	2 λ	80	11	.0605	51
4	In Line	2 λ	80	20	.0107	Moments
4	Parallelogram	2 λ	80	11	.0862	73
4	Parallelogram	2 λ	80	20	.0111	Moments
2	.5 λ Spacing	2 λ	40	10	.0115	52
2	.5 λ Spacing	2 λ	40	11	.0019	Moments
2	.5 λ Spacing	2 λ	100	10	.0961	74
2	.5 λ Spacing	2 λ	100	28	.0226	Moments
2	.5 Spacing	4 λ	200	12	1.23	192
2	.5 Spacing	4 λ	200	85	.173	Moments

References

[1]   R. F. Harrington (1968, "Field Computation by Moment Methods",
      McMillan).
[2]   R. L. Tanner, M. G. Andreasen (1967, IEEE Spectrum, V4,9, p. 53).
[3]   D. A. Pierre (1969, "Optimization Theory with Applications," Wiley).
[4]   A. Leon (1966, "A Comparison Among Eight Known Optimization
      Procedures", p. 23-46 of "Recent Advances in Optimization
      Techniques", T. P. Vogl and A. Levi (Editors) Wiley).
[5]   J. Perini, J. R. Stewart (1972, "Solution of the Scattering by
      Wires and the Conformal Array Problem by Optimization Techniques",
      22nd Symposium WPAFB).
[6]   D. C. Jordan, K. G. Balmain (1968, "Electromagnetic Waves and
      Radiating Systems, p. 333).

PATTERN SYNTHESIS BASED ON OPTIMIZATION
IN A PROBABILISTIC SENSE

Y. T. Lo and W. F. Richards
Electromagnetics Laboratory
University of Illinois, Urbana, Illinois

The precision with which a pattern $f(\theta,\phi)$ approximates a desired pattern $g(\theta,\phi)$ can be measured by $\varepsilon = \| g - f \|^2$. As a purely mathematical problem, it appears [1,2] that given a finite aperture, for any g, ε can be made arbitrarily small by choosing an appropriate excitation. Unfortunately, it also appears [2,3] that large, highly oscillatory excitations may be required if too much precision is demanded. Such ill-behaved excitations give rise to high ohmic losses and narrow bandwidth. Moreover, since the nominal or design excitations can never be realized with absolute precision, the pattern actually produced may bear little resemblance to that which was sought. For the case of arrays with a finite number of elements in a fixed geometry, in general, ε cannot be made arbitrarily small. Nevertheless, the excitation which minimizes ε may have the same undesirable properties described above. To avoid impractical solutions, techniques have been developed [3,4] to obtain excitations which minimize ε (or some other performance index) subject to a constraint on some sensitivity parameter (superdirectivity or Q) which indicates the relationship of the design to errors. A regularization method which achieves this has been described [5]. These methods do yield practical solutions to the synthesis problem, but the sensitivity parameters are somewhat artificial and their specific values are difficult to assign. A fresh approach to this problem is to accept that the excitation can never be realized precisely, but will always have some <u>random</u> error. The performance index ε becomes a random variable which can be "minimized" in some <u>probabilistic</u> sense with respect to the <u>nominal</u> excitation if the statistical nature of the errors is known. After a nominal excitation is obtained, the probability distribution for the performance index can be calculated. A synthesis method which uses this approach for the case of discrete arrays is outlined below.

All quantities denoted by $(\tilde{\cdot})$ are random. The pattern for an array is $\tilde{f} = \tilde{J}^t V$ where $\tilde{J} = J + \delta J$ is the total random excitation column vector, J is the nominal excitation vector, δJ is the error vector, and V is a column vector whose components are the element patterns. (The $(\cdot)^t$ denotes transposition while $(\cdot)^\dagger$ denotes conjugate transposition.) The ε is expressed by means of the metric $\| \cdot \| = \left[\int | \cdot |^2 \, w d\Omega \right]^{1/2}$ where $d\Omega$ is the element of solid angle, $w(\theta,\phi)$ is a positive weighting function, and the integral is over all directions. The nominal and random performance indices are respectively $\varepsilon = \| g - f \|^2$ and $\tilde{\varepsilon} = \| g - \tilde{f} \|^2$. The random variable $\tilde{\varepsilon}$ must be "minimized" in some probabilistic sense. The minimization of its mean $\bar{\varepsilon}$ is an example. Of course, to evaluate $\bar{\varepsilon}$, some of the statistical properties of δJ must be known. Therefore, the errors are assumed to obey the general first-order model $\delta J = A + RJ$ where

the random column vector $\tilde{A}$ represents the "absolute" error and the random square matrix $\tilde{R}$ represents the "relative" error. It can be shown that $\overline{\varepsilon} = \varepsilon + J^\dagger K_2 J + 2\text{Re}\{J^\dagger K_1\} + K_0$ where the K's are given by simple formulas in terms of the first and second moments of elements of $\tilde{A}$ and $\tilde{R}$, and by the properties of the array and g as embodied in the matrix $G = \int VV^\dagger \, wd\Omega$ and the vector $C^\dagger = \int gV^\dagger \, wd\Omega$. The minimum of $\overline{\varepsilon}$ is achieved by a nominal excitation of $J = (G + K_2)^{-1}(C - K_1)$. The form of $\overline{\varepsilon}$ is a generalization of the performance index used in other regularization methods. Here the choice of the regularization "parameter" is more direct.

Optimization schemes exist which exploit other attributes of the distribution function of $\tilde{\varepsilon}$ besides its mean. An excitation which is "optimum" in one scheme may not be "optimum" in another. Therefore, to fully evaluate the merit of any nominal excitation, the distribution function of $\tilde{\varepsilon}$ should be computed. To do this, $\tilde{\varepsilon}$ is written equivalently as $\tilde{\varepsilon} = \tilde{x}^\dagger G\tilde{x} + \varepsilon_0$, where $\tilde{x} = J - J_0 + \delta\tilde{J}$ and ε_0 is the minimum of ε achieved by $J_0 = G^{-1}C$. Assuming the components of δJ are jointly normally distributed, $\tilde{\varepsilon}$ can be expressed by a linear transformation as $\tilde{\varepsilon} = \tilde{Y}^\dagger\tilde{Y} + \varepsilon_0$, where the components of $\tilde{Y}$ are independent and normally distributed. Thus, $\tilde{\varepsilon}$ has a generalized non-central χ^2 distribution which can be asymptotically evaluated by an Edgeworth series [6].

The method described was applied to a planar array of the form shown in Figure 1. The elements were vertical monopoles over a ground plane. The array consisted of ten concentric rings of radii $\rho_K = 1/4(K - 2/\pi) - 1/2\pi \ (1/2)10^{-K}$ wavelengths (K = 1, 2, . . . , 10). Each ring consisted of twenty equispaced, identically excited elements. The desired pattern was uniform in azimuth with a variation in elevation as shown in the polar plot in Figure 2.

The errors were assumed to obey the probability law described by $\tilde{A} = 0$ with probability 1, $\tilde{R}$ a diagonal matrix whose elements were independent random complex numbers with a Gaussian distribution of zero mean and standard deviation of 0.05. For these statistics, the nominal excitation J_1 that minimizes $\overline{\varepsilon}$ was computed. For comparison J_0 was computed and its E-plane pattern in the $\phi = 0$ plane is shown in the polar plot in Figure 3. The corresponding pattern for J_1 is shown in Figure 4. (The H-plane patterns were nearly uniform in azimuth.) The nominal and mean performance indices, ε and $\overline{\varepsilon}$, were computed for both nominal excitations. Expressed as a percentage of $\| g \|^2$, they are: for J_0, $\varepsilon = 0.059\%$, $\overline{\varepsilon} = 390\%$; for J_1, $\varepsilon = 0.132\%$, $\overline{\varepsilon} = 0.318\%$. As seen from Figures 3 and 4 and as indicated by the values of the nominal ε's, there is a slight degradation in the <u>nominal</u> pattern of J_1 from the <u>nominal</u> pattern of J_0. However, the thousandfold decrease in $\overline{\varepsilon}$ from the J_0 to the J_1 solutions dramatically shows that the latter is the more practical design. In fact, a number of excitations corresponding to J_0 were randomly generated according to the assumed statistics. In no case did the pattern obtained even remotely resemble the desired pattern. The same was done for J_1, but in this case, all the patterns generated were very nearly the same as the nominal pattern of Figure 4.

The probability distribution function for $\tilde{\varepsilon}$ with nominal excitation J_1 was also computed and compared with Monte Carlo simulation of 100 samples. The result in Figure 5 shows good agreement between simulation and the Edgeworth series computation.

In conclusion, it is claimed that, since the actual excitation that will be realized can only be known a priori in terms of probabilities, the synthesis problem should be approached from this viewpoint. Such an approach, which minimizes the mean of a random performance index, has been described for an array. It can easily be extended to continuous aperture antennas.

1. G. W. Bouwkamp and N. G. DeBruij (1945 Philip Research Reports 1, p. 135).
2. P. M. Woodward and J. D. Dawson (1948 J. Inst. Elec. Engrs. (London) Part 3, 95, p. 363).
3. D. R. Rhodes (1963 IEEE Trans. AP-11, 4, p. 440).
4. Y. T. Lo, S. W. Lee, and Q. H. Lee (1966 Proc. IEEE 54, 3, p, 268).
5. G. A. Deschamps and H. S. Cabayan (1972 IEEE Trans. AP-20, 3, p. 268).
6. H. Cramer (Mathematical Methods of Statistics, 1945, Princeton, N.J., Princeton University Press, p. 221).
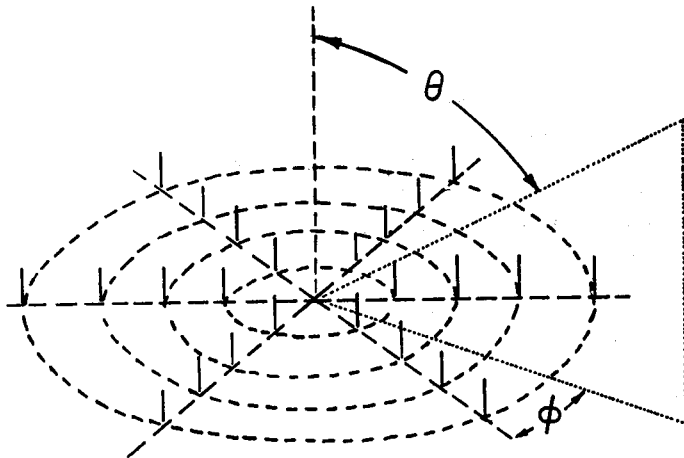
Figure 1. General form of array geometry.
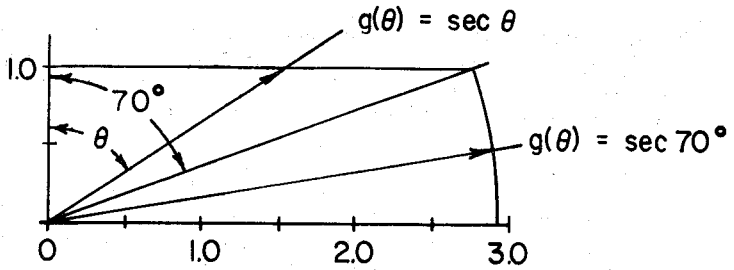
Figure 2.   Polar plot of E-plane variation
of desired pattern.

Figure 3.   Nominal pattern corresponding to the
excitation which minimizes ε.
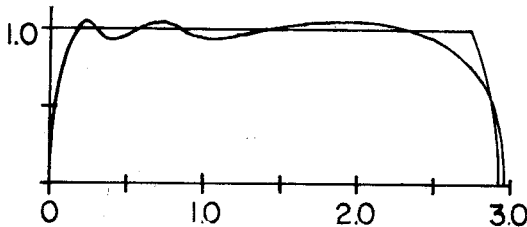
Figure 4.   Nominal pattern corresponding to the
excitation which minimizes $\bar{\varepsilon}$.

PROBABILITY $(\tilde{\varepsilon} < \varepsilon)$

Figure 5.   Probability distribution of $\tilde{\varepsilon}$ calculated by the
Edgeworth series and by simulation.

270

THE NUMERICAL SOLUTION OF SCATTERING PROBLEMS*
IN THE VICINITY OF INTERIOR RESONANT FREQUENCY

C. A. Klein and R. Mittra
Electromagnetics Laboratory
University of Illinois
Urbana, Illinois 61801

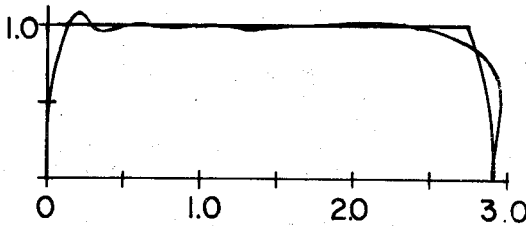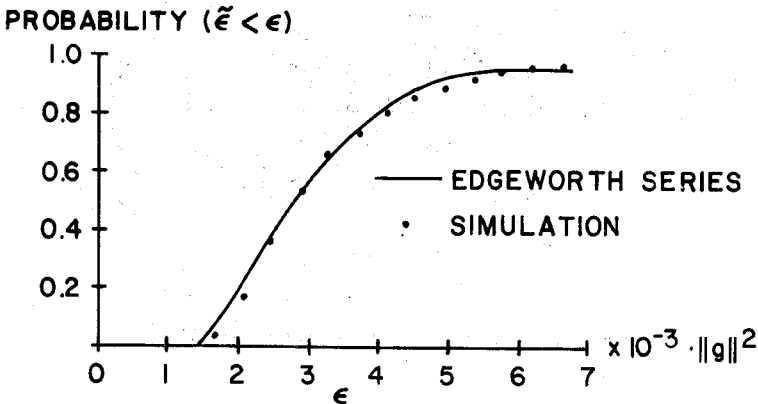In this paper we investigate the numerical solution of integral
equations for scattering problems in the neighborhood of inter-
nal resonance of the scatterer. As is well known, the corre-
sponding matrix equation has a zero eigenvalue at the internal
resonant frequency, and is therefore singular. The problem of
scattering by a rectangular cylinder has been numerically
studied as a test case and it has been found that in the vicinity
of the internal resonant frequency the solution for the surface
current contains a substantial error contribution which is
associated with the eigenvector corresponding to the resonance
current on the scatterer. Two methods have been investigated
for supressing this error contribution. The first of these is
a posteriori filtering of the unwanted eigenvector from the
solution of the matrix equation; the second is modifying the
original matrix equation either via regularization or the intro-
duction of an auxiliary condition that discriminates against
the undesired eigenvector. An example of such an auxiliary
condition is that the desired solution be orthogonal to the
resonant current eigenvector. A comparison of results obtained
by these approaches are presented in the paper and the relative
advantages and disadvantages of various algorithms are discussed.

SINUSOIDAL REACTION FORMULATION FOR SCATTERING BY CONDUCTING
BODIES OF ARBITRARY SHAPE*:   J.H. Richmond and N.N. Wang,
The Ohio State University, Columbus, Ohio

The reaction integral equation developed by Rumsey[1] has been applied
by Richmond[2,3] to thin-wire antennas. In this paper the piecewise-
sinusoidal reaction technique is extended to scattering by conducting
bodies of arbitrary shape. The conducting surface is divided into cells
and the surface current density is expanded in overlapping sinusoidal
bases. Via Galerkin's method, the integral equation is reduced to a
system of simultaneous linear equations: [Z](I)=(V). From a physical
viewpoint, this variational solution follows from enforcement of
reaction tests with an array of sinusoidal electric test sources. The
current distribution over the conducting surface is determined via
matrix inversion. Finally, the scattered field is obtained by inte-
grating the surface currents.

Most previously published solutions have employed pulse bases and col-
location[4,5], whereas, in this paper the current distribution is modeled
as a continuous function with no line charges. It was found that using
pulse bases, the cells should not be greater than 0.1 wavelength on a
side to provide reasonably accurate results. However, using these new
basis functions, the cells can be as large as 0.5 wavelength on a side.

A new technique for evaluating the impedance matrix is developed which

proves to be much more efficient than the standard numerical techniques.

The sinusoidal reaction formulation has been applied to bistatic

scattering by a rectangular plate and the radiation pattern of a half-

wavelength dipole in the presence of a corner reflector. With a few

current samples, good agreement is obtained between the calculated

and measured data[6,7]. With only one current sample over a square

plate, satisfactory data are obtained for the echo area with broadside

incidence over a range from 0.1 wavelength to 1.0 wavelength on a side.

REFERENCES:

1.   V.H. Rumsey, "Reaction Concept in Electromagnetic Theory," The

      Physical Reviews, Vol. 94, No. 6, June 1954.

2.   J.H. Richmond, "Admittance Matrix of Coupled V Antennas," IEEE

      Trans. on Ant. and Prop., Vol. AP-18, No. 6, pp. 820-821,

      November 1970.

3.   P.K. Agrawal, G.A. Richards, G.A. Thiele and J.H. Richmond,

      "Analysis of Design of TEM-Line Antennas," IEEE Trans. on Ant.

      and Prop., Vol. AP-20, No. 5, pp. 561-568, September 1972.

4.   F.K. Oshiro, "Source Distribution Technique for the Solution of

      General Electromagnetic Scattering Problems," Proc. First GISAT

      Symposium, Vol. 1, Part I, Mitre Corporation, 1965.

5.   D.L. Knepp, "Numerical Analysis of Electromagnetic Radiation

      Properties of Smooth Conducting Bodies of Arbitrary Shape in

      the Presence of Known External Sources," Ph.D. Dissertation,

      University of Pennsylvania, 1971.

6.   R.G. Kouyoumjian, "The Calculation of the Echo Area of Perfectly

     Conducting Objects by the Variational Method," Ph.D. Dissertation,

     The Ohio State University, 1953.

7.   A.C. Wilson and H.V. Cottony, "Radiation Pattern of Finite-

     Size Corner-Reflector Antennas," IEEE Trans. on Ant. and Prop.,

     Vol. AP-8, No. 2, March 1960

PROPAGATION AND INTERFERENCE
MEASUREMENTS WITH THE
COMMUNICATIONS TECHNOLOGY SATELLITE

Louis J. Ippolito
NASA Goddard Space Flight Center
Greenbelt, Maryland

This paper describes an experiment designed to measure and characterize the radio frequency links of the SHF transponder on the Communications Technology Satellite (CTS). The CTS, under joint development by the Canadian Department of Communications and NASA, is an experimental satellite designed to provide user communications capability in the recently allocated 12 and 14 GHz bands. A primary objective of the CTS is to test and demonstrate new techniques in satellite communications utilizing a high power downlink with low-cost ground terminals.

A number of the User experiments will be dependent on small aperture, relatively inexpensive ground terminals which will operate with small link power margins. It is essential that the propagation effects of the CTS communications links be thoroughly understood and characterized to assure the achievement of user experiment objectives.

The propagation effects of interest at the CTS wavelengths occur primarily during precipitation periods (rain or wet snow), and result in attenuation, depolarization, and possibly phase distortion of the transmitted signal. In addition, for low elevation earth stations, such as in Alaska or northern portions of Canada, multipath effects could produce signal scintillations which would degrade operations on the communication channel.

Session 35   Rain Scatter

Very little experimental data presently exists on the effects of precipita-

tion on earth-satellite signals in the 12 to 14 GHz band. Data measurements

at 15.3 GHz and 31.65 GHz using the ATS-5 satellite have indicated that

extrapolation from one frequency to another or from one location to another

in the determination of rain attenuation effects can lead to misleading

and often incorrect conclusions. It is, therefore, desirable to obtain

rain attenuation data at the frequencies and locations of interest directly,

hopefully with the same antennas and receivers intended for use on the

operational system.

The CTS Communications Link Characterization Experiment will address the

problems of both natural and man-made components of the electromagentic

environment which could adversely affect the reliability of CTS user

communications links. The experiment will be used to collect data on

communication link quality to ensure that all CTS users have sufficient

margin to provide high quality transmissions.

The natural characteristics of importance in the CTS frequency bands,

(14.0-14.3 GHz up-link, 11.7-12.2 down-link), include attenuation and

signal degradation due primarily to absorption and scattering induced by

precipitation.

The Experiment will also measure and characterize man-made, earth-based

signals which could interfere with the 14.0-14.3 GHz up-link frequency

band of the geostationary CTS.

It is also desirable to utilize meteorological support equipment at the

ground stations to aid in the accurate prediction of rain attenuation. A

number of techniques developed on the ATS-5 and ATS-F Millimeter Wave

Experiment programs on the use of rain gauge networks, radiometers, and

backscatter radars will be employed on the experiment to provide a complete

evaluation of the earth-space channel.

A SIMPLE METHOD FOR DETERMINING EFFECTIVE
RAIN CELL DIAMETERS

D.B. Hodge
The Ohio State University ElectroScience Laboratory
Department of Electrical Engineering
Columbus, Ohio 43212

A simple, tractable model of a rain cell provides an important tool for the prediction of rain attenuation statistics. Such a model was used successfully to predict attenuation statistics on the ATS-5 15.3 GHz downlink for both single paths and spatially separated paths (Zintsmaster, URSI 1972 Spring Meeting). This model was a simple cylindrical cell model having a homogeneous rain rate and a diameter which depended upon the rain rate. The relationship between the cell diameter and rain rate that was used was an empirical relationship generated from attenuation and rain rate measurements (Hogg, 1971 G-AP International Symposium).

It would be desirable to establish a direct link between rain rate measurements and effective cell diameters which did not rely upon attenuation measurements; this would permit the prediction of attenuation statistics without being dependent upon previous attenuation measurements. A simple method for the determination of cell diameter-rain rate relationship will be described. This method utilizes rain rate data recorded simultaneously at only two rain gauges separated by one or two kilometers. The method has been tested using previously published rain gauge data. The resulting cell diameters agree well with cell diameters deduced from attenuation measurements. Thus, a simple, inexpensive method is available for determining effective cell diameter-rain rate relationships.

Fine Scale Probing of Rain Showers

Using Narrow Beam Radars

Thomas G. Konrad
Applied Physics Laboratory
Johns Hopkins University

One of the serious problems facing communications satellite systems is the interference expected due to precipitation scatter at the frequencies being considered, in the tens of GHz range. Good statistical models of the small, strongly reflecting rain cells and the field of cells is lacking, however. A program has been designed to provide these statistics via fine temporal and spatial scale probing of intense rain storms. The program involves the use of a sensitive, high power, narrow beam radar located at Wallops Island, Virginia, in a four month observational program started in May 1973 to study summer thunderstorms. This paper briefly reviews the overall program, its objectives, etc. and the experimental program as conceived and carried out during the summer. The various equipments being used, including the radar, signal processing and recording instrumentation and meteorological equipment will be discussed and preliminary results presented.

Session 35   Rain Scatter

EFFECT OF DROP-SIZE DISTRIBUTIONS ON RAINFALL

RATE-ATTENUATION RELATIONS

Rosemary M. Dyer and Vincent J. Falcone
Air Force Cambridge Research Laboratories
Bedford, Massachusetts 01730

Rain-induced attenuation of centimeter waves is generally considered
to be solely a function of wavelength and rainfall intensity, with observed
variability attributable to measurement errors, temperature differences,
differences in raindrop size distributions and non-sphericity of the drops,
all lumped together as an uncertainty factor. This factor can be as high
as ± 100% when comparing the published results of various measurements.

Computations of attenuation of centimeter waves have been made for a
variety of rain intensities, wavelengths, temperatures, and drop-size distri-
butions. It was found that, assuming errorless measurements, the most important
factor contributing to the observed variability in the rainfall rate vs
attenuation relation is the difference in drop-size distribution for a
given rainfall rate. The variability due to drop-size distribution alone
(holding all other parameters constant) ranges between 5% and 33% standard
deviation about the mean.

BISTATIC SCATTER FROM RAIN[*]

R. K. Crane

Lincoln Laboratory, Massachusetts Institute of Technology

An experimental investigation of bistatic scatter from rain was conducted using a 143 km scatter path at frequencies of 4.5 and 7.7 GHz.[1] The ratio of transmitted to received power (transmission loss) was measured for scattering angles ranging from 6° to 130°. Simultaneous weather radar observations were made at a frequency of 1.3 GHz. Transmission loss estimates for the bistatic scatter path were computed using the weather radar data, the bistatic scattering equation, and a model for the scattering cross section per unit volume based upon Rayleigh scattering by an ensemble of water spheres. The measured and estimated transmission loss values were compared to test the use of the scattering cross section model for the estimation of interference.

The bistatic scatter system used continuous wave (cw) transmission from a horn antenna with a gain of 18 dB. The receiving system used the 60-foot Westford Communications Terminal antenna. The Millstone Hill L-Band radar was used for the weather radar. Both the Westford antenna and the 84-foot Millstone radar antenna were scanned in azimuth at a fixed elevation angle to observe the rain illuminated by the horn antenna. The two antennas were scanned to point in the same direction at the same time. Figure 1 presents a computer generated PPI display for an azimuth scan depicting a number of rain cells. The bistatic scatter system geometry is also indicated on this figure with the transmitter located at Avon, Connecticut and the receiver located at the origin of the coordinate system (north and east positive). The angular resolution of both the bistatic scatter receiver system and the weather radar system were nearly identical. The transmission loss for the bistatic scatter system was estimated by computing the contribution to the received signal for each range resolution cell of the radar and summing the contributions along the radar beam. This process was repeated for each azimuth pointing direction. The results of the transmission loss measurements and estimates at 4.5 GHz for the scan depicted in Fig. 1 are given in Fig. 2.

Two computations are presented in Fig. 2, one for the assumption that the local horizon at the transmitter was at an elevation angle of 0.7° for all azimuth angles from the transmitter and the other for the assumption that the local horizon corresponded with the tops of the trees (shielding table). In both cases, the assumption was made that only the lines-of-sight between the transmitting antenna and the scattering volume that passed above the horizon contributed to the received signal. The area marked clear lines-of-sight on Fig. 1 corresponded to the region reached by lines-of-sight passing above the tree tops. The two calculated curves on Fig. 1 coincide when the scattered signal is from rain within the clear lines-of-sight area. The data show appro: mately a 4 dB difference between the measured and calculated values for the cell at 259° azimuth and an 8 dB difference at 260° azimuth.

Session 35   Rain Scatter

Measurements were made at 7. 7 GHz during a two week period during the summer of 1968 and at 4. 5 GHz during a two week period during the summer of 1970. [2] Figure 3 displays the histogram of comparisons between measured and calculated transmission loss for all the 7. 7 GHz data that was obtained for cells both within the clear lines-of-sight areas and the -10 dB points on the horn antenna directivity pattern. Figure 4 displays the histogram of comparisons for the 4. 5 GHz data. The histograms given in Figs. 3 and 4 were generated using the constants of the monostatic and bistatic radar equations for the respective systems together with transmitter and receiver calibration data. The data were not corrected for attenuation along the measurement paths.

A comparison between the computed and measured transmission loss values requires an absolute calibration of both the monostatic and bistatic [1] radar systems. An exhaustive, redundant calibration procedure was used to maintain the absolute calibration uncertainty of the monostatic radar system to less than 1. 4 dB (3 standard deviations, σ) during the summer of 1970 and 2. 4 dB (3σ) during 1968. The uncertainty in the ratio of measured-to-calculated transmission loss was estimated to be less than 2. 7 dB (3σ) during the summer of 1970 and 3. 7 dB (3σ) during 1968. The width of the ratio histogram was estimated to be 3. 2 dB due to statistical fluctuation of the rain target and horn antenna pointing uncertainties. The bistatic scatter system had an additional correction factor that depended upon the doppler spread of the scattered data. For off path scattering (angles more than 5° from the 229. 6° azimuth direction toward Avon) the doppler spread AGC loop and an additional 1. 05 dB correction to the measured transmission loss is required.

The averaged ratio of measured-to-calculated transmission loss for the 4. 5 GHz data is 1. 2 $\pm$. 4 dB after correction for gaseous absorption along the path and the effect of doppler spread. The averaged ratio for the 7. 7 GHz data is -1. 6 $\pm$. 5 dB after correction. These values are both within the combined calibration uncertainties of each measurement system. The results show that the use of the simplified Rayleigh scattering cross section model for an ensemble of water spheres adequately describes bistatic scatter for a wide range of scattering angles and frequencies below 7. 7 GHz for the hydrometeor types (rain, snow, and mixed rain and snow) encountered in summer showers in New England.

1.   R. K. Crane, "Description of the Avon-to-Westford Experiment," Technical Report 483, Lincoln Laboratory, MIT (29 April 1971).

2.   R. K. Crane, "Analysis of Data from the Avon-to-Westford Experiment," Technical Report 498, Lincoln Laboratory, MIT (8 January 1973).
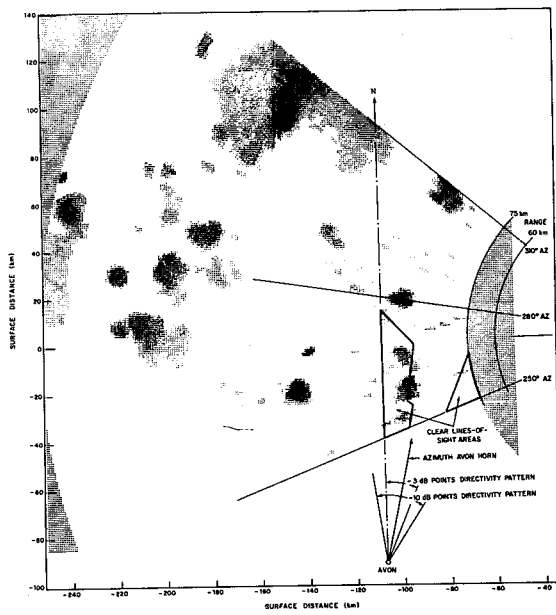
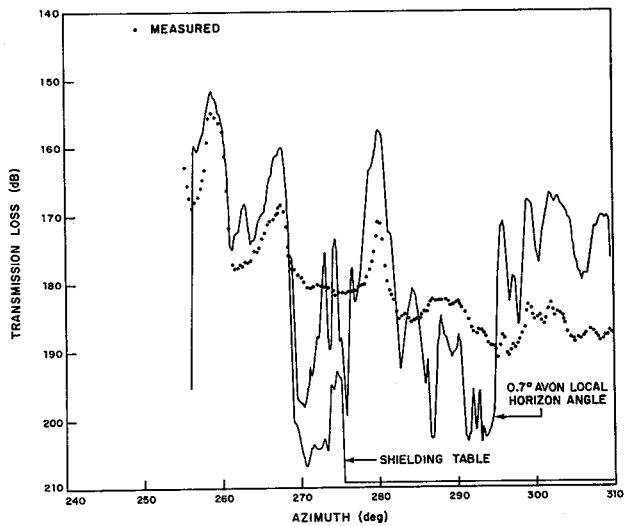Fig. 1 PPI display, Millstone Hill radar, 1.5° elevation 2046-2056 GMT, 28 July 1970.

Fig. 2 Calculated and measured transmission loss, Avon-to-Westford scatter path, 4.5 GHz, 1.5° elevation (Westford), 2046-2056 GMT, 28 July 1970.
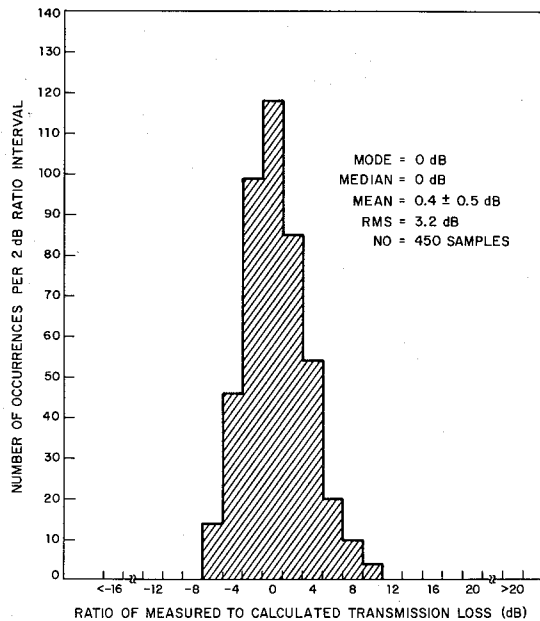
283

MODE = 0 dB
MEDIAN = 0 dB
MEAN = 0.4 ± 0.5 dB
RMS = 3.2 dB
NO = 450 SAMPLES

NUMBER OF OCCURRENCES PER 2 dB RATIO INTERVAL

RATIO OF MEASURED TO CALCULATED TRANSMISSION LOSS (dB)

Fig. 3 Histogram of ratios measured-to-calculated transmission loss, 7.7 GHz, summer 1968.

MODE = 4 dB
MEDIAN = 4 dB
MEAN = 3.0 ± 0.4 dB
RMS = 3.7 dB
NO = 661 SAMPLES

NUMBER OF OCCURRENCES PER 2 dB RATIO INTERVAL

RATIO OF MEASURED TO CALCULATED TRANSMISSION LOSS (dB)
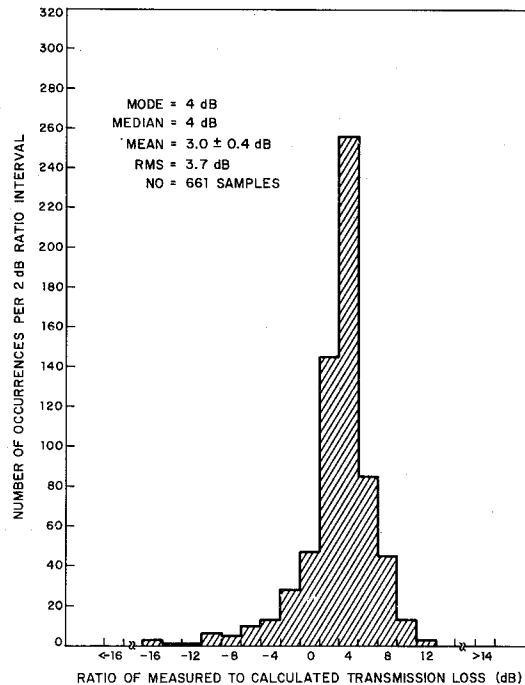
Fig. 4 Histogram of ratios measured-to-calculated transmission loss, 4.5 GHz, summer 1970.

SOME EXPERIMENTAL RESULTS ON 20 GHZ BAND
RAIN ATTENUATION AND DEPOLARIZATION

Kazuo Morita, Yoshio Hosoya and Akira Akeyama
Yokosuka Electrical Communication Laboratory, N.T.T., Japan

1. Introduction
    The use of frequencies above 10 GHz is limited by
attenuation and cross-polarization distortion due to rain.
Cross-polarization discrimination was distorted beyond
expectation on the propagation test carried out at Musashino
in 1971 (1), (2). So a propagation test was carried out
at Owase, which is famous for its heavy rainfalls, from July
to October in 1972 and the rain attenuation and the
depolarization due to rain was measured.
    From experimental results, it was confirmed that there
was a clear differnce in attenuation between horizontal and
vertical polarizations. But the depolarization was less
than the results obtained in Musashino. This report
describes some of the results obtained on this propagation
test.

2. Outline of the propagation test
    The antenna heights of transmitting and receiving site
were 420 m and 50 m, respectively. The distance between
two sites was 4 km. The test period was from July 1 to
October 22 in 1972.   The Yukinoura
site had transmitters of about 100 mW output power at
frequencies of 19.3 and 19.4 GHz, using horizontal and
vertical polarization, respectively. Receivers at the Owase
site sampled signals at both frequencies on both the
transmitted(in-line) and the orthogonal(cross) polarizations.
The amplitude data were continuously recorded and read out
at intervals of thirty seconds. Reading accuracy was one
dB or less with an approximately 70 dB dynamic range.
Three tipping-bucket rain gauges were located along the
transmission path and one minute rainfall rate was measured.
The transmitting and receiving antennas were of identical
1.8 m diameter cassegrain type with radome to avoid
depolarization due to raindrops on the antenna. The antenna
gain was about 48.5 dB and the overall cross-polarization
discrimination of antenna and polarizer system was as follows:
    XPDHv=46 dB, XPDVh=56 dB, XPDVv=46 dB and XPDHh=56 dB
where XPD : cross-polarization discrimination
      H,V : transmitted(in-line) signal
      h,v : orthogonal(cross) polarization signal generated
            due to antenna system imperfections and rainfalls.

285

3.   Measured results
    Figure 1 shows the cumulative distributions of the point
rainfall rate and the path average rainfall rate for the whole
test period. The 0.01% value of the path average rainfall
rate distribution was 145 mm/hr. Figure 2 represents
cumulative distributions of attenuation for horizontally
and vertically polarized signals and Figure 3 shows corres-
ponding measured values of rain attenuation for both
polarizations. From these figures, it is clear that
the rain attenuation for horizontal polarization was about 10
% larger than for vertical polarization. Figure 4 and 5
represent the instantaneous correspondence of the observed
cross-polarization level to the co-polarized signal level.
When the rain attenuation for horizontal polarization was
50 dB, the cross-polarization discrimination XPDHh was about
27 dB. Figure 6 shows measured distribution for the above-
mentioned four kinds of cross-polarization discrimination.
The depolarization measured in Owase area was small in
comparison with the data which have already been published.
For example, the 0.01 % value of XPDHv distribution at Owase
and that at Musashino was 33 dB and 25 dB, respectively,
and the 0.01 % value of XPDHh distribution at Owase and that
measured by W.T.Barnett (3) was 29 dB and 17 dB, respectively.

4.   Conclusion
    As is shown in Figure 5, the correlation between rain
attenuation and depolarization was not necessarily high.
The mechanism of the rain-induced depolarization has not yet
been fully ascertained and the cross-polarization distortion
may be affected by many factors, such as velocity and
direction of wind, the inclination angle of the slanting
path and so on. So it is necessary to continue the research
to determine the mechanism and the characteristics of the
cross-polarization distortion, both theoretically and
experimentally.

References
1. M.Shimba and K.Morita(1972 International IEEE/G-AP Symposium
                p.246)
2. H.Yamamoto, K.Morita and Y.Nakamura(1973 IEEE International
            Conference on Communications)
3. W.T.Barnett(1972 IEEE National Telecommunication Conference,
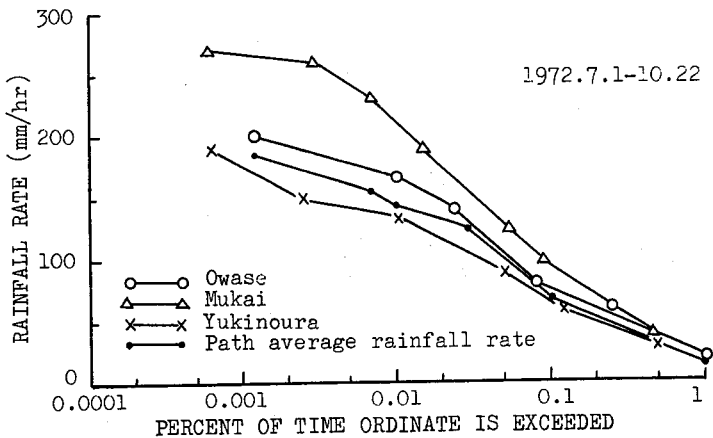   p.10E-1)

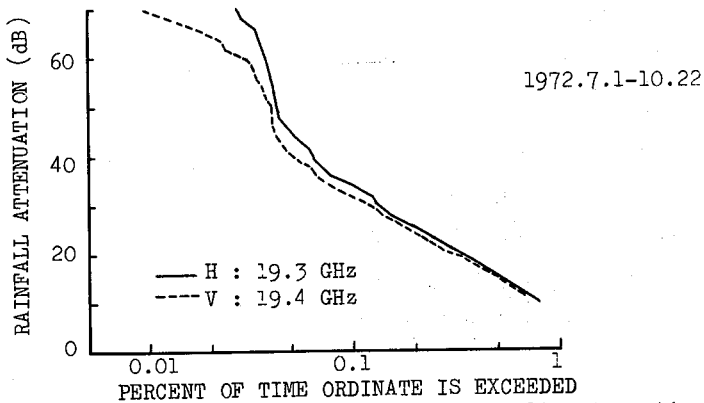Fig.1   Cumulative distribution of rainfall rate
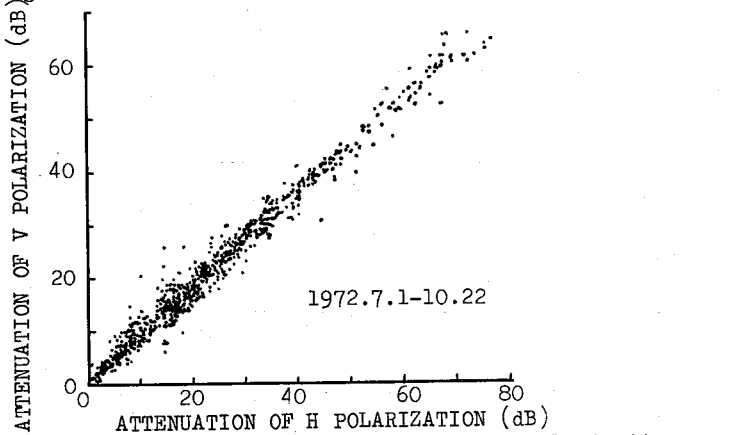

Fig. 2   Cumulative distribution of rainfall attenuation

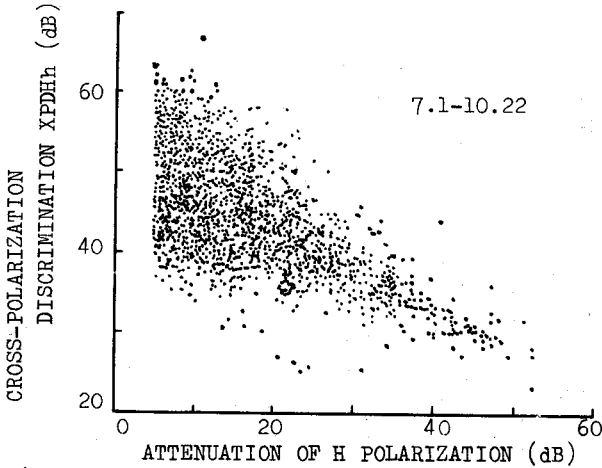Fig. 3   Relation of attenuation for both polarizations

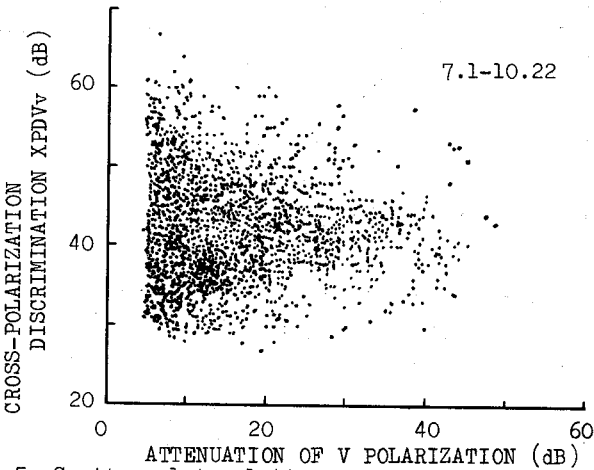Fig. 4   Scatter plot relating cross-polarization to attenuation

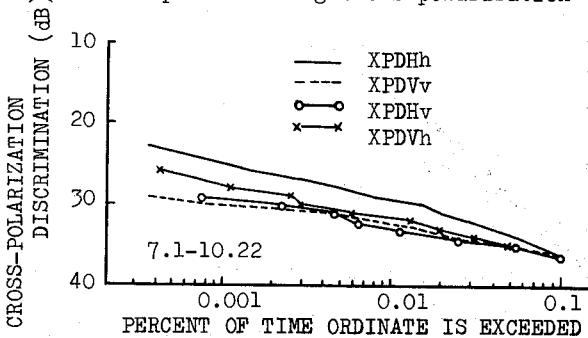Fig. 5   Scatter plot relating cross-polarization to attenuation

Fig. 6   Distribution of cross-polarization distortion

Millimeter Wave Rain Depolarization:
Some Recent 17.65 GHz Measurements*

C. W. Bostian, W. L. Stutzman, Paris H. Wiley and R. E. Marshall
Virginia Polytechnic Institute and State University,
Blacksburg, Virginia 24061

The authors are conducting an experiment in which 17.65 GHz sig-
nals linearly polarized at ±45° from vertical are transmitted over
a 1.43 km path. A computer-controlled system monitors the weather
along the path and measures +45° attenuation, -45° attenuation,
+45° to -45° depolarization, and -45° to +45° depolarization. Some
data from this experiment have been reported previously [1] and
compared with theoretical prediction based on Thomas's model [2].
This paper presents some new results and compares them to values
predicted by a new analysis [3] involving scattering rather than
differential attenuation [2] or differential attenuation and phase
shift [4].

Figure 1 displays the average cross polarization level for each
integer rain rate during a storm on August 17, 1973. The plotted
points were obtained by first charting the 15 second running aver-
age signal levels for both channels and path rainfall rates at one
second intervals and then averaging the signal levels corresponding
to each integer value of rain rate above 9 mm/hr. The error bars
extend one standard deviation on either side of the averages and
indicate the amount of scatter present in the raw data. A solid
curve illustrates the theoretical values predicted by the scatter-
ing model for 40% oblate drops. Most of the observed deviation of
the experimental averages from the theoretical predictions results
from the inability of the tipping bucket raingauge network to char-
acterize fully the instantaneous rain rate along the path. This is
evidenced by Figure 2 where observed and predicted attenuation
values are plotted against corresponding cross polarization levels.

Figures 3 and 4 display average cross polarization levels for a
storm on March 16, 1973. This storm produced the highest rain rates
that we have observed to date.

References
[1] C. W. Bostian et.al. (1973 G-AP International Symposium Digest,
     pp. 250-253).
[2] D. T. Thomas (1971 Radio Science, 6, pp. 833-840).
[3] P. H. Wiley (1973, Ph.D. Dissertation, VPI&SU, Blacksburg, Va.)
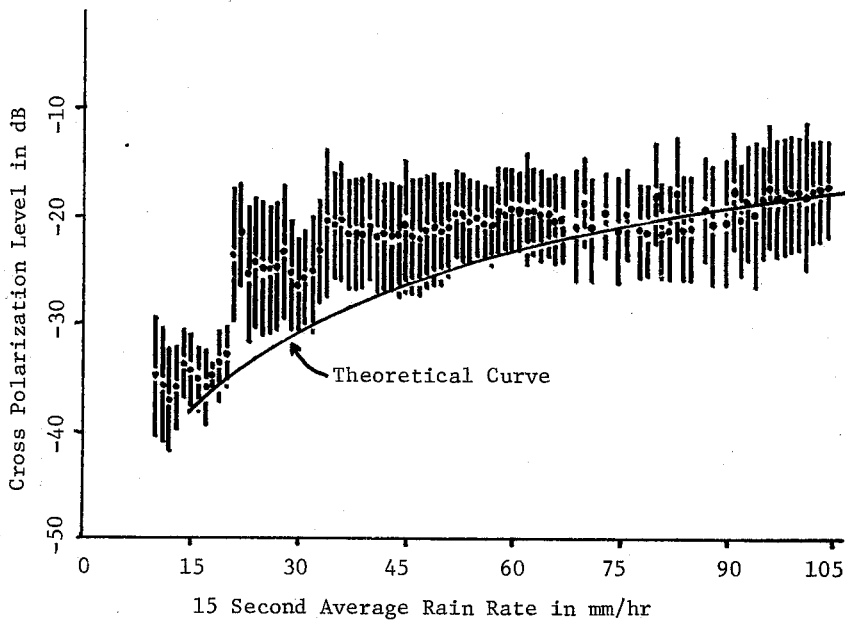[4] P. A. Watson (1973 Proc. IEE, 120).

Figure 1.   Storm of August 17, 1972.
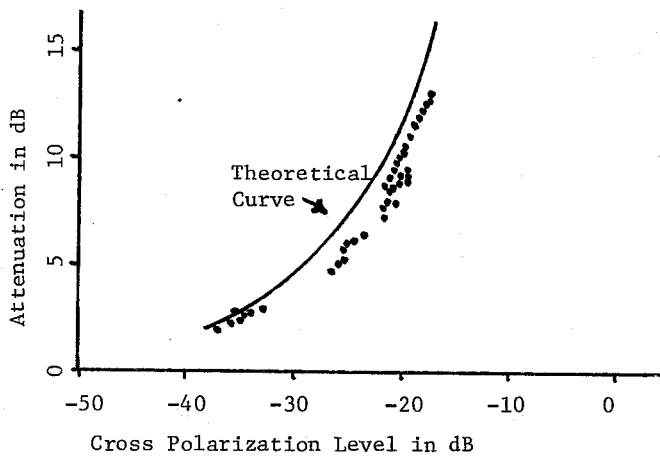

Figure 2.   Storm of August 17, 1972.
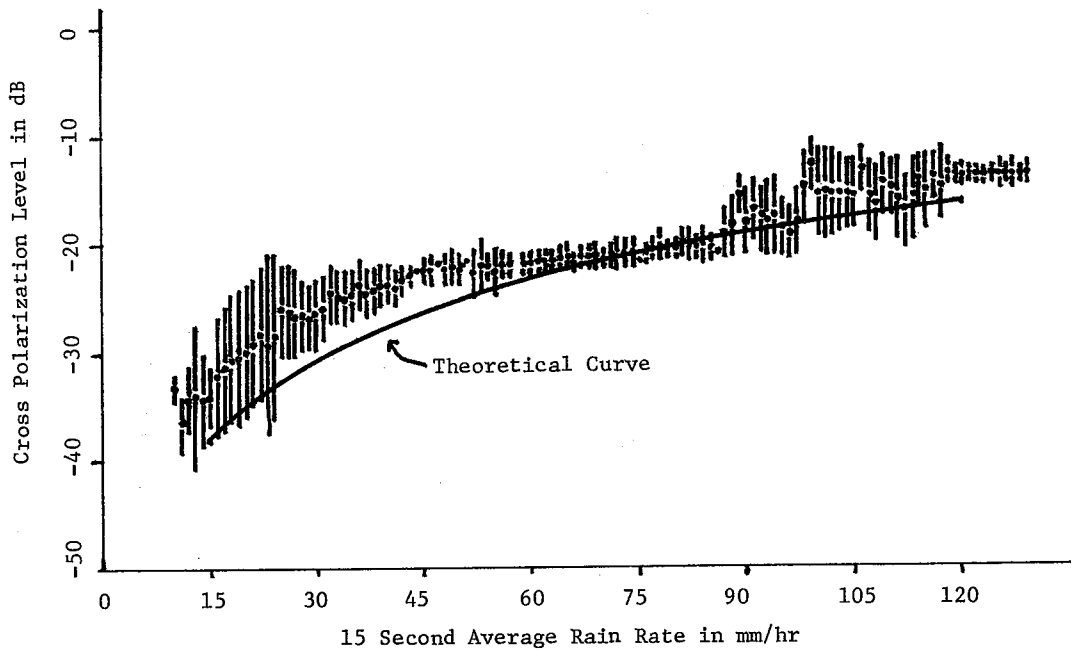
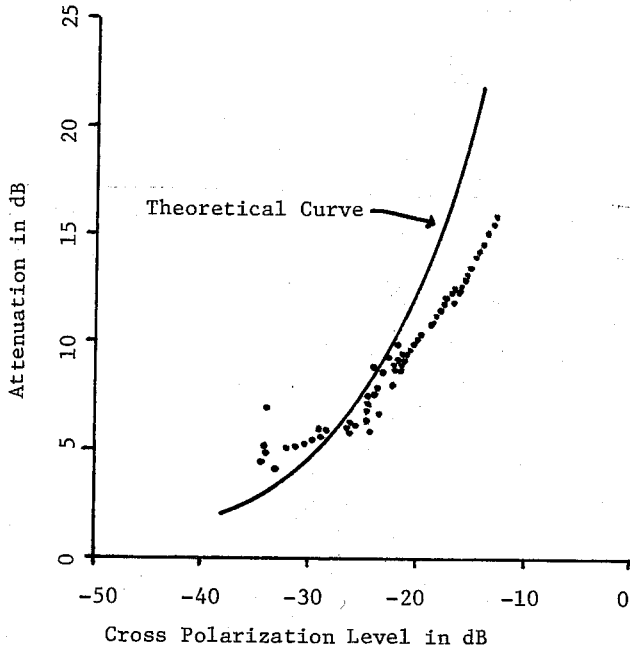Figure 3.   Storm of March 16, 1973.

Figure 4. Storm of March 16, 1973.

EXPERIMENTAL EVIDENCE OF
CROSS-POLARIZATION DISCRIMINATION DETERIORATION
DURING RAIN AND MULTIPATH FADING AT 4 GHZ

by W. T. Barnett
Bell Telephone Laboratories
Holmdel, New Jersey 07733

It has been commonly assumed that the polari-
zation isolation obtained in 4 GHz microwave radio re-
lay systems during free space propagation conditions
would obtain even in cases of substantial multipath
fading or during heavy rains.

From November 1970 to September 1971 ampli-
tude data was obtained on a 42.5 kilometer path between
Atlanta and Palmetto, Georgia. A vertically polarized
signal at 4198 MHz was transmitted and received on
standard horn reflectors. In addition, the orthogonal
horizontal (cross-polarized) received component was
measured. The amplitudes were continuously recorded
on magnetic tape; quantizing intervals were one dB in
amplitude and 0.2 seconds in time. All rain fading
from 11/18/70 to 6/15/71 and all multipath fading dur-
ing August 1971 were subjected to computer analysis.

During multipath fading the amplitude V of
the vertical component faded below a level L according
to the expected relation $P(V \leq L) = aL^2$ with $a = .18$ and
fade depth $= -29 \log L$ (dB). The distribution of the

depolarized component also followed an L^2 relationship
with an offset of 27.5 dB. This offset is identical to
the free space cross-polarization discrimination (XPD)
and one could interpret this result to mean that the XPD
is constant in time. Unfortunately, the effect is quite
different: the main and cross-polarized signals are al-
most completely decorrelated. For example, when the main
signal was faded $40 \pm .5$ dB the cross-polarized signal
was at a power level higher by 2 dB or more for 50 per-
cent of the 40 dB fade time, giving an instantaneous
XPD $\leq$ -2 dB.

During heavy rain when the main signal fade
at 4198 MHz is less than a few dB the XPD deteriorates
by 10 to 15 dB. The worst case observed was a 5 dB
fade coupled with an XPD of 6 dB (21.5 dB degradation
from free space).

MULTI-FREQUENCY MICROWAVE SCANNING
RADIOMETER ANTENNA

R. Meier and R. K. Thomas
General Electric Co.
Space Division
Valley Forge, Pa.

The paper describes the analysis, development and testing of a five-frequency microwave scanning radiometer antenna for use on aircraft or future earth observation satellites for the simultaneous and synergistic radiometric mapping of such characteristics as sea surface temperatures and winds, sea ice, rain, atmospheric water vapor content, soil moisture on a global scale.

The antenna consists of a fixed parabolic torus reflector with a continuously rotating, multi-spoke feed system providing a conical scan pattern as indicated in Fig. 1. The offset geometry, shown in Fig. 2, provides a blockage free aperture. The individual feeds at the five frequencies 5, 10 18/21 and 37 GHz are diagonal horns as shown in Fig. 3, providing low sidelobes in the principal planes.

For purposes of pattern analysis the horn is considered to produce an illuminated reflector zone bounded by the intersection of a cylinder and the parabolic torus. A gaussian taper, truncated at -17 dB, was chosen to represent the aperture illumination, assumed to be zero outside this contour on the instantaneously unused portion of the reflector. The diffraction integral uses the scalar simplification of the physical optics approximation.

Major objectives of the project were to verify the analytically predicted pattern shape and sidelobe levels under the inherently defocussed conditions of the torus reflector and to evaluate the effects of feed spillover onto undesired areas of the reflector. Figure 4 shows a comparison between computed and measured patterns at 5 GHz with only the desired circular spot metalized (per Fig. 3). Figure 5 shows the effects of feed spillover onto the completely metalized reflector. Figure 6 shows a comparison between computed and measured patterns at 37 GHz where reflector tolerances lead to greater discrepancy.

Analytical and measured data is presented at various frequencies and scan angles for two linear, orthogonal polarizations. A novel, low-cost method for building complex reflector models is also presented. It is concluded that a single parabolic torus reflector can provide high efficiency, scanned beams over the frequency range from 5 to 37 GHz provided that a sufficiently large f/$_D$-ratio is selected, the feed sidelobes intercepted by the reflector are kept low and the reflector tolerances and feed/reflector alignment are closely controlled.
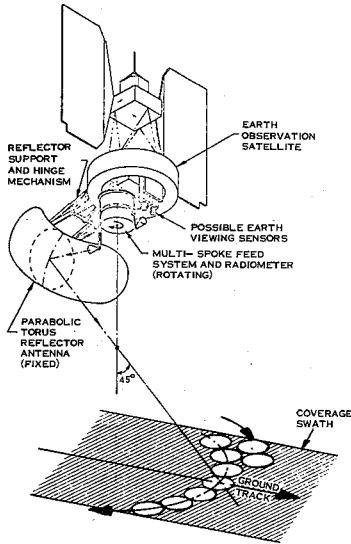
Figure 1.   Arrangement of Radiometer
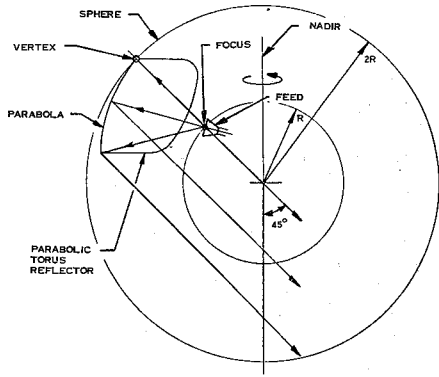and Conical Scan Pattern

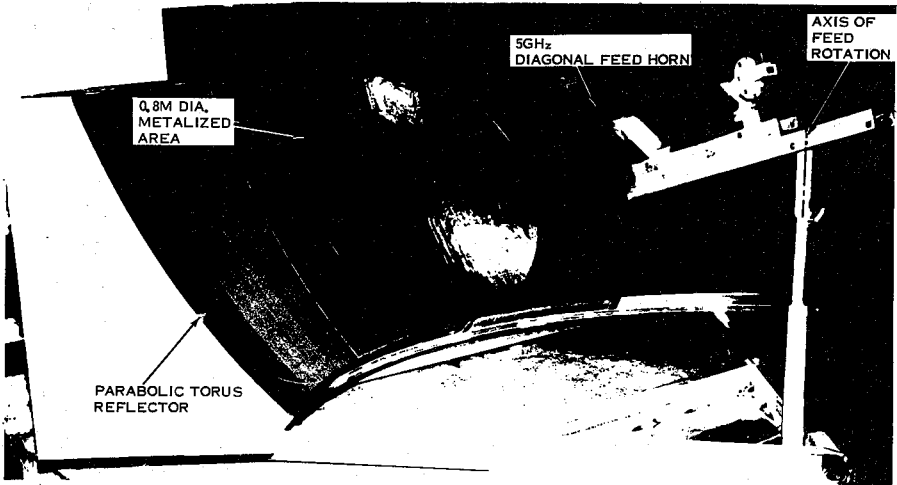Figure 2.   Offset Parabolic Torus
Reflector Geometry

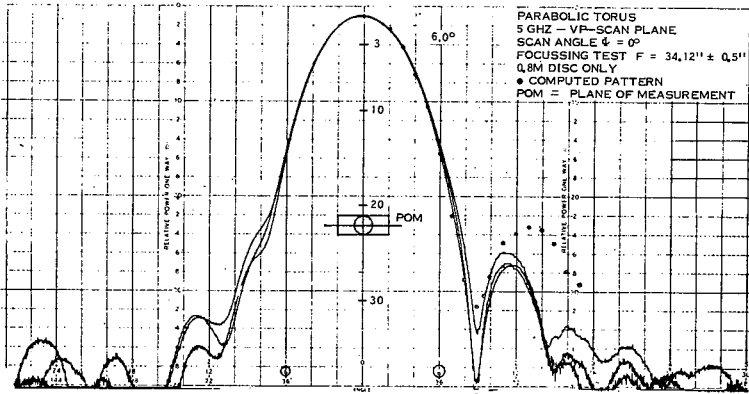Figure 3.   Parabolic Torus Reflector with 5 GHz Diagonal Horn Feed
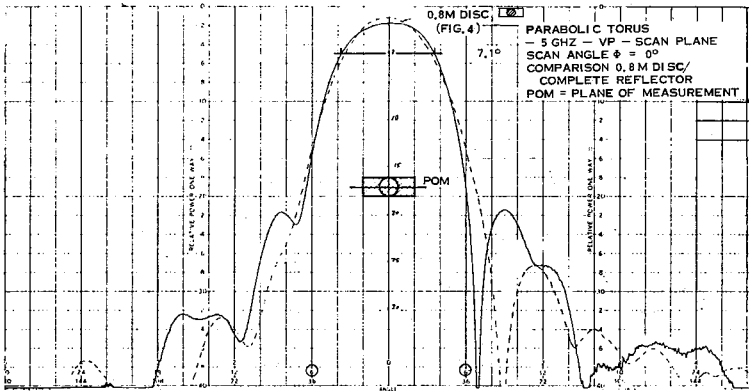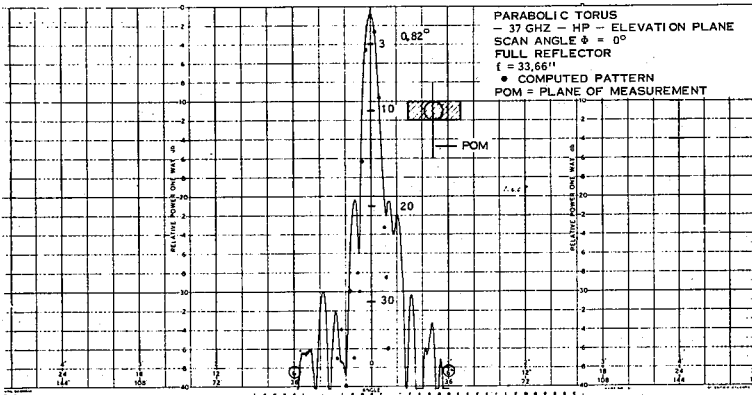
Figure 4.

Figure 5.

Figure 6.

297

INVESTIGATION OF THE CHARACTERISTICS OF A LARGE
REFLECTOR ANTENNA USING MICROWAVE HOLOGRAPHY

J.C. Bennett, A.P. Anderson,
P.A. McInnes[+], A.J.T. Whitaker
(Department of Electronic and Electrical Engineering ,
University of Sheffield, Sheffield, England)

Antenna pattern measurements have traditionally been concerned
with the recording of angular power spectra in which relatively
little emphasis is placed on recording the phase pattern. Hence
Fourier-integral synthesis of the aperture illumination is not
usually possible from such measurements, and information regarding
aperture field deformations, blockages etc. is not readily extrac-
ted. Microwave holographic techniques therefore suggest themselves
as means of relating the antenna pattern to an image of the aper-
ture, with the consequent possibility of using the relationship in
antenna metrology.

The basic microwave system which has been used to obtain the holo-
gram of a large steerable antenna is shown in Fig. 1. The exist-
ing antenna azimuth and elevation system is conveniently utilised
for the field-scanning operation necessary in most microwave holo-
graphic processes. A static microwave horn provides the reference
wave which is combined with the antenna signal via a hybrid-T. The
hologram is obtained in a raster format by performing continuous
scans in elevation and small discrete increments in azimuth. The
hologram signal is sampled at regular intervals during the elevat-
ion scan and the demodulated signal is quantised into 1000 levels
and stored on eight-hole paper tape by a data logging system. The
function of the phase shifter is to synthesise an effective off-
axis reference wave to ensure adequate separation of the recon-
structed image from other interfering outputs. This is accompli-
shed by incrementing the phase shifter by a constant amount between
each elevation scan.

A hologram has been formed in this manner for the 3m paraboloid
(f/D = 0.25) shown in Fig. 2. At the frequency used, 8.15 GHz,
the width of the feed support arms is 1.38λ and the square feed
box has a linear dimension of 8.3λ. The antenna was scanned over
a range of $\pm6^{\circ}$ in elevation and $\pm9^{\circ}$ in azimuth and a total of
approximately 8500 samples of the hologram distribution was
recorded by the data logging system. The hologram, as printed out
on a 32-level intensity display system[1], is shown in Fig. 3.

A reconstruction of the image of the antenna may be performed by
conventional laser-optical methods after forming a reduced-size
transparency of Fig. 3. There are, however, several disadvantages
to this approach. Phase information is not readily available in
the optical image which is also not in a suitable form for obtaining

numerical data. Moreover, the 1000 levels of recorded data must
be reduced to 32 at the hologram formation stage and the system
S/N ratio deteriorates due to optical noise and the photographic
process.

These disadvantages are removed by using a computational technique
to reconstruct the image field distribution in which the rôle of
the optical lens is replaced by the Fast Fourier Transform
algorithm[2]. The recorded data is not in the form of a Fourier
transform hologram since it contains focussing terms arising from
the shift of the focal distribution as the antenna is rotated[3].
Also the antenna rotates about a point distant R behind its aper-
ture and because the reference horn is stationary, the hologram
distribution contains a spherical off-axis reference wave function
$B \exp[-jk(u^2+v^2)/2R] \exp[-jk\alpha u]$ where B is constant, $k = 2\pi/\lambda$,
(u,v) are the hologram co-ordinates and α is a constant denoting
the linear phase change in the azimuthal direction. The resulting
hologram distribution is therefore

$$H(u,v) = |f(u,v)\exp[jk(u^2+v^2)/2R_f]|^2$$
$$+ |B \exp[-jk(u^2+v^2)/2R]\exp[-jk\alpha u]|^2$$
$$+ Bf^*(u,v)\exp[-jk(u^2+v^2)/2R_f] \exp[-jk(u^2+v^2)/2R]\exp[-jk\alpha u]$$
$$+ Bf(u,v)\exp[jk(u^2+v^2)/2R_f]\exp[jk(u^2+v^2)/2R]\exp[jk\alpha u] \quad (1)$$

where $f(u,v)$ is the Fourier transform of the aperture distribution,
R_f is the focal length of the antenna and * denotes the complex
conjugate. The important terms in the hologram distribution are
given by

$$H^1(u,v) = Bf^*(u,v)\exp[-jk(u^2+v^2)/2R_r]\exp[-jk\alpha u]$$
$$+ Bf(u,v)\exp[jk(u^2+v^2)/2R_r]\exp[jk\alpha u] \quad (2)$$

$$\text{where } R_r = \frac{RR_f}{R+R_f} \quad (3)$$

In order to obtain the focussed image of the aperture, it is
desirable to generate, at the FFT input, either $Cf^*(u,v)\exp[-jk\alpha u]$
or $Cf(u,v)\exp[jk\alpha u]$ where C is constant. From equation (2) it is
apparent that premultiplication of the hologram distribution by
spherical wave components $\exp[jk(u^2+v^2)/2R_r]$ or $\exp[-jk(u^2+v^2)/2R_r]$
will suffice.

The computer reconstruction of the aperture amplitude distribution
on the multi-level display is shown in Fig. 4. It is seen that
aperture blockages due to the feed support arms and the square feed
box have been clearly imaged, but that the edge of the dish
(position shown by the dotted circle) is not visible. The edge is
unresolved because a corrugated horn scalar feed was used and
anechoic chamber measurements have shown[4] that the (approximately
Gaussian) illumination function falls off at the dish edge 32dB
below the boresight value.

Before considering details of the reconstructed aperture phase

distribution, it should be mentioned that, during initial radiation pattern measurements, the reflector was found to have two "focal" regions as shown in Figs. 5a and 5b. The two sets of patterns were obtained for two separate axial positions of the feed displaced from each other by one wavelength. In Fig. 5a the azimuth pattern is focussed and the elevation pattern is defocussed whereas in Fig. 5b the reverse is the case. Hence, for a hologram formed with the conditions of Fig. 5a there is approximately 2π radians phase error across the semi-aperture in one direction and uniform phase in the orthoganol direction.

Fig. 6 shows a display of the reconstructed aperture phase distribution produced by adding to the aperture phase distribution an off-axis plane wave function so as to form an interferogram. Uniform phase distribution in the horizontal (azimuth) direction is shown by the constant fringe spacing. In the vertical (elevation) direction, the curvature of fringes shows the presence of almost quadratic phase error which increases from zero at the centre to 2π radians at the aperture edge. It is observed that the feed box has caused the expected π phase change in the distribution at the aperture centre, but that the feed supports do not apparently perturb the phase distribution. The constant visibility of fringes over the whole aperture is due to the equal weighting given to all the phase values in the computation process.

To conclude, a microwave holographic technique has been described which yields quantitative data on the amplitude and phase of the field in the aperture of a microwave antenna. A simple phase detection system and the existing scanning system of the antenna is used. The data is processed computationally and displayed in hard copy with 32 levels. The effects of aperture blockage and profile deformation of the reflector can be measured and a visual concept of the antenna in operation "seen with microwave eyes" is obtained.

REFERENCES
1. A.J.T. Whitaker and A.P. Anderson (1973 Optics and Laser Technology 5, pp.28-29).
2. W.T. Cochran et al. (1967 Proc. I.E.E.E. 55, pp. 1664-1674).
3. R.E. Collin and F.J. Zucker (Antenna Theory, Part II pp. 57-60).
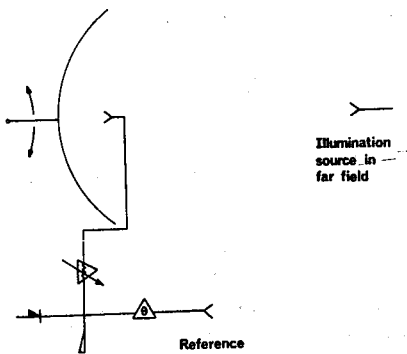4. D.D. Booker and P.A. McInnes (1970 Electron. Lett. 6, pp. 18-20).

Fig. 1   Formation Process

Fig. 2   Antenna under test
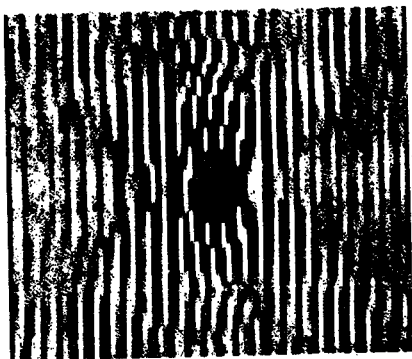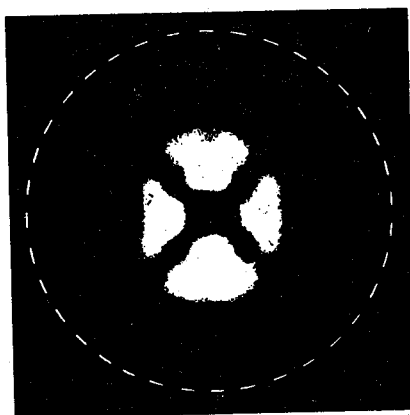

Fig. 3   Hologram

Fig. 4   Amplitude Distribution
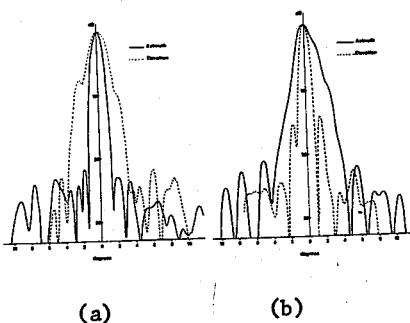

(a)   (b)

Fig. 5   Radiation Patterns

Fig. 6   Phase Distribution

301

POLARIZATION CHARACTERISTICS OF OFFSET REFLECTORS
WITH MULTIPLE ELEMENT FEEDS

D. F. DiFonzo and W. J. English   J. L. Janken

COMSAT Laboratories   Hughes Aircraft Company
Clarksburg, Maryland   El Segundo, California

The increased communications capacity obtainable by reuse
of available frequency bands via multiple isolated beams
has motivated the study of communications satellite an-
tenna designs which can yield high beam isolation by means
of sidelobe and polarization control.[1] Offset reflectors
are attractive for this application. They are capable of
superior sidelobe performance compared to symmetrical
reflectors because of the absence of aperture blockage.
These antennas have been shown to have inferior "cross-
polarization" characteristics compared to symmetrical
reflectors for linear polarization because of their in-
herent asymmetry.[2,3] However, it has also been shown
that a circularly-polarized Huygen's source feed can
yield a secondary pattern from an offset parabola which
is free of cross polarization.[3,4]

For a dual polarized antenna which reuses frequencies on
"orthogonal" polarizations, the usual definitions of
cross polarization may not correctly describe the ob-
tainable beam isolation.[1] This is particularly true for
offset parabolas with multiple element feed arrays.

Polarization Orthogonality
Consider two complex vector fields $\vec{E}_a$ and $\vec{E}_b$ in the far
field of a dual linearly-polarized reflector antenna as
depicted in Figure 1. In general, the fields may be
elliptically polarized and their major axes may not be
orthogonal due to depolarization caused by the reflector.
For a dual linearly-polarized receiving antenna having
orthogonal port orientations $\hat{x}$ and $\hat{y}$ as shown, the beam
isolation or signal-to-interference ratio (S/I) is
given, for the $\hat{x}$ port, as $|\vec{E}_a \cdot \hat{x}|^2 / |\vec{E}_b \cdot \hat{x}|^2$. The curves
in Figure 1 illustrate the beam isolation for the sim-
plified case where the fields have equal strength and
axial ratio and the receiving ports are oriented to
equalize S/I in both x and y ports. The adjustment to
satisfy this condition can be made independently at
each earth station site. Therefore, the quantities of
interest in determining beam isolation are the polar-
ization purity (i.e., the axial ratio) and the amount
by which the major axes of the waves depart from perfect
orthogonality.

Offset Reflectors with Array Feeds
The aperture plane fields for an offset reflector are
shown in Figure 2 for a dual polarized feed. The

transformation of the feed polarization into the aperture
plane fields of a parabola is a stereographic projection.[5]
For a dual polarized Huygen's source feed, the field lines
for the two polarizations are everywhere orthogonal.
Therefore, the aperture plane fields are also orthogonal
everywhere although tilted with respect to the vertical
axis of the reflector. This explains the fact that if a
dual polarized Huygen's source feed (closely approximated
by a corrugated horn, for example) is excited in cir-
cular polarization, the aperture fields will be circularly
polarized. Then, the secondary pattern will have virtually
no "cross polarization."

Array feeds may be utilized to provide secondary beam
pattern shaping. Another application involves the
connection of alternate closely spaced frequency bands
to isolated ports of a multiple beam feed array to pro-
vide a form of spatial multiplexing. The excitation of
each port of the orthogonal beam forming network excites
a given antenna "mode."

Figure 2 also depicts illumination contours for a two-
beam feed array. For circularly-polarized Huygen's
source feeds, two spatially coincident shaped secondary
beams are formed which have very low cross-polarization
levels and therefore permit the existence of an orthog-
onally polarized pair of coincident beams which reuse
the same frequencies.

The excitation of one input port of a dual mode feed
array produces a squinted primary beam illuminating a
portion of the offset reflector. The beam isolation for
a dual linearly-polarized feed is not given by the cross-
polarization level as conventionally measured. For
angles away from the axis in the array plane, the polar-
ization vectors tilt from their on-axis orientations but
they typically remain almost perfectly orthogonal. The
axial ratio of each wave degrades by an amount depending
on the effective f/D of the illuminated region. This
effect is illustrated in Figure 3 for an offset parabola
having an aperture diameter of 18 wavelengths fed with
three rectangular waveguides. For the geometry of
Figure 2, horizontal polarization does not suffer as
much depolarization as vertical polarization due to the
reduced curvature of the illuminated portion of the
reflector. It is seen that the typical value of cross-
polarization levels as conventionally measured are in
the 25 dB range. However, the beam isolation obtained
by aligning a hypothetical dual polarized receiving
antenna to equalize (S/I) as in Figure 1 is much higher
as shown. However, if both ports of the beam forming
network are excited for dual "mode" operation, the
polarization vectors for each "mode" will rotate in

opposite directions at a given off-axis angle. Then,
in addition to the orthogonality of the two polarizations,
the absolute tilt angles relative to a fixed reference
axis become important.

Examples of polarization phenomena for several array feeds
are presented.

<u>References</u>

1.   D. DiFonzo, R. W. Kreutel (1971 P-GAP Symposium)
2.   D. DiFonzo (January 1972, Calif. State Univ.)
3.   D. DiFonzo (November 1972, ICSC/T-47-12E)
4.   T. S. Chu, R. H. Turrin (May 1973, G-AP, p. 339)
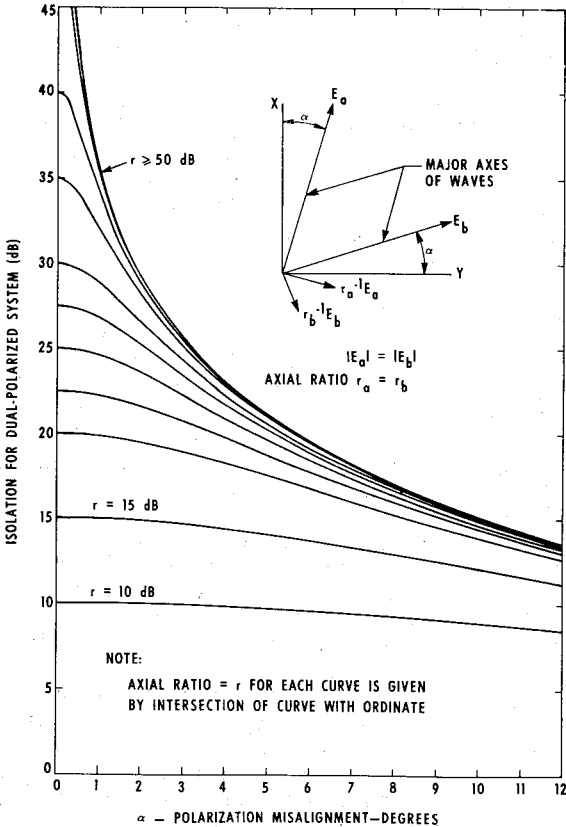5.   J. D. Hanfling (May 1969, G-AP, p. 392)

Figure 1.   Isolation for Two Nonorthogonal
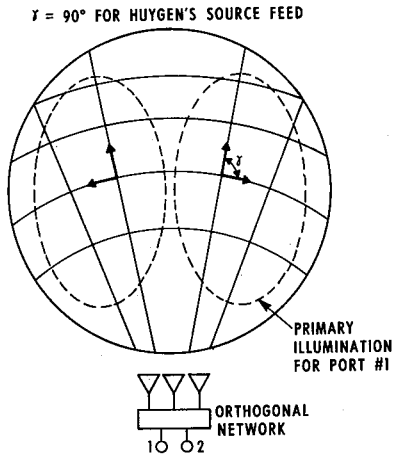   Elliptically-Polarized Waves

γ = 90° FOR HUYGEN'S SOURCE FEED

PRIMARY
ILLUMINATION
FOR PORT #1

ORTHOGONAL
NETWORK

1 ○ ○ 2

Figure 2. Aperture Plane Fields for Offset Reflector
with Dual Polarized Array Feed

BEAM ISOLATION

PRINCIPAL POL.

——— VERT. POL. FEED

— — — HORIZ. POL. FEED

25 dB

CROSS-POL.

GAIN OR ISOLATION (dB)
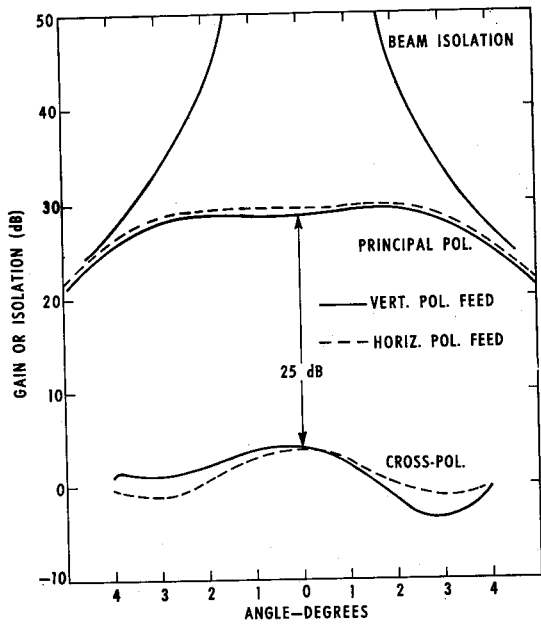
ANGLE—DEGREES

Figure 3. "Cross-Polarization" and Polarization
Isolation for Offset Reflector with
Dual Polarized Array Feed

305

RADIATION FROM "MULTIMODE" REFLECTOR ANTENNAS

J. L. Janken   W. J. English and D. F. DiFor

Hughes Aircraft Company   COMSAT Laboratories
El Segundo, California   Clarksburg, Maryland

Multiple Mode Antennas

Communications satellites presently employ an output
multiplexer to combine many closely spaced frequency
channels which are to be transmitted via the satellite
antenna to a common coverage region. To alleviate the
severe restrictions which are placed on the output mult
plexer due to the small frequency separation between
channels, frequency bands may be connected to orthogona
ports of a multiple-beam array which feeds a reflector.
The input ports of the orthogonal beam array are isolat
and the phase center for each beam remains at the refle
focus resulting in secondary beams which are spatially
coincident. In general, an array of M elements, pro-
viding spatial multiplexing via $N \leq M$ beams, can be use
but the case of most practical interest and the one
discussed here is for $N = 2$ beams since this adequately
minimizes the selectivity required of the satellite out
multiplexer filters. Use of a single reflector and fee
array to provide spatial multiplexing minimizes the wei
and shroud area requirements of the antenna system. Fo:
this application, the excitation of each port of the
orthogonal beam forming network excites a given antenna
"mode."

The Mode-Shift Effect

The primary patterns from the feed array are nominally
identical except for beam tilts caused by the progressive
phase shift across the array elements as illustrated in
Figure 1(a) for a dual mode two-element feed system. In
this case, the feeds are excited in phase quadrature.
Excitation of each port of the quadrature network produce
a primary beam which illuminates a different portion of
the reflector yielding asymmetrical aperture amplitude
distributions but with phase centers remaining at the
reflector focus. For a curved reflector such as a parab-
oloid, the secondary patterns which result from the
complex sum of the patterns from each feed element are
not symmetrical due to the higher order phase error effects
associated with the displacement of the feed elements
from the reflector focus as shown in Figure 1(b). If
the aperture phase distributions are purely linear (no
higher order phase aberrations) then the secondary phase
patterns of each constituent main beam are uniform. The
complex sum of these beams therefore yields symmetrical
and identical composite patterns for each mode. However,

for curved reflectors, the higher order phase terms produce secondary constituent beams whose phase is not uniform over each main beam as shown in Figure 2. In this case, the relative phasing is such that the beams tend to add on one side of the reflector axis and subtract on the other side. The result is that the net secondary beam for "mode 1" is shifted in one direction and that for "mode 2" is shifted in the opposite direction.

For a symmetrical paraboloid, the mode shift occurs in the plane of the feed array. For offset paraboloids, additional phase error terms are present which give rise to rotations of the mode patterns as well as an asymmetry in the array plane.
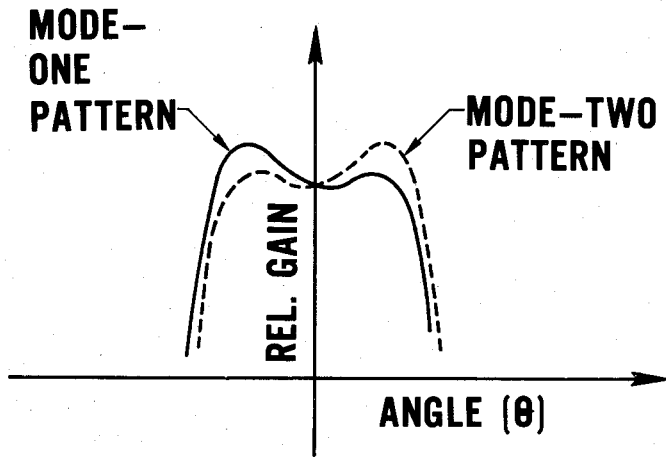
Minimizing Mode Shift Effects

Mode shift arises from reflector phase curvature and can be minimized by increasing the ratio of focal length to dish diameter (f/D). This approach is not always practical due to spacecraft physical constraints. Another less effective approach which is applicable for an odd number of feed elements is to introduce fixed phase shifts, symmetrically disposed in the array plane, to each of the feed elements to alter their relative phase from that produced by the beam forming network. The appropriate phase lead or lag between any two adjacent elements is determined by examining the phase of each constituent beam in the far field and adjusting the feed element phase to equalize the differential phase between two adjacent secondary patterns at symmetrically disposed off-axis angles. This is illustrated in Figure 2 for a three-feed element array. The net mode patterns will then be approximately symmetrical although further iterative adjustments may be required when several feeds are used.

As an illustration of the mode shift phenomenon and its minimization, Figure 3 shows the azimuth plane pattern for an offset parabola having an aperture diameter of 18 wavelengths, a focal length of 16.6 wavelengths, and an array of three rectangular waveguide feeds. The uncompensated pattern is for the condition where the outer two feeds are phased +66° relative to the center element. For a uniform feed excitation, the phase differences would be +60° but this is not satisfied exactly in this case due to amplitude tapering of the outer elements. The compensated pattern shows the effect of adding 9° phase shift to the outer elements. Axial defocusing of the feed array can also affect the symmetry of the mode patterns. Dramatic asymmetry effects as a function of axial feed displacement are noted in Fresnel zone testing. Examples of these effects are presented for multiple element feeds.

FEED
ELEMENTS

REFLECTOR

QUADRATURE
HYBRID

MODE
ONE PORT

MODE TWO
PORT
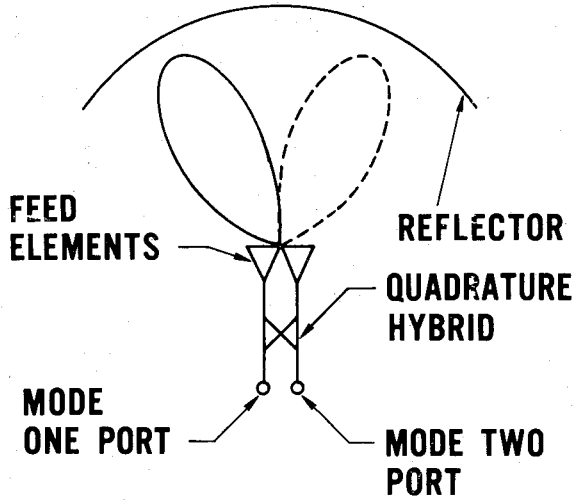
(a) Primary Illumination

MODE—
ONE
PATTERN

MODE—TWO
PATTERN

REL. GAIN

ANGLE (θ)

(b) Secondary Patterns

Figure 1.   Two-"Mode" Reflector

correct this effect if blockages are small and properly located to maintain pattern symmetry. The soundness of this technique has been proved experimentally.

References

1. Han, C. C., et al., "Optimization in the Design of a 12 GHz Low Cost Ground Receiving System for Broadcast Satellites," ICC, June 1973.

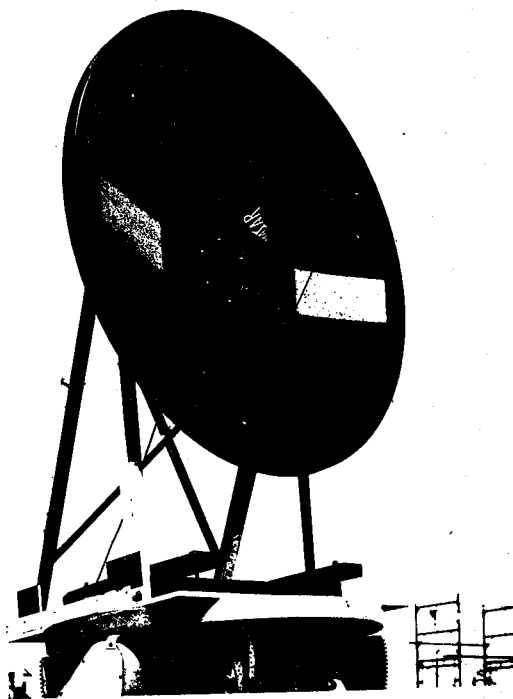2. Silver, S., "Microwave Antenna Theory and Design," McGraw-Hill, 1949, P. 158.
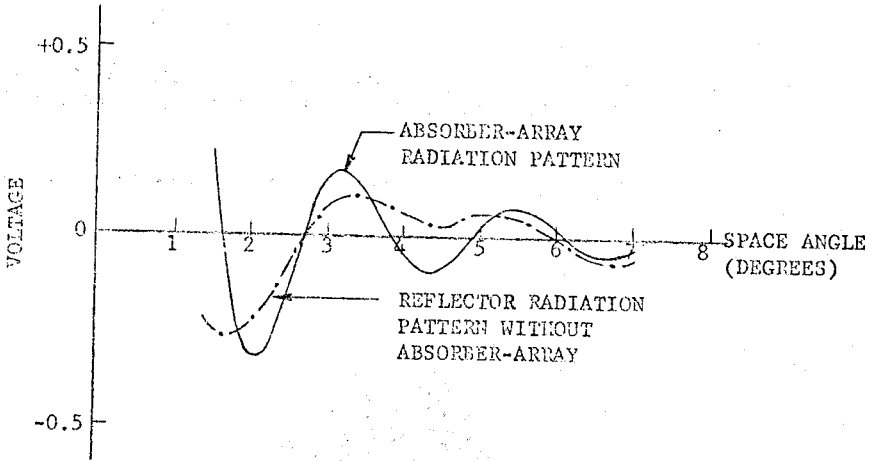

Figure 1-Reflector with absorbers mounted.
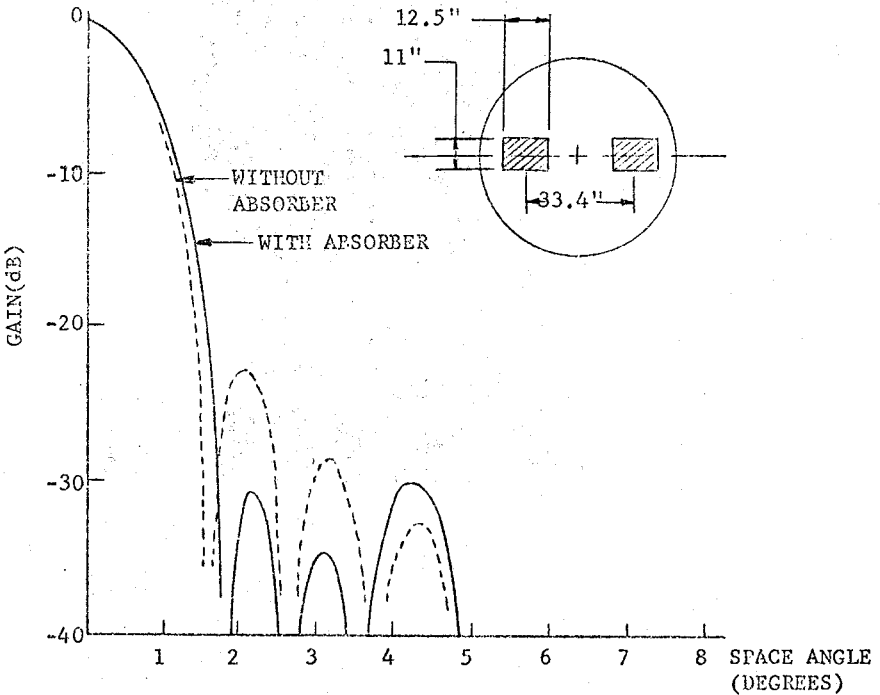
Figure 2-Illustration of matching sidelobe
structure

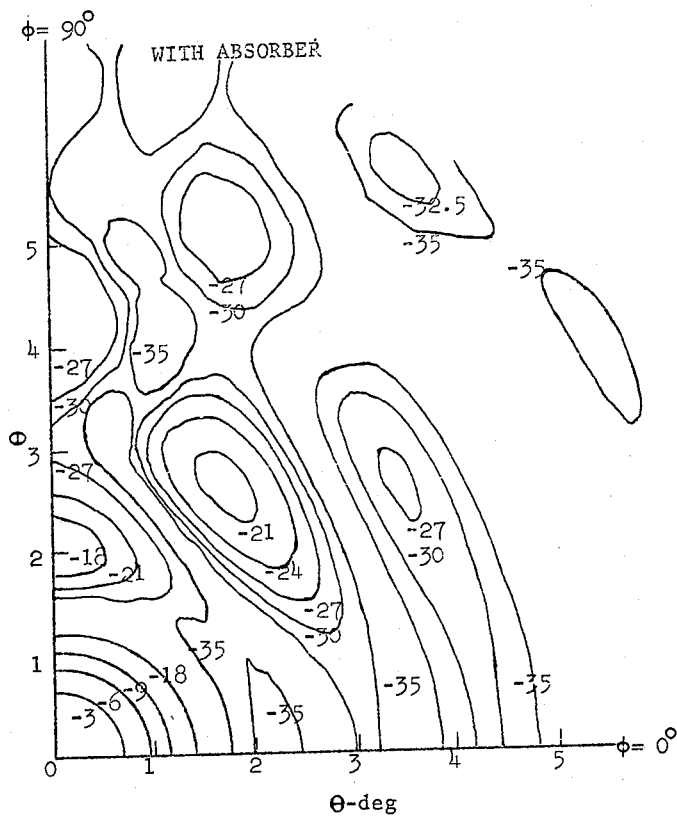Figure 3-Radiation pattern resulting from sidelobe
cancellation

Figure 4-Two-dimension radiation contours

RECENT DEVELOPMENT OF CONICAL REFLECTOR ANTENNAS*

Arthur C. Ludwig, Kenneth Woo, J. J. Gustincic** and J. C. Hardy
Jet Propulsion Laboratory, Pasadena, Calif.

The conical reflector is receiving increased interest for use as unfurlable spacecraft antenna due to the mechanical advantage of the singly-curved surface. A large, high precision, furlable surface can be obtained at relatively low cost. In this paper, the recent development of the conical reflector antenna for use at Ku-, X- and S-band is reported. In particular, the excellent RF performance of the antenna achieved with an X-band line feed is described.

Fig. 1 shows three designs of the antenna. In the absence of a high-efficiency line feed at the onset of the program, the conical-gregorian design[1] was conceived. The conical reflector is illuminated by a corrugated conical horn via a subreflector (generated by a parabolic arc). The large subreflector size required by the design introduces substantial blockage loss. The conical-quadreflex design[2] was conceived to reduce the subreflector size. The conical reflector in this design is illuminated by a corrugated conical horn via two subreflectors, one elliptic-shaped and the other urn-shaped. The reduced sub-reflector size (diameter) significantly decreases the blockage loss but also degrades the capability for multiband operations. Since the design requires multiple reflections on the conical surface, the surface losses are increased. Recently, a line source feed for the conical reflector was obtained. The feed (Fig. 2) consists of a uniform length of circular waveguide with radiating holes and fin phase correctors. The feed utilizes the radiation principles upon which a line feed constructed for the Arecibo spherical reflector[3] was based. The conical-line-source design not only minimizes the blockage and surface losses, but also reduces the antenna weight. Although the line feed is a narrow band device, its bandwidth is more than adequate for deep space applications.

Fig. 3 shows the methods of furling the reflector. The sheet-metal design consists of a conical reflector made of thin aluminum panels connected together by radial ribs and supported by stiffeners on the back of each panel. To furl the reflector, the panels are folded into lobes as shown. The ring-membrane design consists of a conical reflector formed by very lightweight reflecting panels (such as aluminized mylar) stretched between two relatively rigid circular rings. To furl the reflector, the outer ring collapses into a serpentine shape as shown.

Prototype antennas of 6-ft and 14-ft in diameter have been fabricated and tested. It has been found that for 6-ft reflector, the best surface tolerance achievable is 0.008-in rms for the sheet-metal design, and 0.009-in rms for the ring-membrane design, and for 14-ft reflector, the best surface achievable is 0.017-in rms for the ring-membrane design. Fig. 4 shows the RF performance of the antennas, measured at each frequency with an optimum feed in place. As can be seen, the conical-line-source design achieves a high efficiency of 70%. The results are so encouraging that a combined X- and S-band line feed is being developed based on the design of the existing feed. The calculated loss breakdowns for the antennas are compared in the following table, for the 6-ft size at X-band:

Loss Factor	Computed Loss (dB)		
	Gregorian	Quadreflex	Line Source
Subreflector and/or feed blockage	1.07	0.14	0.05
Spillover	0.26	0.83	0.34
Illumination	0.45	0.44	?
Phase	0.09	0.15	?
Load dissipation	0	0	0.36
Reflector distortion	0.02	0.34	0.03
Reflector resistivity	0	0.80	0
Subreflector support blockage	0.10	0.10	0
Total loss	1.99	2.80	?
Calculated Gain (dB)	42.2	41.4	?
Measured Gain (dB)	42.0	41.3	42.6

The breakdowns for the line source case are yet to be completed pending the results of loss calculations for illumination and phase. The quadreflex design shows relatively low performance because of the small size (7.5 wavelengths at X-band) of the elliptical subreflector and the unusually large reflector resistivity loss. This resistivity loss can easily be reduced for later models.

Acknowledgement
The authors wish to thank P. W. Cramer for computing the performance of the quadreflex design, and G. C. Voyles for assisting the measurements.

References
1. A. C. Ludwig (1972 IEEE AP-20, p. 146)
2. R. E. Oliver (1971 JPL Quarterly Technical Review, Vol. 1, No. 1, p. 78)
3. A. W. Love and J. J. Gustincic (1968 IEEE AP-16, p. 132)
4. R. E. Oliver, M. R. Trubert, and A. H. Wilson (1972 JPL Quarterly Technical Review, Vol. 2, No. 2, p. 42)
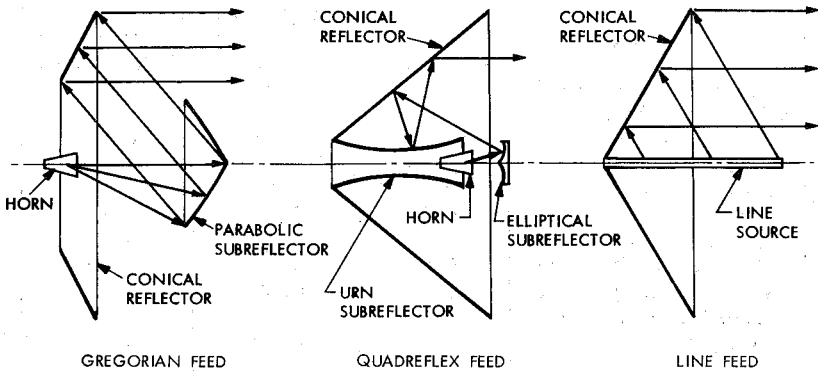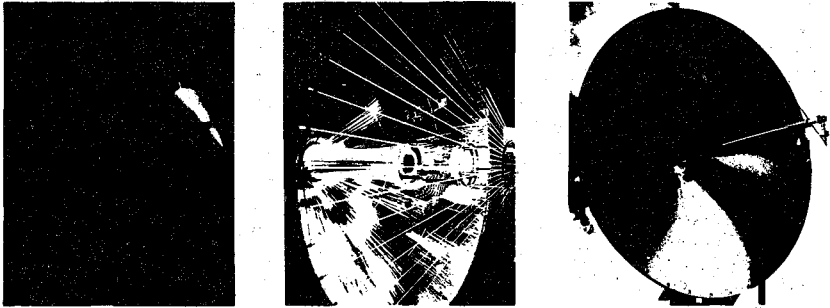
CONICAL
REFLECTOR

CONICAL
REFLECTOR

HORN

PARABOLIC
SUBREFLECTOR

CONICAL
REFLECTOR

HORN

URN
SUBREFLECTOR

ELLIPTICAL
SUBREFLECTOR

LINE
SOURCE

GREGORIAN FEED   QUADREFLEX FEED   LINE FEED

Figure 1.   Alternate Designs of Conical Reflector Antennas
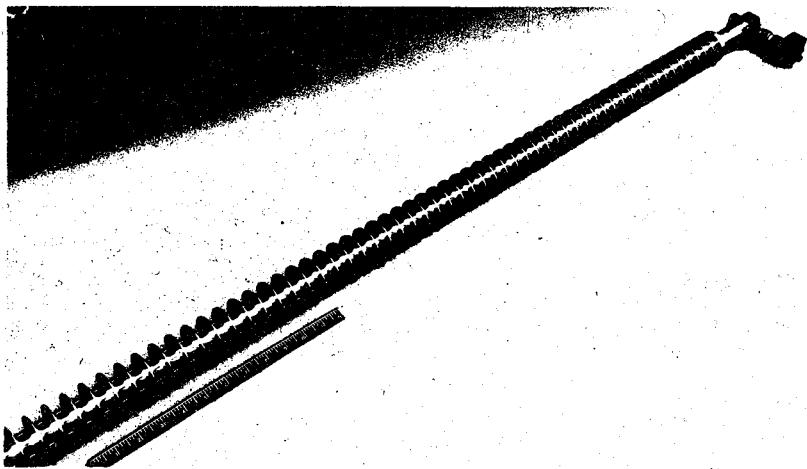
Figure 2. X-Band Line Source

SHEET–METAL DESIGN   RING–MEMBRANE DESIGN
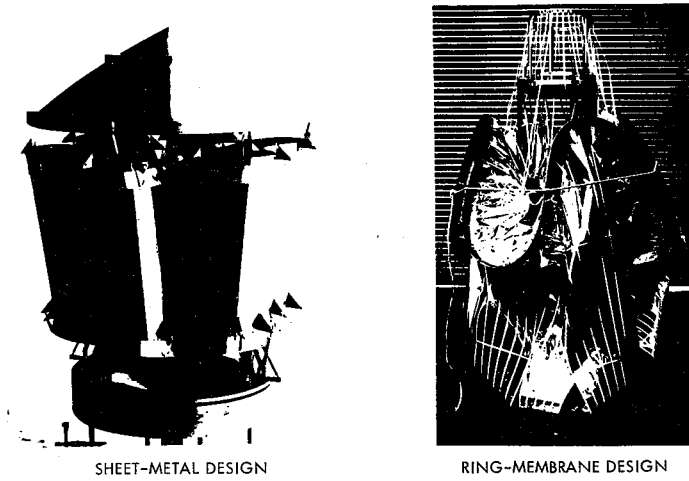
Figure 3.   Furling Techniques
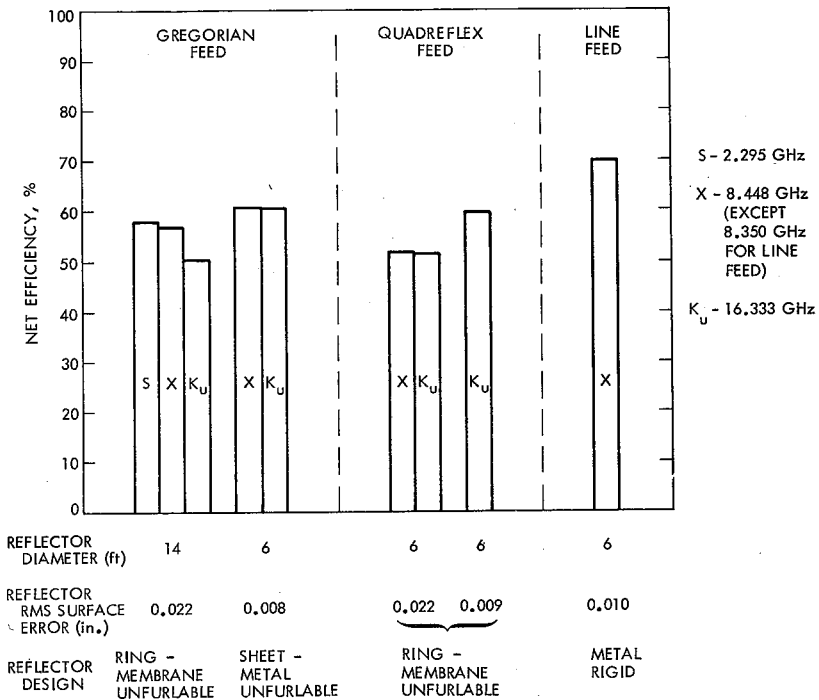

Figure 4. Measured RF Performance of Conical Reflector Antennas

PERFORMANCE OF A REFLECTOR-ARRAY LIMITED SCAN TECHNIQUE

A. C. Schell
Microwave Physics Laboratory
Air Force Cambridge Research Laboratories (AFSC)
L. G. Hanscom Field, Bedford, Massachusetts 01730

Antennas that provide scan coverage over a limited angular sector are used for applications such as aircraft landing systems and communications satellites. A design goal for this type of antenna is to achieve a specified gain and pattern for the minimum number of active radiating elements. Representative examples of limited scan antennas are lenses, stepped reflectors, arrays of directive elements, and multiple reflectors. In much of the earlier work the feed was treated as a movable point source. For current uses it is often desirable to scan electronically by phase control. This implies the use of a phased array for a feed, with at least as many elements as there are half-power beamwidths in the scan sector.[1]

Limited scan sector antennas consisting of a reflector with a phased array have been built and tested.[2] This antenna design is usually based on the idea of an active subreflector; that is, the array simulates the displacement of a feed in the focal region of the main paraboloidal reflector. In this paper an attempt is made to devise a limited scan sector antenna for which the electromagnetic performance parameters can be readily related to the geometry and array size. The antenna consists of a stepped reflector and a circular arc array, and is designed to scan in one plane. The element currents of the circular array are equal in amplitude and have a progressive phase given by $\beta n \Delta \theta$, so that the phase variation of the feed radiation as measured along a circle near the reflector approximates a variation proportional to the angle θ. The reflector surface is chosen to transform this phase variation into a linear wavefront normal to the beam direction. The scan condition to be imposed is that a constant incremental phase change in θ of the feed radiation causes a constant incremental phase change of the output wave with the aperture coordinate y (see Fig. 1). Thus,

$$\frac{dy}{d\theta} = \text{const.} = R$$

and, as $y = \rho \sin \theta$,

$$\rho = \frac{R\theta}{\sin\theta} \tag{1}$$

The curve of eq. (1) is a statement of a scan requirement, but it does not transform the feed radiation appropriately into a desired wavefront such as a plane wave. To do this, the reflector must be stepped so that a satisfactory beam is formed over the scan range.

The resultant reflector consists of confocal parabolic sections with their centers arrayed along the curve given by eq. (1). Alternatively, if the antenna consists of the array and a lens, the path lengths within the lens would be adjusted for equal paths at some beam angle.

The far field beam is scanned according to the relation

$$\beta = kRsin\theta_B$$

and the total scan range, expressed as a number of half-power beamwidths, is approximately

$$N_B \approx \frac{2\beta sin\theta_o}{\pi}$$

where θ_o is the half-angle of the feed arc. For this type of antenna, the reflector is usually not in the far field of the feed array, and the radiation of the array is found from the sum

$$F(\theta) = \sum_{-N}^{N} I_o e^{j\beta\theta_n} e^{jkr_n} [1+cos(\theta-\theta_n)]$$

where an appropriately directed Huygens source has been assumed for each element pattern.

Calculation of the deviation of this pattern from the ideal illumination of the reflector leads to a measure of the gain decrease with scan. In Fig. 2 is shown the gain variation for a typical feed of 25 elements. For this case, $\beta = 40$ corresponds to a scan angle of approximately 9°. Similar curves illustrate the relation between feed size, scan range, and the geometry of the antenna. Pattern calculations show the effect of phase error on the beamwidth and sidelobe level as the beam is steered to the sector edge.

References

1.   W. T. Patton (1972 Phased Array Antennas, A. Oliner and G. Knittel, Eds., Artech House, Inc., p. 330.
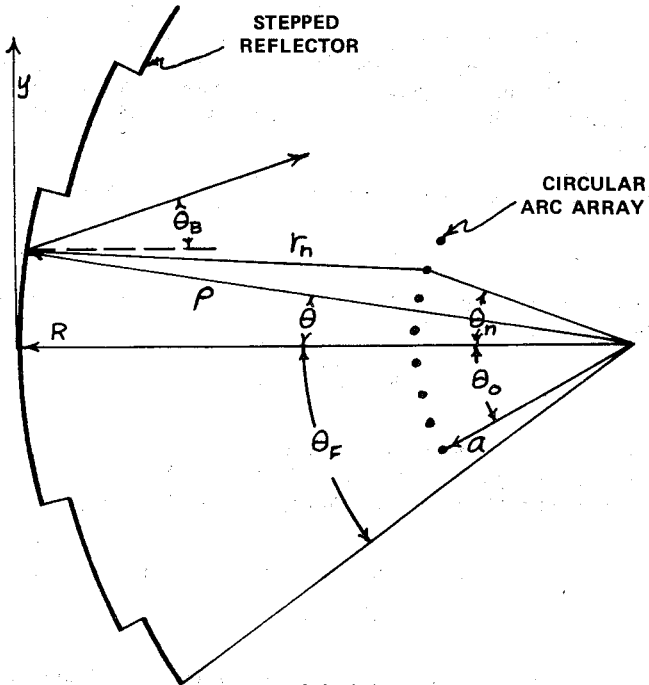
2.   C. Winter (1968 Proc. IEEE, 56, p. 1984.
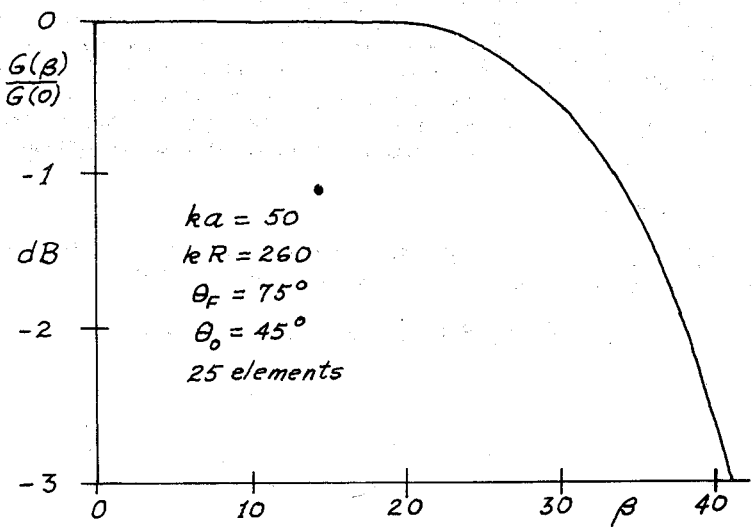
FIG. 1
ANTENNA GEOMETRY

$ka = 50$
$kR = 260$
$\theta_F = 75°$
$\theta_0 = 45°$
$25 \ elements$

FIG. 2
GAIN VARIATION WITH SCAN

320

TWISTREFLECTOR DESIGN USING E-TYPE AND H-TYPE MODES

J. D. Hanfling, G. Jerinic, L. R. Lewis
Raytheon Company
Missile Systems Division
Bedford, Massachusetts

In many antenna applications, unidirectional periodic gratings are used to rotate or twist the polarization of an incident plane wave. For example, in Cassegrain antennas main dish polarization twisting is used in conjunction with a transreflector to prevent subdish blocking, and subdish polarization twisting is used to suppress reflections back into feed (Reference 1). Presented herein are formulas, in terms of E-type and H-type modes, for predicting twistreflector performance and curves showing ideal twistreflector performance as compared to that measured with a practical configuration.

The basic concept of the polarization twistreflector is simply illustrated for the case of normal incidence (TEM), as shown in Figure 1. A periodic strip grating spaced above a metallic reflector is oriented so that the incident electric field is at +45° and is designed to rotate the polarization to -45° upon reflection. The grating and height above the reflector are determined such that the decoupled polarizations, parallel ($E_{||}$) and perpendicular ($E_\perp$) to the strip direction are 180° out of phase. The reflection phases of $E_{||}$ and $E_\perp$ are determined via equivalent circuits of the infinite periodic structure.

For arbitrary incidence and polarization, twistreflector design is facilitated by plane wave decomposition into E- and H-type modes, in the strip direction, that remain decoupled at the reflecting interface (Reference 2). The modal transmission lines, corresponding to $h_y = 0$ (E-type) and $e''_y = 0$ (H-type), are terminated by the corresponding susceptance of the grating in parallel with shorted transmission lines, as shown in Figure 2. The equivalent circuit is a dominant mode approximation. For plane wave incidence, as illustrated in Figure 3, the total reflected electric field in spherical coordinates and in terms of the E- and H-type mode reflection coefficients, is as follows:

$$E_{\theta_r} = -\left(a_x \Gamma'' \frac{k}{k_z} \cos \phi + a_y \Gamma' \frac{k\, k_z}{(k^2 - k_y^2)} \sin \phi \right.$$

$$\left. + a_y \Gamma'' \frac{k}{k_z} \frac{k_x k_y}{k^2 - k_y^2} \cos \phi \right) e^{-j(\underline{k}_r \cdot \underline{r})}$$

(1)

$$E_{\phi_r} = \left(-a_x \Gamma'' \sin \phi + a_y \Gamma' \cos \phi \right.$$

$$\left. - a_y \frac{k_x k_y}{(k^2 - k_y^2)} (\Gamma'' - \Gamma') \sin \phi \right) e^{-j(\underline{k}_r \cdot \underline{r})}$$

(2)

321

where $\underline{k}_r = k_x \underline{x}_0 + k_y \underline{y}_0 - k_z \underline{z}_0$; a_x and a_y are the incident wave
amplitudes; k_x, k_y, and k_z are the incident wave propagation con-
stants; and Γ', Γ'' are the corresponding E-type and H-type mode
reflection coefficients.

For a wave polarized in the plane of incidence perfect twisting will
occur when the ratio E_{ϕ_r}/E_{θ_i} approaches infinity. This occurs when
$\Gamma''/\Gamma' = -1$, and the twisting then becomes only a function of the angle
of incidence, θ, and the angle the incidence plane makes with the
periodicity, $90 - \phi$. The formula for perfect twisting, e.g., com-
plete power transfer from E_{θ_i} to E_{ϕ_r} or E_{ϕ_i} to E_{θ_r}, is expressed by
$\tan \phi = \sec \theta$ as plotted in Figure 4. The performance of an ideal
twistreflector obeys the $\Gamma''/\Gamma' = -1$ condition and provides the limits
of best performance that can be achieved over the range of θ and ϕ,
as given in Figure 5. This figure shows curves of $E_{\theta_r}/E_{\theta_i}$ or E_{ϕ_r}/E_{ϕ_i}
for ϕ = constant as a function of θ. For $\phi = 45°$ the perfect twisting
condition is at $\theta = 0°$ and then slowly falls off with increasing θ; as
ϕ is increased optimum twisting occurs for larger values of θ and the
optimum twisting region becomes sharper.

The geometry of a practical twistreflector utilizing a metallic strip
grating supported above a ground plane is shown in Figures 2 and 3.
Formulas for the inductive reactance and capacitive susceptance for
H-modes and E-modes for the strip grating interface (Reference 3)
are converted to formulas for E-type and H-type modes by substitution
of $\sqrt{k^2-k_y^2}$ for k and $\sqrt{k_\epsilon^2-k_y^2}$ for k_ϵ. Combining the strip grating sus-
ceptance and reactance with that of the short circuited transmission
lines results in expressions for Γ' and Γ''. The performance of the
twistreflector has been obtained by appropriate substitution of Γ' and
Γ'' into (1) and (2), as plotted in Figure 6.

An 18λ square panel with a strip grating supported by a plexiglass
(k = 2.57) sheet over a ground plane was designed and evaluated at
$\phi = 66°$, built and tested. The dimensions were as follows: strip width
(d') of $.114\lambda$, grating periodicity (a) of $.228\lambda$ and distance to the
ground plane (D) of $.164\lambda$. The performance was measured by a
standard arch technique and is compared with predicted values and
ideal twisting, as shown in Figure 6. Both curves show significant
polarization twisting about the optimum $\theta = 62°$. In view of the
excellent agreement of the curves it can be concluded that the domi-
nant mode analysis for calculations, and the construction of and size
of the sample for measurement, do not introduce significant errors.

1)   Hannan, P. W., "IEEE AP-9", p. 140, 1961.
2)   Altschuler, H. M., and Goldstone, L. O., "IEEE MTT-7",
     p. 213,   1959.
3)   Marcuvitz, N., "Mass. Boston Tech. Pub., p. 280, 1964.
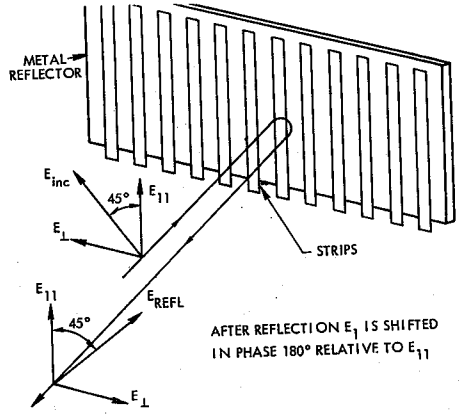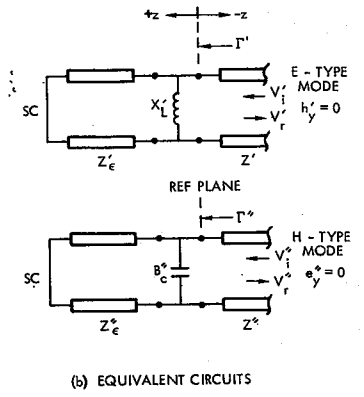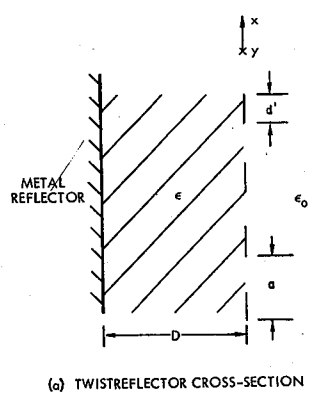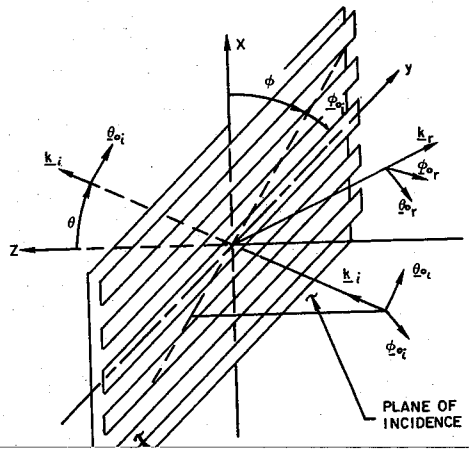
Figure 1 - Principle of Twistreflector
Operation

(a) TWISTREFLECTOR CROSS-SECTION

(b) EQUIVALENT CIRCUITS

Figure 2 - Network Representation of Twist-
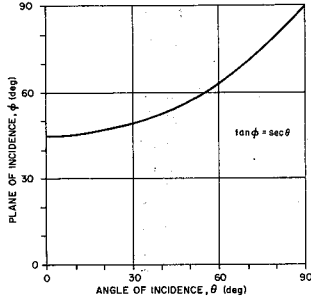reflector for E-Type and H-Type Modes

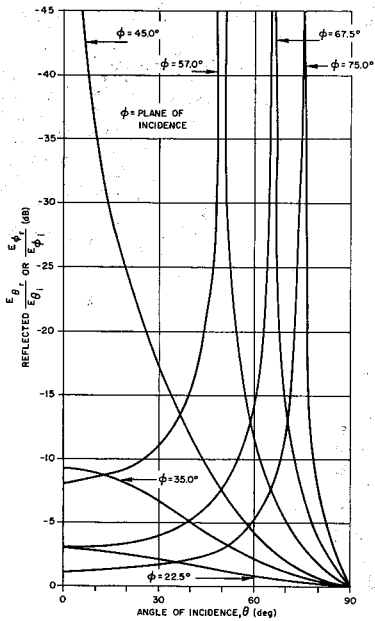Figure 4 - θ - ϕ Pairs for Perfect Twisting

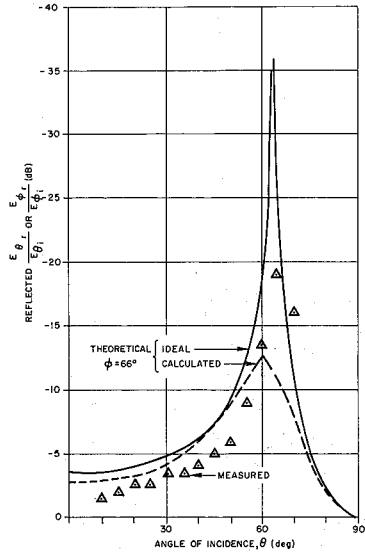Figure 5 - Ideal Twistreflector Performance

Figure 6 - Comparison of Theoretical and Measured Parallel-strip Twist-reflector Performance for $\phi = 66^{\circ}$

ELECTRONIC SCANNING BEAM ANTENNAS
FOR THE MICROWAVE LANDING SYSTEM (MLS)

A.W. Moeller, Bendix Communications Division, Towson, Maryland
W.G. Jaeckle, Bendix Research Laboratories, Southfield, Michigan

INTRODUCTION - This paper describes an electronic scanning beam antenna system which is one of four different systems competing for the ultimate Microwave Landing System (MLS) presently under development by DOT/FAA.[1,2 & 3]   The ultimate MLS systems are intended to replace the existing VHF/UHF ILS facilities at all civil and military airports and will be recommended by the U.S. for adoption as an international standard by ICAO. In addition, the optimum MLS configuration will have capability to provide Category III landing (guidance to touchdown under zero visibility conditions) with variable approach path selection that has applicability to noise abatement procedures which should serve to increase runway capacity. The electronic scanned array system described in this paper is intended to meet the requirements imposed upon the ultimate MLS.

SYSTEM DESCRIPTION - Angular guidance information is derived in the MLS equipped aircraft from ground transmitted scanning beams that are angle encoded with a frequency modulation. As the beam sweeps past the aircraft, the aircraft processor measures this modulation frequency to determine angular position with respect to the runway.

A MLS-equipped runway for Category III landing is shown in Figure 1. The antenna complement consists of C-band azimuth (AZ-1) and elevation (EL-1) scanners for angle guidance to runway threshold and a precision Ku-band elevation (EL-2) scanner for angle guidance through flare out and touch down. All antennas in the system are simple, electronically scanned, linear phased arrays. Linear phased arrays inherently form conical type beams as the beam is scanned off axis. Since planar beam guidance is preferred for some operational requirements, each antenna function has both a primary and an optional small orthogonal array so that planar guidance information can be derived by the aircraft processor from the two orthogonal conical beams. Two basic types of arrays are employed in the system - azimuth type scanners and elevation type scanners. The orthogonal array for the azimuth antenna is simply a small size elevation scanner and the orthogonal array for the elevation antenna is a small azimuth scanner. The same basic line array design is used for both the azimuth and elevation scanners, the only difference being in the radiating apertures. The radiating aperture for an elevation scanner is a vertical array of dipoles, while the radiating aperture for an azimuth scanner is a multiple, probe-fed, extended horn radiator operated with a ground plane. Identical design approaches are used for both the C-band and Ku-band antennas. This approach naturally leads to a high degree of antenna design and component commonality which, in turn, results in reduced system cost.

ARRAY DESCRIPTION - A block diagram of a typical MLS phased array antenna is shown in Figure 2. The array can be divided into four major sections: (1) the radiating elements, (2) the phase shifters, (3) the RF power divider, and (4) the beam steering electronics. The phase shifters are electronically controlled, 6-bit, ferrite latching type with an integral solid-state driver. The phase shifter has a phase accuracy of 3.5-degrees RMS with a 1-dB insertion loss and a 2 microsecond maximum switching time. The power divider is a center-fed, series-parallel type employing directional coupling elements. The coupling values of these elements are designed to produce a 27-dB sidelobe Taylor illumination function across the array. The directional coupler approach minimizes antenna gain variation with scanning as reflected energy due to mutual coupling and impedance variations is absorbed in the coupler loads instead of being reradiated,as in the case of a reactive type power divider. The center-fed feed arrangement minimizes the effect of temperature on beam pointing accuracy.

325

The beam steering electronics consists of a scan timing generator, a sequence generatoi and a steering word compiler with storage units. Upon receipt of a scan gate pulse from the central timing generator, the scan timing generator supplies a series of coarse scan clock pulses to a steering word compiler. The scan timing generator also produces a series of fine scan clock pulses for each coarse scan clock pulse which are then sent to the sequence generator. The coarse scan clock pulses are spaced at 80-microsecond intervals which are equivalent to a 0.1-beamwidth scan increment. The fine scan clock pulses are spaced at an interval of 80/(N-1)/2 microseconds, which are equivalent to 0.1/N-1)/2 beamwidth scan increments, where N is the number of ele-ments in the array. This is equal to a fine scan increment of 0.0025 degrees in the case of an 81 element array having a 1-degree beamwidth. The steering word compiler computes a new set of 6-bit steering words for each phase shifter in the array for each coarse scan pulse. These words are held in the storage units until the units are gated oi by the sequence generator. The storage units are switched on two at a time at the fine scan clock rate by the sequence generator. Since only two phase shifters are reset at ar time, the switching transient effect on the antenna pattern is negligible. This unique coarse-fine steering scheme results in an extremely low degree of beam granularity and a minimum of circuit complexity and cost. [4]

Two types of performance monitors are employed in the array: (1) an RF beam monitor, and (2) a steering electronics monitor. RF beam monitoring is accomplished by coupling a small amount of energy from each element into a common feed line. The phase of the coupled energy is controlled to produce the equivalent of a received far-field RF beam signal at the feed line output as the antenna is scanned through a selected angle. The steering electronics and phase shifter operation is monitored by means of a sensing circuit in each bit of the phase shifters which gives an indication of the phase state. These circuits are used to operate a bank of LED indicator lights (486 in the case of an 81 element array) and an automatic array monitoring system which is integrated into the overall system monitor.

Figure 3 is a picture of the C-band 81 element elevation array. The array generates a one-degree fan beam which scans from 0 to 20 degrees in elevation and provides coverage out to $\pm$ 60 degrees in azimuth. Static type patterns for this array over the 0 to 20 degrees scan range are shown in Figure 4. A typical dynamic scanning pattern demonstrating the ultra-low granularity characteristics of the beam is shown in Figure 5. The measured beam pointing accuracy was better than $\pm$ 0.02 degrees over the full 20 degrees scan range. The measured data showed that this developmental array met all design objectives and that the electronic scanning beam antenna approach should satisfy all MLS functional requirements.

REFERENCES

1. DOT/DOD/NASA Joint Planning Group (National Plan for Development of the Microwave Landing System, July 1971 AD 733-268 National Technical Information Service)

2. RTCA SC-117 Committee Report ("A New Guidance System for Approach and Landing," December 1970, Volumes I and II, Document No. DO 148)

3. R. J. Kelly ("The Bendix/Bell MLS Signal-In-Space," Proceedings of the ION National Aerospace Meeting, March 13-14, 1973 Institute of Navigation)

4. T. C. Chester and J. Frank ("Array Antennas," Radar Handbook, Chapter pages 11-37 to 11-39, M. L. Skolnik (Editor) McGraw-Hill, 1970).
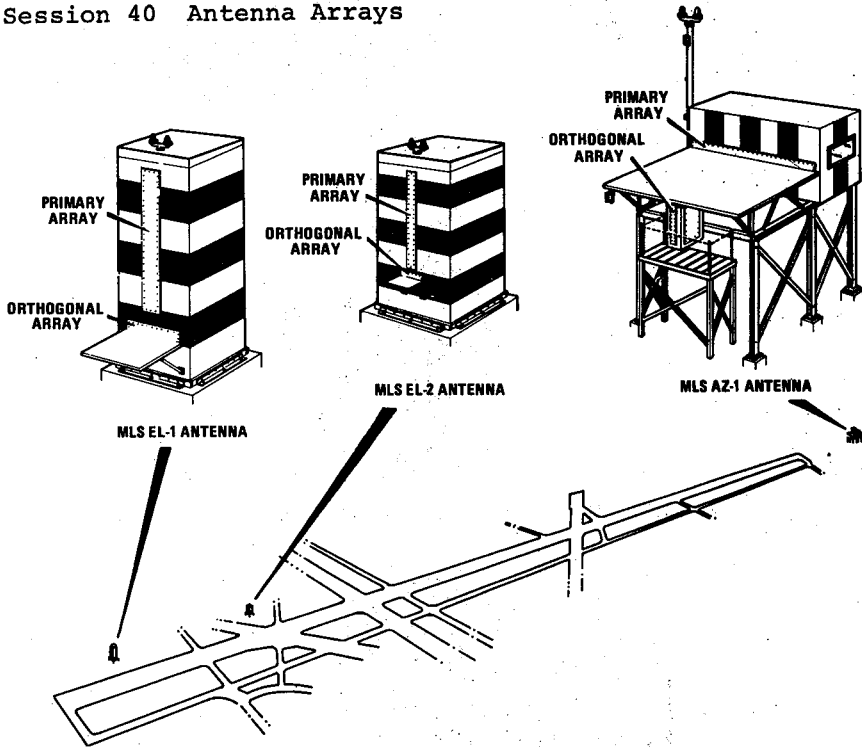
FIGURE 1. CONCEPTIONAL VIEW OF RUNWAY EQUIPPED
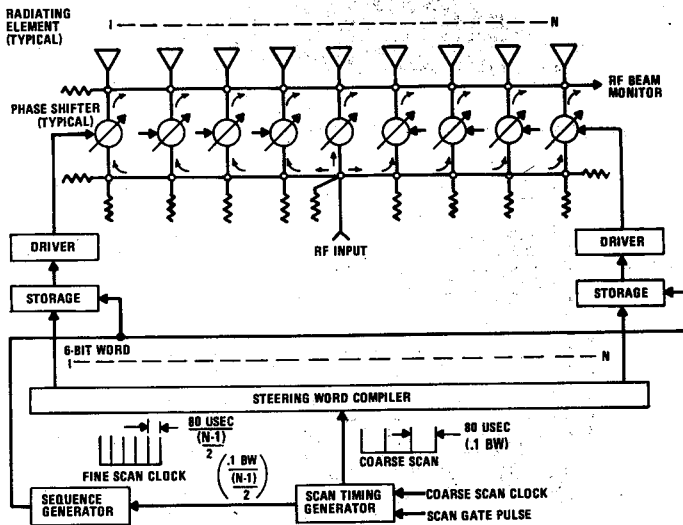WITH MLS PHASED ARRAY ANTENNAS

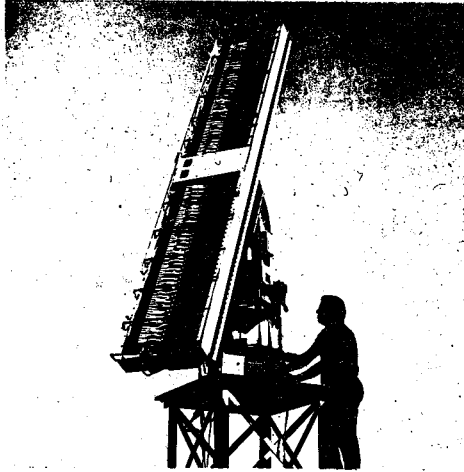FIGURE 2. MLS PHASED ARRAY ANTENNA BLOCK DIAGRAM

327

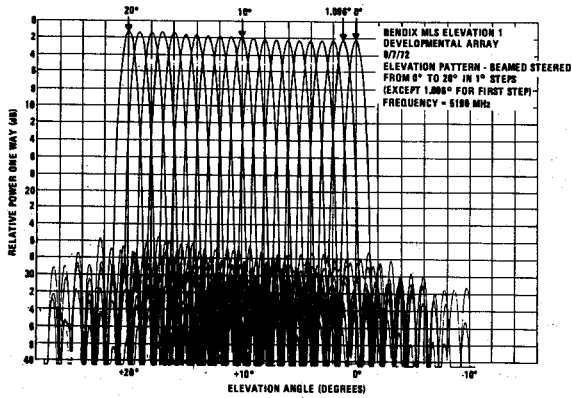FIGURE 3. MLS C-BAND ELEVATION-1 PHASED ARRAY ANTENNA

FIGURE 4. STATIC PATTERNS OF MLS PHASED ARRAY ANTENNA
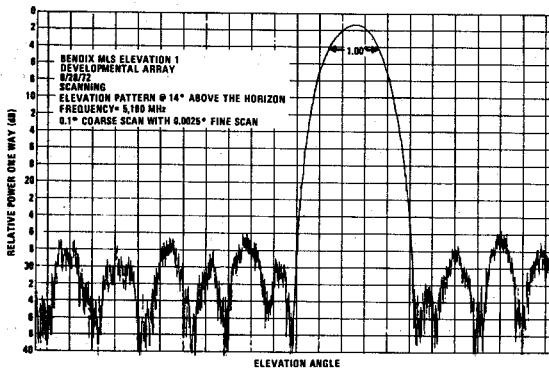

FIGURE 5. DYNAMIC SCANNING PATTERN OF MLS PHASED ARRAY ANTENNA

328

AN EXPERIMENTAL ARRAY PROGRAM FOR LIMITED SCANNING STUDIES

R. J. Mailloux and G. R. Forbes
Air Force Cambridge Research Laboratories
Microwave Physics Laboratory
L. G. Hanscom Field, Bedford, MA

Previous studies[1,2] have indicated that large elements can be used in an array for limited scan applications if odd modes are excited in the apertures to cancel the dominant grating lobes. This paper describes several facets of an experimental program devoted to evaluating and extending this technology. The main effort of the experimental program was the design, construction and testing of an eight element array for $\pm 12^\circ$ E-plane scan. In addition, some H-plane scanning element pattern data was obtained to predict H-plane and intercardinal plane scanning results.

The array technique allows scanning in one or several planes over a limited angular sector out to the maximum angle θ_{max}, measured in any plane and given by

$$D \sin \theta_{max} = 0.6$$

where D is the interelement distance in the plane of scan normalized to wavelength. This factor corresponds to element spacings of about 3.5λ on each side for $\pm 10^\circ$ scan, and 4.6λ for $\pm 7.5^\circ$ scan, with accompanying phase shifter reduction ratios of about 4 and 6.5 for the two-dimensional case.

The experimental array shown in Figure 1 has been used at 11 GHz to study the E-plane scanning characteristics of the technique with a particularly simple form of odd mode control. The array consists of eight horn elements, each about three wavelengths across. After dividing the input signal eight ways, the eight signals are fed to power dividers through varied lengths of coaxial line to provide a progressive phase shift for beam positioning. Each phase-shifted signal is split into two equal signals by a power divider, and then excites two X-band waveguides through probe transitions. The difference in length of the coaxial lines exciting the two probes determines the ratio of even to odd mode signals produced at the junction between the X-band waveguides and the square waveguide at each horn throat. Equal line lengths excite only an odd mode (LSE11) and one half wavelength difference in the line lengths produce a purely even mode (LSE10). Line length differences other than a half wavelength produce an even and odd mode combination with fixed relative phase but with the odd mode either positive or negative depending upon whether the difference is more or less than the half wavelength. This sign change is required in order to scan the beam to either side of the broadside position.

Session 40 Antenna Arrays

The phase velocities of the two modes are different and so the
total electrical phase length difference between them must be
set to an integral number of half-wavelengths in order to excite
the odd mode $\pm 90°$ out of phase with the even mode in each aper-
ture. This was done by adjusting the lengths of the square
waveguides to compensate for the path length difference through-
out the horn.

Thus equipped, the array has been used to simulate actual scan
conditions. The odd mode amplitude was adjusted to form an ele-
ment pattern zero at the grating lobe nearest broadside for each
beam position by inserting pre-cut cable phase shifters. A more
practical configuration could perform the beam steering and odd
mode control functions together by using one phase shifter in
each waveguide rather than the sequential phase shifts introduced
for convenience in this experiment.

Figures 2A and 2B show E-plane patterns of the array of Figure 1.
In Figure 2A, the array is phased at broadside and all elements
are excited with equal power (-13 dB sidelobes). This figure
shows grating lobes at approximately $\pm 19°$ (-16 dB) and also at
$\pm 40°$ (-26 dB). These would be zero if the horn elements were
perfect, and they can be reduced somewhat by using a dielectric
lens to collimate the beam of each horn. Figure 2B shows two
cases at the maximum scan angle $+12°$. The dashed curve in this
figure shows the horn array radiation pattern without odd modes,
and clearly indicates the impossibility of using such a design.
In this case, the main beam gain is reduced over 5 dB with
respect to the broadside array and the grating lobe at $-7°$ is
larger than the main beam by 1.8 dB. Other grating lobes are
at tolerable levels. The solid curve of 2B shows that when each
element is excited with an odd mode signal by changing the rela-
tive lengths, the offending grating lobe is reduced to approxi-
mately the -20 dB level, and the main beam gain is increased to
approximately -1.2 dB with respect to the broadside case.

The results of other experiments and investigations including
element pattern data for H-plane scan, bandwidth and cross polari-
zation data and some sidelobe data for an amplitude tapered array
will be discussed in the oral presentation.

References:

1. R.J. Mailloux (AFCRL Technical Report #72-0421, 19 July 1972).
2. R.J. Mailloux, G.R. Forbes (1972 G-AP Symposium Digest,
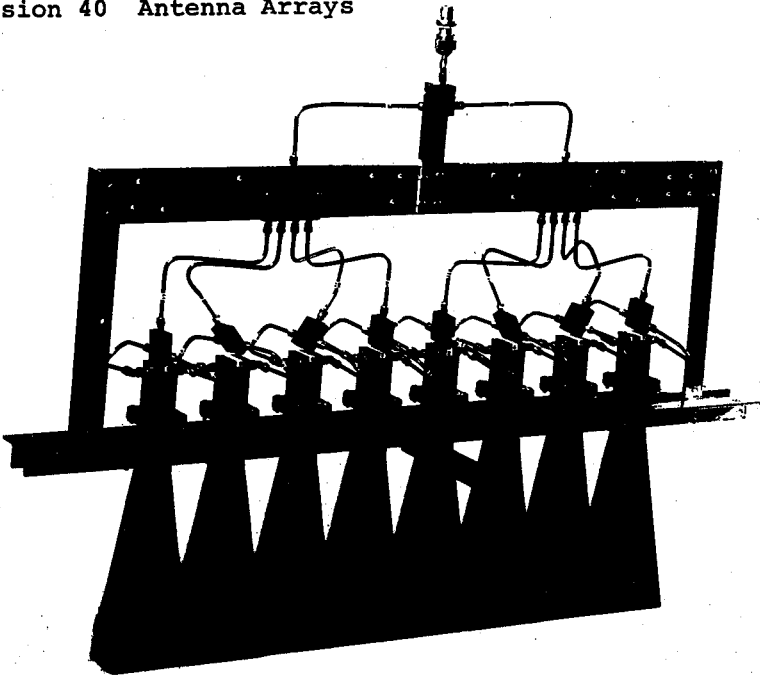   December 1972, pp. 229-232).
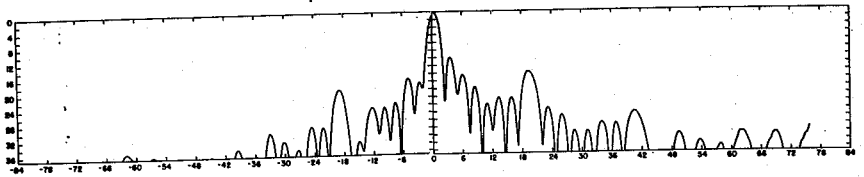
Figure 1.   E-Plane Experimental Array

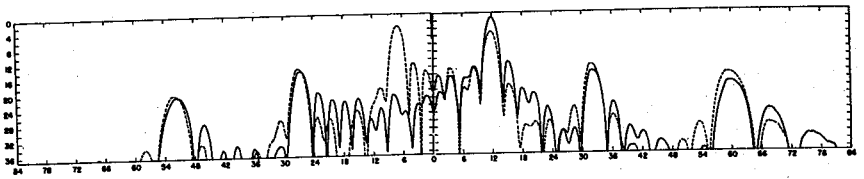Figure 2A. Array Radiation Pattern (Broadside)

Figure 2B. Array Radiation Patterns (12° scan)
————————— With Odd Mode Control
---------- Without Odd Mode Control

331

ON THE DESIGN OF A CIRCULARLY POLARIZED
WAVEGUIDE NARROW WALL RADIATING ELEMENT

N. G. Alexopoulos
University of California
Los Angeles, California
M. E. Armstrong
Hughes Aircraft Company
Fullerton, California

The circularly polarized radiating element consists of co-located longitudinal and transverse slots cut in the narrow wall of region I of the T-septum dual-mode[1] waveguide illustrated in Figure 1. The orientation, method of excitation and location of the crossed slots has been determined by examination of the sum and difference mode wall and septum current density characteristics. The results indicate that the transverse wall slot should be excited by a transverse septum slot. A more convenient location for the crossed slots is the narrow wall of region II, however, this choice is precluded since the difference mode current density is approximately 18 dB below the sum mode current. It is further noted that the longitudinal wall slot is excited only by the sum mode and the transverse wall slot and transverse septum slot combination is excited only by the difference mode. The crossed slots have orthogonal components of radiation when excited by the sum and difference modes and the amplitude and phase of each polarization is controlled independently by its mode of excitation thus facilitating the implementation of this radiating element in a circular polarized application.

The immittance characteristics of the crossed slot element have been determined theoretically by a variational formulation[2] and measured by the "Cavity Method."[3] The results[4] compare satisfactorily and were used in the design of a 20 element linear nonresonant circularly polarized array. A photograph of the crossed slot array is shown in Figure 2 where it is noted that a modified dumbell or H-type transverse wall slot has been used. The effective length of the transverse wall slot is also dependent upon the length and orientation of the septum slot. Since the undesired cross polarized component of radiation from the transverse wall slot is enhanced by the presence of the modified dumbell its dependence upon the septum slot configuration should receive further attention.

Pattern measurements of the initial design indicated that the sum and difference mode principle plane radiation maxima were separated by approximately 9 degrees. The principle plane patterns of a second design are shown in Figure 3, where it is seen that the sum mode and difference mode directions of maximum radiation are within approximately 1.5 degrees of one another. The latter design involves only a change in the T-septum insertion depth to compensate for the difference in phase velocities between the two modes. This is an excellent demonstration of the versatility of the T-septum configuration and its

application to circular or dual polarized antenna requirements. The linear array axial ratio patterns have been measured and indicate that polarization circularity is within ±1 dB at least to the half power beamwidth limits. The axial ratio should improve for exact alignment of the sum and difference beams and the sidelobe level for the difference mode of excitation should improve by accounting for mutual coupling effects.

References

1. Elliott, R. S., "Two-Mode Waveguide for Equal Mode Velocities," IEEE Transactions on Microwave Theory and Techniques, Vol. MTT-16, No. 5, pp. 282-286, May 1968.

2. Oliner, A. A., "Equivalent Circuits for Slots in Rectangular Waveguide," Polytechnic Institute of Brooklyn, R-234-50, PIB-179, August 1951.

3. Wong, N. S., Tang, R., and Okubo, G. H., "Investigation of Characteristics and Practical Implementation of Arbitrarily polarized Radiators in Slot Array, "Hughes Aircraft Company, Fullerton, California, Report 1, Contract No. F19628-70-C-0142, February 1971.

4. Armstrong, M. E., "A Circularly Polarized Waveguide Narrow Wall Slot Radiator," Ph.D. Dissertation, University of California, Los Angeles, 1973.
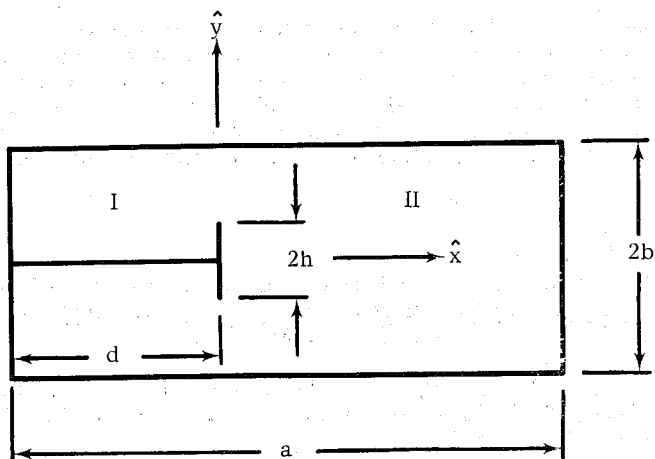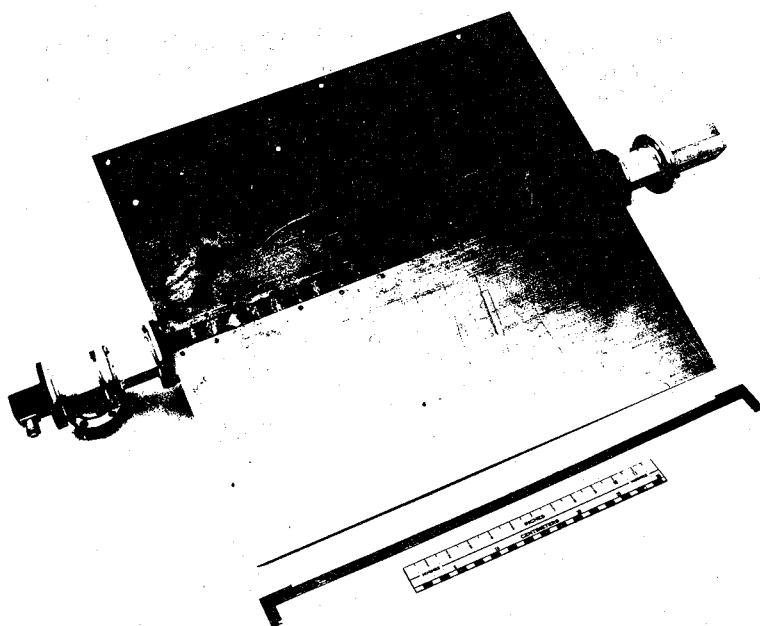
Figure 1. Dual-Mode Waveguide Geometry.

Figure 2. Photograph of 20 Element Crossed Slot Linear Array.

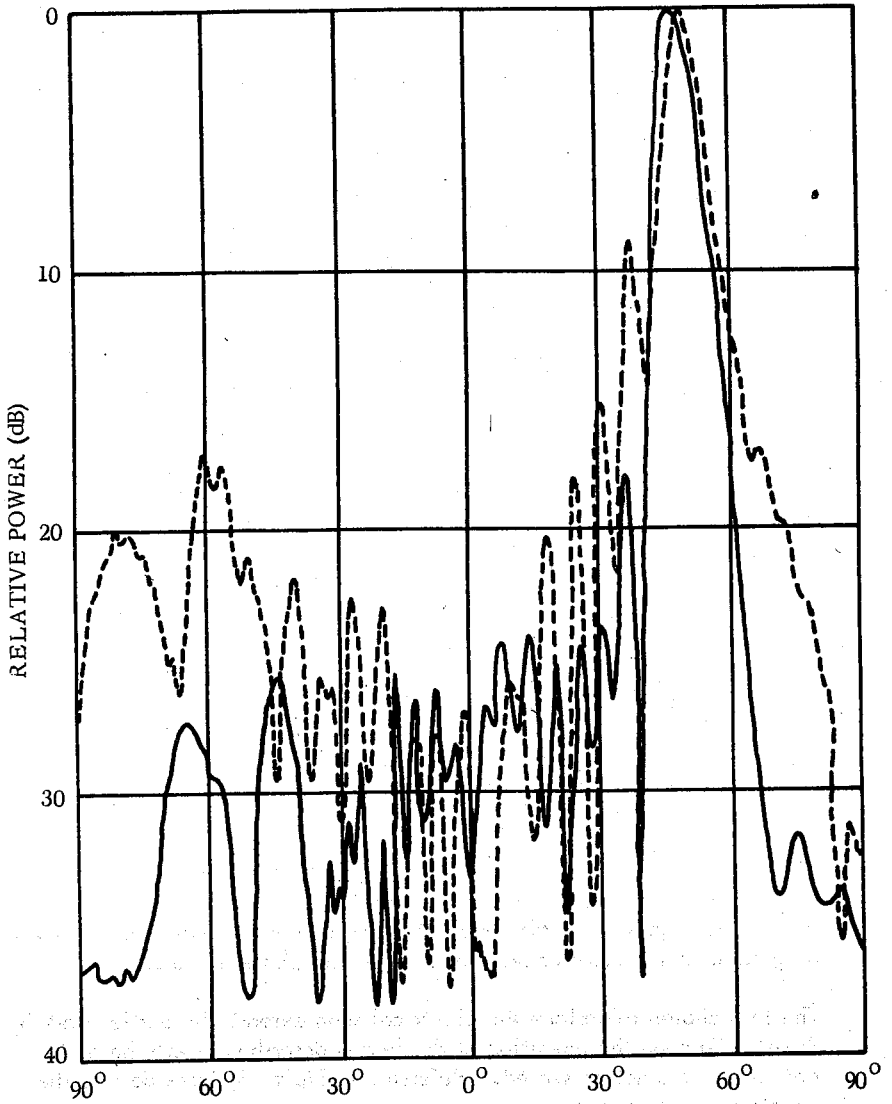Figure 3.   Linear Array Patterns--d/a = 0.328
Σ Mode ———— , Δ Mode — — — — — .

A LARGE EDGE-SLOT ARRAY FOR SATELLITE COMMUNICATIONS

By J. L. Harrison and B. D. Cullen
Radiation
A Division of Harris-Intertype Corporation
Melbourne, Florida

This paper describes a very large electrically scanned slot array (comprising 25,000 slots) that has been built for communication with a synchronous satellite. It uses a new type of lens as the scan mechanism.

The major objective of the array development was to provide sky coverage of ±15° about some nominal in elevation. The external physical appearance of the array is shown in Figure 1. As shown, the antenna receive aperture comprises some 75 waveguides, each with 215 slots. For scanning in elevation, each waveguide is driven by a corresponding lens waveguide, which is a traveling-wave array of edge slots designed to radiate 95 percent of the input power. Circular polarization is provided externally by covering the entire array aperture with a transmission polarizer.

The feed for the slot arrays is shown in Figure 2, with the constrained lens feed tucked under the slot arrays. This configuration is spatially economical; the trombones are required in order to optimize scan performance. The array is scanned by physically displacing the corrugated feed horn along a predetermined arc. This motion produces a scanned beam with correction for quadratic and cubic aberrations to assure a well-focused, wide-angle scan. The advantages of the lens feed are:

a. No need for directional couplers or power dividers

b. No need for digital phase shifters

c. Analysis shows the efficiency of a single-plane, constrained lens would be greater than a more conventional feed with phase shifters.

The lens chosen to perform the electrical scan extends the earlier work by Ruze[1]. (Though the operation of the lens is described briefly here, the derivations are not presented.) Referring to Figure 3, Ruze derives the equations of the lens as:

$$x^2 + a_o y^2 + 2a_o f_o x = 0 \qquad (1)$$

$$\left[(\mu - a_o)d - (\mu_o - a_o)d_o \right] = a_o x \qquad (2)$$

Equation (1) describes the inner lens contour while (2) describes the variation of the refractive index across the lens. Thus, two conditions are specified. There is, however, a third degree of freedom – the outer surface contour. For mechanical and cost reasons, the condition that the outer surface be flat was imposed. This feature provides a planar interface for the waveguide slot arrays (refer to Figure 2).

Having defined the inner and outer contours, the implications of Equation (2) should be analyzed. For simplicity, assume that $\alpha = 0°$; i.e., the focal points are coincident. Thus:

$$\mu_o d_o = \mu d \tag{3}$$

Equation (3) implies that as the length of the guide gets longer – as determined by the contour – its index of refraction should get smaller. This implication dictates that each waveguide be a unique size. Further examination, however, indicates a way out of the dilemma. Consider the phase shift through an individual waveguide as:

$$\phi = \mu d$$

Thus, an alternate writing of Equation (3) could be:

$$\phi = \phi_o$$

ϕ_o is the electrical length of the central waveguide/trombone of the lens. It would not be necessary to vary the index of refraction if another means of maintaining a constant ϕ can be found. One technique is to vary the length, d. To do so, it would be necessary to introduce a trombone between the inner and outer lens contours. The trombone would permit independent length adjustment so a constant ϕ could be maintained regardless of the lens contour.

The lens designed will provide a focused beam for only two source points, 0 and 0', radiating $\pm\alpha$ respectively. For this array, we wish to radiate a beam at any angle between $10°$ and $45°$. To scan the beam $45°$ from the lens axis would result in some pattern deterioration because quadratic and cubic phase errors could develop. In Figure 2, note that the trombones allow the phase at each element to be independently adjusted. By proper selection, a linear phase gradient could be developed in the trombone to steer the beam $30°$ off-axis; i.e., $30°$ down from the zenith. The lens could then provide steering $\pm15°$ about the nominal position, thereby cutting the lens-scan requirements by half, and reducing quadratic and cubic error.

A further refinement in the lens steering can also be accomplished. Equation (4) represents a focal curve that completely eliminates quadratic error.

337

The equations also show that for the contours chosen – flat outer face – the correction for quadratic phase almost cancels the cubic error. The lens designed, therefore, would have excellent scanning properties if the feed is properly displaced.

$$f_c = f_o + 1/2(\alpha^2 - \theta^2)f_o \tag{4}$$

where f_c is the new focal length, α is the angle of perfect focus, and θ is the displacement angle of the feed.

The excitation across the lens and the efficiency of the lens as a collector will be determined by the feed horn. To obtain maximum efficiency, a multichoked horn was designed to eliminate the normally high spillover that occurs in the E-plane of a horn. The choked horn uses higher order modes to reduce sidelobes. In this case, over 90 percent of the energy is collected, a 1-dB gain increase over the conventional horn.

A typical scanned pattern at 30° of scan is shown in Figure 4. The peak sidelobe level is -20 dB for 30° elevation scan. In addition, excellent wide-angle sidelobes are evident. The minimum gain measured was 41 dB, at 45° of scan. The gain at 15° scan was 43 dB. The measured axial ratios for the array varied from 1.0 dB at 15° scan to 3.0 dB at 45° scan.

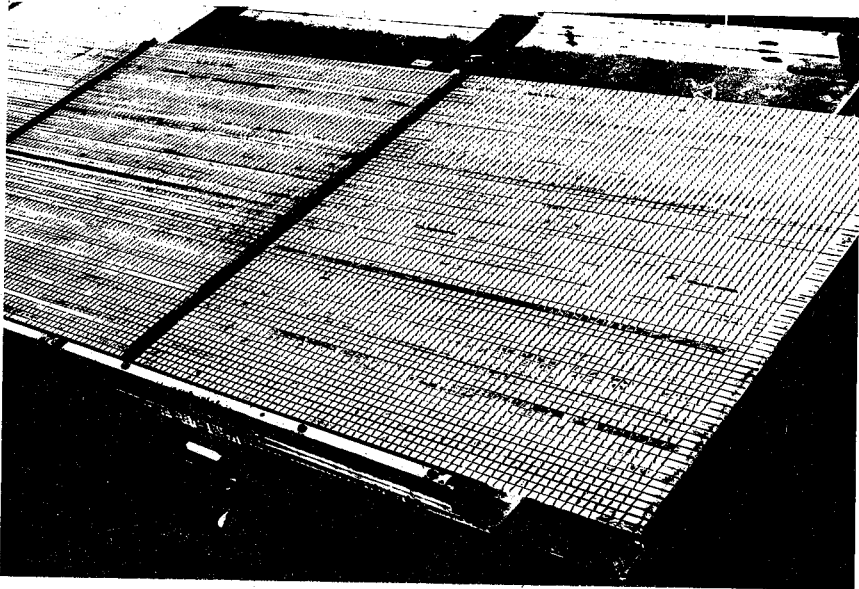1.   J. Ruze (1950 Proceedings IRE, p. 53)
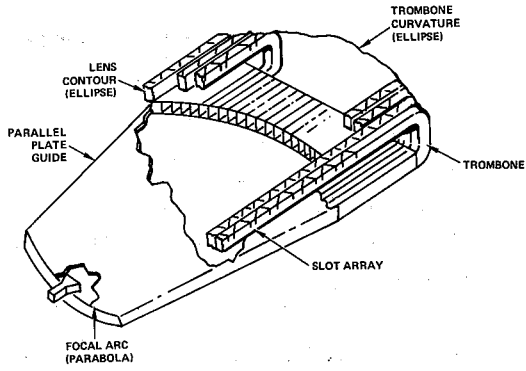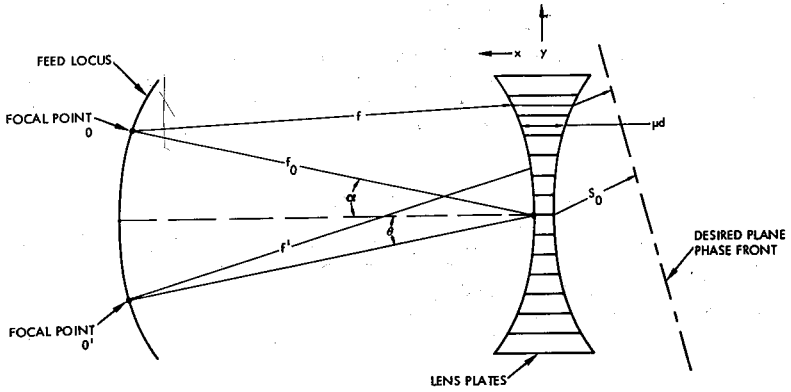

Figure 1.   Array

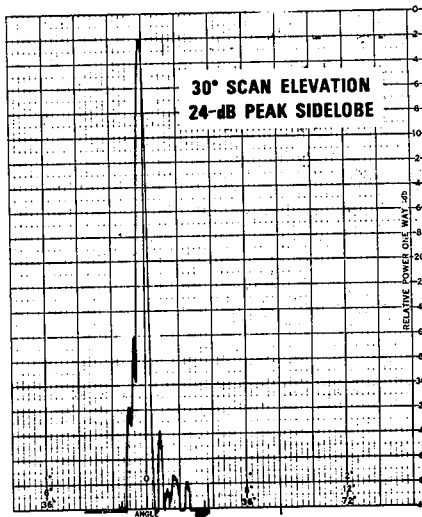Figure 2.   Feed

Figure 3.   Lens

Figure 4.   Typical Scanned Pattern

A NEW MATRIX-FED CYLINDRICAL ARRAY TECHNIQUE

by

R. Rudish, G. Skahill, and W. White
AIL, a division of Cutler-Hammer, Deer Park, New York

INTRODUCTION

A new method of forming and steering a beam with a cylindrical array
has been conceived and experimentally demonstrated at AIL. The new approach
combines the best parts of two other approaches previously published, the
transfer-switch matrix array (Giannini, reference 1), and the Butler matrix
array (Shelton, Shelig, and Chadwick and Glass, references 2, 3, and 4).

For synthesis and collimation of a beam with specified characteristics
preferred relative values of signal amplitude and phase must be established at
the array elements. Since these values are dependent upon the angular loca-
tions of the elements with respect to the nominal direction of the radiated beam,
steering of the beam requires rotation of the preferred distribution around the
array by an amount equal to the angular displacement of the beam. Since the
distributions can be established by means of a simple feed network using power
dividers and delay cables, it is only necessary to find a mechanism for keeping
the feed network connected to the proper array elements as the array is
scanned.

DESCRIPTION OF APPROACH AND ITS OPERATION

A power divider and fixed phase shifters (delay cables) are used to obtain
illumination tapering and beam collimation for a quadrant of the array (Fig-
ure 1). A Butler matrix and variable phase shifters are used to commutate
the tapered collimated distribution; also a set of SP4T switches are used to
connect the desired quadrant of radiating elements to the commutation network.
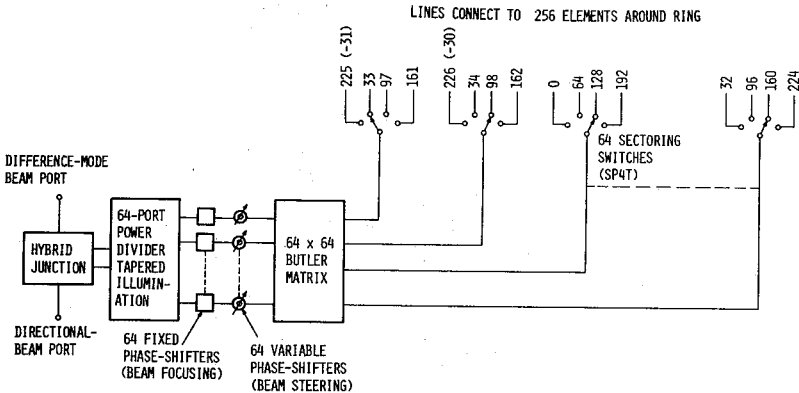
Figure 1. New Approach for Forming and Steering a
Beam with a Cylindrical Array

Figure 2 depicts the relative amplitude and phase distribution across the 64 outputs of the Butler matrix for three different settings of the phase shifters.

A. REFERENCE CONDITION: ALL PHASE SHIFTERS SET TO 0.

B. INTERMEDIATE CONDITION 1: PHASE SHIFTERS SET TO ADD 90°
PROGRESSIVELY ACROSS INPUTS TO BUTLER NETWORK

C. INTERMEDIATE CONDITION 2: PHASE SHIFTERS SET TO ADD 180°
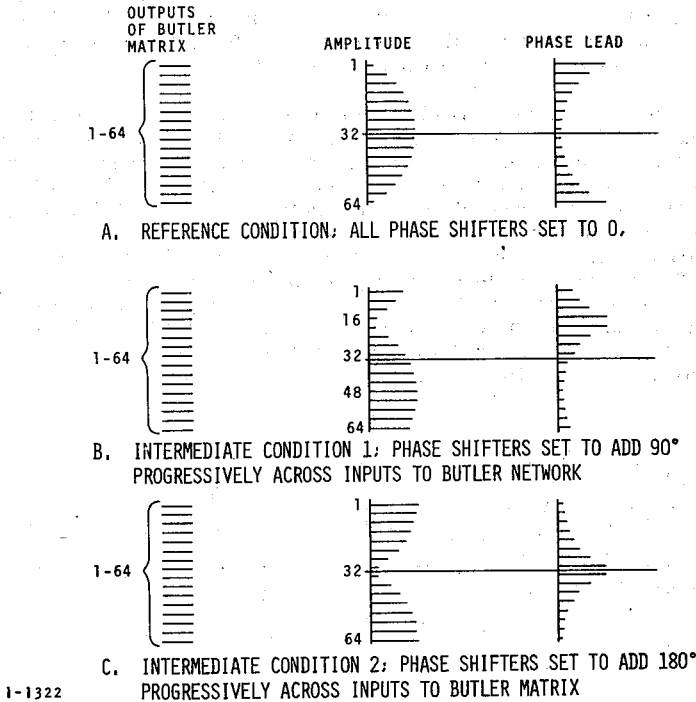PROGRESSIVELY ACROSS INPUTS TO BUTLER MATRIX

I-1322

Figure 2. Amplitude and Phase Distributions at Outputs of Butler
Matrix for Three Settings of Phase Shifters

In the reference condition, the outputs are the desired amplitude and phase distributions. In intermediate condition 1, the distributions have been shifted one-quarter of the way toward one end, and the portion of the distributions which spilled over that end are tacked on the other end. At the same time as the phase shifters were being adjusted to commute the distributions, the sectoring switches were being exercised to drop the first 16 elements and add elements 65 through 80 to the set which is connected to the Butler matrix. The sectoring switches are so arranged that the newly added set of elements will pick up the amplitude and phase distribution values on the first 16 outputs of the Butler matrix; thus, the entire form of distribution on the illuminated elements has remained intact, but the distribution has been rotated 16/256 of the way around the circle of elements. Intermediate condition 2 demonstrates the same phenomena but with twice as much rotation. Continuing the process twice as far again will restore the reference condition to the outputs of the Butler matrix, but now the elements which are connected to these outputs form a set which is 90 degrees removed from the original set. Continuing the process causes steering through the second quadrant, and if further continued, through the entire 360 degrees.

341

EXPERIMENTAL MODEL AND RESULTS

A technique was devised to verify the new beam forming and scanning approach with only a quadrant of a 32-element cylindrical array. The model consisted of eight dipole radiators in front of a cylindrical reflector, fixed cables for connecting lines and differential phase shift, and individual directional couplers interconnected to form a Butler matrix.

First, each of the eight matrix outputs was connected in consecutive order to the eight dipoles. The measured radiation pattern for this configuration (Figure 3A) agreed well with the computed pattern. Then cable lengths were changed to cause the beam to steer 1/32 of a revolution. Also, all of the matrix outputs were reconnected to the dipoles in such a way that it simulated the dropping of an element at one end of the excited group of dipoles and picking up a previously unexcited element at the other end (as would have been done with a full 32-element array by exercising one SP4T switch). This operation shifted the boresight reference by an amount equal and a direction opposite to the amount steered so as to cause this second beam to directly overlay the first one. That this actually happened was confirmed by measurement. The second radiation pattern (Figure 3B) also agrees well with computations.
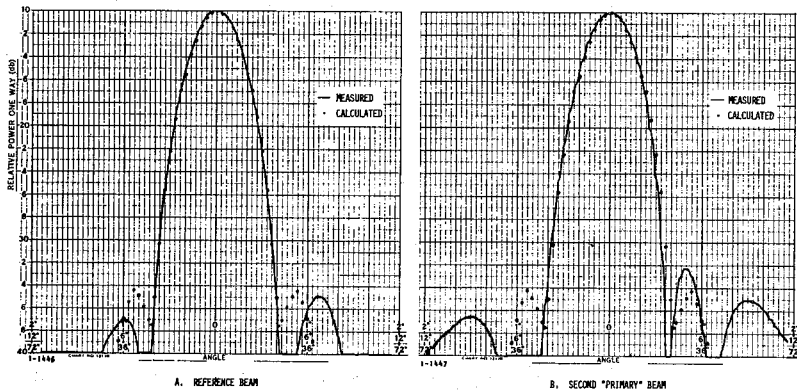

Figure 3.   Radiation Patterns

Then the cable lengths were changed to values which were intermediate between those in the first and those in the second case. However, the matrix outputs were left connected to the dipoles in accordance with the second sequence. As expected, the beam scanned 1/64 of a revolution while essentially retaining its original shape. A composite of the measured radiation patterns for both primary (beam boresight between two elements) and intermediate beam positions is shown in Figure 4 as it would have appeared for a full 32-element array scanned to corresponding angles.
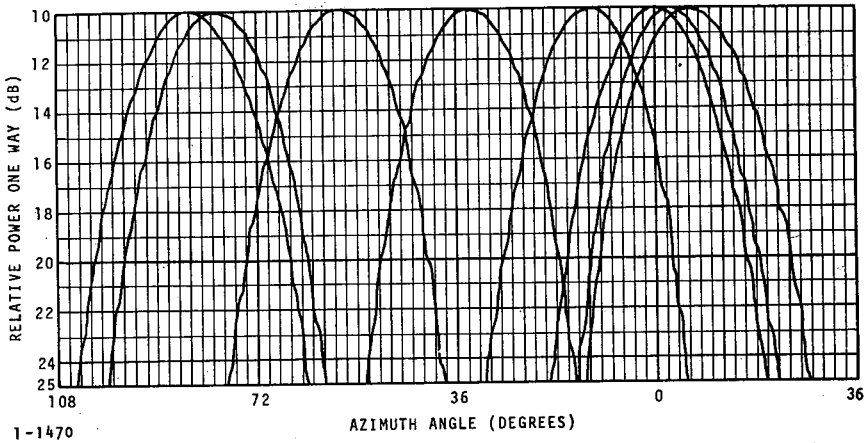
Figure 4. Scan Patterns of Matrix-Fed Array

CONCLUSION

The experimental demonstration verified the capability of the new Butler-matrix-fed cylindrical array to form and scan a beam of specifiable shape. The new method uses a much smaller matrix than with previously reported Butler-matrix methods. Also, it enjoys a principle advantage of the transfer-switch matrix-fed array; that is, by feeding only the useful quadrant of radiators, the new method avoids the cost of feeding the remaining elements and the necessity to achieve cancellation of their excitations. Yet, the passive Butler matrix arrangement with phase shifters at each input is simpler to build, control, and maintain than the transfer-switch matrix.

REFERENCES

1. R. S. Giannini, "An Electronically Scanned Cylindrical Array for IFF, Based on Switching and Phasing Techniques," Proc of Conformal Array Antenna Conf, NELC, San Diego, California, January 1970.

2. Paul Shelton, "Application of Hybrid Matrices to Various Multimode and Multi Beam Antenna Systems," IEEE Washington Chapter, PGAP Meeting, March 1965.

3. B. Sheleg, "A Matrix-Fed Circular Array for Continuous Scanning," Proc of IEEE, Vol 56, No. 11, p 2016 to 2027, November 1968.

4. G. G. Chadwick and J. C. Glass, "Investigation of a Multiple Beam Scanning Circular Array," Scientific Report No. 1, USAF Cambridge Research Laboratory, AF19(628)-367, 31 December 1962.

A CIRCULARLY SYMMETRIC RF COMMUTATOR
FOR CYLINDRICAL PHASED ARRAYS

Bruce F. Bogner
RCA Government and Commercial Systems
Missile and Surface Radar Division
Moorestown, New Jersey 08057

A new feed concept is described which greatly simplifies the
problem of commutating the RF distribution system of a cylindri-
cal phased array. The feed consists of a circular parallel-plate
radial transmission line and a central RF control circuit, as
shown in Figure 1. The radial line contains a central circular
array of probes and a peripheral set of equally spaced pick-up
probes, illustrated in Figure 2. The central probes can be
phased to produce an amplitude distribution in the parallel-plate
line in a given orientation by proper setting of two phase
shifters and cause the peripheral probes to be excited with the
proper amplitude necessary to produce a directive pattern with
low sidelobes when the peripheral probes are connected, through
collimating phase shifters, to the active radiating elements of a
cylindrical phased array.
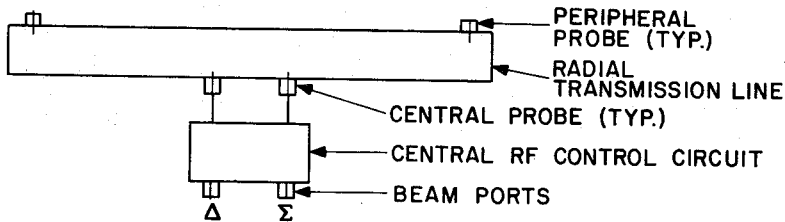
BLOCK DIAGRAM - RF COMMUTATOR
FIGURE 1
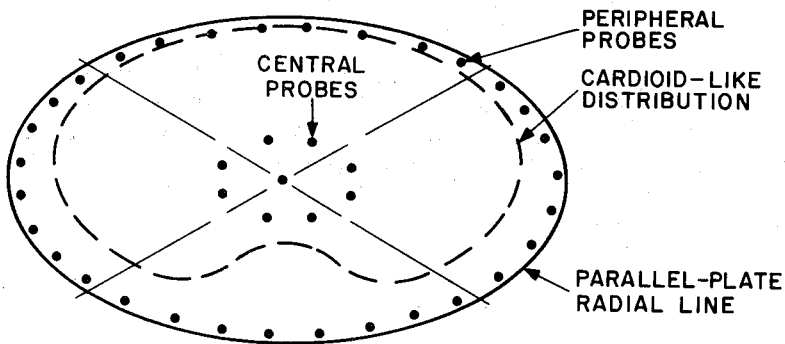
RADIAL TRANSMISSION LINE
FIGURE 2

The control circuit also produces an orthogonal distribution in the parallel-plate line which can be used to form a monopulse difference pattern. This feed technique is the first designed specifically for a cylindrical phased array and is virtually independent of the size of the array. Previous methods of distribution commutation were extensions of linear array scanning techniques and as such rapidly become more complicated and less efficient as the diameter and number of radiating elements of a cylindrical array are increased. The new radial feed commutation technique eliminates the need for complicated and lossy switching matrices, beam forming matrices, power distribution networks or programmable attenuators.

The basic form of the Circularly Symmetric RF Commutator involved a device which contained N outputs connected to a cylindrical array of N radiating elements. To excite only one sector of the array, a fairly directive distribution had to be generated in the radial transmission line and the energy in the undesired directions had to be low. A significant simplification of the device involves the use of a radial transmission line with N/m outputs connected to "m" way switches which connect to the N radiating elements of the array. In this manner the entire periphery of the radial transmission line contributes to the excitation of the active array sector at all times, with all spillover losses in the feed eliminated. The most significant feature of this simplified feed system is that the number of phase shifters required for amplitude commutation can be reduced to a quantity as low as two (2). The central control circuit requires (theoretically) only five probes to produce an angular variation of field possessing the general characteristics of a cardioid. The probe array and the associated central control circuit are designed so that this distribution can be rotated electronically within the power divider for other cases of array beam directions. This is accomplished by programmed control of the two phase shifters in the central control circuit. This feed technique, in conjunction with sector switching, provides N position coarse steering in a uniquely simple way.
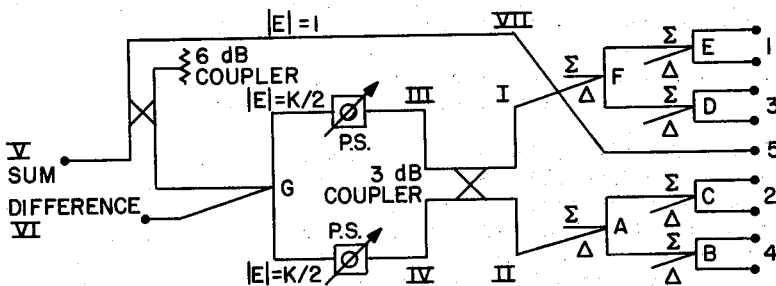

CENTRAL CONTROL CIRCUIT
FIGURE 3

The RF Commutator is a combination of a radial waveguide antenna (central ring of probes) and a radial transmission line termi‐ nated on its periphery by an array of pickup probes (output ring of probes). The principle of operation of the central portion of the proposed circular commutator is a simplified version of the radial waveguide antenna utilizing the "equivalent" of a single ring of four probes. The main features of the central RF Control Circuit are given here with the aid of Figure 3. The wave entering the sum port V is split by the directional coupler in a predetermined ratio so that the waves in the three paths passing beyond the phase shifters have relative amplitudes of 1, k/2 and k/2 as shown. The upper path, with wave amplitude of 1, is fed to the central probe and produces an omni-directional pattern component having no phase variation with angle. Each of the waves of the lower paths emerging from the phase shifters is split by the 90-degree, 3-dB hybrid and are in quadrature, with the upper path leading in phase for one phase shifter while lagging in phase for the other phase shifter. The remaining connection of these paths is to the probes via the difference arms of two 180-degree hybrids (each difference arm giving a figure-of-eight pattern with the axis aligned with the corres‐ ponding diagonal pair of probes in the parallel-plate region). The quadrature relationship introduced by the 90-degree, 3-dB hybrid and the 90-degree spatial orientation of the figure eights results in the transformation of the output wave of each of the phase shifters to an omni-directional pattern in the parallel- plate region. These patterns are distinctive in that each has a phase progression equal to angle change in the parallel-plate region. One progresses in the same sense as the mechanical angle and the other progresses in the opposite sense. When the phase shifters are set to + $\emptyset°$ and - $\emptyset°$ respectively, the two distribu‐ tions rotate together through an angle of $\emptyset°$ in the disc and are always in-phase with the fixed omni-directional distribution. A variable position figure-eight is generated by combining the two counter rotating-phase omni-directional distributions which exist at points III and IV. The RF Commutation is accomplished by combining the variable position figure-eight distribution (at sum port of hybrid G) with the fixed position omni-directional distribution (at point VII) in the directional coupler. The coupling value can be selected to generate a cardioid type distribution of any desired front-to-back ratio. A variable position, orthogonally oriented figure-eight distribution is available at the difference port of hybrid G (point VI).

A model of a Circularly Symmetric RF Commutator designed to operate over the 1200-1400 MHz frequency band, was constructed and evaluated and is shown in Figure 4. The model consists of a 1/4-inch thick 21-inch diameter solid dielectric disc clad on both sides with 2 oz. copper, containing 57 probes. There are eight inner probes on a 1.65 inch radius, 48 outer probes equally spaced on a 9.01 inch radius and one centrally located probe. The power distribution network used to generate the required RF signals consists of seven 180° hybrids, one 90° hybrid, one 6 dB

coupler and interconnecting cables and connectors. The isolation between points I, II and VII were adjusted by varying the lengths of open circuited stubs at hybrids A through F. Orthogonal figure-of-eight probes produce anti-phased signals at hybrids B, C, D and E while the central probe produces in-phase signals at hybrids A and F. Adjustments at these unused ports cause the undesired probes to appear as a high impedance to the desired mode. The stubs on the sum ports of hybrids A and F yielded 23-35 dB coupling between points II and VII and 30-34 dB coupling between points I and VII. The isolation between I and II was adjusted to 26 dB by varying stubs on the difference ports of hybrids B, C, D and E. The measured data taken on the model verified that the desired distributions are realizable over the full design frequency band and that the distributions rotate through the proper angle as the settings of the phase shifters on the central control circuit are changed.

In conclusion, this new method of beam steering accomplishes the commutation of the amplitude distribution of a cylindrical phased array by means of only two variable phase shifters. It also takes full advantage of the geometry of the circular array and all associated circular symmetry to make the extension of the problem to larger diameters, more radiating elements, and/or more beam positions a simple matter.
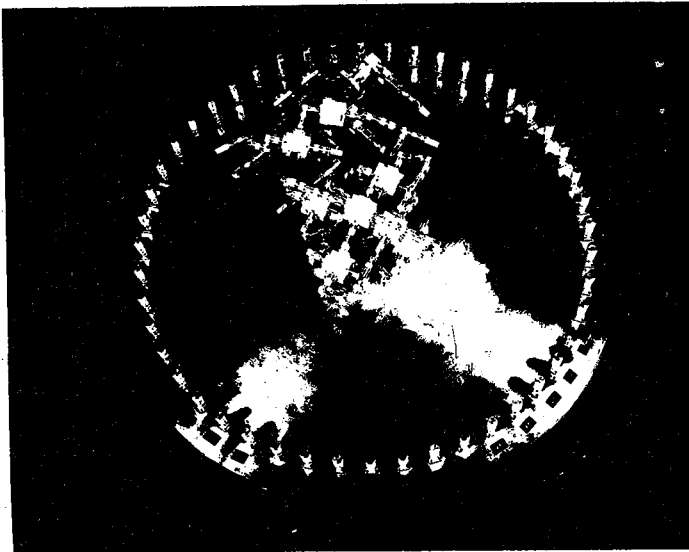
Model of RF Commutator
Figure 4

A MULTI-ELEMENT HIGH POWER MONOPULSE FEED
WITH LOW SIDELOBE AND HIGH APERTURE EFFICIENCY

N. S. Wong, R. Tang, and E. E. Barber
Hughes Aircraft Company
Fullerton, California

A multi-element feed can be employed for many important applications. For example, Ricardi and Niro[1] described the application of a 12-element feed for monopulse applications. Appropriate excitation of the horns results in a much more compatible sum and difference illumination than feeds having fewer horns. Hannan[2] has described several monopulse feed designs in which a multiple number of feed horns up to a maximum number of 12 was used. In his design, more than one waveguide mode may be excited in each feed horn. The design concept is also based on increasing the area of feed aperture illumination of the difference beam over that of the sum beam. More recently, Amitay and Zucker[3] described the employment of a multi-element feed for phase error correction in the spherical reflector, and Dion and Ricardi[4] discussed the employment of a 19-element feed to obtain a shaped beam with variable beamwidth. In this paper, a method of designing multi-element feed is described and applied to the design of a 32-element monopulse feed in which a sidelobe level less than -30 dB is required for both the sum and difference beams. A prototype of this feed design was constructed and excellent agreement between experimental and analytical results was obtained. In addition, a feed design with high power handling capacity was also investigated. Measured results are summarized.

The geometry of the multi-element feed as it is employed in a phased array of the feedthrough lens type is depicted in Figure 1.

The design of the multi-element feed involves the determination of the excitation coefficients on the feed to produce a specific aperture distribution on the feedthrough lens. A method of determining these excitation coefficients has been developed using the reciprocity principle after the following assumptions are made:

1. The element spacings in both the feedthrough lens and multi-element feed are small enough such that they do not support grating lobes.

2. The radiation impedances of both the feedthrough lens and the multi-element feed are matched over the scan angles of interest.

3. Elements in either the feedtrhough lens and the multi-element feed are members of an infinite regularly spaced array.

The first two assumptions are met in most practical cases of interest. The third assumption is equivalent to neglecting the edge effect. It is exactly correct if dummy elements are introduced, and it should be valid if a sufficiently large multi-element feed is used.

The results of the above analysis are summarized:

$$G^*_{mn} = \sum_p \sum_q g_{mnpq} A^*_{pq} e^{-jkR_{mnpq}}$$

and,

$$g_{mnpq} = \frac{\sqrt{A_r \cos \psi_r \, A_t \cos \psi_t}}{R_{mnpq} \cdot \lambda}$$

in which

k	is the free space propagation constant
G_{mn}	is the excitation coefficient of the multi-element feed
A_{pq}	is the aperture distribution
R_{mnpq}	is the path length between the feed element and a lens element, and
g_{mnpq}	is the transmission coefficient between the m, nth feed element to the p, qth lens element
A_r	is the area per element at the multi-element feed
A_t	is the area per element at the lens
ψ_r	is the angle between the Poynting vector and the feed array normal, and
ψ_t	is the angle between the Poynting vector and the lens normal

and,

λ	is the wavelength

Measured Results of the Monopulse Feed in the Experimental Array

A stripline beamforming network was constructed to feed the 32-element feed aperture. This beamforming network provides three beams: the sum beam, the azimuth difference beam, and the elevation difference beam.

This 32-element feed was integrated into the eight-foot S-band feed-through lens. The radiation patterns were measured for the sum beam, azimuth difference, and elevation beams. The measured sum patterns are shown in Figures 2, 3, and 4. Plane cuts were taken in the E-plane, D-plane, and H-plane.

The sidelobe is approximately 32 dB, which is close to the predicted value of 34 dB. The measured azimuth difference patterns are shown in Figures 5 and 6. Plane cuts were taken in H-plane and D-plane. The sidelobe is 27 dB with respect to the peak of the difference beam, and is roughly 30 dB with respect to the peak of the sum beam.

349

The measured elevation difference patterns are shown in Figures 7 and 8. In general, the measured patterns possess slightly higher sidelobe level as compared to the predicted value. This slight difference is attributed to the phase error in the beamforming network and the quantization phase error in the feedthrough lens where the minimum phase step is 22.5°.

The antenna gain of the feedthrough lens with the 32-element feed was also measured. The measured results for all three beams were compared with the estimated value from analytical calculation of spillover loss and aperture tapering loss in addition to direct measurement of other ohmic losses in the antenna system. The agreement is excellent.

Description of the 32-Element Feed Designed for High Power Handling

The multi-element feed possesses a unique advantage in high power handling. For this purpose, the feed aperture is located in front of the focal point as a result of the defocussing. The power is well spread out as compared to an equivalent single horn feed. The focal point is about three wavelengths behind the feed aperture. For this design, a 28 dB circular Taylor aperture design was used. A high power feed based on the above design was constructed and tested.

The agreement between the experimental and analytical result is also excellent.

References

1. L. J. Ricardi and L. Niro, "Design of a Twelve-Horn Monopulse Feed," 1961 IRE International Convention Record, Part 1, pp. 93-102.

2. P. W. Hannan, "Optimum Feed for all Three Modes of a Monopulse Antenna, II: Practice," IEEE Transactions on Antenna and Propagation, Vol. AP-9, pp. 454-461; September 1961.

3. N. Amitay and H. Zucker, "Compensation of Spherical Reflector Aberrations by Planar Array Feeds," IEEE Transactions on Antennas and Propagation, Vol. AP-20, No. 1, pp. 29-56; January 1972.

4. A. R. Dion and L. J. Ricardi, "A Variable Coverage Satellite Antenna System," Proceedings of the IEEE, Vol. 59, No. 2, pp. 252-262; February 1971.
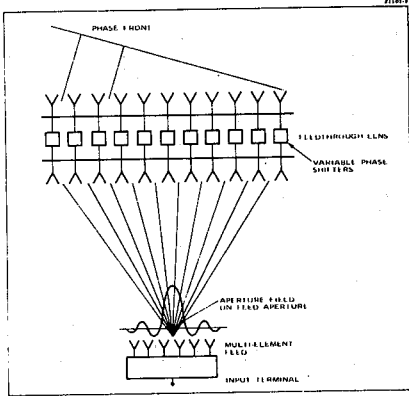
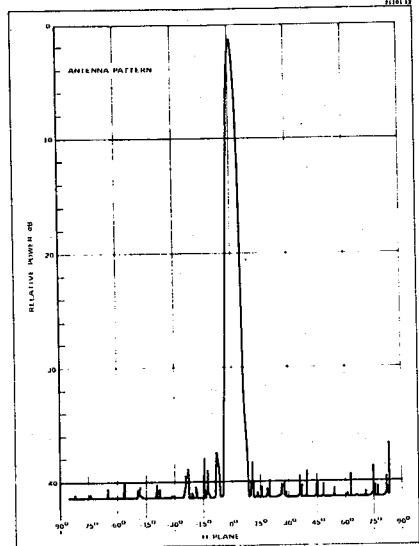Figure 1. A Multi-Element Feed for a Feedthrough Lens Phased Array

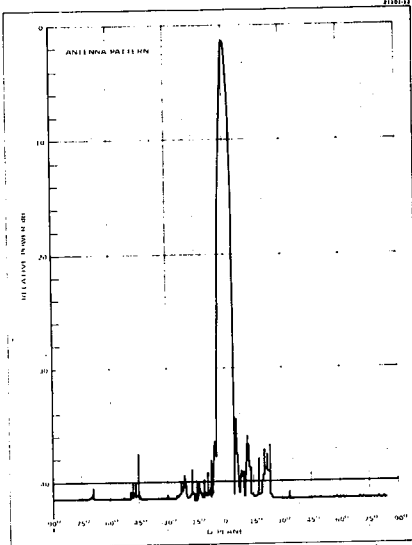Figure 2. Measured Pattern or Sum Beam of the 32-Element Feed

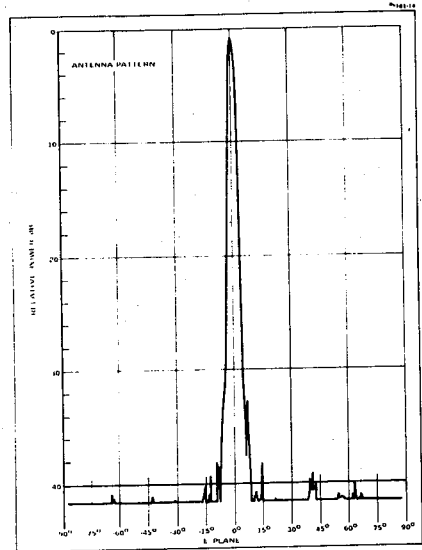Figure 3. Measured Pattern of Sum Beam of the 32-Element Beam

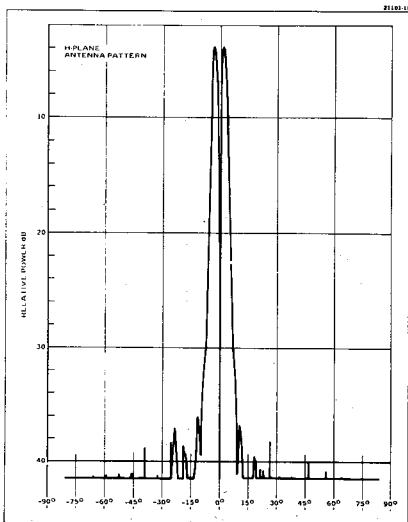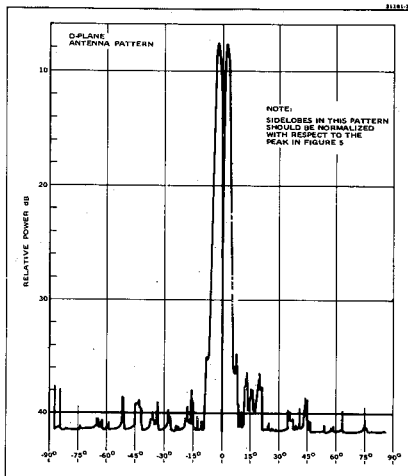Figure 4. Measured Pattern of Sum Beam of the 32-Element Feed

351

Figure 5. Measured Pattern of Azimuth Difference Beam of the 32-Element Feed.

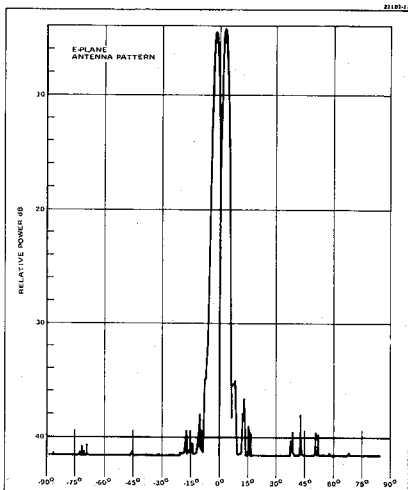Figure 6. Measured Pattern of Azimuth Difference Beam of the 32-Element Feed

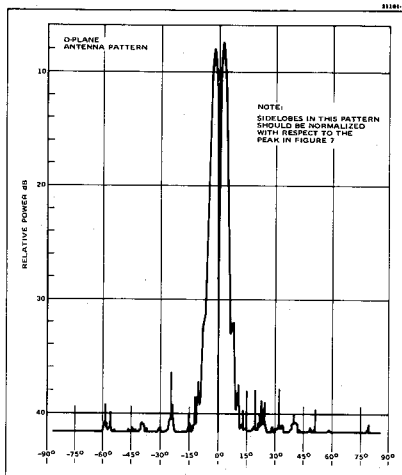Figure 7. Measured Pattern of Elevation Difference Beam of the 32-Element Feed

Figure 8. Measured Pattern of Elevation Difference Beam of the 32-Element Feed.

RETRIEVAL OF TARGET PROPERTIES BY NONCONTACT MICROWAVE METHODS

M.A.K. Hamid and S.S. Stuchly
University of Manitoba
Winnipeg, Canada

Summary

Active and passive microwave noncontact sensors have been of growing interest in recent years in research and industry because they possess many intriguing capabilities and offer many attractive technical, commercial and military possibilities.

One of the most important applications of microwave noncontact sensors is for the measurement of nonelectrical quantities in laboratory, industrial and field environments. Their attractive features are mainly due to the fact that they are non-destructive, contactless, continuous and have a low time constant, high reliability and are free of radiation hazards. In particular, multi-frequency microwave radiometers lend themselves to high altitude all year round airborne operation almost independent of weather and provide greater target to background contrast as sea state increases, when radar clutter would be worse.

While active microwave sensors are based on the interaction of an electromagnetic field with the test object, the passive radiometer sensors are based on the fact that all objects radiate energy over a wide spectrum at ordinary temperatures and that the microwave portion can be detected and interpreted to yield information about the source object. The criteria for comparing the two methods are outlined with reference to accuracy, sensitivity, reliability, time constant, convenience, environment and dynamic vector of motion of the sensor and test object relative to the background.

The basic physical phenomena utilized in relating nonelectrical to electrical quantities at microwave frequencies are presented in the form of transducer response. This response relates electromagnetic wave quantities (field intensity, power, beamwidth, polarization, wave velocity, impedance, etc.) to desired nonelectromagnetic physical quantities (dimension, speed, etc.) or electromagnetic properties of the object (emissivity, permittivity, permeability, conductivity, etc.) to its desired nonelectromagnetic physical properties (moisture, density, temperature, pressure, age, etc.). The first group employs such electromagnetic phenomena as diffraction, scattering and radiation which may be analyzed by Planck's law, geometrical optics, physical optics, geometrical theory of diffraction, boundary value, perturbation or variational techniques depending on the composition and characteristic dimension of the object in comparison to the wavelength. The response in the second group is basically derived from generalized mixture theory and emission models. The usual microwave response quantities are amplitude ratio, phase shift, frequency shift (doppler effect),

polarization shift, resonant frequency shift, Q factor ratio and contrast temperature. These quantities are normally measured using a S-parameter meter, doppler frequency meter, Q factor meter, polarimeter and radiometer.

In order to illustrate the principles of sensor operation, examples are drawn from multitude of applications where the sensor employs the principle of perturbation of an electrical quantity (permittivity, emissivity, frequency, amplitude, phase, polarization, etc.) for measuring geometrical and mechanical quantities of the test object. Examples are process sensors for monitoring sheet metal width and thickness, void fraction, paper moisture content, ice thickness, object speed as well as product sorting, etc.

The latter part of the paper deals with the status of non-contact reconnaissance sensors for determination of subsurface layering (e.g. moisture profiles in soils, snow, stored products, etc.) and classification of man-made (e.g. ships, downed aircraft, oil spills, etc.) vs natural (e.g. icebergs, mineral deposits, etc.) objects. Some specific systems employing radiometric, swept frequency reflectance, complex polarization and short pulse measurement techniques are outlined with reference to resource sensing, target classification, environmental, oceanographic and geological studies. Emphasis is placed on the interaction between measurement quantities which introduces ambiguities and limits the skin depth and overall progress in this field. Attention is also focussed on comparing the effectiveness of these methods with immersion type sensors operating in the time or frequency domain and the potential of hybrid techniques employing beacons interrogated by remote sensors during data gathering missions.

REFERENCES

1. A.T. Edgerton, et al. (1971 Aerojet-General Corp., Tech. Rept. No. 9016R-8).
2. A.W. Adey (1971 AGARD EM Wave Prop Panel XVII Am. Symp. on Prop. Limitations in Remote Sensing, Colorado).
3. A.W. Adey (1970 Dept. of Communications, Ottawa, CRC Rept. 1214).
4. D.B. Harris (1960 Microwave Journal $\underline{3}$, p. 41 & 47).
5. E.M. Sparrow and R.D. Cess, Radiation Heat Transfer (Brooks-Cole, 1966).
6. A. Mayer (1971 NASA TM X-62082).
7. W.E. Lehr (1971 U.S. Coast Guard Rept. project 714104).
8. A. Stogryn (1972 NASA CR-2088).
9. G. Poe, A. Stogryn and A.T. Edgerton (1971 Aerojet-General Corp., Tech. Rept. No. 1684R-1).
10. A.T. Edgerton and D.T. Trexler (1970 Aerojet-General Corp., Tech. Rept. No. 1361R-1).
11. S.S. Stuchly and M.A.K. Hamid (1972 Int. J. Electronics $\underline{33}$, p. 617).
12. R.S. Vickers and G.C. Rose (1971, AFCRL-71-0438).
13. W.A.G. Voss (1969 JMP $\underline{4}$, p. 210).
14. M.A.K. Hamid and J.D. Hunter (1972 Proc. NATO Ad. Study Inst. Meeting on the Science and Technology of Surface Coatings).
15. M.A.K. Hamid (1972 Proc. First Canadian Symp. on Remote Sensing).
16. M.A. Rzepecka and M.A.K. Hamid (1972 IEEE Trans. MTT $\underline{20}$, p. 30).
17. S.S. Stuchly, M.A.K. Hamid and A. Andres (1971 IEEE Trans. IECI $\underline{18}$, p. 85).
18. M.A. Rzepecka, M.A.K. Hamid and A.H. Soliman (1972 IEEE Trans. IECI $\underline{19}$, p. 120).
19. M.A. Rzepecka, S.S. Stuchly and M.A.K. Hamid (1973 IEEE Trans. IM $\underline{22}$, p. 41).
20. P. Bhartia and M.A.K. Hamid (1973 IEEE Trans. IM $\underline{22}$, p. 94).
21. S.S. Stuchly, M.A.K. Hamid and M.A. Halim (1971 IPC Business Press Ltd., Design Electronics Monographs, Microwaves in Industry).
22. S.S. Stuchly (1970 JMP $\underline{5}$, p. 62).
23. N.B. Agdur (1965 U.S. Patent No. 3,458,808).
24. S.S. Stuchly, A. Kraszewski and M.A. Rzepecka (1969 Microwave J. $\underline{12}$, p. 51).
25. S. Sasaki (1959 U.S. Patent No. 3,034,046).
26. S. Summerhill (1967 Inst. Rev. $\underline{14}$, p. 419).
27. M.A.K. Hamid (1972 Defence Research Board of Canada, DREO Rept. No. 611).
28. C.F. Augustine (1965 Electronics $\underline{38}$, p. 65).
29. T.V. Selling and D.K. Nance (1961 Electronics $\underline{34}$, p. 72).
30. D.R.J. White, R.W. Hanford and H. Ihara (1962 Elect. Ind. $\underline{21}$, p. 113).
31. C.D. McGillem and T.V. Selling (1963 IEEE Trans. MIL $\underline{7}$, p. 296).
32. L.D. Dahl and D.R. Hornbaker (1965 ISA 20th Annual Conf., Phys. and Mech. Meas. Inst., p. 6).
33. K. Kuenzi and E. Schanda (1968 IEEE Trans. MTT $\underline{16}$, p. 787).

Session 41 Microwave Sensing

MICROWAVE MEASUREMENTS IN THE STEEL INDUSTRY

B. Dalton, Corporate Engineering Laboratory, BSC

SYNOPSIS
        The paper describes the development and implementation of instruments using microwaves in a heavy industrial environment.

        Four major instrument developments are covered, two in considerable detail. Wherever possible, practical and theoretical accuracies are given. Special emphasis is laid upon the practical diffi- culties of applying such schemes under works conditions.

INTRODUCTION
        The paper covers the work carried out by the Corporate Engineering Laboratory over a period of approximately seven years. As a result of this work, the following instrument developments have been undertaken:

        1. A non-contact rangemeter for level detection.
        2. Thickness gauges for both steel plates and strip.
        3. Position detection of billets and slabs.
        4. Doppler-based length measurement of slabs.

The first two of these will be dealt with in considerable detail.

        Other microwave applications have been recognised and will be briefly mentioned.

THE NON-CONTACT RANGEMETER
        In many parts of the steel industry it is necessary to measure reliably the level of materials loaded into reaction vessels. This is especially true in the blast furnace, where a semi-continuous stream of material is permanently being dumped into the top to match the rate at which the finished product is extracted or tapped at the bottom. The blast furnace is a totally enclosed vessel, possibly under high pressure and containing a particularly erosive and corrosive environment. Because of this, many instruments developed for this application have proved unsatisfactory.

        To circumvent the difficulties, a continuous frequency modu- lated microwave method was proposed, developed and is now being manufactured. Fig. 1 shows the arrangement at the top of the furnace and the position of the head unit of the microwave rangemeter.

        Fig. 2 shows a long-term comparison between such a unit and

a mechanical rod lowered onto the surface (in a slightly different part of the surface), showing the very good agreement obtained.

The paper will describe the microwave method in detail and the full experimental results obtained, and will include latest details of the development state of the first commercial instrument.

THICKNESS GAUGES

The paper describes the development of two steel thickness gauges, one a cavity-based gauge along the same lines as that of Soga (1) for very thin (0.2 mm) strip, the other based upon a microwave interferometer.

The major development work has been carried out upon the interferometer for the measurement of thick (> 8 mm) plate and the experimental set up is shown diagrammatically in Fig. 3.

The gauge works as a simple phase comparison bridge with the plate thickness varying the electrical length of one of the bridge arms. The phase measurement method is after Dropkin (2) and uses a mechanically rotating Fox phase shifter.

Experimental results and future developments will be discussed.

SUMMARY

The paper will end with a short discussion on future needs and trends in the industrial uses of microwave measurement techniques.

The rangemeter obviously has uses outside the blast furnace area and we are looking into uses in such diverse fields as silo and bunker level measurement, crane height, inter-crane distance, etc.

The thickness gauges are open to exploitation and the paper will concentrate on the relative merits and disadvantages of these instruments and their uses outside the steel industry.

The doppler devices will obviously measure both speed and length and possible uses will be discussed.

Brief mention will be made of a wide variety of simple positional measurement problems within the industry.

REFERENCES

1. H. Soga, British Patent Number 1180843.
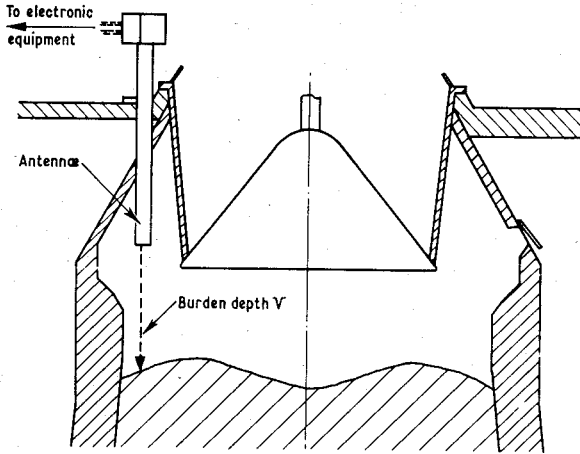2. H.A. Dropkin, IRE Nat'l Conv Rec pt1, Vol 6 pp 57-63.
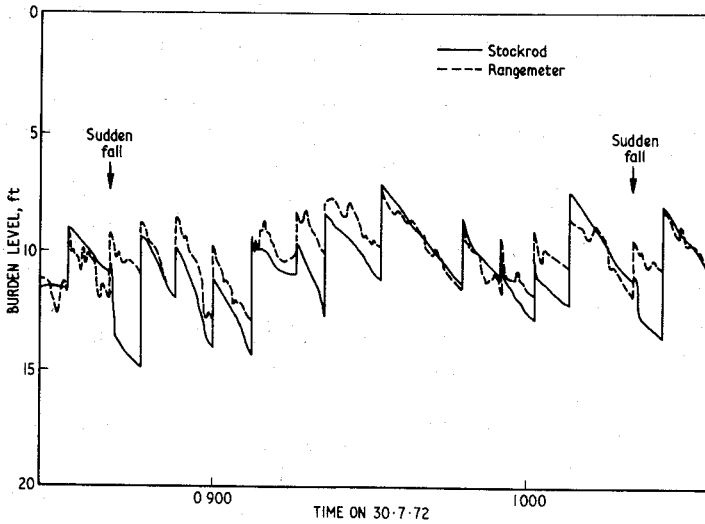
FIG. 1   RANGEMETER IN BLAST FURNACE
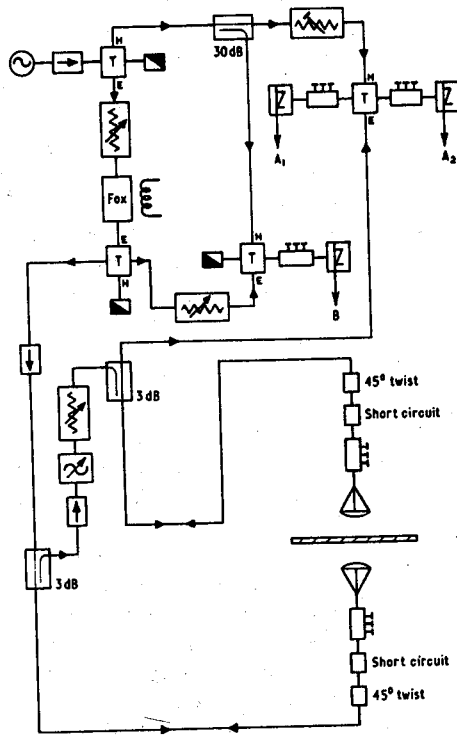

FIG. 2   COMPARISON OF STOCKROD AND RANGEMETER READINGS

FIG. 3 THE PLATE THICKNESS GAUGE

Session 41 Microwave Sensing

AN UNDERGROUND ELECTROMAGNETIC SOUNDER EXPERIMENT

L. T. Dolphin, R. L. Bollen, and G. N. Oetzel
Stanford Research Institute
Menlo Park, California 94025

Motivated by ten years of experience in the application of a novel
short-pulse, high-powered transmitter technique to ionospheric
probing, and the possibility of underground sounding at archaeol-
ogical sites in Egypt, we have developed a lightweight, portable
sounder for underground probing. This equipment has been success-
fully tested in a dolomite mine in California.

The transmitter technique, allowing the generation of tens of
megawatts of power, in the region 5 to 100 MHz, makes use of
pressurized spark gaps as fast switches for discharging stored
electrical energy through a suitable RF pulse circuit. Previous
applications required pulses of the order of one microsecond long,
or typically 8 to 15 RF cycles. The exponentially decaying enve-
lope has frequently been an advantage in our relatively narrowband
applications of ionospheric plasma experiments and long-range prop-
agation studies. However, application of the transmitter technique
to underground sounding has required the development of a very
short pulse free from any tail. The short pulse is required
because of the short ranges to typical underground scattering
objects. The equipment we developed generates one to one-and-one-
half cycles of RF energy at a peak power of 0.2 MW. (Higher-power
versions have been built but were not used in the experiment to be
described.)

High-moisture content in many surface soils and rocks frequently
restricts electromagnetic propagation to very short distances at
the probing frequencies we desired. For example, the attenuation
at 30 MHz in the clay and gravel soil (6 to 10 percent moisture
content), adjacent to our Laboratory, is 9 dB/m in summer and 12
dB/m after winter rains. An abandoned coal mine at Nortonville in
the San Francisco area provided a somewhat improved testing loca-
tion (4.5 dB/m at 30 MHz) from which probable echoes were obtained;
however, a conclusive demonstration of the sounder was not possible
until experiments were conducted in the Inyo Mountains near Lone
Pine, California at a dolomite mine.

The primary experimental objective was to detect a known chamber
in the geometrically complex dolomite mine. After a survey of the
underground workings was completed, the sounder transmitter and

receiver were systematically located at a variety of sites.
Besides observing the received signal on a two-way basis, a
receiver was also located in the mine chamber of interest. This
provided data on one-way propagation time from the surface to the
chamber and an indication of signal strength transmitted through
the rock/air interface into the mine.

The echoes received were complicated in that they did not dupli-
cate the transmitted waveform. There was evidence that the
received waveform was caused by a combination of dispersion and a
time overlap of echoes from reflecting surfaces at greater ranges
than the chamber of interest. The scattering cross section was
aspect-sensitive and at near specularity to the chamber's ceiling
was on the order of 100 m^2.

Another experimental geometry was chosen to obtain a single echo
from a tunnel wall. In that case the echo nearly replicated the
transmitted pulse except for dispersion. The fact that disper-
sion was responsible for differences between the received and
transmitted waveform was verified by computer simulation.

The mine chambers detected were located at depths of 100 to 130
feet. The attenuation coefficient in the dolomite rock was 0.6
dB/m. None of the mine chambers with a favorable geometrical
aspect was located farther than 100 to 130 feet from the hillside
surface, so we did not attempt detection at greater ranges.

Potential applications of this sounder in addition to use in
archaeology include probing in advance of the working face of
deep tunnels, location of old workings from the surface in
advance of surface strip mining, and application in underground
surveying, water table mapping, and prospecting.

Session 41   Microwave Sensing

RADAR SENSING OF SOIL MOISTURE

Fawwaz T. Ulaby and Richard K. Moore
University of Kansas Center for Research, Inc.
Lawrence, Kansas   66044

Remote sensing of soil moisture is of primary concern to hydrologists involved in flood forecasting and in the large-scale water resource management of farming regions and to meteorologists interested in the energy and mass exchange at the air-soil interface. For terrain surfaces such as soil, the dielectric properties are strongly dependent upon the free water content in the soil; it has been shown by Lundien [1] that the effects of soil type on the value of the dielectric constant are greatly overshadowed by the effects of the free water content in the soil, particularly at the lower microwave frequencies. The effects of soil moisture on the radar return have been examined in the laboratory by Lundien [1] and through qualitative evaluation of uncalibrated side-looking airborne radar imagery of Southern Louisiana [2]. In in-between phase, namely that of measuring the radar return under natural conditions and supported with quantitative soil moisture configuration information, up to now has been ignored.

Airborne Scatterometer Results

Radar measurements were made from an altitude of 3000 feet during June, 1970 using 0.4 GHz and 13.3 GHz scatterometers flown by NASA/JSC over a test site near Garden City, Kansas [3]. Antenna patterns are fan-shaped, with narrow beams transverse to the flight path, and wide beams along the flight path. Angle of incidence within the wide beam is determined by filtering out appropriate Doppler-shifted components of the return. The 13.3 GHz antenna has a cross-track beam width of 2.5° and is only vertically polarized. The 0.4 GHz antenna has a cross-track beam width of 6.7° and has both vertically and horizontally polarized elements. Aerial photographs and plant and soil data were obtained simultaneously.

During the flights six fields under irrigation totally within the scatterometer field of view were found to contain both wetted and unwetted sections. The 13.3 GHz vertically-polarized signals at low incidence angles (less than 40°) were observed to fall drastically (about 7 dB) as the effective antenna beamwidth (Doppler-bandwidth limited in the along track direction) moved from irrigated to dry portions of the same field (Figure 1). Although there is some evidence of moisture effects in the 0.4 GHz data, the magnitude of the difference and the range of incidence angles over which the difference is significant varies much more from field to field than with the 13.3 GHz data. It is suspected that reprocessing the 0.4 GHz data to a finer resolution area may yield more conclusive statements regarding the response to moisture [3].

Radar Spectrometer Results

Used in this investigation is the radar section of the University of Kansas 4-8 GHz MAPS (Microwave Active and Passive Spectrometer) system [4] utilizing two parabolic dish antennas mounted parallel on the same platform ontop an antenna positioner. Both transmitting (2.5' diameter) and receiving (3' diameter) antennas

are equipped with ridged waveguide dual-polarized feeds. The antennas and some of the RF components are mounted atop a 75' truck-mounted boom. The operator can point at a target at any incident angle between 0° (normal) and about 75° and at any azimuth angle. The FM-CW radar produces a return averaged over 400 MHz for each of two orthogonal received polarizations, one of which is the same as that transmitted. By properly switching the two polarization ports at the antenna feed of each of the two antennas, the scattering coefficient can be measured for all four linear polarization combinations.

Figures 2a-2c show plots of the HH scattering coefficient for a slightly rough field as a function of soil moisture content by weight at 3 frequencies and 4 look angles. Based on skin depth calculations, it was decided to use the average moisture content in the top 5 cm of the soil as a measure of the moisture content parameters. Two major observations are apparent. First, the linear-portion of the family of curves seems to be between about 15% and 30% moisture content; at low levels of moisture content, the response is "slow" and at very high moisture levels, there is a tendency for "slope reversal". Second, as the microwave frequency is increased from 4.7 GHz to 7.1 GHz, the moisture range of the linear portion of the curves increases. A possible explanation for the decrease in the magnitude of the scattering coefficient as the moisture content increased beyond 30% is that the effect of rain on the soil caused the surface to appear "smooth" in terms of the wavelength. The 36% moisture data was collected a few hours after a reported 2.83" of rain and the 30% moisture data was collected three days later. The smoothing effect of rain caused the backscatter return to decrease at 4.7 GHz, but as the frequency was increased to 5.9 GHz and 7.1 GHz, the surface roughness increased enough to make the surface look "rough" again. We should also keep in mind that increasing the look angle is equivalent to smoothing the surface which explains the apparent successive disappearance of the slope reversal effect as the frequency increased from 4.7 GHz to 7.1 GHz.

The VV polarization moisture response appears to exhibit a similar behavior as the HH curves except for two differences: 1) slightly weaker sensitivity to moisture, and 2) σ^o increases only when soil moisture exceeds about 20% (compared to 15% for HH polarization). Furthermore, the sensitivity of both polarizations to soil moisture appears to decrease with increasing frequency over the 4-8 GHz region.

References

1. J. R. Lundien (1966 U. S. Army Engineer Waterways Experiment Station TR 3-693).

2. H. C. MacDonald and W. P. Waite (1971 Water Resource Research 7, p.100).

3. F. M. Dickey, R. K. Moore, C. King and J. Holtzman (1972 submitted to IEEE-GE, also CRES TM 177-33 University of Kansas Center for Research, Inc.

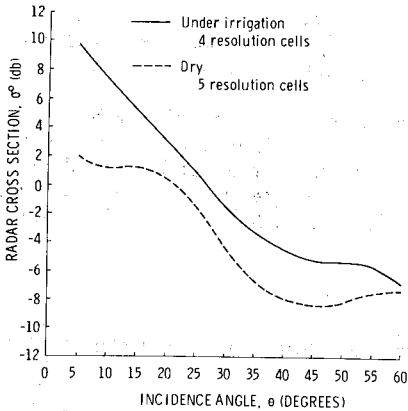4. F. T. Ulaby (1973 submitted to IEEE-AP, also CRES TR 177-35 University of Kansas Center for Research, Inc.).
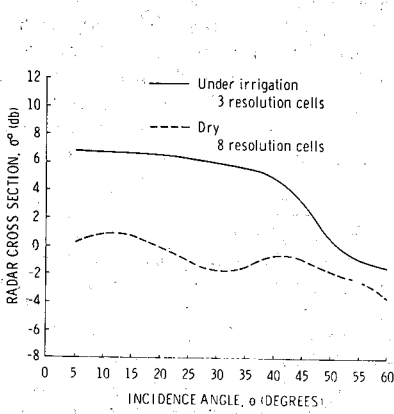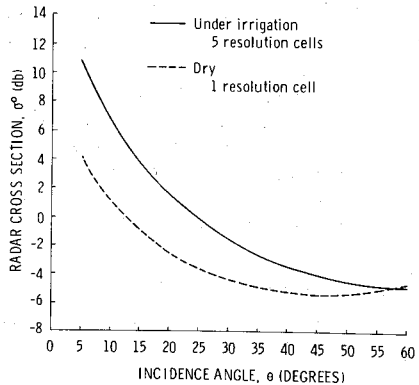
a. Corn 19" High.
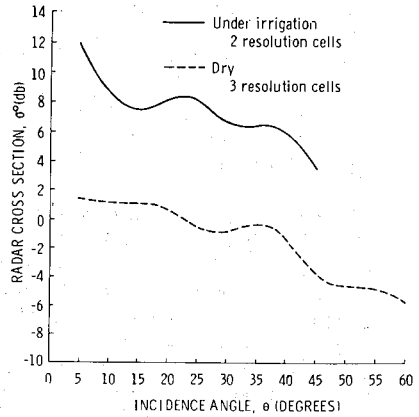
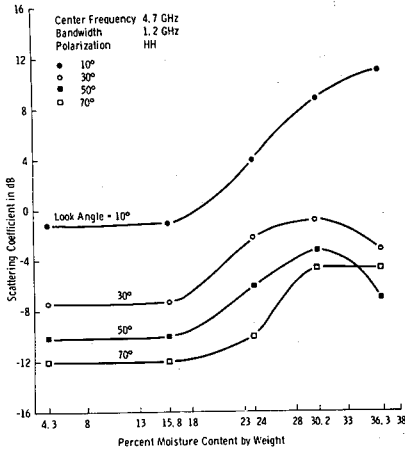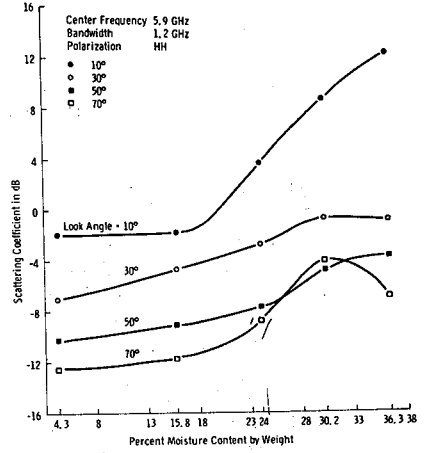b. Corn 36" High.

c. Alfalfa 10" High.

d. Alfalfa 13" High.

Figure 1 (a-d).   Radar Cross-Section of Corn and Alfalfa at 13.3 GHz,
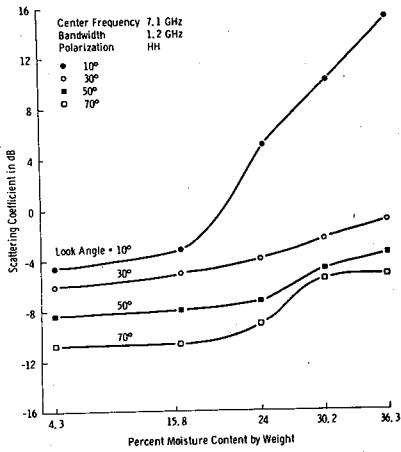   VV Polarization (June, 1970, Garden City, Kansas).

2a

2b

2c

Figure 2. Scattering coefficient as a function of moisture content.
Soil type = Pawnee Clay Loam, RMS surface height = 2.5 cm.
a) 4.7 GHz, b) 5.9 GHz, and c) 7.1 GHz.

EARTH-SPACE PATH DIVERSITY:
DEPENDENCE ON BASE LINE ORIENTATION

D. A. GRAY
Bell Telephone Laboratories
Crawford Hill Laboratory
Holmdel, New Jersey 07733

Attenuation by rainfall is the propagation phenomenon
which severely constrains the use of millimeter wave-
lengths in radio communication systems. Large attenu-
ations, say greater than 3 dB, usually occur in thunder-
storms (and hurricanes which are not discussed here).
To improve millimeter wave radio system reliability
in the rain environment, D. C. Hogg proposed path
diversity,[1] i.e., the use of two transmission paths
sufficiently spaced so that storm cells can cause large
attenuation on only one path at a time. This diversity
scheme has since been studied by various means[2,3,4,5,6]
on both terrestrial and earth-space paths. This paper
discusses a three radiometer experiment designed to
study how diversity advantage in an earth-space system
depends on the compass orientation of the straight line
(base line) drawn between two ground receiving sites.

The layout of the radiometers is shown in the Figure.
The antenna beams were pointed approximately in the
direction of a satellite located south of the mid-U.S.,
and in synchronous equitorial orbit. The Crawford
Hill-Asbury Park (C-A) base line is normal to the
direction of the satellite, whereas the Perrineville-
Crawford Hill (P-C) base line is perpendicular to the
former. It is to be noted that the beam from the
Crawford Hill radiometer passes over the Perrineville
site at an altitude of 17 km. It is therefore believed
that a single intense rain cell should not seriously
affect any two radiometers simultaneously.

The data were obtained using Dicke radiometers as in
earlier experiments conducted at Holmdel.[4] The output
of the radiometers are voltages directly proportional
to the sky temperature measured. The voltage outputs
were recorded on Esterline-Angus strip charts from
which the data have been reduced. There are two primary
assumptions made in the reduction of the data: (1) the
rain is a pure absorber at temperature 270 K, and (2) no
correction for drift in radiometer output is necessary.
The first assumption is well justified. For example,
Wilson[4] found that a pure absorber at 273 K was suitable
for analysing 16 GHz radiometer data. Strickland[7]
assumed 278 K for similar data reduction, and added
retrospectively, that 268 K would better fit his results.
From empirical evidence, 270 K appears valid, and from

theoretical calculations[8] which take into account the
effects of scatter by the raindrops, the assumption of
a pure absorber at 270 K appears valid so long as the
range of derived attenuation is limited to 10 dB: The
choice of 270 K is believed conservative since it is on
the colder side of values obtained in experimental
studies, and consequently, should lead to slightly high
derived attenuations (that 270 K is conservative has
been verified by W. L. Mammel and R. W. Wilson.[9]) As
far as the second assumption is concerned, experience
shows that if the radiometer mixers are tuned for
minimum noise, drift is toward increased noise, and
increased noise results in higher recorded temperatures.
Thus, if no correction for drift is made, the derived
attenuations will err on the high side in the long-term
average. Furthermore, experience shows drift is seldom
large, and error introduced by ignoring it is less than
0.5 dB at the 10 dB level.

Data was removed from Esterline-Angus strip charts in a
straightforward way. For each minute, a value for the
attenuation was transcribed, and from these values
the appropriate distribution functions of the attenuation
for each radiometer, each pair of radiometers, and the
triplet were obtained. The figure provides plots of these
functions for the period 1 November 1971 through
1 November 1972: the curves give the number of minutes
the abscissa was exceeded on the single paths, simulta-
neously exceeded on two given paths, and simultaneously
exceeded on all three paths.

The data in the figure clearly shows a greater diversity
advantage for the C-A pair than for the P-C pair. If
the path length between radiometers were the only
variable determining diversity advantage, we would have
expected the C-A radiometer pair to exhibit the smallest
diversity advantage. For the experiment at hand, how-
ever, the C-A pair (19 km spacing) not only shows a
larger diversity advantage than the P-C (27 km spacing)
pair, but also, an advantage equal to that of the P-A
(34 km spacing) pair. This suggests the C-A base line
orientation is close to optimum for the immediate
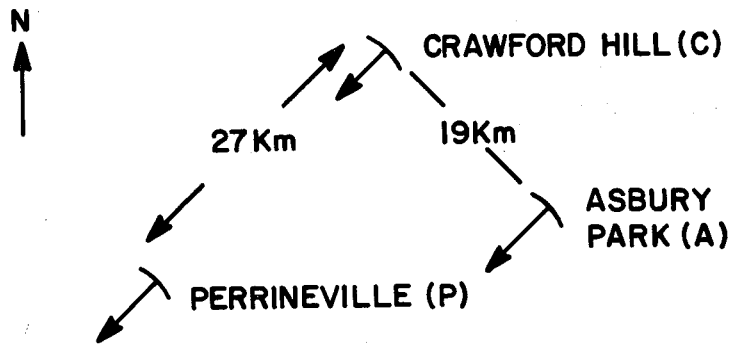Crawford Hill area.

The results in the figure bear on the selection of site
locations for satellite systems which use path diversity;
they imply this: the base line between ground receiving
stations would best be oriented normal to the direction
of the assumed satellite. This implication, however,
must be approached reservedly, for only data from one
year is involved, the phenomenon measured is not
stationary from year to year, and the number of events
accounting for the marked difference in diversity
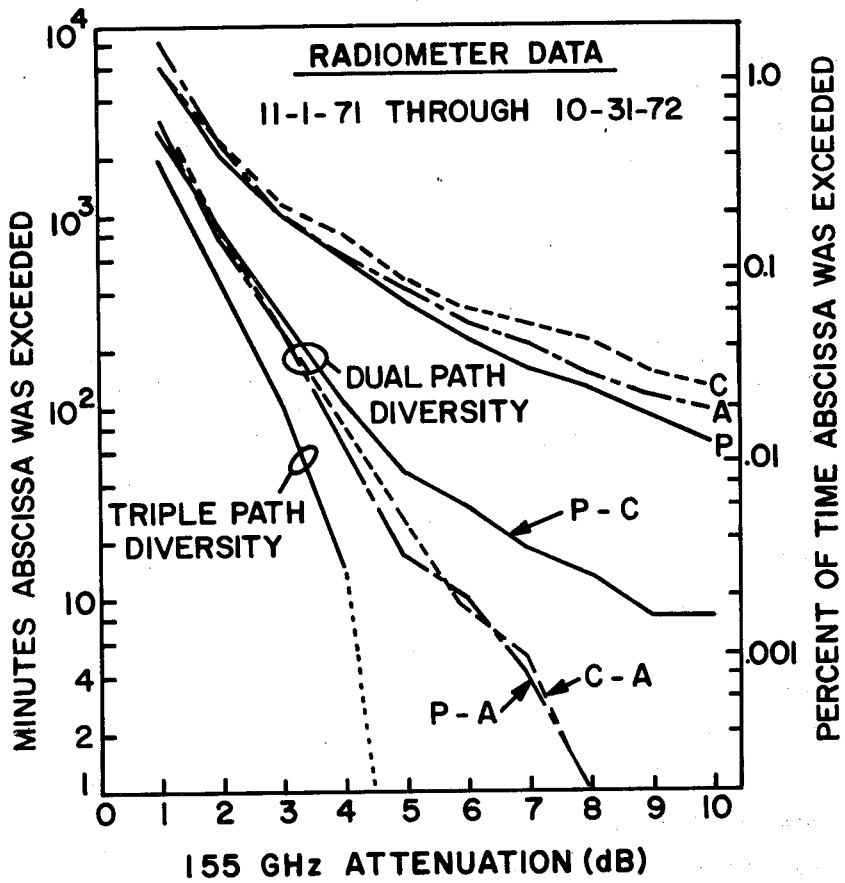advantage is only two. It is of interest that the two

events were both caused by the passage of a cold front,
one with a well developed squall line. Since line
showers in the New Jersey area exhibit a preferred NE
to SW orientation parallel to the P-C base line, it is
believed the above results will be reproduced. Indeed,
an additional five months' data has produced similar
results, with one squall line causing a third joint
outage >10 dB and on the P-C pair.

In applying millimeter waves efficiently to satellite
communications, studies of diversity advantage are
important, and we find that radiometers provide an
economical means for so doing. The experiment at hand
shows their usefulness in answering the question: "Does
base line orientation make a difference in diversity
performance?"

1. D. C. Hogg (1969 IEEE Trans. on Ant. & Prop. AP-10,
    p. 410).
2. R. A. Semplak & H. E. Keller (1969 BSTJ 48, p. 1745).
3. A. E. Freeny & J. D. Gabbe (1969 BSTJ 48, p. 1789).
4. R. W. Wilson (1969 BSTJ 48, p. 1239).
5. K. R. Grimm & D. R. Hodge (1971 OSU Electroscience
    Laboratory Tech. Reps. No. 2374-7).
6. K. N. Wulfsberg (1973 Radio Science 8, p. 1).
7. J. I. Strickland (1972 URSI Spring Meeting, Wash DC).
8. D. A. Gray (1972 URSI Spring Meeting, Wash DC).
9. W. L. Mammel & R. W. Wilson (1973 IEE Conf. on Prop.
    of Radio Waves at Frequencies Above 10 GHz, London,
    April).

N

CRAWFORD HILL (C)

27 Km   19 Km

ASBURY
PARK (A)

PERRINEVILLE (P)

BEAM POINTING : Az − 226° ; El. − 32°

RADIOMETER DATA

11-1-71 THROUGH 10-31-72

MINUTES ABSCISSA WAS EXCEEDED

PERCENT OF TIME ABSCISSA WAS EXCEEDED

DUAL PATH
DIVERSITY

TRIPLE PATH
DIVERSITY

P - C

C - A

P - A

155 GHz ATTENUATION (dB)

Session 41   Microwave Sensing

MEASUREMENT OF SURFACE TOPOGRAPHY USING MICROWAVE SCANNING

TECHNIQUES

By   A.Husain and E.A.Ash

The basic concept of this novel, non-destructive,
non-contacting superresolution microscope has been previously
described[1];   the main features are indicated in the figure.
The aperture in the diaphragm has a diameter which is very
much less than the wavelength. Some of the radiation is
perturbed by the object immediately below the hole. This
component is tagged by vibrating the object and can therefore
be recovered and measured. Using this technique, a grating with
a period of 250 μ could be clearly resolved and displayed,
using 3 cm radiation.

The microscope is capable of detecting small
variations in dielectric constant, and also small changes in
the topography of a surface. The former ability makes it
potentially useful in high resolution testing of microstrip
substrates. The ability to detect small changes in topography
can be exploited to measure surfaces, and particularly to
detect surface cracks. The method is particularly sensitive
for the detection of fine cracks in thin metallic films; cracks
only 20 μ wide have been detected in this way. There is
evidence that even smaller cracks could be detected, even at
the present X-band frequency.

In the proposed talk experimental results on dielectrics,
thin metallic films and solid metal surfaces will be presented
together with some of the essential limitations of the device.

370

The capability of the technique, using higher microwave frequencies and more sophisticated signal processing methods will be assessed.
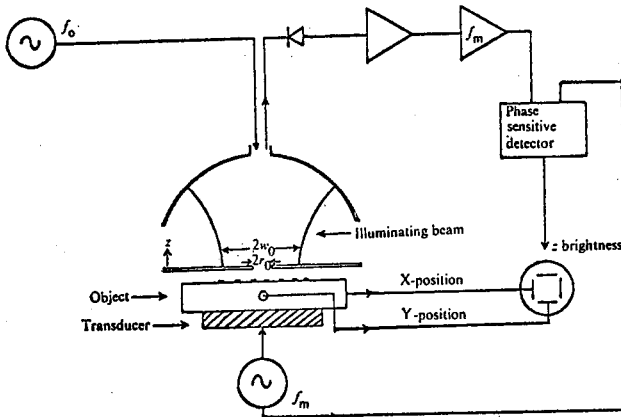
References

1. Superresolution Aperture Scanning Microscope.

   E. A. Ash and G. Nicholls.

   Nature, Vol. 237, No. 5357, pp. 510-512, June 30 1972.

Session 41 Microwave Sensing

DEPENDENCE OF MICROWAVE EMISSION ON MOISTURE CONTENT
FOR THREE SOILS

John C. Blinn III*
Space Sciences Division
Jet Propulsion Laboratory, Pasadena, California   91103

Jack G. Quade
Mackay School of Mines
University of Nevada, Reno, Nevada   89507

INTRODUCTION:

During the summer of 1972 a study of the microwave emission from
moist soils was performed by the Jet Propulsion Laboratory and the
University of Nevada. It was an extension of a previous study of
moist sands (Ref. 1) and was designed to demonstrate the effect of
soil type on the emission characteristics of moist geological mate-
rials and the effect of a regular roughness pattern superimposed on
the surface of the moist material.

EXPERIMENT DESCRIPTION:

The experiments were conducted with three dual-polarized microwave
radiometers operating at 0.95, 2.8 and 21 cm wavelengths. The radio-
meters were mounted four meters above the target area on the front
of a van which housed the electronics and a minicomputer for real
time processing of the data. A detailed description of the system
characteristics and calibration procedures is contained in Ref. 2.

A controlled target area formed by a 2.4 x 2.4 m box with a wooden
floor and movable sides was placed in front of the van and filled
with 15 cm of soil. A fixed increment of water was added, the sur-
face smoothed, vertically then horizontally polarized data taken
with the three radiometers, and soil samples collected from the
centers of each quadrant and one from the center of the target. A
viewing angle of approximately 25° from nadir was used to avoid
reflections from the van and instrument package. Three soil types
were studied, Cave Rock Loamy Sand, Mottsville Coarse Sandy Loam,
Godecke Clay Loam. Moisture data is presented as a percentage of
dry weight.

The effect of a regular roughness pattern was examined by pulling
a triangular toothed template over the surface of the water satur-
ated sandy loam. Ninety degree apex angles and tooth spacings of
2.5, 5, 7.5, and 10 cm were used. The grooves were run first in
the direction of horizontal polarization (perpendicular to the truck
axis) and then in the direction of vertical polarization (parallel
to the truck axis).

*Now with Environmental Research & Technology, Lexington, Mass. 02173

EXPERIMENTAL RESULTS:

Figures 1, 2a and 2b show the effect of moisture content of three
soils on emissivity at 0.95, 2.8 and 21 cm wavelengths (31.4, 10.69,
and 1.42 GHz frequencies) for horizontal and vertical polarization.
In all cases, the emissivity remains approximately constant until a
certain moisture content, then shows a marked decrease as water con-
tent is increased. The following table shows the incremental change
in emissivity for a one percent change in water content assuming a
linear decrease from the listed breakpoint moisture. It shows that

		Sensitivity ($-\Delta e/\%$)			Breakpoint (%)		
	Frequency (GHz)	1.42	10.69	31.4	1.42	10.69	31.4
SOIL	Cave Rock	.026	.046	.044	4.5	9.5	10
	Mottsville	.022	.040	.037	1.5	9.0	10
	Godecke	.023	.030	.028	11	15	15

the sensitivity decreases as the loam and clay content increases,
the clay loam has a higher breakpoint than the other soils, the 21
cm data has a breakpoint significantly lower than the 0.95 and 2.8
cm responses, and because of item 3, the 21 cm sensitivity is less,
even though the total change in emissivity at 21 cm is the same
order or larger than the other channels.

Figures 2c and 2d show the results of the roughness experiments
performed in saturated Mottsville Coarse Sandy Loam, moisture
content 18.3%. The data, presented in the experimental sequence
from left to right, shows that roughness has a marked effect which
is dependent on the wavelength and scale of the roughness.

This experiment shows that microwave emission from moist soils
is a function of both soil type and surface roughness. The data
exhibits a degree of scatter which is believed to be due to non-
specular surfaces and inhomogenities in the material rather than
a variation in calibration. The scatter does not detract from
the conclusions, but provides a good indication of the trouble
one might expect in interpreting data from an in-situ measurement
program.

REFERENCES:

1. Blinn, John C., III, and Quade, Jack G., Microwave Properties
    of Geological Materials: Studies of Penetration Depth and
    Moisture Effects, Fourth Annual Earth Resources Program Review,
    NASA Manned Spacecraft Center, Houston, Texas, Jan. 17 - 21, 1972

2. Blinn, J. C. III, Conel, J.E., and Quade, J. G., Microwave
    Emission from Geological Materials: Observation of Interference
    Effects, Journal of Geophysical Research, Vol. 77, No. 23,
    August 10, 1972.
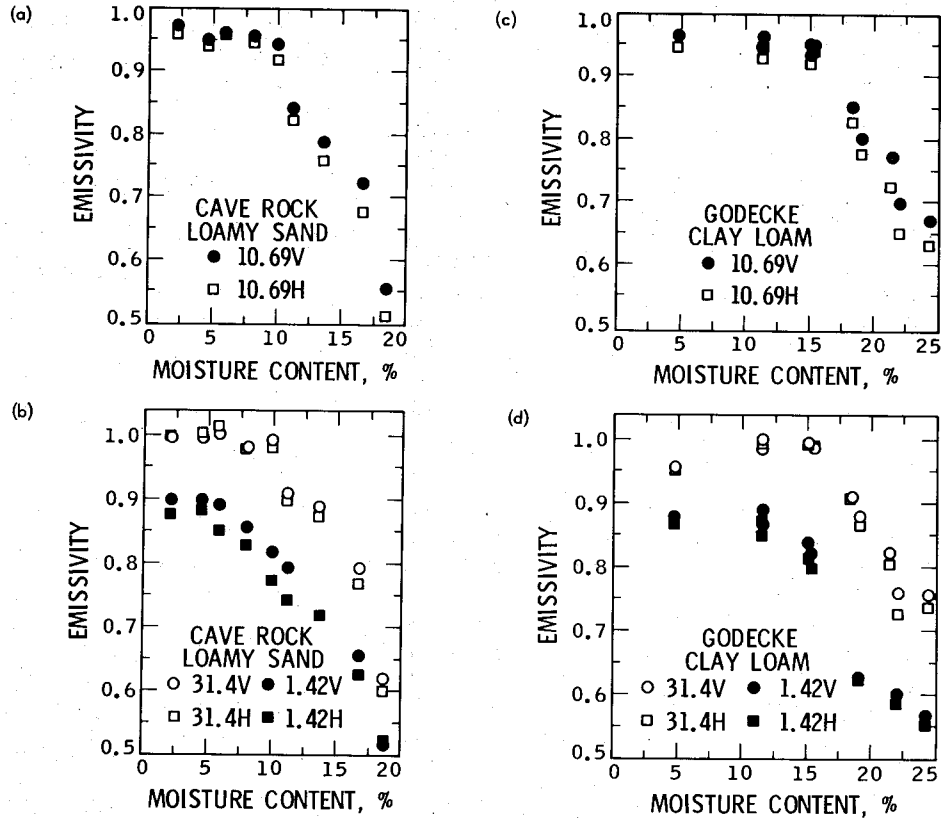
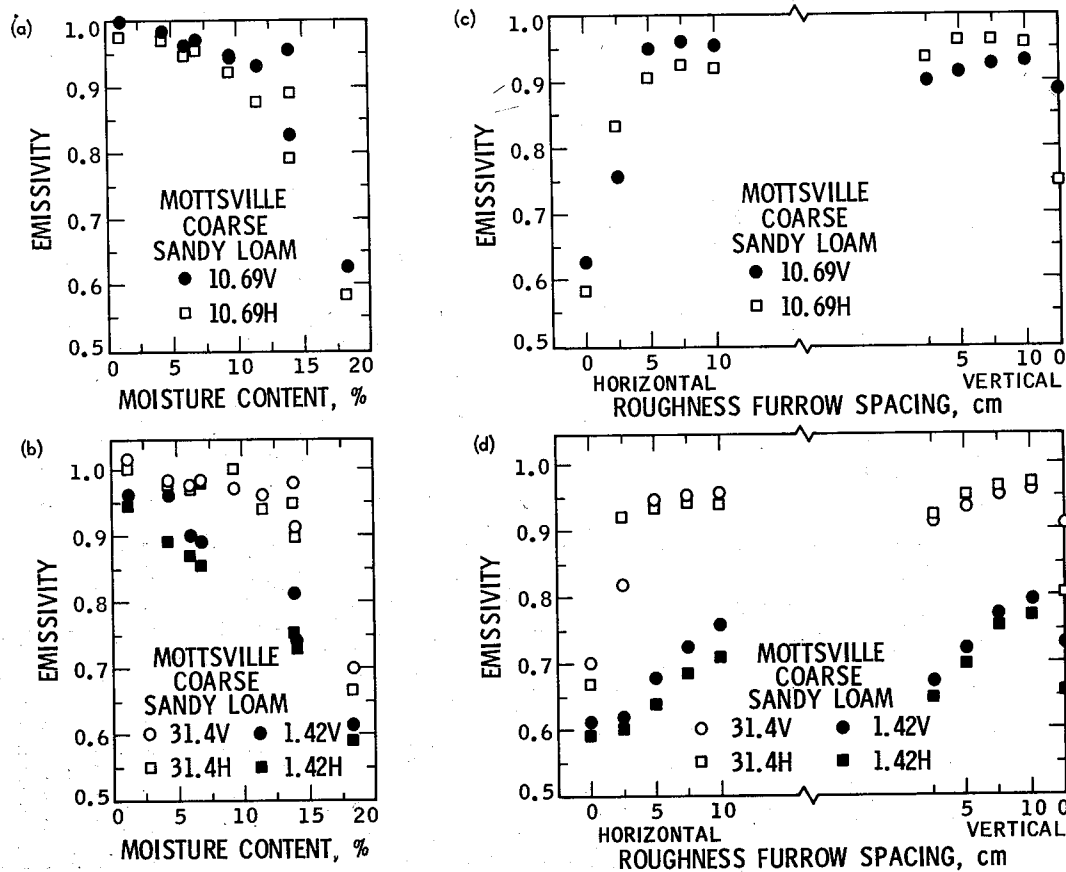Figure 1. Moisture Effects for Loamy Sand and Clay Loam.

Figure 2. Moisture and Roughness Effects for Sandy Loam.

OCTAVE BAND WAVEGUIDE RADIATORS FOR
WIDE-ANGLE SCAN PHASED ARRAYS[†]

C. C. Chen
Hughes Aircraft Company
Fullerton, California

The maximum tunable bandwidth of rectangular waveguide phased arrays is limited to 58 percent.[1] A typical design uses thin iris in the aperture to obtain an impedance match having a maximum VSWR of 2.3:1 over a 50 percent band for a 60-degree half-angle conical coverage.[2] This paper presents a method for extending the useful bandwidth over 2:1 band.

Configuration of the element is shown in Figure 1. The radiating element is a double ridge rectangular guide with the ridge tapered to zero thickness at the open end, and a pair of thin irises which partially cover the aperture. The size of ridges is so chosen that it raises the TE_{20} mode cutoff and lowers the TE_{10} mode cutoff so as to propagate more than octave band of frequencies without higher order modes.

The design objective of the tested array is 2:1 bandwidth for a ±60 degree conical scan volume. The rectangular guide used has a 1.1" x .226" cross section arranged in an equilateral triangular lattice so that it has a unit cell area of .293 λ_h^2, where λ_h = 1.1315" free space wavelength at the high frequency end, f_h = 10.438 GHz. Twenty-five percent width of the aperture is covered with iris. A .03125" thick fiberglass radome with ϵ_r = 7.5 is placed at .1" off the aperture. The cross section of the ridges is .300" x .125". The measured TE_{10} cutoff frequency of the ridge-loaded guide is about 4.4 GHz and TE_{20} cutoff is about 11.8 GHz. Both ridges are linearly tapered to zero height at the aperture within a distance of .375". This taper does not create a mismatch of more than 1.25:1 VSWR from an unloaded guide to a ridge-loaded guide in the high frequency region. Therefore, no significant affects on aperture matching is expected in the high frequency region. However, it lowers the TE_{10} cutoff by 20 percent so that the array can be operated near or below the cutoff frequency of the straight rectangular guide.

The measured amplitude of reflection in three H-plane waveguide simulators are shown in Figure 2. The designed frequency range for ±60° conical coverage is from 5.22 GHz to 10.44 GHz. Without the radome, the average measured reflection loss in these simulators is about .6 dB higher than the case shown in Figure 2. Without iris, radiation blindness is observed in the high frequency region. The estimated maximum VSWR of this array is about 3.6:1 throughout the 2:1 band.

References

1. G. N. Tsandoulas (1972 Microwave Journal, September, pp. 49-54).

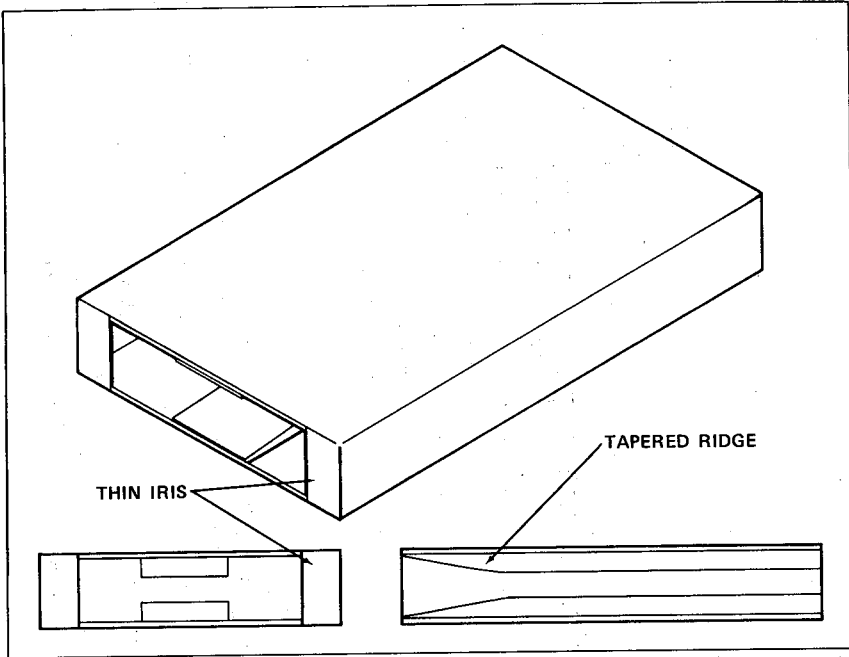2. C. C. Chen (1973 IEEE Transactions AP, May, pp. 298-302).

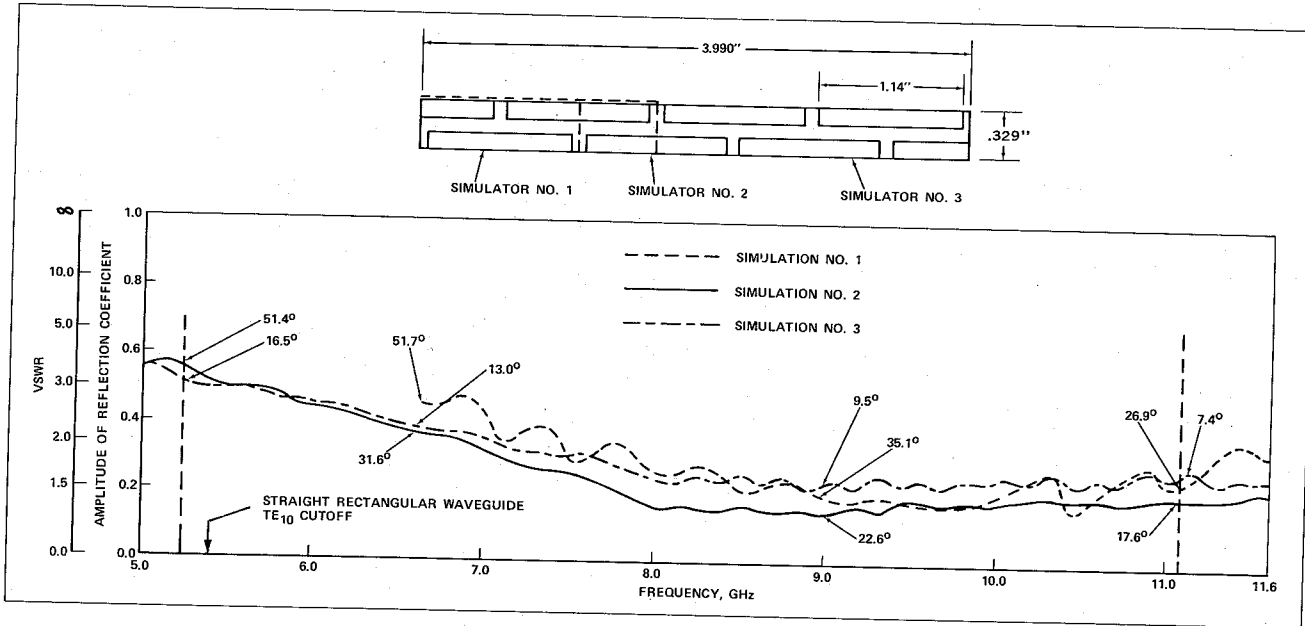Figure I. Configuration of Double Ridge Waveguide Element

Figure 2. Reflection Measurements from Three Different Simulated Apertures

OMNI-DIRECTIONAL BICONICAL HORN ANTENNA
USING METAL-PLATE LENS FOR SHF TV BROADCASTING

T. Saito, K. Uenakada, K. Yasunaga   Y. Shibano and S. Yamashita
   Nippon Hoso Kyokai (NHK)   Sumitomo Electric Industries, Ltd.
        Tokyo, Japan   Osaka, Japan

In order to provide a large number of TV channels, the 12 GH$_z$ band in addition to the VHF and UHF bands must be used. We developed the omni-directional biconical horn antenna using a metal-plate lens (b.h.a.l.) shown in Fig. 1 for this purpose and tested at the NHK's experimental station. This antenna consists of a horizontal polarization biconical horn antenna (b.h.a.)[1] and a cylindrical-shaped metal-plate lens around the aperture of the b.h.a.. The particular features of this antenna are a high gain and a null-filled vertical radiation pattern (v.r.p.) which can be obtained by adjusting the phase distribution of the b.h.a. by using the metal-plate lens.

The amplitude distribution and the phase front in the vertical direction on the aperture of the b.h.a. can be approximated by the half cosine function and the circular arc with its center at the equivalent point source of the b.h.a., respectively. The calculated antenna gain based on the above two approximations is shown in Fig. 2. Figure 2 shows that the size of a high gain b.h.a. is too large to be economically realized. This enormous size is caused by the large deviation of the phase distribution from the constant phase distribution.

The zoned metal-plate lens shown in Fig. 1 is used to obtain a constant phase distribution. This lens consists of phase correction elements composed of two adjacent metal plates. Each of the metal plates is almost equally spaced from the adjoining one and set parallel to both the radial vector of the circular arc and the electric-field vector. This lens was designed to approximate the phase at the middle point of each space between two adjacent metal plates to the constant one. Therefore, the correction error of the phase becomes greater as the distance from the middle point becomes larger and as the aperture angle becomes larger. This error also restricts the improvement of the gain. For example, the measured gain for a b.h.a.l. whose aperture length was 22 λ and aperture angle was 36° was 14.0 dB, where λ is the wavelength. This value is 1.2 dB lower than the calculated gain for an antenna having a half cosine amplitude constant phase distribution, but 6.3 dB higher than that of the b.h.a. with the same dimensions.

A consecant v.r.p. gives an approximately uniform field strength over the prescribed service area. Two methods for synthesizing a cosecant v.r.p. were developed by us. We called one the half cosine amplitude stepped phase method and the other the half cosine amplitude perturbed phase method. The aperture distribution of the former consists of a "half cosine" for the amplitude and a "slanting step function" for the phase. The slanting step

function shown in Fig. 3 is expressed by the equation below;

$$\varphi = \delta \, x/L \quad \left[0 \leq x \leq L \right] \, , \quad -\delta \, x/L \quad \left[-L \leq x < 0 \right] \quad (1)$$

where φ is the phase difference between the upper and lower section and 2L is the aperture length. If $\varphi = -90°$, the v.r.p. $D(\theta)$ of this antenna can be written as:

$$D(\theta) = \frac{\sin \, (S/2 - \pi/4)}{S/2 - \pi/4} \, \tan(S/2) + \frac{\sin \, (S/2 + \pi/4)}{S/2 + \pi/4} \quad (2)$$

where $S = 2\pi L/\lambda \sin \theta$ and θ is a declination angle defined in Fig. 3. Equation (2) shows that $D(\theta)$ is the cosecant beam in the sidelobe region when $S \gg \pi/2$. The beam tilt angle can be adjusted to the required value by δ . When $L = 10 \lambda$, $\varphi = 90°$ and $\delta = 0°$, then the calculated beam tilt angle is $1.37°$, the calculated gain reduction due to null-filling is 0.81 dB and the calculated level at the first null point of the original pattern can be improved to -18.2 dB. The measured gain of the b.h.a.l. for this case is less than the calculated gain by 1.6 dB.

The principle of the half cosine amplitude perturbed phase method is illustrated in Fig. 4 for a 2L aperture. The original pattern for the half cosine amplitude constant phase aperture distribution is expressed by the function $Po(S/\pi)$ with the null points as shown in Fig. 4(a). In order to fill the ith null point, the imaginary pattern $jPi(S/\pi)$ as shown in Fig. 4(b) is required in addition to Po. The resultant complex aperture distribution $\dot{A}(x)$ can be approximated by the equation:

$$\dot{A}(x) \doteqdot \left[\cos \, (\frac{\pi x}{2 \, L}) \right] \, \exp(ja_i \cos(\pi \, x \frac{2i+1}{L})/\cos \, (\frac{\pi \, x}{2 \, L}) \right] \quad (3)$$

$$\text{for} \quad | \, x \, | < L/(i + 0.5)$$

$$= \cos \, (\pi \, x/2L) \, \text{for} \, L/(i + 0.5) < |x| < L$$

where a_i is corresponded to the null-filling level and assumed to be infinitesimally small. The measured cosecant radiation patterns by these two methods for a 21λ aperture b.h.a.l. are shown in Fig. 5. The latter method has two important features. First, the gain reduction due to null-filling is less than that of the former method. For example, the gain reduction for a null-filling of -18 dB at the first null point is 0.8 dB for the former method and 0.5 dB for the latter. Second, the sidelobes in the v.r.p. are greatly distorted from the cosecant envelope when there is a little deviation from the designed phase distribution. This means that a higher quality of design and manufacturing are required in comparison to the former method.

The diameter of the 15 dB omnidirectional b.h.a.l. was 1592 mm which is about 1/6 of the diameter of a.b.h.a. without a lens. The aperture height was 902 mm. The electrical characteristics of this antenna are described in Fig. 1.

Reference 1) Katsuaki Uenakada & Keiichi Yasunaga, "Horizontal polarization biconical horn antenna excited by TE_{11} mode in circular guide". 1971-ISAP, 2-1) D4 Sept., 1971

1592

Biconical horn

Metal-plate lens

E ⊕

902

Metal post array

Circular wave guide

Circular polarizer

TE_{11} mode
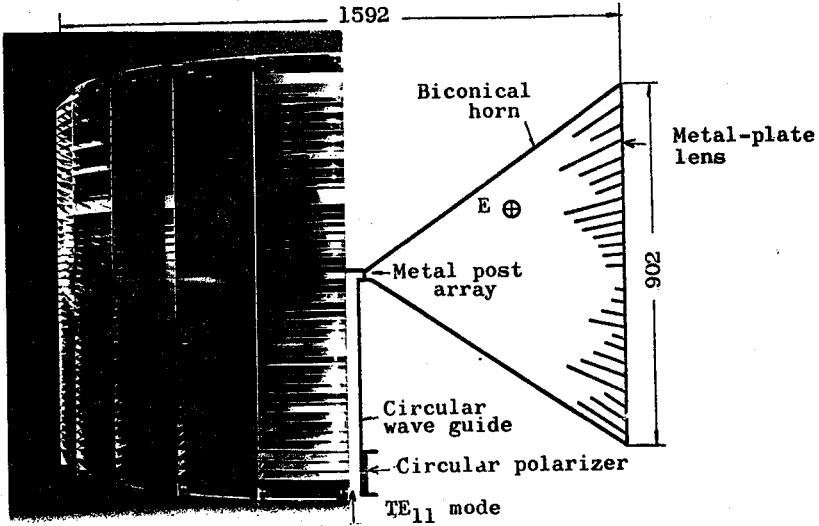
Note: 1. Frequency band is from 11.8 GH_z to 12.2 GH_z.
       2. Antenna gain is 15 dB.
       3. Circularity is from 3.3 to 5.0 dB.

Fig. 1 Structure and three dimentional view of omni-
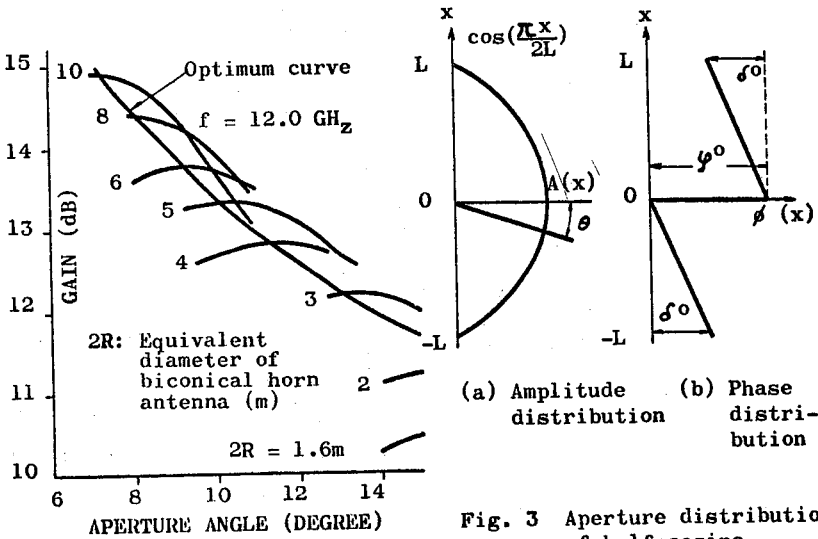   directional biconical horn antenna using metal-
        plate lens.

15
14
13
12
11
10

GAIN (dB)

10
8
6
5
4
3
2

Optimum curve

f = 12.0 GH_z

2R: Equivalent
diameter of
biconical horn
antenna (m)

2R = 1.6m

6   8   10   12   14
APERTURE ANGLE (DEGREE)

Fig. 2 Gain for biconical
        antenna

x

$\cos(\frac{\pi x}{2L})$

L

0

A(x)

θ

-L

x

L

δ^o

φ^o

0

ϕ (x)

δ^o

-L

(a) Amplitude
    distribution

(b) Phase
    distri-
    bution

Fig. 3 Aperture distribution
        of half cosine
        amplitude stepped
        phase method

381
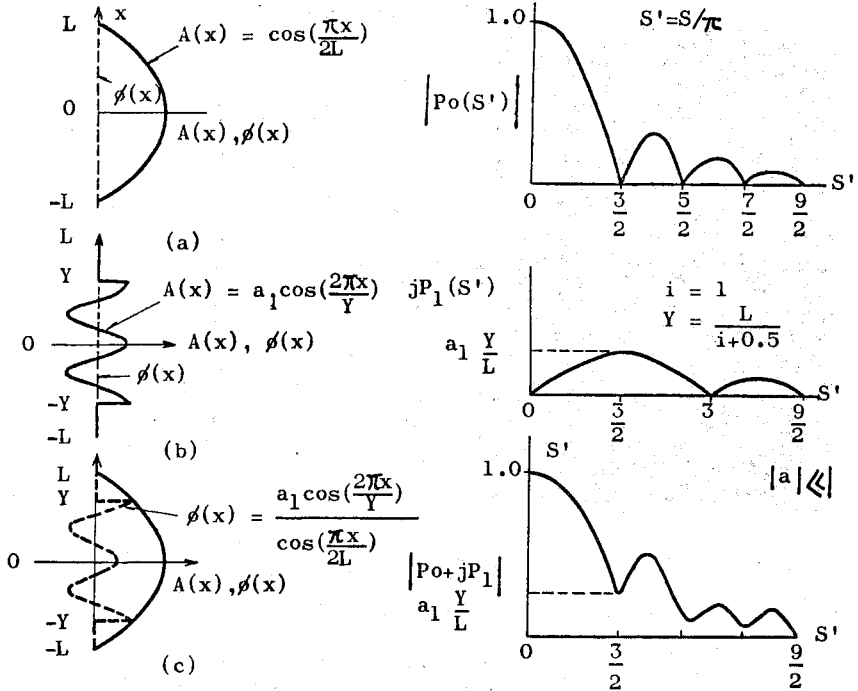
Fig. 4 Principle of the half cosine amplitude perturbed
       phase method

(a) Half cosine distribution and primary pattern Po
(b) cos $(2\pi i \frac{x}{Y})$ - distribution and it's pattern P_1
(c) Equivalent distribution and c.r.p. $\left| Po + jP_1 \right|$
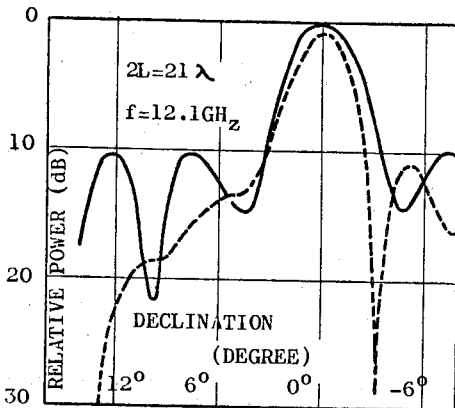
Fig. 5

Measured cosecant radiation
patterns for biconical
horn antenna using metal-
plate lens:
Null filling by stepped
phase method and perturbed
phase method.

--- by stepped phase method $(\varphi = 90^{\circ})$

— by perturbed phase method $(a_1 = 0.4)$

382

ADAPTIVE ARRAY RETRODIRECTIVE EIGENVECTOR BEAMS

William F. Gabriel
Naval Research Laboratory
Washington, D.C. 20375

Consider the adaptive array[1] configuration of Fig.1 and its co-variance matrix, $\underline{M}$,

$$\underline{M} = \overline{[\underline{E}^* \cdot \underline{E}_t]}$$

where $\underline{E}$ is a column vector of array element input signals consist-ing of external interference source contributions plus internal receiver noise. The eigenvalues, $\beta_i{}^2$, and eigenvectors, $\underline{e}_i$, of the Hermitian matrix $\underline{M}$ are solutions to the eigenvalue problem state-ments,

$$\left|\underline{M} - \beta_i{}^2\,\underline{I}\right| = 0 \quad\text{and}\quad \underline{M}\,\underline{e}_i = \beta_i{}^2\,\underline{e}_i$$

Now the components of the unique eigenvectors of $\underline{M}$ may be inter-preted as array element weights, giving rise to a set of unique, orthogonal, normalized, retrodirective, eigenvector beams. The eigenvalues themselves, in fact, represent the output powers delivered by their respective beams.

$$g_i(\theta) = (\underline{s}_t \cdot \underline{e}_i) \quad \text{ith eigenvector beam}$$

where $\underline{s}$ is a vector consisting of the array element phasing associated with far field angle, θ. This set of eigenvector beams can be further related to an equivalent beam forming net-work which constitutes an orthonormal matrix transformation for the element signals.

By solving for the adaptive weights generated in the equivalent network orthonormal system, one can derive a rather simple ex-pression for the output pattern function in terms of the retrodirective eigenvector beams. For the Fig.1 configuration, assuming the use of simple RC filters in the correlation integrators, the output pattern function, $G(\theta,t)$, reduces to the form,

$$G(\theta,t) = G_q(\theta) - \sum_{i=1}^{K} (1-e^{-\alpha_i t})\left(\frac{\mu_i-\mu_o}{\mu_i+1}\right)\hat{W}_{qi}\,g_i(\theta)$$

where $G_q(\theta) = (\underline{s}_t \cdot \underline{W}_q)$ quiescent beam pattern

$\hat{W}_{qi} = (\underline{e}_{it}^* \cdot \underline{W}_q)$ eigenvector component of quiescent beam vector

$\mu_i = \mu_o\left(\dfrac{\beta_i{}^2}{\beta_o{}^2}\right)$ equivalent servo gain factor, where μ_o is quiescent servo gain

$$\underline{W}_q = \quad \text{quiescent beam array weighting vector}$$

$$\alpha_i = \left(\frac{1 + \mu_i}{RC}\right) \text{ transient decay factor}$$

$$\beta_o^2 = \quad \text{eigenvalue for quiescent receiver noise}$$

This expression shows that the performance of the adaptive array is completely controlled by the unique eigenvalues and their associated unique eigenvector beams. All non-unique contributions to the summation are eliminated by the term $\left(\mu_i - \mu_o\right)$.

For the case of a single narrow band interference source, there is only one unique eigenvalue and one unique eigenvector, which produces a uniform illumination retrodirective eigenvector beam centered on the interference source at angle θ_1.

$$g_1(\theta) = \frac{1}{\sqrt{K}} \left[\frac{\sin K(u - u_1)}{\sin (u - u_1)}\right]$$

$$\hat{W}q_1 = G_q(\theta_1)/\sqrt{K} \quad \text{and} \quad \mu_1 = \mu_o(1 + KP)$$

where $u = (\pi d/\lambda)\sin\theta$, K is the number of elements, and P is the ratio of jammer power to receiver noise power at the inputs.

For the case of two narrow band interference sources, there are usually two unique eigenvalues and two unique eigenvector beams, but the beams may differ considerably depending upon the strengths and locations of the sources. Figs. 2, 3, and 4 illustrate the patterns and transient performance for two equal sources of power ratio, 1250, located close together at angles of 18 and 22 degrees respectively. The eigenvalues for this case, $\beta_1^2 = 18544$ and $\beta_2^2 = 1057$, differ by a large factor which may be related to the associated eigenvector beams. Note in Fig. 3 that eigenvector beam $g_1(\theta)$ covers both sources in the manner of a centered sum beam, and its power gain of approximately 7.43 leads to a total power output of 2x7.43x1250 = 18544, the first eigen-value. Eigenvector beam $g_2(\theta)$, on the other hand, splits the sources in the manner of a difference beam, and its power gain of approximately 0.422 at the source locations leads to a total power output of 1057, the second eigenvalue. The sum and difference nature of these two beams explains why their outputs will have zer average cross correlation, even though both beam outputs contain power from the two sources. In Fig.4, note the two distinct slope in the transient response caused by the two different eigenvalues.

Other multiple source distributions have been computed.

---

[1] S.P.Applebaum (1966 Syracuse Univ.Res.Corp.Report SPL TR-66-1)

$$Output = \sum_{i=1}^{6} W_i E_i$$
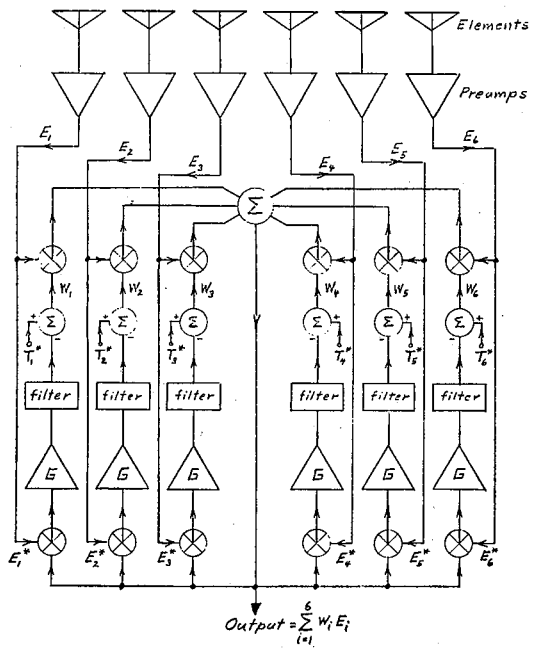
FIG. 1 - AN ANALOGUE LINEAR ADAPTIVE ARRAY CIRCUIT
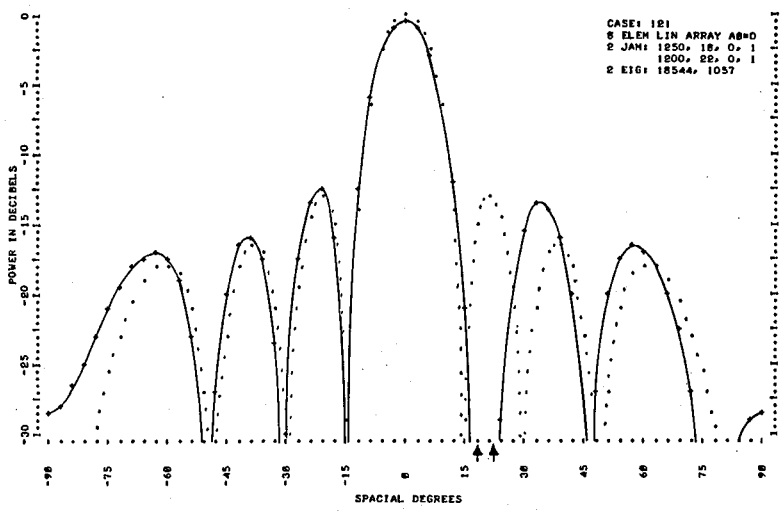
FIG. 2 - QUIESCENT (dotted) AND ADAPTED (solid) PATTERNS FOR TWO JAMMER CASE

385
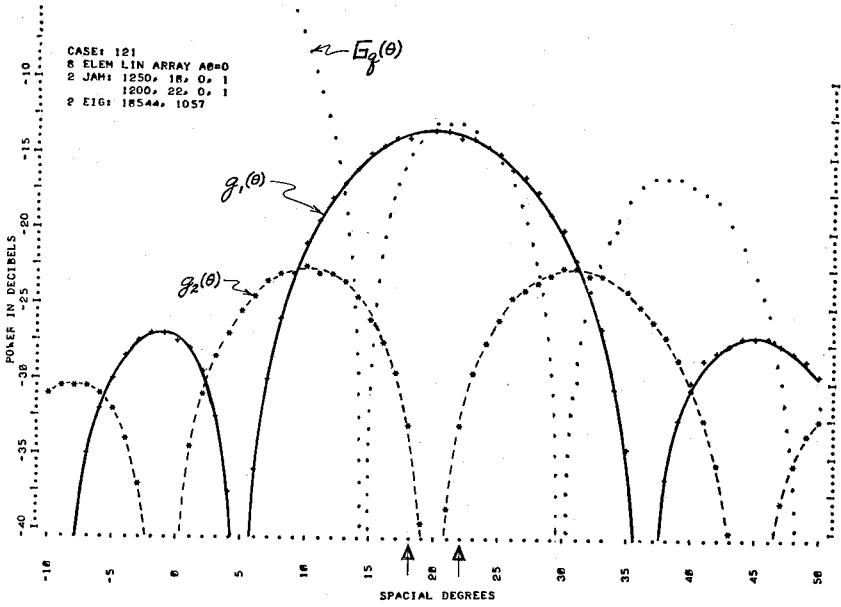
FIG. 3 - RETRODIRECTIVE EIGENVECTOR BEAMS FOR THE TWO JAMMER CASE
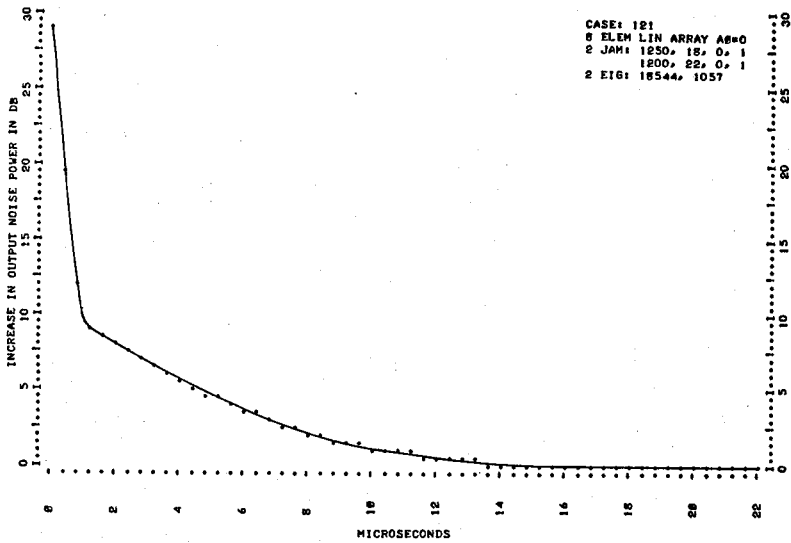
FIG. 4 - OUTPUT NOISE POWER TRANSIENT RESPONSE FOR THE TWO JAMMER CASE

386

ADAPTIVE BEAMFORMING IN THE SPECTRAL DOMAIN

Sam M. Daniel*
System Analysis Group
Motorola, Inc.
Scottsdale, Arizona 85252

ABSTRACT

The adaptive array process is cast into a constrained optimization problem in the spectral domain. Basically, the process allows the array to maintain constant gain in a desired look-direction while simultaneously rejecting undersired interference. The solution to the problem leads to two versions of a "spectral-domain constrained least-mean-squares" (SD-CLMS) iterative algorithm. Convergence considerations lead to optimization of the algorithm in the noiseless case. Smoothing techniques are recommended for the noisy case. A numerical example is included.

STATEMENT OF THE PROBLEM

Consider an array of N omnidirectional sensors and assume no cross-coupling between them. In the spectral domian, a conventional narrowband array has the configuration shown in Figure 1. The inner product $\underline{S}^T\underline{W}$ constitutes the array's processed signal where:

$\underline{S}$: N-component complex-valued spectral-domain column signal vector

$\underline{W}$: N-component complex-valued spectral-domain column weighting vector

Vector $\underline{W}$ characterizes the array's radiation pattern. When properly chosen, $\underline{W}$ gives rise to a single-beam low-sidelobe radiation pattern. The fundamental purpose for such a choice is, of course, to receive main-beam power and attribute it to the look-direction sector of the main beam. However, this passive conventional approach is unrealiable in an interference environment; e.g., when a strong interference happens to be incident on a sidelobe as shown in Figure 1. The purpose of an adaptive array [1], [2] is to minimize the effects of interference while maintaining constant gain in a specific look-direction by means of a process that continually varies $\underline{W}$ in an appropriate fashion.

One possible version of an adaptive array process [4] is based on a policy of iteratively seeking to minimize total received power with respect to a real-valued amplitude distribution $\underline{A}$ over an initial feasible weighting vector $\underline{W}^0$ under the constraint that the component sum of $\underline{A}$ remain constant. The mathematical statement of the process is simply:

$$\left.\begin{array}{l} \min_{\underline{A}} \underline{A}^T(\Omega^0\underline{S})^*(\underline{S}^T\Omega^0)\underline{A} \\[2mm] \text{Subject to: } \underline{C}^T\underline{A} = N \end{array}\right\} \tag{1}$$

---

where

$\underline{A}$:   N-component real-valued column amplitude distribution vector

Ω^0:   N x N complex-valued diagonal matrix whose diagonal elements correspond to $\underline{W}^0$

$\underline{C}^T$:   N-component uniform row vector [1 1 ... 1]

The amplitude constraint guarantees constant gain in the look-direction associated with W^0. Minimization of total received power can only reject interference power under this constraint.

THE SD-CLMS ALGORITHM

Understanding of the problem at hand can be greatly enhanced by appealing to its geometrical interpretation demonstrated in Figure 2 for the 2-dimensional case. Note that the received power P_{REC} is a non-negative quadratic functional of $\underline{A}$ representing a paraboloidal surface with a unique minimum of zero at the origin. The amplitude constraint, on the other hand, is a vertical plane that intersects the axes in the first quadrant at 45°; it constitutes the plane of feasible $\underline{A}$'s. The curve of intersection comprises the continuum of admissible received power levels. Minimum received power is identical to the minimum distance from the curve to the $\underline{A}$-plane corresponding to an optimal vector $\underline{A}^{opt}$. It is the purpose of the adaptive array process described below to approach $\underline{A}^{opt}$ along the projected curve on the $\underline{A}$-plane.

Given an initial weighting vector $\underline{W}^0$, it is clear that $\underline{A}^0 = \underline{C}$, the uniform vector. Using a projected gradient procedure, it can be shown that subsequent improved estimates of $\underline{A}$ are given by

$$\underline{A}^{k+1} = \underline{A}^k - \lambda_k \{\underline{\Gamma}^k - \underline{\Gamma}^k_{avg}\} \qquad (2)$$

where

$\underline{A}^k$:   the current estimate

λ_k: step-size, a positive scalar

$\underline{\Gamma}^k$: $Re\{(\Omega^0\underline{S})^*(\underline{S}^T\underline{W})\}$, the N-component sensitivity vector or gradient vector of P_{REC} with respect to $\underline{A}^k$, namely, $\nabla_A^k P_{REC}$

$\underline{\Gamma}^k_{avg}$:   the average sensitivity uniform vector

Defining initial and current processed complex-valued scalar signals $\underline{S}^T\underline{W}^k$ by Z_0 and Z_k, respectively, and using the fact that $\underline{W}^k = \Omega^0\underline{A}^k$, it can be shown that $\underline{W}$ may be updated directly according to:

$$\underline{W}^{k+1} = \underline{W}^k - \lambda_k Re\{(\Omega^0\underline{S})^*Z_k - \frac{Z_0^* Z_k}{N}\underline{C}\} \qquad (3)$$

This expression constitutes the standard form of the algorithm. Absorbing consecutive $\underline{A}$ estimates into the weighting vector, one obtains the alternate form of the algorithm, namely,

$$\underline{w}^{k+1} = \underline{w}^k - \lambda_k \text{Re}\{ (\Omega^k \underline{S})^* z_k - \frac{|z_k|^2}{N} \underline{C} \} \tag{4}$$

Note the similarity of expression (4) to the first iteration in (3). Figure 3 shows the mathematical block diagram that exercises the standard form of the algorithm. It should be clear that the alternate form, being fully recursive, would correspond to a simpler block diagram; however, one more prone to roundoff error.

CONVERGENCE CONSIDERATIONS

The choice of λ_k has an important bearing in the convergence of the algorithm. Under noiseless conditions, the standard form of the algorithm will exercise optimal power relaxation if

$$\lambda_k = \frac{\text{Re}\{ (\underline{\Gamma}^k - \underline{\Gamma}^k_{avg})^T (\Omega^0 \underline{S})^* z_k \}}{\| \underline{S}^T \Omega^0 (\underline{\Gamma}^k - \underline{\Gamma}^k_{avg}) \|^2} \tag{5}$$

The corresponding optimal step-size for the alternate form may be obtained by simply replacing Ω^0 in (5) by Ω^k.

Choosing λ_k according to (5) results in maximum rate of convergence in the noiseless case. Under noisy conditions, the step-size needs to be a sufficiently small fraction of (5) to be practical. Alternatively, [5] the full value of the step-size may be retained if a sufficiently smoothed sensitivity vector $\underline{\Gamma}^k$ is used.

NUMERICAL EXAMPLE

The standard form of the algorithm has been applied to a concentric tricircular planar array of 15 omnidirectional sensors. The look-direction was chosen at 0° with no desired signal available there. A single interference was put at 36°. After 10 iterations, the received power level dropped to -140 dB of its initial value. Figure 4 shows the situation before and after adaptation. The gain in the desired direction has been maintained while the interference has been practically eliminated.

BIBLIOGRAPHY

[1] O. L. Frost, III, "An Algorithm for Linearly Constrained Adaptive Array Pro-
     cessing," Proc. IEEE, vol. 60, p 926, August 1972.

[2] B. Widrow, et al, "Adaptive Antenna Signals," Proc. IEEE, vol. 55, p. 2143,
     December 1967.

[3] S. M. Daniel and R. Mittra, "An Optimal Solution to a Scattering Problem,"
     Proc. IEEE, vol. 58, P. 270, February 1970.

[4] S. M. Daniel, "Adaptive Beamforming in the Spectral Domain Using a Constrained
     Least-Mean-Squares Algorithm," Magnavox Report No. MX-TM-6-7-301372, November
     1972.

[5] S. M. Daniel, "Analysis, Simulation and Realization of an Automatic Digital
     Wireline Equalizer System," Magnavox Report No. MX-TM-6-7-300473, January
     1973.
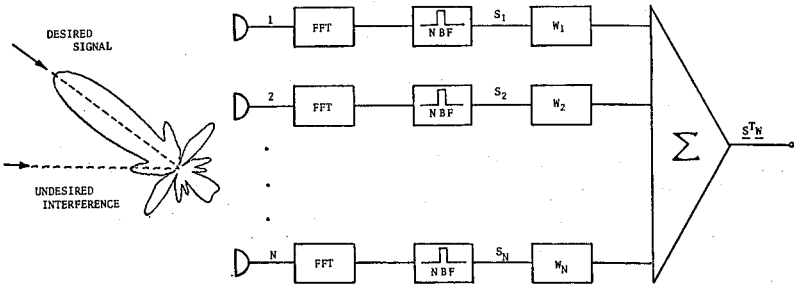
Figure 1.   Conventional Spectral-Domain Narrowband Array
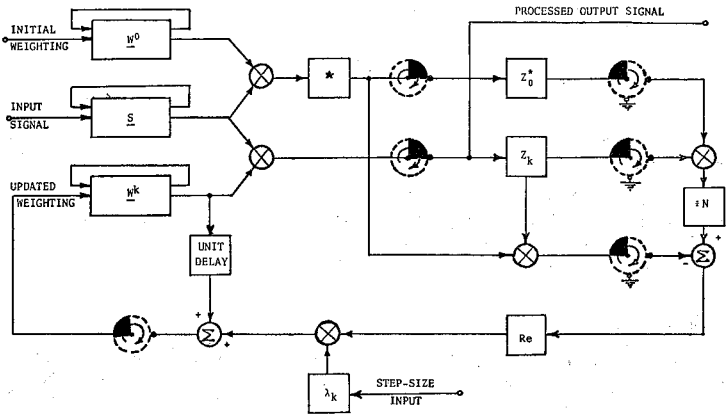
Figure 3.   Mathematical Block Diagram for Standard Form
of the SD-CLMS Algorithm
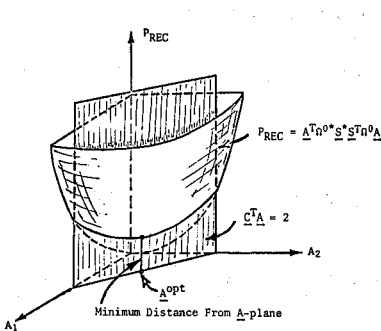
Figure 2.   Geometrical Interpretation
of (1) for 2-dimensional $\underline{A}$
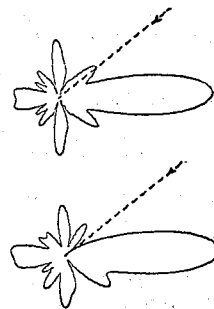
Figure 4.   Radiation Pattern
Before and After Adaptation

BANDWIDTH PROPERTIES OF QUADRUPLE-RIDGED
CIRCULAR AND SQUARE WAVEGUIDE RADIATORS*

M. H. Chen and G. N. Tsandoulas
M.I.T. Lincoln Laboratory, Lexington, Mass.

For dual-polarization arrays, it is desirable to use radiators
with at least two planes of identical symmetry such as circu-
lar and square waveguides. Based on the cutoffs of the first
two (TE_{10}, TE_{11}) waveguide modes, maximum available bandwidth
for square waveguides is about 34% of center frequency[1].
For circular waveguides the TE_{11}-TM_{01} bandwidth is only about
26.5% of center frequency. Thus circular waveguides compare
unfavorably with square waveguides as far as maximum bandwidth
is concerned. The first-higher-order-mode limitation on band-
width has been shown to be valid[1,2] in order to avoid
mode resonance effects that may give blind spots in the array
scan pattern.

In many phased array applications, the circular radiator shape
is advantageous for symmetry and other reasons. If bandwidths
much in excess of about 17% (maximum bandwidth reduced by about
10% to allow good matching to the exciter at the low end of
the frequency band) are required, some way of increasing the
available bandwidth is desirable. It has been known that
ridged rectangular waveguides exhibit greatly enhanced
bandwidth[3]. The quadruple-ridged circular guide has also
been considered as a very wideband radiator, until now. Our
careful theoretical and experimental investigation, however,
has shown that only a limited increase in bandwidth may be
available and then only if the design parameters are properly
chosen. Previous investigations[4] have identified the
bandwidth-determining TM_{01} mode experimentally by symmetrical
excitation of the quadruple-ridged circular guide. However,
if asymmetrical excitation is applied, the next higher mode,
the TE_{21}, propagates and supercedes the TM_{01}. In the
resulting modal inversion the TE_{21} mode is heavily loaded by
the ridges and so its cutoff point is lowered, reducing
bandwidth (Fig. 1). The computed bandwidth is shown in
Fig. 2.

This phenomenon is particularly important in phased arrays in
which off-boresight scanning is equivalent to asymmetrical
excitation with the concomitant entrance of the TE_{21} mode in
the excited or near-cutoff waveguide modal spectrum which may
give rise to blind spots.

Quadruple-ridged square waveguides do not exhibit any bandwidth
increase. In fact, bandwidth is always less than the empty

---

guide value for any ridge size. The bandwidth dependence on ridge size is shown in Fig. 3.

The cutoff wavelength, λ_c, and the transverse field distribution of a circular or square double-ridged waveguide was computed by means of a computer program using the triangular-finite-element method[5]. The program calculates the eigenvalue, $2\pi/\lambda_c$, and the scalar potential ϕ, which is related to the transverse field distribution. From the Helmholtz equation, $\phi = E_z$ for TM modes, and $\phi = H_z$ for TE modes. Therefore, the boundary conditions at the waveguide wall are $\phi = 0$ for TM modes and $\partial\phi/\partial n = 0$ for TE modes. It follows that the equal potential lines inside the waveguide represent the magnetic field lines for TM modes and the electric field lines for TE modes. In this manner a complete set of field lines for the significant modes was obtained. Of interest in Fig. 1 is the splitting of the TE_{21} mode. This happens because the quadruple ridge loads one of the two orthogonal TE_{21} empty-guide modes capacitively and the other inductively; hence the lifting of the degeneracy.

In the case of the circular guide the perimeter was approximated by a 16-sided polygon. Increasing the number of sides to 32 changed the fundamental eigenvalue by less than 1%.

The experimental verification of the theoretical predictions was carried out by creating a C-band cavity and exciting it both symmetrically and asymmetrically by means of a rectangular waveguide. The mode resonances were then identified from the known cavity length. The agreement between theory and experiment is shown in Fig. 4 for the circular waveguide and in Fig. 5 for the square waveguide.

It is seen that the maximum bandwidth increase for the circular waveguide (Fig. 2) may be obtained with very small ridges. In terms of wavelength, the ridge size is so small as to have a negligible effect on mutual coupling throughout most of the microwave band for arrays with reasonable scan volumes and bandwidths.

Acknowledgement

References

1. G.N.Tsandoulas, G.H.Knittel (1972 G-AP Intern. Symp. Digest, p. 157, Williamsburg, Va.).

2. G.H.Knittel (1971 G-AP Intern. Symp. Digest, p.69, UCLA).

3. S.Hopfer (1955 IRE Trans. MTT-3, No.5).

4. J.K.Shimizu (1961 IRE Trans. AP, p.223).

5. A.Konrad, P.Sylvester (1971 IEEE Trans. MTT-19, p.952).
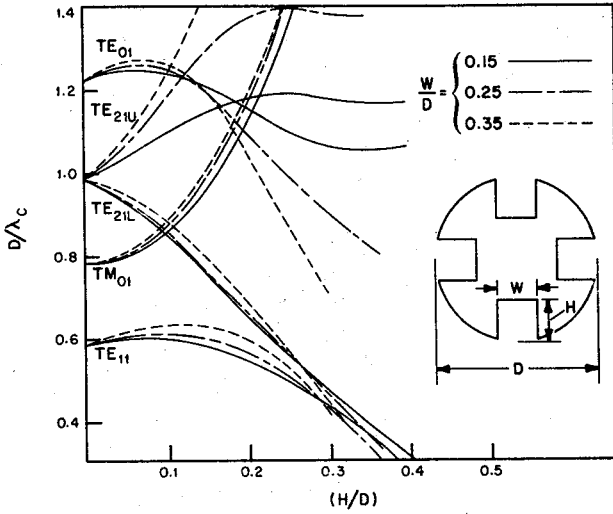
Fig. 1 Modal cutoffs of quadruple-ridged circular waveguide vs. ridge height.
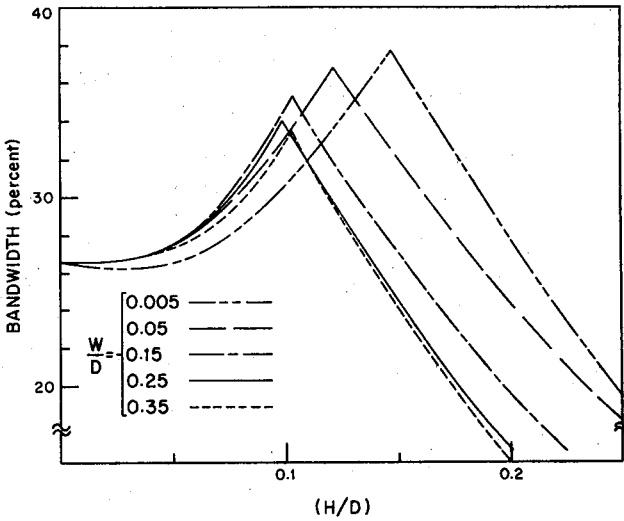
Fig. 2 Bandwidth dependence of quadruple-ridged circular waveguide on ridge height. The region to the left of the peak is determined by the TE_{01} cutoff whereas the region to the right by the TE_{21} cutoff.

393
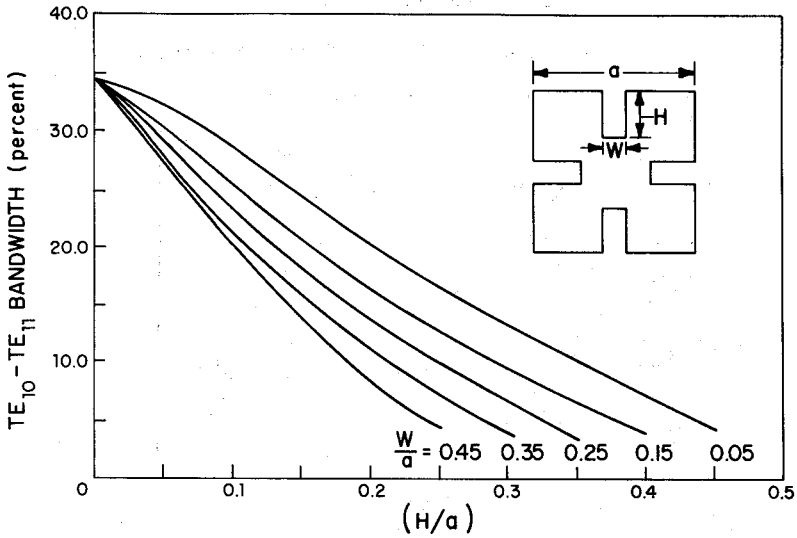
Fig. 3. Bandwidth dependence of quadruple-ridged square waveguide vs. ridge height.
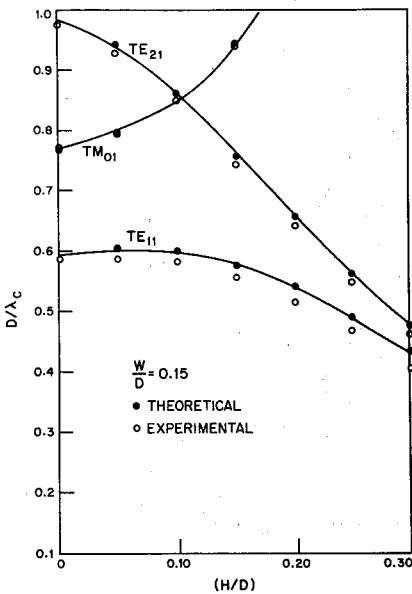
Fig. 4. Experimentally determined modal cutoffs for the quadruple-ridged circular waveguide showing very good agreement with theory.
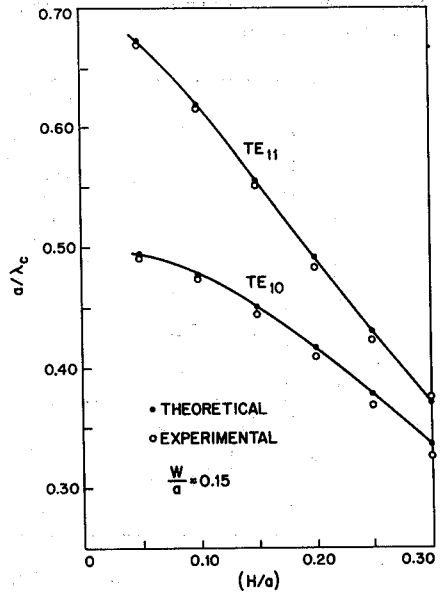
Fig. 5 Same as Fig. 4 but for quadruple-ridged square waveguide.

SIGNAL-TO-NOISE RATIO OPTIMIZATION FOR DISCRETE NOISE SOURCES

Gilles Y. Delisle, Jules A. Cummins
Department of Electrical Engineering
Laval University, Quebec G1K 7P4, Canada

The signal-to-noise power ratio (SNR) of a receiving array of antennas
is often expressed as the ratio of two Hermitian forms [1, 2] which
can be optimized by the technique described by Cheng [2] provided that
the Hermitian form appearing in the denominator be positive-definite.
The procedure fails, however, when the denominator is a semi-positive-
definite Hermitian form. This situation arises, for instance, when
only discrete monochromatic noise sources are considered in the formu-
lation. The performance of the array with respect to signal and noise
may, nevertheless, be optimized by using a different approach which
will be described in this paper.

It is assumed that the system has a narrow bandwidth and that the
direction of both the noise sources and the desired signals are known.
The method consists essentially in optimizing the array gain in the
direction of the desired signals under the constraint that the array
pattern presents nulls in the direction of the noise sources. Follow-
ing Harrington [3], the problem is formulated in terms network para-
meters defined at the antenna terminals. Using the admittance matrix
representation of a system consisting of an N-element array and a
distant test antenna, the array gain may be expressed as [3]:

$$G = K \frac{[\tilde{V}_a{}^*] [\tilde{Y}_{ta}{}^*] [Y_{ta}] [V_a]}{[\tilde{V}_a{}^*] \left[\dfrac{Y_{aa} + \tilde{Y}_{aa}{}^*}{2} \right] [V_a]} \tag{1}$$

where $[V_a]$ is the column matrix describing the array port voltages
$[Y_{ta}]$ is the row matrix of mutual admittances between the arra·
  ports and a distant test antenna and
$[Y_{aa}]$ is the matrix of admittances between the antenna array
  ports.

If the noise sources are assumed to exist in (p - r) directions (with
p < N) and the desired signals in the remaining r directions, then
the current I_t^i flowing at the short-circuited terminals of the test
antenna may be represented by the following matrix equation:

$$
\begin{bmatrix}
I_t^1 \\
I_t^2 \\
\vdots \\
I_t^r \\
\vdots \\
\vdots \\
I_t^p
\end{bmatrix}
=
\begin{bmatrix}
Y_{t1}^1 & Y_{t2}^1 & \cdots & Y_{tN}^1 \\
Y_{t1}^2 & Y_{t2}^2 & \cdots & Y_{tN}^2 \\
\vdots & & \ddots & \vdots \\
\vdots & & & \vdots \\
\vdots & & & \vdots \\
Y_{t1}^p & \cdots\cdots\cdots & & Y_{tN}^p
\end{bmatrix}
\begin{bmatrix}
V_1 \\
V_2 \\
\vdots \\
V_r \\
\vdots \\
\vdots \\
V_N
\end{bmatrix}
\tag{2}
$$

where the upper subscript indicates the direction of the incoming signals and the lower subscript refers to the array port terminals.

In view of the constraints imposed upon the radiation pattern in the direction of the noise sources, eq. (2) is rewritten in a partitioned form as follows;

$$
\begin{bmatrix} [0] \\ \hline [I_c] \end{bmatrix} = \begin{bmatrix} [T_{11}] & \vdots & [T_{12}] \\ \hline [T_{21}] & \vdots & [T_{22}] \end{bmatrix} \begin{bmatrix} [E_1] \\ \hline [E_2] \end{bmatrix} \tag{3}
$$

where $[0]$ is a $(p - r)$ column matrix of zeros corresponding to the desired nulls in the direction of the noise sources, $[I_c]$ is a $(r \times 1)$ column matrix corresponding to the direction of the desired signals and $[T_{11}]$, $[T_{12}]$, $[T_{21}]$, $[T_{22}]$, $[E_1]$ and $[E_2]$ are sub-matrices of dimensions $(p - r) \times (p - r)$, $(p - r) \times (N - p + r)$, $r \times (p - r)$, $r \times (N - p + r)$, $(p - r) \times 1$ and $(N - p + r) \times 1$ respectively.

The problem to be solved is then the optimization of eq. (1) under the constraints imposed by eq. (3). A solution was obtained for a circular array of four cylindrical dipoles using a method proposed by Adams and Strait [4]. For the purpose of illustration, Fig. 1 shows the numerical results computed for the following case; array diameter = 0.25λ (λ is the wavelength), dipole height = 0.5λ, dipole radius a = 0.007λ, direction for maximum gain $\theta_0 = 90^\circ$, $\phi_0 = 45^\circ$ and noise sources symmetrical about the signal direction at the indicated angles. This figure shows the progressive deformations of the optimum pattern as the noise sources approach the direction of the signal source.

Experimental pattern measurements were made at the frequency of 750 MHz with the signal processing method shown in Fig. 2.a. Figs 2.b and 2.c show the measured pattern for a circular array of four dipoles. These results indicate that the theoretical computations can be closely approched at least for arrays having a small number of elements.

References

1. J.A. Cummins et al. (1972 G-AP Symposium Digest, p. 121).
2. D.K. Cheng (1971, Proc. IEEE, 59, p. 1664).
3. R.F. Harrington (1968 – Field Computation by Moment Methods, Macmillan).
4. A.T. Adams et al. (1970 G-EMC Symposium Record, p. 383).
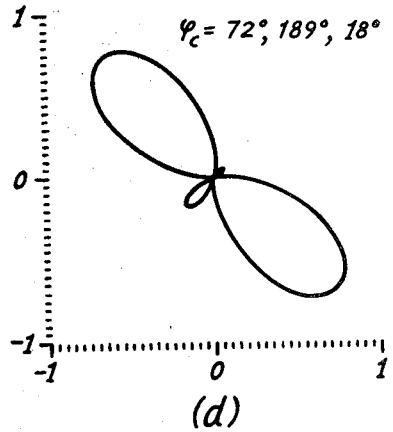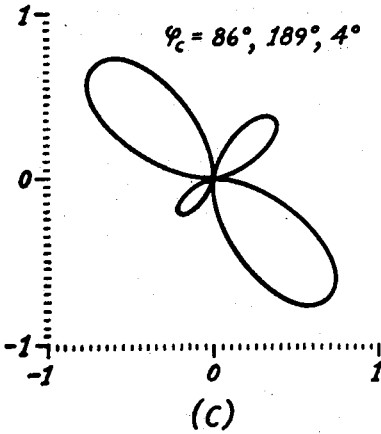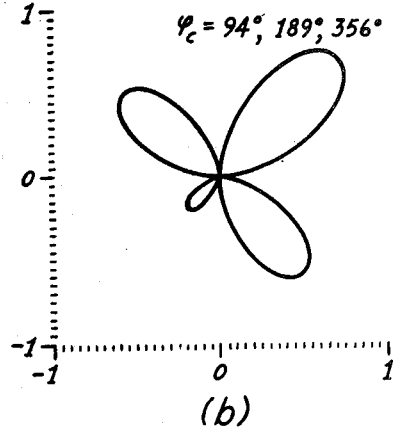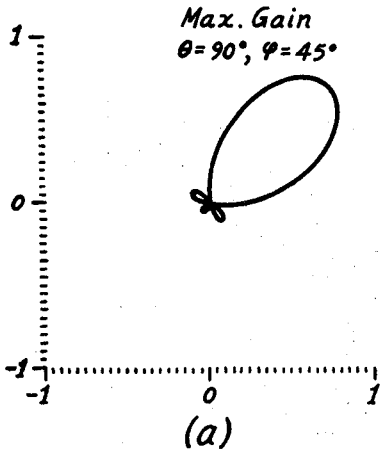
Fig. 1 - Progressive deformations of the optimum pattern of a
4-element circular array. Discrete noise sources
located in the azimuthal plane at the indicated angles.
(dipole height = 0.5λ , array diameter = 0.25λ , λ =
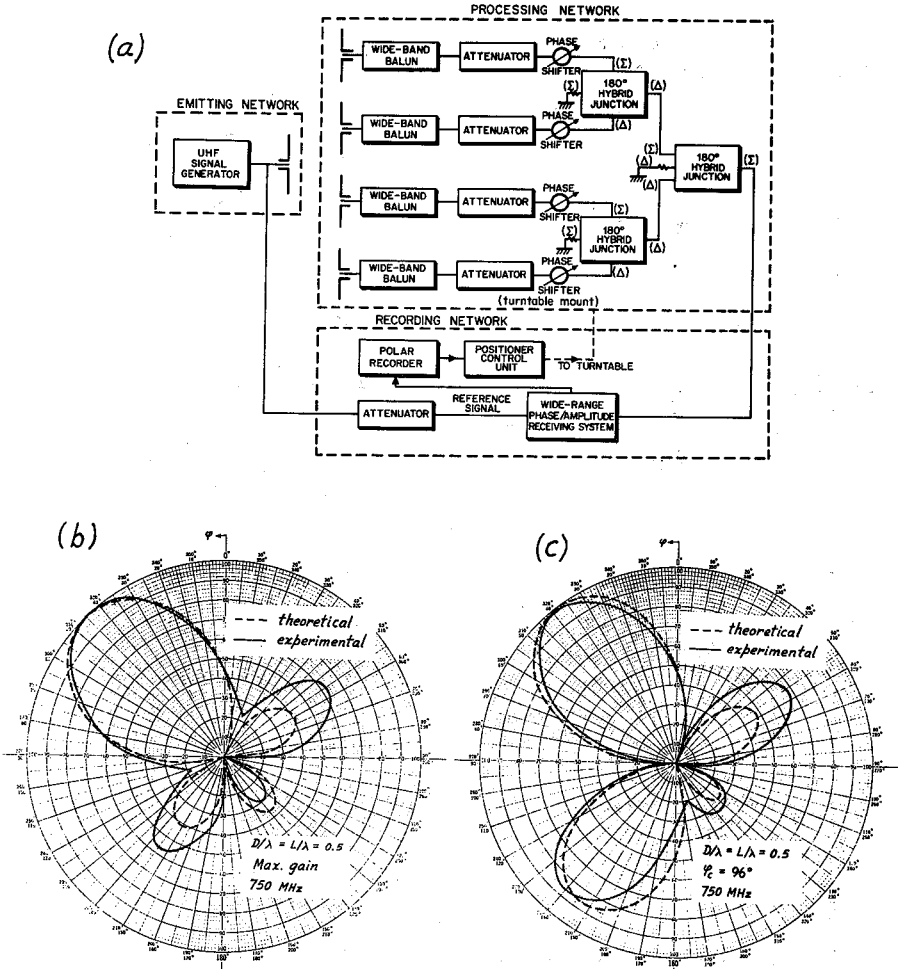wavelength).

Fig. 2 - a) signal processing network b) unconstrained expe-
         rimental pattern c) resultant experimental pattern
         with a discrete noise source located at $\phi_c = 96^o$.
         (D = array diameter, L = height, λ = wavelength).

OPTIMUM SIGNAL BANDWIDTHS
FOR PLANAR PHASED-ARRAY ANTENNAS[*]

George H. Knittel
M. I. T. Lincoln Laboratory

Several studies have been made of the effects of dispersion in linear phased arrays (1-3). The latter study includes planar phased arrays also and examines S/N loss for two matched filter options. An extension of this study considers pulse broadening of a constant-frequency pulse caused by array dispersion (4). However, there is no consideration of the effects of array dispersion on a linear frequency modulated (LFM) pulse and no discussion of whether there exists an "optimum" or maximum-useful bandwidth for a phased-array system.

In this paper, the effects of array dispersion in a radar system using a LFM pulse are considered. There are two principal effects of dispersion, loss of resolution (decrease of effective bandwidth) and loss of S/N ratio. The relative amounts of these losses depend on the choice of the matched and weighting filters in the receiver. It happens that there is an "optimum" signal bandwidth for a given phased array such that a single matched filter (MF), weighting filter (WF) combination provides both minimum S/N loss and the full resolution of the LFM pulse generated by the transmitter.

Figure 1 is a block diagram of the important parts (for the purpose of this study) of a phased-array radar system. Only the dispersive effects of the feed network and phase shifters will be considered here; perfect radiating elements will be assumed.

Figures 2 and 3 show the computed two-way array transmission-coefficient magnitude (voltage) versus normalized frequency for a square array with a 40 x 40 wavelength aperture and either a center-fed-series by center-fed-series feed or a parallel (equal line length) by parallel feed. The feed is assumed to provide a Taylor 30 dB SL, $\bar{n}$ = 6 aperture excitation in each principal plane. The figures show that the series feed limits the effective bandwidth at broadside (θ = 0) and that phase-shifter scanning further limits bandwidth at θ = 60°. The parallel feed has a broader bandwidth at all scan angles between 0° and 60° than does the series feed. In both cases the dispersion is almost entirely in the transmission-coefficient magnitude; the phase of the transmission coefficient is constant for the parallel feed and linear vs. frequency for the series feed.

Figure 4 shows S/N loss for the array for two MF-WF options which provide either full resolution or minimum S/N loss. Both options require filters which are adaptive; i.e., filters whose transfer functions vary with scan angle. The first option produces a perfect compressed pulse; the MF is designed for the incoming waveform and the

---

WF to provide a perfect Taylor 40 dB SL, $\bar{n} = 8$ compressed-pulse frequency spectrum. The second option uses only a MF designed for the incoming waveform; no WF is included. This results in the minimum S/N loss, but yields a compressed pulse shape which has either too broad a main lobe or sidelobes which are too high. Notice that there is a point for each feed network at which the two filter-option curves are tangent. The value of signal bandwidth at this point is termed "optimum" bandwidth. If one chooses to operate the array at a greater signal bandwidth and wants full resolution (that associated with the LFM transmitter pulse bandwidth), he must pay heavily in S/N loss. On the other hand, if one chooses the minimum S/N loss design, he pays heavily in loss of effective bandwidth because of pulse broadening (not shown by the figure). Hence the optimum bandwidth is the maximum signal bandwidth which should be used with the array. At greater bandwidths, one rapidly loses either effective bandwidth or S/N ratio. The S/N loss shown in Figure 4 is relative to that of a perfect system. This is a system with a dispersionless array antenna, a MF designed for the LFM transmitter pulse, and a WF to provide a Taylor 40 dB SL, $\bar{n} = 8$ compressed-pulse frequency spectrum.

It happens that for the parallel feed there is a relationship which permits one to calculate "optimum" scan angle, "optimum" aperture size, or "optimum" broadside beamwidth rather than optimum bandwidth. It is

$$\frac{BW}{B_u} \frac{D}{\lambda_o} \sin \theta = C \quad ,$$

where BW is the percent bandwidth, B_u is the broadside beamwidth relative to that with uniform aperture excitation, D/λ_o is the midband aperture size in wavelengths, and θ is the scan angle. All square arrays with a parallel feed having the same C will have the same array transmission coefficient vs. frequency. Hence Figure 4 is a universal curve for parallel feed networks and the abscissa could be calibrated in units of C where

$$C = \frac{BW}{1.27} (40) \sin 60^\circ = 27.3 \ BW.$$

Thus, an array with uniform excitation, $D/\lambda_o = 30$, and BW = 5% has an "optimum" scan angle of about 50° with $C = 117.4$. A similar relationship exists for series feed networks.

It is interesting to note that the optimum bandwidth (or other parameter) can easily be determined from the two-way array-transmission-coefficient curves in Figure 3. If one wants a compressed pulse with 40 dB SL, $\bar{n} = 8$,the desired edge-band taper on the pulse frequency spectrum is 0.11 relative to midband. At the optimum bandwidth point, the MF is identical (in transfer function magnitude) with the incoming signal (Figure 3) and there is no WF. Hence the array transmission coefficient magnitude should be $\sqrt{0.11} = 0.34$. From

Figure 3, this yields an optimum bandwidth of about 4% (for the parallel feed), which confirms the value actually determined in Figure 4. Therefore, the frequency which causes an array transmission-coefficient magnitude equal to the square root of the desired edgeband pulse-spectrum taper is the edge frequency of the optimum bandwidth.

There are two principal conclusions from the work presented here.

1. There is an optimum or maximum-useful bandwidth or aperture size or scan range for a phase - steered array.

2. A planar series-fed phased array has a substantially smaller useful signal bandwidth or aperture size or scan range than a planar parallel-fed array. For the case shown in Figure 4, the optimum bandwidths are 2.8% and 4.3% respectively.

References

1. J. Frank (Phased Array Antennas; Oliner, Knittel, eds., p. 243)

2. R. R. Kinsey and A. L. Horvath (Phased Array Antennas; Oliner, Knittel, eds., p. 261).

3. C. Rothenberg and L. Schwartzman (1969 G-AP Int'l, Symp. Digest, p. 116).

4. L. Schwartzman (private communication).
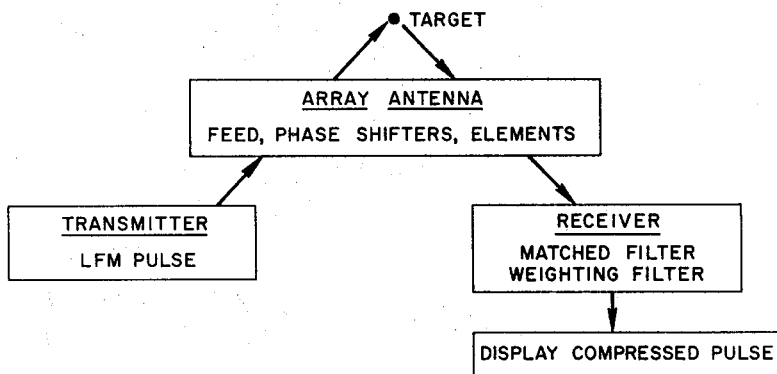
Figure 1 - Important parts of signal processing system including a phased-array antenna.
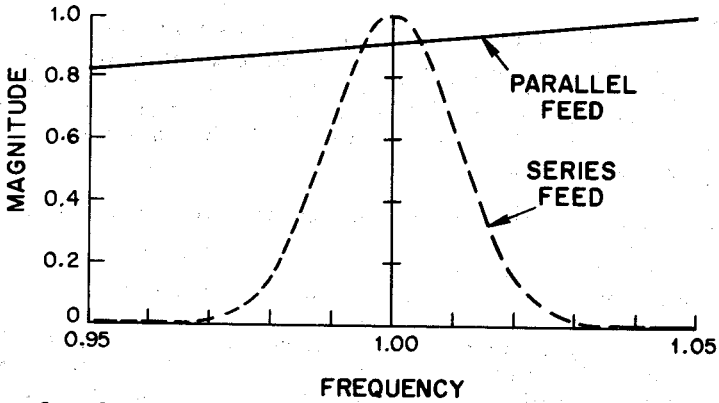
Figure 2 - Two-way array transmission coefficient magnitude vs. frequency; D/λ_o = 40, $\theta = 0^o$ 30 dB SL, $\bar{n}$ = 6 excitation.
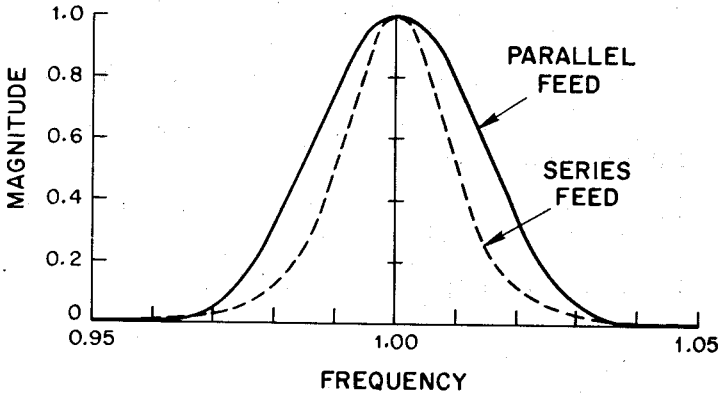
Figure 3 - Two-way array transmission-coefficient magnitude vs. frequency; D/λ_o = 40, $\theta = 60^o$, 30 dB SL, $\bar{n}$ = 6 excitation.
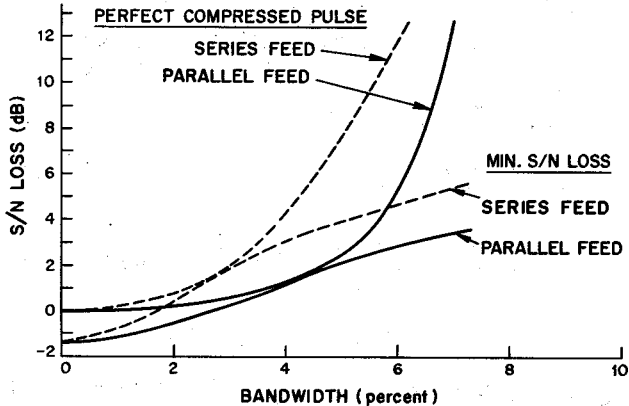
Figure 4 - S/N loss vs. bandwidth for two match-weighting filter options; D/λ_o = 40, $\theta = 60^o$, 30 dB SL, $\bar{n}$ = 6 excitation.

ENHANCEMENT OF MICROWAVE ANTENNA PERFORMANCE IN A REENTRY PLASMA:
FLIGHT TEST RESULTS OF CHEMICAL ALLEVIATION

D. T. Hayes, S.B. Herskovitz, J.F. Lennon, J. L. Poirier
Air Force Cambridge Research Laboratories, Bedford, Mass.

The effect of the injection of an electrophilic liquid into the ionized flow field surrounding a reentry vehicle was observed during the fourth in a series of Trailblazer II flight tests. A high vapor pressure liquid, Freon 114B2, was injected in a sequence of pulses and the subsequent modification of the plasma was measured by a variety of microwave techniques and flush mounted electrostatic probes. The modification consists in the attachment of free electrons to the Freon molecules thus forming negative ions.

The purpose of this paper is to report on the observed changes in the performance of the plasma covered microwave antennas resulting from the introduction of the electrophilic liquid into the medium. This will be done by comparing present test results with those from the third flight of the series which had the same configuration of microwave experiments. This established the basic level of operation of the instruments in the presence of plasma since no attempt was made to reduce free electron concentrations over the antennas during the third flight.

The final component of the four-stage Trailblazer II rocket produces a powered atmospheric reentry. Its configuration is a blunt 9^0 cone with a 6-inch nose radius. The reentry vehicle is spin-stabilized and descends almost vertically. The present flight took place on 28 July 1972. During reentry, the payload achieved a peak velocity of 16,240 fps and was oriented at a relatively large (16.5^0) angle of attack.

The electrophilic liquid was injected into the flow field from a number of ports located at the junction of the hemispherical nose and the conical afterbody. An S-band (2290.5 MHz) aperture transmitting antenna was situated directly behind the injection ports followed by a similar receiving antenna. The relative position of these elements is shown in Figure 1 along with a simplified block diagram of the S-band test system components.

The additive was injected into the flow in a sequence of pulses. Since there is considerable variation in the atmospheric density over the reentry trajectory, two different injection modes were used. The high altitude mode (300 kft down to 170 kft) consisted of just low flow pulses separated by a pause. During the second mode (down to around 100 kft) the pulsing cycle consisted of low flow, high flow (immediately following), and then a pause. This allowed the effect of different additive concentrations to be observed. The pulsed operation produced varying levels of plasma modification while keeping within the weight and volume constraints

403

of the vehicle payload.

   The effect of the plasma-additive interaction on antenna
performance was quite evident. The microwave phenomena observed
during the flight were antenna impedance mismatch, signal attenua-
tion, and interantenna coupling.

   These factors exhibited a complex behavior during the course
of reentry as a result of the nonzero angle of attack which intro-
duced assymmetry into the flow around the vehicle. Thus, as the
nosecone rotated, the antennas on the surface were exposed to con-
tinually varying plasma levels. If readings for windward and lee-
ward orientations of the antennas are examined, the corresponding
changes in antenna performance are clear.

   An example of this is shown in Figure 2. This depicts the
high altitude results for the power reflection coefficient of the
third flight S-band transmitting antenna. During the period
where the reflection began to rise, the windward level at a given
altitude was always higher than that at the leeward position.   Of
course, once both orientations represented complete reflection
there was no longer any variation in response.

   The effect of the additive on the power reflection coefficient
for windward side conditions is shown in Figure 3a. (The rectangles
on the time axis in each additive flight figure represent injection
pulses:⌐⌐ low flow;⌐⌐combined).   It is immediately obvious that
the reflection coefficient, which was expected to reach levels of
0.8 to 0.9 in the absence of chemical additives as indicated Fig-
ure 2, did not approach that level at any time. In fact, its max-
imum was only about 0.3. The gross structure of Figure 3a generally
shows that there was a decrease in reflection coefficient related
to each chemical additive pulse.

   There is also some finer structure which should be pointed
out. As the Freon entered the flow field, the reflection coeffi-
cient sometimes increased by a small amount before the expected
generally larger decrease appeared. This behavior was most likely
due to the nonmonotonic dependence of the reflection coefficient
on increasing (or decreasing) plasma density. In Figure 2 the pow-
er reflection coefficient for the leeward side of the third flight
also shows this effect, so it was not an unexpected phenomena.

   On the leeward side as shown in Figure 3b, the power reflection
coefficient reached values of 0.8. The fact that the leeward re-
flection coefficient is greater than the windward is an unexpected
result. At the higher altitudes, the reflection coefficient was
generally reduced by the chemical additive pulses and then return-
ed to higher levels during the interpulse interval. At the lower
altitudes, the high flow pulses sometimes increased the steady
state reflection coefficient. As mentioned before, this is thought
to be due to the complexity of the response of the reflection coef-
ficient to the changing electron densities.

In the absence of additive the signal attenuation (peak sig-
nal received at a ground station minus the corresponding instant-
aneous vehicle transmitter reflection loss) is a sharply increas-
ing function of altitude (Figure 4a). During the additive flight
the attenuation increased much more gradually (Figure 4b). The
effect of the pulsed nature of the additive injection is apparent.

In summary, the additive reduced reflection levels, enhanced
received signal intensity and altered interantenna coupling
although space limitations have restricted discussion of this
last aspect.
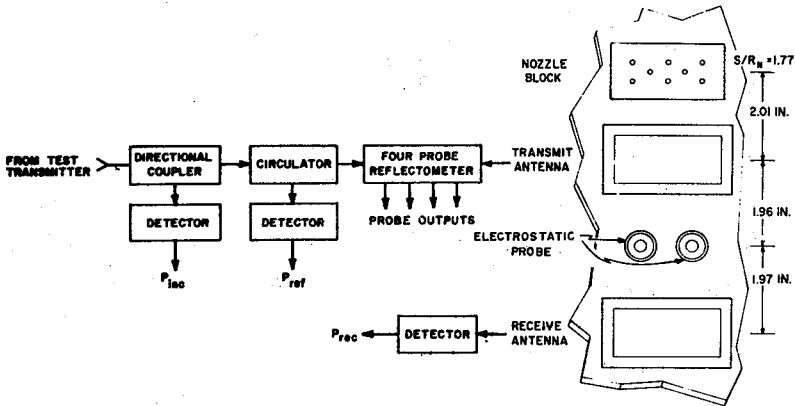
Figure 1. S-Band Test System
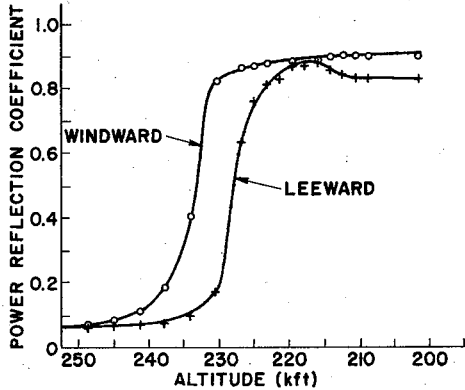
Figure 2.   Power Reflection Coefficient
            (Flight No. 3)
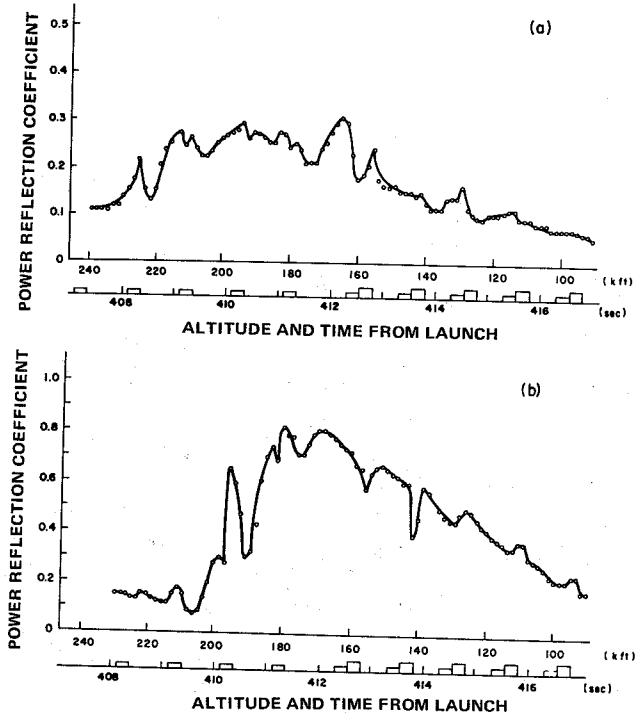
Figure 3. Additive Flight Power Reflection Coefficient (a) Windward Side (b) Leeward Side.
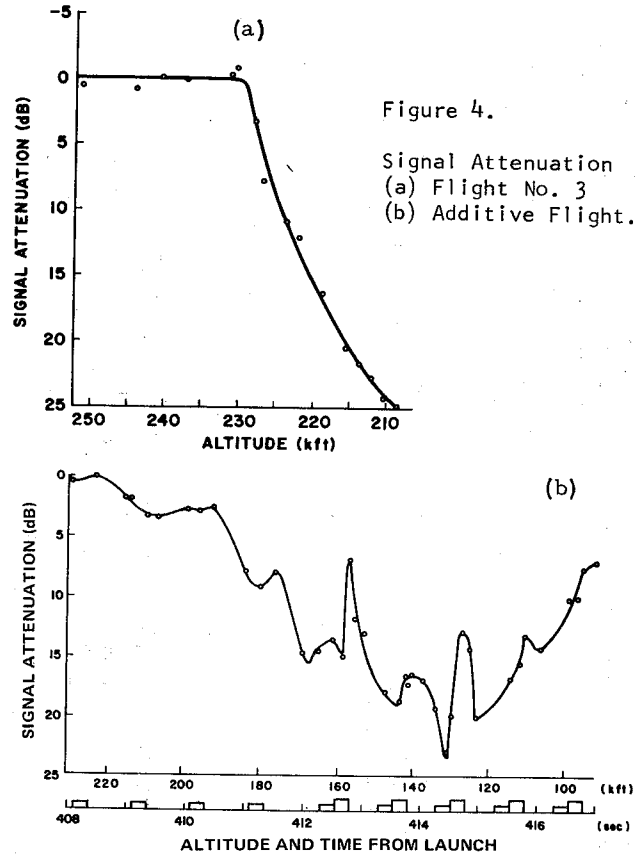
Figure 4.

Signal Attenuation
(a) Flight No. 3
(b) Additive Flight.

RADAR-SYSTEM CONSIDERATIONS IN ASPECT-SENSITIVE
IONOSPHERIC SCATTERING MEASUREMENTS

J. Minkoff
Riverside Research Institute, New York, N.Y. 10023

Introduction

Observations of anisotropic radar scattering from the
aurora were originally explained[1] on the basis of very
long columns of ionization aligned along the direction
of the earth's magnetic field, $\vec{B}$. Although this model
gave a maximum echo when the radar line of sight was
perpendicular to $\vec{B}$, which agreed with experimental re-
sults, it provided an aspect sensitivity which was
found to be too great to fit actual observations. As
will be discussed below, however, because of fundamen-
tal limitations imposed by experimental parameters —
particularly the antenna — these measurements most
likely underestimated the true aspect sensitivity of
the scattering, possibly to a very great extent.

Following this original scattering model for the auro-
ral radar echoes, Booker[2] derived a per-unit-volume
differential scattering cross section for the ionosphe-
ric medium in terms of the three-dimensional wave-
number spectrum, S, of the random electron-density fluc-
tuations, and the variance (mean-square deviation) of
the fluctuations, $\overline{|\Delta n|^2}$. In this model the scattering
is characterized by the longitudinal and transverse
scale sizes or coherence lengths, L and T, which des-
cribe, respectively, the average distances parallel and
perpendicular to $\vec{B}$ over which collective scattering ef-
fects take place. Accordingly, the 3-dB widths of the
wave-number spectrum in the longitudinal and transverse
directions are, respectively, $\sim 2\pi/L$ and $\sim 2\pi/T$; for the
condition of strong aspect sensitivity of interest here
we must have $L \gg T$.

Within this picture of the scattering process, the pur-
pose of radar measurements is to determine $\overline{|\Delta n|^2}$,
L and T. Considering an experimental situation in
which the radar line of sight lies within the magnetic-
meridian plane, the angular distribution of the back-
scatter in the meridian plane, or equivalently the as-
pect sensitivity, is determined by the spectrum of the
electron-density fluctuations along the direction of $\vec{B}$,
with the angular width of the scattering being of the
order of λ/L, λ = radar wave-length. The strength of

the backscattered signal is determined by the transverse spectrum of the fluctuations evaluated at $2k = 4\pi/\lambda$ (Bragg scattering condition) and by the variance $\overline{|\Delta n|^2}$.

Measurements

To determine L the procedure is to measure the received signal strength as a function of angle of incidence to $\vec{B}$ of the transmitted signal. Ideally, using a very narrow antenna beam this would be relatively straightforward. In practice, however, because of the finite angular resolution of the antenna, this is not the case. An analysis of the scattering process,[3] in which the effects of the finite antenna beamwidth, radar waveform, as well as the scattering geometry relative to the direction of $\vec{B}$ have been included, has shown that the extent to which L can actually be determined depends on the relationship between L and the vertical antenna aperture D. If D $\gg$ L then L can be measured. However if D $\lesssim$ L it is shown that the apparent measured value of L will always turn out to be equal to D regardless to the true value of L. Stated another way, under this condition one measures the aspect sensitivity of the antenna rather than that of the scatterers; in fact, turning things around, this provides a means of measuring the antenna beam pattern. The situation is shown to be an exact mathematical analogue of that encountered in a communication system, in which an unknown signal having a spectral width L is passed through a receiver having a bandwidth D. Unless the measured output spectral width is significantly less than D, say by a factor of at least 3 or 4, one can never be certain whether or not the input has actually been faithfully reproduced at the output or whether band-limiting by the receiver has occurred, in which case the spectral width of the output is determined by the system frequency response. Depending on the geometry relative to $\vec{B}$, an additional "band-limiting" effect can occur if the transmitted pulse is too long. In practice however this requirement will not be as restrictive since, for a receiver fractional bandwidth as small as 1%, it can be shown that values of L as large as 5 km will not be truncated by pulse-width effects. Because the pulse-width effect occurs in series with the antenna effect, antenna considerations will always dominate receiver considerations in any practical experimental situation. It is likely that the rather small estimate of ~7 meters for L as given by Booker[2] is due to "band-limiting" by D, since the vertical antenna dimensions mentioned in this reference in connection with the experimental results were evidently quite comparable with this estimate. Hence the true value of L for these observations may in fact have actually been considerably larger than 7 meters.

As noted above, the transverse scale size T can be de-
termined from measurements of backscattered power vs
frequency. Since the strength of the received signal
also depends on the size of the per-pulse scattering
volume, it is necessary to normalize the data with res-
pect to the dimensions of the scattering volume if the
quantity of interest is actually to be obtained. How-
ever, merely normalizing with regard only to the size
of the illuminated volume will not give the correct re-
sult since, because of aspect sensitivity, the contri-
butions to the received signal across the illuminated
volume are not uniform. Thus the proper normalization
may be difficult to achieve in practice since for this
purpose the aspect sensitivity must first be known. It
is found however that this problem can be considerably
simplified by proper choice of the experimental parame-
ters. In particular, for this purpose it is shown[3] that
it is desirable to choose D $\ll$ L. Physically the effect
of this choice is to cause the antenna beam to be very
broad in comparison with the scattering beam and, as a
result, all of the energy in a scattering lobe is col-
lected by the antenna and the aspect sensitivity there-
fore effectively becomes integrated out.

The quantitative result is as follows. For line of
sight within the meridian place and normal incidence to
$\vec{B}$ we write the per-unit-volume differential backscatter
cross-section, σ , as:

$$\sigma = b(k)\, S_L(2k\alpha)$$

$$b(k) = r_e^2\, \overline{|\Delta n|^2}\, S_T(2k)$$

where r_e = classical electron radius = e^2/mc^2 and α
is the scattering angle measured with respect to the
normal to $\vec{B}$. For L/T $\gg$ 1 it is assumed that the wave-
number spectrum S can be written separably as $S = S_L S_T$;
discussion concerning the reasonableness of this assump-
tion is presented in Ref. (3). It is also assumed, be-
cause of the symmetry imposed by $\vec{B}$, that S_T is azimuth-
ally symmetric with respect to $\vec{B}$ and hence a function of
a single variable only. It can then be shown that to
determine b(k) from measurements of P_k, the backscat-
tered power as a function of wave number k, the proper
normalization is given by:

$$b(k) = \frac{2R^2 P_k}{K\, G_\alpha^2\, \lambda\Delta\, \int_{\beta(R)} G_\beta^2(\beta)d\beta}$$

where R = range to scattering cell, K = $P_T \lambda^2/(4\pi)^2$
P_T = transmitted power, Δ = range-resolution cell. The
antenna gain G is written as G = $G_\alpha(\alpha)\, G_\beta(\beta)$ where
α and β are the elevation and azimuth angles; $\beta(R)$ is

the observed azimuthal extent of the target at the range R; since D $\ll$ L, G_α is effectively constant. The extra normalization factor λ in the denominator comes about because the effective thickness of the scattering volume is wavelength dependent, being of the order of $R\lambda/2L$.

Both $\overline{|\Delta n|^2}$ as well as S_T are obtained from $b(k)$. To determine $\overline{|\Delta n|^2}$ we make use of the standard normalization of S — which follows from the requirement that the spatial correlation function of the electron-density fluctuations be unity at the origin — and, letting

$$m_1 = \int_0^\infty k\, b(k)\, dk, \quad \text{we obtain directly,} \quad \overline{|\Delta n|^2} = 2m_1 \big/ \pi\, r_e^2$$

Antenna Configuration

From the above discussion we note that interesting fact that, whereas in order to measure L we must have D $\gg$ L, for purposes of measuring T it is most convenient to choose D $\ll$ L. Of course in general L will not be known, but in any case D $\ll$ L can be achieved by using simple radiating elements having very broad vertical beamwidths. Furthermore the azimuthal angular extent $\beta(R)$ should be as small as possible and we wish to make measurements over a relatively wide range of frequencies. From these considerations we conclude that the ideal antenna for purposes of measuring S_T and $\overline{|\Delta n|^2}$ would be a linear row-array of broad-band (e.g. log periodic) elements with the row oriented perpendicular to the magnetic-meridian plane. For purposes of measuring S_L it is also seen that an array would be required since it is evident than any sort of moveable reflector-type antenna would not be suitable for this purpose. In this case however the array would be oriented parallel to the meridian plane, and the ideal antenna for measurement of all the quantities of interest would therefore be some form of two-dimensional planar array.

As noted above however, true representative values for L are not known at this time. Hence, should L prove to be very large, it could turn out that a prohibitively large number of rows for the array would be required. Moreover, for situations requiring an angle of incidence θ between the radar line of sight and the array columns, the effective number of rows would be reduced by a factor $\cos\theta$. From this it is seen that, in fact, measurements of longitudinal scale sizes may prove to be very difficult to achieve.

References

. S. Chapman (1952 JATP, Vol. 3 p.1)
. H.G. Booker (1956 JATP, Vol. 8 p. 204)
. J. Minkoff (1973 JGR, to be published July or Aug.)

CONTROL OF RADIATION PATTERNS
OF ION ACOUSTIC WAVES

T. Ohnuma, Y. Tamura, T. Fujita, and S. Adachi
Department of Electrical Engineering,
Tohoku University, Sendai, Japan

Only a few have been reported on the observations of radiation
patterns of an electron plasma wave or an ion acoustic wave.[1]
We report here the results of the experimental and theoretical
investigation on the control of the radiation patterns of an ion acou-
stic wave from an circular disk-shaped antenna. The radiation
pattern is controlled by applying a D.C. bias voltage to another
mesh. The change of the radiation pattern is explained as a re-
sult of the in-phase reflection at an electron-rich sheath.

Experiments were performed in a vacuum chamber which is 160
cm in length and 32cm in diameter. Argon gas is used at a pres-
sure of $P \approx 5.6 \times 10^{-4}$ Torr.. Four oxcide-coated cathodes are set
at different positions near the wall of the chamber in order to ob-
tain an uniform plasma. The wall of the chamber is used as an
anode. The diffused plasmas are used for the experiments. The
typical plasma parameters are $N_0 = 5 \times 10^8$ Te =1.5 eV. The space
potential of the experimental regions is nearly zero volt. The ex-
citation of the signals are performed with one or double grids(3cm
in diameter). The detection of the signals are performed with a
grid (1cm in diameter). The wave-patterns of the signals were
displayed of an X-Y recorder using interferometer technique.

For the case of the excitation with double meshes, two meshes
with a same size are set parallel to each other as shown in Fig. 1,
where V_E and V_R show the bias voltage of the two meshes. The
mesh of V_E is used for the excitation of an ion acoustic wave.
The mesh of V_R is used for the control of the radiation pattern
of the ion acoustic wave by changing the bias voltage V_R. The
typical wave-patterns of an ion acoustic wave is shown in Fig. 1.
The bias voltage V_E for the excitation is fixed to $V_E = -25V$. The
applied voltage for the wave-excitation is $V_{ex} = 1V$ peak to peak.
The observed phase velocity is 1.5×10^5 cm/sec, which is nearly
in accord with the calculated value by $C_p = (\kappa T_e/m_i)^{1/2}$. The pha-
se velocity is constant for the experimental frequency region of
f=50kHz~150kHz. The phase velocity is also independent of the
exciting voltage V_{ex} which is smaller than 5V peak to peak. In
Fig. 1(A), the signals which propagate for the inverse direction to
V_R mesh are shown when V_R is changed. The signals will be

called "forward" ones. When the bias voltage V_R is negative, the
signals do not change largely. When V_R is positive, the ampli-
tude of the signals becomes large and nearly twice the signals of
V_R=0V for V_R=40V. In Fig.1(B), the signals which propagate th-
rough the potential barrier V_R are shown when V_R is changed. In
what follows, such signals are called "backward" ones. In case
of $V_R \lesssim 0V$, the signals do not change largely. In case of $V_R > 0V$,
the amplitude of the signals tend to vanish with increasing V_R.

Figure 2 shows the relative amplitude of the signals for both di-
rections when the bias vlotage V_R is changed, in which the change
of the forward (F) and backward (B) signals is clearly shown. The
fact that the sum of the amplitude of F and B is roughly constant
says that there happens the reflection of the ion acoustic wave
near the mesh of V_R. That is, the amplitude of F is thought to be
the sum of the direct signal from V_E-mesh and the reflected one
from V_R-mesh. The reflection of the ion acoustic wave is obser-
ved at an electron-rich sheath and the absorption is not observed
even in an ion-rich sheath.

Figure 3 shows the typical radiation patterns for d/λ=1 and 2. The
radiation patterns are obtained from the spatial wave patterns de-
tected by a lock-in amplifier. For the case of V_R=0V, in which
there is no reflection at V_R-mesh as shown in Fig. 2, the radiation
patterns are nearly the same as that for only one mesh excitation.
In that case, the ion acoustic wave is radiated equally in both si-
des. The dashed curves are the theoretical radiation patterns
from an circular disk-shaped antenna and the open circles are the
experimental results, which are nearly in accord with the theore-
tical ones. When the V_R bias voltage is chaged to V_R=40V, the
radiation patterns are extremely deformed to uni-directional radi-
ation pattern due to the reflection of the ion acoustic wave at V_R=
mesh. The solid circles show the experimental results. The so-
lid curves are the theoretical radiation patterns obtained by assum-
ing the reflecting mesh as an infinite in-phase reflecting plane. Na-
mely, by applying the image priciple the theoretical pattern is ex-
pressed as

$$\frac{\sin(2kD\cos\theta)}{\sin(kD\cos\theta)} \quad \frac{J_1(ka\sin\theta)}{ka\sin\theta} \quad , \qquad (1)$$

where J_1, k and D are the Bessel function of order 1, the wave num-
ber of the ion acoustic wave, and the spacing between the meshes,
respectively. The radius a is $d/2$. The direction perpendicular to
the circular disk is chosen as θ=0. The theoretical and experimen-
tal results are expressed with respect to the standard value at V_R
=0V. and θ=0. Although the reflection of the ion acoustic wave by
V_R at V_R=40V is nearly 90%(Fig. 2), the theoretical and experimen-
tal results are found to be in good agreement (Fig. 3). By apply-

ing two different signals with phase difference to two meshes as shown in Fig. 4, we find the fact that due to sheath around the mesh the electrical distance is 1mm whereas the physical distance between two meshes is 4mm.   Therefore, we have assumed D= 1mm for the curves of Fig. 3.

In conclusion, by use of double meshes spaced apart a little, the in-phase reflection of an ion acoustic wave at an electron-rich sheath was observed. As a result, the radiation field pattern of an ion acoustic wave from an exciter is found to be controlled easily.   This type of antenna may be available for detecting the direction of incident signals and for the excitation of plasma waves to one direction.

1.   K. Shen, S. Aksornkitti, H. C. S. Hsuan, and K. E. Lonngren (1970 Radio Science $\underline{5}$, p. 611)
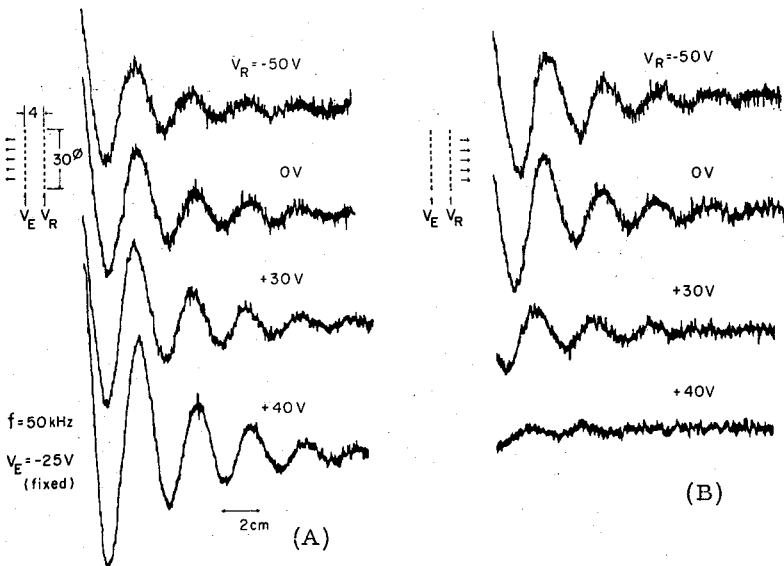
Fig. 1.   Typical spatial wave-patterns of an ion acousrtic wave when the bias voltage V_R is changed.   RF signals are applied to V_E-mesh only, and V_E is the bias voltage. V_R-mesh used only to apply the bias voltage V_R.   The patterns of (A) show (forward) signals which detected for the inverse direction to V_R-mesh as shown by arrawa.   The patterns of (B) show (backward) signals which passed through the potential barrier at V_R= mesh.
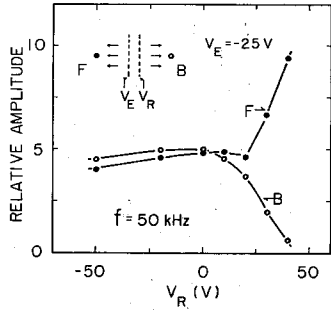
Fig. 2. Relative amplitude of an ion acoustic wave excited by a double-type mesh for both directions(F and B), when the bias voltage V_R is changed.
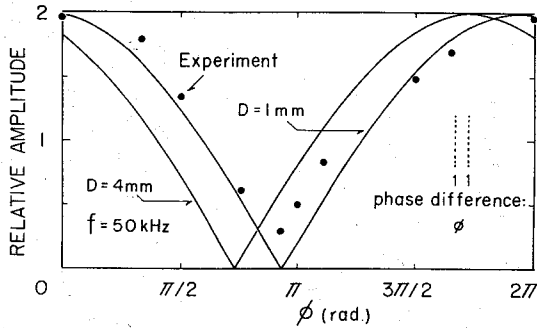
Fig. 4. Amplitude of an ion acoustic wave at $=0°$ with a change in the phase difference with which two external signals are applied to two meshes. The bias voltages of both meshes are fixed to -25 V. Solid lines are the theoretical curves.
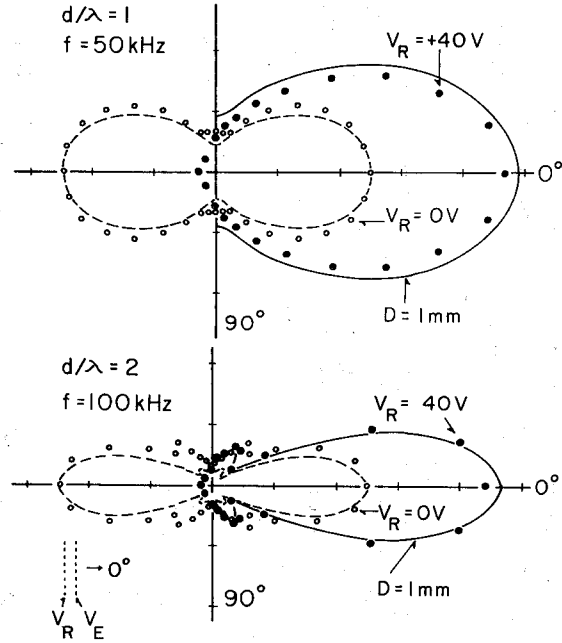
Fig. 3. Typical radiation patterns when the wave frequency is fixed at F=50kHz and 100kHz. Dashed lines are the theoretical curves of the monopole-excitation. Solid lines are the theoretical ones obtained from Eq. (1).

APERTURE ANTENNA WITH NON-GAUSSIAN PHASE ERRORS

Petr Beckmann
Electrical Engineering Department
University of Colorado, Boulder, Colorado 80302

Abstract: The paper derives the mean radiation pattern of an aperture antenna with random phase errors when the errors are a stationary random, but not necessarily normal, function with given probability distribution and correlation coefficient. The case of exponential errors is investigated as an example.

The field radiated into a direction θ, ϕ by an antenna with aperture S is given by

$$f(\theta,\phi) = \iint_{S(x,y)} e^{ik \sin \theta(x \cos \phi + y \sin \phi) + \Psi(x,y)} \, dxdy \quad (1)$$

where an irrelevant constant factor has been discarded, and it has been assumed that the amplitude excitation over the aperture is uniform. The term $\Psi(x,y)$ is the phase error, which ideally should be absent; we assume it to be a stationary random function over the aperture with probability density $p(\psi)$ and isotropic correlation coefficient $\rho(\tau)$, where τ is the distance between two points of the aperture.

Then the mean radiation pattern is

$$\langle ff^* \rangle = \iint_S \iint_{S_1} \langle e^{i(\Psi_1 - \Psi_2)} \rangle \exp[ik(x-x_1)\sin \theta \cos \phi$$

$$+ ik(y-y_1)\sin \theta \sin \phi] dx \, dx_1 dy \, dy_1 \quad (2)$$

where Ψ_1 and Ψ_2 are the values of Ψ at two points separated by τ.

In particular, if the aperture is circular with radius R, we have on setting $x - x_1 = \tau \cos \alpha$, $y - y_1 = \tau \sin \alpha$, and integrating over α,

$$\langle ff^* \rangle = \int_0^R \langle e^{i(\Psi_1 - \Psi_2)} \rangle J_0(k\tau \sin \theta) \tau \, d\tau \quad (3)$$

Relations (2) and (3) are the general solutions of the problem; but the actual computation necessitates the knowledge of the mean value (characteristic function)

involved in the integrand. This is well known when Ψ
is normal, and this case (for a rectangular aperture)
has been treated thoroughly by Shifrin [1].

When Ψ is not (necessarily) normal, we can find the
required function from $p(\psi)$ and $\rho(\tau)$ as follows.
If $p(\psi)$ is proportional to the weighting function of
a set of classical orthonormal polynomials $q_n(\psi)$ (and
if it is not, a simple transformation will make it so),
then as shown in [2],

$$\langle e^{i(\Psi_1-\Psi_2)}\rangle = \sum_{n=0}^{\infty} \rho^n(\tau)\, \Big|\int p(\psi) q_n(\psi) e^{i\psi} d\psi\Big|^2 \qquad (4)$$

and this relation substituted in (2) or (3) will solve
the problem when only $p(\psi)$ and $\rho(\tau)$ are given.

If, for example, Ψ is exponential with variance
$\sigma^2 = 1/\nu^2$,

$$p(\psi) = \nu e^{-\nu\psi} \quad (\psi \geq 0) \qquad (5)$$

then the associated orthogonal polynomials $q_n(\psi)$ are
simple Laguerre polynomials $L_n(\nu\psi)$;   then [2]

$$\Big|\int_0^{\infty} p(\psi) L_n(\psi) e^{i\psi} d\psi\Big|^2 = \nu^2/(\nu^2+1)^{n+1} \qquad (6)$$

and (4) reduces to a geometric series, so that the
solution (3) for a circular aperture is

$$\langle ff^*\rangle = \int_0^R \frac{J_0(k\tau \sin\theta)\tau\, d\tau}{1+\sigma^2[1-\rho(\tau)]} \qquad (7)$$

which differs markedly from the mean radiation pattern
of the same antenna with normal errors,

$$\langle ff^*\rangle = \int_0^R e^{-\sigma^2[1-\rho(\tau)]} J_0(k\tau \sin\theta)\tau\, d\tau \qquad (8)$$

except for small errors $(\sigma^2 \ll 1)$,   in which case

$$e^{-\sigma^2(1-\rho)} \approx \frac{1}{1+\sigma^2(1-\rho)} \approx 1 - \sigma^2(1-\rho) \quad . \qquad (9)$$

References

[1] Y.S. Shifrin, "Statistical Antenna Theory," Golem
     Press, Boulder, Colo., 1972.

[2] P. Beckmann, "Orthogonal Polynomials for Engineers
     and Physicists," Golem Press, Boulder, Colo., 1973.

Session 48   Special Topics

ELECTROMAGNETIC WAVE PROPAGATION IN INHOMOGENEOUS
MULTILAYERED STRUCTURES OF ARBITRARY THICKNESS--FULL WAVE SOLUTIONS

E. Bahar
Electrical Engineering Department, University of Nebraska
Lincoln, Nebraska   68508

Summary

Full wave solutions are derived to the problem of propagation of
electromagnetic waves in multilayered structures of arbitrarily
varying thickness (see Fig. 1). The electromagnetic parameters ε
and μ, characterizing the medium of propagation in each layer, are
also assumed to vary along the propagation path (the x axis). The
sources and observation point may be located in any of the $(m + 1)$
media of the structure.

Exact boundary conditions are imposed and the solutions are not
restricted by the approximate surface impedance concept.

For the purpose of the full wave analysis, generalized transforms
are used to provide a suitable complete expansion for the trans-
verse components of the electromagnetic fields. Thus for verti-
cally polarized waves the z directed magnetic field is expressed
as follows:

$$H_z(x,y) = H_o(x,y) + H_m(x,y) + H_s(x,y) \equiv \Sigma \, H_p(x,u) \, \psi_p(u,y)$$

$$= \int_0^\infty H_o(x,u)\psi_o(u,y)d_o + \int_0^\infty H_m(x,u)\psi_m(x,u)du_m + \sum_{n=1}^N H_s^n(x,u)\psi_s^n(x,u) \tag{1a}$$

and

$$H_p(x,u) = \int_{-\infty}^\infty H_z(x,y)Z(u,y)\psi_p(u,y)dy \ , \ p = o, \ m \ or \ s. \tag{1b}$$

The basis functions $\psi_p(u,y)$ satisfy the differential equation

$$(\partial^2/\partial y^2 + u^2)\psi(u,y) = 0 \tag{2a}$$

and the boundary conditions at each interface, $y = h_{r,r+1}$,

$$\psi(u,h^+) = \psi(u,h^-) \ and \ \frac{\partial}{\partial y} [\frac{1}{\varepsilon_r} \psi(u,h^+) - \frac{1}{\varepsilon_{r+1}} \psi(u,h^-)] = 0. \tag{2b}$$

In a similar manner, the transverse component of the electric
field E_y can be expressed in terms of its transform $E(x,u)$. In
this case, the appropriate basis function is $Z(x,y)\psi(u,y)$; where
$Z(x,y)$ is the transverse wave impedance; thus

$$E_y(x,y) = \Sigma \, E_p(x,u)Z(u,y)\psi_p(u,y) \tag{3a}$$

and

$$E_p(x,u) = \int_{-\infty}^\infty E_y(x,y)\psi_p(u,y)dy \ , \tag{3b}$$

and Σ is to be interpreted as in (1).

The transform functions H(u,y) and E(u,y) can be expressed in terms of the forward and backward wave amplitudes $a(x,u)$ and $b(x,u)$ respectively. Thus, we define

$$H(x,u) = a(x,u) + b(x,u) \; , \; E(x,u) = a(x,u) - b(x,u) \qquad (4)$$

The continuous parts of the wave number spectrum (two infinite integrals) correspond to the radiation and the lateral wave terms, while the discrete part is identified as the finite set of trapped waveguide modes or surface waves. These solutions satisfy the reciprocity relationships in electromagnetic theory.

A wide class of problems such as propagation in the nonuniform and inhomogeneous ionosphere layers or the earth's crust as well as artificial layered structures may be solved using the analysis derived in this paper. In the special case when the bounding media of the structure are regarded as perfect electric or magnetic walls ($\mu/\varepsilon \to 0$ or $\varepsilon/\mu \to 0$ respectively) or when they are characterized by surface impedances, the electromagnetic fields are expressed exclusively in terms of an infinite set of waveguide modes and the radiation and lateral wave terms vanish. Thus, in these cases, when m = 2 and the electromagnetic parameters ε, μ are constant, our problem reduces to the problem of propagation in a waveguide of variable height which has been treated extensively in the technical literature. On the other hand, when only one of the bounding media is regarded as an electric or magnetic wall or if it is characterized by a surface impedance, only one of the infinite integrals in the field expansions vanishes.

In the special case when m = 1, our solutions reduce to those derived recently [1] for the two-medium problems. The solutions can also be used to determine the scattering of electromagnetic waves from objects of finite cross section embedded in the earth's crust or in free space.

The transform pairs (1) and (3) provide a convenient basis for converting Maxwell's equations for $E_y(x,y)$ and $H_z(x,y)$ (in conjunction with the exact boundary conditions) into the following coupled set of ordinary differential equations for the wave amplitudes (4).

$$- \frac{d}{dx} a_p(x,u^*) - i\beta^* a_p(x,u^*)$$

$$= \Sigma \; S_{pq}^{BA}(u^*,u) a_q(x,u) + \Sigma \; S_{pq}^{BB}(u^*,u) b_q(x,u) + J_p(x,u^*)/2 \qquad (5a)$$

and

$$- \frac{d}{dx} b_p(x,u^*) + i\beta^* b_p(x,u^*)$$

$$= \Sigma \; S_{pq}^{AB}(u^*,u) b_q(x,u) + \Sigma \; S_{pq}^{AA}(u^*,u) a_q(x,u) - J_p(x,u^*)/2 \qquad (5b)$$

where Σ is interpreted as in (1) $S_{pq}^{BA} = S_{pq}^{AB}$ and $S_{pq}^{AA} = S_{pq}^{BB}$ are transmission and reflection scattering coefficients, respectively and J_p is the transform of a z directed magnetic line source.

Session 48 Special Topics

Similar sets of coupled first order differential equations are encountered in nonuniform waveguide problems where the wave spectrum is discrete. Iterative solutions for the wave amplitude (5) may be readily derived and substituted into (1a) to obtain the desired solution for H_z. When the source and observation point are at large distances for the principal regions of scattering, this procedure may be simplified by using the steepest descent method for integration.

Excitation of horizontally polarized waves by infinite z directed electric line sources may be treated along the same lines. For three dimensional problems in which the irregular multilayered structure is excited by arbitrary distributions of electro-magnetic sources, both vertically and horizontally polarized waves need to be considered simultaneously since they are generally coupled. In this case, the scalar basis functions $\psi(u,y)$ are replaced by two dimensional vector functions.

Acknowledgement

References

[1] E. Bahar (1972 Canadian Journal of Physics 60, No. 42, pp. 3132-3142).
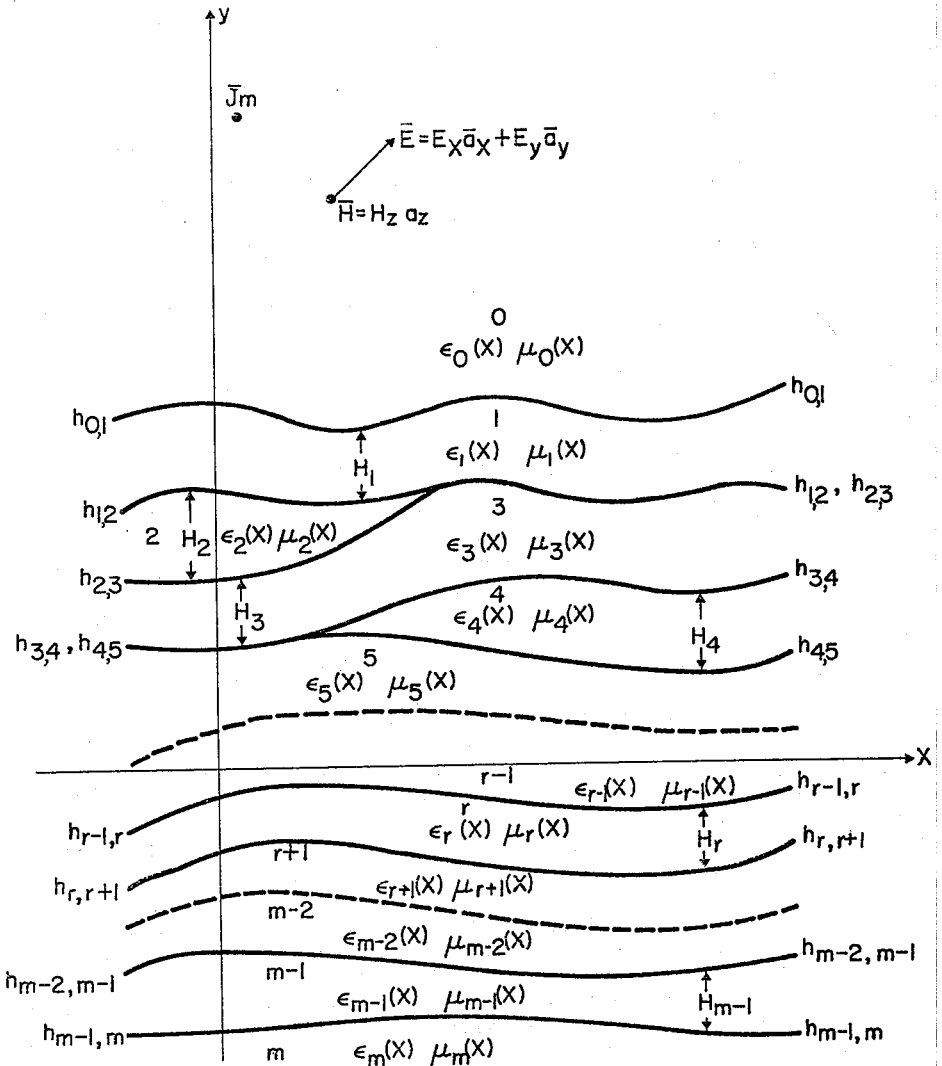
Fig. 1. Line source over a nonuniform multilayered structure.

Session 48 Special Topics

RADAR CROSS SECTION OF A CONDUCTING PLATE
BY WIRE MESH MODELING*

Juang-Lu Lin, Walter L. Curtis & Mervin C. Vincent
The Boeing Aerospace Co., P. O. Box 3999
Mail Stop 4A-41, Seattle, Washington 98124

I. Introduction: In analyzing vulnerability and hardening of an
aeronautic system subject to an incident electromagnetic pulse
(EMP), one is often confronted with solving the problem of scatter-
ing by apertures. Instead of resorting to the complicated rigorous
solutions available in the literature, numerical techniques have
been widely used in recent years. One approach presented here is
to determine the aperture field distribution by solving the dual
problem of the diffraction of a conducting plate modeled by a wire
mesh. In this way existing computer programs for solving wire
antennas may be used directly. The computer program used here was
formulated on the basis of a moment method with point matching and
pulse expansion functions.

In the course of determining the surface current density, it is
quite appropriate to find the far zone field in terms of radar
cross sections as a first check. For this purpose, the radar cross
sections of a conducting rectangular plate are studied numerically
as a function of plate sizes and incident angles on the basis of
wire mesh models. The numerical results are then compared with
measurements of radar cross section made with a series of models
consisting of both wire mesh and conducting plates.

II. Formulation of Problem: The geometry of the problem is as
shown in Figure 1. Consider a perfectly conducting rectangular
plate of height H and length L modeled into wire mesh of square
grid with side Δ and wire radius r_o. A plane electromagnetic wave
with E field parallel to height H is assumed to be incident on the
plate at an arbitrary angle θ. The case $\theta=0°$ corresponds to the
broadside incidence whereas $\theta=90°$ is the case of edge on incidence.

From physical intuition, one expects that Δ should be small compar-
ed to wavelength λ and also $r_o << \lambda$ such that a thin conducting
plate can be well represented by the wire mesh model. Reviewing
the results of antenna and scattering theory known in the past, we
understand that the current distribution and radar cross section
of a linear scatterer are functions of radius r_o or so called
thickness parameter Ω [1]. Following the first order approximate
solution for a loop [2], it is found that a thin plate can be well
represented by different square wire mesh models as long as segment-
to-radius-ratio, Δ/r_o, is kept constant.

III.   Numerical and Experimental Results: To check the accuracy of the numerical results, an experiment was performed with a short pulse radar cross section range at the frequency of 3.15 GHz.

Figure 2 shows the radar cross section of a square plate plotted as a function of θ.   It is found that the numerical results for a wire mesh model with $\Delta/r_o=20$ agree well with those of experiment. For small incidence angles ($\theta \leq 20°$), the echo area of a wire mesh model is almost the same as that of a solid plate, however, it tends to deviate as θ increases.   This tendency is reasonable considering the difference between the discrete distribution in the wire mesh and the continuous distribution of current on the solid conducting plate.   The calculated values for broadside incidence compare well with Richmond's results [3].

In Figure 3, the echo area of a rectangular plate is plotted as a function of incidence angle θ.   An excellent agreement between the calculated and experimental values can be found.

Another important case solved here is the edge-on incidence where physical optics and the geometrical theory of diffraction fail [4]. With $\Delta/r_o=20$, the echo areas of a rectangular plate and a wire mesh model with $\Delta=0.53\lambda/4$ are plotted as a function of L/λ in Figure 4. The calculated values compare well to our measurements and those by Senior, et al. [5].

An important result can be seen in Figure 5 where the radar cross section is shown for a square plate modeled with 3 different mesh sizes (4x4, 5x5, and 6x6 segments) but with the ratio Δ/r_o kept equal to 20.   If the mesh is to represent a solid plate then each model should produce approximately the same results over an appropriate range of frequencies.   Figure 5 shows this to be the case for the square plate example.

IV.   References

[1]   R. W. P. King, The Theory of Linear Antennas,   Harvard
      University Press, 1956.

[2]   R. W. P. King, IRE Trans. AP-7, p. 53, Jan. 1959.

[3]   J. H. Richmond, IEEE Trans. AP-14, p. 782, Nov. 1966.

[4]   R. A. Ross, IEEE Trans. AP-14, p. 329, May 1966.

[5]   E. F. Knott, V. V. Liepa, T. B. A. Senior, IEEE Trans. AP-19,
      p. 788, Nov. 1971.
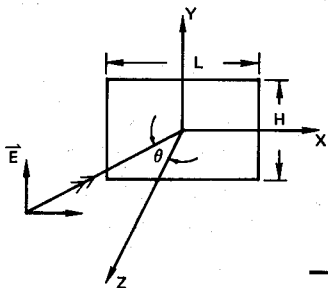
Figure 1: A Plane Wave Is Incident on a Rectangular
Plate at an Angle θ

——— Exp. (Plate)
----- Exp. (Wire-mesh)
● ● ● ● ● Cal. (Wire-mesh)
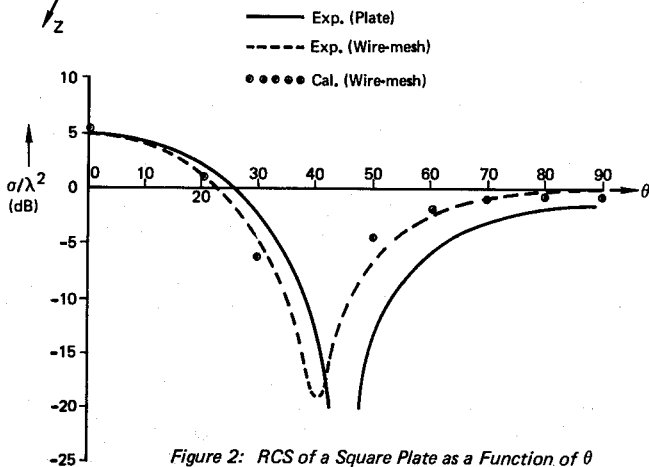
Figure 2: RCS of a Square Plate as a Function of θ
($L/\lambda = 0.6$, $\Delta/r_0 = 20$, 4 x 4 Segments)

Exp. (Plate)   ———
Exp. (Wire-mesh) -----
Cal. (Wire-mesh) ● ● ● ● ●
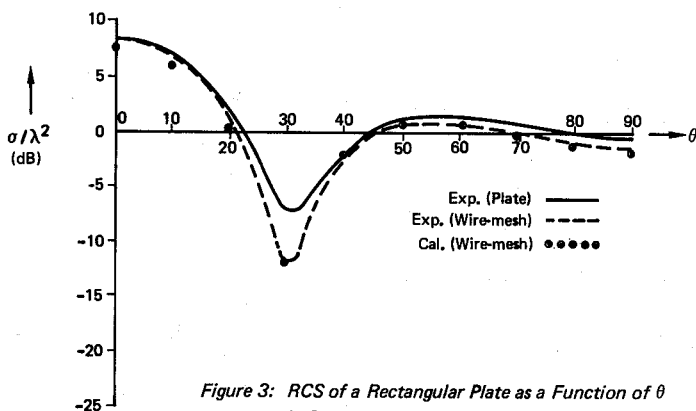
Figure 3: RCS of a Rectangular Plate as a Function of θ
($L/\lambda = 0.795$, $\Delta/r_0 = 20$, 4 x 6 Segments)
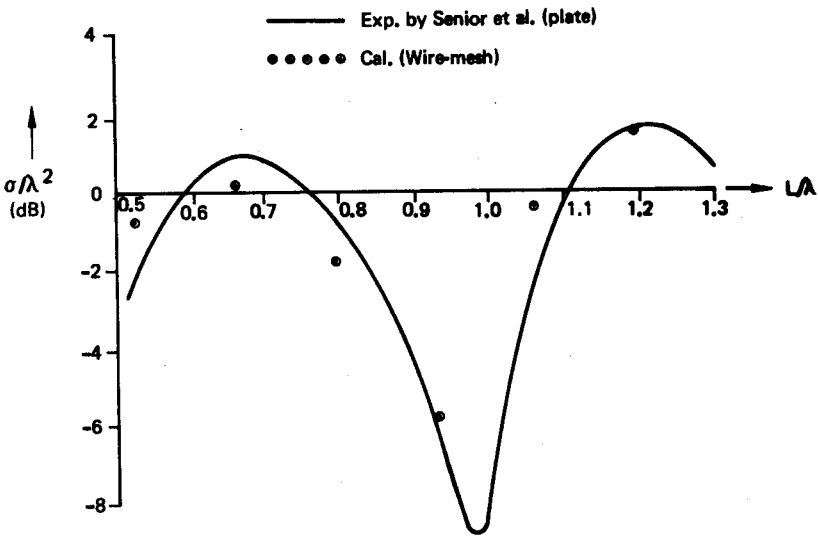
Figure 4: RCS of a Rectangular Plate as a Function of L/λ at Edge-On Incidence
$(H/\lambda = 0.53, \quad \Delta/r_0 = 20)$
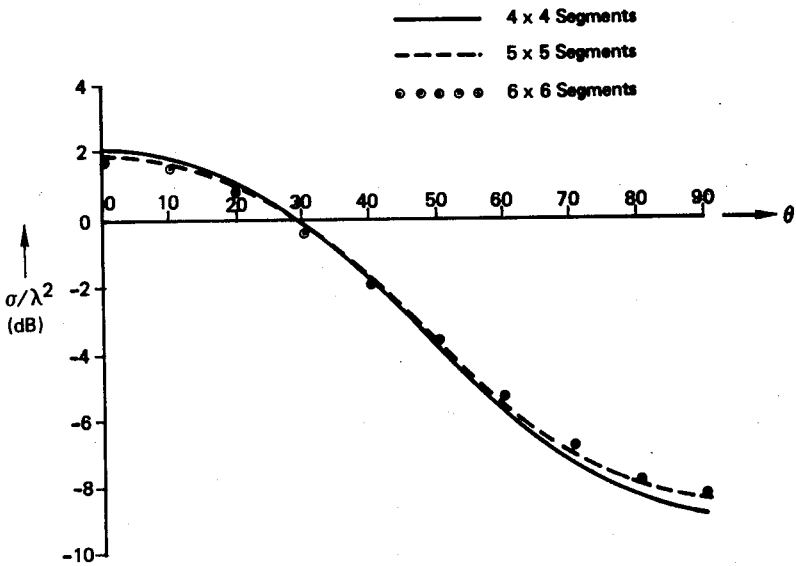
Figure 5: RCS of a Square Plate of a Wire-mesh Model as a Function of θ With Wire-
Size as Parameters. $(L/\lambda = 0.4)$

425

A NEW MULTIMODE RECTANGULAR HORN ANTENNA
GENERATING CIRCULARLY-POLARIZED ELLIPTICAL BEAM

Dr. Ching C. Han and Adam N. Wickert
Philco-Ford Corporation
Western Development Laboratories Division
Palo Alto, California

A new concept is described, which utilizes a multimode rectangular horn antenna to generate a circularly-polarized elliptical shaped beam. This antenna, used in conjunction with a spacecraft to illuminate an elliptical shape earth coverage zone, offers high edge-of-coverage gain, low sidelobes, low edge-of-coverage axial ratio, less RF sensitivity to the space environment and low cost.

To effectively radiate a circularly polarized wave from an aperture, the two orthogonal far-field spherical components, E_θ and E_ϕ, must have equal amplitude and proper phase. For illustration, consider only the two principal orthogonal planes of a conventional rectangular horn simultaneously propagating only the TE_{10} and TE_{01} modes. The E_θ and E_ϕ component do not have equal amplitude off the antenna axis. If a portion of the TE_{10} and TE_{01} mode energy is now converted to the higher order $TE_{12} + TM_{12}$ and $TE_{21} + TM_{21}$ modes with proper amplitude and phase, the E-plane aperture field distributions can be tapered as shown in Figure 1. Thus, by virtue of the higher order TE/TM modes, the effective E-plane pattern width will be matched to the H-plane width of the other orthogonal set of modes as depicted in Figure 2. This figure illustrates the equalization of the E_θ and E_ϕ components in the two principal pattern planes and the significant reduction of sidelobe level of the E-plane components.

The higher order modes can be generated by a symmetrical discontinuity such as a step in an oversized waveguide. The radiation pattern can be calculated by the use of aperture field method.[1] Proper phasing of all wanted modes at the aperture and proper polarizer phase to compensate for the phase difference between two orthogonal modes in the rectangular horn section must be warranted to arrive at a sound design.

An experimental X-band model was fabricated to provide maximum gain[2] (-4.34 dB level) over an elliptical edge-of-coverage angle of 8.8 x 15.2 degrees. Axial ratios for every 15 degrees pattern plane cut are shown in Figure 4, in which an axial ratio less than 2 dB over the desired edge-of-coverage angle is achieved. The corresponding circular polarization patterns are shown in Figure 5. If one took the desired beamwidth at $\phi = 0°$ and $90°$ (in this case $8.8° \times 15.2°$) as the mathematical major and minor axis and plotted a true elliptical contour, the deviation of the measured beam shape from this true ellipse is negligibly small. As shown in Figure 6, the multimode rectangular horn did produce an elliptical cross-section beam.

References

1. Silver, S., "Microwave Antenna Theory and Design," McGraw-Hill, 1949, P. 158.

2. Duncan, J.W., "Off-Axis Gain of Pencil Beams," Proceedings of IEEE, January 1970.
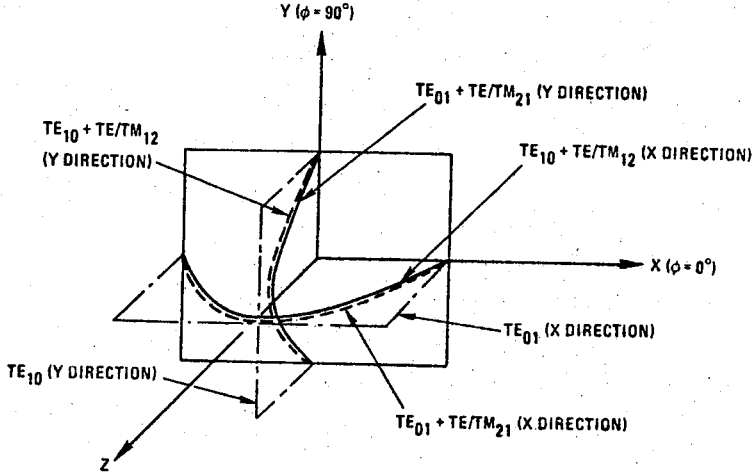
Figure 1--Aperture E-Field Distributions
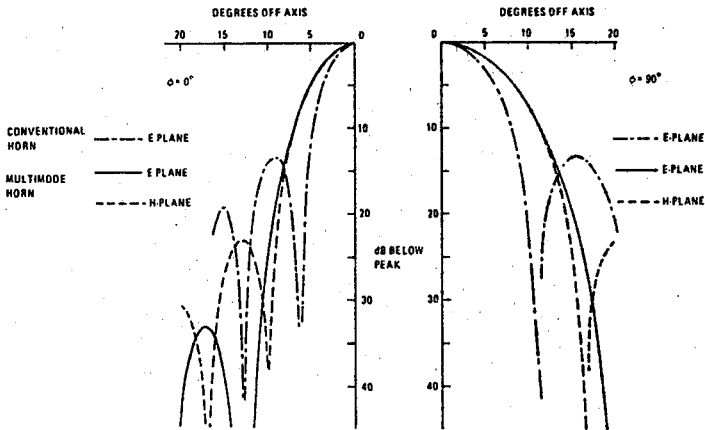
Figure 2--Computed Radiation Patterns of a Multimode Horn
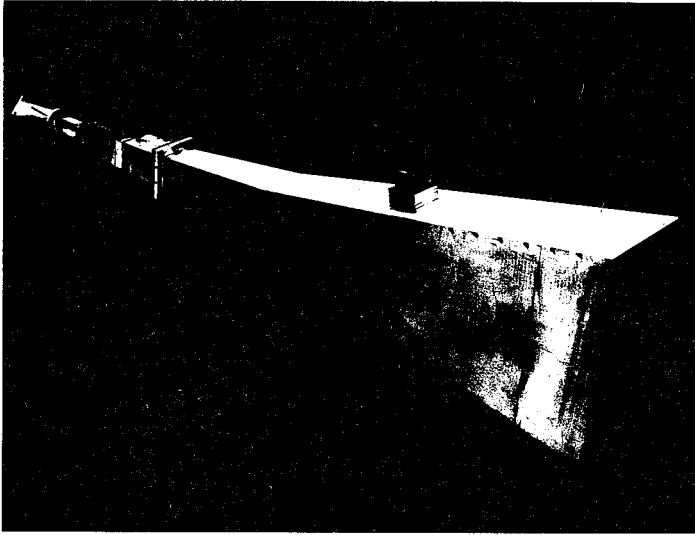
Figure 3--X-Band Multimode Horn Test Model
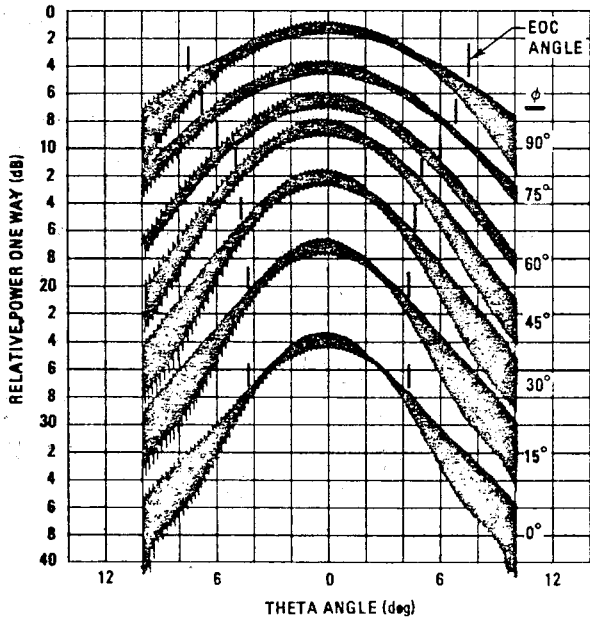
Figure 4--Axial Ratios as a Function of Phi Angle
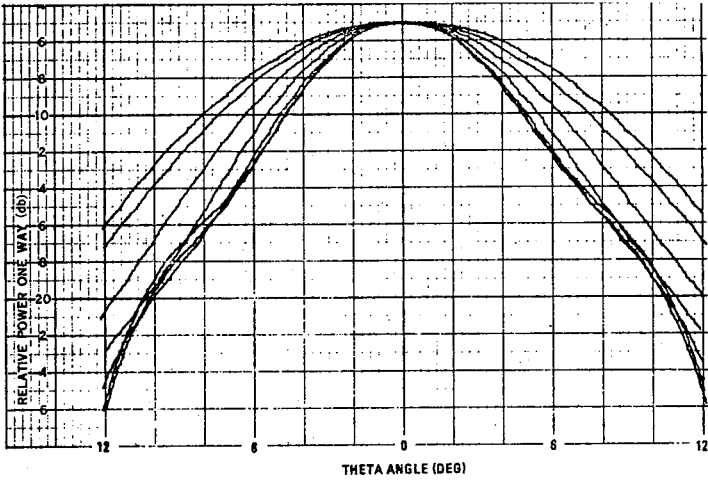
Figure 5--Measured Circular Polarization Patterns
for every 15 Degrees Pattern Plane Cut
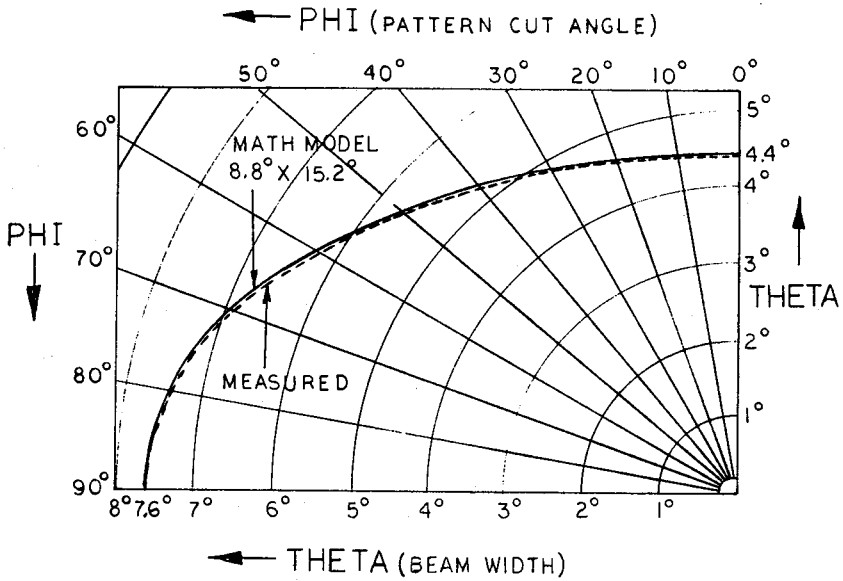
Figure 6--Calculated and Measured Beam Shape

429

Session 48   Special Topics

THE BARE BURIED WIRE NEAR AN INTERFACE

Virgil R. Arens
Arens Applied Electromagnetics, Inc.
15801 White Rock Road, Gaithersburg, Md. 20760

Introduction

A significant part of many antennas that operate below
30 mHz and nearly all antennas that operate below 300 KHz
is the bare buried wire acting as a counterpoise.
Considerable interest has been shown these past few years
in buried antennas both in the HF and UHF regions[1] [2]
because of their potential to providing communications
to and from physically hardened facilities.   Great
interest has also been exhibited in the use of buried
antennas in mine-rescue techniques and geophysical
prospecting.   Thus the concern here is not the solution
to a half-wave dipole antenna in an infinite homogeneous
dissipative medium[3] but rather an antenna that consists
of a three dimensional arbitrary arrangement of bare
wires located below, near and above the surface of a
homogeneous finitely conducting half-space.   The use
of insulated wires is noted.   They are now under study
and will be included in this presentation if completed
in time.

Discussion

Following Dr. Wait[4] most work in the past in this field
has been broken down into three overlapping distance ranges.
These are:

$$
\begin{array}{ll}
\text{(i)} & \rho \gg \lambda_0 \\
\text{(ii)} & \rho \sim \lambda_0 \\
\text{(iii)} & \rho \ll \lambda_0
\end{array}
$$

Where ρ is the horizontal separation between transmitter
and receiver and λ_0 is the free space wavelength.   Further,
the refractive index, η, defined by

$$
\eta^2 = \varepsilon_r - j\sigma/\omega\varepsilon_0
$$

is often assumed to be purely real, where only displacement
current is considered, or purely imaginary where only the
conduction current is considered.

Lastly most efforts in the past have either considered
an infinitismal dipole, an infinitely long wire, or have

assumed some form of current distribution. We have
developed a numerical approach that is valid for all
horizontal distances with no restrictions on the
location of the antenna or the observation point in
their relationship to the interface. The index of
refraction is always assumed to be complex as
defined above. The current distribution is
determined taking into proper consideration the
antenna's environment; it is not assumed to be of
some predetermined form.

Approach

The method used results in a set of simultaneous linear
equations which can be solved for the unknown currents.
As in the past[5] the first step is to appeal to thee principl
of superposition and replace the wire antenna by a finite
set of straight wire segments. Further, we assume the
current on a segment can be represented by the now well
known three term Fourier series whose coefficients are
obtainable in terms of the unknown current on the ends of
the wire and at the center of each segment.

The next step is the development of an expression for the
electric field at any arbitrary point in either half-space
in terms of the unknown current flowing on the wire
segments. It is the development of this expression for
the electric field that differs significantly from the
free space case. Even the free space Green's function
becomes far more complex since the exponent changes from
purely imaginary to complex when one is in a finitely
conducting medium. The evaluation of the infamous
Sommerfeld integrals, while important for antennas in
the upper half-space, becomes exceedingly important for
antennas in the lower half-space. The differences
from the approach necessary over the upper half-space
method[6] will be presented.

Results

Comparisons of input impedance, current distributions,
and fields will be made with the work of others[3] [7] where
we have lowered the antenna into the medium to minimize
the interface effects since the other work was in an
homogeneous space. Comparisons will be made with the
measurements of Fitzgerrell, et al,[2] for antennas of
various configurations in the UHF region. Curves will
be presented to demonstrate how the system loss between
a pair of antennas varies as a function of depth in the
ground for various horizontal displacements. This is a

limited study of the creeping wave phenomenon.   Lastly
the far field pattern in the upper half-space of a buried
HF antenna that would be useful for skywave propagation
will be presented.

---

1.   Entzminger, J. N. et. al. ("Measured Performance of
       HF Subsurface Dipoles," Rome Air Development Center
       Technical Report -69-221 AD-690609, June 1969)
2.   Fitzgerrel, R. G. et. al. ("Buried Vertically
       Polarized UHF Antennas," Office of Telecommunications
       Research Report OT/ITSRR8, November 1970)
3.   King, R. W. P. and Harrison, C. W. (Antennas and Waves
       A Modern Approach, The M.I.T. Press 1969)
4.   Wait, J. R. ("The Electromagnetic Fields of a
       Horizontal Dipole in the presence of a Conducting
       Half-Space," Can. J. Phys. Vol. 39 (1961))
5.   Arens, V. R. and Murphy J. ("Wire Antenna Analysis,"
       1972 G-AP/URSI International Symposium Digest and
       Abstract December 1972)
6.   Arens, V. R. and Murphy J. ("The Ground Correction
       Problem," Submitted to the 1973 G-AP/URSI Symposium.)
7.   Irzuka, K. and King, R. W. P. ("The Dipole Antenna
       Immersed in a Homogeneous Conducting Medium,"
       IRE Trans. on Ant. and Prop. July 1962 pp 384 - 392)

ON THE PULSE RESPONSE OF A DIPOLE
OVER AN IMPEDANCE SURFACE

James R. Wait

C. I. R. E. S. /N. O. A. A. /C. U. and I. T. S. /O. T.
Boulder, Colorado 80302

In both telecommunication and in applied geophysics one needs to understand the transient behavior of an electromagnetic ground wave. While the time domain solution can be obtained formally by an inverse Fourier transform of the known time harmonic solution, there are numerous analytical difficulties to overcome. For this reason, recourse is often made to approximations in both the time harmonic problem and the derived pulse response.

Following the original ideas of Van der Pol (1931) we draw attention to the possible deficiency in the Sommerfeld theory for the plane earth model when detailed information on the pulse response is sought for long times. To simplify our discussion we consider the idealized situation of a vertical electric dipole located on the plane boundary of an idealized ground that exhibits a surface impedance $Z(i\omega)$ for a time factor $\exp(i\omega t)$. Specifically we deal with the case where the source dipole moment $p(t)$ varies as a ramp. function of time. $p(t) = P_0 t\, u(t)$ where P_0 is a constant and $u(t)$ is the unit step function at $t = 0$. Then the radiation component $e(t)$ of a the vertical electric field at distance d on the surface is given by (Wait 1956)

$$e(t) = -[\mu_0/(2\pi d)]\, P_0 B(t')\, u(t') \tag{1}$$

where $\mu_0 = 4\pi \times 10^{-7}$, $t' = t - d/c$, c is the velocity of light and $B(t')$ is the normalized time dependence of the observed field. In the case where the ground is a perfect conductor we know that $B(t') \equiv 1$. Thus ideally the waveform at the radiated vertical electric field is a step-function. In the case where the surface impedance is non-zero we must evaluate $B(t')$ as an inverse Laplace transform that can be written

$$B(t) = \mathcal{L}^{-1}[F(s)/s] \tag{2}$$

where $F(s)$ is analogous to the Sommerfeld attenuation function if s is identified with $i\omega$ in the corresponding time harmonic problem.

For the surface impedance model we know that an exact definition of $F(i\omega)$ is

$$\frac{e^{-ikd}}{d}\, F(i\omega) = \frac{1}{2} \int_{-\infty}^{+\infty} \frac{H_0^{(2)}(\lambda d)\, \lambda\, d\lambda}{(\lambda^2 - k^2)^{\frac{1}{2}} + i k \Delta} \tag{3}$$

where $k = \omega/c$, $\Delta = Z(i\omega)/120\pi$ and $H_o^{(2)}$ is the Hankel function of the second kind. As we can readily verify $F(i\omega) = 1$ for $\Delta \to 0$. For engineering estimates of $F(i\omega)$ and related quantities it is assumed usually that $|\Delta|$ is small compared with unity. Also the parameter kd is considered to be large compared with unity. Obviously the latter assumption will be violated at extremely low frequencies or at corresponding long times in the transient response. In fact, as pointed out by Chang (1973) the relative error in $F(i\omega) - 1$ may be appreciable. The crucial physical question however is whether this will influence the total field to any significant extent. To provide insight to this question we examine (3) under less restrictive assumptions.

Following an ingenious suggestion of Van der Pol (1931), we utilize the following integral representation

$$\frac{1}{(\lambda^2 - k^2)^{\frac{1}{2}} + i k \Delta} = - \frac{\Delta}{(1-\Delta^2)^{\frac{1}{2}}} \int_{(1-\Delta^2)^{-\frac{1}{2}}}^{\infty} \frac{1}{[\lambda^2 - k^2(1-\Delta^2)u^2]^{\frac{1}{2}}} d\left(\frac{1}{(u^2-1)^{\frac{1}{2}}}\right) \quad (4)$$

Thus (3) is equivalent to

$$F(i\omega)\frac{e^{-ikd}}{d} = \frac{e^{-ikd}}{d} - i k \Delta \int_{(1-\Delta^2)^{-\frac{1}{2}}}^{\infty} \frac{e^{-ikd(1-\Delta^2)^{\frac{1}{2}}u}}{(u^2-1)^{\frac{1}{2}}} du$$

$$\quad (5)$$

$$= \frac{e^{-ikd}}{d} - \pi k\Delta H_o^{(2)}[kd(1-\Delta^2)^{\frac{1}{2}}] + 2 i k \Delta \int_1^{(1-\Delta^2)^{-\frac{1}{2}}} \frac{e^{-ikdu(1-\Delta^2)^{\frac{1}{2}}}}{(u^2-1)^{\frac{1}{2}}} du \quad (6)$$

It is suggested that for a valid transient calculation the inverse transform indicated by (2) be evaluated using (6) for the functional form of (2). In general this requires a numerical treatment. Here we consider an approximate evaluation that requires $|\Delta|^4 << 1$ but does not require kd to be small. Thus for the range of integration in (6), we can replace $(u^2-1)^{-\frac{1}{2}}$ by $[2(u-1)]^{-\frac{1}{2}}$. Without difficulty it is then found from (6) that

$$F(i\omega) = - \frac{\pi k\Delta d}{2} \left[H_o^{(2)}(kd) - \left(\frac{2i}{\pi kd}\right)^{\frac{1}{2}} e^{-ikd} \right] e^{ikd} + F_o(i\omega) \quad (7)$$

where $F_o(i\omega) = 1 + 2p^{\frac{1}{2}} e^{-p} \int_{p^{\frac{1}{2}}}^{-i\infty} e^{z^2} dz = 1 - i(\pi p)^{\frac{1}{2}} e^{-p} \operatorname{erfc}(ip^{\frac{1}{2}}) \quad (8)$

where $p = -ik[1 - (1-\Delta^2)^{\frac{1}{2}}]d \simeq -ikd\Delta^2/2$. Here $F_o(i\omega)$ can be identified as the Sommerfeld Attenuation Function and p is analogous to the numerical distance. Clearly if $kd >> 1$, the square bracket term in (7) can be neglected and $F(i\omega) \simeq F_o(i\omega)$.

We can define $\Delta F(i\omega) = F(i\omega) - F_o(i\omega)$ as the low frequency correction to the attenuation function; it is given by

$$\Delta F = -\frac{\pi k \Delta d}{2} H_o^{(2)}(kd)\, e^{ikd} + (\pi/2)^{\frac{1}{2}} \Delta (ikd)^{\frac{1}{2}} \tag{9}$$

Not only does this vanish as $kd \to \infty$ but also it disappears as $kd \to 0$. Apparently ΔF is most significant for kd at the order of one and for values of $|\Delta|$ that are not too small.

To consider the implications of the transient problem, we assume that $\Delta \cong (i\omega e_o/\sigma)^{\frac{1}{2}}$ corresponding to a highly conducting homogeneous ground of conductivity σ. The transient response following (21) is then given by $B(t) = B_o(t) + \Delta B(t)$
where (Wait 1956) $B_o(t) = \mathcal{L}^{-1} F_o(s)/s = 1 - \exp[-t^2/(4Kd)]$
with $K = (2\sigma\mu_o c^3)^{-1} = (240\pi\sigma c)^{-1}$ and $\Delta B(t) = \mathcal{L}^{-1}\Delta F/s$

$$= \mathcal{L}^{-1} \left(\frac{\pi d e_o}{2c\sigma}\right)^{\frac{1}{2}} \left[1 - \left(\frac{2d}{\pi c}\right)^{\frac{1}{2}} s^{\frac{1}{2}} e^{sd/c} K_o\left(\frac{sd}{c}\right)\right]$$

$$= \left(\frac{\pi d\varepsilon_o}{2c\sigma}\right)^{\frac{1}{2}} \left\{\frac{d}{dt}\left[1 - \frac{1}{\pi}\left(\frac{2d}{c}\right)^{\frac{1}{2}} \int_0^t \frac{d\tau}{[(t + \frac{2d}{c} - \tau)(t-\tau)\tau]^{\frac{1}{2}}}\right]\right\} u(t) \tag{10}$$

The latter is expressible as a complete elliptic integral K of the first kind. Thus,

$$\Delta B(t) \simeq \left(\frac{\pi d\varepsilon_o}{2c\sigma}\right)^{\frac{1}{2}} \left\{\frac{d}{dt}\left[1 - \frac{2}{\pi}\frac{(2d/c)^{\frac{1}{2}}}{(t+2d/c)^{\frac{1}{2}}} K\right]\right\} u(t) \tag{11}$$

where $\quad K = \frac{\pi}{2}(1+m)\left[1 + \frac{1^2}{2^2}m^2 + \frac{1^2 \cdot 3^2}{2^2 \cdot 4^2}m^4 + \ldots\right]$

with $\quad m = \dfrac{1 - [1+2d/(ct)]^{\frac{1}{2}}}{1 + [1+2d/(ct)]^{\frac{1}{2}}}$

For $t \to \infty$ we see that

$$\Delta B(t) \sim \frac{d}{2ct}\left[\frac{\pi \varepsilon_o}{\sigma t}\right]^{\frac{1}{2}} \tag{12}$$

Even though $\Delta B(t) \ll 1$ it may be true that $\Delta B(t)$ is greater than $1 - B_o(t)$ for these long times. Thus as pointed out by Chang (1973) the previous analysis based on the conventional Sommerfeld attenuation does not predict this slow tail portion of the transient response of the ground wave. From a physical standpoint, however, it is doubtful if the neglect of $\Delta B(t)$ or ΔF is significant. In the range where $\Delta B(t)$ exceeds $1 - B_o(t)$ the

resultant response B(t) has essentially reached its final value of unity. Also we should stress that the induction and static field contributions (Wait, 1956) will become important at long times not to mention ionospheric influences.

I wish to thank D. C. Chang and J. A. Fuller for their suggestions.

References

1. D. C. Chang, Dept. of Elect. Eng., Univ. of Colorado (NOAA Grant No. N22-126-72 (G), Tech. Report No. 8, April 1973).
2. Balth van der Pol (Ueber die Ausbreitung electromagnetischer Wellen), Zts. f. Hochfreq. Techn. 37, 152 (1931).
3. J. R. Wait (Transient fields of a vertical dipole over a homogeneous curved ground) Can. Jour. Phys. 34, 27 (1956).
4. J. R. Wait (Propagacao de pulsos sobre a terra) Revista Brasilera de Tecnologia 2, 193-199 (1971).

THE IMPULSE RESPONSE AUGMENTATION TECHNIQUE*

C. L. Bennett
Sperry Research Center
Sudbury, Massachusetts 01776

This paper described a new technique for obtaining the total impulse response and the frequency response (system function) of a target over the entire frequency spectrum. This technique can be viewed as an extension of the space-time integral equation approach to the large body problem. The validity of the technique is illustrated by considering the case of a perfectly conducting sphere and comparing the results with those obtained by the classical approach.

The impulse response augmentation technique deals directly with the smoothed impulse response of targets in the far field. The smoothed impulse response is computed using the space-time integral equation approach[1] which has yielded good results up to body sizes of several pulse widths or, equivalently, up to body sizes of several wavelengths.[2] A Gaussian-shaped pulse is used for the incident wave in the numerical formulation to yield a smoothed impulse response whose regions of slow variation are the same as those in the exact impulse response. Moreover, the singular portions of the exact impulse response that result from scattering by specular points on the target can be computed by alternate formulations such as physical optics. This technique combines this known singular structure with the smoothed impulse response to yield the impulse response and frequency response of the target.

The impulse response augmentation technique consists of first computing the smoothed impulse response of the target by solution of the space-time integral equation. The smoothed impulse response is then augmented to remove the contributions due to the singular portions of the impulse response that are known exactly. The form of the augmentation function used for this purpose is chosen to contain the known singular portion of the impulse response, together with a suitable amplitude and phase form in the frequency domain.

Next, the Fourier transform of the augmented smoothed impulse response is divided by the transform of the incident pulse to yield the augmented frequency response. This function is accurate in the low-frequency region, but at higher frequencies, it contains numerical noise which increases exponentially with frequency. However, it is known that the augmented frequency response must go to zero with increasing frequency and by a suitable choice of augmentation function, this high-frequency tail is due mainly to the creeping wave contribution in the impulse response. An estimate of this high-frequency variation is applied to yield an estimate of the augmented frequency response over the

entire frequency spectrum. Finally, the impulse response and frequency response
are obtained by then applying the augmentation procedure in reverse.

As an example of this technique, consider the case of scattering from a per-
fectly conducting sphere. Figure 1 displays the Gaussian pulse whose width is
two-sphere diameters incident on a sphere with radius a . The smoothed im-
pulse response that results from the solution of the space-time integral equa-
tion is displayed in Fig. 2.

The impulse response of the sphere obtained by application of this technique is
displayed in Fig. 3 along with the theoretical result. In this figure, the
impulse at $t/a = -2$ that results from the specular point is immediately
followed by a negative step. This leading edge response is precisely what
physical optics would have predicted. The "cusp like" peak at approximately
$t/a = 3.2$ is due to the creeping wave which travels around the rear of the
sphere. From this figure, the agreement is seen to be excellent including the
neighborhood of the creeping wave.

The frequency response of the sphere that the impulse response augmentation
technique yields is shown in Fig. 4 along with the theoretical result that was
obtained by the classical solution of the boundary value problem. Again the
agreement is excellent.

Results which have been obtained for the prolate spheroid and the sphere-capped
cylinder using this technique will also be presented and discussed.

References

1.   C. L. Bennett (1968, Ph.D. Dissertation, Purdue University).

2.   C. L. Bennett, et al (RADC-TR-70-177, October 1970).
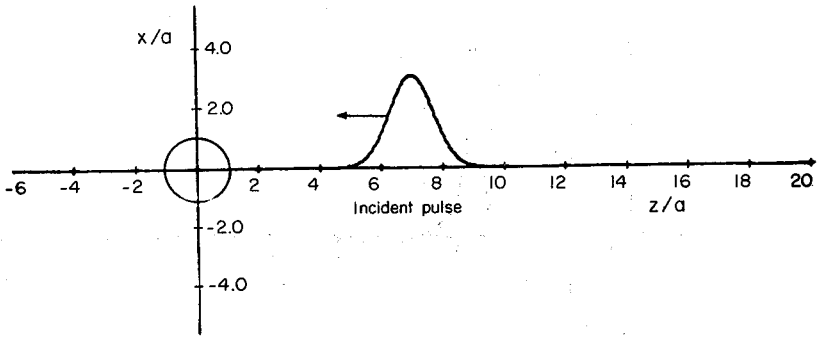
FIG. 1   Incident pulse and sphere with radius a.
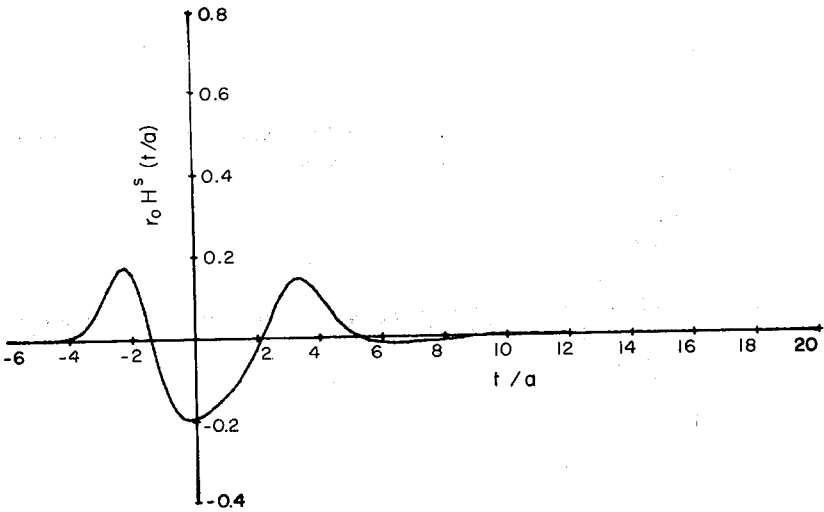
FIG. 2   Smoothed impulse response of sphere with radius a.

439
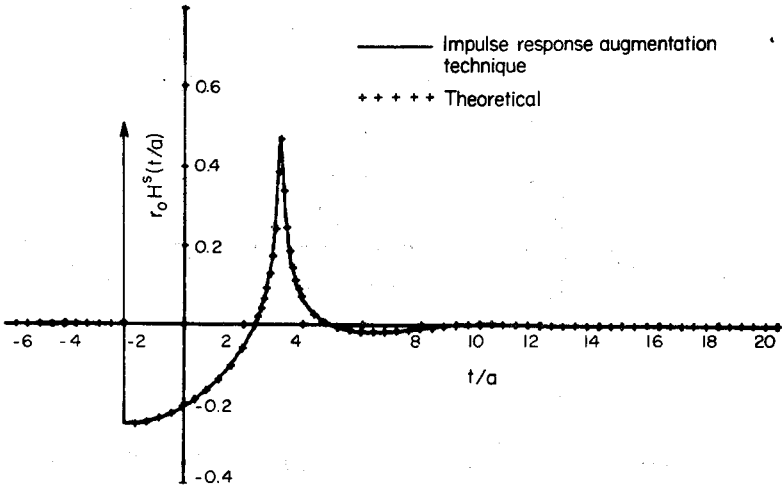
FIG. 3   Impulse response of sphere with radius a.
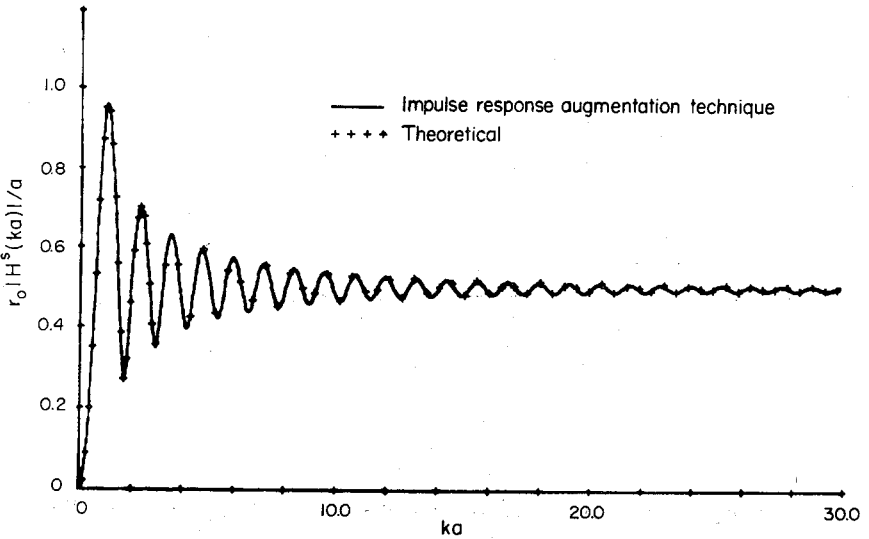
FIG. 4   Frequency response of sphere with radius a.

RADIATION FROM MOVING CHARGED PARTICLES NEAR A CONDUCTOR

K.S.H. Lee and L. Marin
Dikewood Corporation, Westwood Research Branch
Los Angeles, Calidornia

In finding the electromagnetic field of charged particles moving near a conductor there are several advantages, from both the mathematical and physical viewpoint, in first splitting the field into its irrotational and solenoidal part. A general procedure of doing this is contained in the Helmholtz theorem on vector fields. For non-relativistic charged particles the irrotational part of the field can be obtained with sufficient accuracy by solving an appropriate quasi-electrostatic problem and the solenoidal part by solving an appropriate quasi-magnetostatic problem. Let $\underline{K}$ be the surface current density on a perfect conductor, and $\underline{K} = \underline{K}' + \underline{K}''$, $\underline{K}'$ being the irrotational part of $\underline{K}$ and $\underline{K}''$ the solenoidal part. Then, the two quasi-static problems can be stated as follows:

$$\underline{K}' = -\nabla_s \frac{\partial \chi}{\partial t} , \qquad \nabla_s^2 \chi = \sigma \tag{1}$$

$$\frac{1}{2} \underline{K}'' + \int \underline{n} \times (\nabla' G \times \underline{K}'') dS' = \underline{n} \times \underline{H}^{inc} \tag{2}$$

where ∇_s is the surface gradient, G is the static Green's function and σ is the surface charge density determined from an electrostatic problem with the instantaneous positions of all particles specified. Equation (2) directly gives $\nabla_s \cdot \underline{K}'' = 0$.

The field of a point charge orbiting about a perfectly conducting sphere in the equatorial plane is calculated rigorously with the aid of Debye's potentials. The quantities $\underline{K}'$, $\underline{K}''$ and σ are reduced exactly to those deduced from the two quasi-static problems (1) and (2) when $\beta a/b$ is small, a being the radius of the sphere, b the radius of the particle's orbit, and $\beta = v/c$ (v is the particle's velocity). A numerical comparison between the exact results and the corresponding quasi-static results for $\underline{K}'$, $\underline{K}''$ and σ shows exceedingly good agreement for $\beta a/b < \sqrt{3}/2$. A physical explanation for this good agreement can be found in the Singularity Expansion Method applied to a sphere. From physical arguments the quasi-static solutions should give an accurate description of the electromagnetic phenomenon involving a charged particle of arbitrary motion in the presence of a sphere provided that the particle velocity v and its instantaneous radial position r_p satisfy the condition $\beta a/r_p < \sqrt{3}/2$; explicit quasi-static solutions are obtained for this general case.

Session 49   EM Theory

INPUT RESPONSE OF SPHEROIDAL ANTENNAS IN DISPERSIVE MEDIA [†]

Ovidio M.Bucci and Giorgio Franceschetti
Istituto Elettrotecnico, Università, Via Claudio 21, 80125 Napoli
(Italy) and Istituto Universitario Navale, via Acton 38, 80135 Napo-
li (Italy).

1. _Introduction_. This paper is concerned with input response of sphe
roidal antennas in dispersive media, whose geometry is specified in
terms of interfocal distance 2ℓ, the major and minor axes a and b.
The antenna is assumed to be excited at a small equatorial gap, of
width 2s, by an azimuthally independent voltage. In the subsequent a
nalysis, a spheroidal coordinates system (ξ,η,ϕ) will be needed, in
which the antenna surface is represented by $\xi=\xi_0$, $\xi_0=a/\ell$, and the gap
periphery by $\xi=\xi_0,\eta=\pm\eta_0$, $\eta_0\approx+s/a$. The transition to the thin antenna
case (linear antenna) is obtained by letting $b\rightarrow o$, while the transi-
tion to the spherical case by letting $\ell\rightarrow o$, $\xi_0\ell=a=$radius of the sphere.

The input response of the antenna is fully described by its input ad-
mittance $Y(s)$, or by its time response $i(t)$ to a δ-voltage (Dirac pul
se) of unit amplitude. Since $Y(s)$ is the Laplace transform of $i(t)$, it
will suffice to compute the input admittance $Y(s)$ of the antenna. This
will be done by assuming the antenna to be surrounded by a homogene-
ous isotropic time-invariant medium described by (s-dependent) permit
tivity $\varepsilon(s)$ and permeability $\mu(s)$.

Input admittance of linear antennas has been extensively studied by
applying integral equation formulations to the problem [1]. However,
we prefer to use here a modal approach based on the field expansion
in spheroidal coordinates. This is also a well known procedure, for
spheroidal antennas in essentially non-dispersive media [2] or spheri
cal antennas in dispersive media [3]. In this older formulations, how-
ever, the computation of the input susceptance of the antenna has not
received a satisfactory answer, for the case of small gaps. The solu-
tion of this last problem, as extension of our previous results [4,5
6], is a specific contribution of this paper. It allows us to give a
reply to a question of probably fundamental nature, i.e. under which
assumptions an input admittance characteristic of the antenna can be
defined, irrespective of the feeding system (and therefore of the field
distribution across the gap). In addition, we present an equivalent
lumped network for $Y(s)$, which sheds light on both the steady-state
and transient input response of the antenna, this last comprising po-
le (non-dispersive media) as well as branch-cut contributions (disper
sive media).

A further notice about transient response seems in order. Generally
speaking, a transient calculation will need specification of transfer
functions of several other parts of the link (e.g., of the feeding sy
stems). However, in the case of thin antennas, voltages and current
just across the gap can be measured, so that the computation of the
input response $i(t)$ of the antenna makes sense. This response can be
used for a wide-band diagnosis or probing of the environmental elec-
tromagnetic properties.

---

2. Splitting of the modal series for the input admittance of the antenna. The input admittance of the antenna is given in terms of the series [6]

$$Y(\xi_o,\eta_o,q)=s\pi\sqrt{\frac{\varepsilon}{\mu}}\sum_1^\infty T_{2n-1}(\xi_o,q)\;\Theta_{2n-1}(\eta_o,q)/N_{2n-1}(q)=\sum_1^\infty y_n \qquad (1)$$

where $q=js\sqrt{\varepsilon\mu}\ell$, s is the complex frequency, $T_n(\xi_o,q)$ is expressed in terms of radial spheroidal functions, $\Theta_n(\eta_o,q)$ in terms of angular spheroidal functions and integral of the applied voltage across the gap, and $N_n(q)$ is a normalization constant. Let

$$Y(\xi_o,\eta_o,q)=Y(\xi_o,\eta_o,o)+[Y(\xi_o,\eta_o,q)-Y(\xi_o,\eta_o,o)]=j\omega C_s(\xi_o,\eta_o)+Y_d(\xi_o,\eta_o,q)$$
$$(2)$$

Examination of Y_d shows that it is uniformly convergent with respect to η_o, being majorate by the series $(q/n)^2$. Only few terms of it will be needed for antennas of reasonable dimensions in terms of the wavelength, and the series can be computed for $\eta=o$ (δ-gap).

The series $C_s(\xi_o,\eta_o)$ needs a more sharp analysis, whose result is the following

$$C_s(\xi_o,\eta_o)=C_s'(\xi_o,o)+2\varepsilon b\left[\ell n\frac{4}{\eta_o}+\frac{1}{2}\int_o^2\left[\frac{\phi(t)}{t}-1\right]dt-\frac{\pi\eta_o}{4}+O(\eta_o^2\ell n\;\eta_o)\right] \quad (3)$$

where $\phi(t)$ is the normalized voltage distribution across the gap, equal to zero at its lower rim. Note that the integral appearing in (3) equals 0 or 0.345, according to an assumed field constant across, or satisfying the proper edge conditions at the rims of the gap. The value C_s' can be easily computed for any ξ_o. In particular, for (i) linear and (ii) spherical antennas, we have

(i) $C_s' \sim \pi\varepsilon a/\left[\ell n\frac{2a}{b}-1\right]$;   (ii) $C_s'=0$ (4)

When the integral in (3) is negligible with respect other terms, C_s becomes independent of the field distribution across the gap, up to terms of order η_o included. Since this is also the case for Y_d, the above is recognized as the condition under which an input admittance Y specific of the antenna can be defined.

3. Equivalent network. Let us expand the numerator and the denominator of y_n in a series power of s near s=o:

$$y_n=\frac{\pi}{2}\sqrt{\frac{\varepsilon}{\mu}}\;s\sum_{o_p}^\infty \alpha_p^n(\xi_o)\;s^p/\sum_{o_p}^\infty \beta_p^n(\xi_o)\;s^p \qquad (5)$$

where α_p^n, β_p^n are coefficients which can be obtained starting from [7]. The radius of convergence of (5) is unfortunately unknown, increasing, however, with increasing n [7]. Expanding (5) in a continuous fraction for s=o, and taking into account the results of Sect.2, an equivalent lumped network for Y can be sinthesized. For $\omega|\sqrt{\varepsilon\mu}|a\leq2$, the network of fig.1 is obtained, where the box represents a reciprocal gyrator, and the constants y_o^2,ℓ,c,g are known in terms of α's and β's. In particular for (i) linear and (ii) spherical antennas we have

(i) $y_o^2=\frac{1}{4}\left[\ell n\frac{2a}{b}-1\right]^2$; $\ell=22\left[\ell n\frac{2a}{b}-\frac{17}{22}\right]/55$; $c=(2\left[\ell n\frac{2a}{b}-1\right])^{-1}-$

$-2/55\ell$; $g=4/9\ell^2$;

(ii) $y_o^2=\ell=c=g=1$

Fig.2 represent a comparison between our theory (dots)and King-Middleton second order results,while Fig.3 shows a comparison with experiments (dots and triangles) relative to an antenna immersed in water [8].

4. Input response. The steady-state input response of the antenna is now completely known. Note that the equi
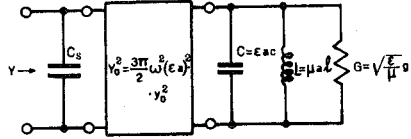
Fig.1. Equivalent network for the input admittance of the antenna.

valent circuit for Y is consistent with scaling properties of the antennas [9]. Furthermore, each network component is given as the product of two terms, one depending on the geometry of the antenna the other on the environment. This is a very useful property in diagnosis or probing applications.

The transient input response i(t) can be inferred as the inverse Lapace transform of Y(s). For a non-dispersive environment, the response is expressed in terms of pole contributions only. Resonant angular frequency ω_e and radiation damping α_o are given by

$$\omega_e^2=(1/\varepsilon\mu\ell ca^2)-\alpha_o^2 \quad ; \quad \alpha_o=g/2c\sqrt{\varepsilon\mu}a \qquad (6)$$

For a dispersive environment, pole locations are altered: specific results have been obtained for some practical cases. Furthermore,new branch-cut contributions appear, these last decaying as $t^{-3/2}$, for t→∞,
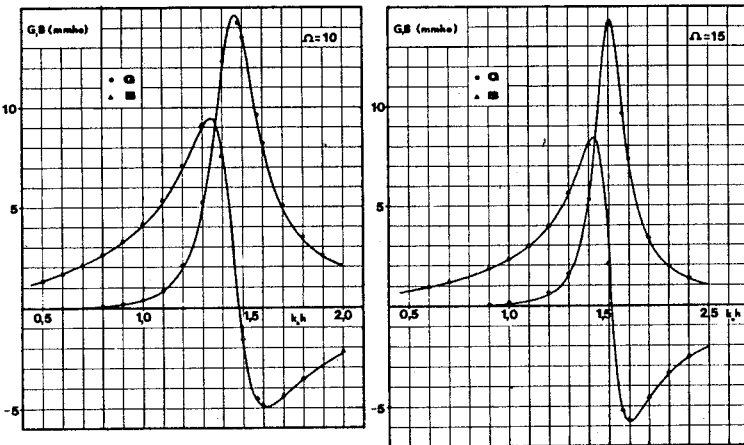
Fig.2. Input admittance of thin antenna: comparison with King-Middleton second order theory.

- 4 -
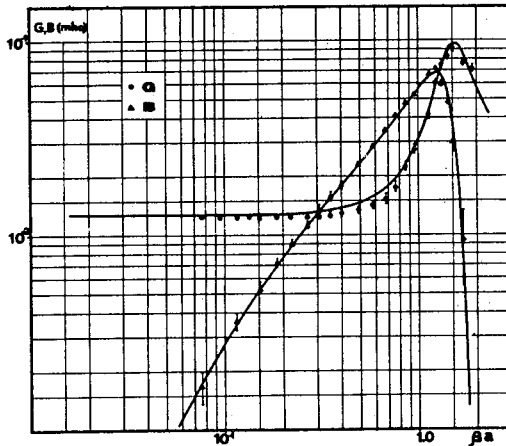
Fig.3. Spheroidal antenna: comparison between
experimental and theoretical results.

when the antenna environment is a conductive medium, or a collision-
less plasma. These are therefore the dominant contributions at large
observation times, and their physical role can be inferred in terms
of reversible and irreversible parts of power [10].

5. References

1. R.W.P.King, C.W.Harrison (1969 MIT Press).
2. J.A.Stratton, L.J.Chu (1940 Appl.Phys.12, p.236 and p.241).
3. J.R.Wait (1964 Radio Science 68D, p.1127 and p.1137).
4. G.Franceschetti, O.Bucci, G.Latmiral (1970 Radio Science 5, p.1475).
5. G.Franceschetti (1970 Proc.AGARD Symp. EM of Sea, 7, p.1)
6. G.Franceschetti (1973 Radio Science, in print).
7. C.Flammer (1957 Stanford Un. Press, p.27 and 90).
8. O.M.Bucci, A.de Bonitatibus, V.G.Vaccaro (submitted to IEE Proceedings)
9. G.A.Deshamps (1967 IEEE Trans. AP-10, p.648).
10. K.S.H.Lee, C.H.Papas (1965 Radio Science 69D, p.1313).

APPROXIMATE SOLUTION OF A VERTICAL ELEMENTARY
DIPOLE OVER A CONDUCTING HALF-SPACE

Richard J. Fisher and David C. Chang
Department of Electrical Engineering
University of Colorado
Boulder, Colorado 80302

The electromagnetic field of a vertical electric dipole of current moment $I_0 dz$ located a distance z_0 above a homogeneous half-space of conductivity σ and dielectric constant ϵ can be determined from a Hertz vector Π which has only a z component. The solution for the time harmonic case is given by

$$\Pi_z(\rho,z) = \left(\frac{i\zeta_0 I_0 dz}{4\pi}\right) K(z,z_0,\rho)$$

where the response function K consists of a direct contribution from the source, K_1, and a scattering contribution from the presence of the conducting half-space, K_2:

$$K = K_1 + K_2$$

where

$$K_1(z,z_0,\rho) = \frac{e^{ik_0 [(z - z_0)^2 + \rho^2]^{1/2}}}{k_0 [(z - z_0)^2 + \rho^2]^{1/2}}$$

$$K_2(z,z_0,\rho) = i \int_0^\infty R(\alpha) e^{ik_0 (z + z_0)(1 - \alpha^2)^{1/2}} J_0(k_0 \rho\alpha) \frac{\alpha d\alpha}{(1 - \alpha^2)^{1/2}} \qquad (1)$$

and

$$R(\alpha) = [n^2(1 - \alpha^2)^{1/2} - (n^2 - \alpha^2)^{1/2}] [n^2(1 - \alpha^2)^{1/2} + (n^2 - \alpha^2)^{1/2}]^{-1}.$$

Here n is the complex index of refraction, ζ_0 is the intrinsic impedance of free space wave number, $\bar{a}_z$ is the unit vector in the z direction, and a time dependence of $e^{-i\omega t}$ is assumed.

Under the conditions that $n(z + z_0) \gg 4$ or $n\rho \gg 50$ or both, the assumption that $(n^2 - \alpha^2)^{1/2} \approx 1$ in $R(\alpha)$ leads to an approximate expression for K_2 which is valid over a wide frequency range. Incorporating this expression yields

$$K(d,e) = K_1 + K_2 = \frac{e^{i\sqrt{(z-z_0)^2+\rho^2}}}{\sqrt{(z-z_0)^2+\rho^2}} + \frac{e^{i\sqrt{d^2+\rho^2}}}{\sqrt{d^2+\rho^2}} - \frac{\pi}{n} e^{-d/n} H_0^{(1)}(w_0',\Omega) \quad (2)$$

where $d = z + z_0$, $w_0 = (d + \sqrt{d^2 + \rho^2/n})/(\rho\sqrt{1 - 1/n^2})$, and $\Omega = \rho\sqrt{1 - 1/n^2}$.
$H_0^{(1)}(w_0',\Omega)$ is an incomplete Hankel function defined by

$$H_0^{(1)}(a,\Omega) = -\frac{i2}{\pi} \int_a^\infty \frac{e^{i\Omega\sqrt{w^2+1}}}{\sqrt{w^2+1}} dw .$$

Equation (2) is valid for any combination of ρ and d. However, provided that $d/\rho \ll 1$ and $|n|^2 \gg 1$, an expression for the incomplete Hankel function may be obtained in terms of the Fresnel integral defined by

$$F(\tau_0) = \int_0^{\tau_0} e^{i\pi t^2/2} dt$$

and the complete Hankel function $H_0^{(1)}(\Omega)$. Allowing $\tau_0 = (2/\pi)\left[\sqrt{d^2 + \rho^2} + d/n - \Omega\right]^{1/2}$ yields from (1)

$$K(d,\rho) \doteq \frac{e^{i\sqrt{(z-z_0)^2+\rho^2}}}{\sqrt{(z-z_0)^2+\rho^2}} + \frac{e^{i\sqrt{d^2+\rho^2}}}{\sqrt{d^2+\rho^2}} - \frac{\pi}{n} e^{-id/n} \left[H_0^{(1)}(\Omega) + \frac{i2}{\sqrt{\Omega\pi}} e^{i\Omega} F(\tau_0) \right],$$
$$(3)$$

a form which is readily evaluated on a computer. It can be shown that (2) and (3) have a wide range of applicability than the so-called Sommerfeld-Norton attenuation function. Also, it can be used to obtain other asymptotic formula in various regions . Curves comparing an exact numerical integration of (1) with the results obtained using the approximation contained in the last three terms of (3) indicates that, in the case of frequency = 1 MHz and conductivity = 10^{-3} mhos/m, the agreement in magnitude of K is virtually complete for a horizontal observation distance of one free-space wavelength. Error in the phase of the K-function is nowhere greater than 4% for source height up to 0. 6 wavelength. For a larger source height, (2) instead of (3) is needed. The approximate formula is then used to compute the variation of K as a function of operating frequency in Figures 1 and 2 for a fixed observation distance of 30 Km. Compared with the solution obtained from a perfect image theory, the contribution from the groundwave term appears to be very significant in providing the phase information. Detailed discussion on the behavior of the electromagnetic fields will be presented.

Figure 1

$\sigma = 10^{-3}$ mho m^{-1}; $\epsilon_r = 10$; $\rho = 30$km
1. $2K_1$ (perfect image theory); h = 500m
2. $K_1 + K_2$ (ground loss corrected); h = 500m
3. $2K_1$; h = 3500m
4. $K_1 + K_2$; h = 3500m

FREQUENCY (HZ)

Figure 2

449
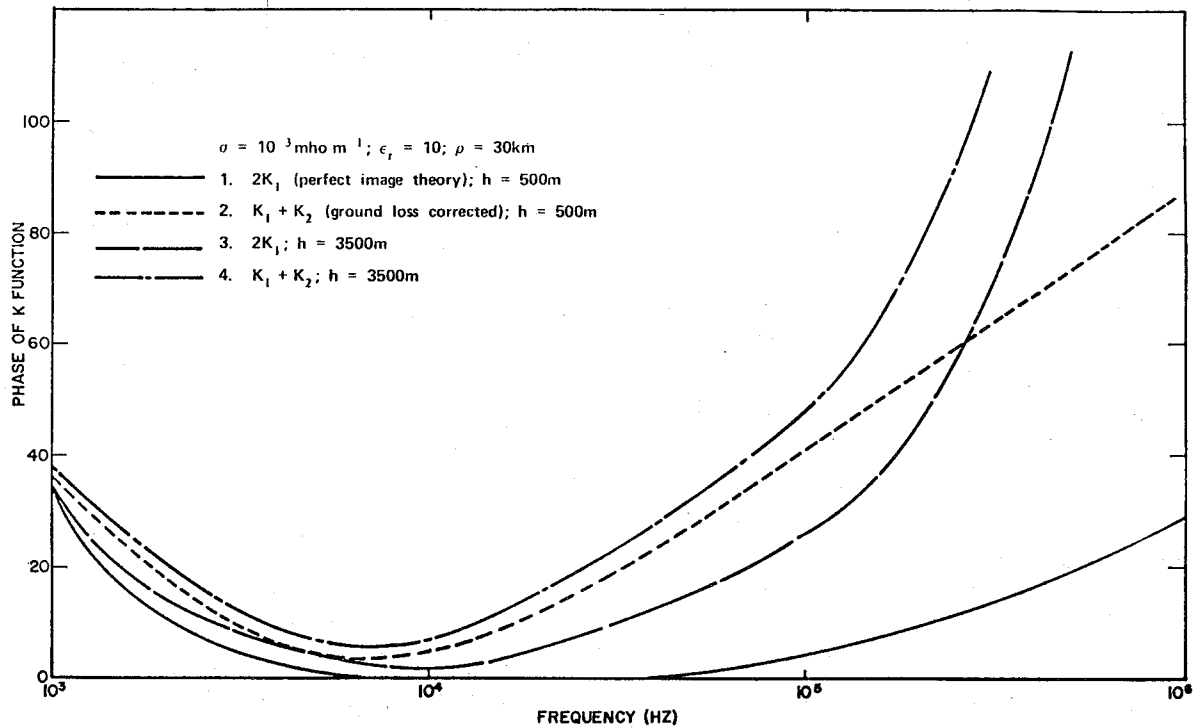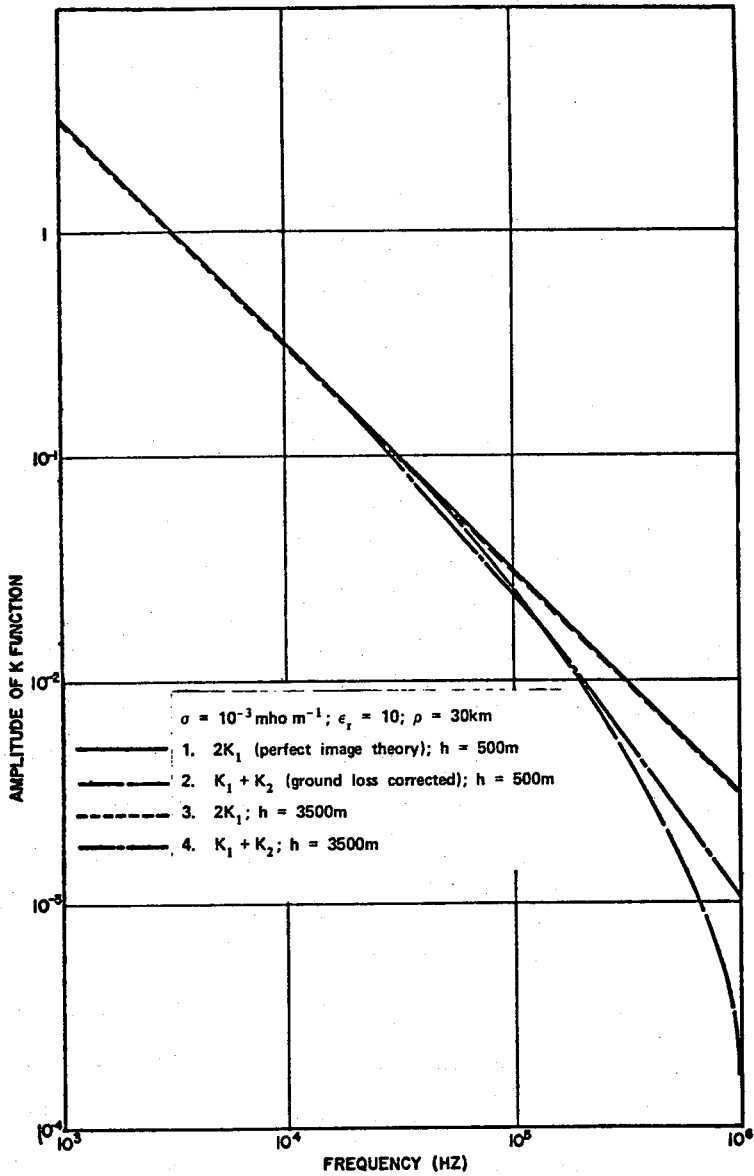
DIFFERENTIAL-GEOMETRY SCALING METHOD

FOR ELECTROMAGNETIC FIELD AND

ITS APPLICATIONS TO COAXIAL WAVEGUIDE JUNCTIONS[*]

Tse Chin Mo and C. H. Papas

Electrical Engineering Department
California Institute of Technology
Pasadena, California

and

Carl E. Baum

Air Force Weapons Laboratory
Kirtland Air Force Base
New Mexico   87117

Summary

It is well-known that in mechanics and fluid dynamics one can transform or scale one problem and its solution to create a whole class of equivalent problems and their solutions[1]. Different problems and their solution behaviors of one equivalent class may look very different, but among them there are properties they share. The essence of such a scaling is to get appropriate dimensionless parameters that are common to them all.

However, in electromagnetic (EM) theory the nature and application of such a similar scaling method[2], except for conformal mappings of static fields, has not been given extensive attention. Only a few articles have recently been devoted to it[3]. The purpose of this work is to thoroughly investigate and develop the nature, the limitation, the usefulness, and the application of such a scaling method for EM theory by using differential-geometry approach.

We first explore and develop the general framework of the method that can carry an EM problem P of complicated geometry into an equivalent problem P' of simple Cartesian or other simple geometry with its accompanying transformations for medium, geometry, source, and field. The advantage of such a procedure is, hopefully, to make the complexities of the geometry and of the medium "cancel" each other in such a way that the resulting problem is simple and solvable. Then we obtain various conditions and limitations of the method as imposed by special choices of geometry, medium, and field modes. These include time independent scaling, orthogonal coordinates, diagonal media, and especially emphasized coaxial systems.

We then present an application of this differential geometry scaling method to two specific problems. In one a perfect matching section between a cylindrical and a conical coaxial waveguide is obtained by appropriately loading the section with inhomogeneous μ and ε, and all relevant electromagnetic quantities and geometrical boundaries are tabulated. In the other a perfect matching section between two cylindrical coaxial waveguides is found with the appropriately shaped matching section loaded by inhomogeneous ε, anisotropic conductivity $\underline{\sigma}$, and constant μ. All results are tabulated and plotted.

Finally we noticed that the parallel-plate Cartesian scaled version of the fixed μ matching may give the fixed μ matchings of other geometrical shapes by permitting some variances in its P'→P scaling procedure. This aforesaid aspect, the criterions for a continuous tapered matching section, and the non-orthogonal scaling which can make use of the Brewster angle transmission in a natural way are discussed for work of future interest.

Footnotes and References

*   Part of this work has been published by T. C. Mo, C. H. Papas, and

C. E. Baum in the J. of Math. Phys. <u>14</u>, 479 (April 1973). Also this

report is mostly based on EMP Sensor and Simulation Note 169, (March

1973) by these same authors. Also this work was partly supported by

the Air Force Weapons Laboratory.

1. See, e.g., L. D. Landau and E. M. Lifshitz, <u>Fluid Dynamics</u>, Pergamon

Press (1959), Secs. 19, 53, 118, 119; also, <u>Mechanics</u>, Pergamon Press

(1960), Sec. 10; for an earlier example of such transforms, see E. J.

Routh, Proc. London Math. Soc. <u>12</u>, 73-89 (1881).

2. Some different examples of the electromagnetic scaling can be found

in the following. For conformal mapped waveguide see, e.g., F. E.

Borgnis and C. H. Papas, in <u>Handbuch der Physik</u>, Springer-Verlag,

Berlin (1958) <u>16</u>, 358; also F. J. Tischer, (Correspondence) Proc. IEEE

<u>51</u>, 1050 (July 1963), and (Correspondence) Proc. IEEE <u>53</u>, 168 (Feb.

1965); also J. A. Stratton, <u>Electromagnetic Theory</u>, McGraw-Hill (1941),

217; also P. Krasnooshkin, J. Phys. USSR <u>10</u>, 434 (1946); for a

frequency scaling of reflection see, J. H. Davis and J. R. Cogdell,

IEEE Trans. <u>AP-19</u>, 58 (Jan. 1971); for a scaling for reducing

constantly moving uniform simple media, see R. J. Pogorzelski, IEEE

Trans. <u>AP-19</u>, (Communication) 455 (May 1971).

3. C. E. Baum, EMP Sensor and Simulation note <u>32</u> (Jan. 1967) and note <u>64</u>

(1968); see also P. L. Uslenghi, IEEE Trans. <u>AP-17</u> (Communication),

644 (Sept. 1969).

TOWARD "ANALYTIC" CONTINUATION OF
ELECTROMAGNETIC FIELDS

Z. A. Typaldos (deceased) and R. J. Pogorzelski
School of Engineering and Applied Science
Electrical Sciences and Engineering Department
University of California
Los Angeles, California 90024

The elegance and power of complex variable theory in electromagnetics is well known. (We refer here to the direct applications in potential theory rather than integral transforms.) A current application is to scattering of electromagnetic waves from a grating.[1] However, many, if not all, of the existing techniques are limited to two dimensional problems. In view of the fact that electrodynamics is inherently four dimensional (reducing to three only upon assumption of a particular dependence on one of the variables) this limitation is a serious one indeed. What is obviously required if we are to proceed much further is some sort of "analytic theory" in four dimensions. Unfortunately, such a theory in the full complex variable sense is known to be impossible. However, in a limited sense a four dimensional "analytic theory" (perhaps better termed a regularity theory) already exists. This theory was developed by Rudolph Fueter and his students and colleagues[2-9] in the 1930's. We have applied this formalism to electrodynamics.

We have found that the regularity (analyticity) conditions; i.e., the four dimensional analog of the Cauchy-Riemann conditions of complex variable theory, are Maxwell's equations of electrodynamics. Some familiar and some rather curious solutions of these equations have been obtained by means of the Fueter formalism. Among the familiar are the field of a point charge, the electrostatic multipole fields, and the field of a time harmonic point dipole. A more exotic result is a four dimensional analog of the simple pole singularity of complex variable theory. Associated with this is a whole set of four dimensional multipole fields.

We suggest that Maxwell's electrodynamics is in reality a limited four dimensional analytic theory. Thought of in this manner the theory could easily possess an analog of the analytic continuation of complex variable theory.

Session 49 EM Theory

References

1.M. Neviere, M. Cadilhac, and R. Petit (1973 IEEE
   Trans. AP-21, p. 37).

2.R. Fueter (1932 Comm. Math. Helv. 4, p. 9).

3.R. Fueter (1935 Comm. Math. Helv. 7, p. 307).

4.R. Fueter (1935 Comm. Math. Helv. 8, p. 371).

5.R. Fueter (1936 Comm. Math. Helv. 9, p. 320).

6.B. Schuler (1938 Comm. Math. Helv. 10, p. 327).

7.M. Eichler (1940 Comm. Math. Helv. 12, p. 212).

8.H. Häfeli (1944 Comm. Math. Helv. 17, p. 135).

9.A. Rose (1950 Comm. Math. Helv. 24, p. 135).

ELECTRICAL CHARACTERISTICS OF A THIN BICONICAL ANTENNA OVER A CONDUCTING HALF SPACE

P. DEGAUQUE, J. FONTAINE and R. GABILLARD
Electronics Department, University of LILLE
LILLE, FRANCE

Previous theoretical works about the determination of the electrical characteristics of biconical antennas supposed that the surrounding medium is infinite in extent or, at least, that this medium has a revolution symetry. Such assumptions are valid if the antenna is situated at a sufficiently great distance from an interface in order to neglect its influence. We have studied the general case of a thin biconical antenna which could be located near the air-ground interface. In a recent paper[1] we have supposed that the antenna is situated in the ground, in a low-loss encapsulant. We present here the case of a vertical antenna above the earth.

The perfectly conducting biconical antenna of length 2a and cone angle θ_0 defines a spherical region (1) of radius a, at a distance h from the air-ground interface, as shown in fig.1.a. The regions(1) and (2) correspond to the air, and the medium (3) to the earth.
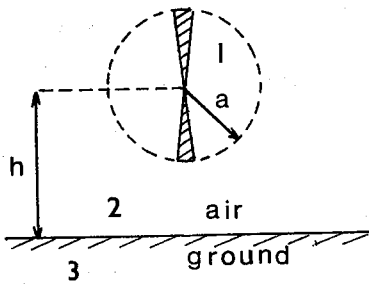
fig.1.a.
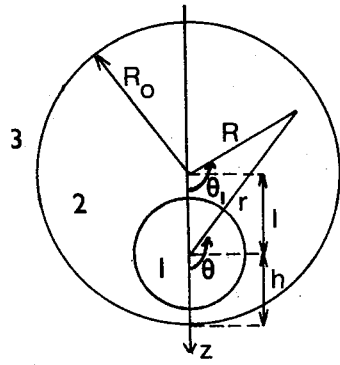
fig.1.b.

To find the boundary conditions between the different media, we use a method investigated by D'JAKONOV[2], by treating the problem of two non concentric spheres. If R_0 is the radius of the outer sphere (fig.1.b.), the result for a plane interface is obtained by letting $R_0 \to \infty$ while holding h constant. Two systems of spherical coordinates are used. The first (r,θ,ϕ) is referred to the center of the internal sphere and the second (R,θ_1,ϕ) to the center of the external sphere. The centers are located on the z axis at a distance ℓ from each other. The propagation constant γ_i and the wave impedance η_i are defined by :
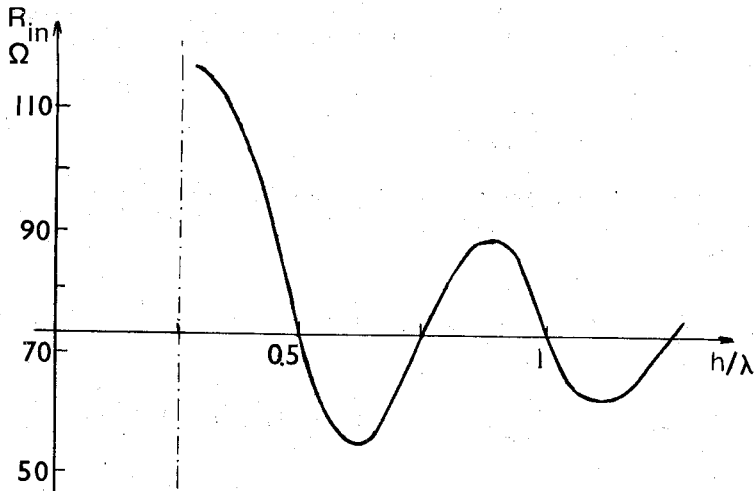
fig.3.

Fig.3. shows the variation of the input resistance, for a half
wave antenna, as a function of the ratio h/λ. In this last case,
we have supposed that the ground is a perfect conductor. From these
curves, we see that the magnitude of the total current is affected
by the presence of the ground even at a distance of a wavelength.

REFERENCES

1. P. DEGAUQUE, J. FONTAINE and R. GABILLARD (1972, Electronics
letters 8, n°25)
2. B.P. D'JAKONOV (1959 Izv.Geophys.Ser., pp.1579-1590)
3. J.G. NEGI (1963 Geophysics 28, pp.665-668)
4. J.R. WAIT (1969 in Antenna theory ed. by COLLIN and ZUCKER,
pp.483-522)

Introduction to SEM

Carl E. Baum
Air Force Weapons Laboratory
Kirtland AFB, New Mexico 87117

I. Introduction

The Singularity Expansion Method (SEM) historically is an outgrowth of an experimental observation concerning the transient response of a wide variety of complicated objects.[1] The observation of damped sinusoids and other apparently simple waveforms in the response implied pole terms in the response considered in the complex ·frequency or s plane. This led to a consideration of the response of various, types of objects in the s plane and the description of the response in terms of the singularities of the analytic functions of s describing the response (hence the name of the method). While in general one can have poles, branch cuts, and essential singularities in the finite s plane as well as entire functions (singularities at infinity) the important singularities are limited to certain kinds depending on the type of problem at hand. Particularly in the important case of pole singularities[1,2] the singularity expansion is equally simple in form in frequency and time domains without needing numerical Fourier transforms; the same expansion coefficients are used with either poles or damped sinusoids. While SEM has been developed to treat electromagnetic problems the formalism can be applied directly to other linear problems such as acoustics. The basic concept from analytic function theory can perhaps be applied to some nonlinear problems as well.

II. Expansion of Currents and Charge Densities

For some objects solutions can be obtained in terms of analytic functions from which a singularity expansion can be obtained. For more general objects of finite size one follows the procedure for a delta function excitation in time (Laplace transformed) with only first order poles included here as[1,8]

$$\langle \overset{\leftrightarrow}{\Gamma}; \vec{U} \rangle = \vec{I} \text{ (integral equation)}, \quad \overset{\approx}{U} = \sum_{\alpha} \tilde{\eta}_{\alpha} \vec{v}_{\alpha} (s - s_{\alpha})^{-1} + \text{possible entire function}$$

$$\langle \overset{\leftrightarrow}{\Gamma}_{o}; \vec{v} \rangle = \overset{\rightarrow}{0}, \quad \langle \overset{\rightarrow}{\mu}; \overset{\leftrightarrow}{\Gamma}_{o} \rangle \text{ (natural frequencies, modes, and coupling vectors)}$$

$$\overset{\approx}{\Gamma} = \sum_{n=o}^{\infty} (s - s_{\alpha})^{n} \overset{\rightarrow}{\Gamma}_{n}, \quad \overset{\approx}{U} = \tilde{\eta} \vec{v}(s - s_{\alpha})^{-1} + \overset{\approx}{U}', \quad \overset{\approx}{I} + \sum_{n=o}^{\infty} (s - s_{\alpha})^{n} \vec{I}_{n} \text{ (near } s_{\alpha})$$

$$\tilde{\eta}(s_{\alpha}) = \frac{\langle \overset{\rightarrow}{\mu}; \vec{I}_{o} \rangle}{\langle \overset{\rightarrow}{\mu}; \overset{\leftrightarrow}{\Gamma}_{1}; \vec{v} \rangle} \text{ (coupling coefficient at } s_{\alpha})$$

There are two presently used forms of coupling coefficients

459

$$\tilde{\eta}_\alpha(s) = e^{(s_\alpha - s)t'} \frac{\langle \vec{\mu}; \vec{I}_o \rangle}{\langle \vec{\mu}; \vec{\Gamma}_1; \vec{\nu} \rangle}$$ Class 1 coupling coefficient special-
ized to exponential form with turn on
time t'

$$\tilde{\eta}_\alpha(s) = \frac{\langle \vec{\mu}; \vec{I}(s) \rangle}{\langle \vec{\mu}; \vec{\Gamma}_1; \vec{\nu} \rangle}$$ Class 2 coupling coefficient (convolution form)

The charge density response is found from

$$\nu_\alpha^{(\rho)} = -(ca_\alpha/s_\alpha) \nabla \cdot \vec{\nu}$$

with an additional coefficient of $(a_\alpha c)^{-1}$ in the terms of the nor-
malized response. For more general excitation waveforms f(t) the
Laplace transform $\tilde{f}(s)$ is used to define object and waveform parts
of the response as

$$\vec{\tilde{V}} = \tilde{f}\vec{\tilde{U}} = \vec{\tilde{V}}_o + \vec{\tilde{V}}_w + \text{possible entire function}$$

$$\vec{\tilde{V}}_o = \sum_\alpha \tilde{f}(s_\alpha)\tilde{\eta}_\alpha \vec{\nu}_\alpha(s - s_\alpha) , \quad \vec{\tilde{V}}_w = \sum \text{terms from singularities of } \tilde{f}(s)$$

Note that the different terms in the expansion depend on different
variables of the problem of interest so that the response factors
somewhat.

III. Expansion of Radiated or Scattered Fields

Having calculated the current density (or surface current density
or line current) one can then calculate the potentials and fields
using the Green's functions

$$\tilde{G}_o = \frac{e^{-\gamma|\vec{r}-\vec{r}'|}}{4\pi|\vec{r}-\vec{r}'|} , \quad \vec{\tilde{G}}_o = \left[\vec{\tilde{I}} - \frac{1}{\gamma^2}\nabla\nabla\right]\tilde{G}_o , \quad \gamma \equiv \frac{s}{c}$$

and the far field forms

$$\tilde{g}_{o_f} \equiv \lim_{r\to\infty} re^{\gamma r}\tilde{G}_o = \frac{e^{\gamma \vec{e}_r \cdot \vec{r}'}}{4\pi} , \quad \vec{\tilde{g}}_{o_f} \equiv \lim_{r\to\infty} re^{\gamma r}\vec{\tilde{G}}_o = \tilde{g}_{o_f}\left[\vec{\tilde{I}} - \vec{e}_R\vec{e}_R\right]$$

From these one can have a singularity expansion of the far field,
for example, in the form of a normalized delta function response
as

$$\vec{\tilde{U}}_f(r\vec{E}) = \sum_\alpha \tilde{\eta}_\alpha \frac{z_o}{c_\alpha\gamma_\alpha} \ell_\alpha \vec{\nu}_{f_\alpha}^{(\vec{E})} (s - s_\alpha)^{-1} , \quad \vec{\nu}_{f_\alpha}^{(\vec{E})} = -\frac{c_\alpha\gamma_\alpha^2}{\ell_\alpha}\langle\vec{\tilde{g}}_{o_f}(s_\alpha);\vec{\nu}_\alpha^{(\vec{J})}\rangle$$

There are other forms of far field expansion in which s is in-
cluded with the natural mode (similar to the variation among the
classes of coupling coefficient).

IV. Problems and Extensions

While SEM is clearly a very useful way to consider the electromagnetic response of various objects there are still many questions concerning the relative efficiency of various SEM forms and extensions of the theory to more powerful results. The coupling coefficients have various forms with different rates of convergence. In some cases second and perhaps higher order poles enter the expansion. Efficient procedures for evaluating branch cuts integrals associated with infinite objects and the presence of lossy semi infinite media are needed. By relating the natural modes to other forms of modal expansions one may find more efficient ways to evaluate other kinds of modes and provide other useful relations among the natural modes. SEM expansion forms can be used to analyze experimental data on the response of complicated objects by decomposing it into the SEM quantities. It seems that the more we find the more questions are naturally raised.

References (Bibliography)

1. Carl E. Baum (Dec. 1971, IN 88, On the Singularity Expansion Method for the Solution of Electromagnetic Interaction Problems) (also 1972 Spring URSI Meeting).

2. Lennart Marin and R. W. Latham (Jan. 1972, IN 92, Analytical Properties of the Field Scattered by a Perfectly Conducting, Finite Body) (also May 1972 Proc. IEEE pp. 640, 641 for very abbreviated version).

3. S. W. Lee and B. Leung (Feb. 1972, IN 96, The Natural Resonance Frequency of a Thin Cylinder and Its Application to EMP Studies).

4. F. M. Tesche (April 1972, IN 102, On the Singularity Expansion Method as Applied to Electromagnetic Scattering from Thin Wires) (also 1973 IEEE Trans. AP-21 no. 1).

5. Joe P. Martinez, Zoe Linda Pine, and F. M. Tesche (May 1972, IN 112, Numerical Results of the Singularity Expansion Method as Applied to a Plane Wave Incident on a Perfectly Conducting Sphere).

6. Lennart Marin (June 1972, IN 116, Application of the Singularity Expansion Method to Scattering from Imperfectly Conducting Bodies and Perfectly Conducting Bodies within a Parallel Plate Region).

7. Lennart Marin (Aug. 1972, IN 119, Natural-Mode Representation of Transient Scattering from Rotationally Symmetric, Perfectly Conducting Bodies and Numerical Results for a Prolate Spheroid).

8. Carl E. Baum (Oct. 1972, IN 129, On the Singularity Expansion Method for the Case of First Order Poles).

9. T. T. Crow, B. D. Graves, and C. D. Taylor (Dec. 1972, MaN 27, Numerical Techniques Useful in the Singularity Expansion Method as Applied to Electromagnetic Interaction Problems).

10. Lennart Marin (Mar. 1973, SSN 173, Transient Electromagnetic Properties of Two Parallel Wires).

11. C. D. Taylor (1973, IN 134, On the Singularity Expansion Method Applied to Aperture Penetration: Part I Theory).

12. F. M. Tesche (SSN to be published, Application of the Singu-
     larity Expansion Method to the Analysis of Impedance Loaded
     Linear Antennas).
13. Carl E. Baum (SSN to be published, Singularity Expansion of
     Electromagnetic Fields and Potentials Radiated from Antennas
     or Scattered from Objects in Free Space).
14. Lennart Marin (note to be published on fat finite length cyl-
     inder near a ground plane).
15. T. H. Schumpert (note to be published on thin wire near a
     ground plane).
16. D. R. Wilton (note to be published on L-wire response).
17. R. Blackburn and D. R. Wilton (note to be published on toroid
     response).
18. P. R. Barnes (note to be published on cylindrical antenna re-
     sponse with loading).
19. C. D. Taylor and T. Crow (note to be published on crossed
     wire response).
20. J. Lytle (note to be published on prolate spheroid response).

\

NUMERICAL ASPECTS OF THE APPLICATION OF SEM TO ELECTROMAGNETIC BOUNDARY VALUE PROBLEMS

F. M. Tesche

The Dikewood Corporation

Albuquerque, New Mexico 87106

I. Introduction

The Singularity Expansion Method (SEM) which was proposed by Baum,[1] has been employed by a number of other investigators[2,3,4] for the purpose of obtaining the time domain solution to various electromagnetic boundary value problems. Although many different structures have been considered by using SEM, the numerical difficulties associated with obtaining the solutions in each case are very similar. This paper discusses some general aspects of the numerical implementation of SEM along with an overview of the work to date in this field.

II. Theory

This technique describes the scattering or radiating properties of an obstacle in terms of its exterior natural resonances which, in the Laplace transform domain, correspond to poles of a response function in the complex s plane. At each complex pole, it is possible to define a natural mode and a coupling vector which form a matrix of residues. The time domain response of the structure can be determined as in classical circuit theory by using Cauchy's integral theorem to perform the inverse Laplace transform.

Following Baum's notation, the current $\bar{J}$ induced on the surface of a conducting obstacle due to an incident field (scattering) or an impressed field (antenna) is the solution to an integral equation

$$\int_S \bar{\bar{K}}(\bar{r}, \bar{r}'; s) \cdot \bar{J}(\bar{r}', s) dS' = \bar{F}(\bar{r}, s) , \tag{1}$$

where F is the incident field which excites the currents on the body. This represents the H field or E field equation, depending upon the application. This equation is conveniently represented as

$$< \bar{\bar{K}}; \bar{J} > = \bar{F} \tag{2}$$

The natural frequencies, s_α, are those such that Eq. (2) has a nontrivial solution for $\bar{F} = 0$. This solution, denoted by $\bar{\nu}_\alpha$, and referred to as the natural mode, satisfies the equation

$$< \bar{\bar{K}}_\alpha ; \bar{\nu}_\alpha > = \bar{0} \tag{3}$$

Another vector $\bar{\mu}_\alpha$ which satisfies

$$< \bar{\mu}_\alpha ; \bar{\bar{K}}_\alpha > = \bar{0} \tag{4}$$

can be defined, and is called the coupling vector. Using these definitions, the obstacle current may be represented as

$$\bar{J}(\bar{r},s) = \sum_\alpha \frac{\eta_\alpha \, \bar{\nu}_\alpha(\bar{r})}{(s - s_\alpha)} + \text{possible entire function of s} \tag{5}$$

where the coupling coefficient η_α has the definition

$$\eta_\alpha = \frac{< \bar{\mu}_\alpha ; \bar{F}_\alpha >}{<\bar{\mu}_\alpha ; \bar{\bar{K}}_{1_\alpha} ; \bar{\nu}_\alpha >} \tag{6}$$

with $\bar{F}_\alpha \equiv \bar{F}(\bar{r},s_\alpha)$ and $\bar{\bar{K}}_{1_\alpha} \equiv \frac{d}{ds}(\bar{\bar{K}})\Big|_{s=s_\alpha}$. Transforming this to the time domain yields

$$\bar{J}(\bar{r},t) = \sum_\alpha \eta_\alpha \bar{\nu}_\alpha(\bar{r}) \, U(\bar{r},t) \, e^{s_\alpha t} + \text{possible response at} \tag{7}$$
$$\text{poles of F(s)}$$

where $U(\bar{r},t)$ is the Heaviside function introduced to insure causality.

III. Numerical Results

The first application of SEM to particular structure was in a thin-wire scattering problem.[3] This has since been extended to the antenna problem. The poles, natural modes and coupling vectors are the same, with only the coupling coefficient being different. The poles for a thin-wire antenna of $a/h = .01$ $(\Omega = 10.59)$ is shown in Figure 2. Associated with each pole is a natural current mode as shown in Figure 3, and a natural far field mode, as in Figure 4. Figure 5(a) shows the time dependent currents at the input and at $z = \pm h/2$ as constructed by SEM. Figure 5(b) shows the linear charge density at $z = h$. The time domain radiated electric field is shown for various angles of observation in Figure 6.

References

1. Baum, C.E. (1972 Spring URSI Meeting, Washington, D.C.)

2. Shumpert, T. (1972 Fall FULMEN Meeting, Ann Arbor, Mich.)

3. Tesche, F.M. (1973 IEEE Trans. A.P., Vol. AP-21, No. 1, pp. 53-62)

4. Wilton, D.R. (1972 Fall URSI Meeting, Williamsburg, Va.)

radius a

z = h

Source of
V_o volts

z = -h
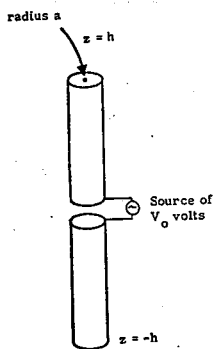
Fig. 1. Linear, center fed antenna.

× even
• odd

$\ell = 3$

$\ell = 2$

$\ell = 1$
layer

$\ell = 4$

$\frac{k_0 \ell}{c\pi}$

$\frac{g\ell}{c\pi}$
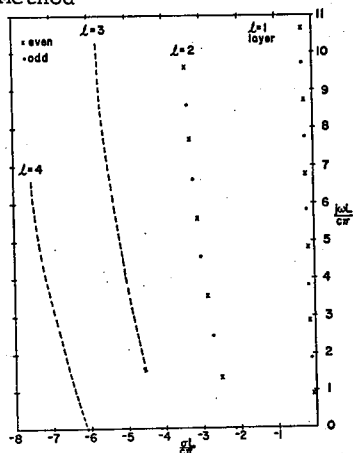
Fig. 2. Pole pattern for unloaded antenna of a/h = .01.

Real ($C_{\ell,n}(z)$)

n = 2

n = 1

n = 3

z/h

Img ($C_{\ell,n}(z)$)

n = 3

n = 2

n = 1

z/h
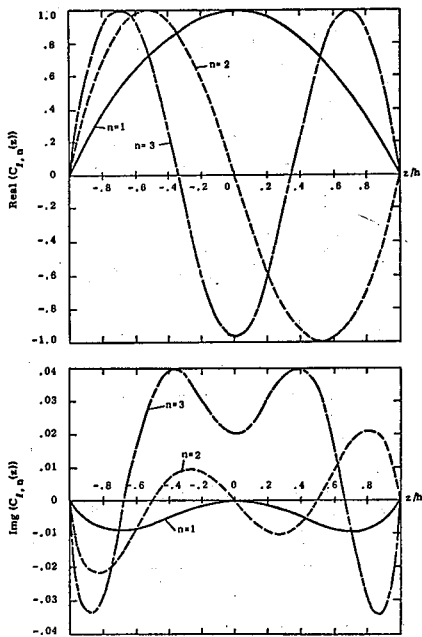
Fig. 3. Real and imaginary parts of normalized natural
modes for $\ell = 1$ layer.

n = 1

n = 2

θ

n = 3

n = 4
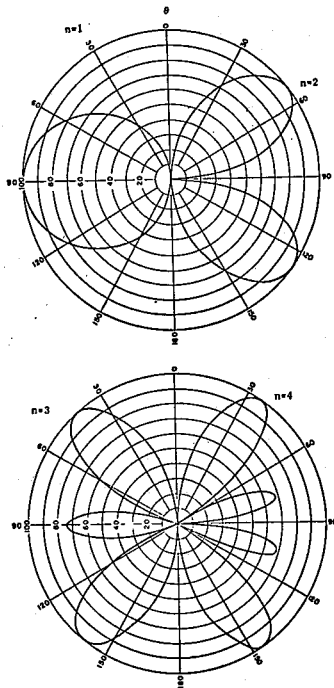
Fig. 4. Magnitudes of far field modes for $\ell = 1$ layer.

465

(a)

(b)
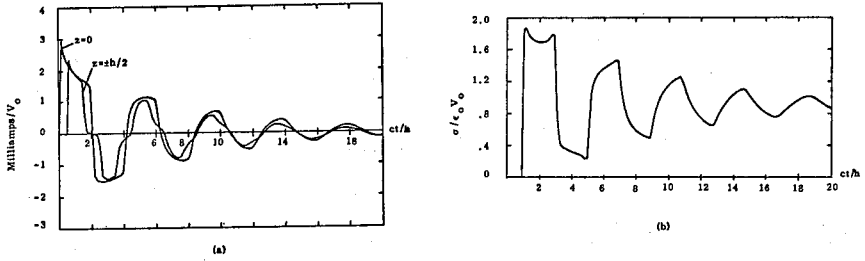
Fig. 5.   Current on antenna (a) and charge at end (b) in
time domain for step input.
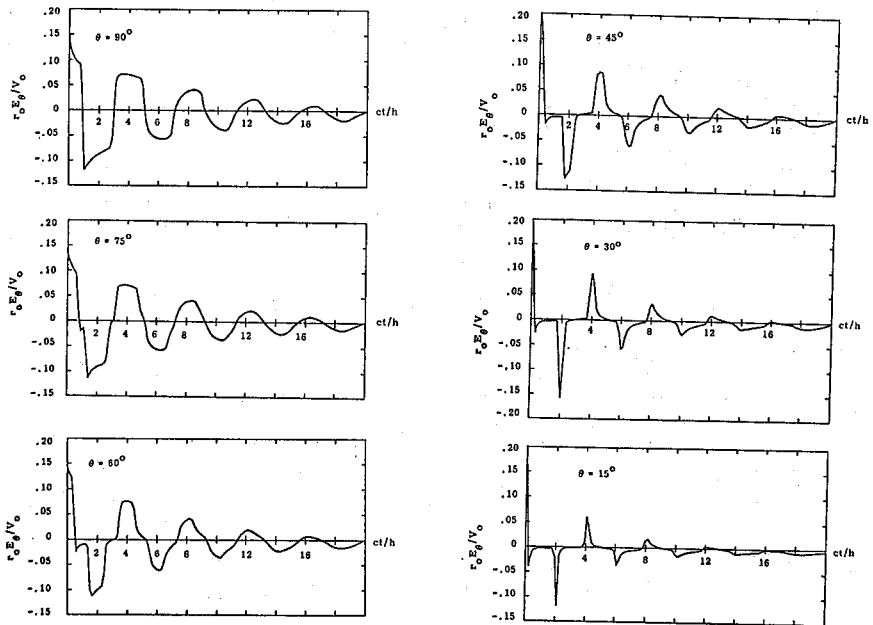
Fig. 6.   Radiated field in time domain for step input.

466

NATURAL-MODE REPRESENTATION OF TRANSIENT SCATTERED FIELDS

Lennart Marin
Dikewood Corporation, Westwood Research Branch
Los Angeles, California

The analytical properties in the complex frequency (s) plane of the field scattered from a perfectly conducting, finite body are investigated from an integral equation point of view. The investigation is based on the magnetic-field integral equation,

$$\left[\tfrac{1}{2}\underline{\underline{I}} - \underline{\underline{L}}(s)\right] \cdot \underline{j} = \underline{j}^{inc}, \qquad \underline{\underline{L}} \cdot \underline{j} \equiv \int_S \underline{n} \times (\nabla G \times \underline{j}) \, dS', \qquad (1)$$

$G(\underline{r},\underline{r}';s) = (4\pi|\underline{r} - \underline{r}'|)^{-1} \exp(-s|\underline{r} - \underline{r}'|/c)$, and the surface S is finite. From the Fredholm theory for the solution of integral equations of the second kind it is shown that the inverse operator $(\tfrac{1}{2}\underline{\underline{I}} - \underline{\underline{L}})^{-1}$ is a meromorphic operator-valued function of s. The locations of the poles of the inverse operator (the natural frequencies are given by those values of s (s_n) for which the homogeneous integral equation has a nontrivial solution $\underline{j}_n$,

$$\left[\tfrac{1}{2}\underline{\underline{I}} - \underline{\underline{L}}(s_n)\right] \cdot \underline{j}_n = 0, \qquad \left[\tfrac{1}{2}\underline{\underline{I}} - \underline{\underline{L}}^\dagger(s_n)\right] \cdot \underline{h}_n = 0 \qquad (2)$$

and $\underline{\underline{L}}^\dagger$ is the adjoint operator of $\underline{\underline{L}}$, $\underline{\underline{L}}^\dagger \cdot \underline{h} = -\int_S \nabla G^* \times (\underline{n} \times \underline{h}) \, dS'$.

Since poles are the only singularities in the s-plane of the inverse operator the Mittag-Leffler theorem can be invoked to find an explicit representation of this inverse operator in terms of the natural frequencies, the nontrivial solutions of the homogeneous integral equation and the nontrivial solutions of the homogeneous adjoint integral equation,

$$\left[\tfrac{1}{2}\underline{\underline{I}} - \underline{\underline{L}}(s)\right]^{-1} = \sum_n \left\{ (s - s_n)^{-1} \left[<\underline{\underline{B}}_n \cdot \underline{j}_n, \underline{h}_n> \right]^{-1} \underline{j}_n \underline{h}_n^* + \underline{\underline{E}}_n(s) \right\} \quad (3)$$

where $\underline{\underline{B}}_n = (d\underline{\underline{L}}/ds)(s_n)$ and $\underline{\underline{E}}_n(s)$ is an entire operator-valued function of s. In deriving (3) it has been assumed that all poles are simple poles. This assumption has been substantiated numerically for all perfectly conducting, finite, bodies investigated so far. From the representation (3) of the inverse operator, it can be seen that many transient scattering and antenna problems involving finite bodies can be treated by employing the same methods as those used in transient network theory.

A procedure for calculating the natural frequencies and the current distribution of the natural modes of a perfectly conducting body of revolution is presented. The analysis is based on the magnetic-field integral equation simplified to account for rotational

ymmetry. This procedure is used in a numerical sample calculation
f certain natural frequencies and modes of a prolate spheroid.
ɔ get some idea of the number of natural modes needed to accurately
ɛscribe an actual scattering situation the time response is
ɑlculated of the induced current on a prolate spheroid due to
 step-function incident plane wave as a function of the number
f modes used in the series expansion of the inverse operator,

$$\underline{J}(\underline{r},t) = \sum_{n} cs_n^{-1} a_n(t) \left[<\underline{B}_n \cdot \underline{j}_n, \underline{h}_n > \right]^{-1} \underline{j}_n \exp(s_n t),$$

$$a_n(t) = \int_{S'} \underline{j}_o(\underline{r}') \cdot \underline{h}_n(\underline{r}') \exp(-s_n \hat{e} \cdot \underline{r}'/c) dS', \qquad (4)$$

$$S' = S'(\underline{r},t) = \{\underline{r}' : \underline{r}' \in S \quad \text{and} \quad |\underline{r} - \underline{r}'| + \hat{e} \cdot \underline{r}' < ct\}.$$

ɛre, ê is the direction of propagation of the incident wave and
ɔ = $\underline{n} \times \underline{H}_o$ where $\underline{H}_o$ is the strength of the incident plane wave.

ɔattering from a perfectly conducting, finite body located within
 parallel-plate region is also considered. A series representation
f the kernel of the integral equation (1), valid on the imaginary
ɑxis of the complex s-plane, can be constructed from image theory.
ɪ analytic continuation into the entire complex frequency plane
f this series representation is then found. It can be shown that
ɪis analytic continuation is an analytic function except along a
ɔuntable number of branch cuts C_n,

$$C_n = \{s : \text{Re}\{s\} = n\pi c/d, \text{Im}\{s\} < 0, n = 0, \pm 1, \pm 2, \ldots\}, \qquad (5)$$

being the separation between the parallel plates. It now follows
ɪat the solution of the integral equation has two types of
ɪngularities in the complex s-plane: one type being poles at
ɪose values of s for which the homogeneous integral equation has
ɔntrivial solutions, the other type being the branch cuts C_n. The
ɔcations of these branch cuts are uniquely determined by the plate
ɛparation.

    Transient electromagnetic problems involving open, uniform
ɑveguides can be treated using methods similar to those discussed
ɔove. The pulse response of a source sheet perpendicular to the
ɕis of the waveguide has the following form

$$F(x,y,z,t) = \frac{1}{2\pi i} \int_{\Gamma} H(x,y,p) I_o(p\tau) dp , \quad ct > z \qquad (6)$$

ɪere $I_o(x)$ is the modified Bessel function of order zero, $\tau^2 = (ct)^2 - z^2$
ɪd Γ is the Bromwich contour. The function $H(x,y,p)$ has two types

of singularities: (1) a branch point at p = 0, and (2) poles in
the left half-plane. The complex integral in (6) can be transformed
into a real-valued integral and a sum of residues. The integral
corresponds to the continuous spectrum and the sum to the discrete
spectrum of F(x,y,z,t). The discrete part of the spectrum can be
interpreted as modes. One of the modes is the TEM mode. The propa-
gation constants of all the other modes are complex, i.e., each
mode is attenuated as it propagates, and they grow exponentially
in the transverse direction of the waveguide. It should be noted
that H(x,y,p) is a meromorphic function of p for a closed waveguide
and that in this case all poles of H(x,y,p) are located on the
imaginary axis. The complex variable p is related to the complex
frequency s by $p = \sqrt{s^2/c^2 - \zeta^2}$ where ζ is the Laplace transform
variable with respect to the axial direction.

APPLICATION OF SINGULARITY EXPANSION METHOD TO THE LOOP ANTENNA

K.R. Umashankar and D.R. Wilton
University of Mississippi
University, Mississippi 38677

R.F. Blackburn
Air Force Weapons Laboratory
Albuquerque, New Mexico 87118

The Singularity Expansion Method (SEM) introduced by Baum [1] has demonstrated its utility in the calculation of the transient response of a thin linear cylindrical wire [2]. Another thin-wire problem of interest is the cylindrical wire loop, for which the time-harmonic solution for the loop current can be written in Fourier series form as [3]

$$I(\phi,s) = \sum_{n=-\infty}^{\infty} \frac{V_n(s)}{a_n(s)} e^{jn\phi}. \tag{1}$$

For convenience, the form above is written in terms of the Laplace transform variable $s = jck$ where c is the speed of light and k is the free space wavenumber. $V_n(s)$ is related to the excitation and is called the coupling coefficient in the terminology of SEM. The zeros of $a_n(s)$ are poles of $I(\phi,s)$ and are the natural resonant frequencies of the loop. For each zero of $a_n(s)$ with fixed n, the associated modal current is $e^{jn\phi}$.

The expression for $a_n(s)$ involves integrals of Anger-Weber functions of complex arguments and a parametric study of the roots of $a_n(s)$ has been carried out using a numerical search procedure. The roots, of course satisfy the requirement that they should appear only in the left half of the s-plane and in complex conjugate pairs. In addition, the location of each root of $a_n(s) = a_{-n}(s)$ falls into one of the following three categories:

1) There is a pole very near the $s=j\omega$ axis at approximately $\omega=n$. This pole gives the principal contribution to the time-domain response of the loop at late times and the imaginary part of the pole location corresponds closely to the resonant frequency of the loop for an excitation of the form $e^{jn\phi}$.

2) There are n+1 poles (including conjugate pairs) which lie roughly on the left hand side of an ellipse centered at $s=0$ and with a semimajor axis somewhat larger than n.

3) There is a layer of poles lying almost parallel to the $s=j\omega$ axis. The layer contains an infinite number of poles and they are spaced approximately $\Delta\omega=\pi c/b$ units apart, where b is the loop radius.

This categorization suggests the double indexing system shown in the figures for labeling the various poles. As with thin cylindrical wires, increasing the wire radius has the effect of shifting the poles nearest the $j\omega$ axis away from axis, or equivalently, increasing the damping constants of those modes in the time domain [2].

An asymptotic form of $a_n(s)$ valid in the complex s-plane for large s has been derived which allows one to find poles approximately as solutions to the equation

$$kb = \frac{\pi}{8} + \frac{j}{2} \ln \left\{ (-1)^n \sqrt{\frac{kb}{\pi}} [2 \ln \frac{2b}{a} - 2\gamma - 2 \ln kb - j\pi] \right\} \quad (2)$$

with $k=-js/c$ and where a is the wire radius. We are also able to show that $1/a_n(s)$ may be expanded in the convergent residue series

$$\frac{1}{a_n(s)} = \sum_i \frac{R_{ni}}{s-s_{ni}} \quad (3)$$

where the poles of $a_n(s)$ are at $s=s_{ni}$ and have residues R_{ni} given by

$$R_{ni} = \lim_{s \to s_{ni}} \frac{(s-s_{ni})}{a_n(s)} = \left[\frac{da_n}{ds} \right]^{-1} \bigg|_{s=s_{ni}} \quad (4)$$

An important result is that the function $1/a_n(s)$ may thus be represented by its poles and residues with no additonal entire function required. An asymptotic form for the residues in (4) can also be derived which can be used to show that Eq. (3) is rather poorly convergent and hence is not a useful representation in the frequency domain.

Substituting (3) into (1) and inverse transforming the equation results in the time domain representation,

$$i(\phi,t) = \sum_{n=-\infty}^{\infty} (\sum_i R_{ni} e^{s_{ni}t}) * v_n(t) e^{jn\phi} \quad (5)$$

where $v_n(t)$ is the Laplace inverse of $V_n(s)$ and the asterisk denotes convolution. Despite the fact that (3) converges slowly, the time domain current representation (5) converges relatively quickly, particularly for late times.

A large number of pole locations $s=s_{ni}$ and corresponding residues R_{ni} have been calculated and tabulated for a wide range of the loop parameter $\Omega=2\ln 2\pi b/a$. These results permit one to calculate time-domain loop currents for arbitrary excitation without resorting to the comparatively inefficient process of Fourier transforming.

References

1. C.E. Baum (1972 Spring URSI Meeting, Washington, D.C.)
2. F.M. Tesche (1973 IEEE Trans. Ant. and Prop. 1, pp. 53-62)
3. R.E. Collin and F.J. Zucker, Ed. (1969, Antenna Theory, Pt. I, McGraw-Hill, N.Y.)
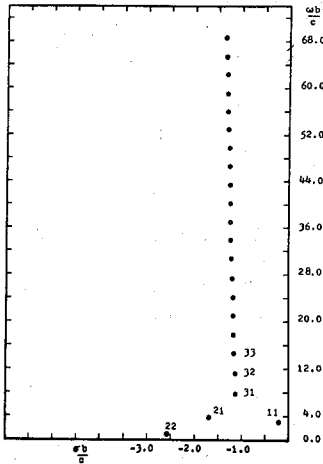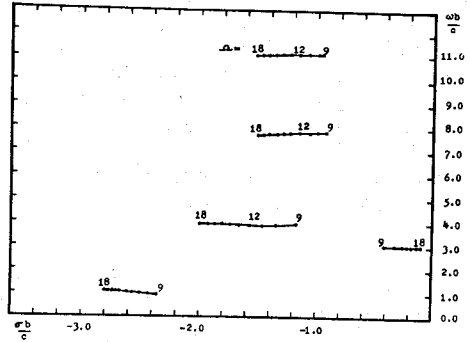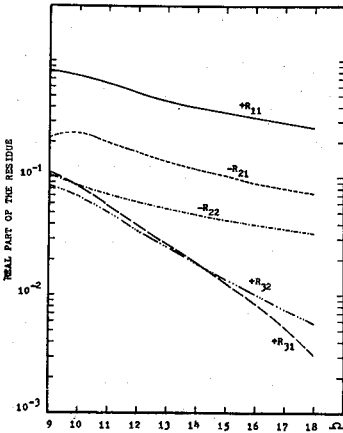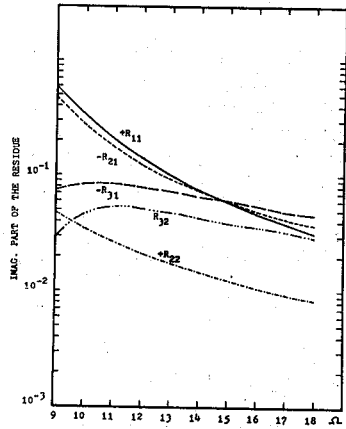
Fig. 1.   (a) Pole locations for a_3 mode in $s = \sigma + j\omega$ plane, (b) Trajectories of the poles for a_3 mode as $\Omega = 2\ell n(2\pi \frac{b}{a})$ varies, (c) Real part of the residues of a_3 mode, (d) Imag. part of the residues of a_3 mode.
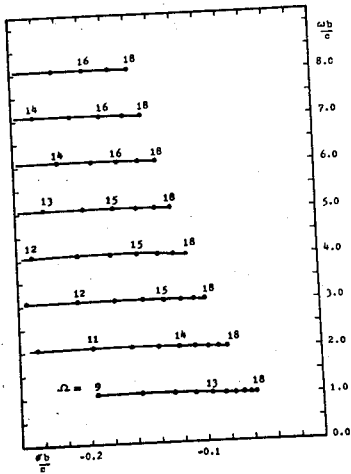
Fig. 2. Trajectories of the poles closest to the $j\omega$- axis for various modes $a_1, a_2 \ldots \ldots a_8$ as Ω varies.
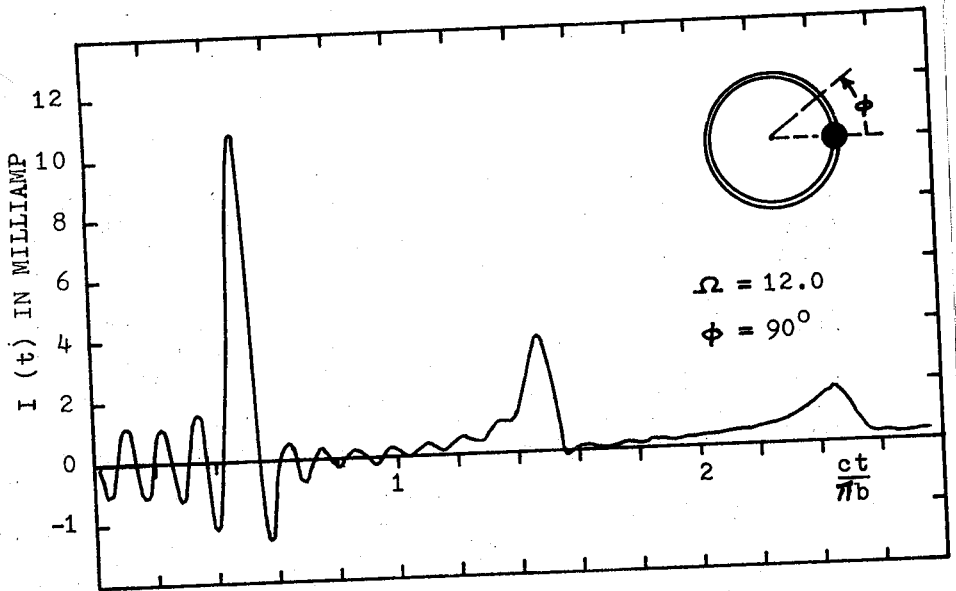
Fig. 3. Time domain current for cylindrical wire loop antenna at $\phi = 90°$ with delta function input, turned on at $t = 0, \phi = 0°$.

473

Session 53   Singularity Expansion Method

$$(\omega')^2 = \omega^2 - \frac{K^2 R^2 \omega^2}{4} - \gamma K R \omega \quad , \tag{9}$$

and

$$\gamma' = \gamma + \frac{K R \omega}{2} \quad . \tag{10}$$

The value of K can be computed from Eq. (4) or approximately from the antenna static capacitance C_0 by

$$K \simeq \frac{C_0 \, (\gamma^2 + \omega^2)}{\omega} \quad . \tag{11}$$

As an example, consider now a dipole antenna with a ratio of half-length to radius equal to 259 and a gap half-width to radius ratio equal to ten. For $\ell/a = 259$, $A = 0.8272 \times 10^{-5}$ mhos, $B = 6.7165 \times 10^{-4}$ mhos, the pole is specified by

$$\omega = \frac{2.961 \, c}{2\ell} \quad \sec^{-1} \quad , \tag{12}$$

and

$$\gamma = \frac{.216 \, c}{2\ell} \quad \sec^{-1} \quad , \tag{13}$$

where c is the speed of light in free space.

In Fig. 1, the normalized current response through a 75 ohm resistor is presented as a function of normalized time. The solid curve is the response due to the first five poles, and the curve composed of short dashes is the response due to the first pole. The curve composed of short and long dashes is the response calculated by the application of the King-Middleton and Wu theories.[4] This curve is shown to permit a comparison between it and those computed by the SEM.

The singularity expansion method provides a simple analytical means to perform an analysis of the cylindrical dipole antenna response to an electromagnetic pulse. For broadside incidence, the response can be accurately calculated for $t > 6\ell/c$ by only two or three poles.[2] As shown in Fig. 1, a calculation involving five singularities gives good agreement with that computed from classical antenna theory. Also, as shown in Fig. 1, the response due to the first pole consisting of two damped sinusoid is a reasonable estimate of the other two response curves.
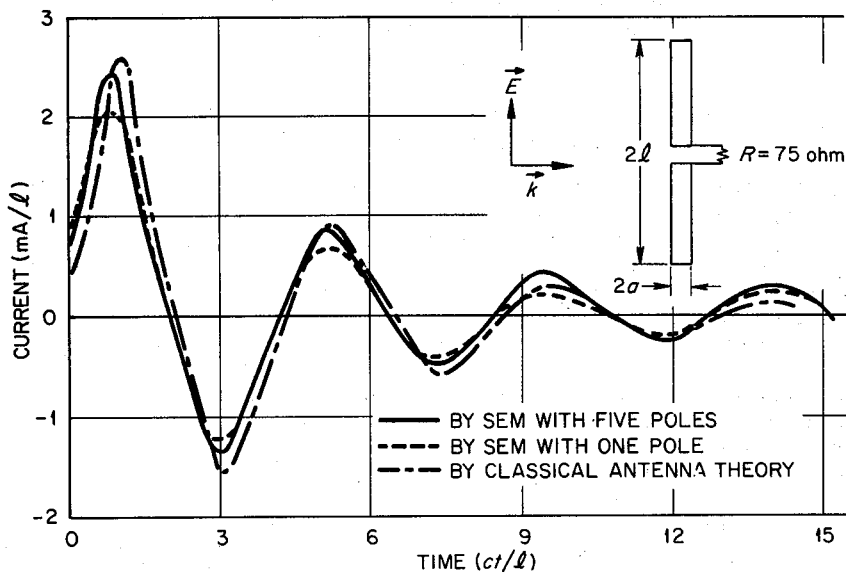
Fig. 1.   The Normalized Current Through a 75 ohm Resistive Load Connected to a Cylindrical Dipole Antenna Excited by a Unit Step Function Plane Wave Pulse.

REFERENCES

1. C. E. Baum (AFWL EMP Interaction Note 88, December 1971).

2. F. M. Tesche (AFWL EMP Interaction Note 102, April 1972).

3. S. W. Lee and B. Leung (AFWL EMP Interaction Note 96, February 1972).

4. D. B. Nelson (Oak Ridge National Laboratory TM-2830, July 1971).

Session 53 Singularity Expansion Method

APPLYING THE SINGULARITY EXPANSION
METHOD TO DETERMINE CURRENT AND
CHARGE INDUCED ON INTERSECTING
THIN CYLINDERS*

T. T. Crow, B. D. Graves and C. D. Taylor
Mississippi State University

Recently Baum developed the singularity expansion method (SEM) for treating general scattering problems.[1] Using the SEM one can determine directly the natural or resonant frequencies of a conducting scattering object and the current distributions associated with these resonances. The time domain response of the induced currents appears simply as a summation of exponentially damped sinusoids, the amplitude of each being determined in a straight-forward manner.

The starting point for the subject study is the Pocklington-type integro-differential equation for the current distribution induced on a structure of intersecting thin cylinders that are solid conductors with flat end faces. However to derive the integro-differential equation certain considerations are made. They are: (1) an extended boundary condition is used, namely the axial component of the total electric field is required to vanish on the axis of the cylinders[2], (2) the cylinders are sufficiently thin that rotational symmetry of the surface current density obtains, (3) the axial currents on the cylinders satisfy the Kirchhoff circuit law at the intersections, (4) the rotational symmetry of the current densities prevails throughout the cylinder junction regions (this is an admittedly unphysical consideration but it obviates a detailed consideration of the probably complex charge flow in the junction region), (5) the leading terms in the quasistatic solution for the current and charge distributions on the cylinder end faces are used[2], and (6) in obtaining the contributions to the axial component of the total electric field on the axis of a cylinder from currents and charges on other cylinders, the electric field from current filaments are used. Accordingly the following integro-differential is obtained for the complex frequency $s = \sigma + j\omega$ and a system of N wires:

$$s\ 4\pi\varepsilon_0 \left[E_s^{inc}(s_n) - E_c(s_n) \right]$$

$$= \sum_{m=1}^{N} \int_{L_m} I_m(s_m') \left[\frac{\partial^2}{\partial s_n \partial s_m'} + \frac{s^2}{c^2}\ (\hat{s}_m' \cdot \hat{s}_n) \right] G(s_n, s_m') ds_m' \tag{1}$$

where

$$G = \exp\left[-\frac{s}{c}\sqrt{(s_n - s_m')^2 + a_n^2 \delta_{nm}} \right] \Big/ \sqrt{(s_n - s_m')^2 + a_n^2 \delta_{nm}} \qquad n = m$$

$$G = \exp\left[-\frac{s}{c}\sqrt{s_n^2 + s_m'^2} \right] \Big/ \sqrt{s_n^2 + s_m'^2} \qquad n \neq m$$

Here $I_m(s_m')$ is the axial current on the mth wire at point s_m', $E_c(s_n)$ is the contribution to the axial component of the electric field from the end cap currents and charges and $E_s^{inc}(s_n)$ is the axial component of the incident electric field.

To apply the SEM, (1) is cast into matrix form by using the method of moments.[1] If a sinusoidal pulse expansion is used for the current distribution then all the integrals may be evaluated analytically. Thus (1) reduces to

$$\overline{\overline{\Pi}}(s)\ \overline{I}(s)\ =\ \overline{E}(s) \tag{2}$$

where the double bar indicates a square matrix and the single bar a column matrix.

At the natural frequencies, denoted by s_α, the determinant of $\overline{\overline{\Pi}}(s)$ must be zero and

$$\overline{\overline{\Pi}}(s_\alpha)\ \overrightarrow{I}(s_\alpha)\ =\ \overline{0} \tag{3}$$

In (3), $\overline{I}(s_\alpha)$ is defined as the mode vector and

$$\overline{\overline{\Pi}}^t(s_\alpha)\ \overline{C}(s_\alpha)\ =\ \overline{0}$$

defines the coupling vector. With the appropriate normalization the time history of the induced current is[1]

$$\overline{i}(t)\ =\ \sum_\alpha \overline{\overline{U}}(t)\ \overline{I}(s_\alpha)\ \overline{C}(s_\alpha)^t\ \overline{E}^{inc}(s_\alpha)\ e^{s_\alpha t} \tag{4}$$

where $\overline{\overline{U}}(t)$ is a diagonal matrix with Heaviside functions along the main diagonal to take into account causality and $\overline{E}^{inc}(s_\alpha)$ is the Laplace transform of the incident pulse. An expression analogous to (4) may be derived for the induced charge distribution via the equation of continuity.

The natural frequencies may be identified with the simple pole singularities of the Laplace transform of the induced current distribution for impulse excitation. The number of poles (or natural modes) necessary to obtain a typical time response of the current is shown in figure 1. In figure 2 the time histories of the junction currents are shown. For both figures the incident electric field is directed parallel to the y axis.

REFERENCES

1. F. M. Tesche (1973 IEEE G-AP, 21, p. 53).
2. C. D. Taylor and D. R. Wilton (1972 IEEE G-AP, 20, p. 772).

Session 53   Singularity Expansion Method
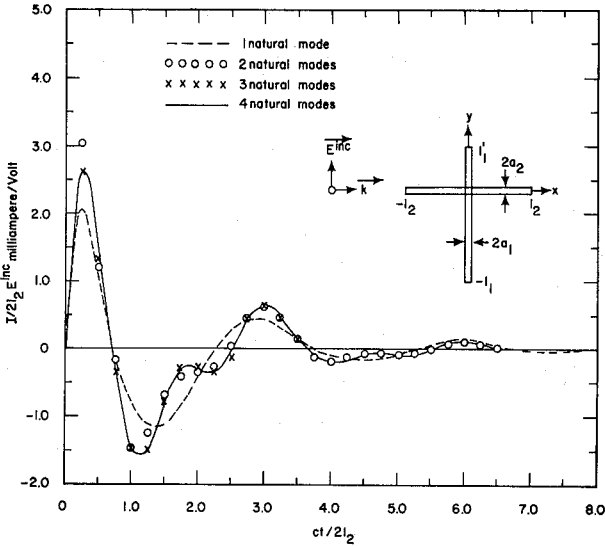
Figure 1. Current at $y=0^+$ for $\ell_1'/\ell_1=0.5$, $2\ell_2/(\ell_1'+\ell_1)=1.0$, $2\ell_2/a_2=20$, $a_1=a_2$
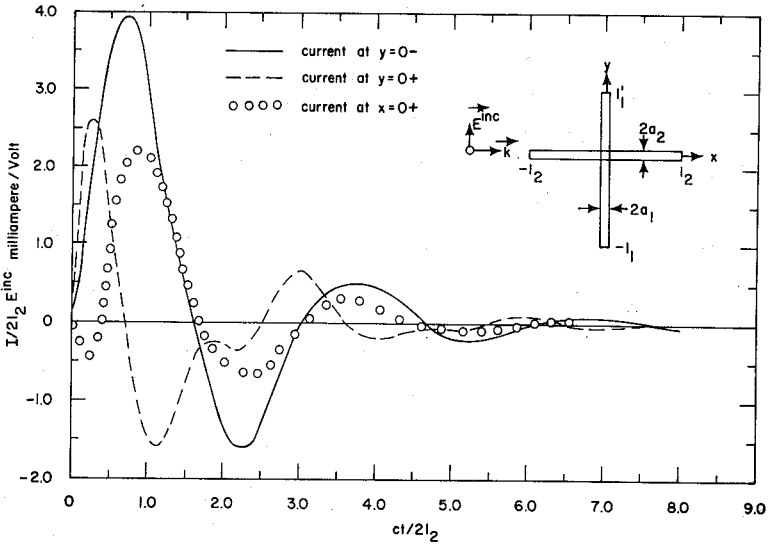
Figure 2. Junction currents for $\ell_1'/\ell_1=0.5$, $2\ell_2/(\ell_1'+\ell_1)=1.0$, $2\ell_2/a_2=20$, $a_1=a_2$, four natural modes.

TRANSIENT RESPONSE OF A THIN-WIRE SCATTERER ARBITRARILY ORIENTED ABOVE A PERFECTLY CONDUCTING GROUND PLANE USING THE SINGULARITY EXPANSION METHOD*

Thomas H. Shumpert
Applied Research Group
The Dikewood Corporation
Albuquerque, New Mexico 87106

ABSTRACT

The singularity expansion method is employed to determine
the transient response of a thin-wire scatterer arbitrarily
oriented above an infinite perfectly conducting ground plane.
An integro-differential equation is formulated for the current
on the scatterer in terms of the complex frequency, $s = \sigma + j\omega$.
The method of moments is used to reduce this integro-differential
equation to a system of linear algebraic equations. The singu-
larity expansion method is then applied to determine the
exterior natural resonances and the transient response of the
scatterer to a unit step incident wave. The analytical and
numerical techniques used to obtain the various terms in the
singularity expansion representation of the transient response
are discussed, and results are presented for several different
orientations of the scatterer with respect to the ground plane.

INTRODUCTION

The singularity expansion method as formalized by Baum [1]
offers a new approach to the transient analysis of scattering
and antenna problems. In a recent paper, Tesche [2] presented
a discussion of the method and applied the general concepts to
analyze the transient response of a thin wire scatterer in free
space. The purpose of this paper is to gain new and additional
insight into the singularity expansion method and its application
to more complicated scattering geometries. In particular,
analytical and numerical techniques similar to those presented
by Tesche [2] are used to determine the transient response of
a thin wire scatterer arbitrarily oriented above a perfectly
conducting ground plane. The transient response of the scatterer

---

481

as determined using the singularity expansion method is com-
pared with that obtained using a classical approach (i.e., plane
wave analysis with Fourier inversion). Various terms in the
singularity expansion representation are calculated and tabu-
lated for several different orientations of the scatterer with
respect to the ground plane, and locations of the exterior nat-
ural resonances as a function of the scatterer orientation are
also presented.

ANALYSIS

Consider the thin-wire scatterer oriented above a perfectly con-
ducting ground plane as shown in Figure 1. A Pocklington type
integro-differential equation for the current induced on the
scatterer by an incident field may be written in terms of some
complex frequency, $s = \sigma + j\omega$. The method of moments may
be used to reduce this integro-differential equation to a system
of linear algebraic equations. In this particular analysis, the
basis functions are piecewise constants (flat pulses) and the
testing functions are Dirac delta functions (collocation). The
resulting matrix equation is then solved using the singularity
expansion method.

A numerical search routine is used to locate the natural reson-
ances (singularities, zeroes) of the impedance matrix. The
natural mode vectors, normalization factors, residue matrices,
and coupling coefficients are calculated in the same manner as
outlined by Tesche [2]. Finally, the transient response is
determined as a weighted sum of damped sinusoids.

RESULTS

A general computer program has been developed for arbitrary
orientations of the scatterer above the plane. Two cases of
particular interest are: (a) Scatterer parallel to the ground
plane, and (b) Scatterer perpendicular to the ground plane.
Figure 2 is a plot of the singularities in the region near the
origin of the sL/c plane for case (a) with $h/L = 0.5$. These
singularities separate into two distinct groups. Those which
lie in the vertical layer nearest the imaginary axis represent
resonances associated with the fundamental length of the
scatterer itself. Those farther out in the plane represent
resonances associated with the distance between the scatterer
and its image. Figure 3 illustrates the movement of this second
group of singularities as a function of the parameter h/L. The
trajectories of the first group are quite different. Figure 4 pre-
sents the trajectory of the singularity associated with the funda-
mental resonance of the scatterer itself as a function of h/L.

Figure 5 shows the trajectories of this same singularity as the center of the scatterer is fixed at a constant distance above the plane and the scatterer is rotated from case (a) to case (b). Finally, Figures 6 and 7 show typical time domain results for case (b) where h/L = 1.0.

REFERENCES

1.   C. E. Baum (1972 Spring URSI Meeting, Washington, D. C.).

2.   F. M. Tesche (IEEE Trans. A. P., Jan. 1973, pp. 53-62).

Figure 1. Thin-wire scatterer arbitrarily oriented above a perfectly conducting ground plane.
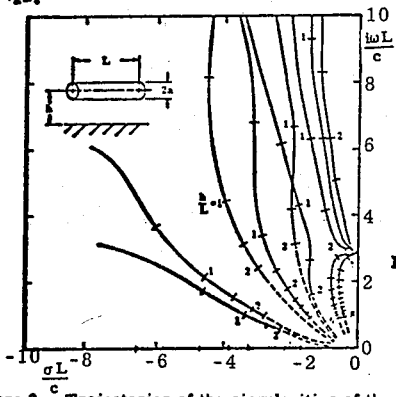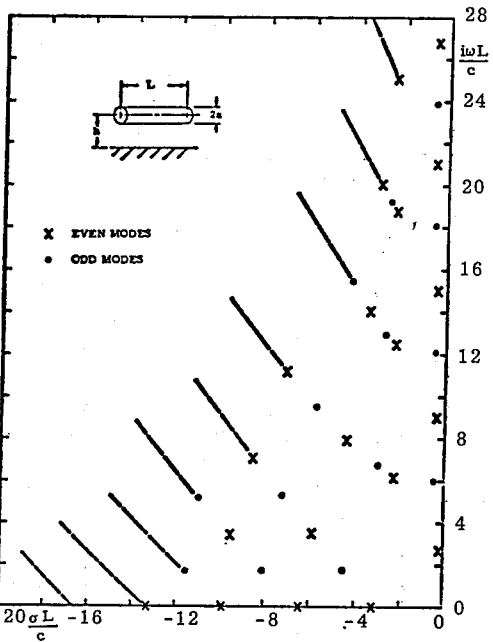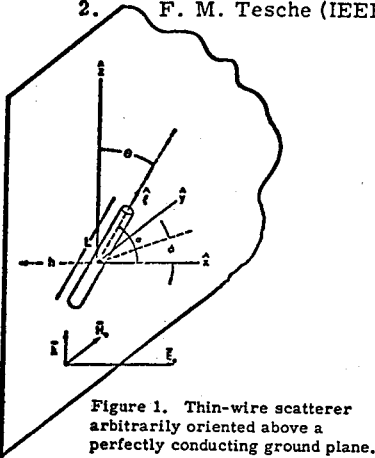
Figure 2. Singularities of a thin-wire scatterer parallel to a perfectly conducting ground plane ($\frac{h}{L}$ = 0.5, ϕ = 0°, θ = 0°, Ω = 10.6).

Figure 3. Trajectories of the singularities of the thin-wire scatterer parallel to the ground as a function of the relative distance from the ground (ϕ = 0°, θ = 0°, Ω = 10.6).

483
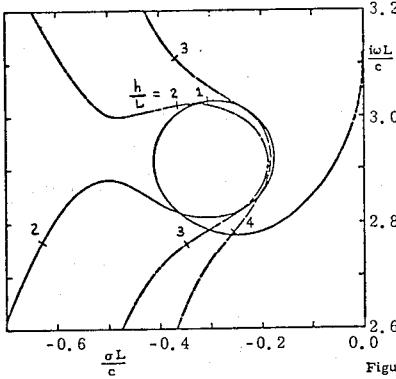
Figure 4. Trajectory of the singularity associated with the fundamental resonance of the scatterer itself ($\phi = 0^\circ$, $\theta = 0^\circ$, $\Omega = 10.6$).
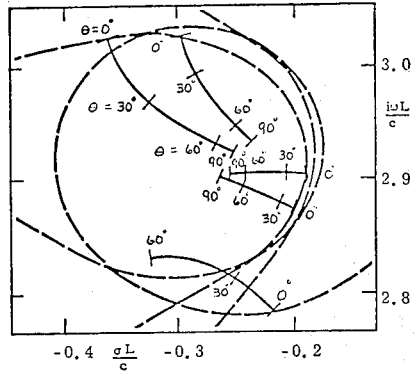
Figure 5. Trajectories of the singularity of Figure 4 as the scatterer is rotated with respect to the plane ($\phi = 0^\circ$, $\Omega = 10.6$).
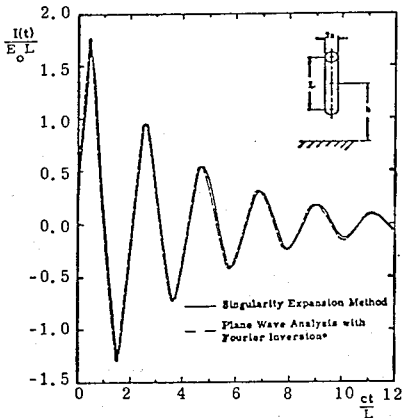
Figure 6. Time response of the current at the midpoint of the scatterer for case (b) (h/L = 1.0, $\phi = 0^\circ$, $\theta = 90^\circ$, $\Omega = 10.6$).
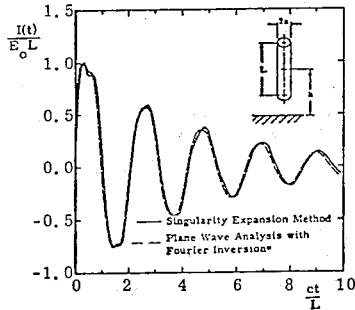
Figure 7. Time response of the current halfway between the midpoint and the end of the scatterer for case (b) (h/L = 1.0, $\phi = 0^\circ$, $\theta = 90^\circ$, $\Omega = 10.6$).

484

486

488

STEERING COMMITTEE
S. W. Maley, Chairman
R. L. Gallawa,
   Associate Chairman, G-AP
A. H. Shapley,
   Associate Chairman, URSI
J. R. Wait, Technical Program
A. Q. Howard, Finance
L. Lewin, Publicity
R. Cohen, Local Arrangements
L. N. Christiansen,
   Local Arrangements
H. Altschuler
D. C. Chang
W. L. Flock
R. C. Kirby
C. G. Little
R. H. Ott

Honorary Members
W. N. Hess
B. W. Birmingham
F. S. Barnes
J. M. Richardson

LOCAL ARRANGEMENTS
R. S. Cohen, Co-Chairman
L. N. Christiansen, Co-Chairman

FINANCE
A. Q. Howard, Chairman
R. G. Olson
T. N. Gautier

PUBLICATIONS
R. L. Gallawa, Chairman
R. L. Lewis
R. E. Munson

PUBLICITY
L. Lewin, Chairman
C. T. Johnk
R. J. Fisher
K. A. Skrivseth

INSTITUTIONAL LISTINGS
R. C. Kirby

TECHNICAL PROGRAM
J. R. Wait, Chairman
R. H. Ott, Associate Chairman
D. C. Chang, Associate Chairman
A. H. Barrett
D. E. Barrick
P. L. Bender
H. G. Booker
G. Birnbaum
N. M. Brice
R. Cohen
F. Einaudi
L. B. Felsen
J. Findlay
R. G. FitzGervell
J. Galejs (deceased)
G. Hagn
M. A. K. Hamid
D. A. Hill
A. Ishimaru
R. Johnson
I. Katz
J. Kelso
W. K. Klemperer
A. A. Ksienski
C. G. Little
J. W. Maley
R. Mittra
G. C. Reid
L. J. Ricardi
V. H. Rumsey
C. J. Sletton
C. T. Tai

HOSTS
University of Colorado
National Oceanic and Atmospheric
   Administration, United States
   Department of Commerce
Office of Telecommunications,
   United States Department of
   Commerce
National Bureau of Standards,
   United States Department of
   Commerce
Boulder-Denver Chapter, G-AP

WE'VE PUT IT ALL TOGETHER IN ATLANTA IN '74

1. 1974 INTERNATIONAL IEEE/G-AP SYMPOSIUM AND USNC/URSI MEETING

   DATES: IEEE/G-AP, 10-12 JUNE 1974
                           URSI, 11-13 JUNE 1974

   GENERAL CHAIRMAN: D. T. PARIS, SCHOOL OF ELECTRICAL ENGINEERING
                           GEORGIA TECH, ATLANTA, GEORGIA 30332
                           TEL. NO. (404)894-2902

2. 1974 INTERNATIONAL IEEE/G-MTT SYMPOSIUM

   DATES: 12-14 JUNE 1974

   GENERAL CHAIRMAN: G. P. RODRIGUE, SCHOOL OF ELECTRICAL ENGINEERING
                           GEORGIA TECH, ATLANTA, GEORGIA 30332
                           TEL. NO. (404)894-2944

3. TWELFTH SYMPOSIUM ON ELECTROMAGNETIC WINDOWS

   DATES: 12-14 JUNE 1974

   GENERAL CHAIRMAN: J. N. HARRIS
                           ENGINEERING EXPERIMENT STATION
                           GEORGIA TECH, ATLANTA, GEORGIA 30332
                           TEL. NO. (404)894-3665

Outline Map of Boulder, Colorado

1 BUS STATION
2 HIGH ALTITUDE OBSERVATORY
3 JILA
4 MEMORIAL CENTER
5 N·CAR
6 POST OFFICE

U.S DEPT OF COMMERCE, BOULDER LABORATORIES
NBS & NOAA

7 RADIO BUILDING
8 CRYOGENIC LABORATORY
9 LIQUEFACTION PLANT
10 PLASMA PHYSICS LAB
11 NOAA

HOUSING
12 HARVEST HOUSE
13 BOULDERADO HOTEL
14 KITTREDGE RESIDENCE HALLS
15 WILLIAMS VILLAGE (UNIV. OF COLO.)
    MOTEL AREAS
    SHOPPING CENTERS
    STATE HIGHWAYS
16 HOLIDAY INN